Synthesis, Oxidation and Electrophilic Functionalization of E_N Ligand Complexes under Weakly Coordinating Conditions

Dissertation

zur Erlangung des
Doktorgrades der Naturwissenschaften

Dr. rer. nat.

am Institut für Anorganische Chemie
der Fakultät für Chemie und Pharmazie
der Universität Regensburg

vorgelegt von

Luis Dütsch

aus Neumarkt i. d. OPf.

im Jahr 2021

Das Promotionsgesuch wurde eingereicht am: 20.12.2021

Tag der mündlichen Prüfung: 11.03.2022

Vorsitzender:	Apl. Prof. Dr. Rainer Müller
Prüfungsausschuss:	Prof. Dr. Manfred Scheer
	Prof. Dr. Henri Brunner
	Prof. Dr. Frank-Michael Matysik

Diese Arbeit wurde angeleitet von: Prof. Dr. Manfred Scheer.

Universität Regensburg

Eidesstattliche Erklärung

Ich erkläre hiermit an Eides statt, dass ich die vorliegende Arbeit ohne unzulässige Hilfe Dritter und ohne Benutzung anderer als der angegebenen Hilfsmittel angefertigt habe; die aus anderen Quellen direkt oder indirekt übernommenen Daten und Konzepte sind unter Angabe des Literaturzitats gekennzeichnet. Die Arbeit wurde bisher weder im In- noch im Ausland in gleicher oder ähnlicher Form einer anderen Prüfungsbehörde vorgelegt.

Luis Dütsch

This thesis was elaborated within the period from January 2016 until December 2021 in the Institute of Inorganic Chemistry at the University of Regensburg under the supervision of Prof. Dr. Manfred Scheer.

Parts of this work (*) as well as results from collaborations, which are not mentioned within this thesis, have already been published during the elaboration of this thesis.

List of Publications:

M. Fleischmann, L. Dütsch, M. Elsayed Moussa, G. Balázs, W. Kremer, Ch. Lescop, M. Scheer
"Self-assembly of reactive linear Cu_3 building blocks for supramolecular coordination chemistry and their reactivity towards E_n ligand complexes"
Inorg. Chem. **2016**, *55*, 2840-2854.

M. Elsayed Moussa, M. Fleischmann, E. V. Peresypkina, L. Dütsch, M. Seidl, G. Balázs, M. Scheer
"Strategies for the Construction of supramolecular dimers versus homoleptic 1D coordination polymers based on the diphosphorus complex $[Cp_2Mo_2(CO)_4(\eta^2\text{-}P_2)]$ and Ag^I salts"
Eur. J. Inorg. Chem. **2017**, 3222-3226.

* L. Dütsch, M. Fleischmann, S. Welsch, G. Balázs, W. Kremer, M. Scheer
"Dicationic E_4 Chains (E = P, As, Sb, Bi) Embedded in the Coordination Sphere of Transition Metals"
Angew. Chem. **2018**, *130*, 3311-3317.
Angew. Chem. Int. Ed. **2018**, *57*, 3256-3261.

M. Elsayed Moussa, S. Welsch, L. Dütsch, M. Piesch, S. Reichl, M. Seidl, M. Scheer
"The Triple-Decker Complex $[Cp^*Fe(\mu,\eta^{4:4}\text{-}P_5)Mo(CO)_3]$ as a building block in Coordination Chemistry"
Molecules **2019**, *24*, 325.

A. Straube, P. Coburger, L. Dütsch, E. Hey-Hawkins
"Triple the fun: tris(ferrocenyl)arene-based gold(I) complexes for redox-switchable catalysis"
Chem. Sci. **2020**, *11*, 10657-10668.

Ch. Riesinger, L. Dütsch, G. Balázs, M. Bodensteiner, M. Scheer
"Cationic Functionalization by Phosphenium Ion Insertion"
Chem. Eur. J. **2020**, *26*, 17166-17170.

N. Reinfandt, Ch. Schoo, L. Dütsch, R. Köppe, S. N. Konchenko, M. Scheer, P. W. Roesky
"Synthesis of unprecedented 4d/4f-polypnictogens"
Chem. Eur. J. **2021**, *27*, 3974-3978.

* L. Dütsch, C. Riesinger, G. Balázs, M. Scheer
"Synthesis of Tetrahedranes Containing the Unique Bridging Hetero-Dipnictogen Ligand EE' (E ≠ E' = P, As, Sb, Bi)"
Chem. Eur. J. **2021**, *27*, 8804-8810.

* L. Dütsch, C. Riesinger, M. Seidl, G. Balázs, M. Scheer
"Structural Diversity of Mixed Polypnictogen Complexes: Dicationic $E_2E'_2$ (E ≠ E' = P, As, Sb, Bi) Chains, Cycles and Cages"
Chem. Sci. **2021**, *12*, 14531-14539.

"It always seems impossible

until it´s done."

Nelson Mandela

To Lilly

and

My Parents

Preface

This thesis deals with the synthesis of new polypnictogen ligand (E_n ligand) complexes (chapter 3) as well as investigations of their reactivity towards one-electron oxidation agents (chapters 4–8) and main-group electrophiles (chapters 9 and 10), and their stabilization as well as characterization in solution and in the solid-state under weakly coordinating conditions. Chapter 11 contains the thesis treasury with separate results, which do not fit to the other chapters thematically.

Some of the presented results have already been published during the preparation of this thesis (*vide supra*). The corresponding citations are given at the beginning of the particular chapters.

Each chapter includes a list of authors. At the beginning of each chapter the individual contribution of each author is described. Additionally, if some of the presented results have already been partly discussed in other theses, it is stated at the beginning of the respective chapters.

To ensure uniform design of this work, all chapters are subdivided into 'Introduction', 'Results and Discussion', 'Conclusion', 'Supporting Information' and 'References'. Furthermore, all chapters have the same text settings and the compound numeration begins anew. In general, starting materials are assigned to capital letters (*e.g.* **A**), products to arabic numerals (*e.g.* **1**) and all others to roman numerals (*e.g.* **I**). Due to different requirements of the journals and different article types, the presentation of figures, *e.g.*, for single crystal X-ray structures or the 'Supporting Information', may differ.

In addition, a general 'Introduction' is given at the beginning and a comprehensive 'Conclusion' of all chapters is presented at the end of this thesis.

Table of Contents

1 INTRODUCTION

1.1 Phosphorus and the Heavy Pnictogens

"Inter inventa nostri seculi non minimum habendum est Phosphorus igneus …" ("Not least amongst the discoveries of our time is phosphorus igneus …").[2] This was written by the famous German philosopher, scientist and historian Gottfried Wilhelm Leibniz in 1710 showing that the element phosphorus is mesmerizing the scientific world since over 300 years. Elemental phosphorus was first discovered by the alchemist Hennig Brand in 1669 in Hamburg (Figure 1) when he boiled down more than 100 litres of his urine under exclusion of air and extracted a liquid, which irradiated green light and turned out as white phosphorus ("phosphoros (gr.) – light-bearer").[3] Interestingly, until the year 1867 this was the only way to synthesize white phosphorus. Brand felt certain that he made the "philosopher´s stone", which can turn non-precious metals into gold and gift everyone with infinite youthfulness. However, it only brought exitus to his dog, for which reason Brand declared phosphorus as the "Element of death".[3] In contrast, it can be regarded as "Element of life" as well, since it is an integral part of various essential functions in living beings such as bones, DNA and within the energy carrier ATP.[3] Apart from that, phosphorus also plays an important role in modern chemistry, *e.g.*, as (poly)phosphorus ligands in organometallic chemistry or within phosphanes, which serve as ligands in catalysts. Moreover, it is a key component of the research of our group, which deals with the reactivity of P_n ligand complexes (*vide infra*) and is also a central part of this thesis.

Figure 1: Hennig Brand and the discovery of white phosphorus.[1]

Phosphorus belongs to group 15 of the periodic table of elements, which is completed by its lighter homologue nitrogen and its heavier congeners arsenic, antimony, bismuth and the yet uncharacterized synthetic element moscovium (eka-bismuth).[4] These elements are also called "The Pnictogens", which derives from the Ancient Greek and can be translated as "causing suffocation" and is referred to the choking properties of nitrogen gas.[5] The pnictogens are of special interest since they differ very much in their properties with nitrogen and phosphorus being non-metals, while arsenic and antimony are metalloids and bismuth a pure metal. Furthermore, the heavier the pnictogens are the less abundant they are.[4b] However, polypnictogen ligand complexes (E_n ligand complexes) are also known with the heavy pnictogens arsenic, antimony and bismuth (*vide infra*).

1.2 Polypnictogen Ligand Complexes

Even today, most phosphorus or arsenic containing ligands in organometallic chemistry bear organic substituents and are of the types R_3E, $R_2E(CH)_2ER_2$ or $RC\{(CH_2)_nER_2\}_3$ (E = P, As; R = alkyl, aryl).[6] However, in the last 50 years, the class of substituent-free P_n and As_n ligands (polypnictogen ligands), in which the pnictogen atoms are only bound to each other and are coordinatively stabilized by organometallic fragments, has strongly evolved[6,7] and, furthermore, also been expanded to Sb_n and Bi_n ligand complexes. Since phosphorus is, on the one hand, isolobal to the {CH} fragment[8] and, on the other hand, associated with carbon through the diagonal relation, it is capable of catenation (formation of pure phosphorus chains, cycles and cages) and so are the heavier pnictogens arsenic, antimony and bismuth. However, while the structural diversity of P_n ligand complexes is particular high, the number of examples decreases by increasing the atomic number of the pnictogen. Interestingly, the first ever E_n ligand complexes reported, $[\{Co(CO)_2R\}_{4-n}As_n]$ (n = 2 (**I**), 3 (**II**); R = CO, PPh_3), bear As_2 or As_3 ligands, respectively, and were reported by *Dahl et. al.* in 1969 (Scheme 1).[9] Only two years later the first P_n ligand complexes, $[ClL_2Rh(\eta^2\text{-}P_4)]$ (L = PPh_3, $P(p\text{-}CH_3C_6H_4)_3$, $P(m\text{-}CH_3C_6H_4)_3$, $AsPh_3$; **III**), where a P_4 tetrahedron is coordinated side-on to a rhodium centre, were accomplished by the group of *Ginsberg*.[10] In the P_4 unit of the latter the coordinating P–P bond is broken leading to a dianionic P_4-butterfly unit.[11] The first coordination complex of an intact P_4 tetrahedron was realized by *Sacconi et. al.* in 1979, where the P_4 unit is coordinated to a nickel fragment in an η^1-fashion (**IV**).[12] Since then, the number of E_n ligand complexes increased

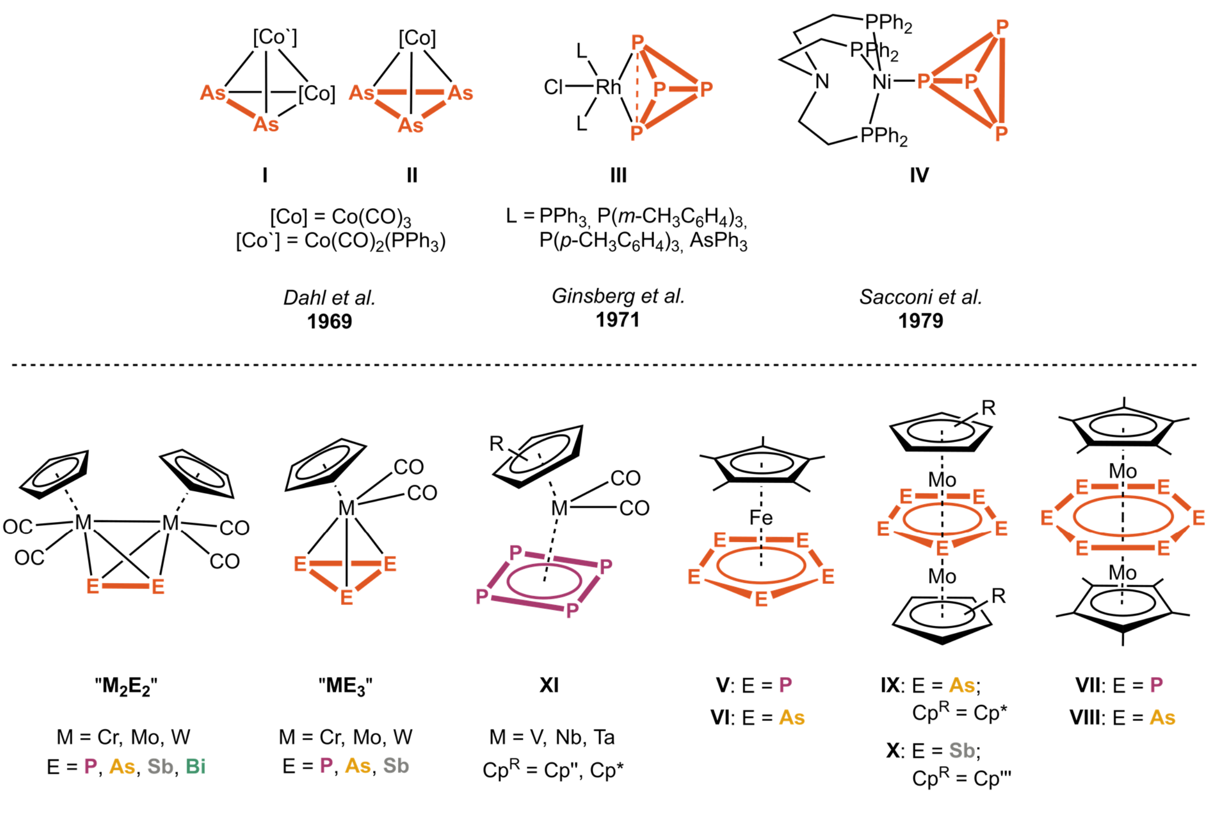

Scheme 1: top: the first E_n ligand complexes; bottom: overview of selected E_n ligand complexes with n = 2–6.

dramatically. To provide a small overview, selected examples for n = 2–6 are presented in the following (Scheme 1, bottom).

Of special interest are aromatic, cyclic E_4, E_5 and E_6 ligands, which are isolobal to organic cyclobutadienyl, cyclopentadienyl (Cp) and benzene ligands and, therefore, can be respected as milestones in organometallic chemistry since they build a bridge between organic chemistry with its endless structural diversity and the inorganic chemistry, which was first described by the Nobel prize winner *Roald Hoffmann*.[8] E_4, E_5 and E_6 ligand complexes are known with a variety of metal fragments mainly incorporating Cp ligands. Pioneering work in this area was accomplished by the group of *Scherer*, which reported first on the sandwich complexes [Cp*Fe(η^5-E_5)] (E = P (**V**), As (**VI**))[13] and the triple-decker complexes [{Cp*Mo}$_2$(μ,η^6:η^6-E_6)] (E = P (**VII**), As (**VIII**)).[14] In the latter, the *cyclo*-E_6 ligands serve as middle-decks bridging two [Cp*Mo] fragments, whereas in the former a *cyclo*-E_5 end-deck is present. However, *cyclo*-E_5 ligands can also act as middle-decks, *e.g.*, in [(Cp*Mo)(μ,η^5:η^5-As_5)] (**IX**).[15] The first and so far only known *cyclo*-Sb_5 ligand was synthesized by *Burford et. al.* in 2000, which is stabilized as a middle-deck within the triple-decker complex [{(Cp'''Mo)(Cp^{R}Mo)}(μ,η^5:η^5-Sb_5)] (**X**: Cp^R = Cp''', 1,4-^{t}Bu$_2$-2-MeC$_5$H$_2$).[16] In contrast, *cyclo*-E_4 ligands are very rare and mainly limited to phosphorus. Moreover, mononuclear *cyclo*-P_4 ligands are only known for group 5 metal complexes [Cp^{R}M(CO)$_2$(η^4-P_4)] (**XI**: M = V,[17] Nb,[18] Ta;[19] Cp^R = Cp*, Cp'') and within the cobalt complex [Cp'''Co(η^4-P_4)].[20] The only reported *cyclo*-E_4 complex of the heavier pnictogens is, to the best of our knowledge, the diiron complex [(LFe)$_2$(μ,η^4:η^4-As_4)] (L = β-diiminate) containing an *cyclo*-As_4 middle-deck.[21]

An interesting class of E_n ligand complexes containing di- and tripnictogen ligands (n = 2, 3) represent the tetrahedrane derivatives [{CpMo(CO)$_2$}$_2$(μ,η^2:η^2-E_2)] (E = P, As, Sb, Bi; "**Mo_2E_2**")[22] and [{CpMo(CO)$_2$}(η^3-E_3)] (E = P, As, Sb; "**MoE_3**"),[22a,23] which are formally derived from white phosphorus, P_4, and its heavier analogues by substituting one or two pnictogen atoms with the isolobal 15 valence-electron (VE) fragments [CpMo(CO)$_2$] (Scheme 1, bottom) and are also known with other group 6 metals (Cr, W) and different substituted Cp^R ligands (*e.g.*, Cp^R = Cp, Cp*, Cp', Cp'').[14a,22b,22d,23b,23c,24]

Besides the homo-dipnictogen ligand complexes **Mo_2E_2**, their respective representatives containing hetero-EE' ligands are known since 1998 when *Mays et. al.* synthesized the complexes

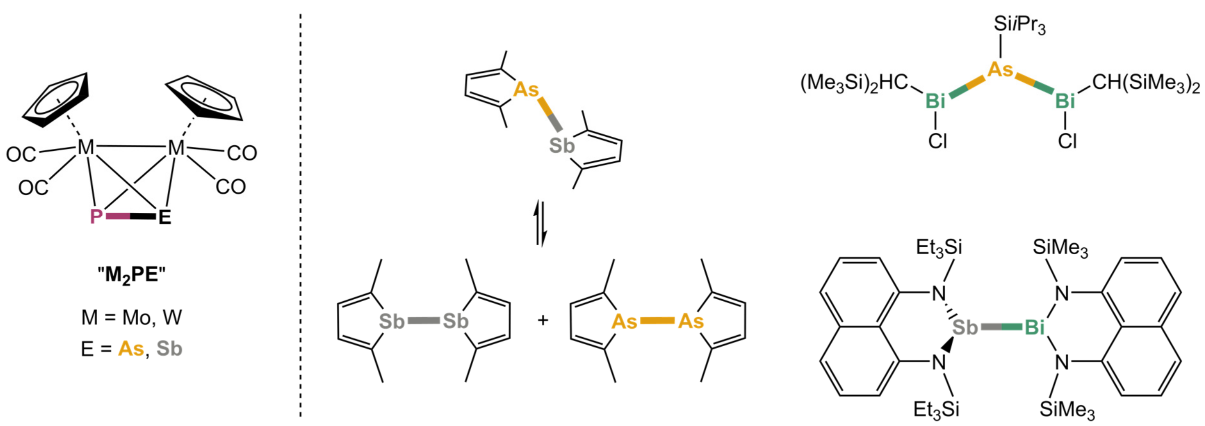

Scheme 2: left: tetrahedral transition metal complexes [{CpM(CO)$_2$}$_2$(μ,η^2:η^2-**PE**)] (M = Mo, W; E = As, Sb; "M_2PE") containing the hetero-dipnictogen ligands **PE** (E = As, Sb); right: selected examples of the rare class of hetero-dipnictogen complexes of the heavier pnictogens As, Sb and Bi.

[{CpM(CO)$_2$}$_2$(μ,η^2:η^2-PE)] (M = Mo, W; E = As, Sb; "**M$_2$PE**"; Scheme 2).[25] The class of hetero-polypnictogen complexes counts, however, only a small number of representatives, especially of the heavier pnictogens. For instance, only three compounds containing covalent As–Sb bonds were reported,[26] and for As–Bi as well Sb–Bi bonds, respectively, even only two examples are known (Scheme 2, right).[27] Furthermore, just half of these were characterized crystallographically. Between As and Sb, only single bonds were observed, whereas the other ones mentioned also form double bonds. However, all of them can only be stabilized by very bulky organic substituents or they have a distinct tendency to disproportionate and form homonuclear bonds (Scheme 2, right).[26a] Therefore, the synthesis of further hetero-polypnictogen complexes is of utmost interest and the tetrahedral complexes **M$_2$PE** represent good precursors for this purpose. However, their elaborate synthesis is low yielding due to many reaction steps and possible side reactions and, more important, does not offer the synthesis of the heavy congeners containing AsSb, AsBi and SbBi ligands.[25] Therefore, the question arose: Is it possible to develop a new and facile synthetic pathway, which eliminates those disadvantages and facilitates the generation of the heavy hetero-dipnictogen complexes? This topic will be discussed in chapter 3.

1.3 Cationic Polypnictogen Complexes

One of the main goals in fundamental research is the synthesis and exploration of new compounds as well as the formation of new bonds between elements with the goal to receive useful materials with interesting properties. In the last century, the number of carbon-based compounds virtually exploded and, subsequently, a multitude of applications were developed such as synthetic polymeric materials,

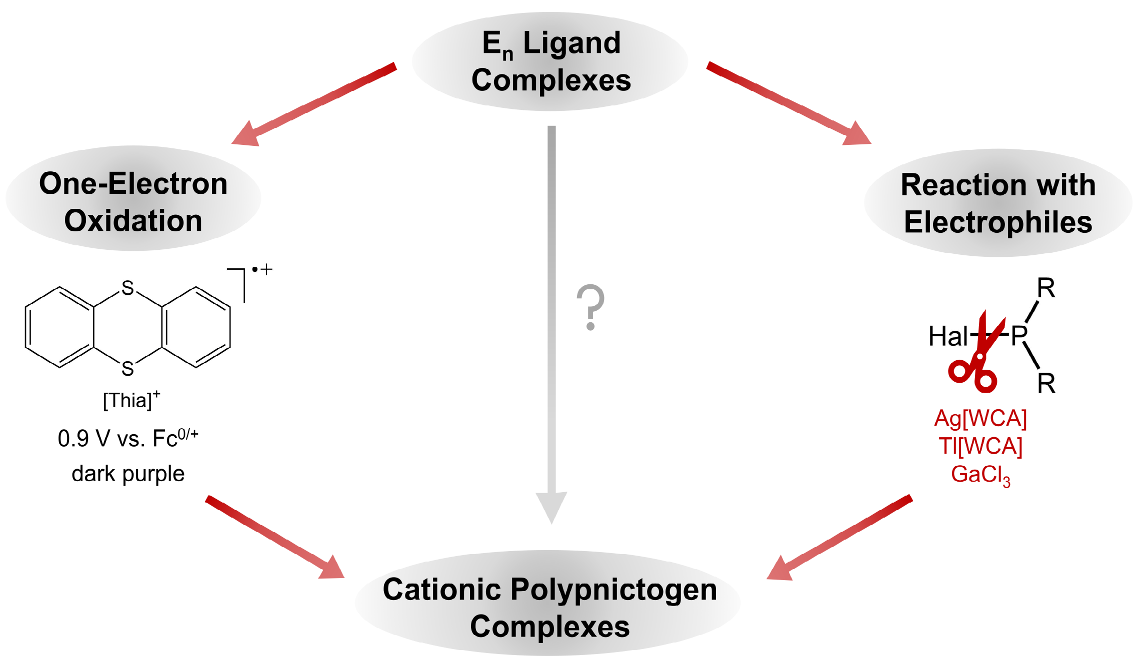

Figure 2: Two synthetic approaches for the synthesis of cationic polypnictogen complexes starting from E$_n$ ligand complexes. Left: Oxidation with strong one-electron oxidants such as thianthrenium ([Thia]$^+$); right: reaction with phosphenium ions R$_2$P$^+$ (R = organic substituent or halides), which are *in situ* generated from the respective halophosphines R$_2$PX (X = Cl, Br, I) *via* halide abstraction.

like polyethylene, polypropylene or polyesters. However, the field of (poly)pnictogen complexes is far less investigated. But, due to the diagonal relation of phosphorus and carbon, and the isolobality of the P atom and the {CH} fragment,[8] phosphorus and also the heavier pnictogen bear a huge potential of forming large chains, cycles and aggregates, and, hence, a big diversity of compounds. Therefore, our group focuses on the formation and reactivity of polypnictogen ligand complexes, which are free from organic substituents. Besides of neutral E_n ligand complexes (*vide supra*), ionic representatives are of interest, too, since they mostly differ in their reactivity as well as their properties. While the chemistry of anionic examples, mainly achieved by reduction[28] or the reactivity towards nucleophiles,[28c,29] is more and more better investigated, only few examples of cationic products are known. Thus, we have set ourselves the objectives to enlarge the area of cationic polypnictogen complexes. In order to achieve this, two main synthetic procedures have shown to be promising (Figure 2):

- Oxidation of (poly)pnictogen complexes
- Reaction of (poly)pnictogen complexes with electrophiles

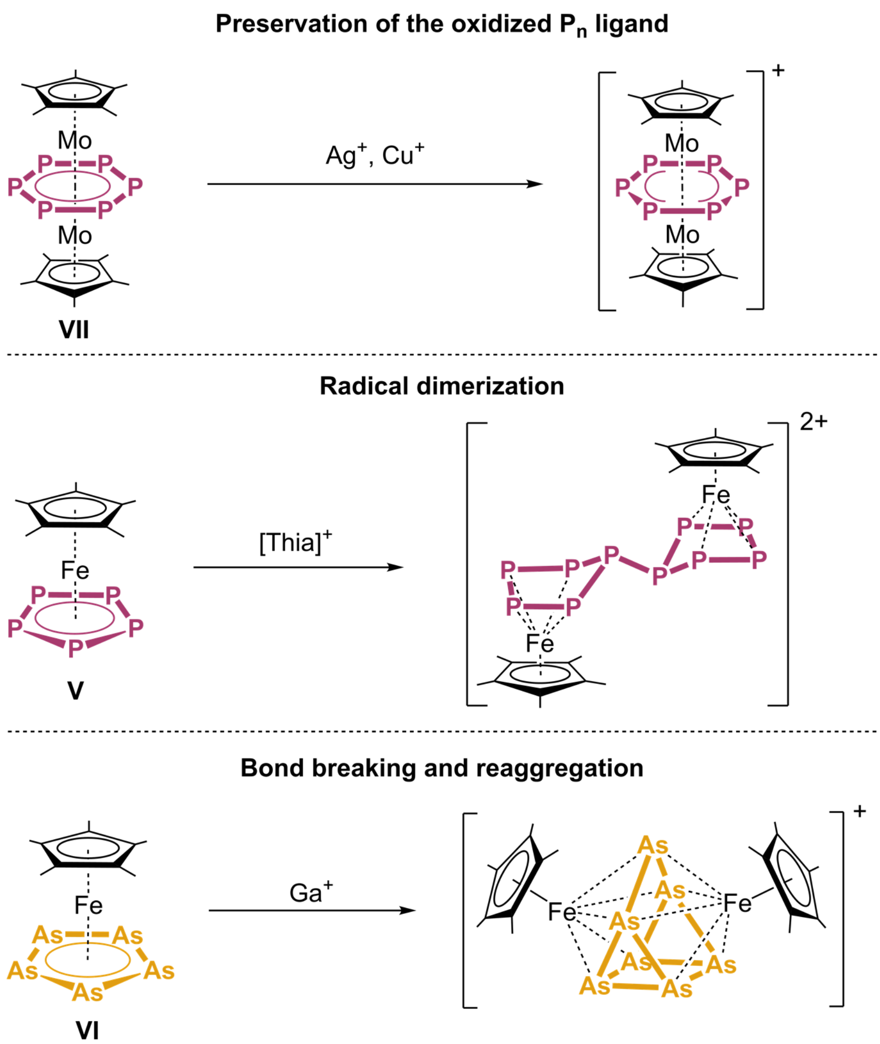

Scheme 3: Three different reactivities of E_n ligand complexes upon one-electron oxidation.

For example, we could show that polyphosphorus ligand complexes represent good starting materials for cationic polyphosphorus compounds upon oxidation. Thereby, three different reactivities could be observed (Scheme 3). On the one hand, reaction of the hexaphosphabenzene[14a] complex $[(Cp^*Mo)_2(\mu,\eta^6:\eta^6\text{-}P_6)]$ (**VII**) with one-electron oxidants such as Ag^+ or Cu^+, respectively, results in the preservation of the triple-decker geometry and a bis-allylic distortion of the P_6 ring.[30] On the other hand, oxidation of $[Cp^*Fe(\eta^5\text{-}P_5)]$ (**V**) with the strong one-electron oxidant thianthrenium ($[C_{12}H_8S_2]^+$ = $[Thia]^+$) leads to dimerization *via* P-P bond formation yielding a formally neutral, bicyclic P_{10} ligand stabilized by two $[Cp^*Fe]^+$ fragments.[28f,31] Finally, oxidation of the arsenic derivative of **V**, $[Cp^*Fe(\eta^5\text{-}As_5)]$ (**VI**), with Ga[TEF] leads to As–As bond breaking, reaggregation and the formation of an As_7 cage, which is stabilized by two [Cp*Fe] fragments.[32] However, in the latter it is not clarified if the oxidation is conducted by the Ga[TEF] or possible decomposition products such as Ga(III) species.

The field of electrophilic functionalization yielding cationic polyphosphorus compounds was pioneered by the groups of *N. Burford* and *J. J. Weigand*. They generated phosphenium ions *in situ* by halide abstraction of halophosphines, and subsequent reaction with additional phosphines led to cationic organosubstituted polyphosphorus chains, cycles and cages.[33] Thereby, typical halide abstracting agents are Ag(I) or Tl(I) salts as well as $GaCl_3$ or $AlCl_3$.

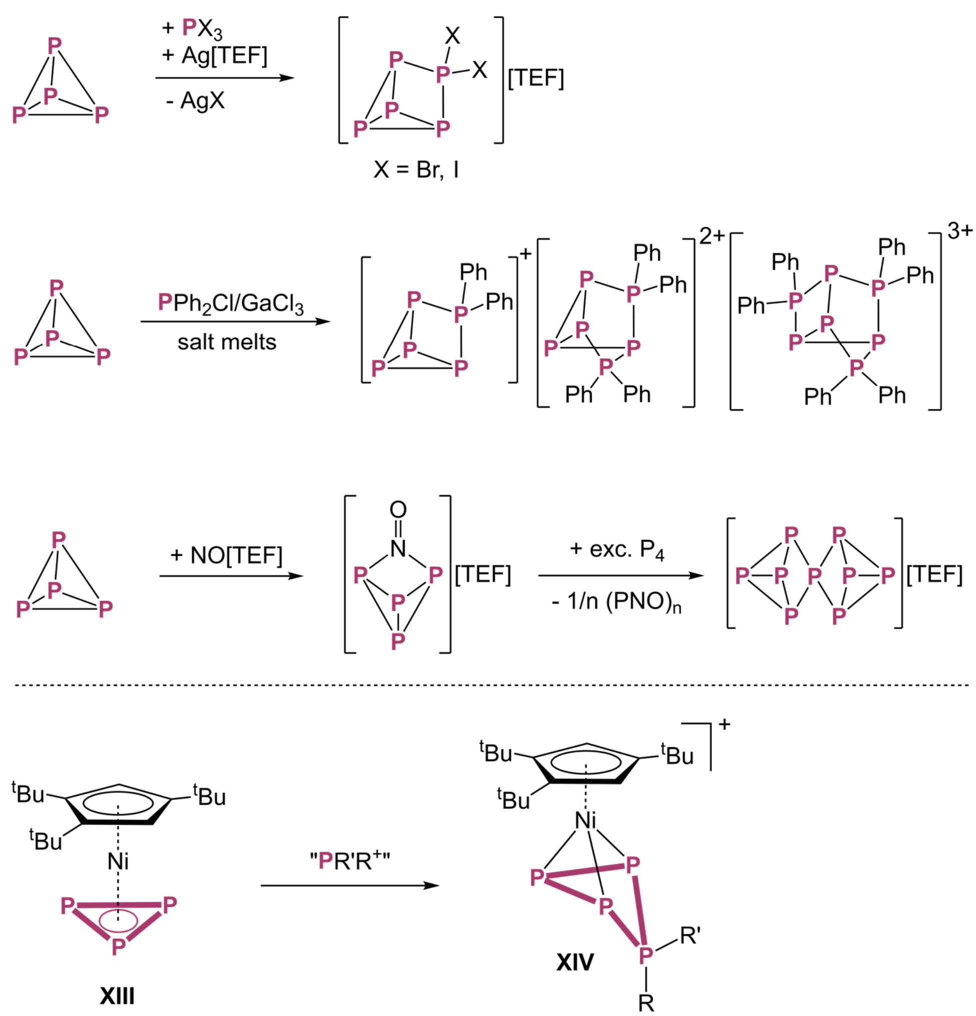

Scheme 4: Top: Reaction of P_4 with various *in situ* generated phosphenium ions and $[NO]^+$ ($[TEF]^-$ = $[Al\{OC(CF_3)_3\}_4]^-$); bottom: electrophilic functionalization of **XIII** with *in situ* generated phosphenium ions (R, R' = organic substituents or halides).

In the same manner the reaction of the phosphenium ions $[PX_2]^+$ (X = Br, I) with white phosphorus led to insertion of the phosphenium ion into one P–P bond forming the cationic P_5 cages $[P_5X_2]^+$ (Scheme 4). Moreover, by using *in situ* generated $[PPh_2]^+$ instead, multiple insertions in up to three P–P bonds of the P_4 tetrahedron could be accomplished (Scheme 4). However, also other main group electrophiles could be introduced into white phosphorus. For example, reaction of P_4 with $[NO]^+$ leads again to insertion of the electrophile into one P–P bond. Subsequent reaction with an excess of P_4 then results in the formation of the first and still only known substituent-free polyphosphorus cation, namely $[P_9]^+$ (**XII**, Scheme 4), which was obtained by Krossing *et al.*[34] This milestone in inorganic chemistry could only be accomplished with the help of weakly coordinating anions (WCAs) such as $[Al\{OC(CF_3)_3\}_4]^-$ ($[TEF]^-$),[35] which are able to stabilize very labile and reactive cations due to their weak nucleophilic properties (*vide infra*).[36]

Only recently, we were able to functionalize the nickel complex [Cp'''Ni(η^3-P_3)] (**XIII**), which bears a naked, *cyclo*-P_3 ligand, *via* reaction with $[PPh_2]^+$ forming a cationic P_4 ligand (**XIV**), which carries two phenyl groups and is stabilized in the coordination sphere of a [Cp'''Ni] fragment (Scheme 4).[37] This synthetic strategy could also be expanded to a large variety of phosphenium ions containing different organic substituents and halides.

Overall, the promising reactivity of P_4 towards oxidation and phosphenium ions, which led to isolation of unique cationic polyphosphorus compounds, prompted us to investigate its isolobal, tetrahedral complexes **Mo₂E₂**, **Mo₂EE'** and **MoE₃** concerning their reactivity towards one-electron oxidants and electrophilic functionalization by main group cations, which are the main objectives of this thesis.

1.4 Excursus: Weakly Coordinating Anions (WCAs)

Four decades ago the concept of "non-coordinating anions" was postulated, where strongly binding anions, like halides, were exchanged by complex anions of the type $[PnF_6]^-$ (Pn = P, As, Sb), $[BF_4]^-$, $[ClO_4]^-$ or $[MX_4]^-$ (M = Al, Ga; X = Cl, Br, I) (Scheme 5).[35] However, ideal "non-coordinating" conditions

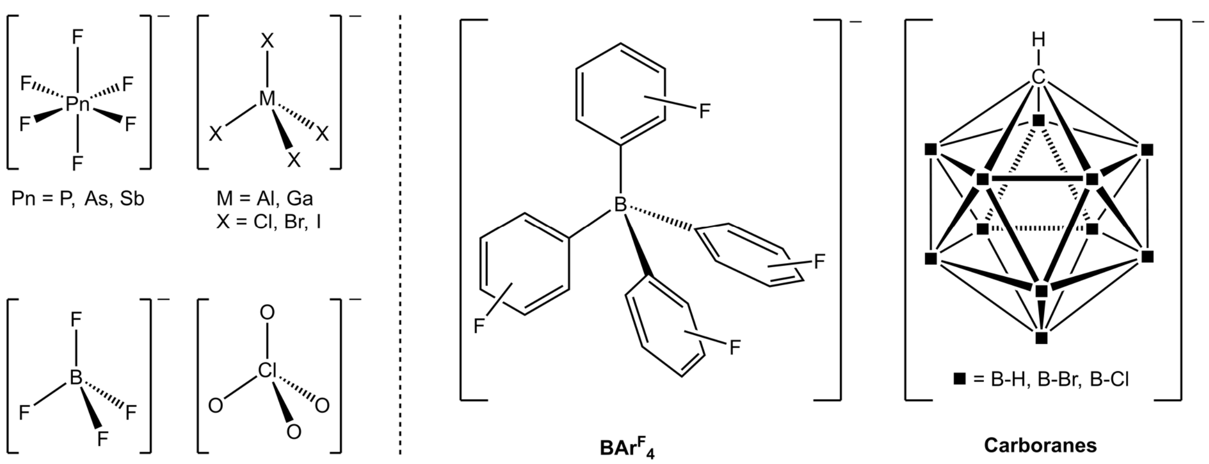

Scheme 5: Left: Representatives of small weakly coordinating anions (WCAs); right: Different classes of WCAs (**BAr^F$_4$** = $[B(C_6F_5)_4]^-$, $[B\{C_6H_3(CF_3)_2\}_4]^-$; **Carboranes** = $[CB_{11}H_{12}]^-$, $[CB_{11}H_6X_6]^-$ (X = Cl, Br)).

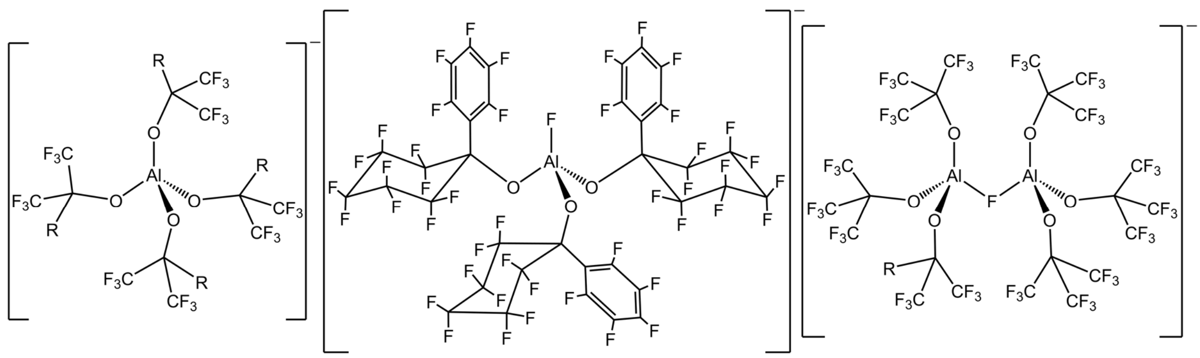

Scheme 6: The weakly coordinating alkoxy- and aryloxy-aluminates $[Al\{OC(CF_3)_3\}_4]^-$ (**[TEF]⁻**), $[Al\{OC(CF_3)_2(CCl_3)\}_4]^-$ (**[TEF^{Cl}]⁻**), $[FAl\{OC(C_5F_{10})(C_6F_5)\}_3]^-$ (**[FAl]⁻**) and $[(R^FO)_3Al–F–Al(OR^F)_3]$ ($R^F = C(CF_3)_3$).

are physically impossible since oppositely charged ions will always attract each other to a certain degree. Thus, very soon it became obvious that these complex anions were indeed able to interact with and coordinate to unsaturated, Lewis acidic metal complexes. For this reason, the term of "weakly coordinating anions" (WCAs) was introduced, which is used nowadays. WCAs proofed to be very useful not only within fundamental research but, moreover, *e.g.*, also as charge carriers in electrochemistry, catalysts or in ionic liquids.[38] Since then, an endless race started with the goal to develop the least coordinating anion, which then again should realize the stabilization of unprecedented, very labile cations. Within that several classes of anions became apparent to exhibit very weak coordinating properties. One of them are borates, which are derived from $[BF_4]^-$ by exchanging the fluorine atoms with fluorinated phenyl groups giving the $[BAr^F{}_4]^-$ anions with the most known representatives $[B(C_6F_5)_4]^-$ and $[B\{C_6H_3(CF_3)_2\}_4]^-$ (Scheme 5), which are widely used in homogenous catalysis.[35] Another well-known class of WCAs is composed of carboranes, which incorporate a stable, univalent, polyhedral central moiety like $[CB_{11}H_{12}]^-$, which is then further halogenated (Scheme 5). Among these the $[CB_{11}H_6X_6]^-$ (X = Cl, Br)[39] anions proofed to be one of the most chemically robust WCAs known, however, their elaborate syntheses restrict their applications. The most important and widely used WCAs in the last two decades are without a doubt per-halogenated alkoxy- and aryloxy-aluminates,[35] which are also mostly used within this thesis. This class of compounds was mainly advanced by the group of *Krossing*, which synthesized, amongst others, the WCAs $[Al\{OC(CF_3)_3\}_4]^-$ ([TEF]⁻) and $[FAl\{OC(C_5F_{10})(C_6F_5)\}_3]^-$([FAl]⁻) (Scheme 6). Moreover, only very recently, they reported on an access towards $[(R^FO)_3Al–F–Al(OR^F)_3]$ ($R^F = C(CF_3)_3$; Scheme 6), which claims to be the least coordinating WCA known to date.[40] These WCAs proofed to be able to stabilize weakly bound Lewis acid base adducts in condensed phase, which were only detected by mass spectrometry prior to that. For example, *Krossing et. al.* could synthesize the silver(I) complex $[Ag(\eta^2\text{-}P_4)_2]^+$, which is coordinated by two P_4 tetrahedra in an η^2 fashion, with the help of the [TEF]⁻ anion.[41] In 2013, the group of *Scheer* could then even realize the analogous arsenic complex $[Ag(\eta^2\text{-}As_4)_2][TEF]$.[42] Moreover, also labile and strongly electrophilic cations such as CX_3^+ (X = Cl, Br, I),[43] PX_4^+, $P_2X_5^+$ or $P_5X_2^+$ (X = Br, I) could be only stabilized by WCAs.[44]

a) $F = \frac{1}{4\pi\epsilon_0}\frac{q_1 q_2}{r^2} = \frac{1}{4\pi\epsilon_0}\frac{z_1 z_2 \cdot e^2}{r^2}$

b) $U_L = -120250\frac{v\cdot|z^+|\cdot|z^-|}{r^+ + r^-}\left(1 - \frac{34{,}5}{r^+ + r^-}\right) {}^{kJ}/_{mol}$

Equation 1: a) Coulomb equation with q_1, q_2 = point charges; z_1, z_2 = ionic charges; e = elementary charge; r = distance between charges; ε_0: dielectric constant; b) Kapustinskii equation: calculation of the lattice energies from the ionic radii with U_L = lattice energy; r^+, r^- = cation and anion radii in pm; v = amount of ions per unit cell; z^+, z^- = ionic charges.

The aluminates $[TEF]^-$ and $[FAl]^-$ are not only characterized by their low coordination properties but, furthermore, they are also chemically robust and can be synthesized in multigram scales with a good price-performance ratio. However, the question arises what makes these anions so weakly coordinating? In general, weak coordination properties are correlated with a low anion-cation interaction, which is mainly dependent on their Coulomb attraction. The Coulomb equation (Equation 1a), which describes the attraction of two point charges, shows that the attractive interaction between two opposite charges is, on the one hand, dependent on the charge quantity (z_1, z_2) meaning that a smaller charge results in weaker interactions. Therefore, WCAs are usually monoanionic. Additionally, they mostly consist of perfluorinated or perhalogenated surfaces, which are able to delocalize the anionic charge, which then again decreases the Coulomb attraction. Due to these perhalogenated surfaces WCAs are also weak Lewis bases and the low polarizability of the C–X bonds weakens dispersive interactions.[38] On the other hand, the Coulomb equation shows that the attraction of two charges also decreases by increasing their distance (r), which can be forced by very large anions. This, as well, has the effect that the lattice energies of the respective salts decrease (*cf.* Kapustinskii equation, Equation 1b). For example, the $[TEF]^-$ possesses an ionic radius of 1.25 nm, which decreases its lattice energy from 1036 kJ/mol in LiF to 361 kJ/mol. Hence, when using large WCAs, conditions in condensed phase can be observed, which resemble those of the gas phase. Therefore, the term of "pseudo gas phase conditions" was postulated for WCAs.[45]

Although the very weak coordinating properties and the low basicity and nucleophilicity of the $[TEF]^-$ anion involve many advantages, this also leads to severe disordering in the solid state in many cases. This effect is intensified by the high symmetry of the perfluorinated alkoxy groups. In order to decrease the tendency of disordering in the solid state, while preserving the excellent weakly coordination properties, the symmetry of the $[TEF]^-$ anion must be lowered. This was accomplished by exchanging one of the -CF_3 groups of each *tert*-butoxy substituent with -CCl_3 groups yielding the WCA $[Al\{OC(CF_3)_2(CCl_3)\}_4]^-$ ($[TEF^{Cl}]^-$; Scheme 6). This anion was synthesized by *Wang et. al.* and it already proofed to have a lower tendency of disordering, but it still can stabilize exotic cations.[46] Additionally, it shows excellent solubility since its lithium salt is already soluble in *n*-pentane.[46]

1.5 References

[1] https://upload.wikimedia.org/wikipedia/commons/9/9f/Hennig_Brand_%28Joseph_Wright%29.jpeg.
[2] F. Krafft, *Angew. Chem. Int. Ed.* **1969**, *8*, 660-671.
[3] W. Jansen, M. Ducci, *CHEMKON* **2006**, *13*, 133-142.
[4] a) R. C. Barber, P. J. Karol, H. Nakahara, E. Vardaci, E. W. Vogt, *Pure Appl. Chem.* **2011**, *83*, 1485-1498; b) A. F. Holleman, E. Wiberg, N. Wiberg, in *Lehrbuch der Anorganischen Chemie, Vol. 102*, Walter de Gruyter, Berlin, **2007**, p. 651.
[5] G. S. Girolami, *J. Chem. Educ.* **2009**, *86*, 1200.
[6] O. J. Scherer, *Acc. Chem. Res.* **1999**, *32*, 751-762.
[7] a) O. J. Scherer, *Chem. unserer Zeit* **2000**, *34*, 374-381; b) O. J. Scherer, *Angew. Chem. Int. Ed.* **1990**, *29*, 1104-1122; c) B. M. Cossairt, N. A. Piro, C. C. Cummins, *Chem. Rev.* **2010**, *110*, 4164-4177; d) M. Caporali, L. Gonsalvi, A. Rossin, M. Peruzzini, *Chem. Rev.* **2010**, *110*, 4178-4235.
[8] R. Hoffmann, *Angew. Chem. Int. Ed.* **1982**, *21*, 711-724.
[9] a) A. S. Foust, M. S. Foster, L. F. Dahl, *J. Am. Chem. Soc.* **1969**, *91*, 5633-5635; b) A. S. Foust, M. S. Foster, L. F. Dahl, *J. Am. Chem. Soc.* **1969**, *91*, 5631-5633.
[10] a) A. P. Ginsberg, W. E. Lindsell, *J. Am. Chem. Soc.* **1971**, *93*, 2082-2084; b) A. P. Ginsberg, W. E. Lindsell, K. J. McCullough, C. R. Sprinkle, A. J. Welch, *J. Am. Chem. Soc.* **1986**, *108*, 403-416.
[11] I. Krossing, L. van Wüllen, *Chem. Eur. J.* **2002**, *8*, 700-711.
[12] P. Dapporto, S. Midollini, L. Sacconi, *Angew. Chem. Int. Ed.* **1979**, *18*, 469-469.
[13] a) O. J. Scherer, T. Brück, *Angew. Chem.* **1987**, *99*, 59-59; b) O. J. Scherer, C. Blath, G. Wolmershäuser, *J. Organomet. Chem.* **1990**, *387*, C21-C24.
[14] a) O. J. Scherer, H. Sitzmann, G. Wolmershäuser, *Angew. Chem. Int. Ed.* **1985**, *24*, 351-353; b) O. J. Scherrer, H. Sitzmann, G. Wolmershäuser, *Angew. Chem. Int. Ed.* **1989**, *28*, 212-213.
[15] M. Schmidt, PhD thesis, University of Regensburg, Regensburg, **2016**.
[16] H. J. Breunig, N. Burford, R. Rösler, *Angew. Chem. Int. Ed.* **2000**, *39*, 4148-4150.
[17] M. Herberhold, G. Frohmader, W. Milius, *J. Organomet. Chem.* **1996**, *522*, 185-196.
[18] O. J. Scherer, J. Vondung, G. Wolmershäuser, *Angew. Chem. Int. Ed.* **1989**, *28*, 1355-1357.
[19] O. J. Scherer, R. Winter, G. Wolmershäuser, *Z. Anorg. Allg. Chem.* **1993**, *619*, 827-835.
[20] F. Dielmann, A. Timoshkin, M. Piesch, G. Balázs, M. Scheer, *Angew. Chem. Int. Ed.* **2017**, *56*, 1671-1675.
[21] F. Spitzer, G. Balázs, C. Graßl, M. Scheer, *Chem. Commun.* **2020**, *56*, 13209-13212.
[22] a) O. J. Scherer, H. Sitzmann, G. Wolmershäuser, *J. Organomet. Chem.* **1984**, *268*, C9-C12; b) P. J. Sullivan, A. L. Rheingold, *Organometallics* **1982**, *1*, 1547-1549; c) J. R. Harper, A. L. Rheingold, *J. Organomet. Chem.* **1990**, *390*, c36-c38; d) W. Clegg, N. A. Compton, R. J. Errington, G. A. Fisher, N. C. Norman, T. B. Marder, *J. Chem. Soc., Dalton Trans.* **1991**, 2887-2895.
[23] a) M. Gorzellik, H. Bock, L. Gang, B. Nuber, M. L. Ziegler, *J. Organomet. Chem.* **1991**, *412*, 95-120; b) L. Y. Goh, R. C. S. Wong, W. H. Yip, T. C. W. Mak, *Organometallics* **1991**, *10*, 875-879; c) H. J. Breunig, R. Rösler, E. Lork, *Angew. Chem. Int. Ed.* **1997**, *36*, 2819-2821.
[24] a) O. J. Scherer, H. Sitzmann, G. Wolmershäuser, *J. Organomet. Chem.* **1986**, *309*, 77-86; b) I. Bernal, H. Brunner, W. Meier, H. Pfisterer, J. Wachter, M. Ziegler, *Angew. Chem. Int. Ed.* **1984**, *23*, 438-439; c) N. Reinfandt, C. Schoo, L. Dütsch, R. Köppe, S. N. Konchenko, M. Scheer, P. W. Roesky, *Chem. Eur. J.* **2021**, *27*, 3974-3978; d) M. Scheer, K. Schuster, A. Krug, H. Hartung, *Chem. Ber.* **1997**, *130*, 1299-1304; e) M. Elsayed Moussa, P. A. Shelyganov, B. Wegley, M. Seidl, M. Scheer, *Eur. J. Inorg. Chem.* **2019**, *2019*, 4241-4248; f) K. V. Adams, N. Choi, G. Conole, J. E. Davies, J. D. King, M. J. Mays, M. McPartlin, P. R. Raithby, *J. Chem. Soc., Dalton Trans.* **1999**, 3679-3686; g) M. Scheer, G. Friedrich, K. Schuster, *Angew. Chem. Int. Ed.* **1993**, *32*, 593-594; h) W. Chen, R. C. S. Wong, L. Y. Goh, *Acta Crystallographica Section C* **1994**, *50*, 998-1000; i) M. Gorzellik, B. Nuber, M. L. Ziegler, *J. Organomet. Chem.* **1992**, *429*, 153-168; j) B. P. Johnson, M. Schiffer, M. Scheer, *Organometallics* **2000**, *19*, 3404-3409.
[25] a) J. E. Davies, L. C. Kerr, M. J. Mays, P. R. Raithby, P. K. Tompkin, A. D. Woods, *Angew. Chem. Int. Ed.* **1998**, *37*, 1428-1429; b) J. E. Davies, M. J. Mays, P. R. Raithby, G. P. Shields, P. K. Tompkin, A. D. Woods, *J. Chem. Soc., Dalton Trans.* **2000**, 1925-1930.
[26] a) A. J. Ashe, E. G. Ludwig, *J. Organomet. Chem.* **1986**, *303*, 197-204; b) D. Nikolova, C. von Hänisch, *Eur. J. Inorg. Chem.* **2005**, *2005*, 378-382; c) J. G. Stevens, J. M. Trooster, H. F. Martens, H. A. Meinema, *Inorg. Chim. Acta* **1986**, *115*, 197-201.
[27] a) S. Traut, A. P. Hähnel, C. von Hänisch, *Dalton Trans.* **2011**, *40*, 1365-1371; b) K. M. Marczenko, S. S. Chitnis, *Chem. Commun.* **2020**, *56*, 8015-8018; c) T. Sasamori, N. Takeda, N. Tokitoh, *Chem. Commun.* **2000**, 1353-1354.
[28] a) M. Schmidt, D. Konieczny, E. V. Peresypkina, A. V. Virovets, G. Balázs, M. Bodensteiner, F. Riedlberger, H. Krauss, M. Scheer, *Angew. Chem. Int. Ed.* **2017**, *56*, 7307-7311; b) C. Schoo, S. Bestgen, M. Schmidt, S. N. Konchenko, M. Scheer, P. W. Roesky, *Chem. Commun.* **2016**, *52*, 13217-13220; c) E. Mädl, G. Balázs, E. V. Peresypkina, M. Scheer, *Angew. Chem. Int. Ed.* **2016**, *55*, 7702-7707; d) N. Arleth, M. T. Gamer, R. Köppe, S. N. Konchenko, M. Fleischmann, M. Scheer, P. W. Roesky, *Angew. Chem. Int. Ed.* **2016**, *55*, 1557-1560; e) N. Arleth, M. T. Gamer, R. Koppe, N. A. Pushkarevsky, S. N. Konchenko, M. Fleischmann, M. Bodensteiner, M. Scheer, P. W. Roesky, *Chem. Sci.* **2015**, *6*, 7179-7184; f) M. V. Butovskiy, G. Balázs, M. Bodensteiner, E. V. Peresypkina, A. V. Virovets, J. Sutter, M. Scheer, *Angew. Chem. Int. Ed.* **2013**, *52*, 2972-2976; g) T. Li, M. T. Gamer, M. Scheer, S. N. Konchenko, P. W. Roesky, *Chem. Commun.* **2013**, *49*, 2183-2185.
[29] E. Mädl, M. V. Butovskii, G. Balázs, E. V. Peresypkina, A. V. Virovets, M. Seidl, M. Scheer, *Angew. Chem. Int. Ed.* **2014**, *53*, 7643-7646.
[30] M. Fleischmann, F. Dielmann, L. J. Gregoriades, E. V. Peresypkina, A. V. Virovets, S. Huber, A. Y. Timoshkin, G. Balázs, M. Scheer, *Angew. Chem. Int. Ed.* **2015**, *54*, 13110-13115.
[31] R. F. Winter, W. E. Geiger, *Organometallics* **1999**, *18*, 1827-1833.

[32] M. Fleischmann, PhD thesis, University of Regensburg, Regensburg, **2015**.
[33] a) C. A. Dyker, N. Burford, *Chem. Asian J.* **2008**, *3*, 28-36; b) A. P. M. Robertson, P. A. Gray, N. Burford, *Angew. Chem. Int. Ed.* **2014**, *53*, 6050-6069; c) M. Donath, F. Hennersdorf, J. J. Weigand, *Chem. Soc. Rev.* **2016**, *45*, 1145-1172.
[34] a) T. Köchner, T. A. Engesser, H. Scherer, D. A. Plattner, A. Steffani, I. Krossing, *Angew. Chem. Int. Ed.* **2012**, *51*, 6529-6531; b) T. Köchner, S. Riedel, A. J. Lehner, H. Scherer, I. Raabe, T. A. Engesser, F. W. Scholz, U. Gellrich, P. Eiden, R. A. Paz Schmidt, D. A. Plattner, I. Krossing, *Angew. Chem. Int. Ed.* **2010**, *49*, 8139-8143.
[35] I. Krossing, I. Raabe, *Angew. Chem. Int. Ed.* **2004**, *43*, 2066-2090.
[36] M. Fleischmann, L. Dütsch, M. Elsayed Moussa, G. Balázs, W. Kremer, C. Lescop, M. Scheer, *Inorg. Chem.* **2016**, *55*, 2840-2854.
[37] C. Riesinger, L. Dütsch, G. Balázs, M. Bodensteiner, M. Scheer, *Chem. Eur. J.* **2020**, *26*, 17165-17170.
[38] N. Trapp, I. Krossing, *Nachrichten aus der Chemie* **2009**, *57*, 632-637.
[39] a) C. A. Reed, *Acc. Chem. Res.* **1998**, *31*, 133-139; b) T. Jelinek, J. Plesek, S. Hermanek, B. Stibr, *Collect. Czech. Chem. Commun.* **1986**, 819-829.
[40] A. Martens, P. Weis, M. C. Krummer, M. Kreuzer, A. Meierhöfer, S. C. Meier, J. Bohnenberger, H. Scherer, I. Riddlestone, I. Krossing, *Chem. Sci.* **2018**, *9*, 7058-7068.
[41] I. Krossing, *J. Am. Chem. Soc.* **2001**, *123*, 4603-4604.
[42] C. Schwarzmaier, M. Sierka, M. Scheer, *Angew. Chem. Int. Ed.* **2013**, *52*, 858-861.
[43] a) I. Krossing, A. Bihlmeier, I. Raabe, N. Trapp, *Angew. Chem. Int. Ed.* **2003**, *42*, 1531-1534; b) H. P. A. Mercier, M. D. Moran, G. J. Schrobilgen, C. Steinberg, R. J. Suontamo, *J. Am. Chem. Soc.* **2004**, *126*, 5533-5548.
[44] M. Gonsior, I. Krossing, L. Müller, I. Raabe, M. Jansen, L. v. Wüllen, *Chem. Eur. J.* **2002**, *8*, 4475-4492.
[45] T. S. Cameron, A. Decken, I. Dionne, M. Fang, I. Krossing, J. Passmore, *Chem. Eur. J.* **2002**, *8*, 3386-3401.
[46] X. Zheng, Z. Zhang, G. Tan, X. Wang, *Inorg. Chem.* **2016**, *55*, 1008-1010.

2 RESEARCH OBJECTIVES

In order to enlarge the structural diversity of organometallic polypnictogen complexes (= E_n ligand complexes; E = P, As, Sb, Bi) the current work focuses on the synthesis and stabilization of cationic E_n ligand complexes under weakly coordinating conditions. To accomplish this goal the following objectives were set:

– Synthesis of new polypnictogen complexes containing hetero-E_n ligands of the heavy group 15 elements As, Sb and Bi:

- development of a new synthetic approach to the complexes $[\{CpMo(CO)_2\}_2(\mu,\eta^2:\eta^2\text{-PE})]$ (E = As, Sb; "**Mo_2PE**"), which increases the overall yield, decreases the amount of reaction steps and avoids possible side reactions
- synthesis of the heavier analogues **Mo_2AsSb**, **Mo_2AsBi** and **Mo_2SbBi**.
- introduction of bulkier Cp ligands into the complexes **Mo_2EE'** (E = P, As, Sb, Bi)

– Oxidation of E_n ligand complexes with one-electron oxidants:

- synthesis of new oxidizing agents with different oxidation potentials containing the WCAs [TEF], [TEF^{Cl}] and [FAl]
- oxidation of the tetrahedral complexes $[\{CpMo(CO)_2\}_2(\mu,\eta^2:\eta^2\text{-}E_2)]$ (**Mo_2E_2**), $[\{CpMo(CO)_2\}_2(\mu,\eta^2:\eta^2\text{-EE'})]$ (**Mo_2EE'**) and $[\{CpMo(CO)_2\}(\eta^3\text{-}E_3)]$ (**MoE_3**)
- investigation of the influence of metal atom, Cp^R ligand and counter ion on the oxidation chemistry of E_n ligand complexes
- oxidation of different As_n ligand complexes with $n > 4$

– Reaction of E_n ligand complexes with main group electrophiles:

- investigation of the reactivity of the tetrahedral complexes **Mo_2E_2**, **Mo_2EE'** and **MoE_3** towards *in situ* generated phosphenium ions with different substituents as well as borinium ions

Preface

The following chapter has already been published. The article is reprinted with permission of Wiley-VCH.

"Synthesis of Tetrahedranes Containing the Unique Bridging Hetero-Dipnictogen Ligand EE' (E ≠ E' = P, As, Sb, Bi)"

Chem. Eur. J. **2021**, *27*, 8804-8810.

Authors

Luis Dütsch, Christoph Riesinger, Gábor Balázs and Manfred Scheer

Author Contributions

The main part (conceptualization, preparation of the compounds **1**, **2**, **3a**, **3b**, **5**, **6a**–**d**, **7** and **8**, writing, visualization, and execution and evaluation of measurements) of this work was done by the first author (Luis Dütsch). The synthesis and description of compound **1** have already been part of the Master thesis of Luis Dütsch. Christoph Riesinger synthesized and characterized compound **4**. He assisted in the crystallographical characterization of the compounds **6a**–**c**. He also assisted in the synthesis and characterization of the compounds **2** and **3a**, which are part of his Bachelor thesis. Gábor Balázs performed the DFT calculations and contributed the respective parts in the manuscript. Manfred Scheer supervised the research and revised the manuscript prior to publication.

Acknowledgements

This work was supported by the Deutsche Forschungsgemeinschaft within the project Sche 384/36-1. We thank Anna Garbagnati, Matthias Hautmann and Lisa Zimmermann for their support in the preparation of the compounds **7** (A. G.), **E3**, **E4** (M. H.) and **4** (L. Z.). Open access funding enabled and organized by Projekt DEAL.

3 Synthesis of Tetrahedranes Containing the Unique Bridging Hetero-Dipnictogen Ligand EE' (E ≠ E' = P, As, Sb, Bi)

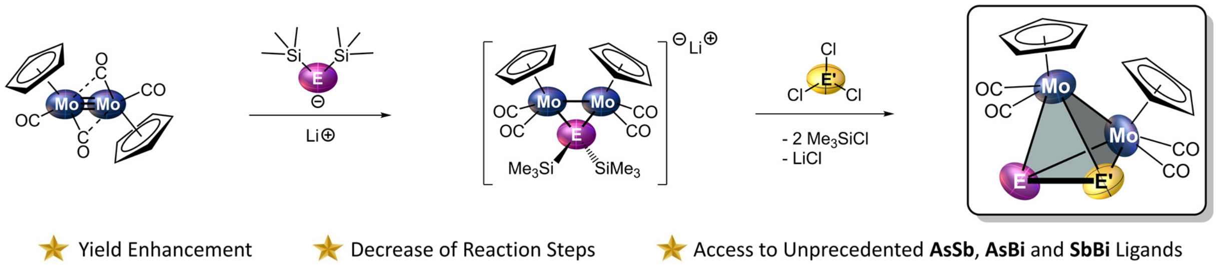

Abstract: *In order to improve and extend the rare class of tetrahedral mixed main group transition metal compounds, a new synthetic route for the complexes [{CpMo(CO)$_2$}$_2$(μ,η^2:η^2-**PE**)] (E = As (**1**), Sb (**2**)) is described leading to higher yields and a decrease in reaction steps. Via this route, also the so far unknown heavier analogues containing **AsSb** (**3a**), **AsBi** (**4**) and **SbBi** (**5**) ligands, respectively, are accessible. Single crystal X-ray diffraction experiments and DFT calculations reveal that they represent very rare examples of compounds comprising covalent bonds between two different heavy pnictogen atoms, which show multiple bond character and are stabilized without any organic substituents. A simple one-pot reaction of [CpMo(CO)$_2$]$_2$ with ME(SiMe$_3$)$_2$ (M = Li, K; E = P, As, Sb, Bi) and the subsequent addition of PCl$_3$, AsCl$_3$, SbCl$_3$ or BiCl$_3$, respectively, give the complexes **1**–**5**. This synthesis is also transferable to the already known homo-dipnictogen complexes [{CpMo(CO)$_2$}$_2$(μ,η^2:η^2-**E$_2$**)] (E = P, As, Sb, Bi) resulting in higher yields comparable to those in the literature procedures and allows the introduction of the bulkier and better soluble Cp' (Cp' = tert-butylcyclopentadienyl) ligand.*

3.1 Introduction

Tetrahedral molecules such as the most simple organic representative, the parent tetrahedrane (tricyclo[1.1.0.0^{2,4}]butane), have always been of great scientific interest, not only due to their aesthetical attraction as a chemical equivalent of a platonic body, but also because of their unusual bonding situation, high ring strain and reactivity.[1] These properties point already to their mostly challenging syntheses and low stability.[1] The probably most prominent inorganic example of this class of compounds is white phosphorus (P_4), which can be prepared by sublimation of red phosphorus and is stable under exclusion of air. In contrast, its heavier counterpart, yellow arsenic (As_4), is highly unstable and undergoes rapid autocatalytic degradation under light exposure already.[2] Furthermore, the heavier homologue Sb_4 has been observed in the solid state only within thin antimony films received by the evaporation of Sb_4 molecules in ultra-high vacuum,[3] while Bi_4 is only known in the gas phase.[4] Heteroatomic tetrahedranes built from p-block elements are extremely scarce. Only three examples, namely AsP_3 (**I**) and the tetrahedrane derivatives $P(C^tBu)_3$ (**II**) and $P_2(C^tBu)_2$ (**III**), have been reported to date (Scheme 1b).[5] They are, however, highly sensitive to air. While **I** and **III** are pyrophoric, compound **II** degrades after 30 mins at room temperature.

By formal substitution of one or two atoms of the E_4 (E = P, As, Sb, Bi) tetrahedra with isolobal 15-valence-electron transition metal fragments, such as [CpMo(CO)$_2$], stable tetrahedra such as the air-stable (in the solid state) polypnictogen ligand complexes [{CpMo(CO)$_2$}(η^3-**E$_3$**)] ("**MoE$_3$**"; E = P, As, Sb)[6] and [{CpMo(CO)$_2$}$_2$(μ,η^2:η^2-**E$_2$**)] ("**Mo$_2$E$_2$**"; E = P, As, Sb, Bi)[6a, 6c, 7] are received (Scheme 1). They can easily be synthesized, characterized and handled and are therefore well-suited starting materials

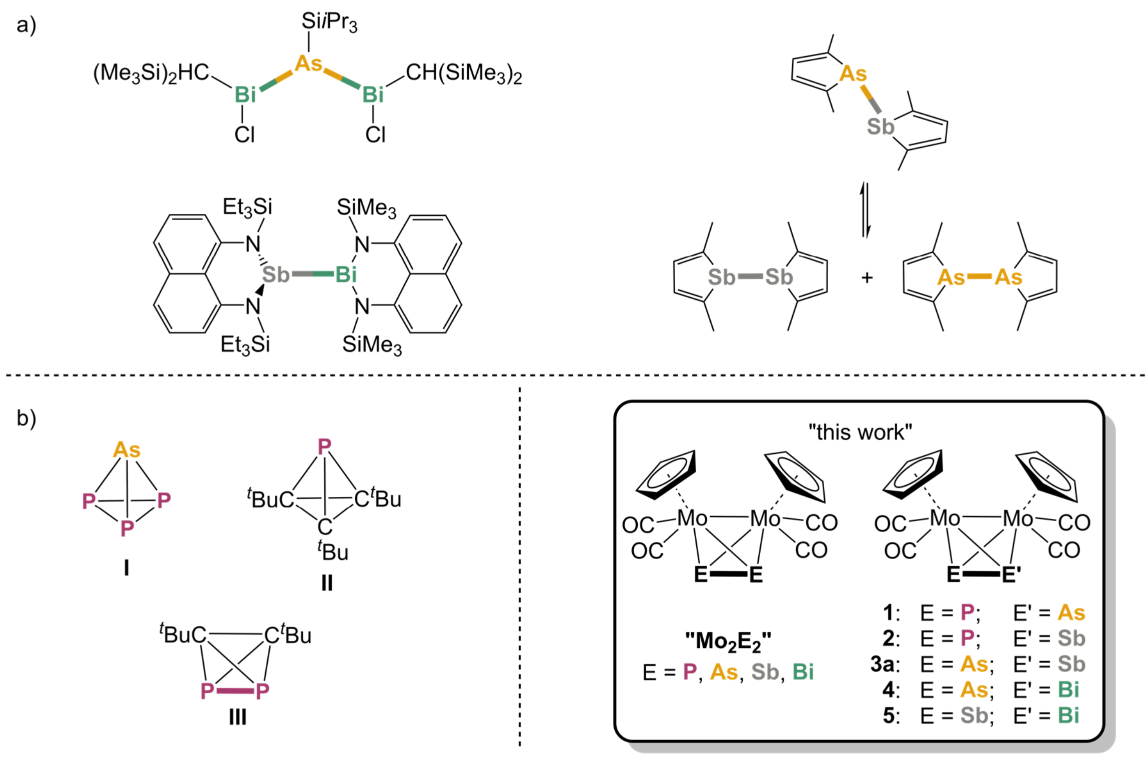

Scheme 1: a) Rare examples of compounds featuring covalent As–Bi and Sb–Bi bonds (left), as well as a covalent As–Sb bond, which is in equilibrium with its respective homo-dipnictogen complexes (right); b) heteroatomic main-group tetrahedranes. *This work*: tetrahedral [{CpMo(CO)$_2$}$_2$(μ,η^2:η^2-**EE'**)] compounds containing scarce covalent hetero-dipnictogen bonds.

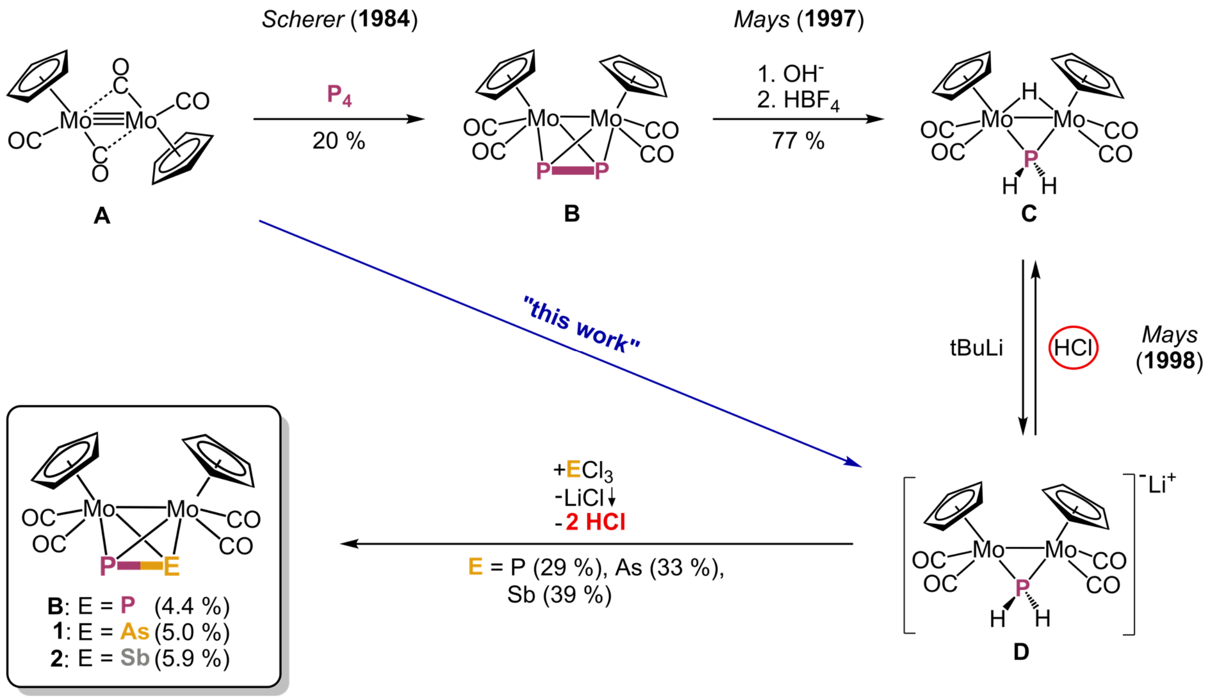

Scheme 2: Synthetic route for the tetrahedral molybdenum pnictogen complexes of the type {[Mo]$_2$(μ,η^2:η^2-**PE**)} (E = P (**B**), As (**1**), Sb (**2**); [Mo] = CpMo(CO)$_2$) by Mays *et al*. in 1998. Yields for **B**, **1** and **2** are calculated for the overall reaction starting from **A**. *This work*: direct synthesis of **D** from **A** and avoidance of HCl elimination by replacing the protons with $SiMe_3$ groups.

for further investigations and have already proved to be excellent precursors for the formation of extended polypnictogen frameworks upon reduction,[8] coordination[9] and oxidation.[10] While for **Mo$_2$E$_2$** complexes all representatives of E (E = P, As, Sb, Bi; except E = N) are known, the respective hetero-dipnictogen complexes **Mo$_2$EE'** have been far less investigated. Until now, only two compounds of this class, [{CpMo(CO)$_2$}$_2$(μ,η^2:η^2-**PE**)] (E = As (**1**), Sb (**2**)), could be synthesized by Mays *et al.* in 1998 (Scheme 2).[11] Their approach based on the deprotonation of [{CpMo(CO)$_2$}$_2$(μ-H)(μ-PH$_2$)] (**C**), which yields the lithium salt of the anion [{CpMo(CO)$_2$}$_2$(μ-PH$_2$)]$^-$ (**D**). Further reaction with $AsCl_3$ or $SbCl_3$, respectively, gives access to **1** and **2** by elimination of one equivalent of LiCl and two equivalents of HCl. However, the latter can also protonate the anion **D** back to **C**, which leads to just moderate yields of 33 % (**1**) and 39 % (**2**), respectively. Another disadvantage of this synthetic route is the elaborate preparation of **C**, where first **Mo$_2$P$_2$** (**B**) is generated by thermolysis of [CpMo(CO)$_2$]$_2$ (**A**) with white phosphorus to be further hydrolysed with NaOH in THF/H_2O. Following this route, **C** can only be obtained in a yield of just 15 %, which leads to an overall yield of 5.0 % for **1** and 5.9 % for **2**, when starting from **A**. Moreover, a direct route affording **C** from **A** was developed by our group in 2003.[12] Additionally, only recently, we were able to show that **D** can be directly synthesized from **B** by a nucleophilic attack of OH$^-$.[13] *Mays et al.* also tried to synthesize the respective **PBi** ligand complex by adding $BiCl_3$ to **D**, but failed, which is not overly surprising as complexes containing a P–Bi bond are very rare and only of a dative bonding nature and/or stabilized by bulky substituents.[14] The number of examples containing a covalent E–E' bond dramatically decreases by moving on to the heavier pnictogen elements.[15] While three compounds for covalent As–Sb bonds were reported,[16] only two are known for As–Bi and Sb–Bi (Scheme 1a),[17] only half of which were characterized crystallographically. Between As and Sb, only single bonds were observed, whereas the other ones mentioned also form double bonds. However, all of them can only be stabilized by very bulky organic substituents or they have a distinct tendency to disproportionate and form homonuclear bonds (Scheme 1a; right).[16a]

These disadvantages and the perspective of making tetrahedral compounds with heavier hetero-dipnictogen ligands accessible prompted us to develop a new synthetic route, which reduces the number of reaction steps and avoids the elimination of HCl to give much higher yields. In the following, we report a facile two-step one-pot synthesis for this type of compounds starting directly from **A** (Scheme 2), which is also transferable to the complexes **Mo_2E_2**, containing different Cp^R ligands such as the *tert*-butyl substituted cyclopentadienyl ligand (Cp' = η^5-C_5H_4tBu) and gives access to the so far unknown heavier hetero-dipnictogen derivatives of **1** and **2** such as [{CpMo(CO)$_2$}$_2$(μ,η^2:η^2-**AsSb**)] (**3a**), [{CpMo(CO)$_2$}$_2$(μ,η^2:η^2-**AsBi**)] (**4**) and [{CpMo(CO)$_2$}$_2$(μ,η^2:η^2-**SbBi**)] (**5**) in higher yields. The latter represent the first examples of compounds containing covalent bonds between mixed heavier group 15 elements that do not bear any bulky organic substituents and are only stabilized by transition metal moieties.

3.2 Results and Discussion

When **A** is reacted with a solution of Li[P(SiMe$_3$)$_2$] (**E1**) in THF, an immediate colour change from orange-brown to greenish red occurs suggesting the formation of the intermediate Li[{CpMo(CO)$_2$}$_2${μ-P(SiMe$_3$)$_2$}] (**6a**) in solution (Scheme 3). Compound **6a** is a derivative of **D** in which the P-bound hydrogen atoms are replaced by SiMe$_3$ groups. Further addition of AsCl$_3$ or SbCl$_3$, respectively, leads to the generation of the tetrahedral molybdenum pnictogen complexes [{CpMo(CO)$_2$}$_2$(μ,η^2:η^2-**PE'**)] (E' = As (**1**), Sb (**2**)) in 69 % and 59 % isolated yields (Scheme 3), respectively, after chromatographic work-up. In the last step, two equivalents of Me$_3$SiCl are released avoiding the disadvantageous elimination of HCl. This method not only avoids elaborate reaction steps,

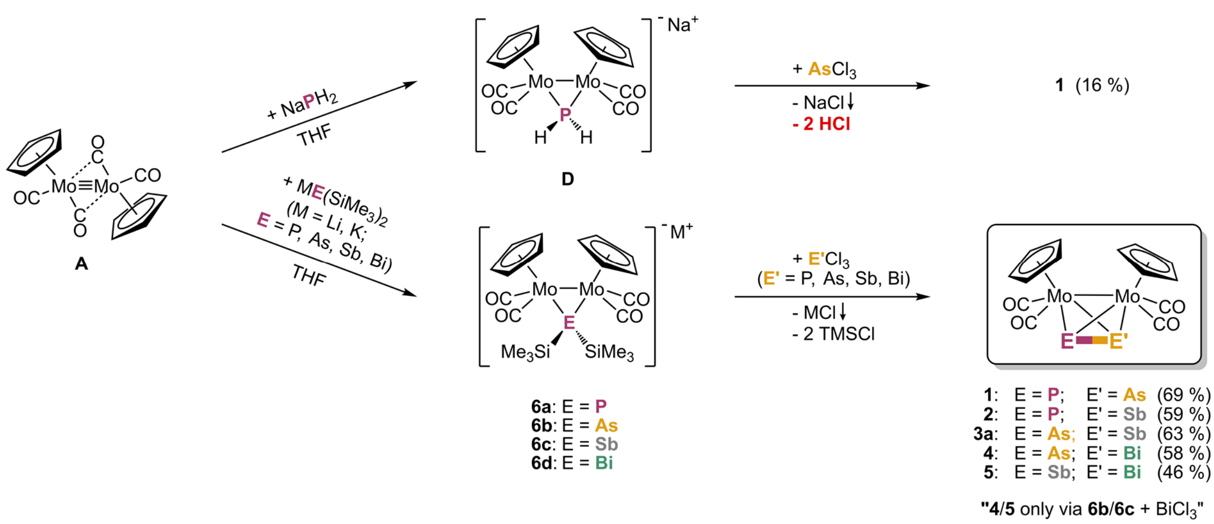

Scheme 3: One-pot synthesis of the tetrahedral hetero-pnictogen complexes **1**-**5**. Top: using NaPH$_2$ for the synthesis of **1** leading to HCl evolution in the second reaction step; bottom: using M**E**(SiMe$_3$)$_2$ (M = Li, K; E = P, As, Sb, Bi) for the synthesis of **1**-**5**, which avoids HCl elimination resulting in higher yields.

Table 1: All possible combinations of the intermediates **6a-d** with **E'**Cl_3 (E' = P, As, Sb, Bi) and the resulting products [{$CpMo(CO)_2$}$_2$(μ,η^2:η^2-**EE'**)]. Yield improvements compared to the literature syntheses are given subjacent (referred to **A**).

	6a ("P")	**6b** ("As")	**6c** ("Sb")	**6d** ("Bi")
PCl_3	P_2 20 % → 57 %	**PAs** (**1**) 5 % → 50 %	**PSb** (**2**) 6 % → 18 %	unsuccessful
$AsCl_3$	**PAs** (**1**) 5 % → 69 %	As_2 35 % → 52 %	**AsSb** (**3a**) 0 % → 63 %	unsuccessful
$SbCl_3$	**PSb** (**2**) 6 % → 59 %	**AsSb** (**3a**) 0 % → 51 %	Sb_2 76 % → 37 %	unsuccessful
$BiCl_3$	unsuccessful	**AsBi** (**4**) 0 % → 58 %	**SbBi** (**5**) 0 % → 46 %	Bi_2 14 % → 25 %

but also increases the yield of the compounds **1** and **2** dramatically, compared to the literature (5.0 % and 5.9 %; Table 1). The purity of **1** and **2** was proven by ^{31}P and ^{1}H NMR spectroscopy as well as by elemental analysis and mass spectrometry. It has to be mentioned that compound **1** can also be synthesized by reacting **A** with $NaPH_2$ (yielding the anion **D** immediately in solution) and the subsequent addition of $AsCl_3$. But, here again, HCl evolves in the second reaction step leading to side reactions and a relatively low yield of 16 %, which, however, still exceeds three times the yield reported by Mays *et al.*

Compound $\mathbf{Mo_2P_2}$ (**B**) can be obtained in the same manner by reacting the solution of the intermediate **6a** with PCl_3. Here, the yield can be increased from 20 % to 57 % (Table 1). However, the synthesis of an analogous complex with a **PBi** ligand by adding $BiCl_3$ to **6a** was not successful, as opposed to the previously reported method of *Mays et al*. Only small traces of $\mathbf{Mo_2P_2}$ could be detected by NMR spectroscopy and mass spectrometry, which might suggest that the P–Bi bond is too unstable and the tetrahedral product is either not formed or decomposes rapidly.

Our synthetic route clearly shows that the number of reaction steps could be reduced and that the yield is considerably increased by an easy one-pot reaction, especially for the hetero-dipnictogen complexes **1** and **2**. But the more challenging question arises whether the yet unknown hetero-dipnictogen ligands, which only contain the heavier elements As, Sb and Bi, are also accessible. The reaction of **A** with either Li[As($SiMe_3$)$_2$] (**E2**), K[Sb($SiMe_3$)$_2$] (**E3**) or K[Bi($SiMe_3$)$_2$] (**E4**) in THF leads to an immediate colour change from orange brown to greenish red (**E2**), greenish brown (**E3**) or bronze-coloured (**E4**) suggesting the formation of the respective intermediates M[{$CpMo(CO)_2$}$_2${μ-E($SiMe_3$)$_2$}] (M = Li, K; E = As (**6b**), Sb (**6c**), Bi (**6d**)) in solution. The subsequent addition of $AsCl_3$, $SbCl_3$ or $BiCl_3$, respectively, and easy purification by column chromatography lead to the unprecedented complexes [{$CpMo(CO)_2$}$_2$(μ,η^2:η^2-**AsSb**)] (**3a**), [{$CpMo(CO)_2$}$_2$(μ,η^2:η^2-**AsBi**)] (**4**) and [{$CpMo(CO)_2$}$_2$(μ,η^2:η^2-**SbBi**)] (**5**) in remarkable isolated yields of 63 %, 58 % and 46 % (Scheme 3, Table 1).

Thus, all combinations of dipnictogen ligands can be synthesized by reacting the respective intermediate **6a**-**d** with the appropriate pnictogen-trihalide ECl_3 (except $\mathbf{Mo_2PBi}$). While compound **3a** can be obtained in two ways, either by combining **6b** with $SbCl_3$ or **6c** with $AsCl_3$, **4** and **5** are only formed by the reaction of **6b** or **6c**, respectively, with $BiCl_3$, not by reacting **6d** with $AsCl_3$ or $SbCl_3$ (Table 1 or Scheme 3). This suggests that either the formation of **6d** is less favoured or that **6d** is less stable than its lighter counterparts.

The incorporated **EE'** ligands feature very rare bonds between different heavier pnictogen atoms, especially within the compounds **3a**, **4** and **5**. Compound **3a** represents the fourth, **4** and **5** only the third example of compounds with covalent As–Sb,[16] As–Bi[17a] or Sb–Bi[17b,17c] bonds, respectively. Moreover, they are the first examples of such covalent E–E' bonds that are only stabilized by transition metals and do not bear any organic substituents. Therefore, these compounds can be regarded as complexes of the exotic diatomic As≡Sb, As≡Bi and Sb≡Bi molecules, respectively, which are the heaviest hetero-pnictogen congeners of N_2.

Analogously to the synthesis of $\mathbf{Mo_2P_2}$, the homo-dipnictogen complexes $\mathbf{Mo_2As_2}$, $\mathbf{Mo_2Sb_2}$ and $\mathbf{Mo_2Bi_2}$ can be synthesized *via* this method, too, again resulting in a remarkable yield enhancement compared to their hitherto existing preparations (except for the antimony complex; Table 1). Additionally, this synthesis could be scaled-up to a multigram scale, which enables the systematic investigation of the reactivity of this class of compounds. All the tetrahedral complexes are well soluble in dichloromethane and toluene and moderately soluble in *ortho*-difluorobenzene and nonpolar solvents such as *n*-hexane or *n*-pentane. Overall, the heavier the pnictogen atoms are, the more the solubility decreases.

The products **1**–**5** can be crystallized from saturated CH_2Cl_2 solutions at -30 °C leading to dark red blocks suitable for single crystal X-ray diffraction. Since **1** and **2** are already described in the literature, only the solid-state structures of **3a**–**5** (Figure 1) will be discussed. They are isostructural with a distorted Mo_2EE' tetrahedron as the central structural motif and crystallize in the monoclinic space groups $P2/n$ (**3a**), $P2_1$ (**4**) or $I2/a$ (**5**), respectively, with two half molecules (**3a**), one (**4**) or one half molecule (**5**) in the asymmetric unit. The **AsSb** ligand of **3a** exhibits a 50:50 disorder over the two sites with an average bond length of 2.515(1) Å,[18] which is in between those of the diarsenic (2.311(3) Å)[7a] and the diantimony complexes (2.678(1) Å).[19] Additionally, it is just slightly longer than the sum of the covalent radii for an As–Sb double bond (2.47 Å).[20] Therefore, it shows a structural similarity to all other existing complexes of the type $[\{CpMo(CO)_2\}_2(\mu,\eta^2:\eta^2\text{-}\mathbf{EE'})]$. It represents, however, the first example of an As–Sb bond with a multiple bond character. The same accounts for the compounds **4** and **5**. The former bears an **AsBi** ligand with a bond length of 2.64(2) Å,[18] the latter an **SbBi** ligand with a bond length of 2.7916(2) Å. Both are again disordered over the two sites in a ratio of 50:50 and the

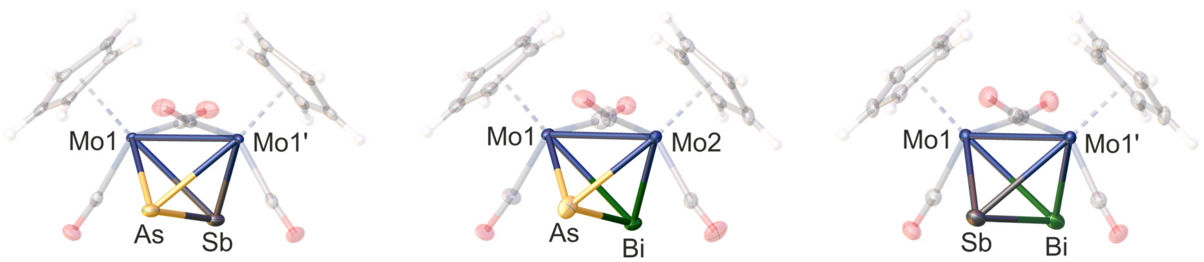

Figure 1: Molecular structure of the unprecedented products **3a** (left), **4** (middle) and **5** (right). Anisotropic displacement is set to the 50% probability level. The Cp ligands as well as the CO substituents are drawn translucent and the disorder is omitted for clarity. Selected bond lengths [Å]: **3a**: As–Sb 2.515(1), Mo1–Mo1' 3.0656(6); **4**: As–Bi 2.64(2), Mo1–Mo2 3.084(2); **5**: Sb–Bi 2.7916(2), Mo1-Mo1' 3.1255(6).

bond distances are in between the sum of the respective single (As–Bi: 2.72 Å; Sb–Bi: 2.91 Å) and double bond (As=Bi: 2.55 Å; Sb=Bi: 2.77 Å) covalent radii, while **5** nears a double bond.[20] Additionally, the bond length of the **SbBi** ligand in **5** is again between those of the diantimony (2.678(1) Å)[19] and the dibismuth (2.838(1) Å) complexes. The same behaviour is observed for the Mo–Mo distances of **3a**–**5**, which are slightly elongated in comparison to the respective lighter homo-dipnictogen complex **Mo_2E_2**, but shortened in comparison to the heavier analogue. The Cp ligands in **3a**–**5** are arranged in an eclipsed manner to each other. Overall, the newly formed complexes **3a**–**5** can, on the one hand, be described as tetrahedra, isolobal to P_4 and As_4 and, on the other hand, as **EE'** dumbbells stabilized by an Mo_2 unit, each featuring a formal triple bond. The rather short E–E' distances are nicely reproduced by DFT calculations (*cf.* the Supporting Information). For example, the As-Sb distance in the optimized geometry of **3a** is with 2.515 Å in excellent agreement with the experimental value (*vide supra*). Moreover, the As-Sb multiple bond character is reflected in the Wiberg bond order with a Löwdin orthogonalized basis (see SI for details) of 1.40. The corresponding Wiberg bond orders of the As-Bi and Sb-Bi bonds in **4** and **5** are 1.35 and 1.36, respectively.

The ^1H NMR spectra of **1**–**5** all feature one singlet in the characteristic region for Cp ligands.[21] Likewise, one singlet is observed in the $^{13}C\{^1H\}$ NMR spectra as well as characteristic signals for the CO ligands. The phosphorus-containing complexes **1** and **2** were characterized by ^{31}P NMR spectroscopy, revealing the expected signals at δ = 34.5 ppm (**1** in C_6D_6)[22] and 98.8 ppm (**2** in C_6D_6)[22] as reported in literature.[11] However, in some cases, both solutions show an additional small signal at -44.5 ppm, which can be attributed to trace impurity of **Mo_2P_2**. This indicates that a slight intermolecular exchange between the pnictogen atoms can take place in these syntheses and, therefore, small amounts of the homo-dipnictogen complexes are generated which cannot be separated by column chromatography. The amount of the produced **Mo_2P_2** is very little (ratio of 20:1 or higher in favour of **1** or **2**, respectively) though. Small amounts of homo-dipnictogen complexes can also be observed in the ^1H NMR spectra of **3a**–**5** in some reactions. The identity of **1**–**5** has been unambiguously proven by mass spectrometry, where the molecular ion peak has been detected. In addition, in some cases, peaks of low intensity

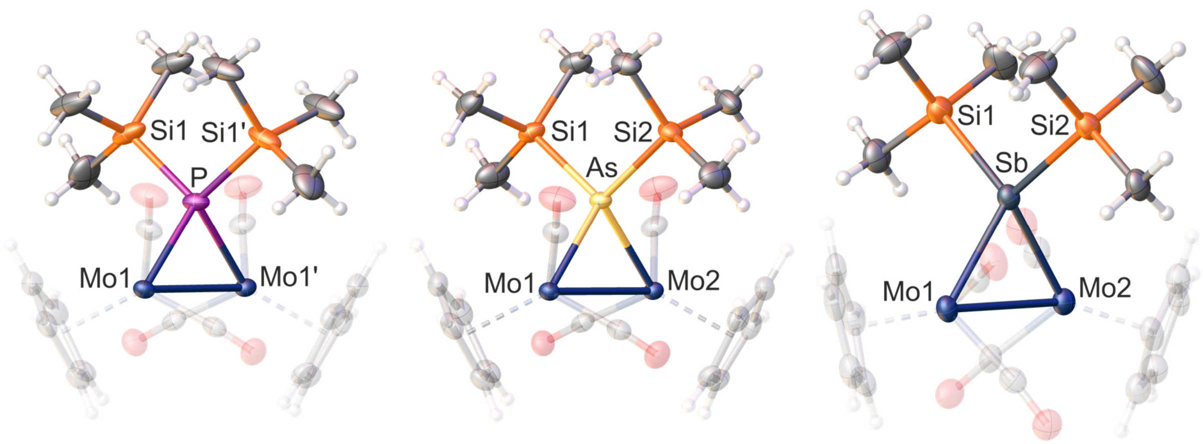

Figure 2: Molecular structures of the intermediates **6a** (left), **6b** (middle) and **6c** (right). Anisotropic displacement is set to the 50% probability level. Only the anionic part is shown. The cations and the crown ethers are omitted, and Cp as well as CO substituents are drawn translucent for clarity. Selected bond lengths [Å] and angles [°]: **6a**: P–Mo1/P–Mo1' 2.4304(6), P–Si1/P–Si1' 2.2574(8), Mo1–Mo1' 3.1889(5), Si1-P-Si1' 103.85(5); **6b**: As–Mo1 2.5213(3), As–Mo2 2.5128(3), As–Si1 2.3410(8), As–Si2 2.3540(8), Mo1–Mo2 3.2445(3), Si1-As-Si2 104.39(3); **6c**: Sb–Mo1 2.6887(8), Sb–Mo2 2.6907(7), Sb–Si1 2.561(2), Sb–Si2 2.559(2), Mo1–Mo2 3.2597(8), Si1-Sb-Si2 105.27(7).

corresponding to the homo-dipnictogen species have been also detected. The composition of **1**–**5** is further supported by elemental analysis. All the synthesized tetrahedral compounds, including **3b**, **7** and **8** (*vide infra*), are stable in air, in contrast to other heteroatomic tetrahedranes.[5a-c]

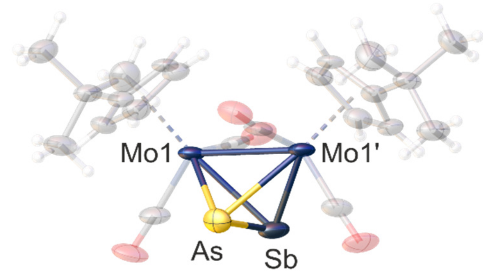

Figure 3: Molecular structure of the Cp' derivative **3b**, exemplifying the isostructural compounds **3b**, **7** and **8**. Anisotropic displacement is set to the 50% probability level. The Cp' ligands as well as the CO substituents are drawn translucent and the disorder is omitted for clarity.

It was also possible to isolate crystals of the intermediates **6a**-**c** (regardless of several attempts, no crystals for **6d** could be obtained), which were suitable for single-crystal X-ray diffraction by adding the respective crown ethers (12-crown-4 for lithium, 18-crown-6 for potassium) within the first reaction step and layering with *n*-hexane at −30 °C (Figure 2). The anions of the intermediates **6a**-**c** are isostructural to each other as well as to **D**, which is a derivative of **6a** where the $SiMe_3$ groups are substituted by protons. They crystallize in the space groups *P*2/*n* (**6a**), $P2_1/n$ (**6b**) and *P*-1 (**6c**), respectively. In the newly formed anions, the pnictogenido $[E(SiMe_3)_2]^-$ units bridge the Mo–Mo bond with E–Mo distances in the range between a single and a double bond (P–Mo: 2.4304(6) Å; As–Mo: 2.5170(3) Å; Sb–Mo: 2.6897(7) Å). The pnictogen atom features a distorted tetrahedral geometry. The Mo–Mo distances (**6a**: 3.1890(5) Å; **6b**: 3.2445(3) Å; **6c**: 3.2598(8) Å) are dramatically increased compared to the starting material **A** (2.4477(12) Å)[23] reasoning that the original triple bond is completely degraded and only an elongated single bond between the molybdenum atoms is left. Additionally, the Mo–Mo distances increase from the lighter to the higher pnictogen elements as expected. Compared to its derivative **D**, compound **6a** shows a similar Mo–Mo distance, but slightly elongated Mo–P bonds (**D**: 2.375(2)–2.378(2) Å). This is caused by the sterically more demanding $SiMe_3$ groups in contrast to the P-bound hydrogen atoms of **D**. A similar derivative of the arsenic compound **6b** is not known yet, but a related structural motif can be found in the neutral compound $[\{CpMo(CO)_2\}_2(\mu\text{-}H)(\mu\text{-}AsH_2)]$ with a bridging $[AsH_2]^-$ unit instead of $[As(SiMe_3)_2]^-$. Interestingly, **6c** is the first crystallographically characterized compound with a stibenido unit bridging a dimolybdenum fragment. And, although the solid-state structure of the bismuth derivative **6d** could not be determined, it probably reveals the same constitution, which is unprecedented for bismuth.

The electronic structures of **6a**-**d** have been investigated by DFT calculations, which are in excellent agreement with the experimentally determined geometric parameters, especially the elongated Mo-Mo distances. Although the Mo-Mo distances in **6a**-**d** are longer than in the corresponding **Mo_2EE'** derivatives **1**–**5**, the Wiberg bond orders in Löwdin orthogonalized basis are only slightly lower (for example: Mo-Mo 3.199 Å, WBI 0.45 in **6a** vs. Mo-Mo 3.048 Å, WBI 0.53 in **1**), indicating the presence of an elongated Mo-Mo single bond. This is also substantiated by the Intrinsic Bonding Orbitals, which show the presence of a Mo-Mo bond, although with additional orbital contribution from the CO groups (see Fig. S34 in the SI).

Besides making the novel hetero-dipnictogen complexes **3a**–**5** accessible, the synthetic strategy reported herein also allows to introduce substituted Cp ligands, such as *tert*-butylcyclopentadienyl (Cp'), to vary the solubility and the electronic as well as the steric properties of the complexes. This might be crucial for further reactivity studies. The following complexes were synthesized by using $[Cp'Mo(CO)_2]_2$ as starting material exemplifying $[\{Cp'Mo(CO)_2\}_2(\mu,\eta^2:\eta^2$-$\mathbf{As_2})]$ (**7**), $[\{Cp'Mo(CO)_2\}_2(\mu,\eta^2:\eta^2$-$\mathbf{Sb_2})]$ (**8**) and $[\{Cp'Mo(CO)_2\}_2(\mu,\eta^2:\eta^2$-**AsSb**$)]$ (**3b**).

The complexes **7** and **8** had already been synthesized by our group in the past,[8b] even though with a remarkably low yield hampering the investigation of further reactivity. Nonetheless, they had already proved to be suitable starting materials for building different anionic pnictogen frameworks upon reduction.[8b] This shows the necessity of making these compounds available in a larger scale, which can be achieved *via* the new synthetic route. That way, the yields of the complexes **7** (5.4 % → 55 %) and **8** (6.0 % → 29 %) can be dramatically increased and also the unprecedented compound **3b** can be obtained in a remarkably good yield of 49 %.

Interestingly, the ^1H NMR spectrum of **3b** (in contrast to the spectra of **7** and **8**) shows three multiplets in a ratio of 1:2:1 for the aromatic protons instead of the expected two triplets, which indicates that the protons in 2,5 and 3,4 position, respectively, are not chemical or magnetical equivalent in **3b**. This is confirmed by $^{13}C\{^1H\}$ NMR spectroscopy, where four singlets instead of two for the proton bound C atoms of the Cp' ring are observed.

Furthermore, orange red crystals suitable for X-ray diffraction of the complexes **3b**, **7** and **8** could be obtained by cooling saturated CH_2Cl_2 solutions from room temperature to −30 °C. Their solid-state structures (*cf.* Figure 3 for **3b**) show tetrahedral Mo_2EE' cores, which are almost identical to their Cp congeners.

3.3 Conclusion

We developed a new and easy one-pot synthesis of air-stable tetrahedral dimolybdenum dipnictogen complexes, which enables not only an impressive yield improvement (see Table 1) for the already known hetero-dipnictogen complexes $[\{CpMo(CO)_2\}_2(\mu,\eta^2:\eta^2$-**PE**$)]$ (E = As (**1**), Sb (**2**)) and the homo-dipnictogen complexes $\mathbf{Mo_2E_2}$ (E = P, As, (Sb), Bi), but, more importantly, also gives access to unprecedented complexes containing the heavier hetero-dipnictogen ligands **AsSb** (**3**), **AsBi** (**4**) and **SbBi** (**5**). Now, these syntheses can also be carried out in a multigram scale. The complexes **3**–**5** extend the very rare class of E_n ligand complexes of the heavy pnictogen elements and the exotic tetrahedrane analogues, with all of them featuring very rare covalent bonds between two different heavy pnictogen atoms as well as representing the first ever examples in which these bonds can be stabilized without any organic substituents. Therefore, these compounds can be understood as the complexes of the exotic diatomic As≡Sb, As≡Bi and Sb≡Bi molecules with reduced E–E' bond order, which are the heavy hetero-pnictogen congeners of N_2. Within that, compound **3** contains the very first As–Sb bond with a multiple bond character.

The intermediates $M[\{CpMo(CO)_2\}_2\{\mu\text{-}E(SiMe_3)_2\}]$ (M = Li, K; E = P (**6a**), As (**6b**), Sb (**6c**)) could also be crystallographically characterized revealing anionic $[E(SiMe_3)_2]^-$ units bridging a dimolybdenum fragment. The salt **6c** contains the first crystallographically characterized single stibenido unit of this kind.

Moreover, the new synthesis allowed to introduce the bulkier *tert*-butylcyclopentadienyl (Cp') ligand to vary the steric and electronic properties and enhance the solubility, which expands the possibilities of further reactivity studies. Overall, the newly synthesized E_n ligand complexes in large scale can be used as promising precursors for the synthesis of extended E_n ligand frameworks upon oxidation or reduction. Furthermore, due to the lack of Sb_n and Bi_n ligand complexes, the almost unexplored coordination behaviour of these compounds towards coinage and other transition metals can now be investigated.

3.4 Supporting Information

3.4.1 General remarks

All manipulations were carried out under an inert atmosphere of dried nitrogen/argon using standard Schlenk and glovebox techniques. The starting materials $[CpMo(CO)_2]_2$,[24] $[Cp'Mo(CO)_2]_2$,[25] $LiP(SiMe_3)_2$,[26] $LiAs(SiMe_3)_2$,[27] $MSb(SiMe_3)_2$ (M = Li, K),[28] $KBi(SiMe_3)_2$[29] and $NaPH_2$[30] were synthesized *via* the respective literature procedures. The reagents PCl_3, $AsCl_3$, $SbCl_3$, $BiCl_3$ and the crown-ethers (12-crown-4 and 18-crown-6) are commercially available and were used after purification by distillation or sublimation, respectively. Solvents were freshly distilled under nitrogen after drying over CaH_2 (CH_2Cl_2, CD_2Cl_2), or over K or Na/K alloy (alkanes, THF = tetrahydrofuran). Dried solvents were also taken from a solvent purification system from MBraun. Silica for column chromatography was dried under vacuum at 200 °C for 7 days. NMR spectra were recorded on a Bruker Avance 300 MHz NMR spectrometer (^{1}H: 300.132 MHz, ^{31}P: 121.495 MHz, ^{13}C: 75.468 MHz) or a Bruker Avance 400 MHz NMR spectrometer (^{1}H: 400.130 MHz, ^{31}P: 161.976 MHz, ^{13}C: 100.613 MHz) with external references of $SiMe_4$ (^{1}H, ^{13}C) and H_3PO_4 (85%, ^{31}P). The chemical shifts δ are presented in parts per million (ppm) and coupling constants J in Hz. The measurements were performed at 300 K. LIFDI-MS and FD-MS spectra were measured on a Jeol AccuTOF GCX by the mass spectrometry department of the University of Regensburg. The respective molecular ion peaks of the desired products **1**–**8** are assigned as [$\mathbf{M}^+$] in each case. IR spectra were recorded either as solids using a ThermoFisher Nicolet iS5 FT-IR spectrometer with an iD7 ATR module and an ITX Germanium or ITX Diamond crystal, or grinded together with dried KBr and pressed to pellets and measured on a VARIAN FTS-800 FT-IR spectrometer. Elemental analyses (EA) were performed by the micro analytical laboratory of the University of Regensburg.

3.4.2 Experimental details

Synthesis of the complexes of the type [{CpMo(CO)$_2$}$_2$(μ,η^2:η^2-EE')] (EE' = PAs (1), PSb (2), AsSb (3a), AsBi (4), SbBi (5)) and [{CpMo(CO)$_2$}$_2$(μ,η^2:η^2-E$_2$)] (E = P ("Mo$_2$P$_2$"), As ("Mo$_2$As$_2$"), Sb ("Mo$_2$Sb$_2$"), Bi ("Mo$_2$Bi$_2$")) – General procedure

The synthesis for all complexes of the type [{CpMo(CO)$_2$}$_2$(μ,η^2:η^2-EE')] are similar and, therefore, a general procedure is provided. The data (amount of substances, colour changes, work-up methods and yields) for the specific reactions are given in Table S1.

Dark orange-brown solutions of [Cp(CO)$_2$Mo]$_2$ (**A**) in 30 mL THF were reacted with LiP(SiMe$_3$)$_2$ (**E1**), LiAs(SiMe$_3$)$_2$ (**E2**), KSb(SiMe$_3$)$_2$ (**E3**) or KBi(SiMe$_3$)$_2$ (**E4**), respectively, in 10 mL THF leading to colour changes to dark greenish red (**E1**, **E2**), dark greenish brown (**E3**) or dark bronze-coloured (**E4**). These solutions were stirred for 30 minutes. Subsequently, E'Cl$_3$ (E' = P, As, Sb, Bi) was added, either as pure liquid (PCl$_3$ and AsCl$_3$) or dissolved in 10 mL THF (SbCl$_3$ and BiCl$_3$), and stirred for another 30 minutes. After evaporation of the solvent, the residue was mixed with silica, redissolved in 10 mL CH$_2$Cl$_2$ and evaporated to dryness. The free-flowing powder was subjected to a column chromatography (silica, 20x4 cm). Elution with a mixture of *n*-hexane and toluene (3:1) leads to a orange red (**1**, **2**), red (**3a**) or dark red (**4**, **5**) fraction containing the desired tetrahedral compounds. For **Mo$_2$P$_2$** and **Mo$_2$As$_2$** sometimes a small yellow fraction can be observed, which elutes already with pure *n*-hexane or *n*-pentane, containing the respective **MoE$_3$** compounds [CpMo(CO)$_2$(η^3-**E$_3$**)]. The solvent of the main fraction was removed *in vacuo* and the residue dried in vacuum for 3 hours. Crystals suitable for single crystal X-ray diffraction analyses could be obtained by cooling saturated CH$_2$Cl$_2$ solutions from room temperature to -30 °C.

Table S1: Data for the syntheses of the complexes **Mo$_2$P$_2$**, **Mo$_2$As$_2$**, **Mo$_2$Sb$_2$**, **Mo$_2$Bi$_2$**, **1**, **2**, **3a**, **4** and **5**.

Product	Amount of **A**	Amount of M**E**(SiMe$_3$)$_2$	Amount of **E'**Cl$_3$	Colour change after **2nd** reaction step	Column chromato-graphy	Yield
Mo$_2$P$_2$	5.60 g 12.9 mmol 1.0 eq.	Li**P**(SiMe$_3$)$_2$(thf)$_{1.6}$ 3.80 g 12.7 mmol 1.0 eq.	**P**Cl$_3$ 1.2 mL 13.7 mmol 1.1 eq.	dark orange red	orange fraction	3.56 g (7.2 mmol = 57 %)
Mo$_2$As$_2$	4.00 g 9.2 mmol 1.0 eq.	Li**As**(SiMe$_3$)$_2$(thf)$_{1.6}$ 3.10 g 9.0 mmol 1.0 eq.	**As**Cl$_3$ 0.8 mL 9.5 mmol 1.0 eq.	dark orange red	orange red fraction	2,7 g (4.7 mmol = 52 %)
Mo$_2$Sb$_2$	1.00 g 2.3 mmol 1.0 eq.	K**Sb**(SiMe$_3$)$_2$(thf)$_{0.4}$ 724 mg 2.15 mmol 0.95 eq.	**Sb**Cl$_3$ 525 mg 2.3 mmol 1.0 eq.	dark red	red fraction	526 mg (0.8 mmol 37 %)

Product	Amount of **A**	Amount of M**E**$(SiMe_3)_2$	Amount of **E'**Cl_3	Colour change after **2**nd reaction step	Column chromato-graphy	Yield
Mo_2Bi_2	2.00 g 4.57 mmol 1.0 eq.	K**Bi**$(SiMe_3)_2(thf)_{0.3}$ 1.90 g 4.95 mmol 1.1 eq.	**Bi**Cl_3 1.43 g 4.57 mmol 1.0 eq.	dark brown	brown fraction	965 mg (1.1 mmol = 25 %)
1 Method A	556 mg 1.28 mmol 1.2 eq.	Li**P**$(SiMe_3)_2(thf)_{1.6}$ 384 mg 1.28 mmol 1.2 eq.	**As**Cl_3 0.09 mL 1.07 mmol 1.0 eq.	dark orange red	orange red fraction	400 mg (0.74 mmol = 69 %)
1 Method B	3.30 g 7.6 mmol 1.0 eq.	Li**As**$(SiMe_3)_2(thf)_{1.6}$ 2.55 g 7.4 mmol 1.0 eq.	**P**Cl_3 0.7 mL 8.0 mmol 1.1 eq.	dark orange red	orange red fraction	1.99 g (3.69 mmol = 50 %)
2 Method A	1.30 g 3.0 mmol 1.0 eq.	Li**P**$(SiMe_3)_2(thf)_{1.8}$ 942 mg 3.0 mmol 1.0 eq.	**Sb**Cl_3 684 mg 3.0 mmol 1.0 eq.	dark orange red	orange red fraction	400 mg (0.74 mmol = 69 %)
2 Method B	434 mg 1.0 mmol 1.0 eq.	K**Sb**$(SiMe_3)_2(thf)_{1.8}$ 437 mg 1.0 mmol 1.0 eq.	**P**Cl_3 87 mL 1.0 mmol 1.0 eq.	dark orange red	orange red fraction	105 mg (0.18 mmol = 18 %)
3a Method A	434 mg 1.0mmol 1.0 eq.	Li**As**$(SiMe_3)_2(thf)_{1.8}$ 358 mg 1.0 mmol 1.0 eq.	**Sb**Cl_3 181 mg 1.0 mmol 1.0 eq.	dark red	red fraction	298 mg (0.51 mmol = 51 %)
3a Method B	152 mg 0.35 mmol 1.0 eq.	K**Sb**$(SiMe_3)_2$ 107 mg 0.35 mmol 1.0 eq.	**As**Cl_3 0.03 mL 0.35 mmol 1.0 eq.	dark red	red fraction	136 mg (0.22 mmol = 63 %)
4 Method A	174 mg 0.4 mmol 1.0 eq.	Li**As**$(SiMe_3)_2(thf)_{1,8}$ 143 mg 0.4 mmol 1.0 eq.	**Bi**Cl_3 126 mg 0.4 mmol 1.0 eq.	dark red	dark red	166 mg (0.23 mmol = 58 %)
4 Method B	**A** + K**Bi**$(SiMe_3)_2(thf)_{0.3}$ + **As**Cl_3 unsuccessful (only traces of **Mo_2As_2** and **$MoAs_3$**)!					
5 Method A	217 mg 0.50 mmol 1.0 eq.	K**Sb**$(SiMe_3)_2(thf)_{0.4}$ 168 mg 0.50 mmol 1.0 eq.	**Bi**Cl_3 173 mg 0.55 mmol 1.1 eq.	dark red brown	dark red fraction	136 mg (0.22 mmol = 63 %)
5 Method B	**A** + K**Bi**$(SiMe_3)_2(thf)_{0.3}$ + **Sb**Cl_3 unsuccessful!					
Mo_2PBi	**A** + Li**P**$(SiMe_3)_2(thf)_{1.6}$ + **Bi**Cl_3 unsuccessful! **A** + K**Bi**$(SiMe_3)_2(thf)_{0.3}$ + **P**Cl_3 unsuccessful!					

Analytical Data:

Mo_2P_2:[31]

^1H NMR (CD_2Cl_2):	δ/ppm = 5.20 (s, Cp)
^{31}P NMR (CD_2Cl_2):	δ/ppm = –43.7 (s, P_2), –351.9 (traces, [CpMo(CO)$_2$(η^3-**P_3**)])

Mo_2As_2:[32]

^1H NMR (acetone-d_6):	δ/ppm = 5.36 (s, Cp)

Mo_2Sb_2:[33]

EA:	calcd. (%) for [$C_{14}H_{10}Mo_2O_4Sb_2$]:	C: 24.81, H: 1.49
	found (%):	C: 24.92, H: 1.47
FD-MS (THF):	Cation *m/z* (%): 677.57 (100) [**M^+**]	

Mo_2Bi_2:[34]

FD-MS (toluene):	Cation *m/z* (%): 851.79 (100) [**M^+**]

Mo_2PAs (**1**):[35]

^1H NMR (CD_2Cl_2):	δ/ppm = 5.20 (s, Cp)	
^1H NMR (C_6D_6):	δ/ppm = 4.51 (s, Cp)	
^{31}P NMR (C_6D_6/CD_2Cl_2):	δ/ppm = 30.2 (s, **1**),	
^{31}P NMR (C_6D_6):	δ/ppm = 34.5 (s, **1**), –44.5 (traces, **Mo_2P_2**)	
^{31}P NMR (CD_2Cl_2):	δ/ppm = 30.1 (s, **1**), –43.2 (traces < 5 %, **Mo_2P_2**)	
$^{13}C\{^1H\}$ NMR (CD_2Cl_2):	δ/ppm = 85.87 (s, Cp), 226.37 (s, CO), 226.85 (s, CO)	
ESI-MS (MeCN/H_2O):	Cation *m/z* (%) = 485.8 (33) [**M**$^+$–2·CO], 457.8 (100) [**M**$^+$–3·CO], 429.8 (55) [**M**$^+$–4·CO]	
EA:	calcd. (%) for [$C_{14}H_{10}Mo_2O_4PAs$]:	C: 30.90, H: 1.85
	found (%):	C: 30.80, H: 1.95
IR (KBr):	$\tilde{\nu}$/cm^{-1} = 2058 (w), 1946 (vs), 1900 (vs), 1420 (w), 1060 (vw), 1007 (w), 819 (m), 567 (m), 531 (m), 498 (m), 456 (m)	

Mo_2PSb (**2**):[35]

^1H NMR (CD_2Cl_2):	δ/ppm = 5.18 (s, Cp), 5.23 (traces, Cp of **Mo_2P_2**)	
^1H NMR ($CDCl_3$):	δ/ppm = 5.15 (s, Cp), 5.21 (traces, Cp of **Mo_2P_2**)	
^1H NMR (C_6D_6):	δ/ppm = 4.48 (s, Cp), 4.54 (traces, Cp of **Mo_2P_2**)	
^{31}P NMR (CD_2Cl_2):	δ/ppm = 90.7 (s, **1**), –43.1 (traces < 5 %, **Mo_2P_2**)	
^{31}P NMR ($CDCl_3$):	δ/ppm = 90.9 (s, **1**), –47.0 (traces < 3 %, **Mo_2P_2**)	
^{31}P NMR (C_6D_6):	δ/ppm = 98.8 (s, **1**), –44.4 (traces < 5 %, **Mo_2P_2**)	
EA:	calcd. (%) for [$C_{14}H_{10}Mo_2O_4PSb$]:	C: 28.63, H: 1.72
	found (%):	C: 29.20, H: 1.80
FD-MS (toluene):	Cation *m/z* (%): 585.75 (100) [**M^+**]	

"Mo_2PBi":

FD-MS (toluene):	Cation *m/z* (%): 495.77 (100) [**Mo_2P_2**], 467.82 (68) [**Mo_2P_2**–CO], several unidentified decomposition products
$^{31}P\{^1H\}$ NMR (CD_2Cl_2):	δ/ppm = –43.3 (**Mo_2P_2**)

Mo_2AsSb (**3a**):

^1H NMR ($CDCl_3$):	δ/ppm = 5.11 (s, Cp), 5.14/5.30 (traces, Cp of **Mo_2As_2/Mo_2Sb_2**)
$^{13}C\{^1H\}$ NMR ($CDCl_3$):	δ/ppm = 83.51 (s, Cp), 226.33 (s, CO), 226.93 (s, CO)
EA:	calcd. (%) for [$C_{14}H_{10}Mo_2O_4AsSb$]·(toluene)$_{0.06}$: C: 27.22, H: 1.66
	found (%): C: 27.34, H: 1.62
FD-MS (toluene):	Cation *m/z* (%): 629.70 (100) [**M^+**], 677.67 (3) [**Mo_2Sb_2**], 583.71 (14) [**Mo_2As_2**]

Mo_2AsBi (**4**):

^1H NMR (CD_2Cl_2):	δ/ppm = 5.13 (s, Cp)
$^{13}C\{^1H\}$ NMR (CD_2Cl_2):	δ/ppm = 83.08 (s, Cp), 84.53 (s, traces, Cp of **Mo_2As_2**), 225.35 (s, CO), 226.49 (s, CO)
EA:	calcd. (%) for [$C_{14}H_{10}Mo_2O_4AsBi$]·(toluene)$_{0.05}$: C: 23.85, H: 1.45
	found (%): C: 23.95, H: 1.30
FD-MS (toluene):	Cation *m/z* (%): 717.74 (100) [**M^+**], 583.65 (5) [**Mo_2As_2**]

Mo_2SbBi (**5**):

^1H NMR (CD_2Cl_2):	δ/ppm = 5.07 (traces, s, Cp of **Mo_2Bi_2**) 5.09 (s, Cp), 5.10 (traces, s, Cp of **Mo_2Sb_2**)
$^{13}C\{^1H\}$ NMR (CD_2Cl_2):	δ/ppm = 81.49 (s, traces, Cp of **Mo_2Bi_2**), 81.93 (s, Cp), 82.50 (s, traces, Cp of **Mo_2Sb_2**), 226.31 (s, CO), 226.92 (s, CO)
EA:	calcd. (%) for [$C_{14}H_{10}Mo_2O_4SbBi$]·(toluene)$_{0.15}$: C: 23.21, H: 1.45
	found (%): C: 23.26, H: 1.30
FD-MS (toluene):	Cation *m/z* (%): 763.65 (100) [**M^+**], 677.57 (31) [**Mo_2Sb_2**]

Synthesis of 1 using $NaPH_2$

A dark orange-brown solution of [$Cp(CO)_2Mo]_2$ (**A**; 2.0 g, 4.61 mmol, 1 eq.) in 30 mL THF was reacted with $NaPH_2$ (280 mg, 5.00 mmol, 1 eq.) in 50 mL THF leading to a colour change to dark purple. The solution was stirred for 30 minutes. Subsequently, $AsCl_3$ (0.45 mL, 4.60 mmol, 1 eq.) was added as a pure liquid. The resulting orange suspension was stirred for another 15 hours. After evaporation of the solvent, the residue was mixed with silica, redissolved in 10 mL CH_2Cl_2 and evaporated to dryness. The free-flowing powder was subjected to a column chromatography (silica, 30 x 3.5 cm). Elution with a mixture of *n*-hexane and CH_2Cl_2 (1:1) leads to an orange red fraction containing **1**. An additional orange fraction could be observed, which could not be further characterized. The solvent was removed and the residue dried in vacuum for 3 hours.

Yield	398 mg (0.75 mmol, 16.4 %)
^{31}P NMR (C_6D_6)	δ/ppm = 33.7 (traces of [$\{CpMo(CO)_2\}_2(\mu\text{-}H)(\mu\text{-}PH_2)$]), 34.7 (s, **1**)

Synthesis of the complexes [{Cp'Mo(CO)$_2$}$_2$(μ,η^2:η^2-EE')] (EE' = AsSb (3b), As$_2$ (7), Sb$_2$ (8); Cp' = η^5-C$_5$H$_4$^{t}Bu) – General procedure

The synthesis for the complexes **3b**, **7** and **8** are similar and, therefore, a general procedure is provided. The data (amount of substances, colour changes, work-up method and yield) for the specific reactions are given in Table S2.

Dark orange-brown solutions of [Cp'(CO)$_2$Mo]$_2$ in 30 mL THF were reacted with LiAs(SiMe$_3$)$_2$ (**E2**) or LiSb(SiMe$_3$)$_2$ (**E3**), respectively, in 10 mL THF leading to colour changes to dark greenish red (**E2**) or dark greenish brown (**E3**). These solutions were stirred for 30 minutes. Subsequently, E'Cl$_3$ (E' = As, Sb) was added, either as pure liquid (AsCl$_3$) or dissolved in 10 mL THF (SbCl$_3$), and stirred for another 30 minutes. After evaporation of the solvent, the residue was mixed with silica, redissolved in 10 mL CH$_2$Cl$_2$ and evaporated to dryness. The free-flowing powder was subjected to a column chromatography (silica, 20x4 cm). Elution with a mixture of *n*-hexane and toluene (5:1) leads to a fraction containing the desired tetrahedral compounds. In the case of **7** a yellow first fraction can be observed, which eluates already with pure *n*-pentane, containing the respective **MoE$_3$** compound [Cp'Mo(CO)$_2$(η^3-**As$_3$**)]. The solvent was removed *in vacuo* and the residue dried in vacuum for 3 hours. Crystals suitable for single crystal X-ray diffraction analyses could be obtained by cooling saturated CH$_2$Cl$_2$ solutions from room temperature to -30 °C.

Table S2: Data for the syntheses of the complexes **3b**, **7** and **8**; dme = dimethoxyethane.

Product	Amount of **[Cp'(CO)$_2$Mo]$_2$**	Amount of M**E**(SiMe$_3$)$_2$	Amount of **E'Cl$_3$**	Colour change after **2nd** reaction step	Column chroma-to-graphy	Yield
3b	500 mg 0.9 mmol 1.0 eq.	Li**As**(SiMe$_3$)$_2$(thf)$_{2.3}$ 355 mg 0.9 mmol 1.0 eq.	**Sb**Cl$_3$ 204 mg 0.9 mmol 1.0 eq.	dark orange red	dark red fraction	325 mg (0.44 mmol = 49 %)
7	2.00 g 3.66 mmol 1.0 eq.	Li**As**(SiMe$_3$)$_2$(thf)$_{2.0}$ 1.44 g 3.84 mmol 1.05 eq.	**As**Cl$_3$ 0.32 mL 3.84 mmol 1.05 eq.	dark orange red	dark red fraction	1.40 g (2.01 mmol = 55 %)
8	500 mg 0.9 mmol 1.0 eq.	Li**Sb**(SiMe$_3$)$_2$(dme) 328 mg 0.9 mmol 1.0 eq.	**Sb**Cl$_3$ 226 mg 1.0 mmol 1.1 eq.	dark orange red	dark red fraction	208 mg (0.26 mmol = 29 %)

Analytical Data:

(Cp')Mo$_2$AsSb (**3b**):

^{1}H NMR (CD_2Cl_2): δ/ppm = 1.27 (s, *t*Bu, 18H), 5.00 (m, Cp, 2H), 5.06 (m, Cp, 4H), 5.15 (m, Cp, 2H)

^{13}C{^{1}H} NMR (CD_2Cl_2): δ/ppm = 31.77 (s, *t*Bu (quart.)), 32.03 (s, *t*Bu (Me)), 81.63 (s, Cp (C-H)), 82.74 (s, Cp (C-H)), 83.11 (s, Cp (C-H)), 83.90 (s, Cp (C-H)), 118.26 (s, Cp (quart.)), 228.03 (s, CO), 228.51 (s, CO)

EA: calcd. (%) for [$C_{22}H_{26}Mo_2O_4AsSb$]: C: 35.56, H: 3.53
found (%): C: 35.70, H: 3.41

FD-MS (toluene): Cation *m/z* (%): 741.79 (100) [**M**$^+$], 695.81 (9) [$Cp'_2(CO)_4Mo_2As_2$]

(Cp')Mo$_2$As$_2$ (**7**):

^{1}H NMR (C_6D_6): δ/ppm = 1.06 (s, *t*Bu, 18H), 4.61 (t, 2.4 Hz, Cp, 4H), 4.75 (t, 2.4 Hz, Cp, 4H)

^{13}C{^{1}H} NMR (C_6D_6): δ/ppm = 31.3 (s, *t*Bu (quart.)), 31.8 (s, *t*Bu (Me), 83.0 (s, Cp (C-H)), 84.8 (s, Cp (C-H)), 119.0 (s, Cp (quart.)), 228.5 (s, CO)

EA: calcd. (%) for [$C_{22}H_{26}As_2Mo_2O_4$]: C: 37.96, H: 3.76
found (%): C: 37.42, H: 3.5

FD-MS (CH_2Cl_2): Cation *m/z* (%): 695.86 (100) [**M**$^+$]; 789.72 (58) [$Cp'_2Mo_2As_4(CO)_2$]

IR (ATR): $\tilde{\nu}$/cm^{-1} = 3098 (w), 2955 (m), 2864 (w), 1965 (vs), 1934 (vs), 1893 (vs), 1872 (vs), 1478 (m), 1461 (m), 1444 (w), 1398 (w), 1360 (m), 1269 (m), 1197 (w), 1148 (m), 1060 (w), 1040 (w), 1019 (w), 921 (w), 906 (w), 880 (w), 842 (m), 830 (m), 815 (s), 801 (s), 673 (w)

(Cp')Mo$_2$Sb$_2$ (8):

^{1}H NMR (C_6D_6):	δ/ppm = 1.08 (s, *t*Bu, 9H), 4.43 (t, 2.4 Hz, Cp, 2H), 4.75 (t, 2.4 Hz, Cp, 2H)
^{13}C{^{1}H} NMR (C_6D_6):	δ/ppm = 31.4 (s, *t*Bu (quart.)), 31.9 (s, *t*Bu (Me), 81.1 (s, Cp (*C*-H)), 81.4 (s, Cp (*C*-H)), 116.8 (s, Cp (quart.)), 228.7 (s, CO)
EA:	calcd. (%) for [{(C_9H_{13})(CO)$_2$Mo}$_2$Sb$_2$]: C: 33.45, H: 3.32 found (%): C: 33.61, H: 3.34
LIFDI-MS (toluene):	Cation *m/z* (%): 789.78 (100) [**M**$^+$]
IR (ATR):	$\tilde{\nu}$/cm^{-1} = 2983 (w), 2965 (w), 2943 (w), 2902 (w), 1918 (vs), 1890 (vs), 1866 (vs), 1842 (w), 1476 (w), 1462 (w), 1443 (w), 1400 (w), 1362 (w), 1269 (w), 1147 (w), 1058 (w), 1041 (w), 1020 (w), 904 (w), 883 (w), 842 (w), 831 (w), 818 (w), 804 (w), 682 (w)

Synthesis of the intermediates M[{CpMo(CO)$_2$}$_2${μ,η^2-E(SiMe$_3$)$_2$}] (6a-d) for X-ray analysis

The syntheses of crystalline sample of the salts **6a-d** are similar and, therefore, a general procedure is provided. The amount of substances, which are used in the specific reactions are given in Table S3.

Dark orange-brown solutions of [Cp(CO)$_2$Mo]$_2$ (**A**) in 5 mL THF were reacted with LiP(SiMe$_3$)$_2$ (**E1**), LiAs(SiMe$_3$)$_2$ (**E2**), KSb(SiMe$_3$)$_2$ (**E3**) or KBi(SiMe$_3$)$_2$ (**E4**), respectively, in 5 mL THF leading to colour changes to dark greenish red (**E1**, **E2**), dark greenish brown (**E3**) or dark bronze-coloured (**E4**). To this solution the respective crown-ether was added, either as a stock solution in DME (12-crown-4 for Li) or as a solid dissolved in 5 mL THF(18-crown-6 for K). After stirring for 30 minutes the solution was layered with *n*-hexane and stored at -30 °C under exclusion from light. After several days the products **6a-c** can be obtained as crystals suitable for single crystal X-ray diffraction. Crystallisation of **6d**, however, was unsuccessful, maybe due to low stability of **6d**.

For NMR characterization of **6a** compound **A** (84 mg, 0.2 mmol) and LiP(SiMe$_3$)$_2$(thf)$_{1.6}$ (65 mg, 0.2 mmol) are both solved in 15 mL toluene and the solutions were combined. After few minutes, **6a** precipitates and the slightly orange coloured mother liquid was decanted off. The residue was dried for 10 minutes and subjected to ^{1}H, ^{31}P and ^{31}P{^{1}H} NMR spectroscopy without further purification (Figure S15-S17).

Table S3: Data for the syntheses of the complexes **6a**-**d** for X-ray analysis.

Product	Amount of **A**	Amount of M**E**($SiMe_3$)$_2$	Amount of crown-ether
6a	87 mg 0.2 mmol 1.0 eq.	Li**P**($SiMe_3$)$_2$(thf)$_{2.3}$ 65 mg 0.2 mmol = 1.0 eq.	**12-crown-4** 0.25 mL of a 0.81 M solution in DME 0.2 mmol = 1.0 eq.
6b	87 mg 0.2 mmol 1.0 eq.	Li**As**($SiMe_3$)$_2$(thf)$_{1.6}$ 69 mg 0.2 mmol = 1.0 eq.	**12-crown-4** 0.25 mL of a 0.81 M solution in DME 0.2 mmol = 1.0 eq.
6c	87 mg 0.2 mmol 1.0 eq.	K**Sb**($SiMe_3$)$_2$ 61 mg 0.2 mmol = 1.0 eq.	**18-crown-6** 58 mg 0.2 mmol = 1.0 eq.
6d	87 mg 0.2 mmol 1.0 eq.	K**Bi**($SiMe_3$)$_2$(thf)$_{0.3}$ 83 mg 0.2 mmol = 1.0 eq.	**18-crown-6** 58 mg 0.2 mmol = 1.0 eq.

Analytical Data:

6a:

^{1}H NMR (CD_2Cl_2): δ/ppm = 0.28 (s, 9H, $SiMe_3$), 0.30 (s, 9H, $SiMe_3$), 1.79/3.66 (t, 16H, two THFs coordinating the lithium cation), 5.22 (s, 10H, Cp)

^{1}H NMR (CD_3CN): δ/ppm = 0.18 (s, 9H, $SiMe_3$), 0.20 (s, 9H, $SiMe_3$), 1.80/3.64 (t, 4H, half THF coordinating the lithium cation), 4.95 (s, 10H, Cp)

^{31}P{^{1}H} NMR (CD_2Cl_2): δ/ppm = 4.0 (s, P($SiMe_3$)$_2$), the signal is broadening in the proton coupled ^{31}P NMR spectrum upon coupling to the methyl groups of $SiMe_3$

^{31}P{^{1}H} NMR (CD_3CN): δ/ppm = 11.4 (s, P($SiMe_3$)$_2$)

^{31}P NMR (CD_3CN): δ/ppm = 11.4 (s, P($SiMe_3$)$_2$)

^{13}C{^{1}H} NMR (CD_3CN): δ/ppm = 4.07 (s, $SiMe_3$), 4.15 (s, $SiMe_3$), 25.83 (s, THF), 67.88 (s, THF), 89.54 (s, Cp); the signals of the CO ligands were too weak and could not be observed

3.4.3 NMR spectra

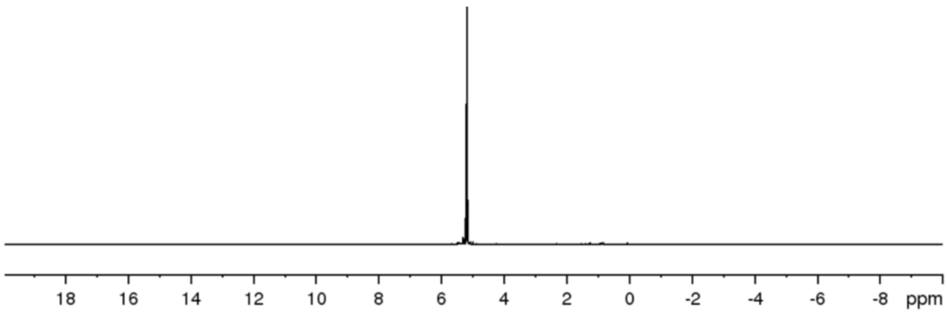

Figure S1: ^{1}H NMR spectrum of [(CpMo(CO)$_2$)$_2$(μ,η^2:η^2-PAs)] (**1**) in CD_2Cl_2.

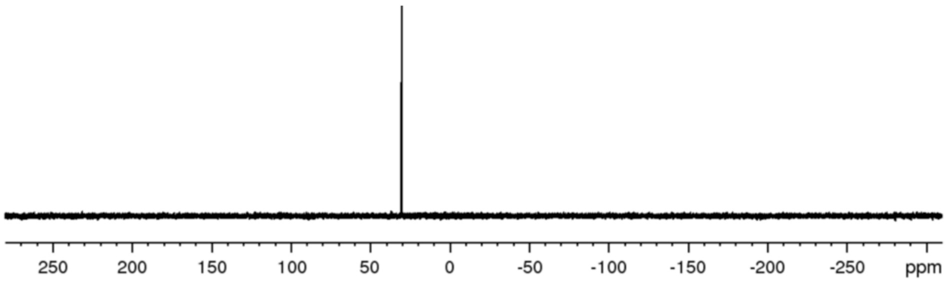

Figure S2: ^{31}P NMR spectrum of [(CpMo(CO)$_2$)$_2$(μ,η^2:η^2-PAs)] (**1**) in C_6D_6.

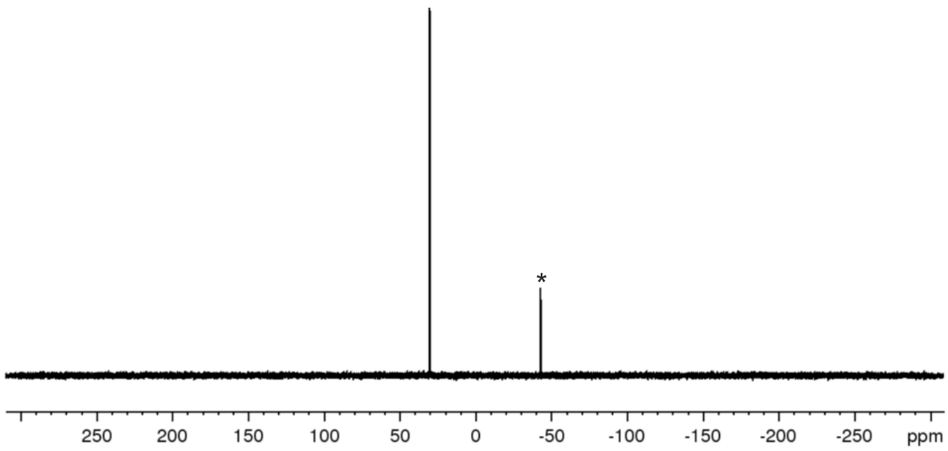

Figure S3: ^{31}P NMR spectrum of [(CpMo(CO)$_2$)$_2$(μ,η^2:η^2-PAs)] (**1**) in CD_2Cl_2 with additional formed traces of **Mo$_2$P$_2$** (*; < 5%).

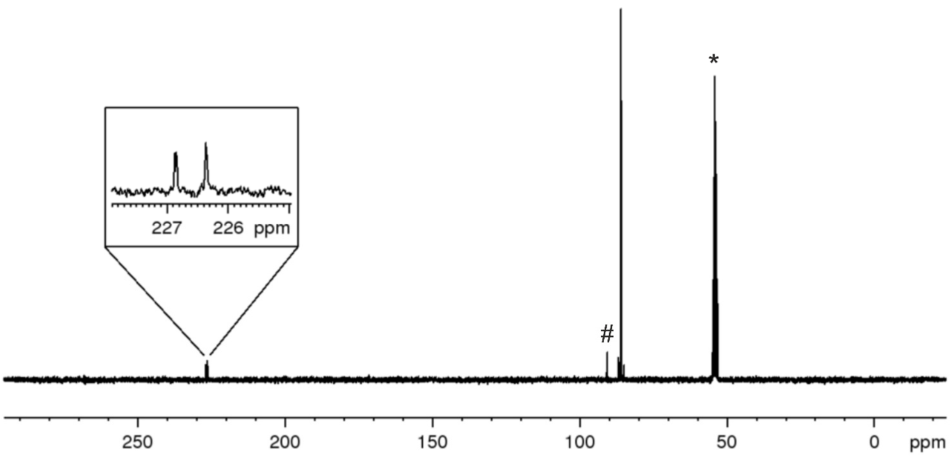

Figure S4: $^{13}C\{^{1}H\}$ NMR spectrum of [(CpMo(CO)$_2$)$_2$(μ,η^2:η^2-PAs)] (**1**) in CD_2Cl_2; * = CD_2Cl_2, # = Cp of traces of **Mo$_2$P$_2$**.

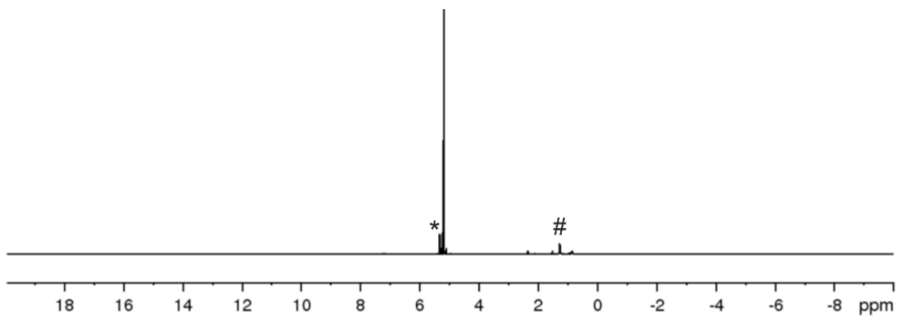

Figure S5: ^{1}H NMR spectrum of [(CpMo(CO)$_2$)$_2$(μ,η^2:η^2-PSb)] (**2**) in CD_2Cl_2; * = CD_2Cl_2, # = H grease.

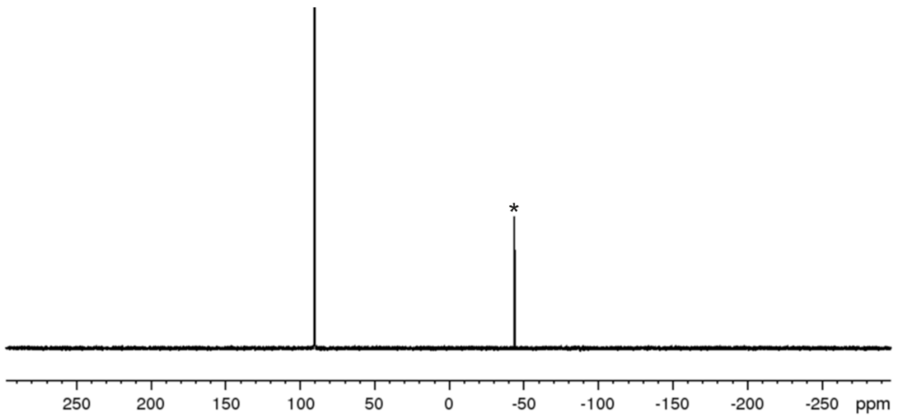

Figure S6: ^{31}P NMR spectrum of [(CpMo(CO)$_2$)$_2$(μ,η^2:η^2-PSb)] (**2**) in CD_2Cl_2; * = traces of **Mo_2P_2** (< 5 %).

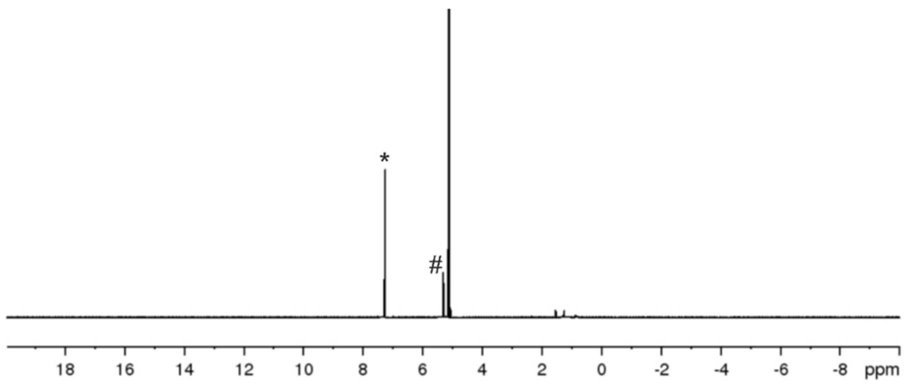

Figure S7: ^{1}H NMR spectrum of [(CpMo(CO)$_2$)$_2$(μ,η^2:η^2-AsSb)] (**3a**) in $CDCl_3$; * = $CDCl_3$, # = Cp of traces of **Mo_2As_2/Mo_2Sb_2**.

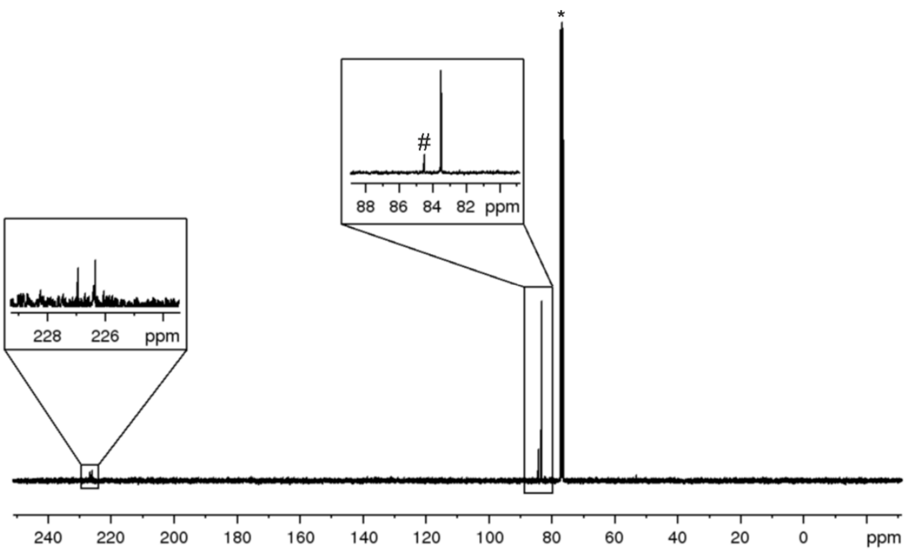

Figure S8: ^{13}C{^{1}H} NMR spectrum of [(CpMo(CO)$_2$)$_2$(μ,η^2:η^2-AsSb)] (**3a**) in $CDCl_3$; * = $CDCl_3$, # = Cp of traces of **Mo_2As_2/Mo_2Sb_2**.

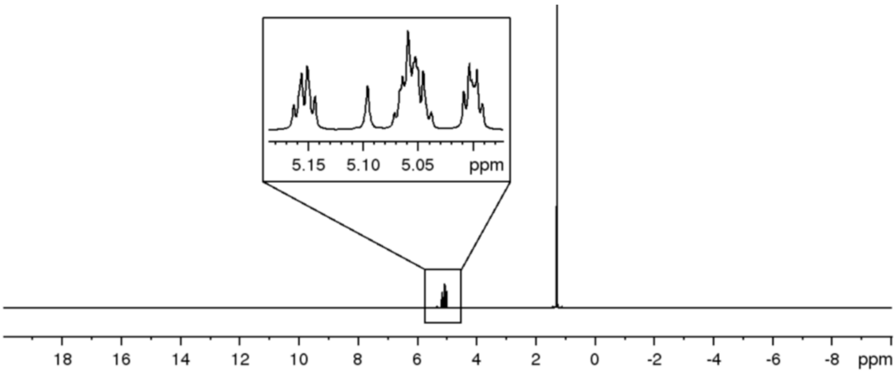

Figure S9: ^{1}H NMR spectrum of [(Cp'Mo(CO)$_2$)$_2$(μ,η^2:η^2-AsSb)] (**3b**) in CD_2Cl_2.

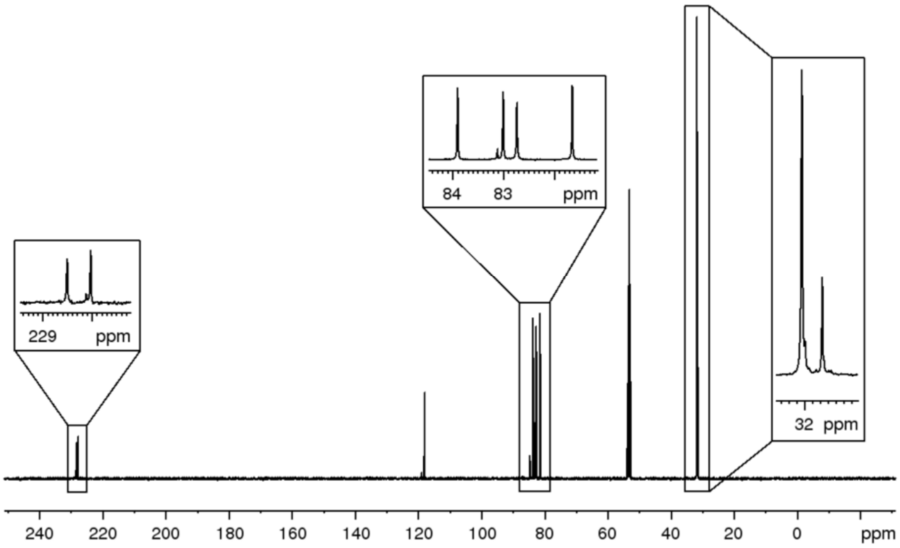

Figure S10: $^{13}C\{^{1}H\}$ NMR spectrum of [(Cp'Mo(CO)$_2$)$_2$(μ,η^2:η^2-AsSb)] (**3b**) in CD_2Cl_2.

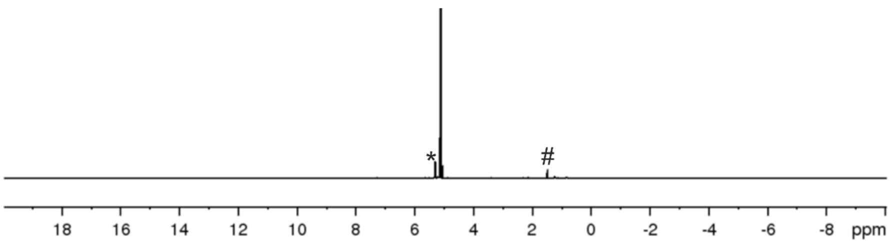

Figure S11: ^{1}H NMR spectrum of [(CpMo(CO)$_2$)$_2$(μ,η^2:η^2-AsBi)] (**4**) in CD_2Cl_2; * = CD_2Cl_2, # = H_2O.

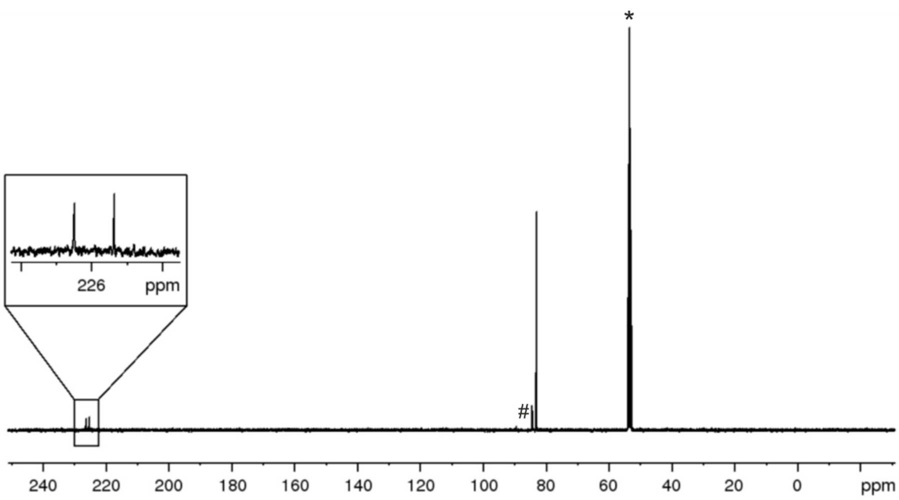

Figure S12: $^{13}C\{^{1}H\}$ NMR spectrum of [(CpMo(CO)$_2$)$_2$(μ,η^2:η^2-AsBi)] (**4**) in CD_2Cl_2; * = CD_2Cl_2, # = traces of **Mo_2As_2**.

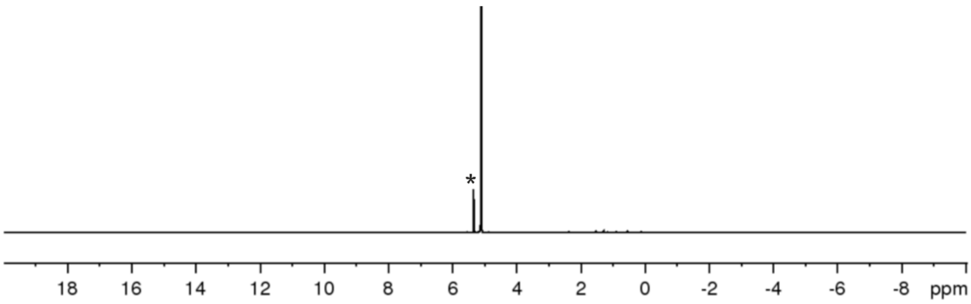

Figure S13: ^{1}H NMR spectrum of [(CpMo(CO)$_2$)$_2$(μ,η^2:η^2-SbBi)] (**5**) in CD_2Cl_2; * = CD_2Cl_2.

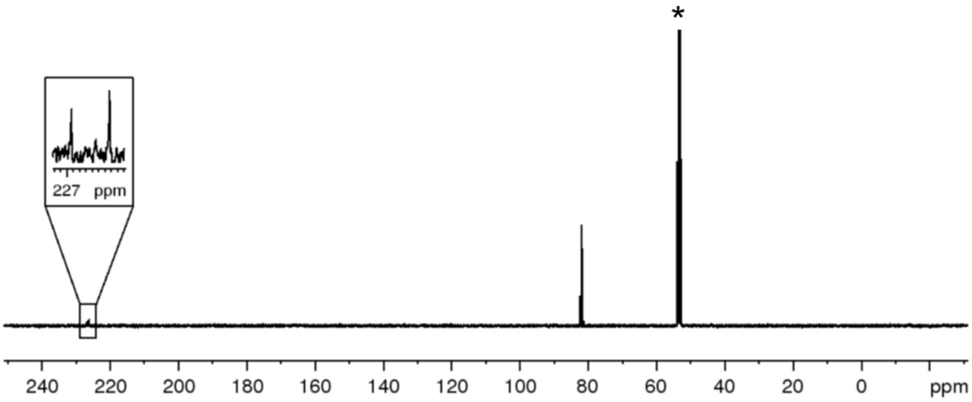

Figure S14: ^{13}C{^{1}H} NMR spectrum of [(CpMo(CO)$_2$)$_2$(μ,η^2:η^2-SbBi)] (**5**) in CD_2Cl_2; * = CD_2Cl_2.

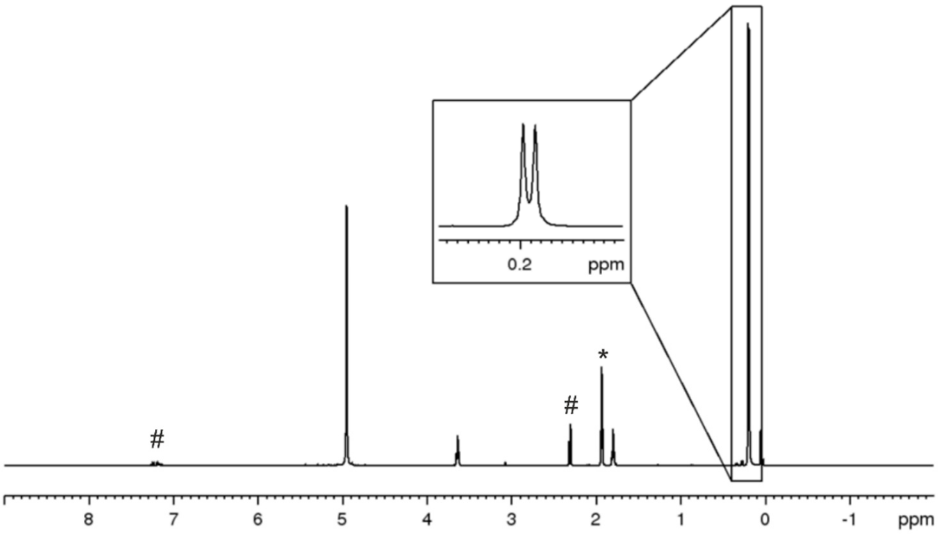

Figure S15: ^{1}H NMR spectrum of Li[{CpMo(CO)$_2$}$_2${μ,η^2-P(SiMe$_3$)$_2$}] (**6a**) in CD_3CN; * = CD_3CN, # = toluene.

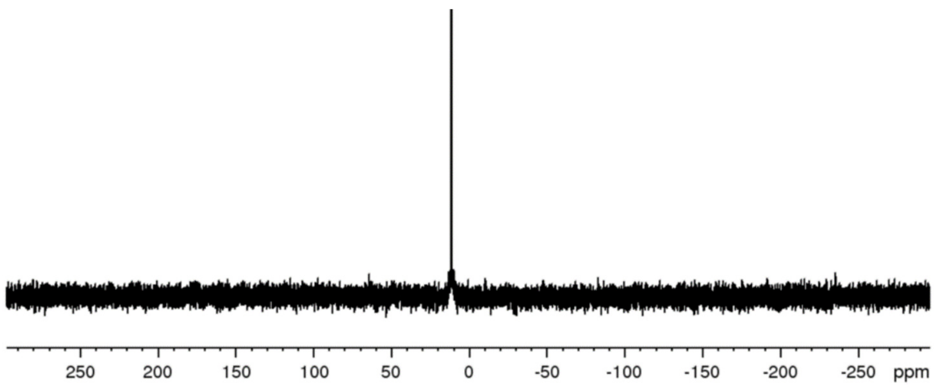

Figure S16: ^{31}P NMR spectrum of Li[{CpMo(CO)$_2$}$_2${μ,η^2-P(SiMe$_3$)$_2$}] (**6a**) in CD_3CN.

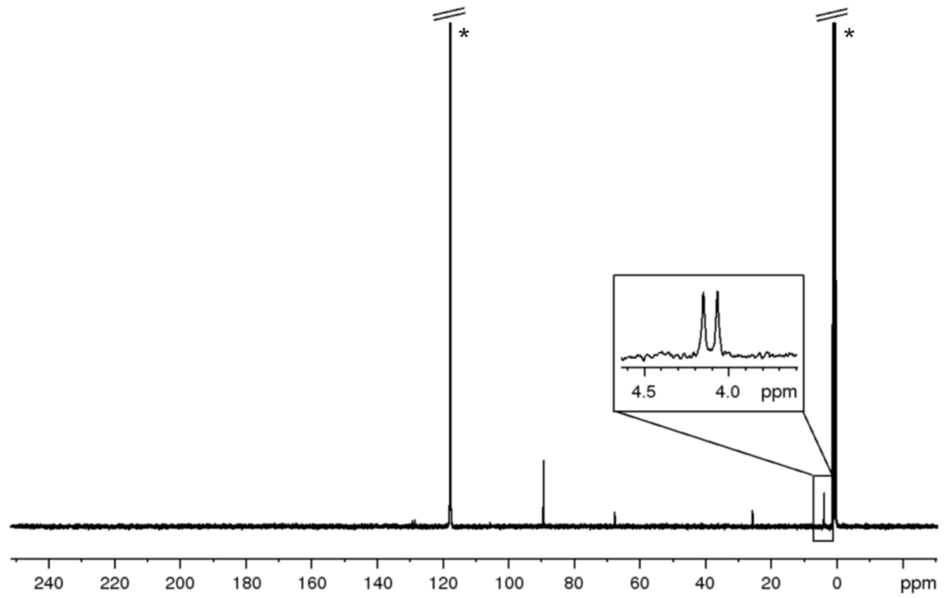

Figure S17: $^{13}C\{^{1}H\}$ NMR spectrum of Li[{CpMo(CO)$_2$}$_2${μ,η^2-P(SiMe$_3$)$_2$}] (**6a**) in CD_3CN; * = CD_3CN.

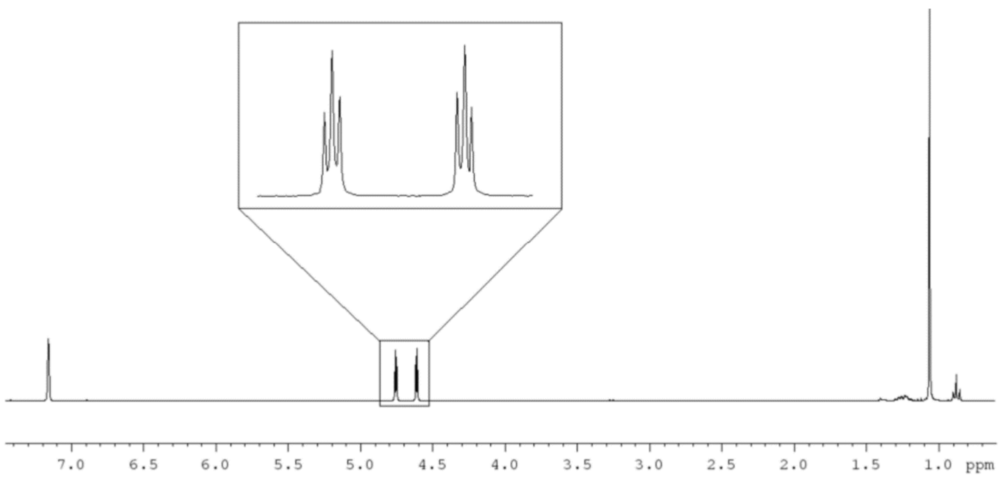

Figure S18: ^{1}H NMR spectrum of [(Cp'Mo(CO)$_2$)$_2$(μ,η^2:η^2-As$_2$)] (**7**) in C_6D_6.

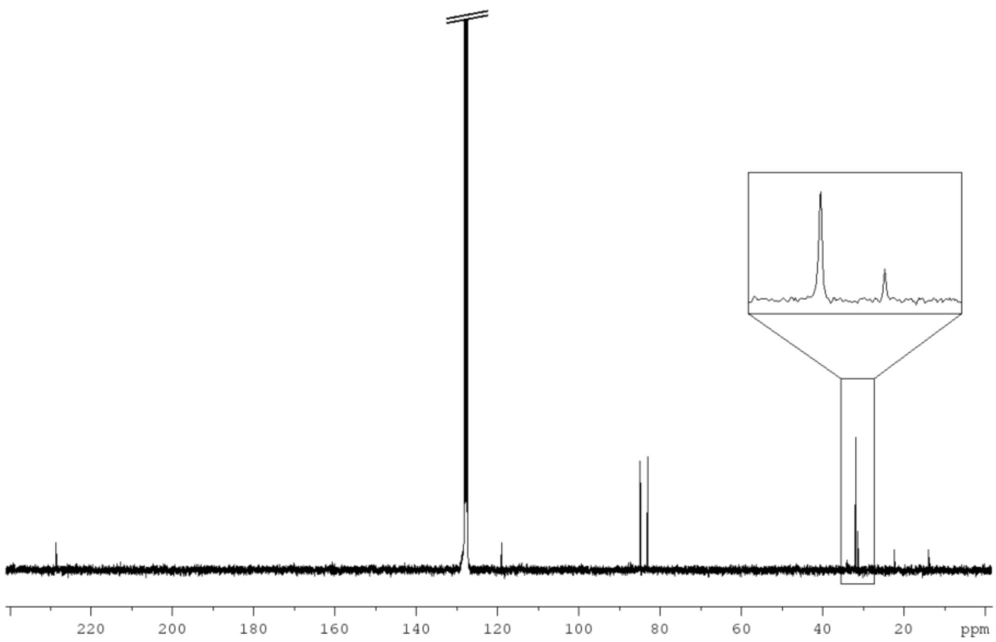

Figure S19: $^{13}C\{^{1}H\}$ NMR spectrum of [(Cp'Mo(CO)$_2$)$_2$(μ,η^2:η^2-As$_2$)] (**7**) in C_6D_6.

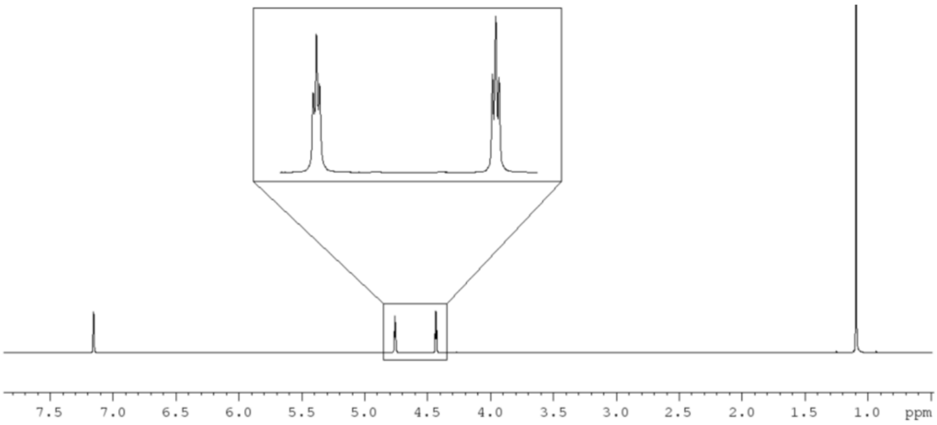

Figure S20: ^{1}H NMR spectrum of [(Cp'Mo(CO)$_2$)$_2$(μ,η^2:η^2-Sb$_2$)] (**8**) in C_6D_6.

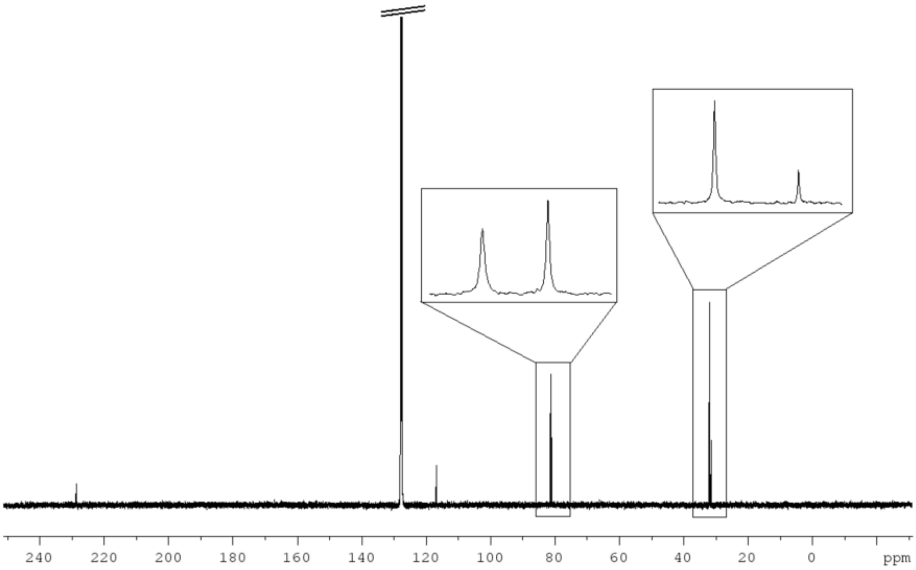

Figure S21: $^{13}C\{^{1}H\}$ NMR spectrum of [(Cp'Mo(CO)$_2$)$_2$(μ,η^2:η^2-Sb$_2$)] (**8**) in C_6D_6.

3.4.4 IR Spectra

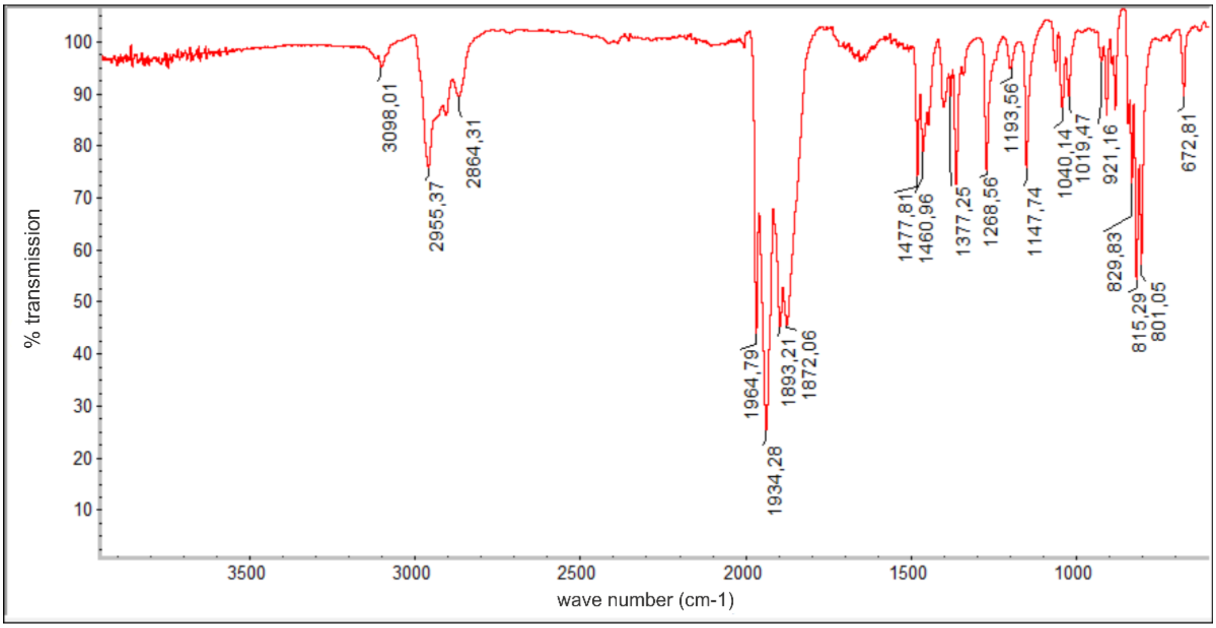

Figure S22: IR spectrum of [(Cp'Mo(CO)$_2$)$_2$(μ,η^2:η^2-As$_2$)] (**7**).

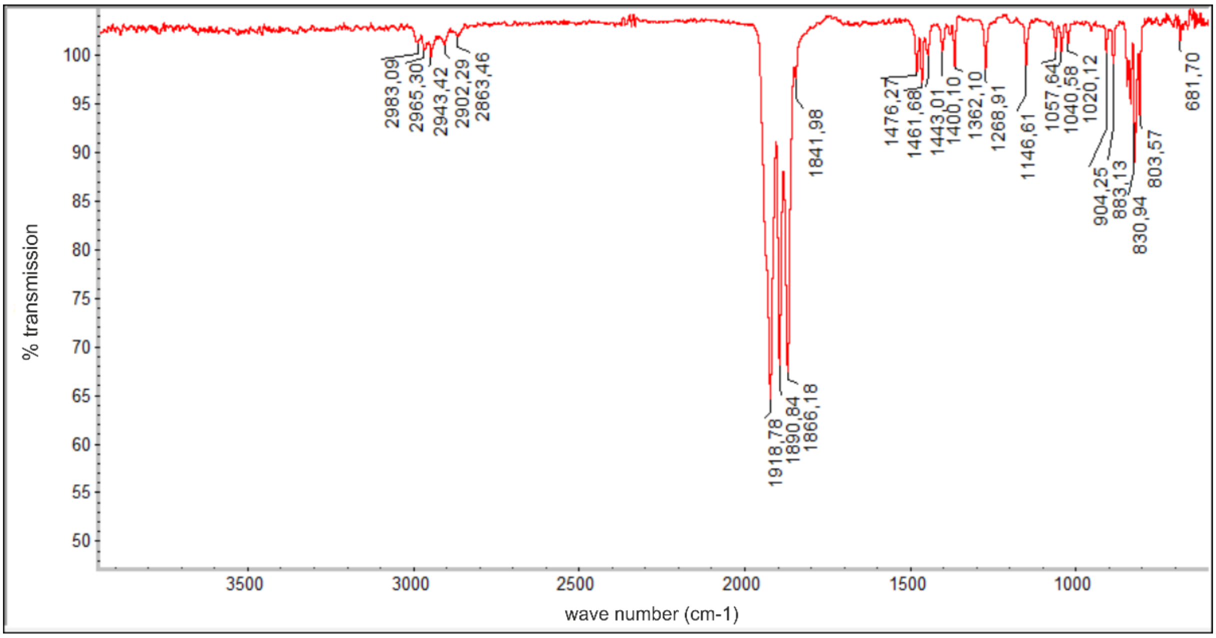

Figure S23: IR spectrum of $[(Cp'Mo(CO)_2)_2(\mu,\eta^2:\eta^2\text{-}Sb_2)]$ (**8**).

3.4.5 X-ray crystallography

All crystal manipulations were performed under mineral oil. The diffraction experiments were performed at 123 K on a Rigaku (former Agilent Technologies or Oxford Diffraction) Gemini Ultra with an AtlasS2 detector, on a GV50 diffractometer with a TitanS2 detector using Cu-K_α, Cu-K_β or Mo-K_α radiation. Crystallographic data together with the details of the experiments are given in Table S4 and Table S5. The cell determination, data reduction and absorption correction for all compounds were performed with the help of the CrysAlis PRO software.[36] All structures were solved by using the programs SHELXT[37] and Olex2.[38] The full-matrix least-squares refinement against F^2 was done using SHELXL[39] and Olex2.[38] If not stated otherwise, all atoms except hydrogen atoms were refined anisotropically. The H atoms were calculated geometrically and a riding model was used during the refinement process.

CIF files with comprehensive information on the details of the diffraction experiments and full tables of bond lengths and angles for **2**-**8** are deposited in Cambridge Crystallographic Data Centre (CCDC) under the deposition codes CCDC-2061901 (**2**), CCDC-2061902 (**3a**), CCDC-2061903 (**3b**), CCDC-2061904 (**4**), CCDC-2061905 (**5**), CCDC-2061906 (**6a**), CCDC-2061907 (**6b**), CCDC-2061908 (**6c**), CCDC-2061909 (**7**) and CCDC-2061910 (**8**).

Crystallographic Data for Compound **2** was already provided by Mays *et*. *al*. in 1998 under the CCDC deposition code CCDC-100650.[35]

Table S4: Crystallographic details for the compounds **2**,[40] **3a**, **3b**, **4**, and **5**.

	2[40]	**3a**	**3b**	**4**	**5**
formula	$C_{14}H_{10}O_4PMo_2Sb$	$C_{14}H_{10}AsMo_2O_4Sb$	$C_{22}H_{26}AsMo_2O_4Sb$	$C_{14}H_{10}O_4AsMo_2Bi$	$C_{14}H_{10}BiMo_2O_4Sb$
weight [g·mol^{-1}]	586.82	630.77	742.98	718.00	764.83
Temperature [K]	123	123	122.9(3)	123(1)	123(2)
crystal system	monoclinic	monoclinic	orthorhombic	monoclinic	monoclinic
space group	$P2/n$	$P2/n$	$P2_12_12$	$P2_1$	$I2/a$
a [Å]	13.4669(2)	13.5271(2)	15.0805(5)	8.8466(2)	16.6083(9)
b [Å]	7.5991(1)	7.6095(1)	10.1597(3)	7.8968(2)	7.6109(3)
c [Å]	15.7859(2)	15.7703(3)	7.8995(2)	11.5419(3)	14.4656(7)
α [°]	90	90	90	90	90
β [°]	95.047(1)	94.625(2)	90	101.576(2)	115.955(6)
γ [°]	90	90	90	90	90
Volume [Å^3]	1609.21(4)	1618.02(4)	1210.31(6)	789.91(3)	1644.1(2)
Z	4	4	2	2	4
ρ_{calc} [g·cm^{-3}]	2.422	2.589	2.039	3.019	3.090
μ [mm^{-1}]	26.861	28.052	14.150	36.782	13.799
F(000)	1104.0	1176.0	716.0	652.0	1376.0
crystal size [mm^3]	0.218 × 0.152 × 0.069	0.126 × 0.097 × 0.072	0.427 × 0.277 × 0.162	0.197 × 0.095 × 0.073	0.703 × 0.306 × 0.281
diffractometer	Gemini Ultra	Gemini Ultra	GV50	GV50	Gemini Ultra
absorption correction	gaussian	gaussian	gaussian	gaussian	analytical
T_{min} / T_{max}	0.343 / 0.668	0.575 / 0.678	0.003 / 0.234	0.023 / 0.277	0.014 / 0.122
radiation [Å]	Cu-Kα (λ = 1.54184)	Cu-Kα (λ = 1.54184)	Cu-Kβ (λ = 1.39222)	Cu-Kα (λ = 1.54184)	Mo-Kα (λ = 0.71073)
2Θ range [°]	8.278 to 133.49	8.288 to 133.458	9.478 to 120.36	7.818 to 147.3	7.3 to 62.908
completeness [%]	99.3	99.4	99.9	98.6	99.7
reflns collected / unique	8840 / 2827	8891 / 2846	6312 / 2418	7411 / 3149	7351 / 2599
R_{int} / R_{sigma}	0.0330 / 0.0336	0.0315 / 0.0307	0.1318 / 0.0866	0.0455 / 0.0344	0.0333 / 0.0303
data / restraints / parameters	2827 / 66 / 210	2846 / 72 / 217	2418 / 0 / 139	3149 / 146 / 218	2599 / 0 / 100
GOF on F^2	1.185	1.100	1.056	1.097	1.093
R_1 / wR_2 [$I \geq 2\sigma(I)$]	0.0331 / 0.0850	0.0263 / 0.0617	0.0746 / 0.1934	0.0468 / 0.1212	0.0317 / 0.0801
R_1 / wR_2 [all data]	0.0349 / 0.0864	0.0306 / 0.0636	0.0761 / 0.1944	0.0476 / 0.1215	0.0336 / 0.0812
max / min $\Delta\rho$ [e·Å^{-3}]	1.02 / –1.59	0.68 / –1.30	2.88 / –1.54	2.34 / –2.15	0.96 / –2.22
Identification code	LD185_CR003_abs	LD190_CR008_abs	LD153_F1_abs	CR492_Cua	LD233_abs

Table S5: Crystallographic details for the compounds **6a**, **6b**, **6c**, **7** and **8**.

	6a	**6b**	**6c**	**7**	**8**
formula	$C_{36}H_{60}LiMo_2O_{12}PSi_2$	$C_{36}H_{60}AsLiMo_2O_{12}Si_2$	$C_{42}H_{71}KMo_2O_{12.5}SbSi_2$	$C_{22}H_{26}As_2Mo_2O_4$	$C_{22}H_{26}O_4Mo_2Sb_2$
weight [g·mol^{-1}]	970.81	1014.76	1184.89	696.15	789.81
Temperature [K]	123(1)	123(1)	123(1)	123(1)	123.0(1)
crystal system	monoclinic	monoclinic	triclinic	monoclinic	orthorhombic
space group	$P2/n$	$P2_1/c$	P-1	$P2_1/c$	$P2_12_12$
a [Å]	23.081(1)	12.4933(1)	9.7702(2)	10.3882(3)	15.1466(4)
b [Å]	9.2777(3)	18.7395(2)	14.1024(3)	14.8930(3)	10.2347(3)
c [Å]	12.4744(6)	18.9341(2)	19.0574(5)	15.2218(3)	7.8972(3)
α [°]	90	90	85.172(2)	90	90
β [°]	125.121(7)	92.476(1)	84.141(2)	90.911(2)	90
γ [°]	90	90	85.419(2)	90	90
Volume [Å^3]	2185.0(2)	4428.68(8)	2596.1(1)	2354.7(1)	1224.23(7)
Z	2	4	2	4	2
ρ_{calc} [g·cm^{-3}]	1.476	1.522	1.516	1.964	2.143
μ [mm^{-1}]	6.037	6.445	7.165	3.880	19.358
F(000)	1004.0	2080.0	1210.0	1360.0	752.0
crystal size [mm^3]	0.211 × 0.127 × 0.064	0.474 × 0.231 × 0.129	0.414 × 0.338 × 0.085	0.958 × 0.553 × 0.381	0.235 × 0.143 × 0.048
diffractometer	Gemini Ultra	Gemini Ultra	GV50	Gemini Ultra	GV50
absorption correction	analytical	analytical	gaussian	analytical	gaussian
T_{min} / T_{max}	0.497 / 0.730	0.140 / 0.480	0.219 / 1.000	0.494 / 0.741	0.298 / 0.858
radiation [Å]	Cu-Kα (λ = 1.54184)	Cu–Kα (λ = 1.54184)	Cu-Kβ (λ = 1.39222)	Mo-Kα (λ = 0.71073)	Cu-Kβ (λ = 1.39222)
2Θ range [°]	7.092 to 132.046	7.082 to 148.448	5.694 to 149.958	7.134 to 70.64	9.416 to 120.458
completeness [%]	99.5	99.4	99.2	99.9	99.7
reflns collected / unique	11658 / 3794	27585 / 8866	41532 / 14134	88121 / 10042	4114 / 2248
R_{int} / R_{sigma}	0.0272 / 0.0284	0.0291 / 0.0257	0.0562 / 0.0454	0.0535 / 0.0283	0.0333 / 0.0479
data / restraints / parameters	3794 / 693 / 465	8866 / 156 / 602	14134 / 0 / 529	10042 / 0 / 307	2248 / 0 / 139
GOF on F^2	1.061	1.055	1.136	1.105	1.031
R_1 / wR_2 [$I \geq 2\sigma(I)$]	0.0235 / 0.0570	0.0341 / 0.0932	0.0793 / 0.1999	0.0255 / 0.0554	0.0337 / 0.0821
R_1 / wR_2 [all data]	0.0268 / 0.0588	0.0374 / 0.0964	0.0892 / 0.2061	0.0331 / 0.0578	0.0366 / 0.0849
max / min $\Delta\rho$ [e·Å^{-3}]	0.72 / –0.43	1.02 / -0.52	4.86 / –2.23	0.73 / –1.03	0.60 / -1.50
Identification code	CR326_GemCua	CR327_Cua	LD370_CR328	LD444_Fr2_abs	LD151_2_abs

Refinement details for 2

Compound **2** can be regarded as isostructural to the compounds **1**, **3a**, **4** and **5**. It crystallizes in the monoclinic space group *P*2/*n* with two half molecules in the asymmetric unit. The refinement of the crystal structure could be done without any difficulty. The **PSb** ligands within the tetrahedral complexes exhibit a disorder over the two sites in a ratio of 50:50 (Figure S24). The anisotropic displacement parameters (ADP) of one Cp ring and one **PSb** ligand were restrained by SIMU commands.

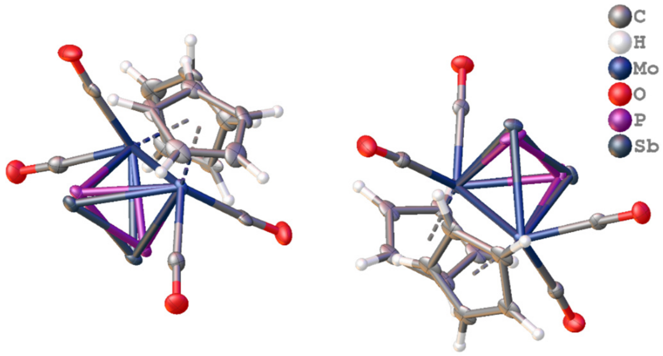

Figure S24: X-ray structure of **2**. The grown structure of the asymmetric unit, which contains two half molecules of **2**, is shown.

Refinement details for 3a

Compound **3a** can be regarded as isostructural to the compounds **1**, **2**, **4** and **5**. It crystallizes in the monoclinic space group *P*2/*n* with two half molecules in the asymmetric unit. The refinement of the crystal structure could be done without any difficulty. The **AsSb** ligands within the tetrahedral complexes exhibit a disorder over the two sites in a ratio of 50:50 (Figure S25). The ADPs of one Cp ring and the two **AsSb** ligands were restrained by SIMU commands.

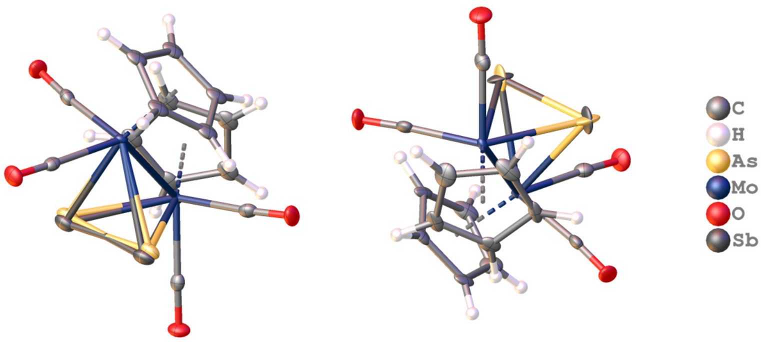

Figure S25: X-ray structure of **3a**. The grown structure of the asymmetric unit, which contains two half molecules of **2**, is shown.

Refinement details for 3b

Compound **3b** can be regarded as isostructural to the compounds **7** and **8**. It crystallizes in the orthorhombic space group $P2_12_12$ with one half molecule in the asymmetric unit. The refinement of the crystal structure could be done without any difficulty. The **AsSb** ligand within the tetrahedral complexes exhibits a disorder over the two sites in a ratio of 50:50 (Figure S26). The disorder was refined by using a EXYZ command as the As and Sb atoms sit on the same position.

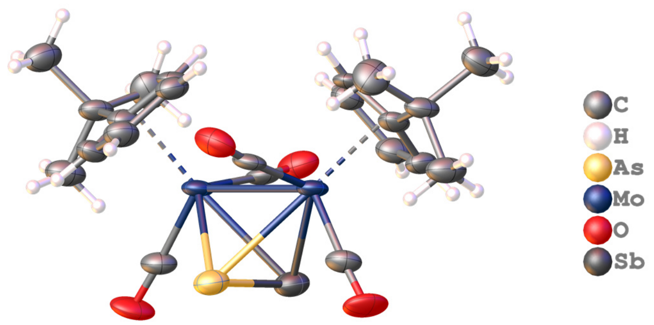

Figure S26: X-ray structure of **3b**. The grown structure of the asymmetric unit, which contains a half molecule of **3b**, is shown.

Refinement details for 4

Compound **4** can be regarded as isostructural to the compounds **1**, **2**, **3a** and **5**. It crystallizes in the monoclinic space group $P2_1$ with one molecule in the asymmetric unit. The refinement of the crystal structure could be done without any difficulty. The **AsBi** ligand within the tetrahedral complex exhibits a disorder over the two sites in ratio of 76:24 (Figure S27). The ADPs of the Cp rings, the two **AsSb** ligands and two CO ligands were restrained by SIMU commands. The **AsBi** ligands were restrained with a SADI command.

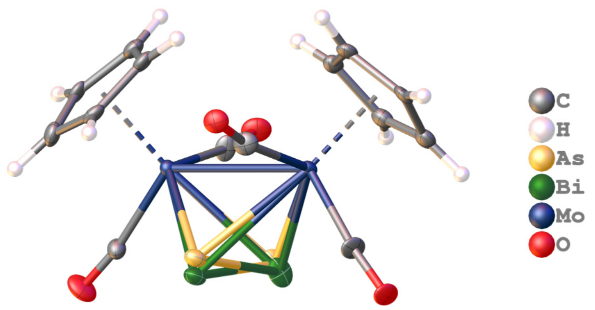

Figure S27: X-ray structure of **4**.

Refinement details for 5

Compound **5** can be regarded as isostructural to the compounds **1**, **2**, **3a** and **4**. It crystallizes in the monoclinic space group $I2/a$ with one half molecule in the asymmetric unit. The refinement of the crystal structure could be done without any difficulty. The **SbBi** ligand within the tetrahedral complex exhibits a disorder over the two sites in ratio of 50:50 (Figure S28). The disorder was refined by using a EXYZ command as the Sb and Bi atoms sit on the same position.

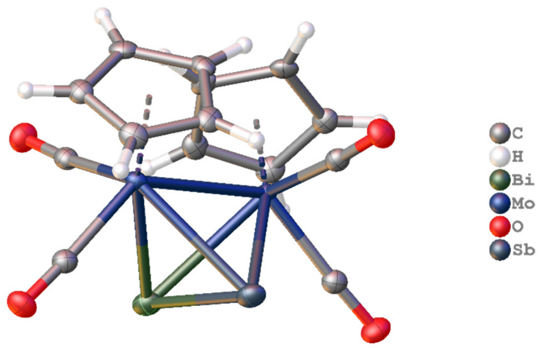

Figure S28: X-ray structure of **5**. The grown structure of the asymmetric unit, which contains one half molecule of **5**, is shown.

Refinement details for 6a

Compound **6a** can be regarded as isostructural to the compounds **6b** and **6c**. It crystallizes in the monoclinic space group *P*2/*n* with one half anion $[\{CpMo(CO)_2\}_2\{\mu\text{-}P(SiMe_3)_2\}]^-$, one half Li^+ cation and one crown-ether (12-crown-4) in the asymmetric unit. The refinement of the crystal structure could be done without any difficulty. Overall, two crown-ethers are coordinating the lithium ion and each exhibits a threefold disorder in a ratio of 50:33:17 (Figure S29). The disordered crown-ethers were restrained by several DFIX, and the ADPs with SIMU commands.

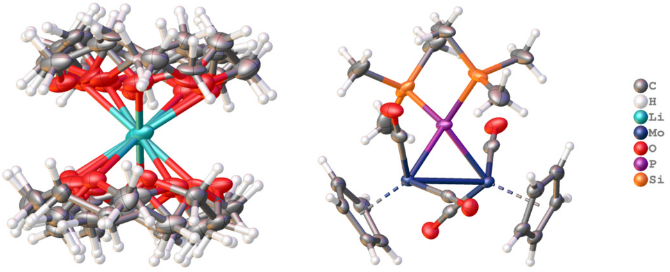

Figure S29: X-ray structure of **6a**. Left: Lithium cation coordinated by two disordered crown-ethers (12-crown-4); right: anionic part of **6a**.

Refinement details for 6b

Compound **6b** can be regarded as isostructural to the compounds **6a** and **6c**. It crystallizes in the monoclinic space group $P2_1/c$ with one anion $[\{CpMo(CO)_2\}_2\{\mu\text{-}As(SiMe_3)_2\}]^-$, one Li^+ cation and two crown-ethers (12-crown-4) in the asymmetric unit. The refinement of the crystal structure could be done without any difficulty. The two crown-ethers are coordinating the lithium ion. One of them exhibits a disorder in a ratio of 70:30 (Figure S30). The ADPs of the disordered crown-ether were restrained by SIMU and RIGU commands.

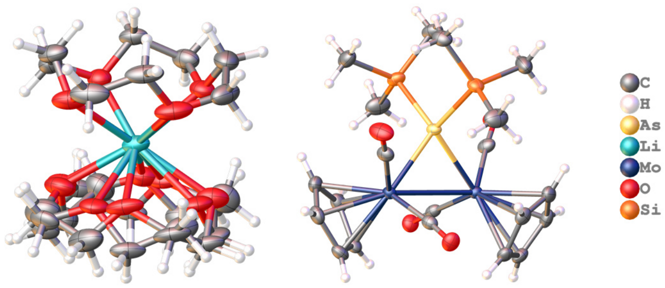

Figure S30: X-ray structure of **6b**. Left: Lithium cation coordinated by one ordered and one disordered crown-ether (12-crown-4); right: anionic part of **6b**.

Refinement details for 6c

Compound **6c** can be regarded as isostructural to the compounds **6a** and **6b**. It crystallizes in the triclinic space group *P*-1 with one anion $[\{CpMo(CO)_2\}_2\{\mu\text{-}Sb(SiMe_3)_2\}]^-$, one K^+ cation, one crown-ether (18-crown-6) and two THF molecules in the asymmetric unit. The refinement of the crystal structure could be done without any difficulty. The potassium cation is coordinated by the crown-ether and the two THF molecules (Figure S31). A solvent mask was calculated and 41 electrons were found in a volume of 171 Å^3 in two voids per unit cell. This is consistent with the presence of half THF per asymmetric unit, which accounts for 40 electrons per unit cell.

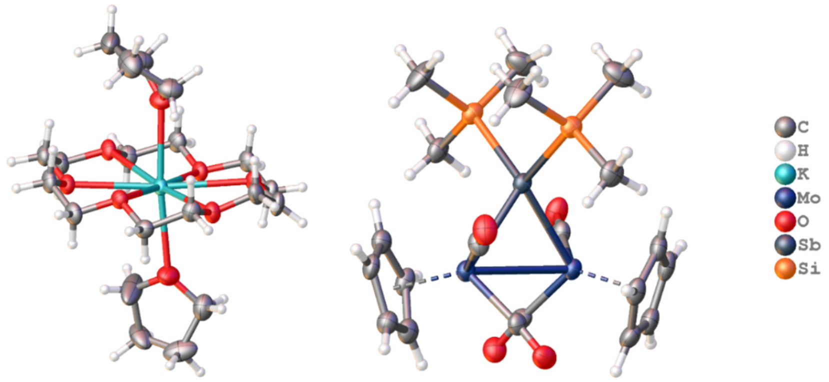

Figure S31: X-ray structure of **6c**. Left: Potassium cation coordinated by one crown-ether (18-crown-6) and two THF molecules; right: anionic part of **6c**.

Refinement details for 7

Compound **7** can be regarded as isostructural to the compounds **3b** and **8**. It crystallizes in the monoclinic space group $P2_1/c$ with one molecule in the asymmetric unit. The refinement of the crystal structure could be done without any difficulty. One of the *tert*-butyl-groups shows a rotational disorder with a ratio of 78:22 (Figure S32).

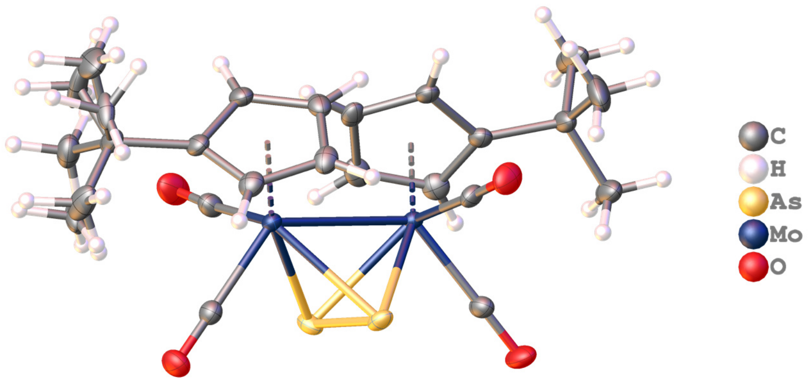

Figure S32: X-ray structure of **7**.

Refinement details for 8

Compound **8** can be regarded as isostructural to the compounds **3b** and **7**. It crystallizes in the orthorhombic space group $P2_12_12$ with one half molecule in the asymmetric unit. The refinement of the crystal structure could be done without any difficulty (Figure S33).

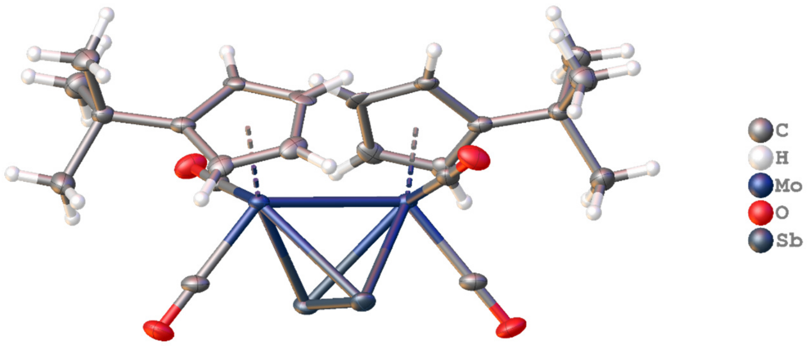

Figure S33: X-ray structure of **8**. The grown structure of the asymmetric unit, which contains one half molecule of **8**, is shown.

3.4.6 Details of DFT Calculations

The geometry of the molecules has been optimized using ORCA,[41] version 4.2 at the B3LYP[42] level together with the def2-TZVP basis set for all atoms.[43] The dispersion effects have been incorporated *via* the D3 corrections together with the Beke-Johnson damping.[44] Additionally, for the complexes **6a**-**d**, the solvent effects has been incorporated *via* the Conductor-like Polarizable Continuum Model (C-PCM)[45] with THF as solvent. The calculation of the Wiberg bond indices in the Löwdin orthogonal orbital basis,[46] which are known to be less basis set dependent have been calculated using the Multiwfn program (version 3.8)[47] It has to be noted that the WBIs computed using the Löwdin orbitals, are sligthly overestimated for polar bonds.[47] The Intrinsic Bonding Orbitals[48] have been generated using the IboWiew program.[49]

Table S6: Total energies calculated at the B3LYP-D3J/def2-TZVP level and additional C-PCM correction for **6a**-**d** as well as selected bond lengths (Å) and the corresponding Wiberg bond order in Löwdin orthogonalized basis.

Compound	Total Energy (a.u.)	E-E' bond length (Å)	WBI	Mo-Mo bond length (Å)	WBI
1	−3554.101344105	2.209	1.48	3.048	0.53
2	−1558.568042740	2.412	1.41	3.073	0.52
[{CpMo(CO)$_2$}$_2$(PBi)]	−1532.946515369	2.504	1.35	3.080	0.51
3a	−3453.050397049	2.515	1.40	3.095	0.51
4	−3427.430176249	2.600	1.35	3.102	0.51
5	−1431.904231562	2.772	1.36	3.138	0.50
6a	−2136.881020368	n. a.	n. a.	3.199	0.45
6b	−4031.346794109	n. a.	n. a.	3.231	0.44
6c	−2035.799910774	n. a.	n. a.	3.305	0.43
6d	−2010.160724327	n. a.	n. a.	3.320	0.42

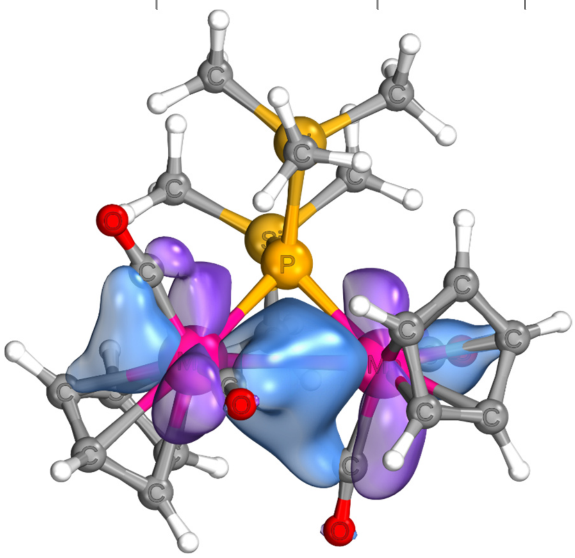

Figure S34: Intrinsic Bonding Orbital representing the Mo-Mo bond in **6a**. AO contributions: Mo2 0.763, Mo1 0.763, C9 0.136, C13 0.136, C12 0.052, C8 0.052 (other: 0.098).

Table S7: Cartesian coordinates of the optimized geometry of [(CpMo(CO)$_2$}$_2$(**PAs**)] (**1**).

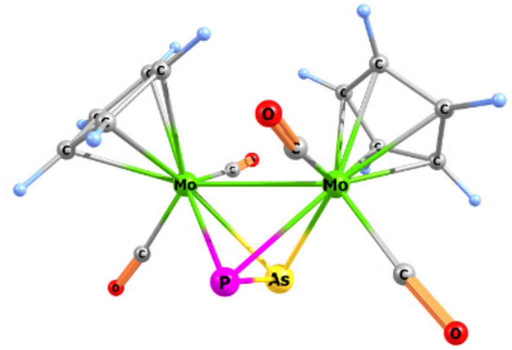

Atom	X	Y	Z
As	−0.619448173	−2.484514211	−0.859089129
P	−1.765412690	−1.657004630	0.838565293
Mo	0.779481442	−1.152782602	0.869319661
Mo	−1.384649976	0.097642499	−0.875305199
C	−0.948918290	2.105542138	0.373157870
H	−0.115877234	2.220854217	1.042614638
C	−3.055385252	1.680323644	−0.430266584
H	−4.097081094	1.410423048	−0.480791604
C	−2.258776948	2.152645410	−1.517171517
H	−2.592929221	2.319795180	−2.527023866
C	−0.954665166	2.407766262	−1.010776353
H	−0.122375091	2.788826208	−1.579317602
C	−2.246959838	1.650850912	0.731227598
H	−2.558670350	1.348253345	1.715645128
C	−2.766739448	−0.783199515	−1.995664350
C	−0.117981210	−0.130400853	−2.376455789
O	−3.606594419	−1.206221087	−2.653284477
O	0.605996614	−0.159802619	−3.274137103
C	2.301319083	0.225935207	−0.378803841
H	1.988266329	0.997529711	−1.058524522
C	2.990663319	−1.800099418	0.449936066
H	3.285104791	−2.834515623	0.512201124
C	2.986085799	−0.864826135	1.528407201
H	3.292595530	−1.058915082	2.542177457
C	2.551798216	0.385445797	1.006019319
H	2.457157504	1.301662760	1.565227522
C	2.567106552	−1.127443460	−0.722262565
H	2.475840172	−1.555956070	−1.705075649
C	0.689286564	−2.794136830	1.983350384
C	−0.045299462	−0.176654705	2.375092027
O	0.726440315	−3.735568907	2.637279230
O	−0.439378364	0.428543408	3.273730634

Table S8: Cartesian coordinates of the optimized geometry of [(CpMo(CO)$_2$}$_2$(**PSb**)] (**2**).

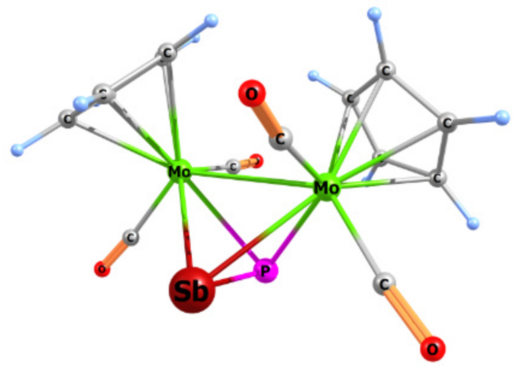

Atom	X	Y	Z
Sb	−0.661486242	−2.690099957	−0.951297907
P	−1.787107348	−1.614468545	0.891215896
Mo	0.785204403	−1.170398080	0.871804175
Mo	−1.399650513	0.088817255	−0.885169074
C	−0.927632734	2.090918918	0.363016608
H	−0.088391613	2.195172491	1.026376827
C	−3.044885034	1.692443672	−0.424658445
H	−4.090120213	1.435193535	−0.467184900
C	−2.250998726	2.156299021	−1.516770606
H	−2.590612778	2.327061230	−2.524214427
C	−0.940077128	2.393221963	−1.021016012
H	−0.107693038	2.764053115	−1.596170696
C	−2.227843614	1.652941411	0.730575732
H	−2.536131793	1.353246189	1.716955111
C	−2.802579224	−0.755964584	−1.999604063
C	−0.134442042	−0.134645108	−2.387637037
O	−3.665378701	−1.137227193	−2.656810603
O	0.593369822	−0.131500790	−3.285175853
C	2.284789039	0.233870299	−0.374844268
H	1.962967350	0.995843131	−1.061128764
C	3.007623758	−1.774785465	0.469307528
H	3.323794421	−2.802317014	0.538601845
C	2.978592789	−0.834868225	1.541880595
H	3.282751377	−1.017524565	2.558476473
C	2.522927257	0.404117521	1.009941127
H	2.408217123	1.321089551	1.564181042
C	2.578501755	−1.115755365	−0.710287212
H	2.513949872	−1.545914969	−1.694390052
C	0.708989346	−2.816926265	1.974125465
C	−0.038873374	−0.202631242	2.382664893
O	0.763021158	−3.758675202	2.628274465
O	−0.420795457	0.399413064	3.288962237

Table S9: Cartesian coordinates of the optimized geometry of [{CpMo(CO)$_2$}$_2$(**PBi**)].

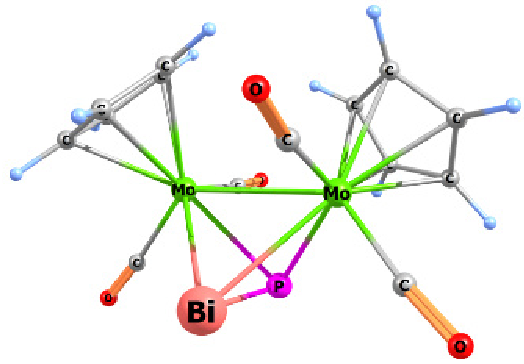

Atom	X	Y	Z
Bi	−0.675044218	−2.783171593	−0.996347412
P	−1.788910107	−1.595617908	0.905495401
Mo	0.785074061	−1.175563511	0.873346569
Mo	−1.402907712	0.086724193	−0.888650558
C	−0.917953559	2.083713866	0.361567153
H	−0.078182633	2.180588169	1.025231236
C	−3.036808098	1.698928731	−0.428221600
H	−4.083378479	1.447362239	−0.471622851
C	−2.239989974	2.159549414	−1.519178773
H	−2.577795776	2.332255762	−2.526843588
C	−0.927873192	2.387373266	−1.022388416
H	−0.092876895	2.753028944	−1.597056828
C	−2.220782287	1.653473992	0.727779185
H	−2.531613778	1.354455016	1.713547615
C	−2.816760147	−0.750304952	−1.992486627
C	−0.140259308	−0.136928692	−2.393893618
O	−3.691291458	−1.118935727	−2.643298629
O	0.591120178	−0.120990912	−3.289564727
C	2.274079689	0.239386725	−0.373676111
H	1.948438536	0.996381288	−1.063459267
C	3.012301078	−1.760039178	0.479669306
H	3.337997323	−2.784287859	0.553273090
C	2.970850619	−0.817857335	1.549255241
H	3.272810330	−0.994943273	2.567427298
C	2.505333701	0.415292493	1.011733123
H	2.380144483	1.332544836	1.563202394
C	2.581918330	−1.108080517	−0.703990794
H	2.528055517	−1.540006183	−1.687896206
C	0.712696021	−2.828220855	1.964466076
C	−0.036651272	−0.217689006	2.389482743
O	0.772977895	−3.772797502	2.615279625
O	−0.414718368	0.384376069	3.297819552

Table S10: Cartesian coordinates of the optimized geometry of [{CpMo(CO)$_2$}$_2$(**AsSb**)] (**3a**).

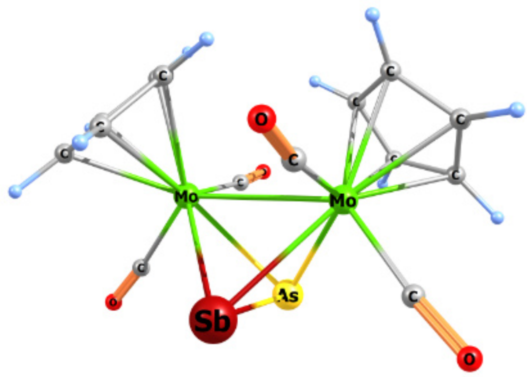

Atom	X	Y	Z
Sb	−0.621511743	−2.686393251	−0.987272421
As	−1.882932640	−1.697473478	0.950648591
Mo	0.787851894	−1.178969691	0.882115728
Mo	−1.410789010	0.088554978	−0.888633901
C	−0.922002562	2.078541311	0.369196833
H	−0.090344104	2.171482184	1.043331842
C	−3.035226867	1.711571960	−0.446059333
H	−4.083821894	1.470955199	−0.501391564
C	−2.221803109	2.163286860	−1.528035621
H	−2.546467737	2.340714555	−2.539140094
C	−0.912845735	2.379899607	−1.015099639
H	−0.068652523	2.740093553	−1.579608775
C	−2.232845280	1.659389966	0.720491832
H	−2.558719592	1.371053947	1.704586167
C	−2.824100719	−0.755204301	−1.989711602
C	−0.156064195	−0.132709203	−2.397377959
O	−3.694286906	−1.134674357	−2.638231630
O	0.569619117	−0.120833285	−3.297027582
C	2.267610144	0.237368331	−0.373237656
H	1.936526900	0.996055307	−1.058510516
C	3.010731476	−1.764691151	0.469089827
H	3.334861337	−2.789774088	0.537440538
C	2.978262949	−0.824872690	1.541525893
H	3.286899042	−1.005000726	2.557142993
C	2.509568959	0.410004761	1.011013496
H	2.388767119	1.325890214	1.565699285
C	2.571481870	−1.109660062	−0.709404018
H	2.508951603	−1.540181995	−1.693421694
C	0.737136667	−2.829626263	1.978509513
C	−0.036567966	−0.209489906	2.391808779
O	0.815256482	−3.775188362	2.625907336
O	−0.404543176	0.409879677	3.293655452

Table S11: Cartesian coordinates of the optimized geometry of [(CpMo(CO)$_2$}$_2$(**AsBi**)] (**4**).

Atom	X	Y	Z
Bi	−0.637790539	−2.778159050	−1.029057149
As	−1.886491304	−1.674702313	0.967345041
Mo	0.787888208	−1.183504176	0.884180177
Mo	−1.414477929	0.087286021	−0.892549322
C	−0.915153003	2.073771547	0.366762926
H	−0.082151750	2.162012094	1.039800811
C	−3.030875787	1.716073891	−0.445944656
H	−4.080400833	1.479305006	−0.499964287
C	−2.217381395	2.165803910	−1.528458851
H	−2.542661940	2.344706690	−2.539092569
C	−0.906798038	2.376075708	−1.017420444
H	−0.061924699	2.732877419	−1.583063682
C	−2.227007523	1.659798834	0.719519297
H	−2.552936957	1.372629656	1.703932313
C	−2.834159863	−0.747209542	−1.990009928
C	−0.157989411	−0.135683900	−2.400521466
O	−3.712780155	−1.112795420	−2.637173124
O	0.568743150	−0.112101762	−3.300360958
C	2.259900070	0.240488992	−0.372711262
H	1.926594784	0.995152339	−1.061188227
C	3.014728394	−1.754133616	0.477471688

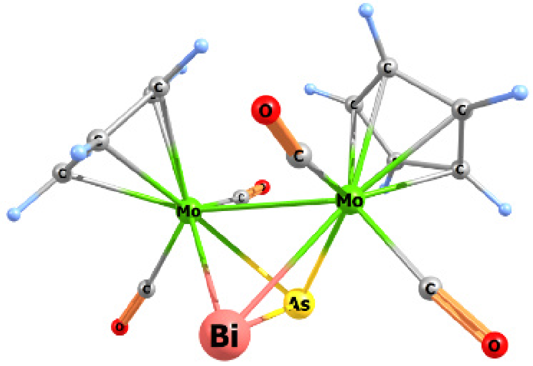

Atom	X	Y	Z
H	3.346878566	−2.776393522	0.549562054
C	2.972592315	−0.812160035	1.547145031
H	3.279886450	−0.987358478	2.564000188
C	2.496095181	0.417889551	1.011871006
H	2.367774314	1.334345129	1.563882808
C	2.574543055	−1.104950749	−0.704555480
H	2.521272117	−1.536592584	−1.688562203
C	0.739666978	−2.837882992	1.972738693
C	−0.029866401	−0.219501507	2.398850097
O	0.824105595	−3.784601898	2.618958968
O	−0.389821850	0.399514358	3.304612610

Table S12: Cartesian coordinates of the optimized geometry of [(CpMo(CO)$_2$}$_2$(**SbBi**)] (**5**).

Atom	X	Y	Z
Bi	0.570368021	6.150784767	7.829125897
Sb	1.397801809	6.038588560	5.186141550
Mo	−0.472497009	4.092782531	5.922350761
Mo	2.446345042	4.093750995	7.074374521
O	−1.475366939	3.256647878	8.758436831
O	−2.696976196	6.275887649	5.710745033
C	−1.064794733	3.654579213	7.752022495
C	−1.835274458	5.523485399	5.841532526
O	3.463679708	3.248116889	4.248683681
O	4.664998399	6.284980646	7.263036423
C	3.049401888	3.645439341	5.252990329
C	3.806059371	5.528200056	7.143706248
C	1.688831822	2.124214318	8.225505394
H	0.747158214	1.641475905	8.039398880
C	2.912593270	1.851002721	7.567855107
H	3.063904232	1.123949583	6.787063223
C	3.923421632	2.672252912	8.141841350
H	4.968808758	2.668437097	7.884388801
C	3.304829742	3.465942004	9.151772073
H	3.801949939	4.182275717	9.784487242
C	1.927886561	3.127952380	9.201801796

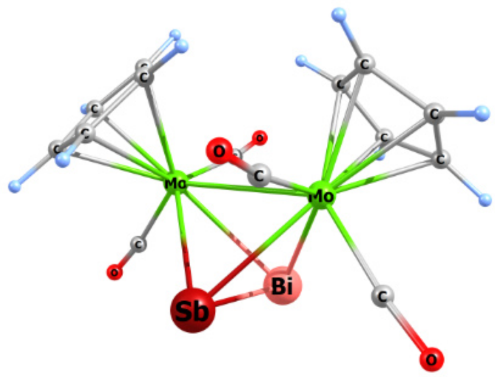

Atom	X	Y	Z
H	1.196730770	3.526735457	9.882839341
C	0.280000974	2.114816866	4.783297426
H	1.218766988	1.629486993	4.977585591
C	−0.948649707	1.849528697	5.435241571
H	−1.107404814	1.126833321	6.218631606
C	−1.952027579	2.673378665	4.852763175
H	−2.998623801	2.676389524	5.105313412
C	−1.324171831	3.460505302	3.843061392
H	−1.813721283	4.177880995	3.205670060
C	0.050958579	3.116000796	3.801994531
H	0.787612633	3.511896825	3.125141734

Table S13: Cartesian coordinates of the optimized geometry of [(CpMo(CO)$_2$}$_2$P(SiMe$_3$)$_2$]$^-$ (**6a**).

Atom	X	Y	Z
Mo	1.421806855	−1.847380882	0.663419393
Mo	−1.421951642	−1.847188120	−0.663605785
P	0.000011820	0.032252906	−0.000016799
Si	0.617011103	1.469304391	−1.690479471
Si	−0.616819772	1.469241777	1.690571352
O	2.463234293	−2.893585023	−2.023854882
O	3.700952159	0.120059569	0.029107539
C	2.775880836	−0.577390138	0.245010739
C	1.960349955	−2.447902944	−1.048503593
O	−2.463492698	−2.893430245	2.023612632
O	−3.700847188	0.120546011	−0.029281974
C	−2.775876660	−0.577033243	−0.245189423
C	−1.960567409	−2.447741965	1.048283899
C	2.000270601	−3.923912925	1.525611493
H	2.175337180	-4.764194156	0.861826945
C	0.773076351	−3.603960077	2.161321660
H	−0.154238247	−4.153943437	2.071046254
C	2.968165767	−2.955754465	1.917554206
H	4.010574960	−2.937265241	1.617693571
C	0.966921221	−2.431381157	2.944682001
H	0.216790063	−1.958644775	3.564815949
C	2.320367725	−2.027478378	2.792924567
H	2.795547245	−1.180864600	3.277255019
C	−1.669778654	0.639879139	3.023775240
H	−2.638141810	0.311786852	2.638673489
H	−1.847496194	1.379785417	3.817251565
H	−1.175876271	−0.224468038	3.472137578
C	−1.636556902	2.978218911	1.141645442
H	−1.114776108	3.628880875	0.433931935
H	−1.873421163	3.578169051	2.032341262
H	−2.582556444	2.662493225	0.690638305
C	0.934532895	2.120306162	2.571942191
H	1.477603169	1.298173334	3.049845039
H	0.637998581	2.833977019	3.354031468
H	1.629398506	2.627369152	1.895856562
C	−2.000831889	−3.923558297	−1.525927068

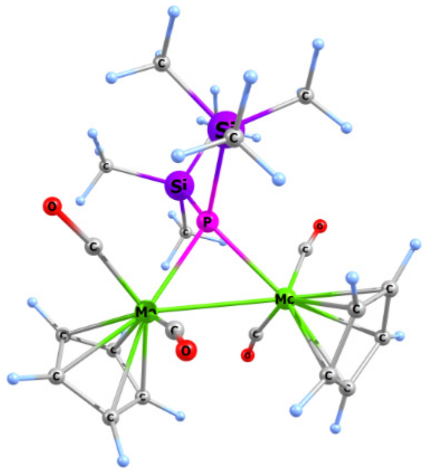

Atom	X	Y	Z
H	−2.176209169	−4.763801470	−0.862176847
C	−0.773460515	−3.603892126	−2.161436886
H	0.153703409	−4.154110002	−2.071035305
C	−2.968420058	−2.955147886	−1.917989643
H	−4.010869195	−2.936403346	−1.618282563
C	−0.966894349	−2.431244777	−2.944803967
H	−0.216541835	−1.958687116	−3.564805957
C	−2.320262868	−2.027018361	−2.793253697
H	−2.795156981	−1.180275567	−3.277639399
C	1.671374573	0.640316692	−3.022805362
H	2.639681788	0.312880058	−2.637007129
H	1.849157467	1.380154509	−3.816329755
H	1.178262364	−0.224425572	−3.471299714
C	1.635367547	2.979057070	−1.141139831
H	1.112628352	3.629521481	−0.433951447
H	1.872504902	3.578975972	−2.031783113
H	2.581238942	2.664044762	−0.689373509
C	−0.934183772	2.119119625	−2.573047220
H	−1.476365787	1.296501511	−3.051129215
H	−0.637599666	2.832811247	−3.355098873
H	−1.629857383	2.625857612	−1.897558867

Table S14: Cartesian coordinates of the optimized geometry of [(CpMo(CO)$_2$}$_2$As(SiMe$_3$)$_2$]$^-$ (**6b**).

Atom	X	Y	Z
Mo	0.301974320	2.024631398	−1.595205595
Mo	−0.431844853	1.991742054	1.551624209
As	0.009704221	0.038067008	−0.024329655
Si	1.911630152	−1.314165476	0.342014832
Si	−1.784555468	−1.453501744	−0.393924802
O	2.062018267	4.262847268	−0.369979962
O	−2.361652846	4.087411871	0.330382108
O	3.096031622	0.995029500	−2.413715943
O	−3.135974560	0.744653072	2.369525981
C	1.377176074	3.383130719	−0.738411512
C	2.036023599	1.341766639	−2.035530500
C	−2.106800061	1.174300674	1.991509161
C	−1.610316803	3.262989761	0.697264048
C	−0.312976251	1.854651826	−3.878128363
H	0.311210316	1.312028145	−4.569764133
C	1.328067209	1.420259450	3.118277544
H	1.746974055	0.430437276	3.172847351

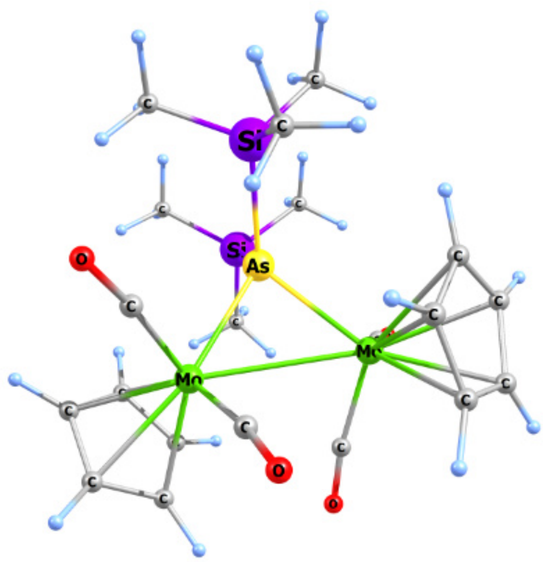

Atom	X	Y	Z	Atom	X	Y	Z
C	−1.411083083	1.320661750	−3.158986988	C	0.192527106	1.872059589	3.835678061
H	−1.754980390	0.302361046	−3.212018607	H	−0.390199796	1.285310800	4.527469749
C	−0.030972121	3.234510298	3.502472146	C	−3.350128942	−0.502177686	-0.821097483
H	−0.802647424	3.868214479	3.907930013	H	−3.453701458	0.392590940	−0.210561451
C	−0.191484358	3.230581654	−3.547091674	H	−4.211867444	−1.148465105	−0.628812790
H	0.530685691	3.919382453	−3.953896676	H	−3.377779053	−0.211879857	−1.870617402
C	0.962887762	3.616282433	2.557151373	C	1.803140511	2.495408490	2.323078189
H	1.072956666	4.587901495	2.106361560	H	2.644813371	2.467254693	1.654234289
C	−1.210713826	3.538660024	−2.601837014	C	1.627767286	−2.541741426	1.742967264
H	−1.392478064	4.500120886	−2.152363293	H	1.235933566	−2.046199807	2.633462646
C	−1.965162680	2.358852109	−2.365866793	H	2.573653074	−3.024004014	2.007724385
H	−2.802229891	2.269072809	−1.696724360	H	0.922813494	−3.322333525	1.452804451
C	−2.101372606	−2.437190819	1.178329942	C	−1.409496586	−2.651600485	−1.798927807
H	−1.239854073	−3.043928714	1.457608430	H	−1.050644542	−2.125515512	−2.685771866
H	−2.954490111	−3.105737313	1.026090112	H	−2.317870316	−3.198574812	−2.069230099
H	−2.334587733	−1.767507089	2.006794927	H	−0.652092444	−3.381603979	−1.509158553
C	2.301750350	−2.266049441	−1.233499661	C	3.400811132	−0.249620365	0.773461616
H	1.492360694	−2.941908940	−1.510183018	H	3.443978729	0.647171286	0.158642902
H	3.208009853	−2.861779908	−1.086106114	H	4.308115737	−0.833189459	0.590180018
H	2.475000528	−1.578534575	−2.062121578	H	3.400342401	0.047166159	1.821476384

Table S15: Cartesian coordinates of the optimized geometry of $[\{CpMo(CO)_2\}_2Sb(SiMe_3)_2]^-$ (**6c**).

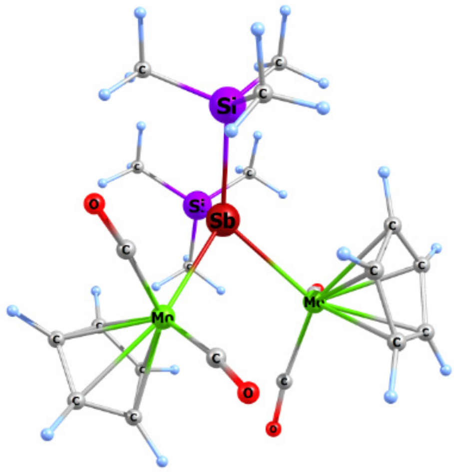

Atom	X	Y	Z
Sb	0.022750682	−0.045185096	0.051254708
Mo	−1.437555806	1.777884551	1.396953355
Mo	0.385750420	−0.679629566	2.645426641
Si	2.008039687	0.796494643	−1.336130307
Si	−1.155691859	−1.752417518	−1.455258683
O	−2.264210944	−0.725638845	4.259964501
O	0.096536543	3.034723885	3.783599254
O	0.138268341	3.950087564	−0.138261640
O	−0.562570489	−3.533415842	1.925363116
C	−0.414262142	3.082093353	0.436640817
C	1.665922475	0.316639918	4.364947747
H	1.197785962	0.972657423	5.078881346
C	2.283398230	0.719434126	3.152028372
H	2.347977845	1.727083114	2.779783799
C	−0.424814667	2.481817221	2.889132927
C	1.786200390	−1.099265884	4.474320085
H	1.445860481	−1.706360508	5.297085785
C	−1.305628409	−0.647240520	3.587141945
C	2.787813473	−0.443269761	2.510551190
H	3.317037561	−0.476997227	1.573620802
C	2.472631858	−1.563688604	3.320108718
H	2.725361800	−2.589056155	3.103153440
C	3.049707439	1.964525562	−0.294202994
H	2.427039614	2.735171366	0.159656424
H	3.790036100	2.453906294	−0.934924632
H	3.583919296	1.440641887	0.497989421
C	−3.494119014	1.175515477	0.277333613
H	−3.505307609	0.647845889	−0.660979473
C	−1.577727026	−0.986406201	−3.123240609
H	−2.174366991	−0.079787316	−3.002359195
H	−2.150428118	−1.695260991	−3.729195599
H	−0.673267871	−0.723440032	−3.675200857
C	−3.459494023	2.881475861	1.819277073
H	−3.464611334	3.866215270	2.256962045
C	−0.231344369	−2.424830297	2.150180222
C	−2.727873729	−2.346450836	−0.613049878

Atom	X	Y	Z
H	−2.517464749	−2.685755643	0.401058598
H	−3.143689863	−3.186693728	−1.178043530
H	−3.485610788	−1.564858452	−0.565217314
C	−3.511288334	1.644569855	2.525444544
H	−3.538730636	1.522966274	3.594900120
C	−3.439902822	2.583973317	0.430177482
H	−3.405412057	3.304093059	−0.371417990
C	−3.531054046	0.593010857	1.572385570
H	−3.558386057	−0.459942917	1.793329885
C	1.340609850	1.739473691	−2.821846578
H	0.717774817	1.104133070	−3.453522520
H	2.168378906	2.118995224	−3.429209307
H	0.740184690	2.588442143	−2.490571656
C	−0.005924744	−3.220914168	−1.707188584
H	0.931476319	−2.919570415	−2.177495312
H	−0.484332676	−3.969000347	−2.347138807
H	0.225762092	−3.686684945	−0.747811954
C	3.067112975	−0.644374738	−1.927648193
H	3.407435847	−1.255847178	−1.089299847
H	3.948118705	−0.270337160	−2.458377583
H	2.509678776	−1.288550007	−2.610360507

Table S16: Cartesian coordinates of the optimized geometry of [(CpMo(CO)$_2$}$_2$Bi(SiMe$_3$)$_2$]$^-$ (**6d**).

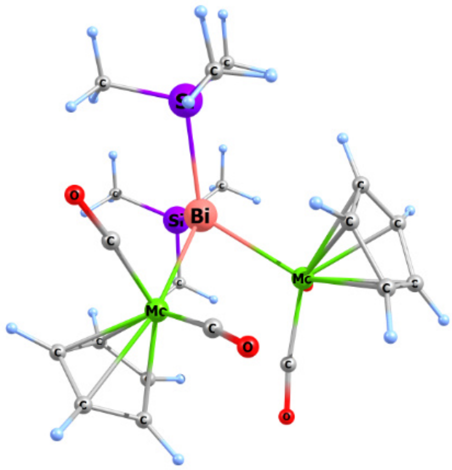

Atom	X	Y	Z
Bi	0.024139401	−0.048531959	0.058948552
Mo	−1.454846698	1.816407404	1.478397505
Mo	0.357966413	−0.661387172	2.741324985
Si	2.070276663	0.824132096	−1.365153764
Si	−1.194143012	−1.814546710	−1.480836423
O	−2.288481455	−0.667876638	4.360106297
O	0.061204025	3.052442340	3.886015577
O	0.152402871	3.981281732	−0.037346067
O	−0.624346528	−3.506435202	2.026709274
C	−0.415675536	3.117914013	0.530549050
C	1.634759037	0.335588209	4.457964055
H	1.164922857	0.989971370	5.172222897
C	2.253392093	0.741095618	3.246642493
H	2.317239122	1.749244415	2.875138225
C	−0.452348320	2.507111569	2.981779618
C	1.754560231	−1.081001222	4.564779155
H	1.416496016	−1.689093522	5.387654064
C	−1.330679685	−0.605851603	3.683786220
C	2.759630271	−0.420408492	2.603834822
H	3.291244787	−0.450463179	1.667969049
C	2.444209151	−1.542903685	3.410617593
H	2.699182421	−2.567508409	3.192767160
C	3.103127992	1.974476700	−0.296287232
H	2.478826895	2.756104829	0.137292317
H	3.873470223	2.450060899	−0.911824204
H	3.600110062	1.440493989	0.513694958
C	−3.504818142	1.195255333	0.357022184
H	−3.513709913	0.656075560	−0.574876393
C	−1.604773077	−1.049574327	−3.151391548
H	−2.229310468	−0.161448296	−3.034849434
H	−2.144683226	−1.768931048	−3.775141865
H	−0.696254087	−0.756466991	−3.681268674
C	−3.473453632	2.919035073	1.880139550
H	−3.483355413	3.908526230	2.306683511
C	−0.277655146	−2.401993265	2.251771504
C	−2.764384278	−2.384437991	−0.620061838
H	−2.539058762	−2.748730902	0.382569488
H	−3.217830805	−3.201319265	−1.190614939
H	−3.496972870	−1.581505327	−0.538298166
C	−3.528067606	1.689410182	2.599817088
H	−3.557821065	1.579272880	3.670397037
C	−3.451145861	2.605487325	0.493698695
H	−3.416059745	3.316420426	−0.315982502
C	−3.545061512	0.627195939	1.658661482
H	−3.571220403	−0.423437565	1.890974365
C	1.393370199	1.782021503	−2.836518368
H	0.768096061	1.150606090	−3.470271772
H	2.216197886	2.169534859	−3.445869213
H	0.792479147	2.626254420	−2.493728896
C	−0.040953136	−3.283089348	−1.713801086
H	0.896581666	−2.983014291	−2.185322509
H	−0.514570795	−4.040700517	−2.346328063
H	0.191121188	−3.737162452	−0.748744297
C	3.116150269	−0.620612019	−1.968804157
H	3.479214990	−1.221359876	−1.132338274
H	3.982533528	−0.252103693	−2.527148597
H	2.540516713	−1.272955591	−2.628537516

3.5 References

[1] G. Maier, *Angew. Chem. Int. Ed.* **1988**, *27*, 309-332.

[2] M. Seidl, G. Balázs, M. Scheer, *Chem. Rev.* **2019**, *119*, 8406-8434.

[3] a) T. M. Bernhardt, B. Stegemann, B. Kaiser, K. Rademann, *Angew. Chem. Int. Ed.* **2003**, *42*, 199-202; b) A. Stock, O. Guttmann, *Berichte der deutschen chemischen Gesellschaft* **1904**, *37*, 885-900: Stock and Guttmann reported on a possible synthesis of yellow antimony by reacting liquid stibane (antimony trihydride) with oxygen at 183 K in 1904. However, an anlytical evidence could not be provided.

[4] A. J. Karttunen, M. Linnolahti, T. A. Pakkanen, *Theor. Chem. Acc.* **2011**, *129*, 413-422.

[5] a) B. M. Cossairt, M.-C. Diawara, C. C. Cummins, *Science* **2009**, *323*, 602-602; b) M.-L. Y. Riu, R. L. Jones, W. J. Transue, P. Müller, C. C. Cummins, *Science Advances* **2020**, *6*, eaaz3168; c) G. Hierlmeier, P. Coburger, M. Bodensteiner, R. Wolf, *Angew. Chem. Int. Ed.* **2019**, *58*, 16918-16922; d) G. A. Ozin, *Journal of the Chemical Society A: Inorganic, Physical, Theoretical* **1970**, 2307-2310, also the existence of the molecules As_2P_2, As_3P and SbP_3 within mixtures of phosphorus and arsenic or phosphorus and antimony vapours, respectively, has been detected by high-temperature gas-phase RAMAN spectroscpy.

[6] a) O. J. Scherer, H. Sitzmann, G. Wolmershäuser, *J. Organomet. Chem.* **1984**, *268*, C9-C12; b) M. Gorzellik, H. Bock, L. Gang, B. Nuber, M. L. Ziegler, *J. Organomet. Chem.* **1991**, *412*, 95-120; c) H. J. Breunig, R. Rösler, E. Lork, *Angew. Chem. Int. Ed.* **1997**, *36*, 2819-2821.

[7] a) P. J. Sullivan, A. L. Rheingold, *Organometallics* **1982**, *1*, 1547-1549; b) W. Clegg, N. A. Compton, R. J. Errington, N. C. Norman, *Polyhedron* **1988**, *7*, 2239-2241.

[8] a) N. Arleth, M. T. Gamer, R. Koppe, N. A. Pushkarevsky, S. N. Konchenko, M. Fleischmann, M. Bodensteiner, M. Scheer, P. W. Roesky, *Chem. Sci.* **2015**, *6*, 7179-7184; b) N. Reinfandt, Ch. Schoo, L. Dütsch, R. Köppe, S. N. Konchenko, M. Scheer, P. W. Roesky, *Chem. Eur. J.* **2021**, *27*, 3974-3978.

[9] a) M. Fleischmann, J. S. Jones, G. Balazs, F. P. Gabbai, M. Scheer, *Dalton Trans* **2016**, *45*, 13742-13749; b) H. V. Ly, M. Parvez, R. Roesler, *Inorg. Chem.* **2006**, *45*, 345-351; c) M. Fleischmann, L. Dütsch, M. E. Moussa, A. Schindler, G. Balázs, C. Lescop, M. Scheer, *Chem. Commun.* **2015**, *51*, 2893-2895; d) M. Fleischmann, L. Dütsch, M. Elsayed Moussa, G. Balázs, W. Kremer, C. Lescop, M. Scheer, *Inorg. Chem.* **2016**, *55*, 2840-2854; e) M. E. Moussa, J. Schiller, E. Peresypkina, M. Seidl, G. Balázs, P. Shelyganov, M. Scheer, *Chem. Eur. J.* **2020**, *26*, 14315-14319; f) J. Schiller, A. Schreiner, M. Seidl, G. Balázs, M. Scheer, *Chem. Eur. J.* **2020**, *26*, 14570-14574; g) O. J. Scherer, H. Sitzmann, G. Wolmershäuser, *Angew. Chem. Int. Ed.* **1984**, *23*, 968-969; h) J. Bai, E. Leiner, M. Scheer, *Angew. Chem. Int. Ed.* **2002**, *41*, 783-786; i) M. Scheer, L. Gregoriades, J. Bai, M. Sierka, G. Brunklaus, H. Eckert, *Chem. Eur. J.* **2005**, *11*, 2163-2169; j) S. Welsch, L. J. Gregoriades, M. Sierka, M. Zabel, A. V. Virovets, M. Scheer, *Angew. Chem. Int. Ed.* **2007**, *46*, 9323-9326; k) M. Scheer, L. J. Gregoriades, M. Zabel, J. Bai, I. Krossing, G. Brunklaus, H. Eckert, *Chem. Eur. J.* **2008**, *14*, 282-295; l) S. Welsch, M. Bodensteiner, M. Dušek, M. Sierka, M. Scheer, *Chem. Eur. J.* **2010**, *16*, 13041-13045; m) M. Fleischmann, S. Welsch, L. J. Gregoriades, C. Gröger, M. Scheer, *Zeitschrift für Naturforschung B* **2014**, *69*, 1348-1356; n) M. Elsayed Moussa, B. Attenberger, E. V. Peresypkina, M. Fleischmann, G. Balázs, M. Scheer, *Chem. Commun.* **2016**, *52*, 10004-10007.

[10] L. Dütsch, M. Fleischmann, S. Welsch, G. Balázs, W. Kremer, M. Scheer, *Angew. Chem. Int. Ed.* **2018**, *57*, 3256-3261.

[11] J. E. Davies, L. C. Kerr, M. J. Mays, P. R. Raithby, P. K. Tompkin, A. D. Woods, *Angew. Chem. Int. Ed.* **1998**, *37*, 1428-1429.

[12] U. Vogel, M. Scheer, *Z. Anorg. Allg. Chem.* **2003**, *629*, 1491-1495.

[13] F. Riedlberger, M. Seidl, M. Scheer, *Chem. Commun.* **2020**, *56*, 13836-13839.

[14] P. S. Nejman, T. E. Curzon, M. Bühl, D. McKay, J. D. Woollins, S. E. Ashbrook, D. B. Cordes, A. M. Z. Slawin, P. Kilian, *Inorg. Chem.* **2020**, *59*, 5616-5625.

[15] E. Conrad, N. Burford, R. McDonald, M. J. Ferguson, *J. Am. Chem. Soc.* **2009**, *131*, 5066-5067.

[16] a) A. J. Ashe, E. G. Ludwig, *J. Organomet. Chem.* **1986**, *303*, 197-204; b) D. Nikolova, C. von Hänisch, *Eur. J. Inorg. Chem.* **2005**, 378-382; c) J. G. Stevens, J. M. Trooster, H. F. Martens, H. A. Meinema, *Inorg. Chim. Acta* **1986**, *115*, 197-201.

[17] a) S. Traut, A. P. Hähnel, C. von Hänisch, *Dalton Trans.* **2011**, *40*, 1365-1371; b) K. M. Marczenko, S. S. Chitnis, *Chem. Commun.* **2020**, *56*, 8015-8018; c) T. Sasamori, N. Takeda, N. Tokitoh, *Chem. Commun.* **2000**, 1353-1354.

[18] **3a**: Two half molecules in the asymmetric unit of **3a**. The given bond lengths are the average bond lengths of both. **4**: The **AsBi** ligand is diordered over the two sites with a ratio of 50:50. The given bond length is the average of both As-Bi distances. For details see Supporting Information.

[19] J. R. Harper, A. L. Rheingold, *J. Organomet. Chem.* **1990**, *390*, c36-c38.

[20] P. Pyykkö, *J. Phys. Chem. A* **2015**, *119*, 2326-2337.

[21] For details see Supporting Informations.

[22] For chemical shifts in other deuterated solvents see Supporting Information.

[23] R. J. Klingler, W. M. Butler, M. D. Curtis, *J. Am. Chem. Soc.* **1978**, *100*, 5034-5039

[24] R. J. Klingler, W. Butler, M. D. Curtis, *J. Am. Chem. Soc.* **1975**, *97*, 3535-3536.

[25] M. Scheer, K. Schuster, K. Schenzel, E. Herrmann, P. G. Jones, *Z. Anorg. Allg. Chem.* **1991**, *600*, 109-119.

[26] G. Fritz, W. Hölderich, *Z. Anorg. Allg. Chem.* **1976**, *422*, 104-114.

[27] a) R. L. Wells, M. F. Self, J. D. Johansen, J. A. Laske, S. R. Aubuchon, L. J. Jones III, A. H. Cowley, S. Kamepalli, in *Inorg. Synth.*, **1996**, pp. 150-158; b) G. Becker, C. Witthauer, *Z. Anorg. Allg. Chem.* **1982**, *492*, 28-36.

[28] a) G. Becker, A. Münch, C. Witthauer, *Z. Anorg. Allg. Chem.* **1982**, *492*, 15-27; b) E. Amberger, R. W. Salazar G, *J. Organomet. Chem.* **1967**, *8*, 111-114; c) C. Marquardt, O. Hegen, M. Hautmann, G. Balázs, M. Bodensteiner, A. V. Virovets, A. Y. Timoshkin, M. Scheer, *Angew. Chem. Int. Ed.* **2015**, *54*, 13122-13125.

[29] a) O. Mundt, G. Becker, M. Rössler, C. Witthauer, *Z. Anorg. Allg. Chem.* **1983**, *506*, 42-58; b) T. M. Rookes, E. P. Wildman, G. Balázs, B. M. Gardner, A. J. Wooles, M. Gregson, F. Tuna, M. Scheer, S. T. Liddle, *Angew. Chem. Int. Ed.* **2018**, *57*, 1332-1336; c) G. Becker, M. Roessler, *Z. Naturforsch. B.* **1982**, *37b*, 91-96.

[30] A. Johannis, *Ann. Chim. Phys.* **1906**, *7*, 106.

[31] O. J. Scherer, H. Sitzmann, G. Wolmershäuser, *J. Organomet. Chem.* **1984**, *268*, C9-C12.

[32] M. L. Ziegler, K. Blechschmitt, B. Nuber, T. Zahn, *Chem. Ber.* **1988**, *121*, 159-171.

[33] J. R. Harper, A. L. Rheingold, *J. Organomet. Chem.* **1990**, *390*, c36-c38.

[34] W. Clegg, N. A. Compton, R. J. Errington, G. A. Fisher, N. C. Norman, T. B. Marder, *J. Chem. Soc., Dalton Trans.* **1991**, 2887-2895.

[35] J. E. Davies, L. C. Kerr, M. J. Mays, P. R. Raithby, P. K. Tompkin, A. D. Woods, *Angew. Chem. Int. Ed.* **1998**, *37*, 1428-1429.

[36] Agilent (2014). CrysAlis PRO. Agilent Technologies Ltd., Yarnton, Oxfordshire, England.

[37] G. Sheldrick, Acta Crystallographica Section A **2015**, 71, 3-8.

[38] O. V. Dolomanov, L. J. Bourhis, R. J. Gildea, J. A. K. Howard, H. Puschmann, *J. Appl. Cryst.* **2009**, *42*, 339-341.

[39] G. Sheldrick, Acta Crystallographica Section C **2015**, 71, 3-8.

[40] Crystallographic Data for Compound **2** was already provided by Mays *et. al*. in 1998 under the CCDC deposition code CCDC-100650.

[41] F. Neese "The ORCA program system" Wiley Interdisciplinary Reviews: Computational Molecular Science, **2012**, Vol. 2, Issue 1, Pages 73–78.

[42] a) A. D. Becke, *J. Chem. Phys.* **1993**, *98*, 5648-5652; b) C. Lee, W. Yang, R. G. Parr, *Phys. Rev. B* **1988**, *37*, 785-789; c) A. D. Becke, *Phys. Rev. A* **1988**, *38*, 3098-3100; d) S. H. Vosko, L. Wilk, M. Nusair, *Can. J. Phys.* **1980**,

58, 1200-1211; e) J. C. Slater, *Phys. Rev.* **1951**, *81*, 385-390; f) P. A. M. Dirac, *Proc. Royal Soc. A* **1929**, *123*, 714-733.
[43] a) A. Schäfer, C. Huber, R. Ahlrichs, *J. Chem. Phys.* **1994**, *100*, 5829; b) K. Eichkorn, F. Weigend, O. Treutler, R. Ahlrichs, *Theor. Chem. Acc.* **1997**, *97*, 119; c) F. Weigend, R. Ahlrichs, *Phys. Chem. Chem. Phys.* **2005**, *7*, 3297; d) F. Weigend, *Phys. Chem. Chem. Phys.* **2006**, *8*, 1057.
[44] S. Grimme, S. Ehrlich, L. Goerigk, *J. Comput. Chem.* **2011**, *32*, 1456-1465.
[45] V. Barone, M. Cossi, M. *J. Phys. Chem. A*, **1998**, *102*, 1995-2001.
[46] O. V. Sizova, L. V. Skripnikov, A. Y. Sokolov, *J. Molec. Struct.: THEOCHEM* **2008**, *870*, 1-9.
[47] T. Lu, F. Chen, *J. Comput. Chem.* **2012**, *33*, 580-592.
[48] G. Knizia, *J. Chem. Theory Comput.* **2013**, *9*, 4834-4843.
[49] IboView v20150427. http://www.iboview.org/

Preface

The following chapter has already been published. The article is reprinted with permission of Wiley-VCH.

"Dicationic E_4 Chains (E = P, As, Sb, Bi) Embedded in the Coordination Sphere of Transition Metals"

German version:
Angew. Chem. **2018**, *130*, 3311-3317.

English version:
Angew. Chem. Int. Ed. **2018**, *57*, 3256-3261.

Authors

Luis Dütsch, Martin Fleischmann, Stefan Welsch, Gábor Balázs, Werner Kremer and Manfred Scheer

Author Contributions

The main part (conceptualization, preparation of the compounds **2**, **3** and **4**, writing, visualization, and execution and evaluation of measurements) of this work was done by the first author (Luis Dütsch).
Compound **1b** was previously obtained as a side-product in trace amounts and has been structurally characterized by Stefan Welsch. The description of the X-ray structure of **1b** and the spectroelectrochemistry have been described by Stefan Welsch in his PhD thesis. Martin Fleischmann synthesized and characterized the compounds [Thia][TEF], **1a** and **1b**, which have already been part of his PhD thesis. He also contributed to the initial draft. Werner Kremer performed the MAS NMR spectroscopic measurements of crystalline and precipitated **1b**. Gábor Balázs performed the DFT calculations and contributed the respective parts in the manuscript. Manfred Scheer supervised the research and revised the manuscript prior to publication.

Acknowledgements

This work was supported by the Deutsche Forschungsgemeinschaft. We thank Dr. Florian Pevny, Prof. Dr. Rainer Winter, Felix Riedlberger (CV measurements), Dr. Michael Bodensteiner (X-ray diffraction), Valentin Vass (MS measurements), and David Konieczny (preparation of [Thia][TEF]) for their support.

4 Dicationic E_4 Chains (E = P, As, Sb, Bi) Embedded in the Coordination Sphere of Transition Metals

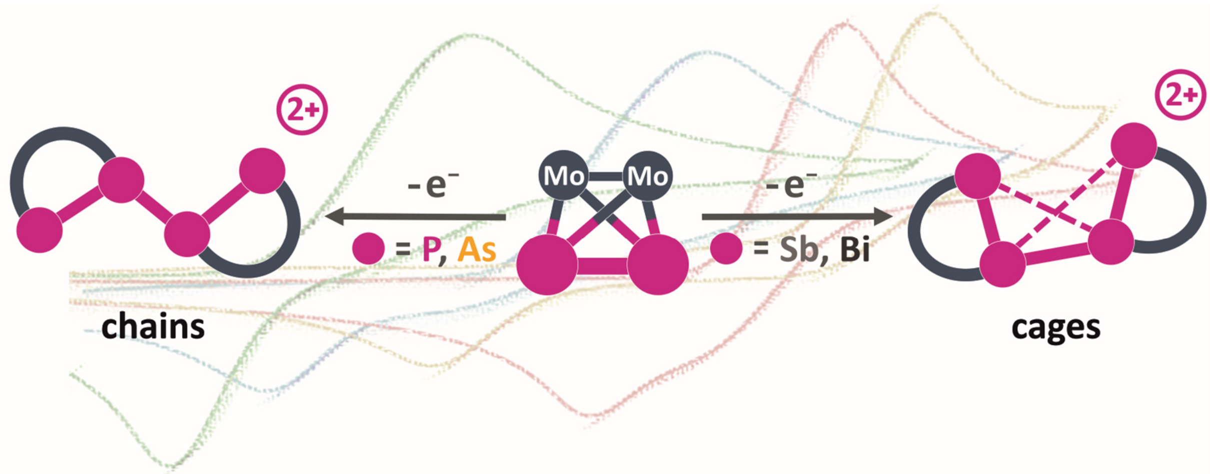

Abstract: *The oxidation chemistry of the complexes [{CpMo(CO)$_2$}$_2$(μ,η^2:η^2-E$_2$)] (E = P (**A**), As (**B**), Sb (**C**), Bi (**D**)) is compared. The oxidation of **A**-**D** with [Thia]$^+$ (= [C$_{12}$H$_8$S$_2$]$^+$) results in the selective formation of the dicationic E$_4$ complexes [{CpMo(CO)$_2$}$_4$(μ$_4$,η^2:η^2:η^2:η^2-E$_4$)]$^{2+}$ (E = P (**1**), As (**2**), Sb (**3**), Bi (**4**)) stabilized by four [CpMo(CO)$_2$] fragments. The formation of the corresponding monocations [**A**]$^+$, [**C**]$^+$ and [**D**]$^+$ could not be detected by cyclovoltammetry, EPR or NMR spectroscopy. This finding suggests that dimerization is fast and that there is no dissociation in solution, which was also predicted by DFT calculations. However, EPR measurements of **2** confirmed the presence of small amounts of the radical cation [**B**]$^+$ in solution. Single crystal X-ray diffraction revealed that the products **1** and **2** feature a zigzag E$_4$ chain in the solid state, while **3** and **4** bear a central E$_4$ cage with a distorted "butterfly-like" geometry. Additionally, **1** can be easily and reversibly converted into a symmetric and an unsymmetric form.*

4.1 Introduction

One of the main features of carbon is its (homo)catenation (formation of long covalent chains) capability, on which the chemistry of polymeric materials, such as polyethylene or polypropylene, is based. Catenation is also known for the heavier tetrels, but, in this case, comes along with a decrease in the chain lengths, and is less common for other elements. For example, boron as an electron-deficient element tends to form cages, although very recent results show that stepwise homocatenation is possible.[1] In combination with phosphorus, boron mimics Group 14 elements and is then able to form inorganic polymers[2] as well as defined anionic and cationic chains.[3] However, phosphorus diagonally related to carbon, is also capable of catenation. Although neutral and anionic polyphosphorus chains and rings have been known for decades,[4] it was only recently that the groups of *N. Burford* and *J. J. Weigand* opened up the field of cationic polyphosphorus arrangements.[5] Through halide abstraction from halophosphines and a subsequent reaction with additional phosphines, they synthesized a large variety of organo-substituted polyphosphorus chains, cycles and cages. Nonetheless, cationic polyphosphorus and polyarsenic compounds with fewer organic moieties have also been reported.[6] Another way to cationic polypnictogen compounds is the oxidation of pnictogen-rich molecules. *Krossing et al.* showed that the oxidation of white phosphorus with $[NO]^+$ leads to the first substituent-free polyphosphorus cation, namely $[P_9]^+$.[7] This fundamental finding could only be achieved with the help of weakly coordinating anions (WCAs).[8] Hence, oxidation is a promising route to access extended polyphosphorus systems without any stabilizing organic substituents and may be a key to generating first representatives of the heavier pnictogen elements as well.

Our research focuses on the formation and reactivity of substituent-free polypnictogen ligands in the coordination sphere of transition metals.[9] While the reduction chemistry[10] and reactivity towards nucleophiles[10c,11] have been investigated more and more, only few examples of oxidation products are known. Generally, oxidation chemistry appears to be very difficult owing to the high sensibility of the products and the influences of the solvent as well as the strong competition between oxidation and coordination reactions. Thus, it was shown that the oxidation of the hexaphosphabenzene complex $[(Cp^*Mo)_2(\mu,\eta^6:\eta^6\text{-}P_6)]$[12] results in a bis-allylic distortion of the P_6 ring (**I**, Scheme 1).[13] In

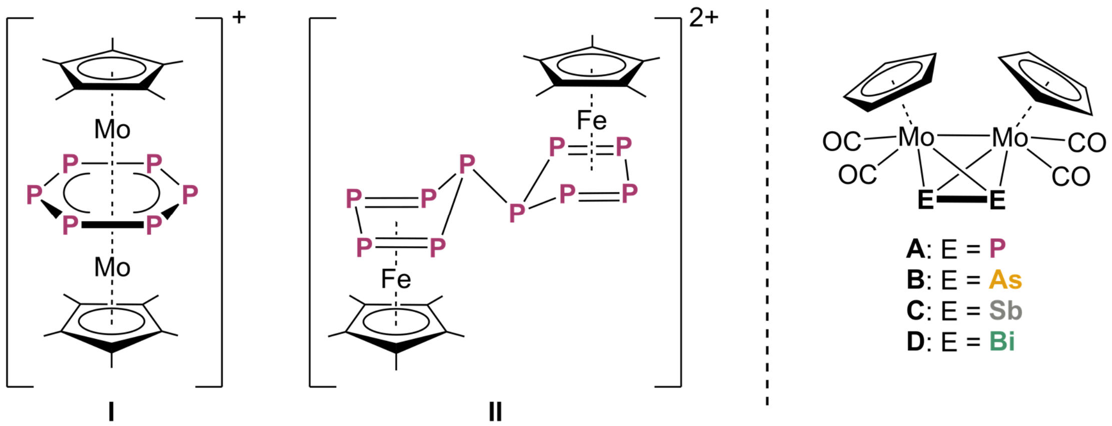

Scheme 1: Oxidized polyphosphorus ligand complexes (**I** and **II**) and structural representation of the tetrahedral complexes **A**–**D**.

contrast, the oxidation of [Cp*Fe(η^5-P_5)][14] leads to P-P bond formation and yields a formally neutral bicyclic P_{10} ligand stabilized by two [Cp*Fe^{II}]$^+$ fragments (**II**, Scheme 1).[10f,15] The obvious general deficit in our knowledge and the lack of examples with heavier group 15 elements motivated us to carry out a first systematic study of the oxidation chemistry of these heavier elements by oxidizing the complexes [{CpMo(CO)$_2$}$_2$(μ,η^2:η^2-E_2)] (Scheme 1, E = P (**A**), As (**B**), Sb (**C**), Bi (**D**)),[16] which are isolobal to P_4 and its heavier analogues. In doing so, oxidation instead of coordination was observed for the first time for these E_2 units, leading, in the case of phosphorus and arsenic, to unprecedented E_4^{2+} chains stabilized in the coordination sphere of transition metals, whereas the heavier antimony and bismuth representatives reacted to unprecedented dicationic E_4 cages.

4.2 Results and Discussion

The cyclic voltammograms of the starting materials (Figure 1a) reveal a pseudo-reversible oxidation at +0.28 V (**A**), +0.19 V (**B**), +0.05 V (**C**) and −0.18 V (**D**) vs. $Cp_2Fe^{0/+}$ with the reduction peaks shifted significantly to lower potentials at −0.22 V (**A**), −0.06 V (**B**), −0.38 V (**C**) and −0.47 V (**D**). This supports the expected trend of a decrease in oxidation potential as the atomic number of the element increases.[17]

When **A** is reacted with the strong one-electron oxidant [$C_{12}H_8S_2$]$^+$[SbF_6]$^-$ ($C_{12}H_8S_2$ = thiantrenium = [Thia]) in CH_2Cl_2, a dark precipitate is formed, and the orange solution decolourizes. The product **1a** (Scheme 2) is obtained as a dark green analytically pure powder in 80% yield. Unfortunately, the ionic product **1a** is insoluble in all common solvents except for MeCN, $MeNO_2$ and acetone but in these

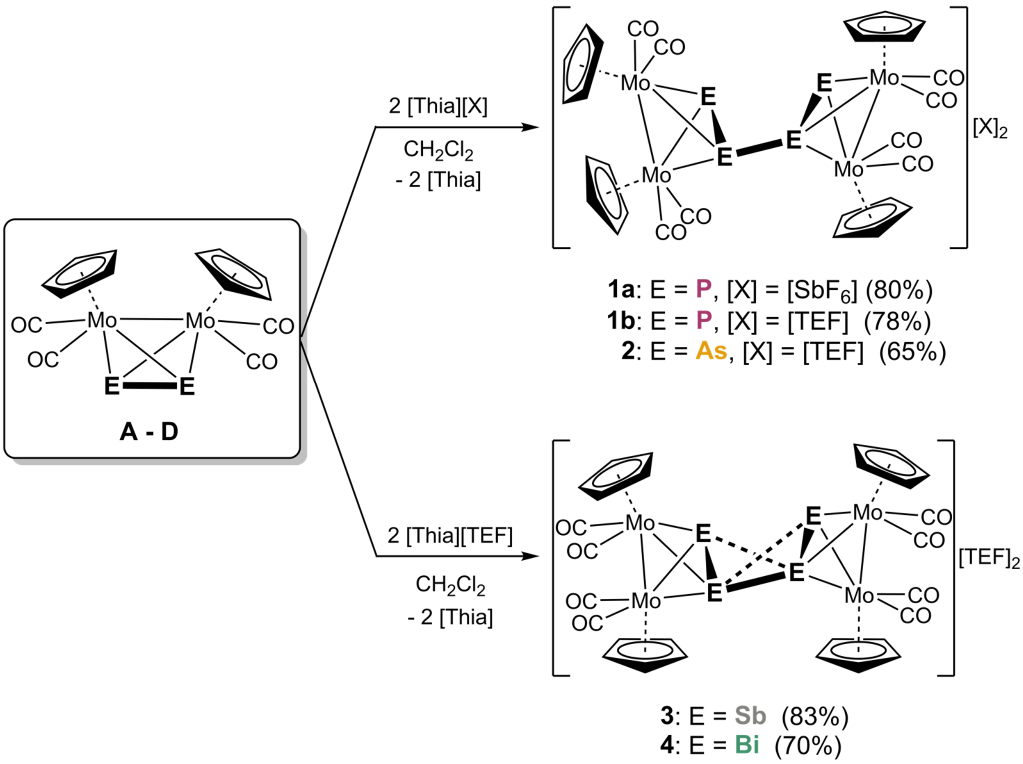

Scheme 2: Oxidation of **A–D**. Yield given in parentheses.

solvents fast decomposition occurs even at low temperatures. Nevertheless, a few dark red crystals of **1a** suitable for single crystal X-ray diffraction were obtained (Figure 1b).

To increase the solubility of the oxidation products and enable the characterization of **1a** in solution, the $[SbF_6]^-$ anion was exchanged for the WCA aluminate anion $[Al\{OC(CF_3)_3\}_4]^-$ (= $[TEF]^-$). Therefore, a route for a high yielding synthesis of the salt [Thia][TEF] had to be developed. We identified two approaches,[17] of which the most promising one is a simple one-step synthesis starting from commercially available reagents, giving the deep purple [Thia][TEF] in 92 % yield (equation 1). The reaction is performed in liquid SO_2 to ensure that Li[TEF] and $[NO][SbF_6]$ are fully solubilized. The product [Thia][TEF], however, is readily soluble in CH_2Cl_2 and crystallizes as dark purple blocks from CH_2Cl_2/*n*-hexane.[17] With the help of this very well soluble strong oxidant, reactions can now be conducted even at very low temperatures and in solvents with lower polarity.

When [Thia][TEF] is reacted with a solution of **A, B** (orange-red), **C** (red) or **D** (dark yellow-brown) in CH_2Cl_2, an immediate colour change to dark red-green without the formation of any precipitate is observed. The addition of toluene results in the precipitation of the almost pure products **1b** and **2**–**4** as dark green powders. Interestingly, recrystallization from CH_2Cl_2/*n*-hexane yields dark red single crystals in all cases (except **4**: black crystals). Dissolution of the crystals in CH_2Cl_2 followed by addition of toluene again yields a dark green powder. Single crystal X-ray diffraction of the dark red crystals reveals the E-E coupled products **1b** and **2–4** (Figure 1c–f). The central structural motif of the dicationic products **1a, 1b** and **2** consists of a zigzag P_4 chain (**1a**,**b**) or an As_4 chain (**2**), respectively, with E-E-E angles between 79.06(7)° (**2**)[18] and 104.91(4)° (**1b**). Whereas there is a center of inversion in **1a** resulting in a symmetric and planar P_4 chain, **1b** and **2** are unsymmetric and show an unexpected gauche conformation of the E_4 unit with a dihedral angle of 133.83(5)° (**1b**) and 129.61(8)° (**2**).[18] The Mo–Mo bonds as well as the E–E bonds inside the tetrahedra are significantly elongated compared to

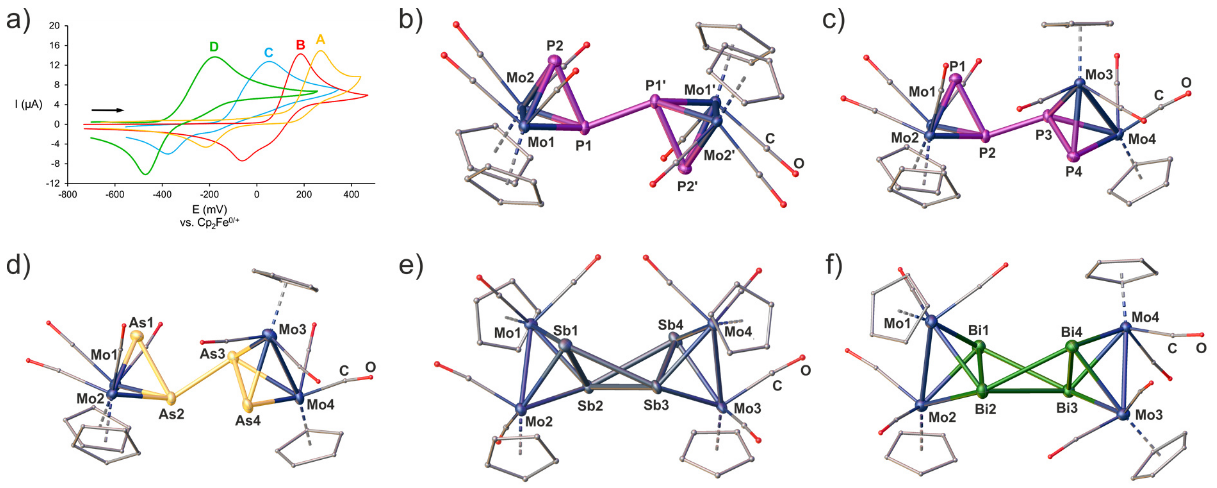

Figure 1: a) CV of **A** to **D** in CH_2Cl_2 solution; (*c*($[NBu_4][PF_6]$ = 0.1 M)). Molecular structures of **1a** (b), **1b** (c), **2** (d), **3** (e) and **4** (f). Ellipsoids are drawn at 50% probability. H atoms are omitted and C as well as O atoms are drawn as small spheres for clarity. Selected bond lengths [Å] and angles [°]: **1a**: P1-P2 2.1762(8), P1-P1' 2.2206(10), Mo1-Mo2 3.1796(2), P2P1P1' 92.96(3); **1b**: P1-P2 2.1277(11), P2-P3 2.2090(10), P3-P4 2.1641(10), Mo1-Mo2 3.1373(3), Mo3-Mo4 3.1669(3), P1P2P3 104.91(4), P2P3P4 98.96(4); **2**: As1-As2 2.467(2), As2-As3 2.562(2), As3-As4 2.447(2), Mo1-Mo2 3.1498(19), Mo3-Mo4 3.1926(17), As1As2As3 79.06(7), As2As3As4 85.61(7); **3**: Sb1-Sb2 2.8729(4), Sb2-Sb3 3.1850(3), Sb3-Sb4 2.8711(4), Sb1-Sb3 3.2920(4), Sb2-Sb4 3.2594(3), Mo1-Mo2 3.2122(4), Mo3-Mo4 3.2193(4), Sb1Sb2Sb3 65.598(9), Sb2Sb3Sb4 64.880(8); **4**: Bi1-Bi2 3.0442(4), Bi2-Bi3 3.3202(3), Bi3-Bi4 3.0642(4), Bi1-Bi3 3.4453(4), Bi2-Bi4 3.4599(4), Mo1-Mo2 3.2129(8), Mo3-Mo4 3.2232(8), Bi1-Bi2-Bi3 65.383(8), Bi2-Bi3-Bi4 65.488(8).

the neutral complexes **A** and **B** (**A**: Mo–Mo: 3.022(1) Å, P–P 2.079(2) Å;[16a] **B**: Mo–Mo: 3.131(2) Å, As–As 2.305(3) Å).[16b] The newly formed central P–P bonds in **1a** and **1b** are similar in length (2.21(1)-2.22(1) Å) and significantly longer than the terminal P–P bonds (2.13(1)-2.18(1)° Å). The central As–As bond (2.562(2) Å)[18] in **2** is similarly elongated compared to the terminal As–As bonds (2.447(2)-2.467(2) Å). An interesting structural feature of **1a/b** and **2** is the almost eclipsed arrangement of the Cp rings in **1a** and on one Mo_2E_2 unit in **1b** and **2**, respectively, (see left side in Figure 1c and 1d), which has not been observed before for the free tetrahedral complexes **A** or **B** in the solid state. This rearrangement suggests a possible free motion of the ligands on the Mo atom in solution as found in the tetrahedral complex $[\{CpMo(CO)_2\}_2(\mu,\eta^2:\eta^2\text{-PAs})]$.[19]

The solid-state structures of **3** and **4** (Figure 1e/f) reveal a zigzag E_4 chain as well with the central E–E bond being significantly elongated compared to the terminal E–E bonds, which are again longer than in free **C** and **D**. The same is true for the Mo–Mo bonds.[16c,16d] However, in contrast to **1a/b** and **2**, the antimony and bismuth derivatives exhibit further short E···E contacts (Sb1-Sb3/Sb2-Sb4: 3.2593(3)-3.2920(4) Å; Bi1-Bi3/Bi2-Bi4: 3.4453(4)-3.4599(4) Å), which are shorter than the sum of the van-der-Waals radii (Sb: Σ = 4.12 Å; Bi: Σ = 4.14 Å),[20] resulting in a distorted "butterfly-like" (bicyclo[1.1.0]butane) framework stabilized by four $[CpMo(CO)_2]$ fragments. The first neutral antimony butterfly complexes have been published only recently,[21] while they are completely unknown as dicationic cores and for bismuth in general. Hence, compound **4** represents the first "butterfly-like" complex of the heaviest group 15 element, even though it is quite distorted.

DFT calculations[17] show that the singly occupied molecular orbital (SOMO) in the paramagnetic monocations $[\mathbf{A}]^+$-$[\mathbf{D}]^+$ (potentially formed first) is delocalized over the molybdenum atoms and the E_2 unit (Figure 2a; see also the Supporting Information, Figure S37). By going from P to Bi (*i.e.*, $[\mathbf{A}]^+$ to $[\mathbf{D}]^+$), the spin density on Mo decreases, while the spin density on the E atoms increases (*e.g.*, 0.75 and 0.51 unpaired e^- on the Mo atoms as well as 0.16 and 0.41 unpaired e^- on the E atoms for $[\mathbf{A}]^+$ and $[\mathbf{D}]^+$, respectively).[17] The dimerization of the transient monocations $[\mathbf{A}]^+$–$[\mathbf{D}]^+$ to the dications **1**–**4** *via* E–E bond formation is exothermic in solution, with a free energy of −118.12 kJ·mol^{-1} to −141.15 kJ·mol^{-1} for **1b** and **4**, respectively. The increase of the dimerization energy is roughly continuous, except for the arsenic derivative **2**, which shows the lowest dimerization energy (Figure 2b). This is in good agreement with the observed experimental data, that is, the partial dissociation of **2** to $[\mathbf{B}]^+$ in solution (*vide infra*). Furthermore, the DFT calculations consistently confirm the experimentally

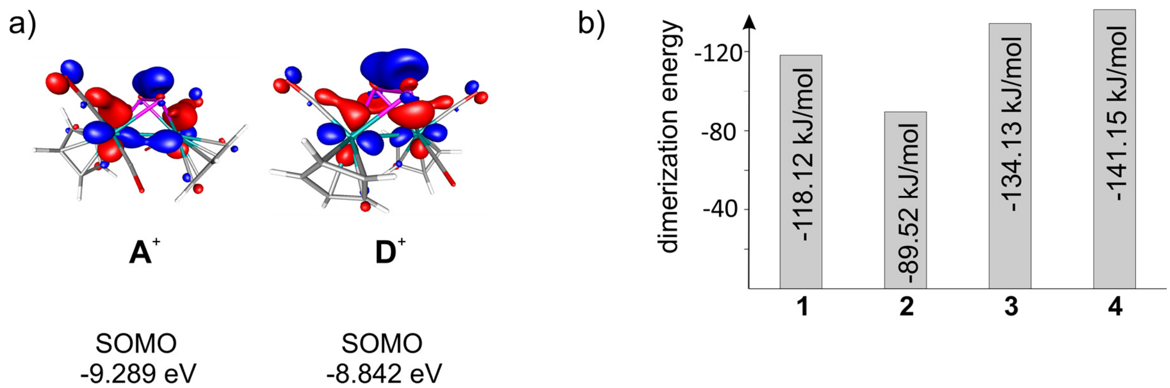

Figure 2: a) Single occupied molecular orbitals in $[\mathbf{A}]^+$ and $[\mathbf{D}]^+$ and b) dimerization energies for **1**–**4**, calculated at the B3LYP/def2-TZVP level of theory.

observed E–E and Mo–Mo bond elongations, although the absolute bond lengths are overestimated by the used DFT method.[17] Additionally, the E-E-E-E torsion angle in the optimized geometry of **1** and **2** closely approaches 180° during the geometry optimization leading to an almost planar E_4 unit. This suggests that the experimentally observed gauche arrangement in **1b** and **2** determined by single crystal X-ray diffraction may be caused by solid state effects. Moreover, the solid-state structures of **3** and **4** are well reproduced by the calculations. All attempts to optimize the geometry of **4** by starting from a geometry similar to that of **1a** lead to the cage-like geometry as found for **4** in the solid state. This indicates that the structures of **3** and **4** are not a result of packing effects in the solid state. Furthermore, the energy difference between **1a** (C_i symmetry) and **1b** (C_1 symmetry) is with 5.39 kJ·mol^{-1} rather small with the latter structure being energetically favored. Natural population analysis (NPA) shows an increase in the positive charge of the E_4 unit from +1.10 to +2.27 from **1** to **4**, while the averaged charge density on the $CpMo(CO)_2$ fragment varies from +0.21e to -0.07e in **1** to **4**.

The rather unusual geometry of **3** and **4** can be rationalized by inspecting the molecular orbital (MO) interaction diagram of **4**, made up of two $[\{CpMo(CO)_2\}_2Bi_2]^+$ fragments (Figure 3). This diagram shows that the orbitals involved in the Bi-Bi σ bond as well as in the Bi-Mo bonds of the two fragments interact with each other leading to a set of five molecular orbitals that are bonding within the Bi_4 unit. Additionally, the SOMO and SOMO-1 orbitals of the fragments interact to give the HOMO, which is bonding within the Bi_4 unit, and to the LUMO of **4**. In contrast to **4**, the interaction of the $[\{CpMo(CO)_2\}_2P_2]^+$ fragment orbitals in **1**, which are mainly P-based, leads to the formation of a P–P σ bond as well as to orbitals with a P–P π bonding character (Figure S38 in SI).[22] The Wiberg Bond Index (WBI) of the central P–P bond in **1** is with 0.85 lower than that of the terminal P–P bonds (1.00 and 1.05). This trend is also observed for **2**, **3** and **4**, but the WBIs are lower (**2**: 0.67 and 0.85/0.86; **3**: 0.30 and 0.62/0.62; **4**: 0.45 and 0.55/0.56). In **3** and **4**, the two additional weak E···E interactions show WBIs of 0.30/0.47 and 0.30/0.27, respectively. Interestingly, when considering only the sum of the WBIs of the E–E bonds and the interactions between the $[\{CpMo(CO)_2\}_2E_2]^+$ fragments, the complexes **3** and **4** (WBI = 1.07/1.02) have a slightly larger bond index than **1** and **2** (WBI = 0.91/0.81). This shows that the central Sb–Sb and Bi–Bi bonds are stabilized *via* the formation of several additional weak E···E interactions.[17]

As **1a** decomposes in solution, we only report on the spectroscopic data of **1b** and **2**–**4**. The ^{1}H NMR spectra of **1b**, **3** and **4** in CD_2Cl_2 feature only one sharp singlet at δ = 5.75 ppm (**1b**), 5.65 ppm (**3**) or 5.78 ppm (**4**), respectively, for the Cp ligands. Likewise, one singlet is observed in the $^{13}C\{^1H\}$ NMR spectra (δ = 92.26 ppm (**1b**), 89.51 ppm (**3**) and 88.54 ppm (**4**)) for the Cp ligands, indicating a highly dynamic behaviour of the Cp ligands in solution, which cannot be resolved on the NMR timescale, not even by going to lower temperatures.

Surprisingly, in the ^{1}H NMR spectrum of **2** at room temperature, a broad signal is observed at δ = 5.79 ppm ($\omega_{1/2}$ = 330 Hz), which is slightly shifted to lower fields and sharpens upon cooling to 193 K (Figure S2 in SI). In the $^{13}C\{^1H\}$ NMR spectrum, a singlet at δ = 91.39 ppm is observed only at 193 K. This behaviour may be attributed to a partial dissociation of **2** into the paramagnetic monocation [**B**]$^+$ at room temperature. At low temperatures, this process is inhibited, and the formation of the dication **2** is favoured. In addition to the described signals for the Cp ligands, characteristic signals for CO ligands and the [TEF]$^-$ anion can be detected in the $^{13}C\{^1H\}$ and $^{19}F\{^1H\}$ NMR

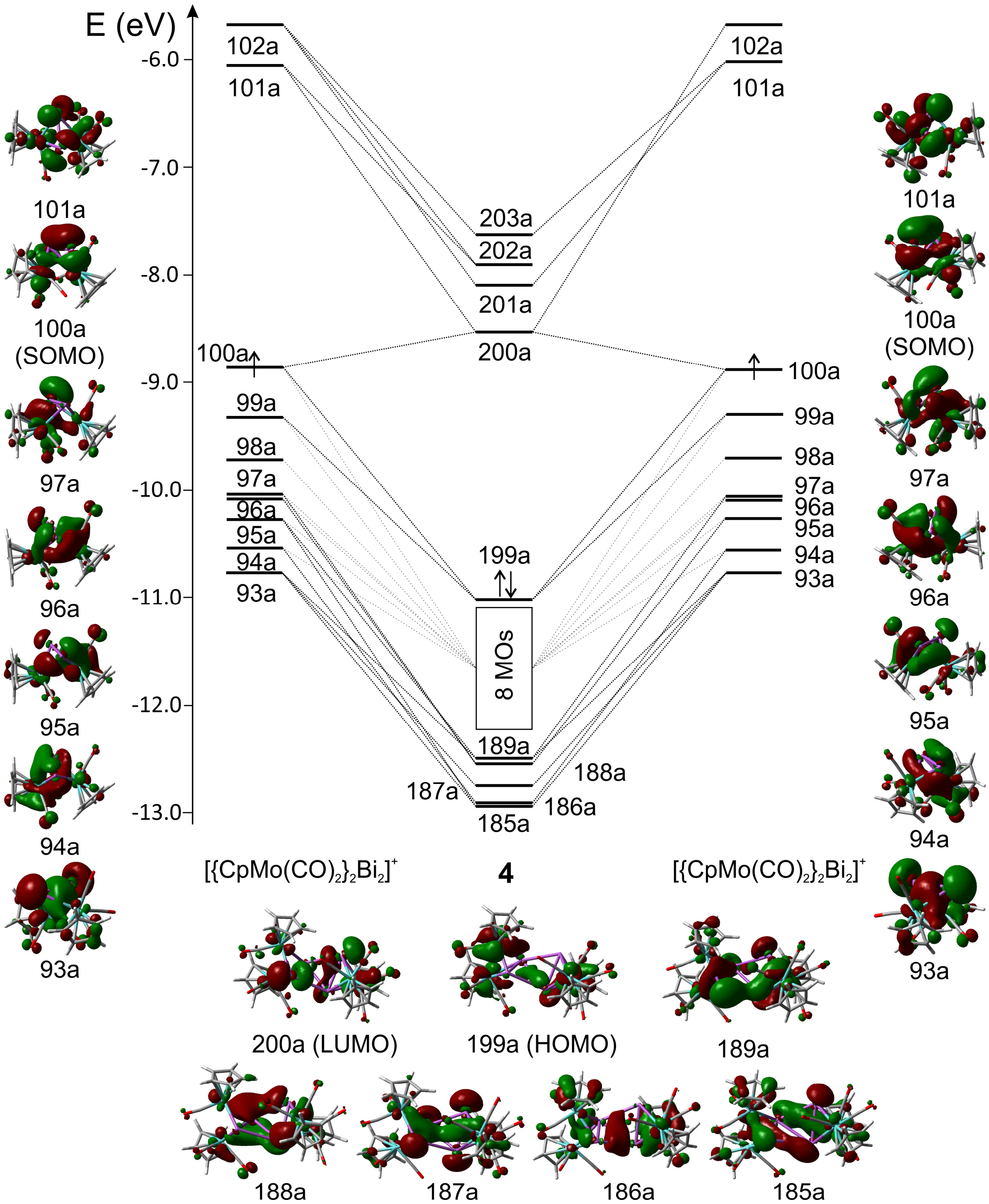

Figure 3: Molecular orbital interaction diagram of **4**, at the B3LYP/def2-SVP level. The MOs marked with the box do not contribute to the bonding within the Bi_4 unit. Only fragment contributions higher than 10% are depicted. For the fragments only the alpha spin orbitals are considered.

spectra, respectively. Interestingly, the $^{31}P\{^1H\}$ NMR spectrum of **1b** shows only one broad signal at δ = −0.1 ppm ($\omega_{1/2}$ = 193 Hz), which moves to higher field (δ = −26.5 ppm) and significantly broadens upon cooling ($\omega_{1/2}$ > 10000 Hz at 213 K), but no signal splitting can be resolved before the compound starts precipitating, indicating a fast dynamic process in solution for the P_4 chain in **1b** as well.

Solutions of **1b**, **3** and **4** in CH_2Cl_2 and solid samples are silent in the X-band EPR spectra at room temperature and at 77 K, indicating that no dissociation of the dicationic species occurs, which is in good agreement with the calculated dissociation energy barriers (*vide supra*). Surprisingly, the same measurements for **2** show a weak isotropic signal (g_{iso} = 2.1110), which is in good agreement with the previously described ^{1}H NMR spectrum and supports the assumption that small amounts of dissociated monocationic radicals [**B**]$^{+}$ are present in solution at room temperature. Additionally, the EPR signal is significantly shifted from $g_{iso} = 2.1110$ to $g_{iso} = 1.9667$ upon cooling from 293 K to 77 K. NMR spectroscopy conclusively shows that the dicationic P_4 complex **1b** undergoes fast dynamic processes rendering all P atoms, all Cp ligands and all CO ligands magnetically equivalent on the NMR timescale at room temperature. To shed light on these dynamic processes, the ^{31}P{^{1}H} MAS NMR and the IR spectra were recorded for a precipitated and a crystalline sample of **1b**. As mentioned before, the precipitated (dark green) and crystalline (dark red) forms of **1b** can be converted into each other in a reversible fashion. Solutions of the precipitated or crystallized of **1b** cannot be distinguished spectroscopically from each other. Additionally, **1b** can be precipitated or crystallized from these solutions. The ^{31}P{^{1}H} MAS NMR spectrum of crystalline **1b** (Figure 4) shows four signals at δ = 118.7, 40.7, –70.0 and –92.5 ppm in a 1:1:1:1 ratio, which correspond to the four magnetically inequivalent P atoms as also found in the crystal structure (see Figure 1c). The signal assignment is based on the calculated isotropic magnetic shielding of the P atoms.[17] In contrast, the green precipitate exhibits two distinctly different singlets at δ = 124.7 ppm (A) and δ = –75.9 ppm (B) in a 1:1 ratio (Figure 4a). This spectrum is in good agreement with a symmetric P_4 chain comparable to that in the X-ray structure of **1a** (Figure 1b). Signal A corresponds to the terminal P atoms and signal B to the central P–P bridged atoms. The similar chemical shifts of signal A and the signal for P1 in the ^{31}P{^{1}H} MAS NMR spectra can also be explained by the similar environment of P1 in **1b** and P2/P2’ in **1a** with the Cp rings on the adjacent Mo–Mo bond in a *cis* arrangement (see Figure 1b,c).

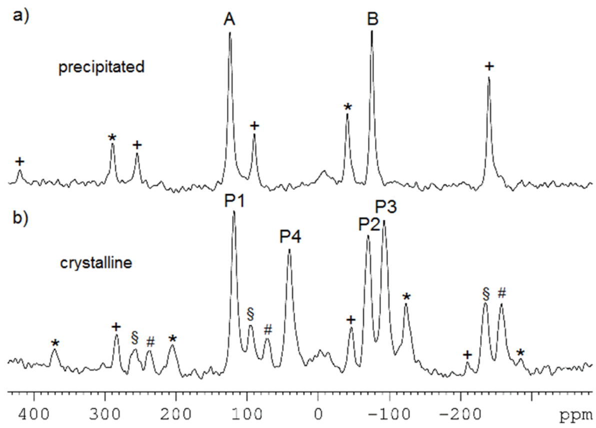

Figure 4: ^{31}P{^{1}H} MAS NMR spectra of **1b** at f = 20 kHz in the precipitated (a) and crystalline form (b), respectively. Rotation side bands are marked corresponding to the signals +(P1, B), §(P2), #(P3) and *(P4, A).

The IR spectra of solid **1b** (symmetric) show only three strong bands corresponding to CO stretching for the green precipitate, while at least six strong bands can be observed for the red brown crystalline sample (unsymmetric), which is in good agreement with a decrease in symmetry. In contrast, the IR spectra of **2** and **3** do not show any differences in the CO bands between the crystalline and precipitated forms; in each case, at least seven bands are observed. Hence, these compounds do not undergo a reversible conversion between a symmetric and an asymmetric form. For the bismuth derivative **4**, a small shift of the CO bands is detected between the crystalline and the precipitated samples. In general, the CO stretching frequencies of **1b** and **2**–**4** are higher than those for the neutral complexes **A**–**D**, which can be explained by a decrease in π back-bonding from the Mo atoms upon oxidation.[17]

4.3 Conclusion

In summary, we have systematically studied the oxidation of polypnictogen moieties in the coordination sphere of transition metals. The used tetrahedral E_2 ligand complexes **A**–**D** are readily oxidized by the organic radical cation $[\text{Thia}]^{+}$. However, the products could only be characterized in CH_2Cl_2 solution once the weakly coordinating anion $[\text{TEF}]^{-}$ had been incorporated. In this context, the newly synthesized oxidation agent [Thia][TEF] has been shown to be a powerful synthetic reagent owing to its oxidation power as well as its solubility and the good solubility of the corresponding products. The initially formed monocations $[\mathbf{A}]^{+}$, $[\mathbf{B}]^{+}$, $[\mathbf{C}]^{+}$ and $[\mathbf{D}]^{+}$ dimerize immediately in solution *via* E–E bond formation giving the dicationic products $[\{CpMo(CO)_2\}_4(\mu_4,\eta^2:\eta^2:\eta^2:\eta^2\text{-}E_4)]^{2+}$ (E = P (**1a**, **b**), As (**2**), Sb (**3**), Bi (**4**)), which reveal unprecedented unsubstituted cationic E_4 chains stabilized in the coordination sphere of transition metals. Although **1a** decomposes in solution, we were able to determine its symmetric (C_i) solid-state structure and compared it to the unsymmetric solid-state structures of the analogous complexes **1b** and **2**, which feature an E_4 chain in gauche conformation. Furthermore, the complexes **3** and **4** of the heavier Group 15 elements Sb and Bi tend to undergo more cage-like aggregation, leading to a distorted “butterfly-like” (bicyclo[1.1.0]butane) geometry. DFT calculations showed that the bonding within the Bi_4 unit in **4** is mainly based on the mixing of Bi–Bi σ and Mo–Bi orbitals of the two $[\{CpMo(CO)_2\}_2(E_2)]^{+}$ fragments. The same can be considered for **3**. In contrast to **1**, which features a strong central P–P bond, the rather weak central E–E bonds in **3** and **4** are supported through additional weak E···E interactions. The P_4 chain of **1b** can be reversibly converted into a symmetric (precipitated) and an asymmetric (crystalline) form. Such a conversion was not observed for the heavier derivatives **2**, **3** and **4**. Dissociation of the dicationic complexes to the free monoradicals was only observed for the As derivative **2**, which is in agreement with the dissociation/dimerization energies of the DFT calculations. Moreover, the P_4 chain of **1b** exhibits very fast dynamic behaviour in solution in contrast to the known catena-polyphosphorus cations or the $[P_9]^{+}$ cation.[7] Therefore, the oxidation chemistry of polypnictogen ligand complexes provides a unique entry to new classes of cationic polypnictogen frameworks stabilized in the coordination sphere of transition metals, which cannot be obtained by other means.

4.4 Supporting Information

4.4.1 General remarks

All manipulations were carried out under an inert atmosphere of dried nitrogen using standard Schlenk and glovebox techniques. CH_2Cl_2 and CD_2Cl_2 were dried over CaH_2, alkanes were distilled from K or Na/K alloy. Dried solvents were also taken from a solvent purification system from MBraun. NMR spectra were recorded in CD_2Cl_2 on a Bruker Avance 300 MHz NMR spectrometer (^1H: 300.132 MHz, ^{31}P: 121.495 MHz, ^{13}C: 75.468 MHz, ^{19}F: 282.404 MHz) or a Bruker Avance 400 MHz NMR spectrometer (^1H: 400.130 MHz, ^{31}P: 161.976 MHz, ^{13}C: 100.613 MHz, ^{19}F: 376.498 MHz) with external references of $SiMe_4$ (^1H, ^{13}C), CCl_3F (^{19}F) and H_3PO_4 (85%, ^{31}P). $^{31}P\{^1H\}$ MAS NMR spectra were recorded on a Bruker Avance 300 NMR spectrometer (^{31}P: 121.495 MHz). The chemical shifts of the MAS NMR spectra are also presented in the δ scale using NaH_2PO_4 as an external standard. X-Band EPR spectra were recorded on a MiniScope MS400 device from Magnettech GmbH with a frequency of 9.5 GHz equipped with a rectangular resonator TE102. Cyclovoltammetry (CV) measurements were performed in CH_2Cl_2 solution containing $[NBu_4][PF_6]$ (c = 0.1 mol·L^{-1}) as supporting electrolyte. Ferrocene (Fc) or cobaltocene were added to the samples after the complete measurements and Fc was used as an internal reference ($E(Fc^0/Fc^+)$ = 0 V). The CV measurement of **A**, **C** and **D** were recorded and analyzed by the first author. The CV of **B** was recorded and analyzed by Felix Riedelberger from Prof. Dr. Scheer's group at the University of Regensburg. The spectroelectrochemistry of **A** was recorded and analyzed by Dr. Florian Pevny and Prof. Dr. Rainer Winter at the University of Regensburg (now University of Konstanz). ESI-MS spectra were either measured on a Finnigan Thermoquest TSQ 7000 mass-spectrometer by the MS department of the University of Regensburg or on a Waters Micromass LCT ESI-TOF mass-spectrometer by the first author. The mass spectrum of **1b** was recorded by Valentin Vass from Dr. Robert Kretschmer's group at the University of Regensburg. IR spectra of **1 a/b** were recorded as KBr discs or in CH_2Cl_2 solution using a Varian FTS-800 FT-IR spectrometer. The IR spectra of **2**, **3** and **4** were recorded as solids using a ThermoFisher Nicolet iS5 FT-IR spectrometer with an iD7 ATR module and an ITX Germanium crystal. Elemental analyses were performed by the micro analytical laboratory of the University of Regensburg.

4.4.2 Experimental details

Preparation of [Thia][TEF]:

In order to achieve a chemical oxidation of **A** to **D**, and the possibility to study the ionic products in solution the best choice was to use a strong oxidant like the organic radical cation of thianthrene $[C_{12}H_8S_2]^+$ (= [Thia], E^0 = 0.86 V vs $Cp_2Fe^{0/+}$)[23] containing the weakly coordinating anion (= WCA) $[Al\{OC(CF_3)_3\}_4]^-$ (= $[TEF]^-$). Two synthetic procedures were developed affording the deep purple salt [Thia][TEF] in good yield (see Scheme S1). Hereby, method 2 represents a simple one-step synthesis starting from commercially available reagents, where [Thia][TEF] is obtained in 92 % yield. The reaction is performed in liquid SO_2 to ensure the solubility of Li[TEF]. The product [Thia][TEF], however, is readily soluble in CH_2Cl_2 and crystallizes as dark purple blocks from CH_2Cl_2/n-hexane.

method 1: $\mathrm{Li[TEF] + [Thia][SbF_6]} \xrightarrow[\bullet)))]{CH_2Cl_2,\ 20\ h} \mathrm{[Thia][TEF] + Li[SbF_6]}\downarrow$
(61%)

method 2:
$\mathrm{Li[TEF] + NO[SbF_6] + (thianthrene)} \xrightarrow[r.\ t.,\ 24h]{SO_2\ (l)} \mathrm{[Thia][TEF] + Li[SbF_6]}\downarrow + \mathrm{NO}\uparrow$
(92%)

Scheme S1. Syntheses of [Thia][TEF]. Crystalline yield given in parentheses.

Method 1: Thia[SbF_6] (135 mg, 0.30 mmol, 1 eq.) and Li[TEF] (330 mg, 0.34 mmol, 1.1 eq.) were placed in a Schlenk flask equipped with a Young valve. Subsequently, 10 mL of CH_2Cl_2 (stored over CaH_2) were condensed onto the solids at –196 °C. The flask was closed under reduced pressure. Upon dissolution of the compounds the formation of a deep violet solution could be observed. The flask was sonicated for 20 h. In order to precipitate the ionic product the reaction mixture was filtered over diatomaceous earth directly into 100 mL of stirred *n*-hexane. The blackish blue precipitate was freed from the colorless supernatant solution, washed with 100 mL of *n*-hexane and dried in vacuum. The solid was dissolved in 15 mL of CH_2Cl_2 and the deep violet solution was carefully layered with 80 mL of *n*-hexane. After storage at +4 °C [Thia][TEF] can be obtained as dark violet crystals in the course of three days. Yield 215 mg (61%).

Method 2: A Schlenk flask with Young valve was equipped with a stirring bar, thianthrene (1.08 g, 4.99 mmol, 1.2 eq.), NO[SbF_6] (1.156 g, 4.36 mmol, 1 eq.) and Li[TEF] (4.23 g, 4.34 mmol, 1 eq.). SO_2 (50 mL) was condensed onto these solids under reduced pressure at –196 °C. The flask was closed under reduced pressure and the cooling was removed. Upon dissolution the reaction turns from light blue to dark blue and finally to dark violet, when everything is dissolved. After stirring at r.t. for 18 h the SO_2 was removed and the dark blue solid was solved in 60 mL of CH_2Cl_2. The deep violet suspension was filtered over diatomaceous earth and the frit was washed with pure CH_2Cl_2 till the filtrate was colorless. 400 mL of *n*-hexane were added to the solution, which led to precipitation of the crude product. The supernatant was decanted off and the precipitate was washed three times with 100 mL of toluene and subsequently dried in vacuum. The crude product was dissolved in 60 mL of CH_2Cl_2. The resulting deep purple solution was filtered and carefully layered with the fivefold amount of *n*-hexane. Storage at +4 °C afforded [Thia][TEF] as dark violet to black blocks. Yield 4.722 g (3.99 mmol, 92 %).
^{1}H NMR (400 MHz, CD_2Cl_2, 300 K) no signal can be resolved for [Thia]$^{+}$. Additionally, the residual solvent signal of CD_2Cl_2 is significantly broadened and usual splitting to a triplet is not observed. ^{27}Al{^{1}H} NMR (104.3 MHz, CD_2Cl_2, 300 K) δ/ppm 34.8 [TEF]$^{-}$. ^{19}F{^{1}H} NMR (282.4 MHz, CD_2Cl_2, 300 K) δ/ppm = –75.4 (s, CF_3). X-band EPR (293 K, solid) g_{iso} = 2.007. Anal. calcd. for [Thia][TEF]: C: 28.42, H: 0.68, S: 5.42. Found: C: 28.82, H: 0.81, S: 5.47.

Preparation of [{CpMo(CO)$_2$}$_4$(μ_4,η^2:η^2:η^2:η^2-P$_4$)][SbF$_6$]$_2$ (1a):

[{CpMo(CO)$_2$}$_2$(μ,η^2:η^2-P$_2$)] (**A**) (99 mg, 0.2 mmol, 2 eq.) was dissolved in 15 mL of CH_2Cl_2 at –35 °C. [Thia][SbF$_6$] (90 mg, 0.2 mmol, 2 eq.) was dissolved in 40 mL of CH_2Cl_2 at –35 °C and slowly added to the stirred solution of **A**. The turbid dark reaction mixture was stirred at –30 °C for 20 min. When the stirring was stopped, a dark green precipitate and a clear light orange solution (small excess **A**) could be observed. The supernatant solution was decanted off and the crude product was washed two times with toluene (30 mL) and dried in vacuum. This affords **1a** as a dark green powder.
Yield 117 mg (80%). ^{1}H NMR (400 MHz, CD_3CN, 273 K, decomposition!) δ/ppm 5.74 (br, Cp), 3.15 (br), 1.93 (br). ^{31}P{^{1}H} NMR (162.0 MHz, CD_3CN, 273 K, decomposition!) δ/ppm 3.2 (br, ω½ = 1300 Hz), –42.2 (s, presumably **A**). ^{13}C{^{1}H} NMR (100.6 MHz, CD_3CN, 273 K, decomposition!) δ/ppm 220.53 (s, CO), 92.45 (s, Cp). Anal. calcd. for [{Cp$_2$Mo$_2$(CO)$_4$P$_2$}$_2$][SbF$_6$]$_2$: C: 22.98, H: 1.38. Found: C: 22.93, H: 1.54.

Preparation of [{CpMo(CO)$_2$}$_4$(μ_4,η^2:η^2:η^2:η^2-P$_4$)][TEF]$_2$ (1b):

Light orange [{CpMo(CO)$_2$}$_2$(μ,η^2:η^2-P$_2$)] (**A**) (109 mg, 0.22 mmol, 2.2 eq.) and dark purple [Thia][TEF] (237 mg, 0.2 mmol, 2 eq.) were combined as solids and grinded together affording a dark brown powder. IR spectroscopy from KBr pellets (see below) did show the CO stretching frequencies of pure **A** (this suggests no reaction of Thia[TEF] and **A** in the solid state). This solid was transferred into a Schlenk flask and pre-cooled CH_2Cl_2 (30 mL) was added at –50 °C and the resulting turbid dark reddish green solution was stirred in a cooling bath for 30 min while the solvent temperature reached –20 °C (The reaction product is the same when a solution of [Thia][TEF] is added to a solution of **A**). The cooling bath was removed and the reaction was stirred for additional 10 minutes at room temperature. The clear dark solution was transferred to a flask containing 100 mL of stirred toluene. The crude product is precipitated as a fine dark green to black powder leaving a clear light orange solution (small excess of pure **A**). The supernatant solution was removed and the precipitate washed two times with 50 mL of pure toluene. The crude product was dried in vacuum yielding 250 mg (85%) of dark green powder. Recrystallization from CH_2Cl_2/*n*-hexane affords pure **1b** as dark red blocks which are suitable for single crystal X-ray diffraction in 227 mg (78%) yield. The crystals were dried in vacuum.
^{1}H NMR (400 MHz, CD_2Cl_2, 300 K) δ/ppm 5.75 (s, Cp). ^{31}P{^{1}H} NMR (162.0 MHz, CD_2Cl_2, 300 K) δ/ppm –0.1 (br, $\omega_{1/2}$ = 193 Hz [(**A**)$_2$]$^{2+}$). ^{13}C{^{1}H} NMR (100.6 MHz, CD_2Cl_2, 300 K) δ/ppm 218.92 (s, CO), 121.65 (q, $^1J_{CF}$ = 293 Hz; CF$_3$), 92.26 (s, Cp). ^{19}F{^{1}H} NMR (282.4 MHz, CD_2Cl_2, 300 K) δ/ppm = –75.5 (s, CF$_3$). ^{31}P{^{1}H} MAS NMR (121.6 MHz, 293 K, f = 20 kHz, precipitated) δ/ppm = 124.7 (s, $\omega_{1/2}$ = 790 Hz, P$_{ex}$), –74.9 (s, $\omega_{1/2}$ = 730 Hz, P$_{int}$). ^{31}P{^{1}H} MAS NMR (121.6 MHz, 293 K, f = 20 kHz, crystalline) δ/ppm = 118.7 (s, $\omega_{1/2}$ = 960 Hz, P$_{ex1}$), 40.7 (s, $\omega_{1/2}$ = 1220 Hz, P$_{ex2}$), –70.0 (s, $\omega_{1/2}$ = 1180 Hz, P$_{int1}$), –92.5 (s, $\omega_{1/2}$ = 1170 Hz, P$_{int2}$). The Evans NMR method of **1b** in CD_2Cl_2 solution does not show any paramagnetic shifted solvent signal (suggests diamagnetic [(**A**)$_2$]$^{2+}$ in solution without dissociation). The compound **1b** is ESR silent in the solid state and in CH_2Cl_2 solution. Anal. calcd. for [($C_{14}H_{10}O_4Mo_2P_2$)$_2$][TEF]$_2$: C: 24.63, H: 0.69. Found: (crude product, contains small amounts of thianthrene) C: 27.33, H: 1.10. (crystalline product **2**) C: 24.99, H: 0.81. Positive ion MS, *m/z* (%): 495.8 (10) [**A**]$^+$, 439.8 (30) [**A**–2(CO)]$^+$, 411.8 (100) [**A**–3(CO)]$^+$, 383.8 (88) [**A**–4(CO)]$^+$. **1b** (precipitated): IR(KBr) cm^{-1}: 3128 (w), 2958 (vw),

2924 (w), 2853 (vw), 2048 (vs), 2039 (s), 2001 (vs), 1969 (vw), 1426 (vw), 1354 (m), 1303 (vs), 1277 (vs), 1244 (vs), 1219 (vs), 1168 (m), 973 (vs), 840 (m), 835 (m), 728 (s). **1b** (crystalline): IR(KBr) cm^{-1}: 3140(w), 2962 (vw), 2919 (vw), 2851 (vw), 2069 (s), 2060 (vs), 2043 (s), 2028 (s), 2016 (s), 1994 (s), 1963 (m), 1426 (vw), 1353 (m), 1303 (vs), 1277 (vs), 1243 (vs), 1219 (vs), 1173 (m), 973 (vs), 843 (m), 728 (s).

Preparation of [{CpMo(CO)$_2$}$_4$(μ_4,η^2:η^2:η^2:η^2-As$_4$)][TEF]$_2$ (2):

A dark purple solution of [Thia][TEF] (100 mg, 0.09 mmol, 2 eq.) in 15 mL CH_2Cl_2 was transferred to an orange-red solution of [{CpMo(CO)$_2$}$_2$(μ,η^2:η^2-As$_2$)] (**B**) (52 mg, 0.09 mmol, 2 eq.) in 10 mL CH_2Cl_2 at r.t. affording an immediate color change to a dark reddish green solution. After stirring for 30 minutes addition of 60 mL *n*-hexane lead to precipitation of a green to black powder of crude **2**. The slightly green supernatant solution was removed and the precipitate washed twice with 20 mL of pure toluene. The crude product was dried in vacuum. Recrystallization from CH_2Cl_2/*n*-hexane at +4 °C afforded pure **2** as dark red to black blocks which are suitable for single crystal X-ray diffraction in 81 mg (62%) yield. The crystals were dried in vacuum.

^{1}H NMR (400.1 MHz, CD_2Cl_2, 300 K) δ/ppm 5.79 (s, $\omega_{1/2}$ = 330 Hz Cp). ^{1}H NMR (400.1 MHz, CD_2Cl_2, 193 K) δ/ppm 5.71 (s, $\omega_{1/2}$ = 1.3 Hz Cp). ^{13}C{^{1}H} NMR (100.6 MHz, CD_2Cl_2, 193 K) δ/ppm 120.50 (q, $^1J_{CF}$ = 292 Hz; CF_3), 91.39 (s, Cp). ^{19}F{^{1}H} NMR (376.5 MHz, CD_2Cl_2, 300 K) δ/ppm = –75.5 (s, CF_3). The compound **2** shows an isotropic signal in the ESR spectra with g_{iso} = 2.1110. The signal is shifted to g_{iso} = 1.9667 upon cooling from 293 K to 77 K. Anal. calcd. for [($C_{14}H_{10}O_4Mo_2As_2$)$_2$][TEF]$_2$: C: 23.23, H: 0.65. Found: (crystalline product **2**): C: 23.63, H: 0.75. Positive ion MS, *m/z* (%): 584.87 (65) [**B**]$^+$, 525.85 (32) [**B**–2(CO)]$^+$, 499.65 (100) [**B**–3(CO)]$^+$, 471.66 (76) [**B**–4(CO)]$^+$, 556.66 (3) [**2**-2(CO)]$^{2+}$, 540.66 (3) [**2**-3(CO)]$^{2+}$, Negative ion MS *m/z* (%): 966.89 (100) [TEF]$^-$. **2** (crystalline and precipitated): IR(ATR) cm^{-1}: 3150 (vw), 3140 (vw), 2373 (vw), 2346 (vw), 2056 (w), 2045 (m), 2028 (m), 2014 (m), 1996 (w), 1983 (w), 1966 (w), 1352 (w), 1299 (m), 1274 (s), 1241 (s), 1215 (vs), 1174 (m), 972 (vs), 842 (m), 727 (vs).

Preparation of [{CpMo(CO)$_2$}$_4$(μ_4,η^2:η^2:η^2:η^2-Sb$_4$)][TEF]$_2$ (3):

A dark purple solution of [Thia][TEF] (60 mg, 0.05 mmol, 2 eq.) in 15 mL CH_2Cl_2 was transferred to an red solution of [{CpMo(CO)$_2$}$_2$(μ,η^2:η^2-Sb$_2$)] (**C**) (34 mg, 0.05 mmol, 2 eq.) in 10 mL CH_2Cl_2 at r.t. affording an immediate color change to a dark reddish green solution. After stirring for 30 minutes addition of 60 mL *n*-hexane lead to precipitation of a green to black powder of crude **3**. The slightly brown supernatant solution was removed and the precipitate washed twice with 20 mL of pure toluene. The crude product was dried in vacuum. Recrystallization from CH_2Cl_2/*n*-hexane at +4 °C afforded pure **3** as dark red to black blocks which are suitable for single crystal X-ray diffraction in 65 mg (83%) yield. The crystals were dried in vacuum.

^{1}H NMR (400.1 MHz, CD_2Cl_2, 300 K) δ/ppm 5.65 (s, Cp). ^{13}C{^{1}H} NMR (100.6 MHz, CD_2Cl_2, 300 K) δ/ppm 217.31 (small, CO), 121.24 (q, $^1J_{CF}$ = 295 Hz; CF_3), 89.51 (s, Cp). ^{19}F{^{1}H} NMR (376.5 MHz, CD_2Cl_2, 300 K) δ/ppm = –75.5 (s, CF_3). The compound **3** is ESR silent in the solid state and in CH_2Cl_2 solution at r.t. and at 77 K. Anal. calcd. for $[(C_{14}H_{10}O_4Mo_2Sb_2)_2][TEF]_2$: C: 21.91, H: 0.61. Found: (crystalline product **3**): C: 22.26, H: 0.68. Positive ion MS, *m/z* (%): 677.57 (100) [**C**]$^+$, 621.62 (30) [**C**-2(CO)]$^+$, 593.59 (79) [**C**–3(CO)]$^+$, 565.59 (30) [**C**–4(CO)]$^+$, ~654 (0.3) [**3**-2(CO)]$^{2+}$. Negative ion MS *m/z* (%): 966.93 (100) [TEF]$^-$. **3** (crystalline and precipitated): IR(ATR) cm^{-1}: 3133 (vw), 2369 (vw), 2036 (w), 2018 (w), 1990 (m), 1984 (m), 1975 (w), 1955 (w), 1946 (w), 1426 (vw), 1353 (w), 1290 (m), 1275 (s), 1245 (s), 1215 (vs), 1169 (w), 971 (vs), 847 (w), 727 (s).

Preparation of $[\{CpMo(CO)_2\}_4(\mu_4,\eta^2:\eta^2:\eta^2:\eta^2\text{-}Bi_4)][TEF]_2$ (4):

A dark purple solution of [Thia][TEF] (79 mg, 0.07 mmol, 2 eq.) in 15 mL CH_2Cl_2 was transferred to a dark brown solution of $[\{CpMo(CO)_2\}_2(\mu,\eta^2:\eta^2\text{-}Bi_2)]$ (**D**) (57 mg, 0.07 mmol, 2 eq.) in 10 mL CH_2Cl_2 at r.t. affording an immediate color change to a dark reddish green solution. After stirring for 60 minutes addition of 60 mL *n*-pentane lead to precipitation of a green to black powder of crude **4**. The slightly brown supernatant solution was removed and the precipitate washed twice with 20 mL of pure toluene. The crude product was dried in vacuum. Recrystallization from CH_2Cl_2/*n*-pentane afforded pure **4** as dark black blocks which are suitable for single crystal X-ray diffraction in 85 mg (70%) yield. The crystals were dried in vacuum.

^{1}H NMR (400.1 MHz, CD_2Cl_2, 300 K) δ/ppm 5.78 (s, Cp). ^{13}C{^{1}H} NMR (100.6 MHz, CD_2Cl_2, 300 K) δ/ppm 213.61 (small, CO), 121.24 (q, $^1J_{CF}$ = 293 Hz; CF_3), 88.54 (s, Cp). ^{19}F{^{1}H} NMR (376.5 MHz, CD_2Cl_2, 300 K) δ/ppm = –75.5 (s, CF_3). The compound **4** is ESR silent in the solid state and in CH_2Cl_2 solution at r.t. and at 77 K. Anal. calcd. for $[(C_{14}H_{10}O_4Mo_2Bi_2)_2][TEF]_2$: C: 19.81, H: 0.55. Found: (crystalline product **4**): C: 19.96, H: 0.66. Positive ion MS, *m/z* (%): 849.90 (81) [**D**]$^+$, 793.91 (29) [**D**–2(CO)]$^+$, 765.89 (100) [**D**–3(CO)]$^+$, 737.88 (38) [**B**–4(CO)]$^+$. Negative ion MS *m/z* (%): 967.00 (100) [TEF]$^-$. **4** (crystalline): IR(ATR) cm^{-1}: 3124 (vw, br), 2006(w), 1978 (m), 1970 (m), 1950 (w), 1931 (w), 1919 (w), 1352 (w), 1297 (m), 1274 (s), 1241 (s), 1213 (vs), 1172 (w), 971 (vs), 837 (w), 727 (s). **4** (precipitated): IR(ATR) cm^{-1}: 3151 (vw, br), 2020 (w), 2001 (m), 1974 (m), 1966 (m), 1934 (w, br), 1919 (w, br), 1352 (w), 1297 (m), 1274 (s), 1241 (s), 1213 (vs), 1172 (w), 971 (vs), 837 (w), 727 (s).

4.4.3 NMR spectroscopy

Variable temperature ^{1}H NMR study of compound 2

The ^{1}H NMR spectrum of **2** at room temperature reveals, in contrast to the compounds **1**, **3** and **4** (sharp singlet), only a very broad signal at δ = 5.79 ppm ($\omega_{1/2}$ = 330 Hz) for the Cp ligands (Figure S1). Therefore, we recorded a variable temperature NMR study, which shows, that the signal slightly moves to lower field and sharpens upon cooling to 193 K (Figure S2). Additionally, in the ^{13}C{^{1}H} NMR spectrum a singlet at δ = 91.39 ppm occurs at 193 K, while at r.t. no signal is observed, suggesting broadening of the signal as well. This NMR behavior may rely to a partially dissociation of **2** to the paramagnetic monocations [**B**]$^{+}$ at r.t., what is inhibited at low temperatures.

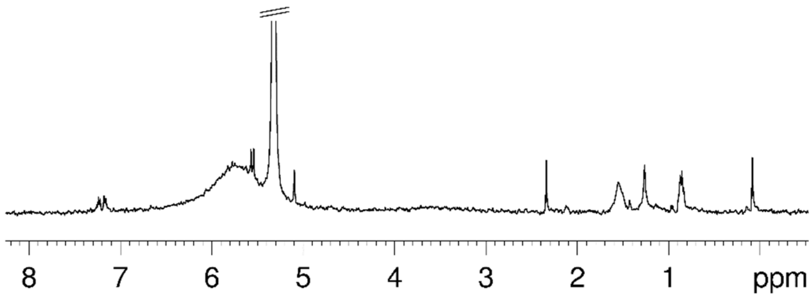

Figure S1: Magnification of the ^{1}H NMR spectrum of **2** at r.t., showing the broad signal at δ = 5.79 ppm ($\omega_{1/2}$ = 330 Hz) for the Cp ligands. The signal at δ = 5.32 ppm belongs to the solvent CH_2Cl_2, showing its ^{13}C satellites as well, and the other small signals can be assigned to toluene, hexane and grease.

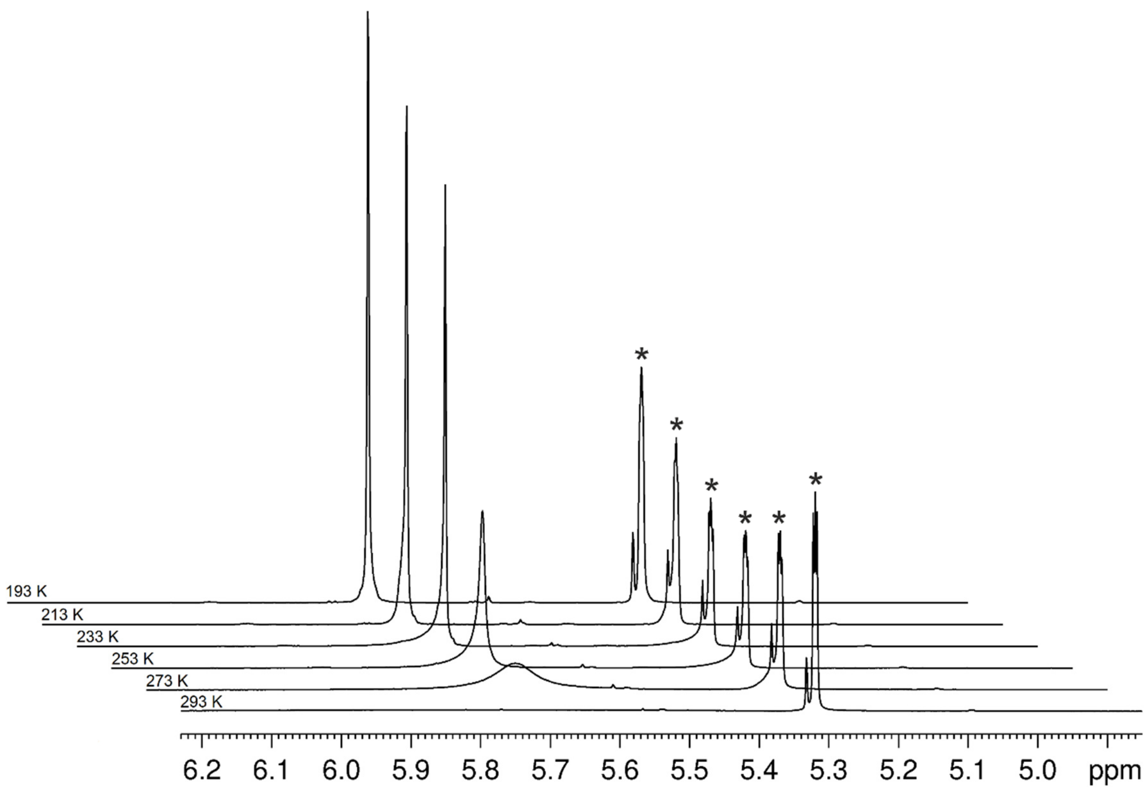

Figure S2: Variable temperature ^{1}H NMR spectra of **2**, showing the sharpening of the Cp assignable signal at δ = 5.79 ppm upon cooling from r.t. to 193 K in steps of 20 K. The signals at δ = 5.32 ppm (*) belong to the solvent CH_2Cl_2 or $CDHCl_2$, respectively.

4.4.4 IR spectroscopy

Reversible interconversion of crystalline and precipitated 1b followed by IR spectroscopy

When the dark red crystals of **1b**, **2**, **3** and **4** are dissolved in CH_2Cl_2, the solution cannot be distinguished from solutions of the dark green crude products by IR and NMR spectroscopy. Additionally, the dissolved crystals can be precipitated by addition of toluene to afford again a dark green powder which cannot be distinguished from the crude products by IR spectroscopy. The following figures describe a detailed IR spectroscopic characterization of 1b in solution and the solid state. Figure S3 shows the IR spectrum of solid **A** grinded together with [Thia][TEF]. The spectrum shows three strong resonances for the CO stretching frequencies which are identical to pure **A** which reveals, that no reaction occurs between **A** and [Thia][TEF] in the solid state.

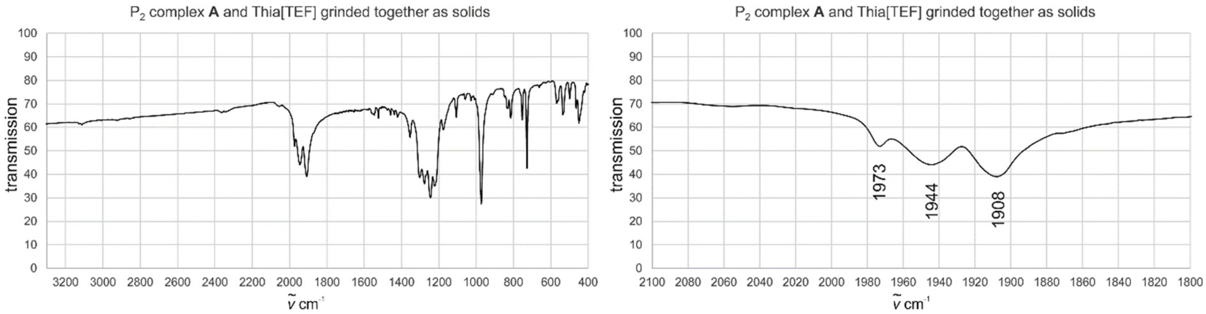

Figure S3: IR(KBr) spectrum of solid **A** and [Thia][TEF] before the reaction.

Figure S4 shows the IR spectrum of the dark red single crystals of **1b** from which the solid state structure of **1b** could be determined (see main text). The spectrum shows at least seven resonances in the region of CO stretching frequencies which in in good agreement with an unsymmetrical dicationic complex that was found by X-ray structure determination. All CO ligands are crystallographically independent in the solid state and exhibit different environments. The increased energy of the stretching frequencies compared to neutral **A** can easily be explained by a decrease in electron density on the Mo atoms due to the chemical oxidation resulting in a weaker π-back bonding to the CO ligands.

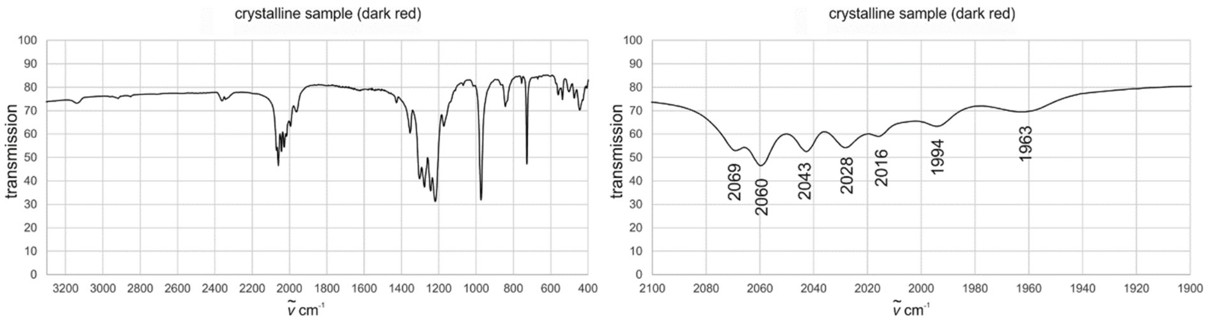

Figure S4: IR(KBr) spectrum of crystalline **1b**.

Figure S5 shows the IR spectrum of solid **1b** in the form of dark green powder which was obtained directly from the reaction mixture (of **A** and [Thia][TEF] in CH_2Cl_2) by precipitation upon addition of toluene. The spectrum shows three very strong resonances in the region of the CO stretching frequencies. The fact that this sample shows less signals than the crystalline sample (in Figure S4) is in good agreement with an increase in symmetry of the dicationic complex by precipitation.

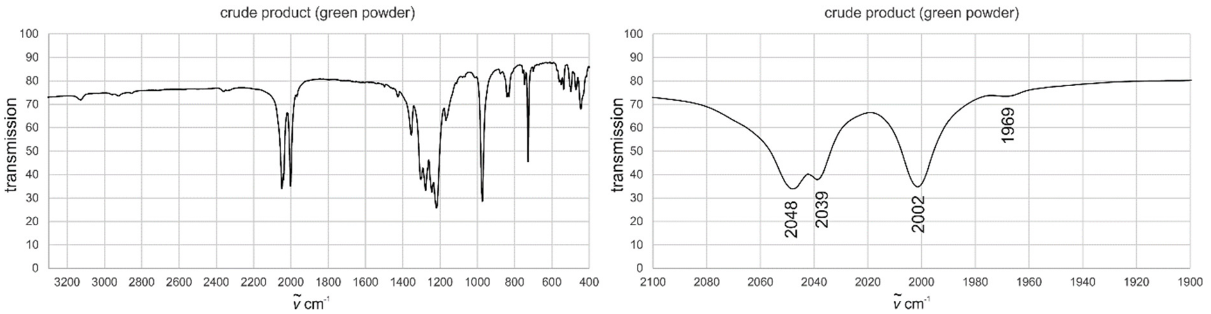

Figure S5: IR(KBr) spectrum of **1b** in the form of dark green powder which was obtained directly from the reaction mixture by precipitation with toluene.

Figure S6 shows the IR spectrum of solid **1b** in the form of dark green powder which was obtained from crystals of **1b** dissolved in CH_2Cl_2 and subsequently precipitated by addition of toluene. The spectrum is identical to Figure S5. This proves, that once **1b** is crystallized, it can be dissolved again and exhibits the same flexibility and dynamics like the product, which is obtained directly after reaction of **A** and [Thia][TEF]. This confirms that **1b** can be converted reversibly between an symmetric (precipitated) and unsymmetric (crystalline) form.

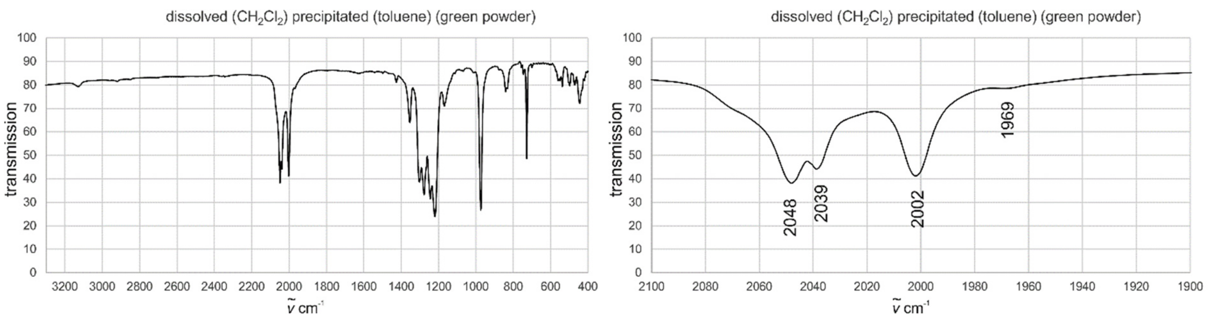

Figure S6: IR(KBr) spectrum of **1b** in the form of dark green powder which was obtained from crystals of **1b** dissolved in CH_2Cl_2 and subsequently precipitated by addition of toluene.

Figure S7 shows the solution spectra of **1b** in CH_2Cl_2. The spectra are identical, when **1b** was previously in crystalline form or in precipitated form. Additionally, it can be noted that no evolution of the signals can be observed depending on time proving that compound **1b** is stable in CH_2Cl_2 solution (in contrast to MeCN), although it exhibits a highly dynamic behavior in solution (see NMR description in the main text).

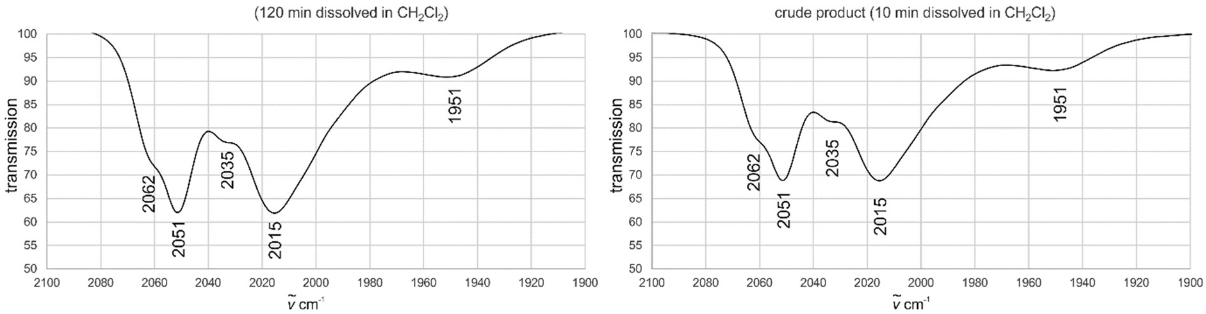

Figure S7: IR(CH_2Cl_2) spectra of crystals of **1b** dissolved in CH_2Cl_2 after 120 minutes of stirring (left); IR(CH_2Cl_2) spectra of dark green powder of **1b** dissolved in CH_2Cl_2 after 10 minutes of stirring (right).

IR spectroscopy of compounds 2, 3 and 4

In contrast to compound **1**, the IR spectra of **2** and **3** (Figure S8 and Figure S9) do not show any difference in the CO resonances between the crystalline and precipitated forms, where in each case at least seven resonances are observed. Hence, a reversible conversion between a symmetric and an asymmetric form can be excluded. For the bismuth derivative **4** the IR spectrum of the precipitated sample (Figure S10, left) shows at least six CO bands, which are slightly shifted in the spectrum of the crystalline sample (Figure S10, right). Thereby, the resonances at 1966 cm^{-1} and 2020 cm^{-1} disappear, while resonances at 1950 cm^{-1} and 1978 cm^{-1} occur. Unfortunately, an exact attribution of the CO bands was not possible.

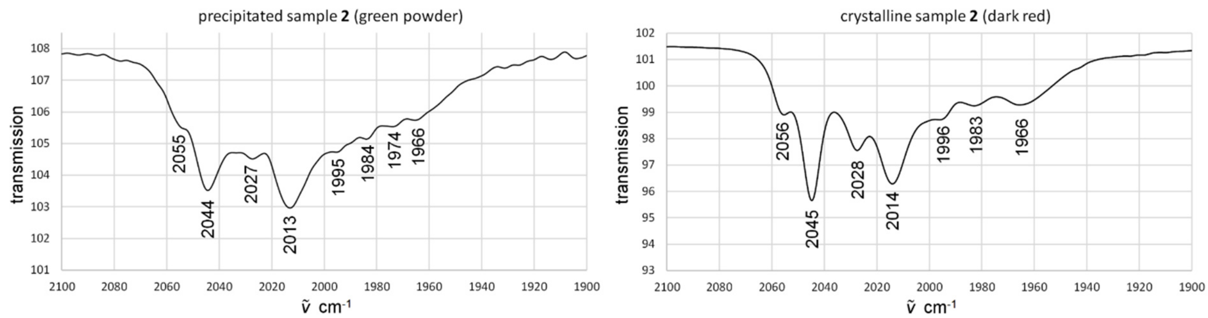

Figure S8: IR spectrum of **2** in its precipitated (left) or crystalline (right) form, respectively. Only CO resonances are shown.

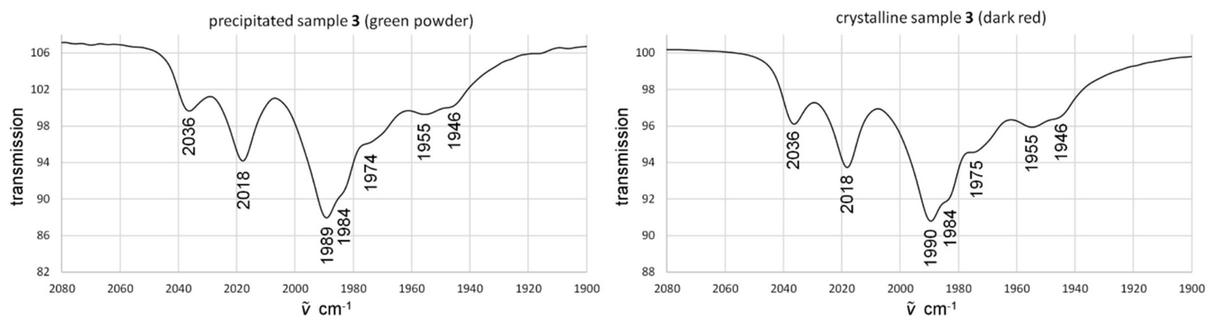

Figure S9: IR spectrum of **3** in its precipitated (left) or crystalline (right) form, respectively. Only CO resonances are shown.

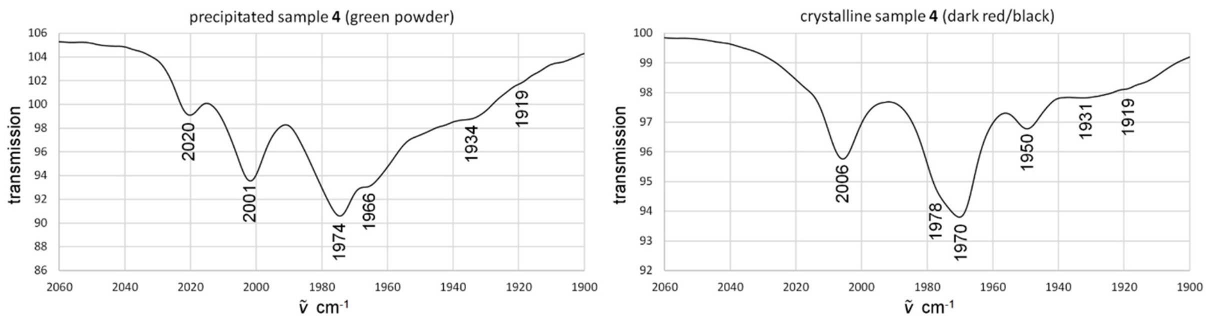

Figure S10: IR spectrum of **4** in its precipitated (left) or crystalline (right) form, respectively. Only CO resonances are shown.

4.4.5 Electrochemical analyses

Cyclovoltammetry of A

The CV of **A** in CH_2Cl_2 solution is depicted in Figure S11. The complex undergoes a pseudo-reversible oxidation with the peak of the anodic wave at +0.28 V vs. $Cp_2Fe^{0/+}$, while the corresponding cathodic wave is significantly shifted to –0.22 V vs. $Cp_2Fe^{0/+}$. This suggests that after the first oxidation of **A**, the shifted peak for the reduction corresponds to the dication of **[A-A]$^{2+}$**. During this study, no decline of the cathodic wave of **[A-A]$^{2+}$** or the observation of any reduction assignable to the monocation [**A**]$^+$ could be observed in the CV regardless of the scan rates, the temperature and the concentration of **A**. This points to a rapid dimerization to the dication. The second (+0.45 V vs. $Cp_2Fe^{0/+}$) and third oxidation (+0.84 V vs. $Cp_2Fe^{0/+}$) are irreversible, as well as the reduction (-1.19 V vs. $Cp_2Fe^{0/+}$), and can be seen in Figure S12 and Figure S13.

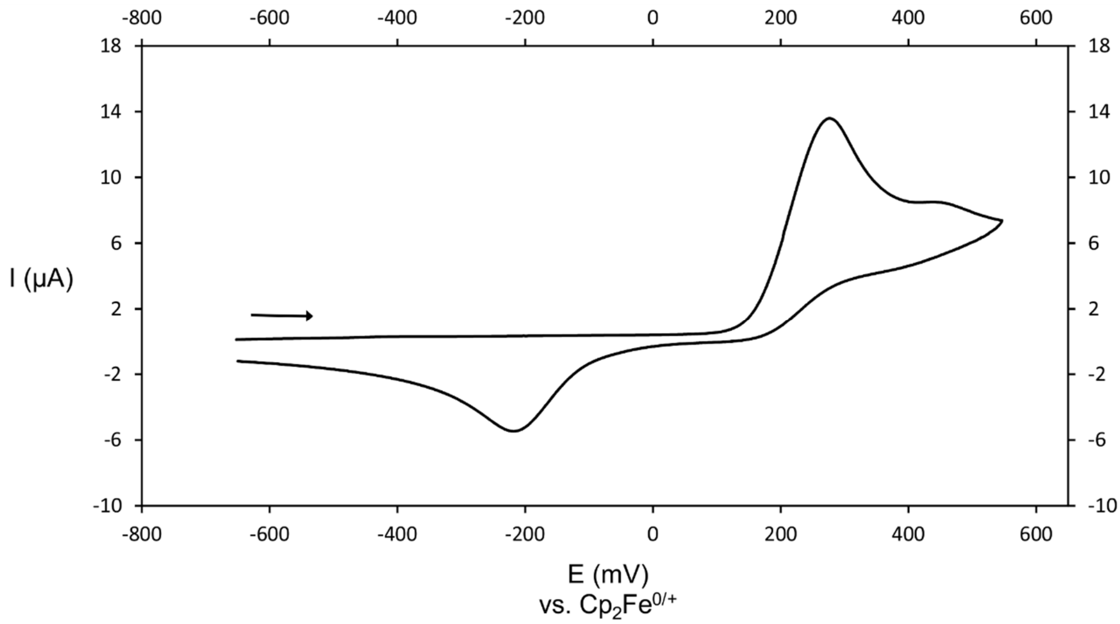

Figure S11: CV of **A** showing only the first (pseudo-reversible) oxidation.

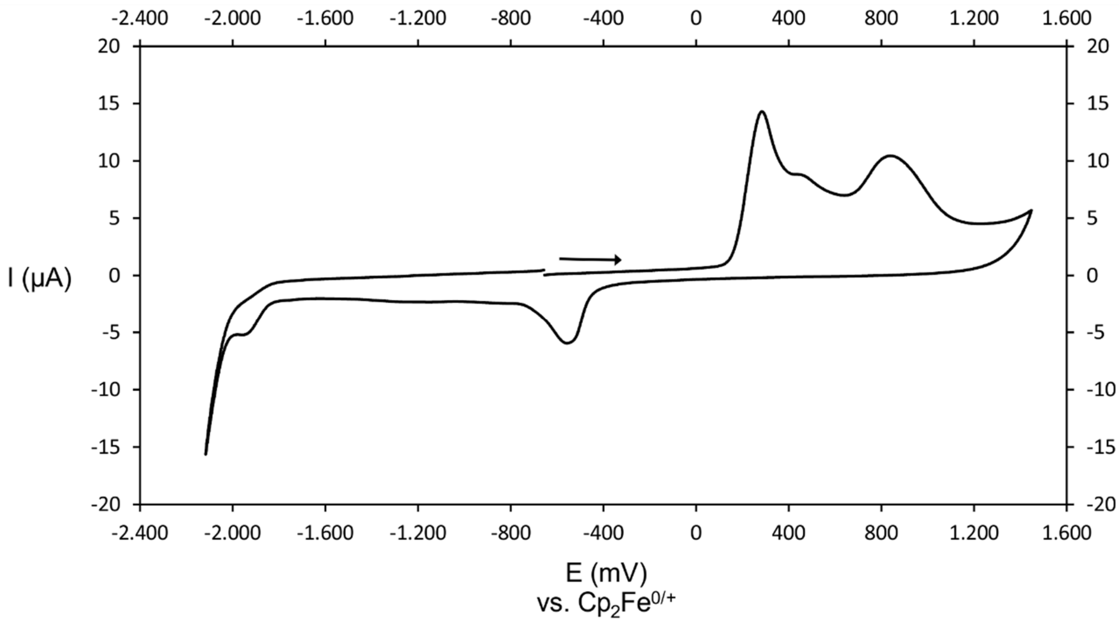

Figure S12: Full CV of **A**

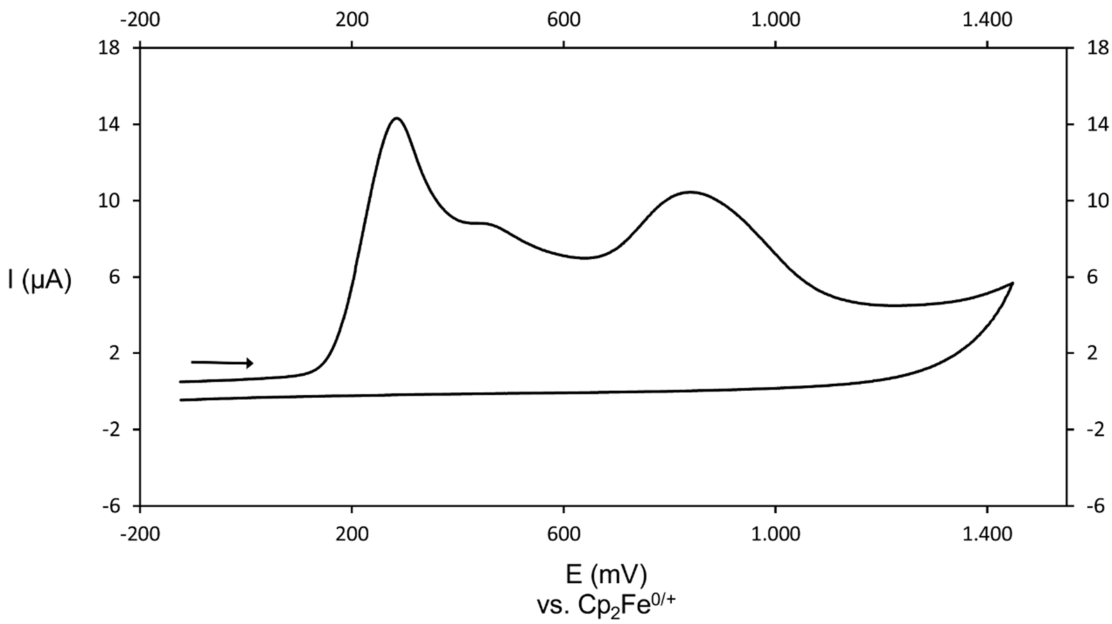

Figure S13: CV of **A** showing the three oxidations.

Spectroelectrochemistry of A

The complexes **A** to **D** contain CO ligands which are excellent probes for IR spectroscopy. During the current study it was possible to follow the oxidation of **A** by spectroelectrochemistry shown in Figure S14. The intensities of the CO stretching bands at 1913, 1962 and 1987 cm^{-1} for neutral **A** decrease during the oxidation, while three new signals at higher energies (~2028, 2044 and 2053 cm^{-1}) evolve. The observed CO stretching frequencies at higher energy for the formed dication can easily be explained by a decrease in π back bonding from the Mo atoms, which are more electron poor compared to neutral **A**. This process is fully reversible as long as **A** is only oxidized once. This is in good agreement with the CV of **A** and the assumption that [**A**]$^+$ immediately dimerizes and the resulting dication [**A-A**]$^{2+}$ can be reduced back to **A**.

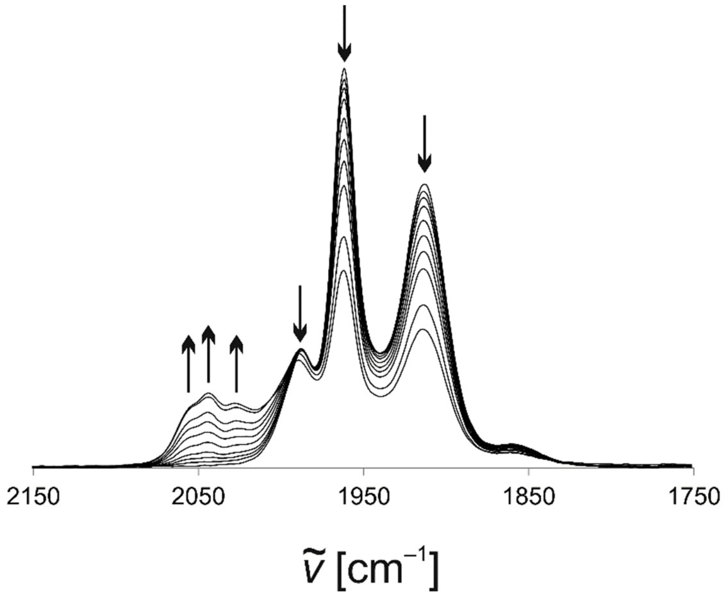

Figure S14: IR spectrum of **A** recorded during the CV measurement. The CO stretching frequencies of neutral **A** (1913, 1962 and 1987 cm^{-1}) decrease, while new bands (~2028, 2044 and 2053 cm^{-1}) evolve during the oxidation of **A**.

Cyclovoltammetry of B

The CV of **B** in CH_2Cl_2 solution is depicted in Figure S15. The complex undergoes a pseudo-reversible oxidation with the peak of the anodic wave at +0.19 V vs. $Cp_2Fe^{0/+}$, while the corresponding cathodic wave is significantly shifted to –0.06 V vs. $Cp_2Fe^{0/+}$. This suggests that after the first oxidation of **B**, the shifted peak for the reduction corresponds to the dication of **[B-B]$^{2+}$**. During this study, no decline of the cathodic wave of **[B-B]$^{2+}$** or the observation of any reduction assignable to the monocation [**B**]$^+$ could be observed in the CV regardless of the scan rates, the temperature and the concentration of **B**. This points to a rapid dimerization to the dication. The second (+0.64 V vs. $Cp_2Fe^{0/+}$) and third oxidation (+1.17 V vs. $Cp_2Fe^{0/+}$) are irreversible and can be seen in Figure S16 and Figure S17. Here no reduction of **B** occurs in CH_2Cl_2.

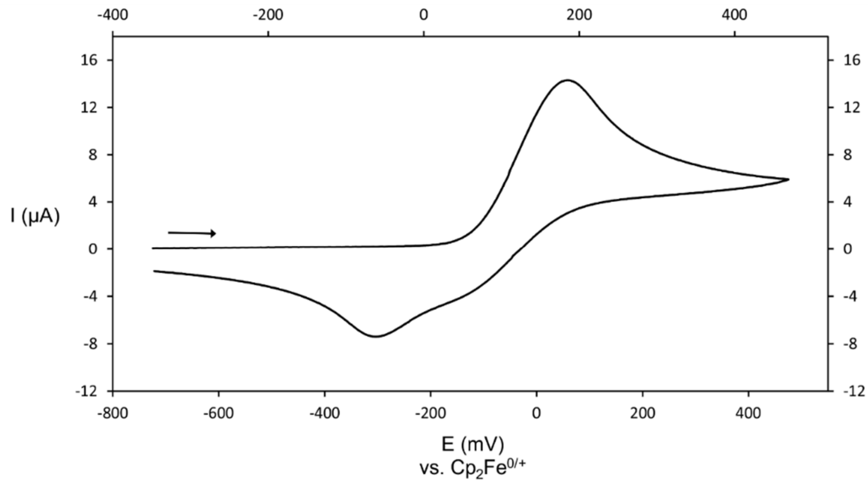

Figure S15: CV of **B** showing only the first (pseudo-reversible) oxidation.

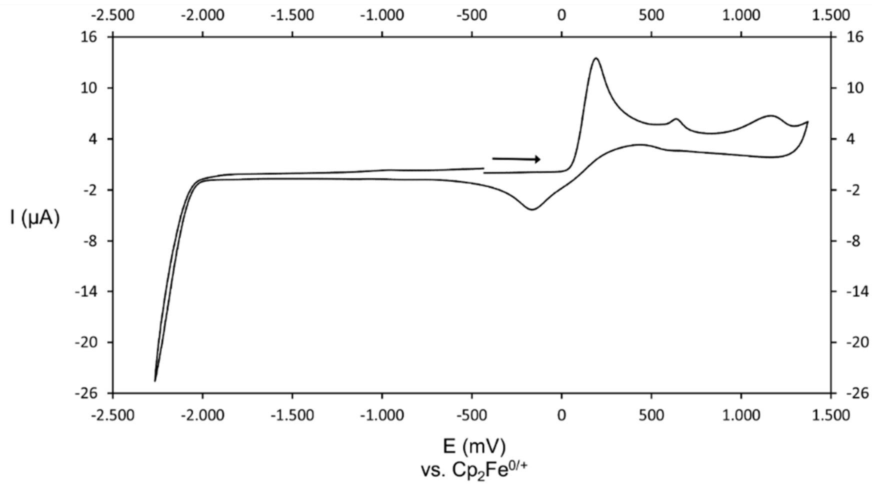

Figure S16: Full CV of **B**.

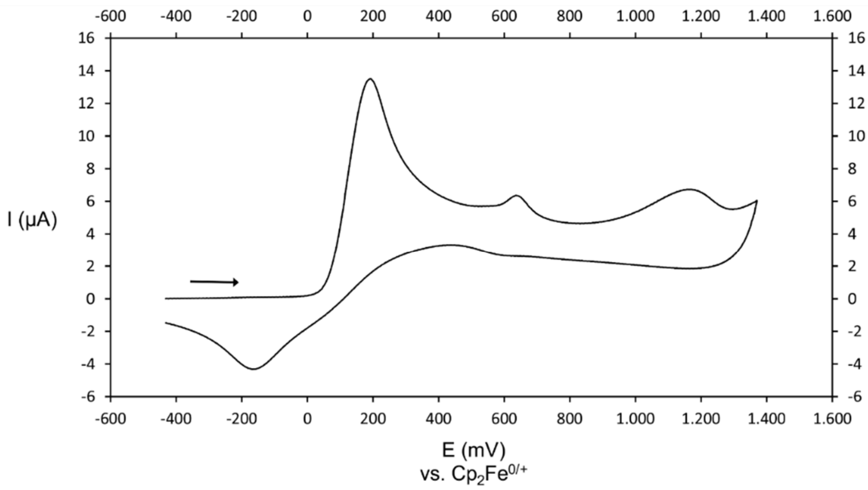

Figure S17: CV of **B** showing the three oxidations and the reduction.

Cyclovoltammetry of C

The CV of **C** in CH_2Cl_2 solution is depicted in Figure S18. The complex undergoes a pseudo-reversible oxidation with the peak of the anodic wave at +0.05 V vs. $Cp_2Fe^{0/+}$, while the corresponding cathodic wave is significantly shifted to –0.38 V vs. $Cp_2Fe^{0/+}$. This suggests that after the first oxidation of **C**, the shifted peak for the reduction corresponds to the dication of **[C-C]**$^{2+}$. During this study, no decline of the cathodic wave of **[C-C]**$^{2+}$ or the observation of any reduction assignable to the monocation [**C**]$^+$ could be observed in the CV regardless of the scan rates, the temperature and the concentration of **C**. This points to a rapid dimerization to the dication. In the case of **C** no second and third oxidation occurs, but instead two pseudo-reversible reductions (Figure S19) with the cathodic waves at –1.54 V and –1.72 V, and the anodic waves shifted to –0.65 V and –0.84 V vs. $Cp_2Fe^{0/+}$.

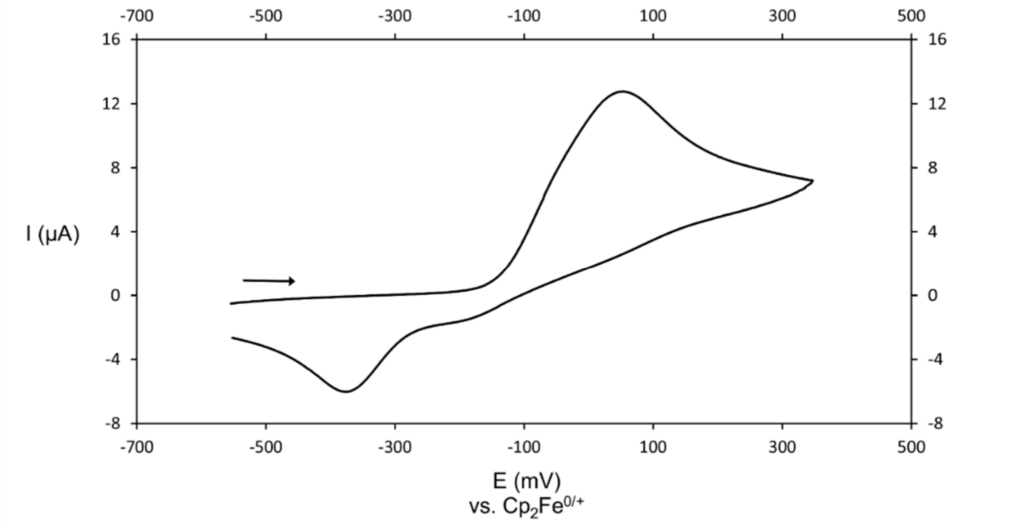

Figure S18: CV of **C** showing only the first (pseudo-reversible) oxidation.

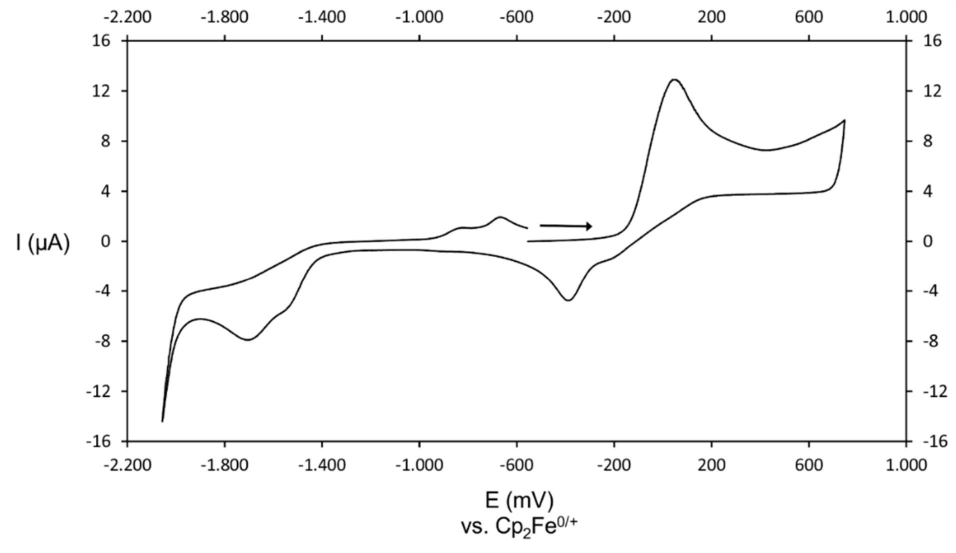

Figure S19: Full CV of **C**.

Cyclovoltammetry of D

The CV of **D** in CH_2Cl_2 solution is depicted in Figure S20. The complex undergoes a pseudo-reversible oxidation with the peak of the anodic wave at –0.18 V vs. $Cp_2Fe^{0/+}$, while the corresponding cathodic wave is significantly shifted to –0.47 V vs. $Cp_2Fe^{0/+}$. This suggests that after the first oxidation of **D**, the shifted peak for the reduction corresponds to the dication of **[D-D]$^{2+}$**. During this study, no decline of the cathodic wave of **[D-D]$^{2+}$** or the observation of any reduction assignable to the monocation [**D**]$^{+}$ could be observed in the CV regardless of the scan rates, the temperature and the concentration of **D**. This points to a rapid dimerization to the dication. In the case of **D** a second oxidation occurs at +0.40 V vs. $Cp_2Fe^{0/+}$, which is reversible. Additionally, a pseudo-reversible reduction of **D** can be observed with cathodic waves at –2.14 V vs. $Cp_2Fe^{0/+}$ and the corresponding oxidation significantly shifted to –1.14 V vs. $Cp_2Fe^{0/+}$ (Figure S21).

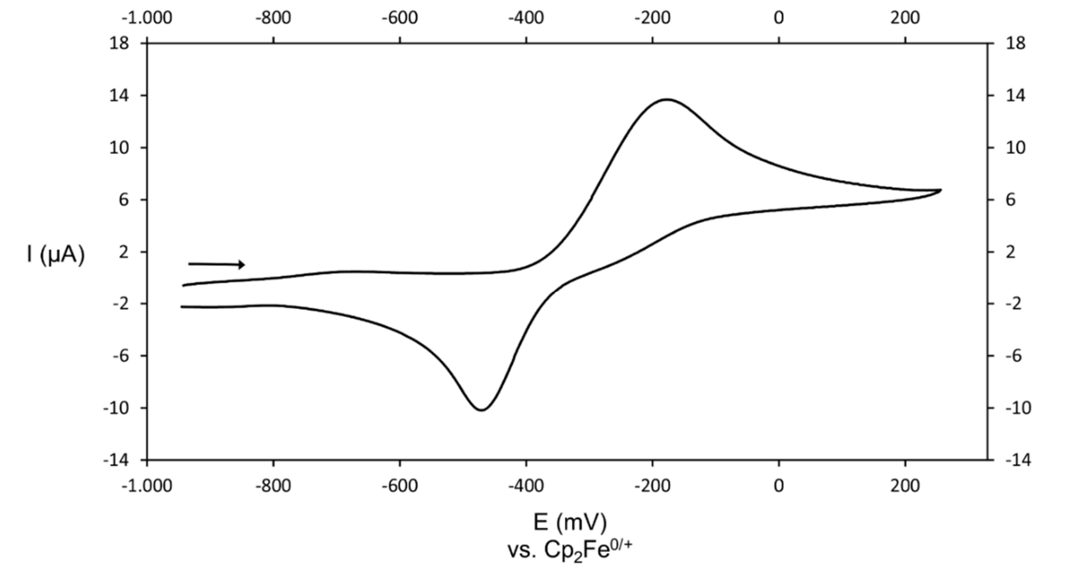

Figure S20: CV of **D** showing only the first (pseudo-reversible) oxidation.

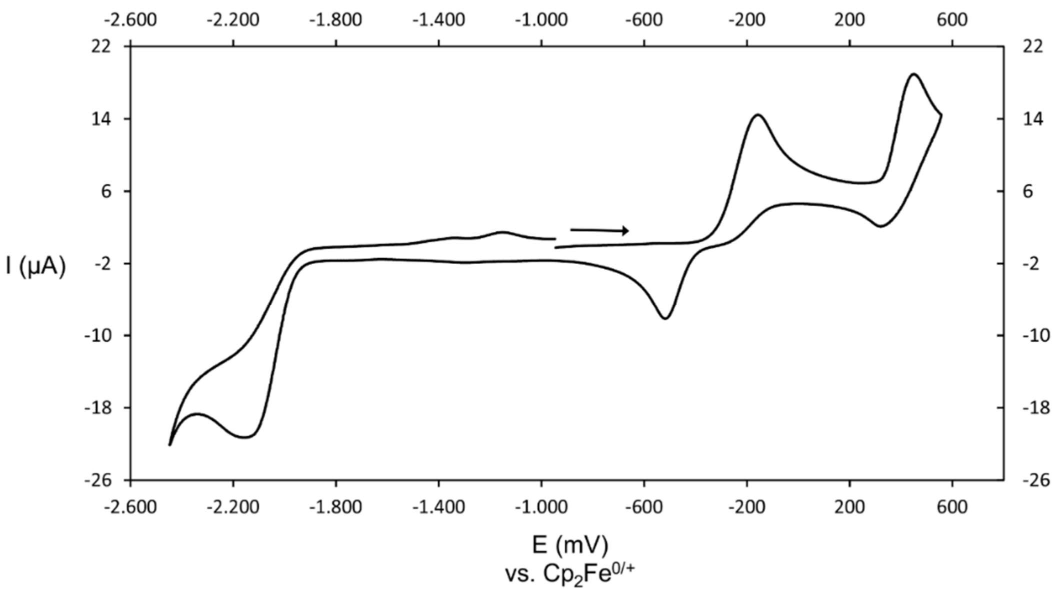

Figure S21: Full CV of **D**.

ESI mass spectrometry of 1b

The ESI mass spectrum of a CH_2Cl_2 solution of **1b** (Figure S22) clearly shows signals assignable to the monocationic species [**A**]$^+$, [**A**–2(CO)]$^+$, [**A**–3(CO)]$^+$ and [**A**–4(CO)]$^+$ which suggests dissociation in the gas phase in accordance with DFT (see below). However, magnification of the signal for [**A**]$^+$ shown in Figure S23 shows some small peaks (≈50:1 intensity, shifted by ~0.5 Da) with the same *m/z* ratio, which are located in between the major signals for [**A**]$^+$. These signals may arise from a small percentage of a dicationic species but the isotopic distribution cannot clearly be resolved due to the small percentage.

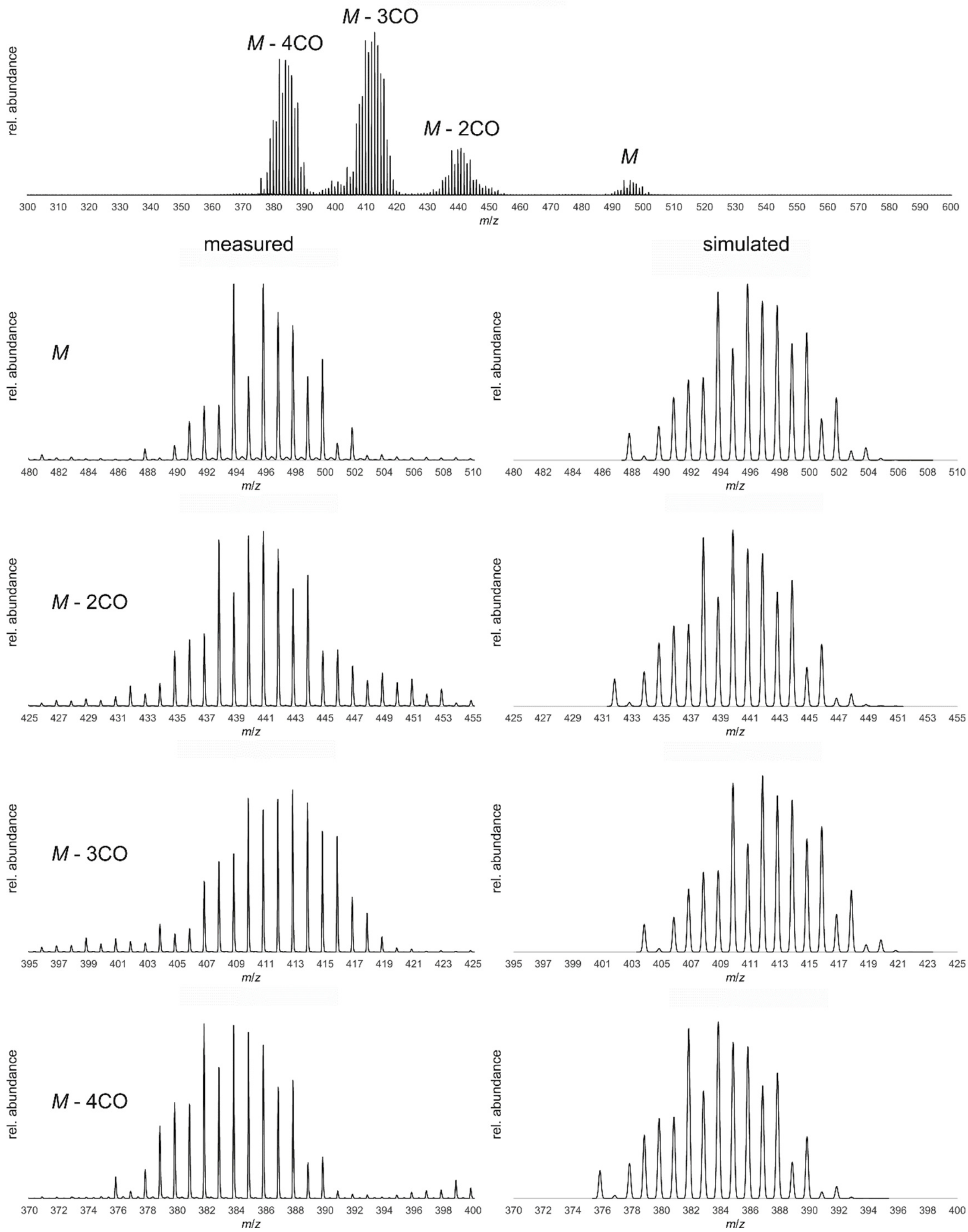

Figure S22: (top) ESI MS spectrum of **1b** from CH_2Cl_2. Measured (left) and simulated (right) isotopic distribution for the assignable peaks. *M* = **A**.

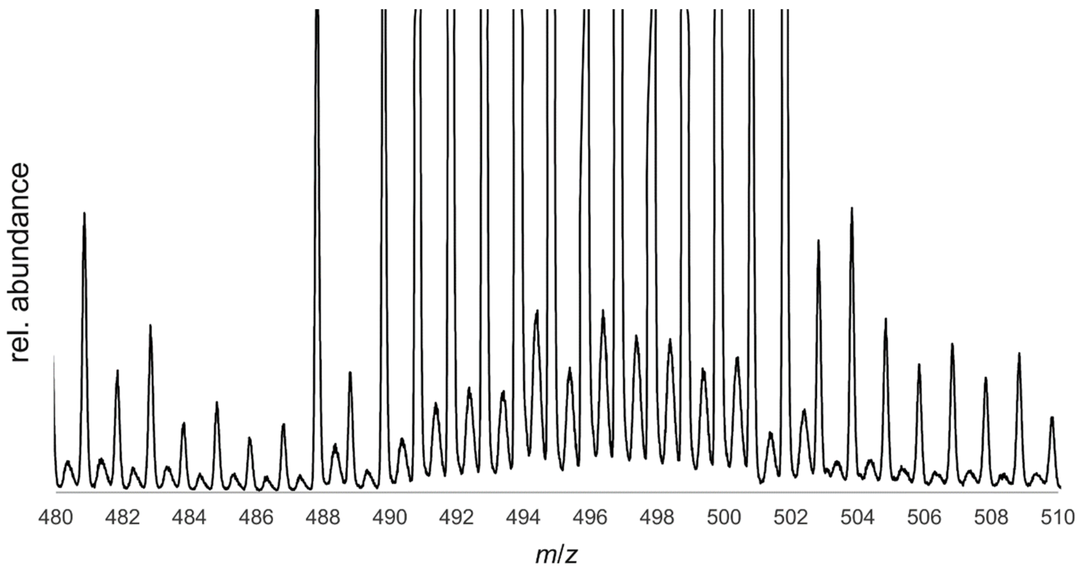

Figure S23: Magnification of the measured peaks for [*M*]$^+$ (=[**A**]$^+$), showing the small peaks shifted by ~0.5 Da compared to the major signal. These may arise from a dicationic species.

ESI mass spectrometry of 2

The ESI mass spectrum of a CH_2Cl_2 solution of crystalline **2** () clearly shows signals assignable to the monocationic species [**B**]$^+$, [**B**–2(CO)]$^+$, [**B**–3(CO)]$^+$ and [**B**–4(CO)]$^+$. However, some small peaks (shifted by ≈0.5 Da) are detected in the *m/z* regions for signals which may be assigned to [**2**–4CO]$^+$ and [**2**–8CO]$^+$. The overlay of the latter signals with monocationic species though does not allow a reliable assignment by isotopic distribution modelling of these species. Additionally, also signals for dicationic species which may be assigned to [**2**-2(CO)]$^{2+}$ and [**2**-3(CO)]$^{2+}$ can be detected (see Figure S25). The anion mode shows only one signal for the [TEF]$^-$ anion.

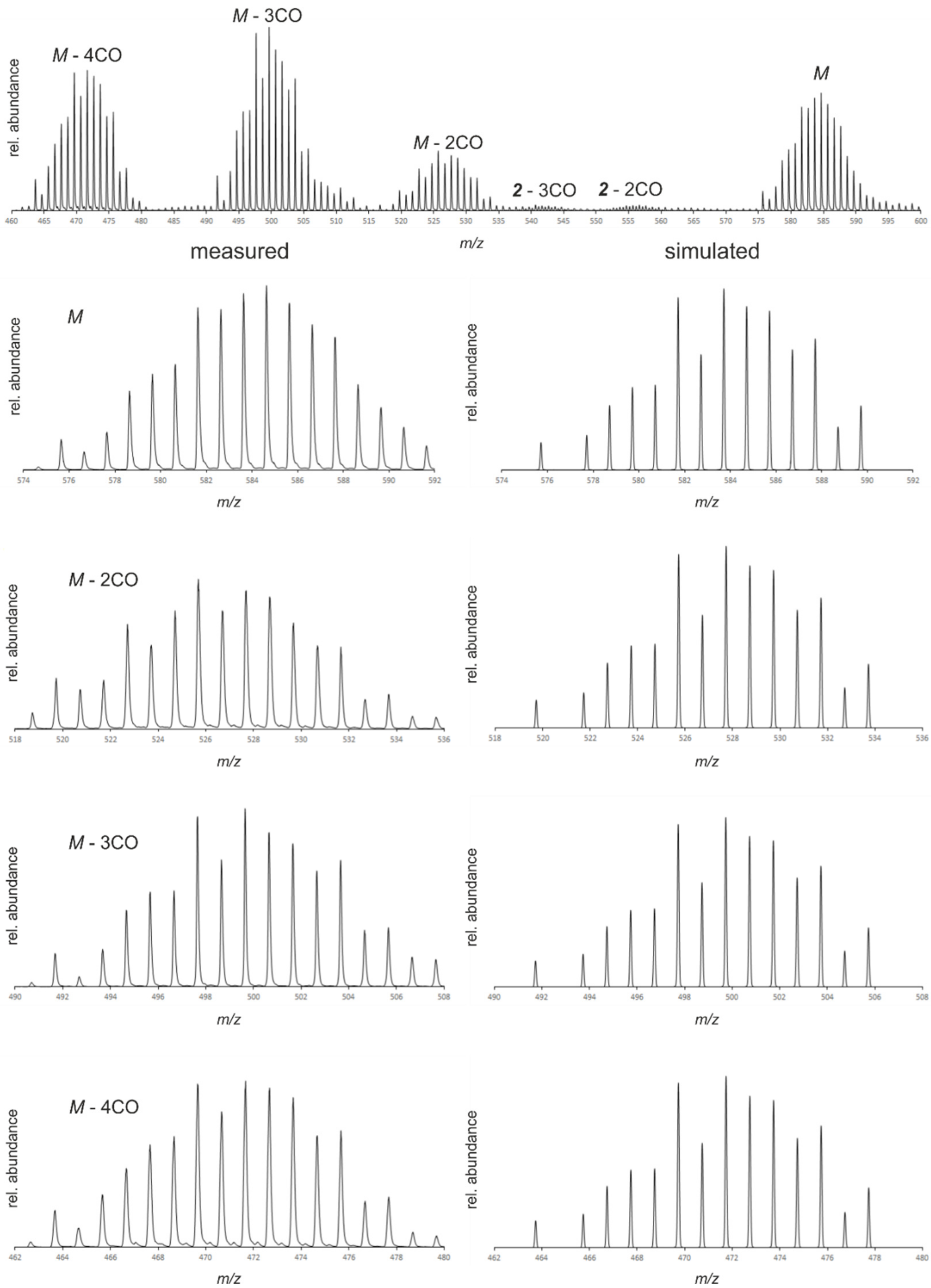

Figure S24: (top) ESI MS spectrum of **2** from CH_2Cl_2 from 460 to 600 Da. Measured (left) and simulated (right) isotopic distribution for the assignable peaks. *M* = **B**.

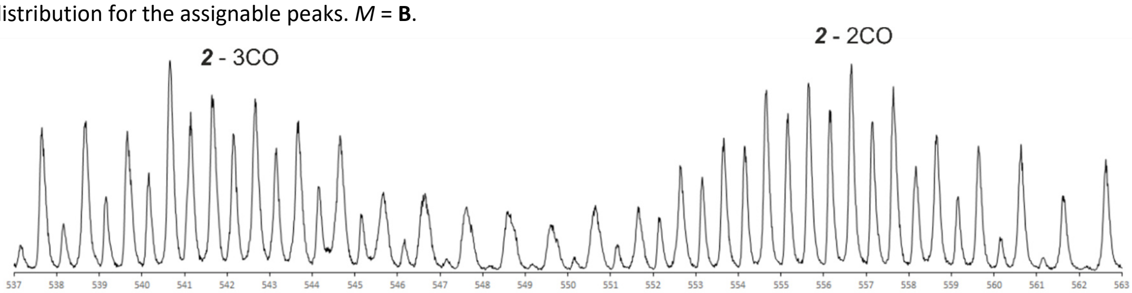

Figure S25: ESI MS spectrum of **2** from CH_2Cl_2 (only the *m/z* region from 537 to 563 Da is depicted) showing dicationic species which may be assignable to $[\mathbf{2}\text{-}2(CO)]^{2+}$ and $[\mathbf{2}\text{-}3(CO)]^{2+}$.

ESI mass spectrometry of 3

The ESI mass spectrum of a CH_2Cl_2 solution of crystalline **3** (Figure S26) clearly shows signals assignable to the monocationic species [**C**]$^+$, [**C**–2(CO)]$^+$, [**C**–3(CO)]$^+$ and [**C**–4(CO)]$^+$. However, magnification of the *m/z* region from 642 to 664 Da (Figure S27) show some small peaks shifted by ≈0.5 Da. These signals may arise from a small percentage of a dicationic species. The overlay of the latter signals with monocationic species though does not allow a reliable assignment by isotopic distribution modelling of these species. The anion mode shows only one signal for the [TEF]$^-$ anion.

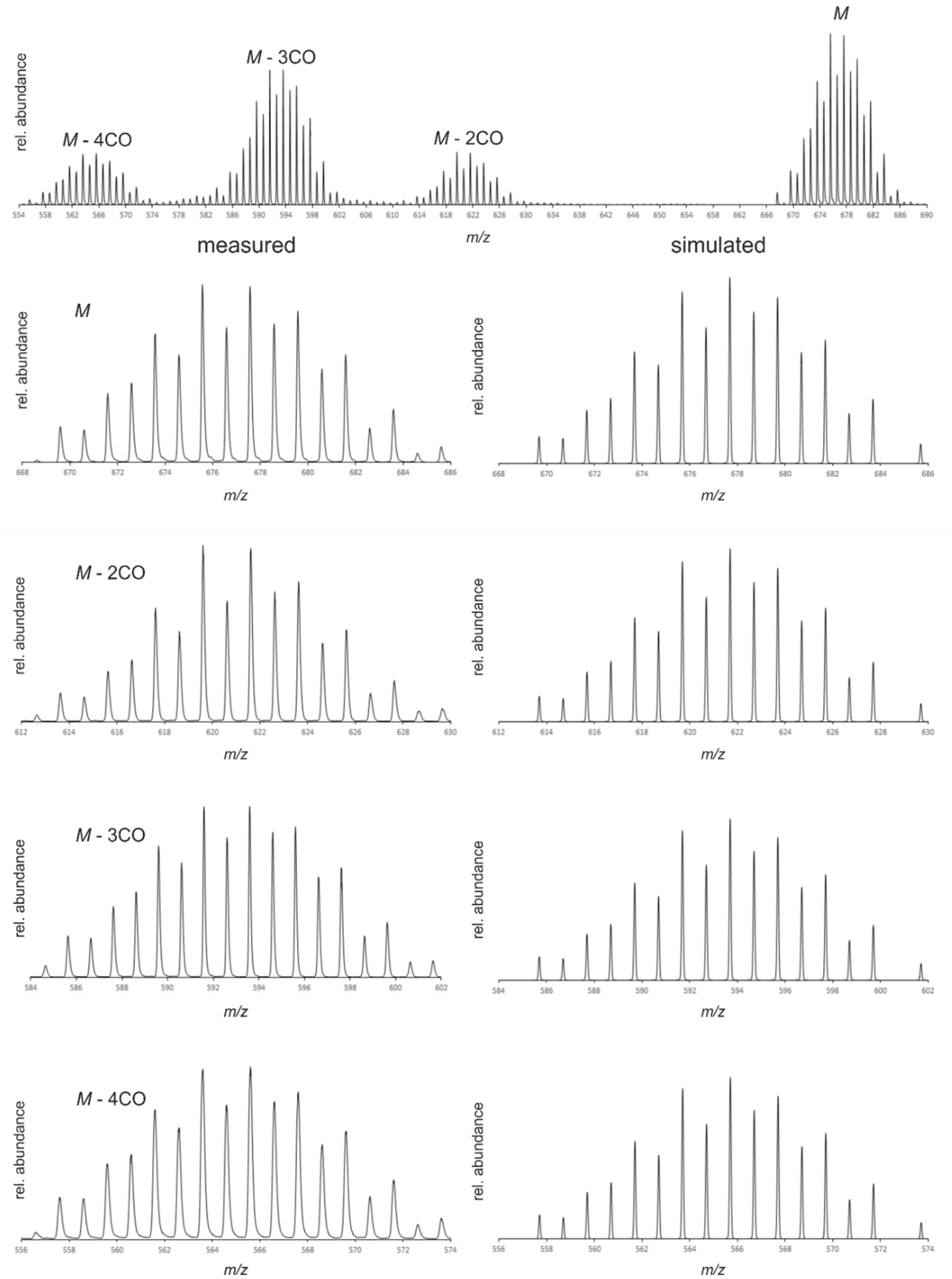

Figure S26: (top) ESI MS spectrum of **3** from CH_2Cl_2 from 554 to 690 Da. Measured (left) and simulated (right) isotopic distribution for the assignable peaks. *M* = **C**.

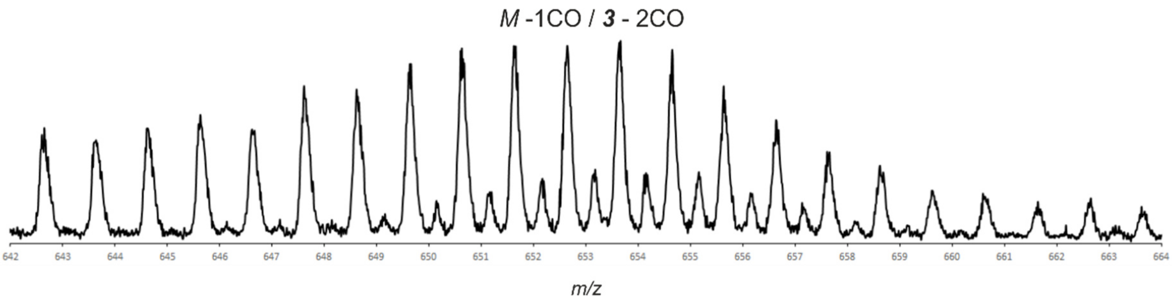

Figure S27: ESI MS spectrum of **3** from CH_2Cl_2 (only the *m/z* region from 642 to 664 Da is depicted) showing the small peaks shifted by ~0.5 Da compared to the major signal. These may arise from a dicationic species.

ESI mass spectrometry of 4

The ESI mass spectrum of a CH_2Cl_2 solution of crystalline **4** (Figure S28) clearly shows signals assignable to the monocationic species [**D**]$^+$, [**D**–2(CO)]$^+$, [**D**–3(CO)]$^+$ and [**D**–4(CO)]$^+$. However, no signals for dicationic species could be observed.

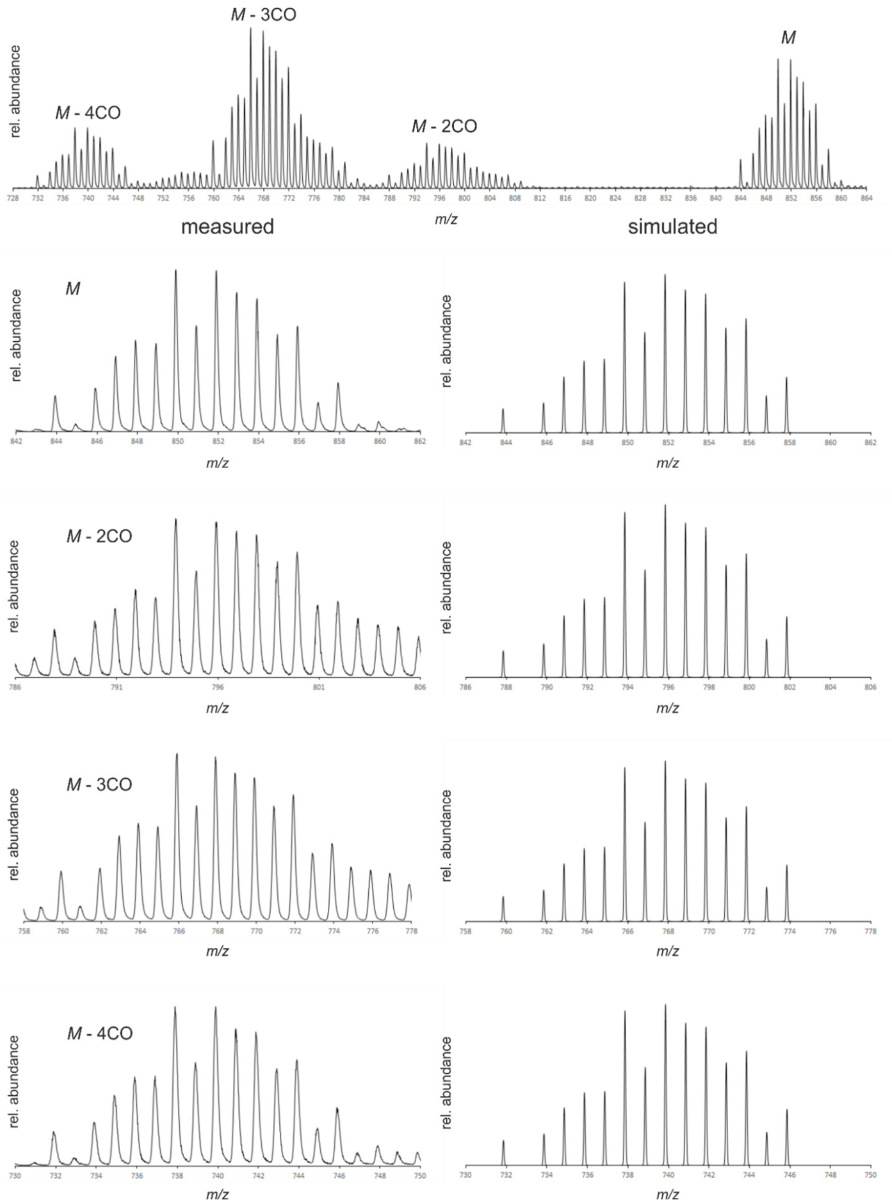

Figure S28: (top) ESI MS spectrum of **4** from CH_2Cl_2 from 728 to 864 Da. Measured (left) and simulated (right) isotopic distribution for the assignable peaks. *M* = **D**.

X-band EPR measurement

CH_2Cl_2 solutions of crystalline **1b**, **3** and **4** are silent in the X-band EPR spectra at r.t. and at 77 K. This concludes that no dissociation of the dicationic species to the paramagnetic monocations [**A**]$^+$, [**C**]$^+$ or [**D**]$^+$, respectively, occurs. This matches with the calculated dissociation energy barriers (*vide infra*). EPR measurements of **2**, instead, show an isotropic signal with weak intensity and a g_{iso} of 2.1110 at room temperature. This assumes small amounts of dissociated monocationic radicals [**B**]$^+$ in solution and agrees with the broad signal in the ^{1}H NMR spectra of **2** (*vide supra*). The signal is shifted to g_{iso} = 1.9667 upon cooling to 77 K (Figure S29). This may be caused by a temperature dependent spin distribution in [**B**]$^+$.

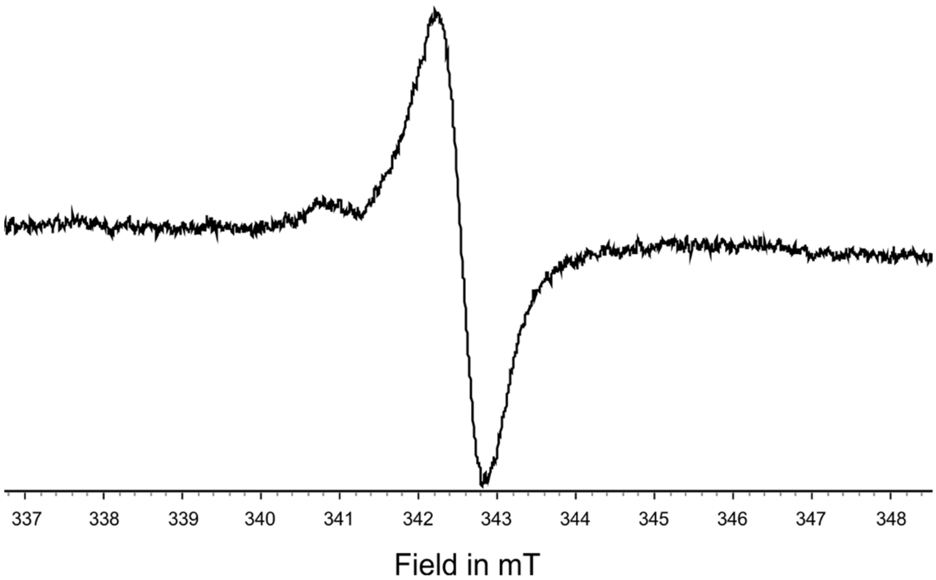

Figure S29: EPR spectrum of **2** in CH_2Cl_2 at 77 K. g_{iso} = 1.9667

4.4.6 X-ray crystallography

All crystal manipulations were performed under mineral oil. The diffraction experiments were performed at 123 K or 110 K, respectively, on a Rigaku (former Agilent Technologies or Oxford Diffraction) Gemini Ultra or GV 50 diffractometer using Cu-K_α or Mo-K_α radiation. Crystallographic data together with the details of the experiments are given in Table S1. The cell determination, data reduction and absorption correction for all compounds were performed with the help of the CrysAlis PRO software. The full-matrix least-square refinement against F^2 was done with ShelXL. If not stated otherwise, all atoms except hydrogen were refined anisotropically. The H atoms were calculated geometrically and a riding model was used during the refinement process.

CIF files with comprehensive information on the details of the diffraction experiments and full tables of bond lengths and angles for [Thia](TEF], **1a**, **1b**, **2**, **3** and **4** are deposited in Cambridge Crystallographic Data Centre under the deposition codes CCDC-1589798 ([Thia][TEF], CCDC-1589799 (**1a**), CCDC-1589800 (**1b**), CCDC-1589801 (**3**), CCDC-1589802 (**2**), and CCDC-1589803 (**4**).

Table S1: Crystallographic details for the compounds [Thia][TEF], **1a**, **1b**, **2**, **3** and **4**.

	[Thia][TEF]	**1a**	**1b**	**2**	**3**	**4**
formula	$C_{28}H_8AlF_{36}O_4S_2$	$C_{32}H_{26}F_{12}Mo_4N_2O_8P_4Sb_2$	$C_{60}H_{20}Al_2F_{72}Mo_4O_{16}P_4$	$C_{30}H_{10}AlAs_2F_{36}Mo_2O_8$	$C_{30}H_{10}AlF_{36}Mo_2O_8Sb_2$	$C_{30}H_{10}Al\ Bi_2F_{36}Mo_2O_8$
weight [g·mol^{-1}]	1183.44	1545.69	2926.36	1551.08	1644.74	1819.20
Temperature [K]	123.00(14)	122.9(4)	123.1(2)	110(1)	122.98(10)	122.99(10)
crystal system	triclinic	monoclinic	monoclinic	triclinic	monoclinic	orthorhombic
space group	*P*–1	$P2_1/n$	$P2_1/n$	*P-1*	$P2_1/n$	*Pbca*
a [Å]	11.6645(2)	13.01605(15)	15.43561(8)	15.3791(3)	15.5970(2)	28.8721(6)
b [Å]	14.21758(15)	7.86712(8)	21.49774(12)	21.7793(5)	22.6102(3)	22.2080(3)
c [Å]	14.28912(15)	22.5281(2)	26.97813(15)	26.8944(6)	26.1177(3)	29.2990(3)
α [°]	91.0927(9)	90	90	90.0326(17)	90	90
β [°]	112.6095(14)	99.6941(11)	89.2667(5)	92.0984(17)	90.6500(10)	90
γ [°]	113.5492(14)	90	90	90.4679(17)	90	90
Volume [Å^3]	1963.21(6)	2273.91(4)	8951.44(8)	9001.8(3)	9209.8(2)	18786.3(5)
Z	2	2	4	8	8	16
ρ_{calc} [g·cm^{-3}]	2.002	2.257	2.171	2.289	2.372	2.573
μ [mm^{-1}]	3.446	20.279	7.350	2.234	15.591	20.703
F(000)	1154.0	1468	5640.0	5928.0	6216.0	13456.0
crystal size [mm^3]	0.385 × 0.325 × 0.207	0.162 × 0.076 × 0.051	0.348 × 0.193 × 0.059	0.215 x 0.136 x 0.027	0.275 x 0.228 x 0.128	0.155 x 0.129 x 0.089
diffractometer	Gemini Ultra	Gemini Ultra	Gemini Ultra	Gemini-Ultra	GV50	GV50
absorption correction	gaussian	gaussian	gaussian	analytical	gaussian	gaussian
T_{min} / T_{max}	0.365 / 0.576	0.105 / 0.517	0.283 / 0.684	0.683 / 0.950	0.510 / 0.713	0.769 / 0.832
radiation [Å]	CuK_α (λ = 1.54184)	CuK_α (λ = 1.54184)	CuK_α (λ = 1.54184)	MoKα (λ = 0.71073)	CuK_α (λ = 1.54184)	CuK_α (λ = 1.54184)
2Θ range [°]	6.928 to 135.572	7.354 to 133.952	7.738 to 132.072	6.376 to 56.696	5.17 to 149.07	5.585 to 150.422
completeness [%]	98.8	99.2	99.4	98.7	99.4	99.9
reflns collected / unique	34878 / 7003	20457 / 4035	66712 / 15518	214503 / 44340	50346 / 18101	78250 / 18874
R_{int} / R_{sigma}	0.0272 / 0.0140	0.0324 / 0.0255	0.0283 / 0.0191	0.0868 / 0.0743	0.0374 / 0.0331	0.0542 / 0.0393
data / restraints / parameters	7003 / 12 / 748	4035 / 0 / 290	15518 / 3 / 1471	44340 / 4382 / 4365	18101 / 402 / 1630	18874 / 522 / 1639
GOF on F^2	1.080	0.993	1.043	1.126	1.032	1.070
R_1 / wR_2 [$I \geq 2\sigma(I)$]	0.0555 / 0.1629	0.0176 / 0.0377	0.0305 / 0.0808	0.1432 / 0.3488	0.0373/ 0.0953	0.0368 / 0.0863
R_1 / wR_2 [all data]	0.0565 / 0.1637	0.0207 / 0.0384	0.0338 / 0.0823	0.1691 / 0.3609	0.0402 / 0.0980	0.0491 / 0.0949
max / min $\Delta\rho$ [e·Å^{-3}]	1.29 / –0.54	0.46 / –0.40	1.09 / –0.50	2.76 / -1.97	1.22 / -1.38	2.02 / -1.56

Refinement details for [Thia][TEF]

[Thia][TEF] crystallizes in the triclinic space group *P*–1 with one formula unit in the asymmetric unit. The refinement could be done without any difficulty. One -C_4F_9 group of the $[TEF]^-$ anion shows a rotational disorder with a 50:50 ratio. Both parts were refined anisotropically. The ADPs of two half-occupied F atoms were restrained by ISOR commands. The crystal structure of [Thia][TEF] is shown in Figure S30 (disorder omitted).

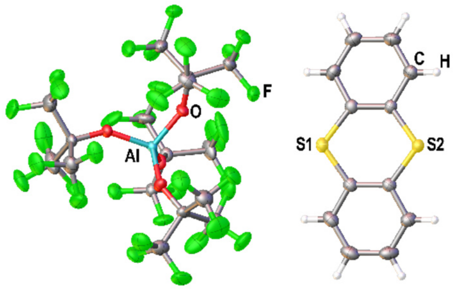

Figure S30: X-ray structure of [Thia][TEF].

Refinement details for 1a

Although **1a** decomposes in MeCN, we were able to obtain a single crystal suitable for X-ray diffraction to determine the solid state structure of **1a**. The compound **1a** crystallizes in the monoclinic space group $P2_1/n$ with one half of the P_4 chain complex, one $[SbF_6]^-$ anion and one MeCN solvent molecule in the asymmetric unit. The second half of the P_4 chain complex is crystallographically generated by a center of inversion. The structure refinement could be done without any problems. The crystal structure of **1a** is shown in Figure S31.

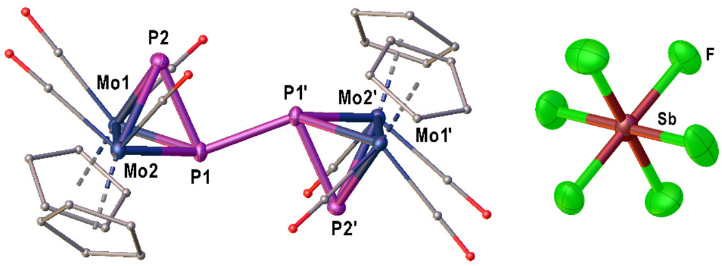

Figure S31: X-ray structure of **1a**. (left) dicationic P_4 zigzag chain complex (only one half in asymmetric unit); (right) $[SbF_6]^-$ anion.

Refinement details for 1b

Compound **1b** can be regarded as isostructural to compound **2**. It crystallizes in the monoclinic space group $P2_1/n$ with one dicationic complex exhibiting a central P_4 zigzag chain and two independent WCAs $[TEF]^-$ in the asymmetric unit. The refinement of the crystal structure of **2** could be done without any difficulty. One $-C_4F_9$ group of one anion shows a rotational disorder with a 60:40 ratio. The minor occupied part was refined isotropically and one of these $-CF_3$ groups was restrained during the refinement by SADI commands. The crystal structure of **1b** is shown in Figure S32.

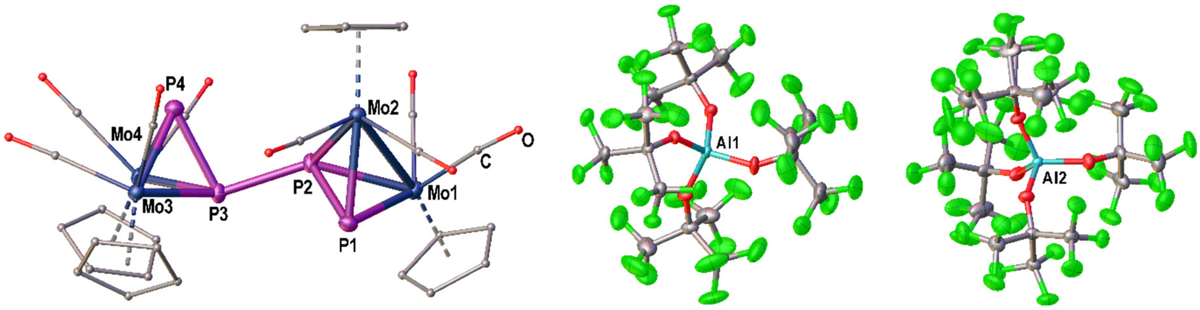

Figure S32: X-ray structure of **1b**. (left) dicationic P_4 zigzag chain complex. (middle + right) two independent $[TEF]^-$ anions.

Refinement details for 2

Compound **2** can be regarded as isostructural to compound **1b**. It crystallizes in the triclinic space group P-1 with four formula units in the asymmetric unit, *i.e.*, two dicationic complexes exhibiting a central As_4 zigzag chain and four independent WCAs $[TEF]^-$. The cell parameter are close to a monoclinic space group but the possibility of monoclinic or pseudo-monoclinic space groups could be excluded definitively. Both, the two cations as well as three of four anions show severe disorder. Due to the weak interaction between the ions the different parts are able to move independently and wobble inside the crystal. One cationic part (Figure S33 top middle) exhibits a disorder of the Mo_4As_4 unit with a ratio of 96:4, the other cationic part (Figure S33 top right) shows a disorder of one Mo_2As_2 unit with a ratio of 95:5 and a threefold disorder of the other Mo_2As_2 unit with a ratio of 55:40:5. The heavy atom frameworks still contains q-peaks with an electron density up to 2.8 e^-. This indicates further disorder of the cations, which cannot be resolved due to a very low occupancy. The geometry of the disordered Cp rings and CO groups was restrained with several AFIX, DFIX and SADI commands and the ADPs were restrained with RIGU and SIMU commands. The $[TEF]^-$ anion including Al1 shows a rotational disorder of all four $-OC_4F_9$ groups with ratios of 54:46, 60:40, 50:50 and 50:50, respectively. The $[TEF]^-$ anions including Al2 and Al3 show a rotational disorder of one $-C_4F_9$ group with a ratio of 62:38 and 60:40, respectively. Hereby, the geometry of the $[TEF]^-$ anions were restrained by several DFIX and DANG commands and the ADPs by RIGU commands.

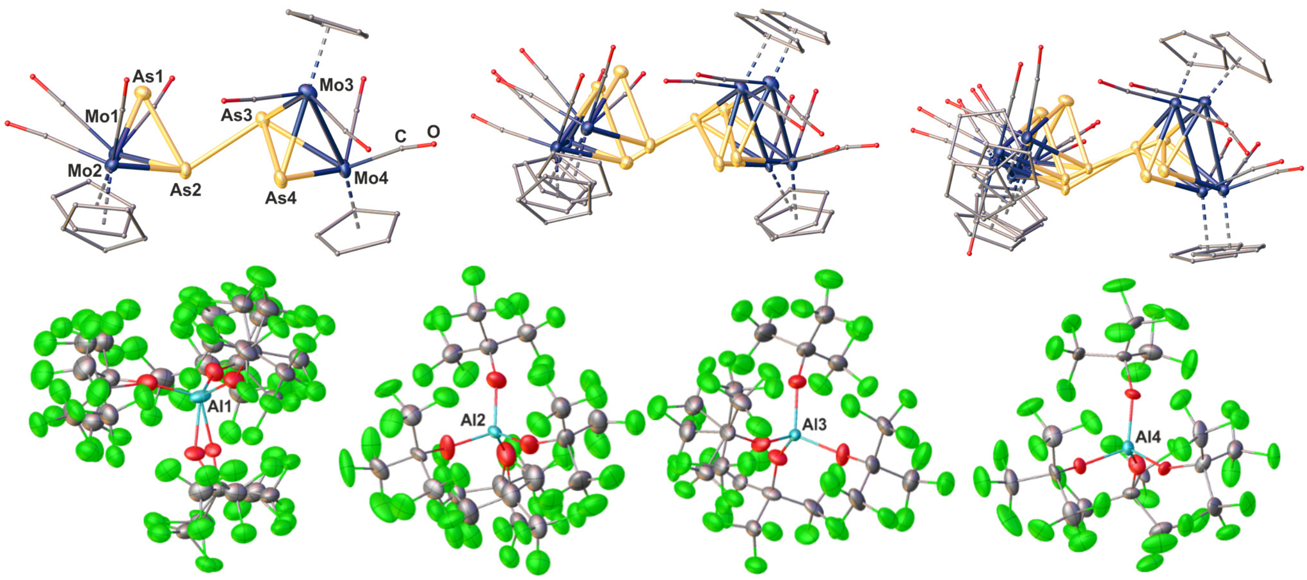

Figure S33: X-ray structure of **2**. (top left) dicationic As_4 zigzag chain complex. (top middle + right) disorder of the two independent cations. (bottom) four independent $[TEF]^-$ anions with disorder.

Refinement details for 3

Compound **3** can be regarded as isostructural to compound **4**. It crystallizes in the monoclinic space group $P2_1/n$ with two formula units in the asymmetric unit, *i.e.*, one dicationic complex and two independent WCAs $[TEF]^-$. The diacationic part exhibits a central Sb_4 cluster-like motif bearing a Sb_4 zigzag chain and further short Sb-Sb contacts leading to a distorted "butterfly-like" geometry. The refinement of the crystal structure of **3** could be done without any severe difficulty. The cation is completely ordered. One of the $[TEF]^-$ anions shows one disordered $-CF_3$ group, the second anion containing Al2 shows a rotational disorder of two $-C_4F_9$ groups with ratios of 52:48 and 63:37. The geometry of the disordered parts were restraint with several DFIX and DANG commands and the ADPs were restraint with RIGU commands. The crystal structure of **1b** is shown in Figure S34.

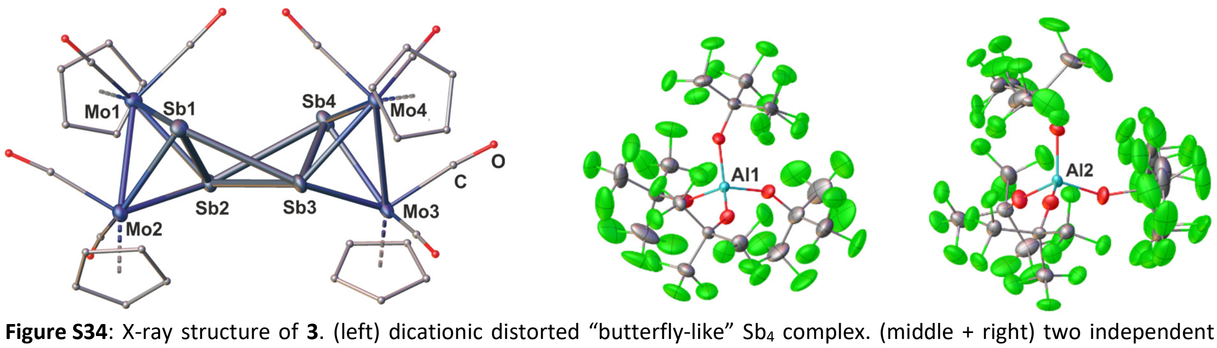

Figure S34: X-ray structure of **3**. (left) dicationic distorted "butterfly-like" Sb_4 complex. (middle + right) two independent $[TEF]^-$ anions.

Refinement details for 4

Compound **4** can be regarded as isostructural to compound **3**. It crystallizes in the orthorhombic space group *Pbca* with two formula units in the asymmetric unit or, more precisely, two halves of the dicationic complex and two independent WCAs $[TEF]^-$. The diacationic part exhibits a central Bi_4 cluster-like motif bearing a Bi_4 zigzag chain and further short Bi-Bi contacts leading to a distorted "butterfly-like" geometry. The refinement of the crystal structure of **3** could be done without any severe difficulty. The cation as well as one $[TEF]^-$ anion is completely ordered. The second anion containing Al1 shows a rotational disorder of two $-C_4F_9$ groups with ratios of 54:46 and 50:50. The geometry of the disordered parts were restraint with several DFIX and DANG commands and the ADPs were restraint with RIGU commands. The crystal structure of **1b** is shown in Figure S35.

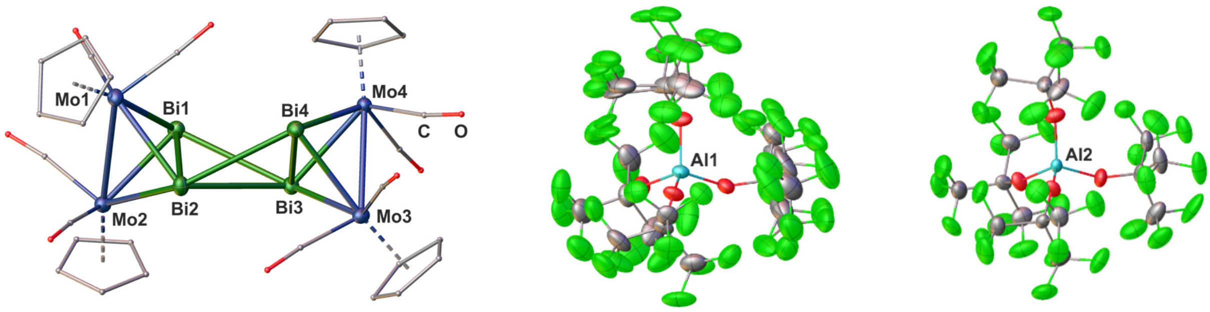

Figure S35: X-ray structure of **4**. (left) dicationic distorted "butterfly-like" Bi_4 complex. (middle + right) two independent $[TEF]^-$ anions.

4.4.7 DFT calculations

The DFT calculations were performed with the TURBOMOLE[24] program package at the D3(BJ)[25]-B3LYP[26]/def2-TZVP[27] level of theory. The geometries have been optimized in the gas phase. The coulomb potentials have been approximated by using the resolution of identity (RI)[28,27b] together with the Multipole Accelerated Resolution of Identity (MARI-J)[29] methods. The solvent effects were incorporated as single point calculation on the gas phase optimized geometries *via* the Conductor-like Screening Model[30] (COSMO) using the dielectric constant of CH_2Cl_2 (ε = 8.930). The reaction energies (Table S2) have been calculated by using the SCF energies without corrections for zero point vibration energy and the entropic effects are not considered. The molecular orbital interaction schemes (Figure S38) were created using single point calculations at the B3LYP/def2-SVP level using Gaussian09[31] and AOMix.[32] The isotropic magnetic shielding of the phosphorus atoms in $[\{CpMo(CO)_2\}_4(\mu_4,\eta^2:\eta^2:\eta^2:\eta^2\text{-}P_4)]^{2+}$ have been calculated at the BP86[33]/def2-TZVP level (Table S5).

Table S2: Reaction energies calculates at the D3(BJ)-B3LYP/def2-TZVP level of theory.

Transformation	Reaction Energy (kJ·mol^{-1})
2 $[\{CpMo(CO)_2\}_2(\mu,\eta^2:\eta^2\text{-}P_2)]^+$ = $[\{CpMo(CO)_2\}_4(\mu_4,\eta^2:\eta^2:\eta^2:\eta^2\text{-}P_4)]^{2+}$ (C_1)	-118.12
2 $[\{CpMo(CO)_2\}_2(\mu,\eta^2:\eta^2\text{-}P_2)]^+$ = $[\{CpMo(CO)_2\}_4(\mu_4,\eta^2:\eta^2:\eta^2:\eta^2\text{-}P_4)]^{2+}$ (C_i)	-112.73
2 $[\{CpMo(CO)_2\}_2(\mu,\eta^2:\eta^2\text{-}As_2)]^+$ = $[\{CpMo(CO)_2\}_4(\mu_4,\eta^2:\eta^2:\eta^2:\eta^2\text{-}As_4)]^{2+}$	-89.52
2 $[\{CpMo(CO)_2\}_2(\mu,\eta^2:\eta^2\text{-}Sb_2)]^+$ = $[\{CpMo(CO)_2\}_4(\mu_4,\eta^2:\eta^2:\eta^2:\eta^2\text{-}Sb_4)]^{2+}$	-134.13
2 $[\{CpMo(CO)_2\}_2(\mu,\eta^2:\eta^2\text{-}Bi_2)]^+$ = $[\{CpMo(CO)_2\}_4(\mu_4,\eta^2:\eta^2:\eta^2:\eta^2\text{-}Bi_4)]^{2+}$	-141.15

Table S3: Wiberg bond indices of selected bonds calculated at B3LYP/def2-TZVP level of theory. Labeling according to Figure S36.

1		**2**		**3**		**4**	
P6-P5	1.05	As6-As5	0.86	Sb2-Sb1	0.62	Bi2-Bi1	0.55
P7-P6	0.85	As7-As6	0.67	Sb3-Sb2	0.30	Bi33-Bi2	0.27
P8-P7	1.00	As8-As7	0.85	Sb4-Sb1	0.30	Bi34-Bi1	0.30
Mo2-Mo1	0.43	Mo2-Mo1	0.42	Sb4-Sb2	0.47	Bi34-Bi2	0.45
Mo4-Mo3	0.40	Mo4-Mo3	0.38	Sb4-Sb3	0.62	Bi34-Bi33	0.56
P7-P5	0.02	As7-As5	0.06	Sb3-Sb1	0.02	Bi33-Bi1	0.02
P8-P6	0.04	As8-As6	0.08	Mo6-Mo5	0.41	Mo4-Mo3	0.41
P7-Mo3	0.68	As7-Mo3	0.72	Mo8-Mo7	0.41	Mo36-Mo35	0.41
P7-Mo4	0.73	As7-Mo4	0.66	Mo6-Sb1	0.83	Mo3-Bi1	0.81
P8-Mo3	0.84	As8-Mo3	0.88	Mo6-Sb2	0.70	Mo3-Bi2	0.71
P8-Mo4	0.85	As8-Mo4	0.88	Mo7-Sb3	0.83	Mo4-Bi1	0.82
P5-Mo1	0.78	As5-Mo1	0.87	Mo7-Sb4	0.70	Mo4-Bi2	0.67
P5-Mo2	0.87	As5-Mo2	0.92	Mo8-Sb3	0.85	Mo35-Bi33	0.82
P6-Mo1	0.73	As6-Mo1	0.67	Mo8-Sb4	0.72	Mo35-Bi34	0.73
P6-Mo2	0.73	As6-Mo2	0.68	Mo5-Sb1	0.84	Mo36-Bi33	0.82
				Mo5-Sb2	0.72	Mo36-Bi34	0.64

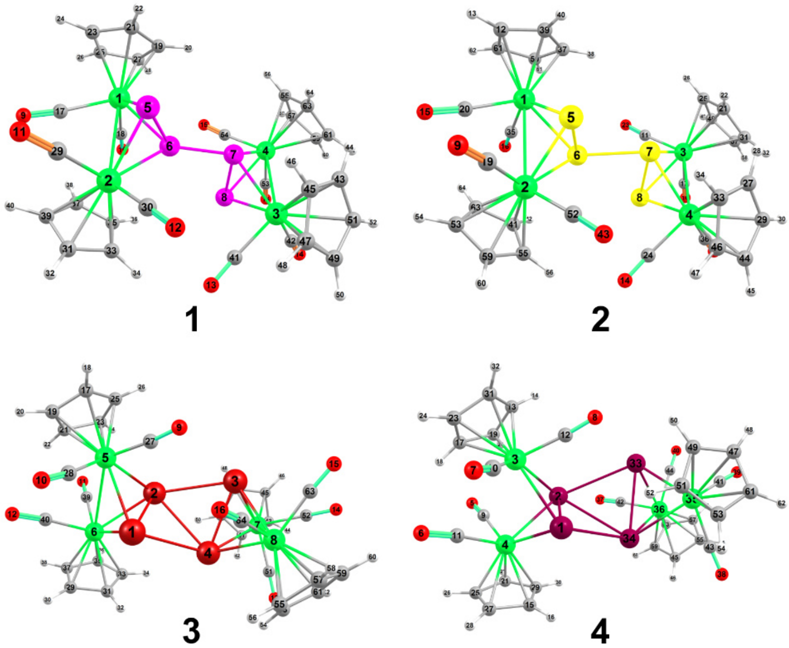

Figure S36: Labeling scheme of compounds **1-4** for the attribution of WBIs.

Table S4: Spin densities on selected atoms in **A**$^+$-**D**$^+$ calculated at the D3(BJ)/B3LYP/def2-TZVP level of theory.

[{CpMo(CO)$_2$}$_2$(μ,η^2:η^2-P$_2$)]$^+$ (**A**$^+$)		[{CpMo(CO)$_2$}$_2$(μ,η^2:η^2-As$_2$)]$^+$ (**B**$^+$)		[{CpMo(CO)$_2$}$_2$(μ,η^2:η^2-Sb$_2$)]$^+$ (**C**$^+$)		[{CpMo(CO)$_2$}$_2$(μ,η^2:η^2-Bi$_2$)]$^+$ (**D**$^+$)	
1 Mo	0.38	1 Mo	0.29	3 Mo	0.29	3 Mo	0.26
2 Mo	0.38	2 Mo	0.29	4 Mo	0.29	4 Mo	0.26
3 P	0.08	3 As	0.15	1 Sb	0.17	1 Bi	0.20
4 P	0.08	4 As	0.15	2 Sb	0.17	2 Bi	0.20

Table S5: Calculated isotropic magnetic shielding (ppm) for the phosphorus atoms of **1b** at the BP86/def2-TZVP level of theory. Labeling of the atoms according to the labeling in the X-ray structure (Figure S32).

Atom	isotropic magnetic shielding
P1	120
P2	176
P3	132
P4	39

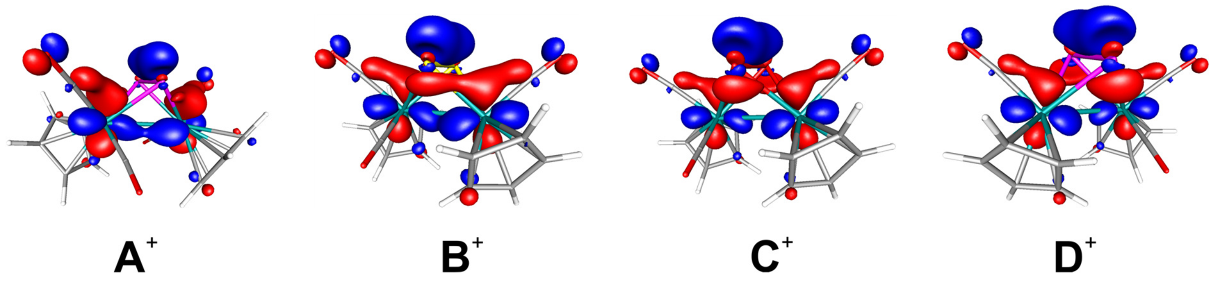

Figure S37: Single occupied molecular orbitals (SOMOs) in the transient monoradical cations [**A**]$^+$, [**B**]$^+$, [**C**]$^+$ and [**D**]$^+$.

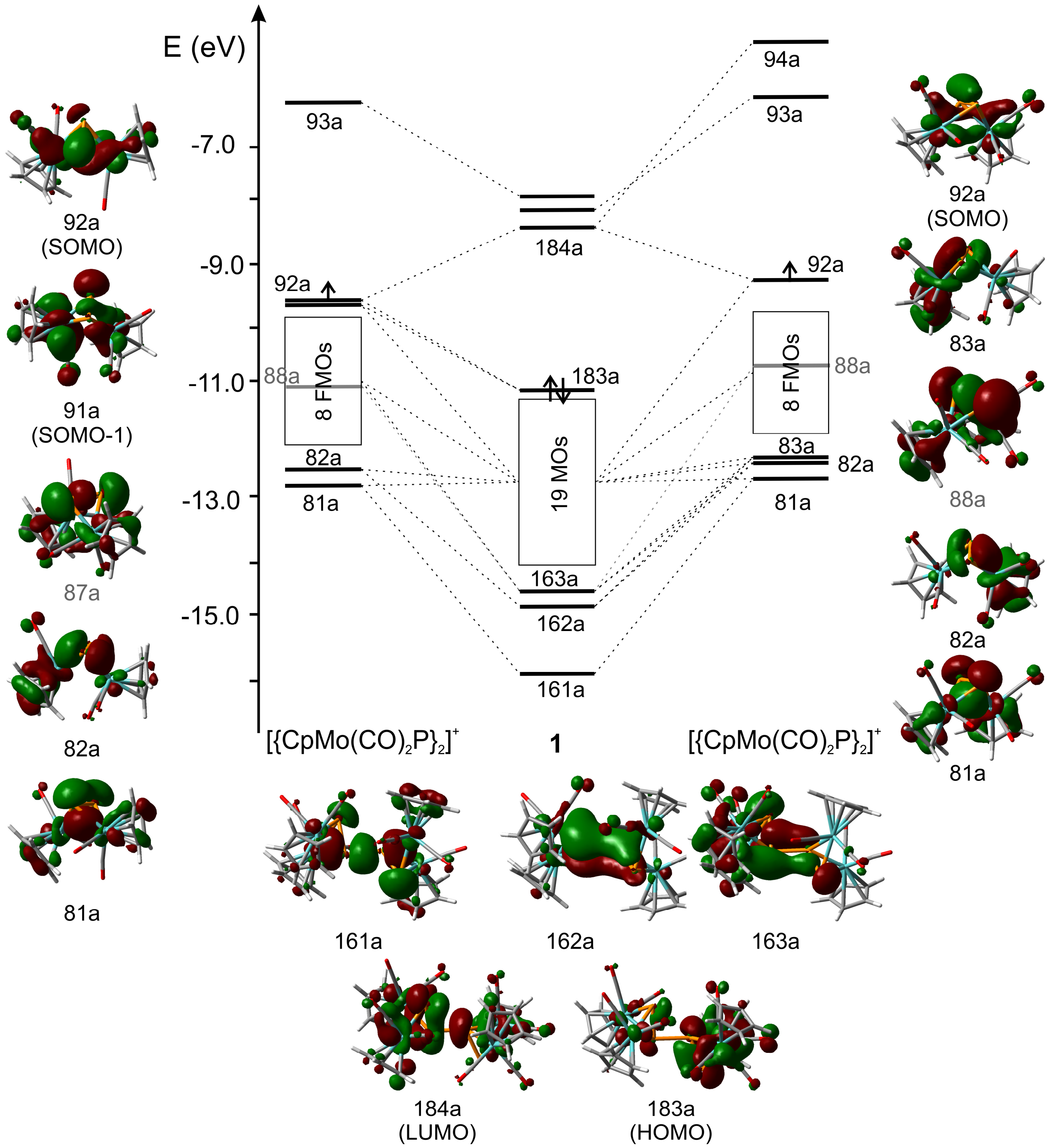

Figure S38: Molecular orbital interaction diagram for [{CpMo(CO)$_2$}$_4$(μ_4,η^2:η^2:η^2:η^2-P$_4$)]$^{2+}$ ([**A**]$_2$$^{2+}$), at the B3LYP/def2-SVP level of theory. The fragment orbital (FMO; 88a) in gray represents the P-P σ-bond in the fragment.

Table S6: Cartesian coordinates of the optimized geometry of $[\{CpMo(CO)_2\}_2(\mu,\eta^2{:}\eta^2\text{-}P_2)]^+$ ([**A**]$^+$), at the D3(BJ)/B3LYP/def2-TZVP level of theory.

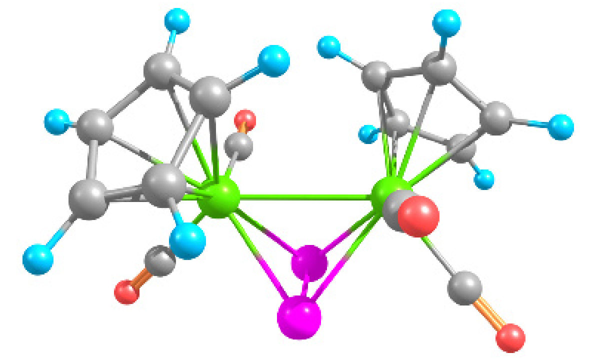

Atom	X	Y	Z
Mo	8.8680078	0.8557528	7.4256032
Mo	11.7695944	0.2185180	8.0505167
P	9.8236276	−1.1592497	8.7318342
P	9.8363509	0.6848925	9.7015666
C	7.2270953	0.0135461	8.1632378
C	8.9636360	−0.6458927	6.1441119
C	12.5869899	−0.2439908	9.8007635
C	11.9274593	2.1179225	8.5732312
C	7.6233772	2.8437643	7.4683108
H	6.8194391	2.9755860	8.1731686
C	7.5107595	2.2641490	6.1681741
H	6.6080326	1.8983455	5.7092283
C	8.8002023	2.3048513	5.5699817
H	9.0459201	1.9571371	4.5800981
C	9.6954743	2.9088931	6.4860643
H	10.7384422	3.1053225	6.3148258
C	8.9685199	3.2376841	7.6623528
H	9.3724487	3.7119200	8.5397381
C	12.1700681	−1.3724646	6.3039551
H	11.5299770	−2.2219987	6.1412358
C	13.2956676	−1.3245504	7.1600512
H	13.6687003	−2.1392223	7.7581591
C	13.8665703	−0.0185231	7.0746899
H	14.7540369	0.3235770	7.5794092
C	13.0780061	0.7326293	6.1603768
H	13.2574074	1.7534837	5.8657097
C	12.0381514	−0.1012398	5.6819502
H	11.2920817	0.1708905	4.9574461
O	6.2357779	−0.4100277	8.5538389
O	8.9850292	−1.4654095	5.3339028
O	13.1287532	−0.5330963	10.7690696
O	12.0929087	3.2307021	8.8239970

ENERGIES [a.u.]: Total energy (+ OC corr.) = −1659.6383829264 (−1659.6386925313)

Table S7: Cartesian coordinates of the optimized geometry of $[\{CpMo(CO)_2\}_2(\mu,\eta^2{:}\eta^2\text{-}As_2)]^+$ ([**B**]$^+$), at the D3(BJ)/B3LYP/def2-TZVP level of theory.

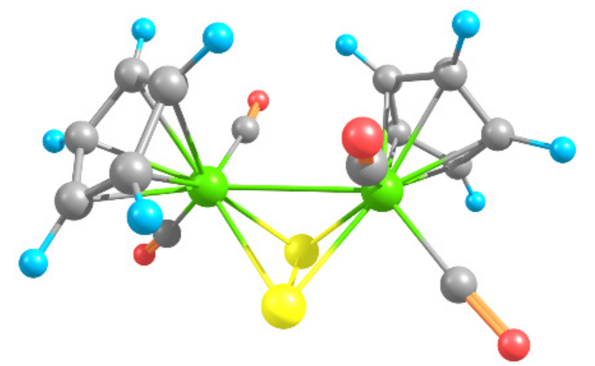

Atom	X	Y	Z
Mo	−1.6641307	0.1527463	0.1796316
Mo	1.3511383	−0.6463090	0.7605984
As	−0.7388288	−2.0400739	1.3090411
As	−0.5191211	0.0538932	2.4790078
C	−3.2771255	−0.9513322	0.5792123
C	−1.3041281	−1.0916469	−1.3208738
C	2.2372846	−0.6929922	2.5473330
C	1.4569594	1.3303137	0.8652320
C	−2.9751078	2.0465949	0.5585139
H	−3.6600973	2.1084858	1.3984839
C	−3.2897165	1.5485581	−0.7502884
H	−4.2535817	1.1694923	−1.0759362
C	−2.1265935	1.6768258	−1.5613365
H	−2.0484271	1.4002333	−2.6084327
C	−1.0910587	2.2456196	−0.7667173
H	−0.0914571	2.4910740	−1.1070831
C	−1.6152673	2.4751358	0.5471431
H	−1.0860840	2.9481624	1.3672978
C	1.7218940	−2.3148872	−0.8548684
H	1.0060059	−3.0919775	−1.1002625
C	2.7533624	−2.3999876	0.1257838
H	2.9469006	−3.2432183	0.7816092
C	3.5151781	−1.1846934	0.0689487
H	4.3862496	−0.9468434	0.6717400
C	2.9538289	−0.3608857	−0.9477698
H	3.3161262	0.6189939	−1.2436804
C	1.8474645	−1.0512798	−1.5189464
H	1.2287300	−0.6943976	−2.3344141
O	−4.2557153	−1.5269142	0.7806854
O	−1.1736221	−1.7577129	−2.2610127
O	2.8179976	−0.7474340	3.5420006
O	1.6309425	2.4764567	0.8893595

ENERGIES [a.u.]: Total energy (+ OC corr.) = −5448.3999799019 (−5448.3974790233)

Table S8: Cartesian coordinates of the optimized geometry of [{CpMo(CO)$_2$}$_2$(μ,η^2:η^2-Sb$_2$)]$^+$ ([**C**]$^+$), at the D3(BJ)/B3LYP/def2-TZVP level of theory.

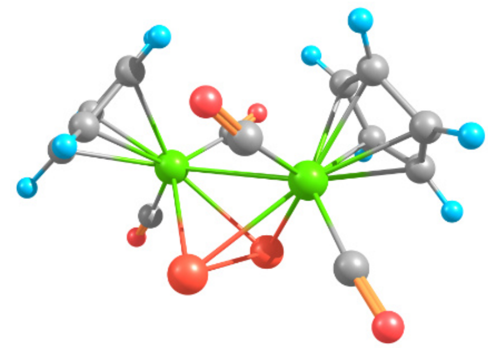

Atom	X	Y	Z
Sb	−0.5103171	−2.4978269	−1.1283388
Sb	−1.9058872	−1.6902181	1.1339255
Mo	0.8902128	−1.2036102	0.8868194
Mo	−1.4880319	0.1669511	−0.8849121
C	−1.2139853	2.2428991	0.2585084
H	−0.3592513	2.4741195	0.8695569
C	−3.3064489	1.5572405	−0.4019476
H	−4.3176764	1.1856893	−0.3839098
C	−2.6320453	2.0942038	−1.5396242
H	−3.0415355	2.1981717	−2.5307794
C	−1.3455858	2.5180045	−1.1232107
H	−0.6024779	2.9840995	−1.7494419
C	−2.4281843	1.6487322	0.7084483
H	−2.6609142	1.3932573	1.7277682
C	−2.6596419	−0.6686285	−2.2793137
C	−0.0042760	0.2004716	−2.2071874
O	−3.3804601	−1.0507560	−3.0767576
O	0.8197722	0.3454639	−2.9927310
C	2.5477903	0.0727306	−0.2584873
H	2.3192948	0.9293573	−0.8679897
C	3.0029886	−2.0827936	0.3982542
H	3.1870953	−3.1442421	0.3784522
C	3.1334040	−1.2315822	1.5365772
H	3.4305264	−1.5353245	2.5267101
C	2.8555301	0.0947252	1.1225197
H	2.8887425	0.9705634	1.7498026
C	2.6399819	−1.2752895	−0.7103249
H	2.5333372	−1.6036391	−1.7297776
C	0.7545245	−2.6332607	2.2845562
C	0.1775529	0.1001066	2.2072271
O	0.7847766	−3.4468235	3.0837300
O	−0.1088107	0.8872076	2.9918776

ENERGIES [a.u.]: Total energy (+ OC corr.) = −1457.3475468129 (−1457.3438683961)

Table S9: Cartesian coordinates of the optimized geometry of [{CpMo(CO)$_2$}$_2$(μ,η^2:η^2-Bi$_2$)]$^+$ ([**D**]$^+$), at the D3(BJ)/B3LYP/def2-TZVP level of theory.

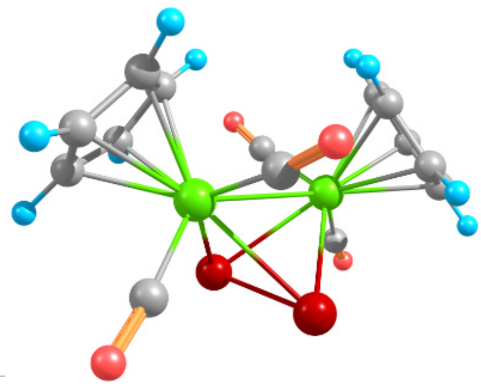

Atom	X	Y	Z
Bi	−0.7436909	2.4905992	1.2664596
Bi	0.7435270	2.4905457	−1.2667552
Mo	1.4515065	0.6092815	0.7668696
Mo	−1.4515429	0.6091246	−0.7670231
C	−0.3145025	−0.1402952	−2.2104212
C	−2.2010476	1.9258658	−2.0724334
C	−2.8511146	−0.2190100	0.9621729
H	−2.8586490	0.1243136	1.9823465
C	−2.1068251	−1.3276305	0.4671860
H	−1.4211789	−1.9317230	1.0347630
C	−2.4599054	−1.5231563	−0.8888249
H	−2.0809972	−2.2970992	−1.5360347
C	−3.4181021	−0.5406929	−1.2453597
H	−3.9048001	−0.4498852	−2.2021423
C	−3.6634594	0.2676958	−0.0951312
H	−4.3718850	1.0769689	−0.0316001
O	0.2440097	−0.6797583	−3.0577299
O	−2.7336670	2.6132672	−2.8136522
C	0.3145352	−0.1400290	2.2103724
C	2.2009733	1.9262898	2.0720230
C	2.8515371	−0.2188268	−0.9620186
H	2.8593932	0.1245869	−1.9821601
C	2.1070521	−1.3274508	−0.4673522
H	1.4215552	−1.9314667	−1.0351909
C	2.4596463	−1.5230687	0.8887659
H	2.0804964	−2.2970490	1.5357876
C	3.4177656	−0.5406556	1.2456987
H	3.9041723	−0.4499504	2.2026370
C	3.6635416	0.2677871	0.0955874
H	4.3720255	1.0770308	0.0323358
O	−0.2439548	−0.6794550	3.0577193
O	2.7335856	2.6138457	2.8131048

ENERGIES [a.u.]: Total energy (+ OC corr.) = −1406.1168610510 (−1406.1126805587)

Table S10: Cartesian coordinates of the optimized geometry of $[\{CpMo(CO)_2\}_4(\mu_4,\eta^2:\eta^2:\eta^2:\eta^2\text{-}P_4)]^{2+}$ ($[\mathbf{A}]_2^{2+}$; C_1 symmetry), at the D3(BJ)/B3LYP/def2-TZVP level of theory.

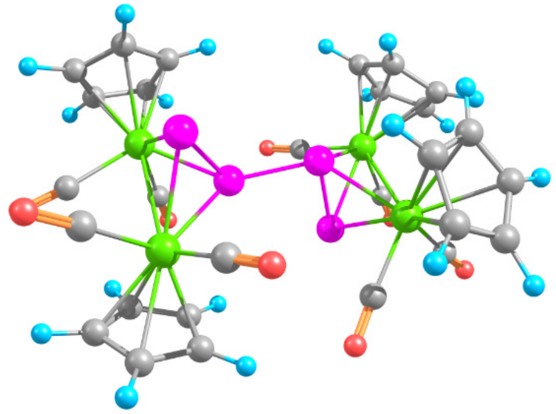

Atom	X	Y	Z
Mo	−3.8589110	18.6774975	13.4760892
Mo	−1.7041565	18.2280207	15.7839495
Mo	−3.3918001	13.1326891	17.0832131
Mo	−6.1817563	13.5946092	15.5644958
P	−1.9525622	17.0252214	13.5553383
P	−3.4722620	16.7842873	14.9967769
P	−3.9890540	14.6628961	15.2903041
P	−4.9888085	15.0440780	17.1973909
O	−2.3835234	21.3955793	13.9875355
O	−5.8914302	19.4550140	15.7476890
O	0.5974662	19.4132491	13.9625744
O	0.0900396	15.7051766	16.3099382
O	−2.0414765	15.0698877	19.1333222
O	−5.2864273	12.1030340	19.3987067
O	−7.5552244	16.3176888	14.8317110
O	−7.9447960	13.4835890	18.1788468
C	−2.8644860	20.3627011	13.8707955
C	−5.1261706	19.1881739	14.9449213
C	−4.9221409	17.5594950	11.6754573
H	−5.1714555	16.5118194	11.7129589
C	−3.7215636	18.1069255	11.1496914
H	−2.9147613	17.5524496	10.7012049
C	−3.7873962	19.5136858	11.2839805
H	−3.0412283	20.2153984	10.9491051
C	−5.0432300	19.8448297	11.8803177
H	−5.4165555	20.8393703	12.0602095
C	−5.7444004	18.6276024	12.1209362
H	−6.7382283	18.5371009	12.5274750
C	−0.2370811	18.9731722	14.5936452
C	−0.5416788	16.6274331	16.0820037
C	−0.7166495	19.1658755	17.6527717
H	0.3437830	19.1004795	17.8317310
C	−1.7072530	18.2443642	18.1087520
H	−1.5251644	17.3582946	18.6919906
C	−2.9812311	18.7407339	17.7233938
H	−3.9315565	18.2836299	17.9432954
C	−2.7841316	19.9638598	17.0368580
H	−3.5563940	20.6054158	16.6509765
C	−1.3912239	20.2213079	16.9749601
H	−0.9315350	21.0893497	16.5309967
C	−2.5757599	14.3964033	18.3812585
C	−4.6183751	12.4953953	18.5690833
C	−2.7267297	11.3889434	15.5905734
H	−3.2691719	11.0916038	14.7116332
C	−1.6721858	12.3370072	15.6240031
H	−1.3002639	12.9032291	14.7864718
C	−1.1692084	12.3947751	16.9464438
H	−0.3449337	13.0035563	17.2797919
C	−1.9104903	11.4748799	17.7412741
H	−1.7331723	11.2476543	18.7795734
C	−2.8811015	10.8561307	16.8956774
H	−3.5645946	10.0769713	17.1911983
C	−7.2857119	13.5337546	17.2545979
C	−7.0622398	15.3399115	15.1463462
C	−6.8604987	12.9691463	13.4329587
H	−6.9603021	13.6779856	12.6281717
C	−7.8880136	12.5931412	14.3503995
H	−8.8983153	12.9675231	14.3654924
C	−7.3608657	11.5762582	15.1933171
H	−7.8981251	11.0622952	15.9740544
C	−6.0252786	11.3201278	14.8025076
H	−5.3880287	10.5680090	15.2315057
C	−5.7125892	12.1846572	13.7207591
H	−4.7798688	12.2220447	13.1835120

ENERGIES [a.u.]:

Total energy = −3318.931372929

Total energy + OC corr. = −3318.926558631

Table S11: Cartesian coordinates of the optimized geometry of $[\{CpMo(CO)_2\}_4(\mu_4,\eta^2:\eta^2:\eta^2:\eta^2\text{-}As_4)]^{2+}$ ($[\mathbf{B}]_2^{2+}$), at the D3(BJ)/B3LYP/def2-TZVP level of theory.

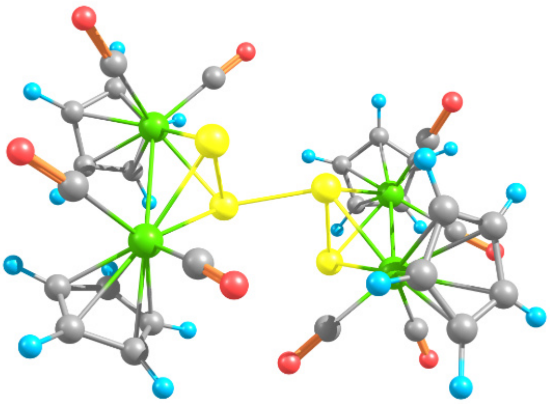

Atom	X	Y	Z
Mo	−0.0121012	3.0471978	−2.1625284
Mo	2.0211131	2.5629519	0.2909386
Mo	−2.4988000	−2.4942620	0.4474318
Mo	0.3850533	−2.5620046	1.9114226
As	1.5368930	1.0671585	−1.7641129
As	−0.2523413	1.0671585	−0.0884044
As	−0.3136609	1.3892673	−0.1692197
As	−1.4366835	−0.7392673	2.0040885
O	4.4448143	3.1356695	−1.6480131
O	−4.1769858	−2.6767617	3.1024003
C	−3.5829532	−0.8933274	−0.0411159
C	0.1154196	3.5208545	−4.4519560
H	0.9657356	4.0085900	−4.8998461
O	1.5976522	−0.3655131	3.7802894
O	2.0273833	5.4289215	−2.1176357
O	−1.7089579	4.7036609	−0.1012048
C	−3.5335442	−2.5829382	2.1680199
O	−1.3687615	−3.6643328	4.2886654
C	3.5507978	2.9109479	−0.9829436
C	1.3298168	4.5233913	−2.0714033
C	−1.9599411	−3.9324490	−1.3643607
H	−1.0779040	−3.8140810	−1.9709608
O	−4.2082259	−0.0080012	−0.3954013
C	1.1030144	−1.1392998	3.0982275
C	−3.2147183	−3.3145111	−1.6050392
H	−3.4556878	−2.6675995	−2.4319211
C	1.2120904	−4.2660054	0.4692215
H	0.7198602	−4.5870298	−0.4311683
C	1.0310024	−4.8053616	1.7676331
H	0.3753030	−5.6158575	2.0401085
C	−2.0875430	−4.7666569	−0.2234810
H	−1.3298225	−5.4058023	0.1921844
C	2.2175575	−3.2651518	0.5450384
H	2.5989121	−2.6833996	−0.2770217
C	−1.0626135	4.0949216	−0.8185248
C	−0.7650546	−3.2291915	3.4284919
C	−1.3485978	1.9000057	−3.7544050
H	−1.7909070	0.9388813	−3.5497520
C	−0.0888256	2.1207238	−4.3703160
H	0.5768953	1.3630007	−4.7476764
C	0.8973647	3.6079929	2.1123746
H	−0.1295759	3.4159431	2.3731281
O	3.5189763	−0.0710729	1.0881969
C	1.9289560	−4.1328103	2.6519768
H	2.0686986	−4.3444724	3.6991732
C	2.6574392	−3.1821448	1.8869603
H	3.4292168	−2.5276906	2.2559305
C	−4.1246016	−3.7655454	−0.6010359
H	−5.1717998	−3.5215062	−0.5334130
C	−1.9333684	3.1599021	−3.4623898
H	−2.9088452	3.3219134	−3.0343469
C	2.9606630	0.8716763	0.7641601
C	2.7736782	4.5862164	1.2212222
H	3.4150869	5.2648893	0.6824932
C	2.0280141	2.8918448	2.5891396
H	2.0098271	2.0689808	3.2839352
C	−3.4172449	−4.6607608	0.2487430
H	−3.8320682	−5.1948063	1.0882887
C	3.1977835	3.5041723	2.0422271
H	4.2181735	3.2314539	2.2549549
C	−1.0278874	4.1713340	−3.8979782
H	−1.1999963	5.2344724	−3.8684954
C	1.3592669	4.6531124	1.2746243
H	0.7475589	5.3903518	0.7843805

ENERGIES [a.u.]:

Total energy = −10896.833702875

Total energy + OC corr. = −10896.829055953

Table S12: Cartesian coordinates of the optimized geometry of $[\{CpMo(CO)_2\}_4(\mu_4\text{-}\eta^2{:}\eta^2{:}\eta^2{:}\eta^2\text{-}Sb_4)]^{2+}$ ($[\mathbf{C}]_2^{2+}$), at the D3(BJ)/B3LYP/def2-TZVP level of theory.

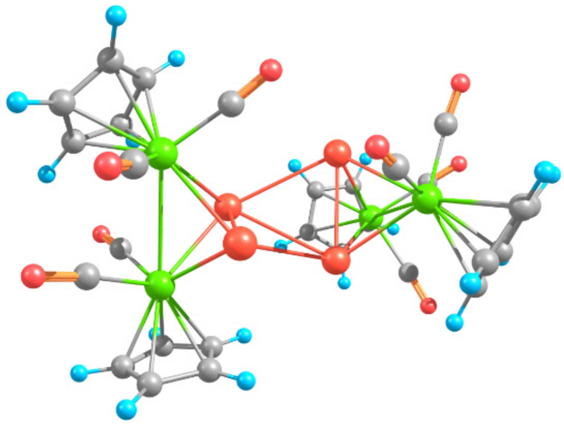

Atom	X	Y	Z
Sb	-1.9585651	-0.9737952	0.9563989
Sb	0.6776734	-1.5661957	-0.1355702
Sb	0.3786940	1.0804334	-2.0952231
Sb	0.2225871	1.5096030	0.7824603
Mo	-1.5713535	-3.1441240	-0.7720651
Mo	-0.3266429	-2.7707598	2.2158074
Mo	2.2390954	2.6439935	-0.8392500
Mo	-0.9450994	3.3136372	-1.0419988
O	-2.4618305	-1.0101121	-2.8730001
O	-4.5420653	-3.3582091	0.2302705
O	1.6309096	-4.9783372	1.1630098
O	-2.5998532	-4.9277416	2.4026951
O	2.0489463	4.7425132	1.4787602
O	1.8984570	4.9679710	-2.9220561
O	-0.9020121	3.7290143	-4.1568391
O	-3.3966985	1.4028495	-1.3557469
C	-2.0892593	-4.5650031	-2.5215811
H	-2.9208621	-4.3793962	-3.1808857
C	-2.1159251	-5.3686967	-1.3481475
H	-2.9782818	-5.8772797	-0.9481531
C	-0.8081117	-5.4203779	-0.8161126
H	-0.5093728	-5.9785393	0.0535219
C	0.0415752	-4.6429121	-1.6490044
H	1.1072381	-4.5383507	-1.5362476
C	-0.7452785	-4.1171424	-2.7085799
H	-0.3836284	-3.5322365	-3.5377929
C	-2.1559658	-1.7457674	-2.0541825
C	-3.4524090	-3.2300236	-0.0804422
C	-0.8947322	-2.4562964	4.4624667
H	-1.8723470	-2.6917061	4.8500265
C	-0.4698340	-1.1855025	3.9947188
H	-1.0587460	-0.2841860	3.9946959
C	0.8966941	-1.2926049	3.6203311
H	1.5115935	-0.4925984	3.2434288
C	1.3192127	-2.6235187	3.8610066
H	2.3152946	-3.0076388	3.7141320
C	0.2117535	-3.3509810	4.3855121
H	0.2237254	-4.3761571	4.7161385
C	0.8741849	-4.1789964	1.4799057
C	-1.7985465	-4.1254085	2.2528796
C	4.2968452	2.2528909	0.1861564
H	4.5035710	2.5623207	1.1974930
C	4.5109207	3.0332743	-0.9868825
H	4.9191703	4.0295625	-1.0216645
C	4.1582785	2.2299594	-2.1098015
H	4.2401196	2.5190836	-3.1447279
C	3.7360932	0.9620569	-1.6319547
H	3.4723612	0.1142663	-2.2409861
C	3.8190375	0.9802910	-0.2135320
H	3.5843961	0.1584830	0.4420568
C	2.0416027	3.9908733	0.6144776
C	1.9356067	4.1126098	-2.1636995
C	-1.1367436	4.7139405	0.8593980
H	-0.7035330	4.5086580	1.8234443
C	-2.4316693	4.3264843	0.4218173
H	-3.1524240	3.7643558	0.9919919
C	-2.6395288	4.8799672	-0.8790461
H	-3.5406832	4.8097533	-1.4652755
C	-1.4692940	5.6090023	-1.2287349
H	-1.3186127	6.1665729	-2.1390408
C	-0.5497660	5.5110754	-0.1605469
H	0.4148192	5.9854334	-0.1215166
C	-0.8684425	3.5239184	-3.0356610
C	-2.4623391	2.0557468	-1.2790523

ENERGIES [a.u.]:

Total energy = −3318.931372929

Total energy + OC corr. = −3318.926558631

Table S13: Cartesian coordinates of the optimized geometry of $[\{CpMo(CO)_2\}_4(\mu_4\text{-}\eta^2{:}\eta^2{:}\eta^2{:}\eta^2\text{-}Bi_4)]^{2+}$ ($[\mathbf{D}]_2^{2+}$), at the D3(BJ)/B3LYP/def2-TZVP level of theory.

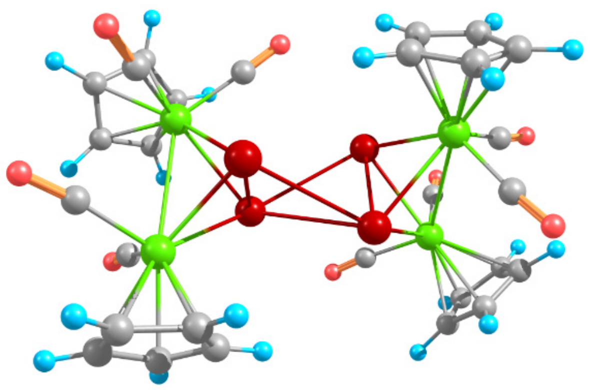

Atom	X	Y	Z
Bi	1.2967122	−0.8448469	−1.8749669
Bi	−0.7458023	−1.7208956	0.2675361
Mo	1.7570428	−3.1439859	−0.1849027
Mo	−0.6173678	−2.8181769	−2.4300194
O	−1.7915328	−5.2134377	−0.7927717
O	1.5363523	−4.7754682	−3.6030399
O	4.0939815	−3.1544205	−2.2856344
O	3.2092196	−0.8958643	1.4136661
C	−1.2939186	−4.3376320	−1.3397912
C	3.2060719	−3.0993061	−1.5702533
C	0.8107951	−4.0413355	−3.1090926
C	2.6670611	−1.6806316	0.7703735
C	1.8227361	−4.1735982	1.8908702
H	1.7741424	−3.6172332	2.8120672
C	−1.3225804	−1.2355783	−4.0769045
H	−0.8436273	−0.3017315	−4.3179697
C	1.2286534	−5.4699922	0.0876169
H	0.6526631	−6.0485545	−0.6128118
C	0.7208998	−4.7579263	1.2080231
H	−0.3068767	−4.7429832	1.5290477
C	−2.8046934	−2.7715190	−3.2215218
H	−3.6231097	−3.2090982	−2.6739239
C	2.6337120	−5.3203330	0.0699295
H	3.3038679	−5.7636157	−0.6488993
C	−1.9858954	−3.4394607	−4.1790542
H	−2.0823287	−4.4654574	−4.4927276
C	−1.0664612	−2.4853060	−4.6999538
H	−0.3329917	−2.6686703	−5.4679696
C	−2.3941627	−1.4160997	−3.1610780
H	−2.8370971	−0.6497901	−2.5471734
C	3.0131800	−4.5210073	1.1835351
H	4.0213312	−4.2729885	1.4708212
Bi	0.3105121	0.8969092	2.2657706
Bi	−0.7296447	1.5631098	−0.5552791
Mo	1.0729953	3.2678470	0.9577830
Mo	−1.9965504	2.5943920	1.8855904
O	−3.3733022	−0.1944160	2.1742069
O	−0.4249240	5.2843665	−0.9099928
O	0.3004350	5.0444731	3.4206033
C	−1.7985465	−4.1254085	2.2528796
C	4.2968452	2.2528909	0.1861564
H	4.5035710	2.5623207	1.1974930
C	4.5109207	3.0332743	−0.9868825
H	4.9191703	4.0295625	−1.0216645
C	4.1582785	2.2299594	−2.1098015
H	4.2401196	2.5190836	−3.1447279
C	3.7360932	0.9620569	−1.6319547
H	3.4723612	0.1142663	−2.2409861
C	3.8190375	0.9802910	−0.2135320
H	3.5843961	0.1584830	0.4420568
C	2.0416027	3.9908733	0.6144776
C	1.9356067	4.1126098	−2.1636995
C	−1.1367436	4.7139405	0.8593980
H	−0.7035330	4.5086580	1.8234443
C	−2.4316693	4.3264843	0.4218173
H	−3.1524240	3.7643558	0.9919919
C	−2.6395288	4.8799672	−0.8790461
H	−3.5406832	4.8097533	−1.4652755
C	−1.4692940	5.6090023	−1.2287349
H	−1.3186127	6.1665729	−2.1390408
C	−0.5497660	5.5110754	−0.1605469
H	0.4148192	5.9854334	−0.1215166
C	−0.8684425	3.5239184	−3.0356610
C	−2.4623391	2.0557468	−1.2790523

ENERGIES [a.u.]:

Total energy = −2812.2849635063

Total energy + OC corr. = −2812.2791215014

4.5 References

[1] H. Braunschweig, R. D. Dewhurst, S. Mozo, *ChemCatChem* **2015**, *7*, 1630-1638.

[2] C. Marquardt, T. Jurca, K.-C. Schwan, A. Stauber, A. V. Virovets, G. R. Whittell, I. Manners, M. Scheer, *Angew. Chem. Int. Ed.* **2015**, *54*, 13782-13786.

[3] a) C. Marquardt, G. Balázs, J. Baumann, A. V. Virovets, M. Scheer, *Chem. Eur. J.* **2017**, *23*, 11423-11429; b) C. Marquardt, T. Kahoun, A. Stauber, G. Balázs, M. Bodensteiner, A. Y. Timoshkin, M. Scheer, *Angew. Chem. Int. Ed.* **2016**, *55*, 14828-14832.

[4] a) M. Baudler, K. Glinka, *Chem. Rev.* **1993**, *93*, 1623-1667; b) M. Baudler, K. Glinka, *Chem. Rev.* **1994**, *94*, 1273-1297.

[5] a) C. A. Dyker, N. Burford, *Chem. Asian J.* **2008**, *3*, 28-36; b) A. P. M. Robertson, P. A. Gray, N. Burford, *Angew. Chem. Int. Ed.* **2014**, *53*, 6050-6069; c) M. Donath, F. Hennersdorf, J. J. Weigand, *Chem. Soc. Rev.* **2016**, *45*, 1145-1172.

[6] a) M. H. Holthausen, J. J. Weigand, *J. Am. Chem. Soc.* **2009**, *131*, 14210-14211; b) M. H. Holthausen, J. J. Weigand, *Dalton Trans.* **2016**, *45*, 1953-1961; c) M. Gonsior, I. Krossing, L. Müller, I. Raabe, M. Jansen, L. v. Wüllen, *Chem. Eur. J.* **2002**, *8*, 4475-4492; d) M. Donath, E. Conrad, P. Jerabek, G. Frenking, R. Fröhlich, N. Burford, J. J. Weigand, *Angew. Chem. Int. Ed.* **2012**, *51*, 2964-2967.

[7] a) T. Köchner, S. Riedel, A. J. Lehner, H. Scherer, I. Raabe, T. A. Engesser, F. W. Scholz, U. Gellrich, P. Eiden, R. A. Paz Schmidt, D. A. Plattner, I. Krossing, *Angew. Chem. Int. Ed.* **2010**, *49*, 8139-8143; b) T. Köchner, T. A. Engesser, H. Scherer, D. A. Plattner, A. Steffani, I. Krossing, *Angew. Chem. Int. Ed.* **2012**, *51*, 6529-6531.

[8] a) I. Krossing, I. Raabe, *Angew. Chem. Int. Ed.* **2004**, *43*, 2066-2090; b) T. A. Engesser, M. R. Lichtenthaler, M. Schleep, I. Krossing, *Chem. Soc. Rev.* **2016**, *45*, 789-899.

[9] a) B. M. Cossairt, N. A. Piro, C. C. Cummins, *Chem. Rev.* **2010**, *110*, 4164-4177; b) M. Caporali, L. Gonsalvi, A. Rossin, M. Peruzzini, *Chem. Rev.* **2010**, *110*, 4178-4235; c) B. P. Johnson, G. Balázs, M. Scheer, *Coord. Chem. Rev.* **2006**, *250*, 1178-1195; d) M. Scheer, *Dalton Trans.* **2008**, 4372-4386; e) O. J. Scherer, *Angew. Chem. Int. Ed.* **1990**, *29*, 1104-1122; f) O. J. Scherer, *Acc. Chem. Res.* **1999**, *32*, 751-762.

[10] a) M. Schmidt, D. Konieczny, E. V. Peresypkina, A. V. Virovets, G. Balázs, M. Bodensteiner, F. Riedlberger, H. Krauss, M. Scheer, *Angew. Chem. Int. Ed.* **2017**, *56*, 7307-7311; b) C. Schoo, S. Bestgen, M. Schmidt, S. N. Konchenko, M. Scheer, P. W. Roesky, *Chem. Commun.* **2016**, *52*, 13217-13220; c) E. Mädl, G. Balázs, E. V. Peresypkina, M. Scheer, *Angew. Chem. Int. Ed.* **2016**, *55*, 7702-7707; d) N. Arleth, M. T. Gamer, R. Köppe, S. N. Konchenko, M. Fleischmann, M. Scheer, P. W. Roesky, *Angew. Chem. Int. Ed.* **2016**, *55*, 1557-1560; e) N. Arleth, M. T. Gamer, R. Koppe, N. A. Pushkarevsky, S. N. Konchenko, M. Fleischmann, M. Bodensteiner, M. Scheer, P. W. Roesky, *Chem. Sci.* **2015**, *6*, 7179-7184; f) M. V. Butovskiy, G. Balázs, M. Bodensteiner, E. V. Peresypkina, A. V. Virovets, J. Sutter, M. Scheer, *Angew. Chem. Int. Ed.* **2013**, *52*, 2972-2976; g) T. Li, M. T. Gamer, M. Scheer, S. N. Konchenko, P. W. Roesky, *Chem. Commun.* **2013**, *49*, 2183-2185.

[11] E. Mädl, M. V. Butovskii, G. Balázs, E. V. Peresypkina, A. V. Virovets, M. Seidl, M. Scheer, *Angew. Chem. Int. Ed.* **2014**, *53*, 7643-7646.

[12] O. J. Scherer, H. Sitzmann, G. Wolmershäuser, *Angew. Chem. Int. Ed.* **1985**, *24*, 351-353.

[13] M. Fleischmann, F. Dielmann, L. J. Gregoriades, E. V. Peresypkina, A. V. Virovets, S. Huber, A. Y. Timoshkin, G. Balázs, M. Scheer, *Angew. Chem. Int. Ed.* **2015**, *54*, 13110-13115.

[14] O. J. Scherer, T. Brück, *Angew. Chem.* **1987**, *99*, 59-59.

[15] R. F. Winter, W. E. Geiger, *Organometallics* **1999**, *18*, 1827-1833.

[16] a) O. J. Scherer, H. Sitzmann, G. Wolmershäuser, *J. Organomet. Chem.* **1984**, *268*, C9-C12; b) P. J. Sullivan, A. L. Rheingold, *Organometallics* **1982**, *1*, 1547-1549; c) J. R. Harper, A. L. Rheingold, *J. Organomet. Chem.* **1990**, *390*, c36-c38; d) W. Clegg, N. A. Compton, R. J. Errington, G. A. Fisher, N. C. Norman, T. B. Marder, *J. Chem. Soc., Dalton Trans.* **1991**, 2887-2895.

[17] See the Supporting Information for details.

[18] The asymmetric unit of **2** consists of two disordered dicationic molecules. Distances and angles are only given for the less disordered molecule. The second molecule is similar in structure. Because of this disorder and especially that of the counteranions, the metrical parameters in **2** should be considered with care. See the Supporting Information for details.

[19] J. E. Davies, M. J. Mays, P. R. Raithby, G. P. Shields, P. K. Tompkin, A. D. Woods, *J. Chem. Soc., Dalton Trans.* **2000**, 1925-1930.

[20] M. Mantina, A. C. Chamberlin, R. Valero, C. J. Cramer, D. G. Truhlar, *J. Phys. Chem. A* **2009**, *113*, 5806-5812.

[21] a) L. Tuscher, C. Ganesamoorthy, D. Bläser, C. Wölper, S. Schulz, *Angew. Chem. Int. Ed.* **2015**, *54*, 10657-10661; b) L. Tuscher, C. Helling, C. Ganesamoorthy, J. Krüger, C. Wölper, W. Frank, A. S. Nizovtsev, S. Schulz, *Chem. Eur. J.* **2017**, *23*, 12297-12304.

[22] The described DFT calculations of the molecular orbital (MO) interaction diagrams were only carried out for the lightest (**1**) and the heaviest derivative (**4**). They can be considered as exemplary for **2** and **3**, respectively.

[23] N. G. Connelly, W. E. Geiger, *Chem. Rev.* **1996**, *96*, 877-910.

[24] a) F. Furche, R. Ahlrichs, C. Hättig, W. Klopper, M. Sierka, F. Weigend, *WIREs Comput. Mol. Sci.* **2014**, *4*, 91-100. b) R. Ahlrichs, M. Bär, M. Häser, H. Horn, C. Kölmel, *Chem. Phys. Lett.* **1989**, *162*, 165–169; c) O. Treutler, R. Ahlrichs, *J. Chem. Phys.* **1995**, *102*, 346–354.

[25] S. Grimme, S. Ehrlich, L. Goerigk, *J. Comput. Chem.* **2011**, *32*, 1456-1465. b) S. Grimme, J. Antony, S. Ehrlich, H. Krieg, *J. Chem. Phys.* **2010**, *132*, 154104.

[26]) P. A. M. Dirac, *Proc. Royal Soc.A*,**1929**, *123*, 714. b) J. C. Slater, *Phys. Rev.***1951**, *81*, 385. c) S. H. Vosko, L. Wilk, M. Nusair, *Can. J. Phys.***1980**, *58*, 1200. d) A. D. Becke, *Phys. Rev. A*, **1988**, *38*, 3098. e) C. Lee, W. Yang, R. G. Parr, *Phys. Rev. B*,**1988**, *37*, 785. f) A. D. Becke, *J. Chem. Phys.* **1993**, *98*, 5648.

[27] a) A. Schäfer, C. Huber, R. Ahlrichs, *J. Chem. Phys.* **1994**, *100*, 5829; b) K. Eichkorn, F. Weigend, O. Treutler, R. Ahlrichs, *Theor. Chem. Acc.* **1997**, *97*, 119. c) F. Weigend, R. Ahlrichs, *Phys. Chem. Chem. Phys.* **2005**, *7*, 3297.

d) F. Weigend, *Phys. Chem. Chem. Phys.* **2006**, *8*, 1057. e) K. Eichkorn, F. Weigend, O. Treutler, R. Ahlrichs, *Theor. Chem. Acc.* **1997**, *97*, 119.

[28] K. Eichkorn, O. Treutler, H. Öhm, M. Häser, R. Ahlrichs, *Chem. Phys. Lett.* **1995**, *242*, 652.

[29] M. Sierka, A. Hogekamp, R. Ahlrichs, *J. Chem. Phys.* **2003**, *118*, 9136.

[30] a) A. Klamt; G. Schüürmann, *J. Chem. Soc. Perkin Trans.2*, **1993**, 799–805. b) A. Klamt; V. Jonas, *J. Chem. Phys.*, **1996**, 105, 9972–9981.

[31] Gaussian 09, Revision E.01, M. J. Frisch, G. W. Trucks, H. B. Schlegel, G. E. Scuseria, M. A. Robb, J. R. Cheeseman, G. Scalmani, V. Barone, B. Mennucci, G. A. Petersson, H. Nakatsuji, M. Caricato, X. Li, H. P. Hratchian, A. F. Izmaylov, J. Bloino, G. Zheng, J. L. Sonnenberg, M. Hada, M. Ehara, K. Toyota, R. Fukuda, J. Hasegawa, M. Ishida, T. Nakajima, Y. Honda, O. Kitao, H. Nakai, T. Vreven, J. A. Montgomery, Jr., J. E. Peralta, F. Ogliaro, M. Bearpark, J. J. Heyd, E. Brothers, K. N. Kudin, V. N. Staroverov, T. Keith, R. Kobayashi, J. Normand, K. Raghavachari, A. Rendell, J. C. Burant, S. S. Iyengar, J. Tomasi, M. Cossi, N. Rega, J. M. Millam, M. Klene, J. E. Knox, J. B. Cross, V. Bakken, C. Adamo, J. Jaramillo, R. Gomperts, R. E. Stratmann, O. Yazyev, A. J. Austin, R. Cammi, C. Pomelli, J. W. Ochterski, R. L. Martin, K. Morokuma, V. G. Zakrzewski, G. A. Voth, P. Salvador, J. J. Dannenberg, S. Dapprich, A. D. Daniels, O. Farkas, J. B. Foresman, J. V. Ortiz, J. Cioslowski, and D. J. Fox, Gaussian, Inc., Wallingford CT, 2013.

[32] A) S. I. Gorelsky, AOMix: *Program for Molecular Orbital Analysis*; version 6.90, 2017, http://www.sg-chem.net; b) S. I. Gorelsky, A. B. P. Lever, *J. Organomet. Chem.* **2001**, *635*, 187-196.

[33] a) P. A. M. Dirac *Proc. Royal Soc. A*, **1929**, *123*, 714–733. b) J. C. Slater *Phys. Rev.*, **1951**, *81*, 385–390. c) S. Vosko; L. Wilk; M. Nusair, *Can. J. Phys.*, **1980**, *58*, 1200–1211. d) A. D. Becke *Phys. Rev. A*, **1988**, *38*, 3098–3100. e) J. P. Perdew. *Phys. Rev. B*, **1986**, *33*, 8822–8824.

Preface

The following chapter has already been published. The article is reprinted with permission of the Royal Society of Chemistry.

"Structural Diversity of Mixed Polypnictogen Complexes: Dicationic $E_2E'_2$ (E ≠ E' = P, As, Sb, Bi) Chains, Cycles and Cages"

Chem. Sci. **2021**, *12*, 14531-14539.

Authors

Luis Dütsch, Christoph Riesinger, Gábor Balázs, Michael Seidl and Manfred Scheer

Author Contributions

The main part (conceptualization, preparation of the compounds [Thia][TEF^{Cl}], **1**, **2**, **3a**, **3b**, **4b** and **5**, writing, visualization, and execution and evaluation of measurements) of this work was done by the first author (Luis Dütsch). Christoph Riesinger synthesized and characterized compound **4a**. He also assisted in the synthesis of **3a**/**b** and [Thia][TEF^{Cl}] in the course of his Bachelor thesis. Gábor Balázs performed the DFT calculations and contributed the respective parts in the manuscript. Michael Seidl assisted in the refinement of the X-ray structures. Manfred Scheer supervised the research and revised the manuscript prior to publication.

Acknowledgements

This work was supported by the Deutsche Forschungsgemeinschaft within the project Sche 384/36-1. Christoph Riesinger is grateful to the Studienstiftung des Deutschen Volkes for a PhD fellowship.

5 Structural Diversity of Mixed Polypnictogen Complexes: Dicationic $E_2E'_2$ (E ≠ E' = P, As, Sb, Bi) Chains, Cycles and Cages Stabilized by Transition Metals

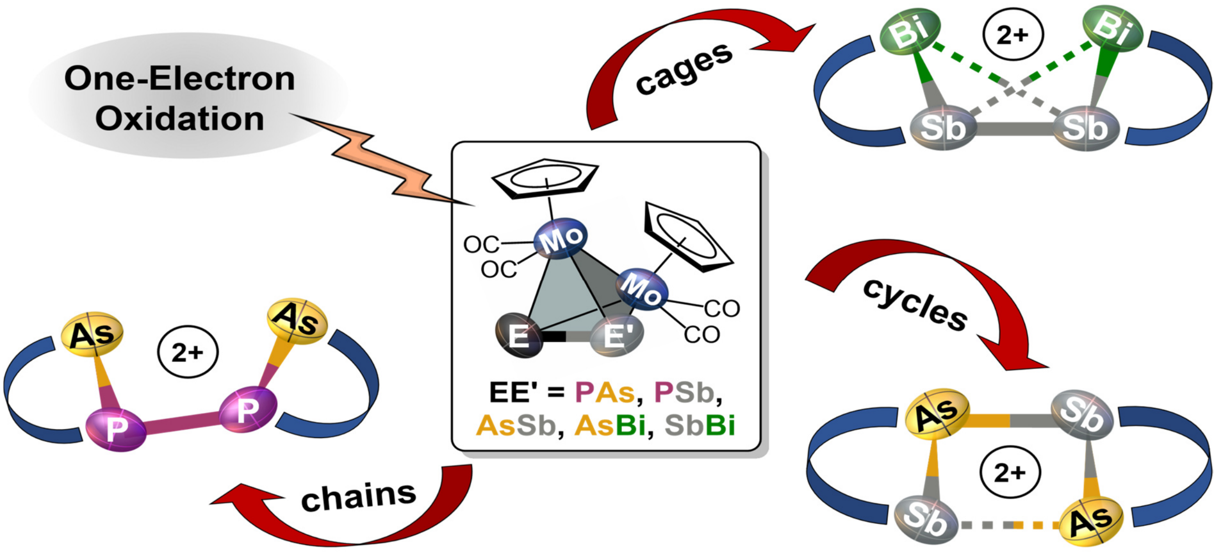

Abstract: *The reactivity of the tetrahedral dipnictogen complexes [{CpMo(CO)$_2$}$_2$(μ,η^2:η^2-EE')] (E, E' = P, As, Sb, Bi; "**Mo$_2$EE'**") towards different one-electron oxidation agents is reported. Oxidation with [Thia][TEF] (Thia$^+$ = $C_{12}H_8S_2^+$; TEF$^-$ = Al{OC(CF$_3$)$_3$}$_4^-$) leads to the selective formation of the radical monocations [**Mo$_2$EE'**]$^{\cdot+}$ which immediately dimerize to the unprecedented dicationic $E_2E'_2$ ligand complexes [{CpMo(CO)$_2$}$_4$(μ$_4$,η^2:η^2:η^2:η^2-**E'EEE'**)]$^{2+}$ via E–E bond formation. Single crystal X-ray diffraction revealed that, in case of **Mo$_2$PAs** and **Mo$_2$PSb**, P-P bond formation occurs yielding zigzag E_2P_2 (E = As (**1**), Sb(**2**)) chains, whereas **Mo$_2$SbBi** forms a Sb_2Bi_2 (**5**) cage, **Mo$_2$AsSb** an unprecedented As_2Sb_2 (**3a**) unit representing an intermediate stage between a chain- and a cage-type structure, and **Mo$_2$AsBi** a novel planar As_2Bi_2 (**4a**) cycle. Therefore, **1**–**5** bear the first substituent-free, dicationic hetero E_4 ligands, stabilized by transition metal fragments. Furthermore, in case of **Mo$_2$AsSb**, the exchange of the counterion causes changes in the molecular structure yielding an unusual, cyclic As_2Sb_2 ligand. The experimental results are corroborated by DFT calculations.*

5.1 Introduction

The element carbon features the same affinity to both electropositive and electronegative elements, which makes it unique among all elements. Furthermore, this property is the basis of its infinite structural diversity.[1] In particular, hydrocarbons form numerous chain- and cage-like as well as cyclic molecules or even combinations of these, which are important starting materials for organic syntheses and a large number of applications. For example, the isoprene molecule (2-methyl-1,3-butadiene) is the basic unit for the class of terpenes, which counts more than 8,000 different molecules, and is widely used as, *e.g.*, flavours and fragrances.[2] In contrast to carbon, the structural diversity of other p-block elements decreases strongly, which is caused by weaker covalent E–E bond energies. Thus, their chemistry is far less investigated. Since carbon and phosphorus are related to each other through the diagonal relationship and the isolobality between the {CH} fragment and the P atom (Scheme 1a),[3] phosphorus is also capable of catenation. While numerous neutral and anionic polyphosphorus chains, cages and cycles have been known for a long time,[4] the field of cationic representatives was only opened during the last two decades, mainly by the groups of *Burford* and *Weigand*.[5] However, these compounds always carry organic substituents. Recently, we could show that polyphosphorus ligand complexes represent good starting materials for cationic polyphosphorus compounds upon oxidation. For example, oxidation of the hexaphosphabenzene[6] complex $[(Cp^*Mo)_2(\mu,\eta^6:\eta^6\text{-}P_6)]$ results in a bis-allylic distortion of the P_6 ring.[7] In contrast, oxidation of

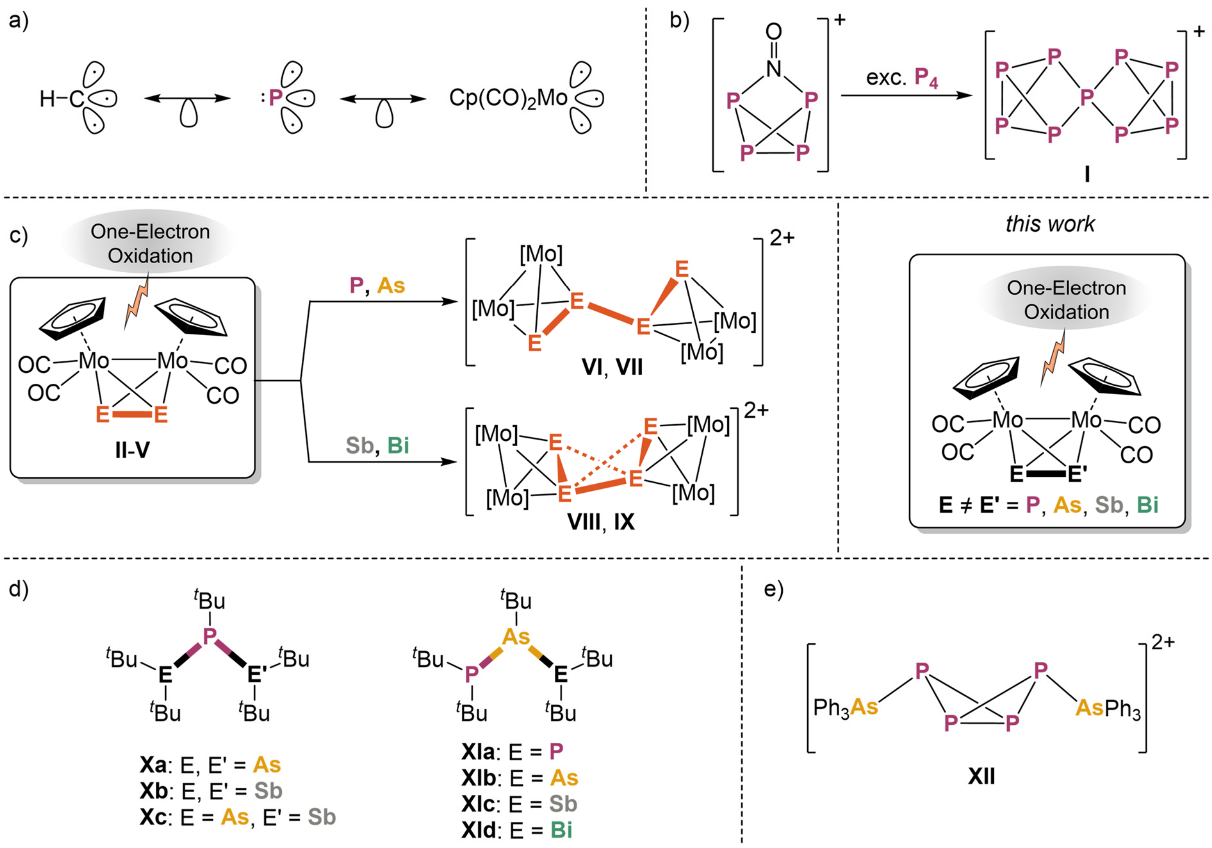

Scheme 1: a) Isolobal relation between the {CH} fragment, phosphorus and the 15 VE fragment $\{CpMo(CO)_2\}$; b) first substituent-free polyphosphorus cation P_9^+ (**I**); c) selected examples of neutral hetero-polypnictogen complexes (**X**, **XI**); d) dicationic hetero-polypnictogen compound **XII**; *this work*: one-electron oxidation of the hetero-dipnictogen complexes $[\{CpMo(CO)_2\}_2(\mu,\eta^2:\eta^2\text{-}EE')]$ (EE' = PAs (**A**), PSb (**B**), AsSb (**C**), AsBi (**D**), SbBi (**E**)).

[$Cp^*Fe(\eta^5-P_5)$] leads to dimerization *via* P-P bond formation yielding a formally neutral, bicyclic P_{10} ligand stabilized by two $[Cp^*Fe]^+$ fragments.[8] The first substituent-free polyphosphorus cation, namely $[P_9]^+$ (**I**, Scheme 1b), was obtained by *Krossing et al. via* oxidation of P_4 with $[NO]^+$.[9] This milestone in inorganic chemistry could only be accomplished with the help of weakly coordinating anions (WCAs),[10] which are able to stabilize very labile and reactive cations due to their weak nucleophilic properties. Since the tetrahedrane derivative $[\{CpMo(CO)_2\}_2(\mu,\eta^2:\eta^2-P_2)]$ (**II**; "$\mathbf{Mo_2P_2}$") is isolobal to P_4, we carried out its oxidation, which leads to dimerization *via* P–P bond formation yielding the dicationic complex $[\{CpMo(CO)_2\}_4(\mu,\eta^2:\eta^2:\eta^2:\eta^2-P_4)]^{2+}$ (**VI**) including a unique P_4 chain free from organic substituents (Scheme 1c).[11] In comparison to polyphosphorus compounds, representatives of the heavier group 15 elements such as arsenic, antimony as well as bismuth are considerably less known. Interestingly, we could transfer the reactivity of **II** towards oxidants to its heavier derivatives $[\{CpMo(CO)_2\}_2(\mu,\eta^2:\eta^2-E_2)]$ (E = As (**III**), Sb (**IV**), Bi (**V**); "$\mathbf{Mo_2E_2}$"), which yield similar dimerization products $[\{CpMo(CO)_2\}_4(\mu,\eta^2:\eta^2:\eta^2:\eta^2-E_4)]^{2+}$ (E = As (**VII**), Sb (**VIII**), Bi (**IX**)) including an analogous dicationic As_4 (**VII**) chain as well as unique dicationic Sb_4 (**VIII**) and Bi_4 (**IX**) "butterfly-like" cages, respectively, which are stabilized by transition metal fragments (Scheme 1c).[11] Even rarer is the field of hetero-polypnictogen complexes, especially the ones containing As–Sb,[12] As–Bi[13] and Sb–Bi[14] bonds, since the hetero-element bond energy decreases. Therefore, they have to be stabilized by bulky organic substituents, as for instance in the neutral hetero-tripnictogen chains $^tBu_2EP(^tBu)E'^tBu_2$ (E, E' = As, Sb; **X**)[15] and $^tBu_2PAs(^tBu)E^tBu_2$ (E = P, As, Sb, Bi; **XI**)[16] (Scheme 1d). Otherwise, they tend to disproportionate by forming homonuclear bonds.[12a] The only example of a cationic hetero-polypnictogen complex is, to the best of our knowledge, the arsane-stabilized dicationic P_4 butterfly compound $[(AsPh_3)_2(\mu,\eta^1:\eta^1-P_4)][AlCl_4]_2$ (**XII**; Scheme 1e),[17] whereas representatives of the heavier pnictogens are unknown, which might be caused by the lack of suitable precursors.

To target this, only very recently we were able to extend the class of tetrahedral $\mathbf{Mo_2E_2}$ (**II**–**V**) compounds by their respective substituent-free hetero-dipnictogen congeners $[\{CpMo(CO)_2\}_2(\mu,\eta^2:\eta^2-$**EE'**$)]$ (EE' = PAs (**A**), PSb (**B**), AsSb (**C**), AsBi (**D**), SbBi (**E**); Scheme 1). They are now accessible *via* a simple procedure in high yields, which makes further reactivity studies feasible.[18] **C**–**E** feature the very first covalent bonds between two different heavy pnictogen atoms that do not possess organic substituents. Hence, **A**–**E** should serve as excellent precursors for the formation of unprecedented extended hetero-polypnictogen frameworks upon oxidation. Thus, the question arises between which pnictogen atoms of the hetero-EE' ligand the new bonds will be formed after oxidation and whether the ionization potential of the pnictogen or the bond energy of the newly formed bond will determine the reaction outcome. Herein, we report on the reactivity of **A**–**E** towards salts of the strong one-electron oxidant thianthrenium ($[Thia]^{\cdot+} = [C_{12}H_8S_2]^{\cdot+}$) to form unprecedented hetero-pnictogen chain and cage moieties. Additionally, the influence of the stabilizing counterion on the reactivity and the solid-state structure was investigated, and a remarkable effect showed.

5.2 Results and Discussion

Cyclic voltammetry

The cyclic voltammograms (CV) of **A**–**E** (Figure 1) reveal a chemically pseudo-reversible oxidation at +0.19 V (**Mo_2PAs** = **A**), +0.08 V (**Mo_2PSb** = **B**), +0.12 V (**Mo_2AsSb** = **C**), −0.10 V (**Mo_2AsBi** = **D**) and −0.07 V (**Mo_2SbBi** = **E**) vs. $Cp_2Fe^{0/+}$ and the reductive back wave significantly shifted to −0.31 V (**A**), −0.43 V (**B**), −0.20 V (**C**), −0.36 V (**D**) and −0.44 V (**E**).[19] Compared to **Mo_2P_2** (**IV**, +0.28 V),[11] the oxidation potential of **Mo_2PAs** is considerably lower but almost equal to that of the heavier congener **Mo_2As_2** (**V**, +0.19 V).[11] The same is observed for **Mo_2PSb**, where the oxidation potential equals the one of **Mo_2Sb_2** (+0.05 V).[11] However, the oxidation potentials of **Mo_2AsSb**, **Mo_2AsBi** and **Mo_2SbBi** are in between the oxidation potentials of their respective homo-dipnictogen complexes, with the latter two being almost similar.[11] Therefore, **Mo_2PSb** steps out of line, as a higher or at least similar oxidation potential compared to **Mo_2AsSb** is expected. **Mo_2SbBi** also shows an additional small oxidation wave at +0.05 V, which can be attributed to small amounts of **Mo_2Sb_2**, which are formed as trace impurities during its synthesis.[18]

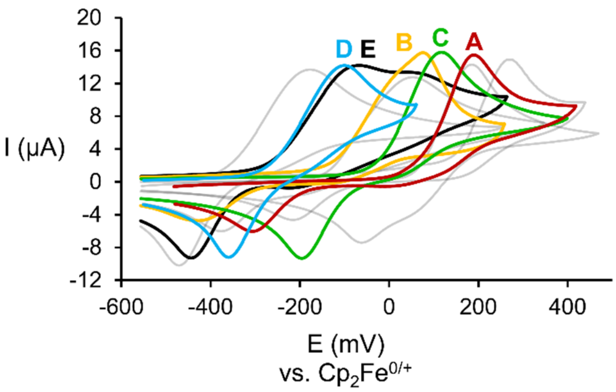

Figure 1: Cyclic voltammograms of the starting materials **A**–**E** (coloured) as well as their homo-dipnictogen congeners (grey; from right to left: **II, III, IV** and **V**) in CH_2Cl_2 solution (only the first oxidation and its respective back wave are shown); $c([NBu_4][PF_6])$ = 0.1 M.

The CVs of **A** and **B** suggest that the heavier pnictogen atom (As in **A** and Sb in **B**) contributes more to the oxidation potential than the P atom and, therefore, a dimerization *via* As–As or Sb–Sb bond formation upon one-electron oxidation should be favoured over P–P bond formation. DFT calculations also show that the heavier pnictogen atom contributes more to the HOMO and that the pnictogen atomic orbital contribution increases with increasing atomic number, *i.e.* P:E(%) = 7:7, 10:12 and 13:18 for E = As, Sb and Bi, respectively. However, this contrasts with the experimental findings, which are discussed in the following.

One-electron oxidation of A–E

When an orange red solution of **A** or **B** is reacted with the very strong one-electron oxidant $[Thia]^+$ (E = 0.86 V vs. $Cp_2Fe^{0/+}$)[20] containing the WCA $[Al\{OC(CF_3)_3\}_4]^-$ (= $[TEF]^-$) in CH_2Cl_2, immediately dark greenish red solutions of the P–P coupled products $[\{CpMo(CO)_2\}_4(\mu_4,\eta^2:\eta^2:\eta^2:\eta^2\text{-EPPE})][TEF]_2$ (E = As (**1**), Sb (**2**)), featuring a P_2E_2 chain, are obtained selectively, and **1** and **2** can be isolated in 73 % and 88 % yields (Scheme 2). DFT calculations show that the formation of the isomers containing a P–P bond are energetically favoured compared to the possible isomers with E–E bonds (42 kJ·mol^{-1} and 38 kJ·mol^{-1} for **1** and **2**, respectively). The next starting materials, the heavier analogues **Mo_2AsSb** (**C**) and **Mo_2AsBi** (**D**), represent very interesting compounds as their lighter homo-dipnictogen congener **Mo_2As_2** (**III**) builds dicationic E_4 chains upon oxidation, whereas their heavier homo-dipnictogen

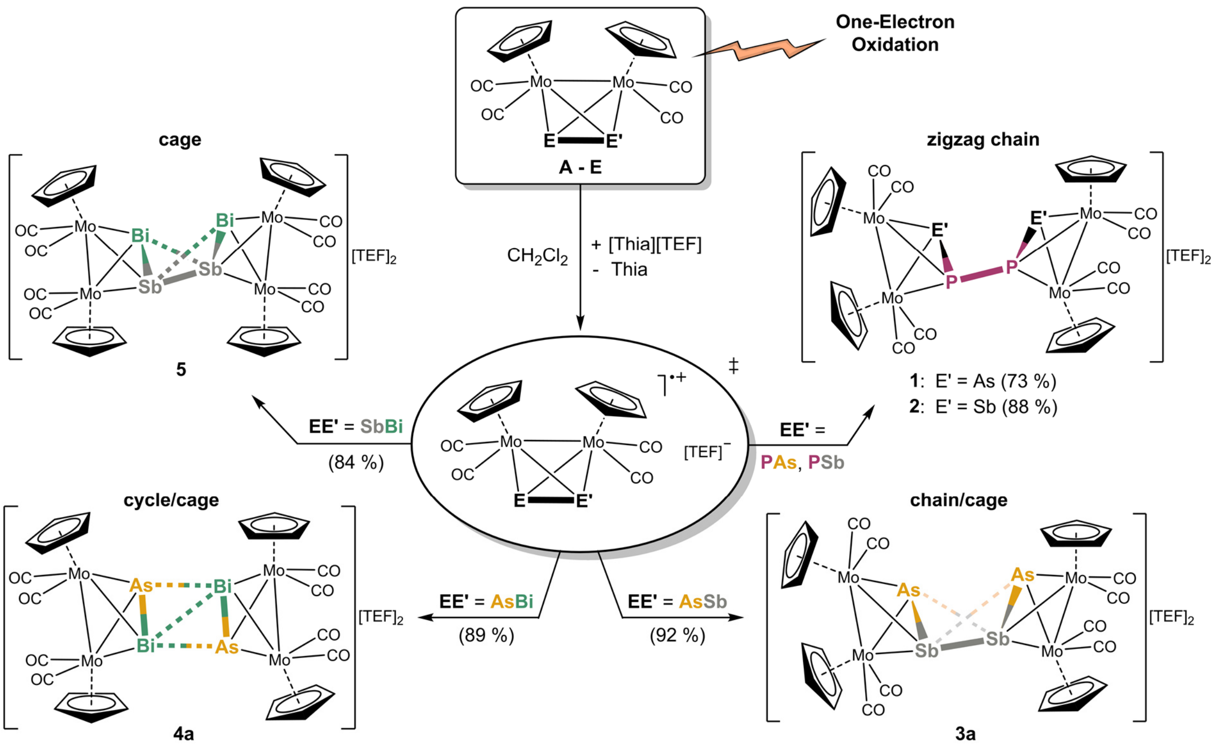

Scheme 2: Oxidation of the tetrahedral hetero-dipnictogen complexes [{CpMo(CO)$_2$}$_2$(μ,η^2:η^2-**EE'**)] (EE' = PAs (**A**), PSb (**B**), AsSb (**C**), AsBi (**D**), SbBi (**E**) resulting in dimerization reactions leading to dicationic $E_2E'_2$ chains, cages and cycles. Isolated yields are given in parentheses.

congeners **Mo$_2$Sb$_2$** (**IV**) and **Mo$_2$Bi$_2$** (**V**) form dicationic E_4 cage-like ligand complexes. Therefore, the question arose which way **C** and **D** tend to follow upon one-electron oxidation. Their CVs (Figure 1) indicate an oxidation behaviour, which is in between their homo-dipnictogen derivatives. Interestingly, the reaction of **C** and **D** with [Thia][TEF] selectively leads to the E'–E' coupled, dicationic products [{CpMo(CO)$_2$}$_4$(μ$_4$,η^2:η^2:η^2:η^2-EE'E'E)][TEF]$_2$ (EE' = AsSb (**3a**), AsBi (**4a**)) in excellent isolated yields of 92 % and 89 % (Scheme 2). **3a** represents an astonishing intermediate stage between the chain- and the cage-type structures and **4a** possess an unprecedented planarized As$_2$Bi$_2$ cyclic ligand which differs significantly from hitherto observed structures. Interestingly, in contrast to **1** and **2**, in both cases, no bonds between the lighter pnictogen atoms (As in **3a** and **4a**) are formed. However, oxidation of **E** leads to an Sb–Sb coupled cage-like compound [{CpMo(CO)$_2$}$_4$(μ$_4$,η^2:η^2:η^2:η^2-BiSbSbBi)][TEF]$_2$ (**5**) in 84 % crystalline yield (Scheme 2), which exhibits an Sb$_2$Bi$_2$ ligand with a butterfly-like structure.

In each case, the potentially first formed radical cations [**A**]$^{\cdot+}$, [**B**]$^{\cdot+}$, [**C**]$^{\cdot+}$, [**D**]$^{\cdot+}$ or [**E**]$^{\cdot+}$, respectively, immediately dimerize and do not dissociate in solution since no signals can be observed in the respective X-band EPR spectra (*vide infra*). This is also supported by DFT calculations which show that the dimerization of the radical cations [**A**]$^{\cdot+}$–[**E**]$^{\cdot+}$ is exothermic (**A**: 147 kJ·mol^{-1}, **B**: 158 kJ·mol^{-1}, **C**: 143 kJ·mol^{-1}, **D**: 144 kJ·mol^{-1} and **E**: 166 kJ·mol^{-1}).

Structural characterization of 1–5

Analytically pure crystals of **1** and **3a**–**5** suitable for single crystal X-ray diffraction are received as dark red (**1**, **3a**) or black (**4a**, **5**) blocks or plates after precipitation with *n*-hexane, washing with toluene

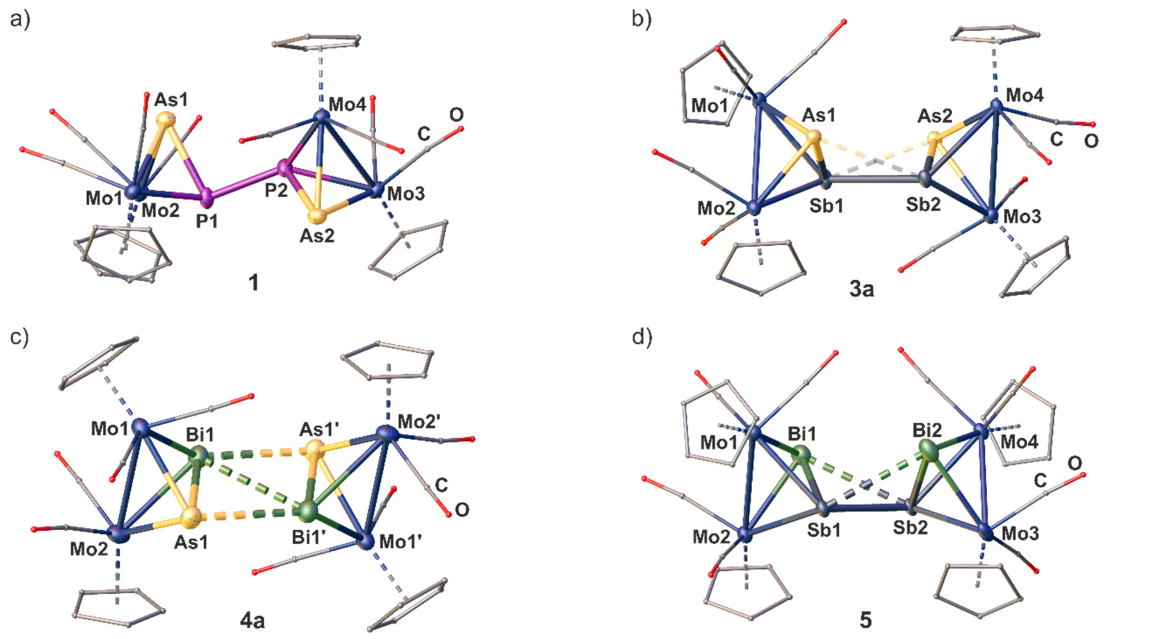

Figure 2: Molecular structure of the dicationic parts of **1** (a), **3a** (b), **4a** (c), and **5** (d). Anisotropic displacement is set to the 50% probability level. H atoms are omitted and C as well as O atoms are drawn as small spheres for clarity. Short E···E and E···E' contacts are drawn as dashed bonds and long E···E' contacts as translucent dashed bonds. Selected bond lengths [Å] and angles [°]: **1**: P1–As1 2.3099(1), P1–P2 2.2163(1), P2–As2 2.2490(1), Mo1–Mo2 3.1853(1), Mo3–Mo4 3.1559(1), As1-P1-P2 96.79(1), P1-P2-As2 103.86(1), As1-P1-P2-As2 134.77(1); **3a**: As1–Sb1 2.6874(1), Sb1–Sb2 3.0024(1), Sb2–As2 2.6795(1), As1–Sb2 3. 3.3214 (1), As2–Sb1 3. 2730(1), As1-Sb1-Sb2 71.18(1), Sb1-Sb2-As2 70.08(1), As1-Sb1-Sb2-As2 128.98(1); **4a**: As1–Bi1 2.8261(1), Bi1–Bi1' 3.2725(1), As1–Bi1' 3.2577(1), Mo1–Mo2 3.1922(1), As1-Bi1-Bi1' 64.09(1), As1-Bi1-Bi1'-As1' 180.00(1); **5**: Sb1–Bi1 2.9760(1), Sb1–Sb2 3.2237(1), Sb2–Bi2 2.9851(1), Sb1–Bi2 3.3236(1), Sb2–Bi1 3.3048(1), Mo1–Mo2 3.2172(1), Mo3–Mo4 3.2205(1), Bi1-Sb1-Sb2 64.69(1), Sb1-Sb2-Bi2 64.18(1), Bi1-Sb1-Sb2-Bi2 112.70(1).

and recrystallization from CH_2Cl_2/*n*-hexane or *o*-difluorobenzene/*n*-hexane at 4 °C. Despite several attempts, **2** could only be crystallized as thin plates which allowed to yield a weak X-ray dataset revealing just a first insight into the heavy-atom framework of the molecular structure and, therefore, no detailed structural data of **2** are discussed in the following.[21]

The cationic moieties of **1**–**5** (Figure 2a-d) each consist of two molecules of the oxidized starting materials [**A**]$^{\cdot+}$, [**B**]$^{\cdot+}$, [**C**]$^{\cdot+}$, [**D**]$^{\cdot+}$ or [**E**]$^{\cdot+}$, respectively, whose Mo_2EE' tetrahedra are linked together *via* a newly formed E–E or E'–E' bond. The received central structural motifs in **1** and **2** are an asymmetrical AsPPAs or SbPPSb zigzag chain, respectively, with a gauche conformation (dihedral angle in **1**: 134.77(1)°). Hence, they are related to their all-phosphorus and all-arsenic derivatives **VI** and **VII**.[11] The P–As distances in **1** are only slightly longer than in free **A** (2.232(1) Å),[22] but still slightly shorter than a P–As single bond (2.32 Å).[23] The newly formed central P–P bond (2.2163(1) Å) matches well with an anticipated classical single bond and with the corresponding distance in the DFT-optimized geometry (2.198 Å). The respective P-P distance in the DFT-optimized geometry of **2** is calculated to 2.201 Å.

In **3a**–**5**, hetero-tetrapnictogen ligands (AsSbSbAs (**3a**), AsBiBiAs (**4a**) and BiSbSbBi (**5**)) are observed, which, however, differ from those of the P–P and As–As coupled derivatives **1**, **2**, **VI** and **VII** and reveal cage-like structural motifs. Thereby, the intra-tetrahedral E–E' bond lengths are elongated by ~0.2 Å compared to the respective starting materials but are all just slightly longer than the respective single bonds.[23] In contrast, the newly formed E–E or E'–E' bonds, respectively, are comparably longer and exceed the respective single bonds by 0.20 Å (**3a**), 0.25 Å (**4a**) and 0.42 Å (**5**). Interestingly, **3a**, **4a** and **5** exhibit two further short E···E' contacts (As···Sb: 3.2730(1)–3.3214(1) Å; As···Bi: 3.2577(1) Å; Sb···Bi: 3.3048(1)–3.3236(1) Å).[24] In **4a** and **5**, they exceed their respective single bonds by 0.4–0.5 Å, whereas, in **3a**, they are elongated even more by 0.7 Å. But all of them are still far below the sum of their van der Waals radii (As–Sb/Bi: Σ = 3.91/3.92 Å, Sb–Bi: Σ = 4.13 Å).[25] Thus, **5** exhibits a cage-like central Sb_2Bi_2 core, which can be described as a distorted "butterfly-like" (bicyclo[1.1.0]butane) framework stabilized by four [CpMo(CO)$_2$] fragments. This is the first example of a mixed polypnictogen butterfly-type compound. So far, only similar metal-coordinated Sb_4 and Bi_4 complexes have been reported either as dicationic (**VIII** and **IX**)[11] or as neutral species.[26] In contrast, **3a** and **4a** exhibit central cage-like As_2Sb_2 and As_2Bi_2 cores, respectively, which differ from the hitherto discussed structures. The structure in **3a** reveals to be a very remarkable intermediate stage between the zigzag E_4 and $E_2E'_2$ chains in **1**, **2**, **VI** and **VII** on the one hand, and the distorted "butterfly-like" E_4 and Sb_2Bi_2 cages in **5**, **VIII** and **IX** on the other hand.[11] This based on the very long distances of the additional E···E' contacts, the arrangement of the Cp ligands (Figure 2 and SI) and the observed angles within the AsSbSbAs unit (*vide infra*). Moreover, compound **4a** represents an entirely unprecedented structure, where the dication is symmetrical and contains a completely planar, central As_2Bi_2 cage. Therefore, it can rather be described as a dicationic As_2Bi_2 cycle or as a planarized, distorted $As_2Bi_2^{2+}$ "butterfly-like" (bicyclo[1.1.0]butane) framework stabilized by four [CpMo(CO)$_2$] fragments (for natural charge distribution see SI). DFT calculations, though, suggest a "butterfly-like" geometry similar to **5**. The fact that the build-up of As–Bi and Bi–Bi interactions, respectively, is favoured over an As–As bond formation is also very remarkable.

The transition from a chain-like (**1**) to a more cage-like structural motif in **3a**–**5** is also reflected by the angles within the E'EEE' chains. While the As1-P1-P2 and P1-P2-As2 angles in **1** are close to 100°, the respective angles in **3a**–**5** decrease considerably to 64° (**4a**, **5**) and 71° (**3a**). Also, the dihedral angles ∢(E'-E-E-E') change from 135° in **1** to 113° in **5** and 180° in the planar As_2Bi_2 cycle of **4a**, while the same angle is just slightly decreased to 128° in **3a** illustrating again that it represents an intermediate stage between a chain and a cage type structure. In each of the compounds **1** and **3a**–**5**, the Mo–Mo bonds are elongated by 0.1–0.2 Å compared to their respective starting materials, while the Mo–E and Mo–E' bonds slightly decrease in length. DFT calculations for the gas phase reproduce well the experimental geometric parameters of **1** and **2** in the solid state, while, for **3**-**5**, cage-like geometries are predicted. The Mayer bond order for the central P–P bonds in **1** and **2** is 0.79 and 0.81, respectively, while the bond order of the central E–E bonds in the cage-like geometries of **3a**, **4a** and **5** lies between 0.42 and 0.52. However, they are supported by two additional E···E' interactions with bond orders between 0.21 and 0.35 (*cf.* the Supporting Information). Hence, the Mayer bond orders of the newly formed bonds and interactions for the compounds with a cage-like geometry add up to a bond order of nearly 1 (*cf.* the Supporting Information).

In general, hetero-polypnictogen chains are almost unknown. While few examples for AsPPAs[27] and SbPPSb[27a] chains and cycles have been reported, which, however, could only be stabilized by organic substituents or were only obtained as an inseparable product mixture,[28] heavier hetero-polypnictogen chains without phosphorus have, to the best of our knowledge, not been observed yet (except for a tetrabismuth-substituted diarsane $As_2(BiClR)_4$ (R = CH(SiMe$_3$)$_2$).[13] Therefore, **1** and **2** are the first E_2P_2 (E = As, Sb) ligands only stabilized by transition metal fragments, and **3a**–**5** the first $E_2E'_2$ ligands of the heavy pnictogen elements As, Sb and Bi in general. Additionally, the polypnictogen cages in **3a** and **4a** show geometries which have not been observed before for p-block elements.

DFT Computations

DFT calculations[19] show that the single occupied molecular orbital (SOMO) in the potentially first formed paramagnetic monocation [**B**]$^{\cdot+}$ is delocalized over the molybdenum atoms as well as the PSb ligand and the CO units with major contributions from Mo, P and Sb (Figure 3). The spin density is mainly localized on Mo (24 and 40%) and with smaller contributions from the pnictogen atoms (14% on P and 16% on Sb). Interestingly, although the spin density on Sb is slightly higher than on P, the dimerization of [**B**]$^{\cdot+}$ occurs *via* P–P bond formation. The spin density on the EE' unit in [**A**]$^{\cdot+}$–[**E**]$^{\cdot+}$ increases with increasing the atomic number of E or E' (*cf.* SI). Furthermore, DFT calculations consistently reproduce the experimentally observed effect of P–As and Mo–Mo bond elongations, although the absolute bond lengths are slightly overestimated.[19] Additionally, the torsion angle in the dimerization product **1** comes close to 180° during the geometry optimization. Therefore, the E_4 chains become planar. This suggests that the experimentally observed gauche arrangement, determined by single crystal X-ray diffraction of **1**, may be caused by crystal packing effects.

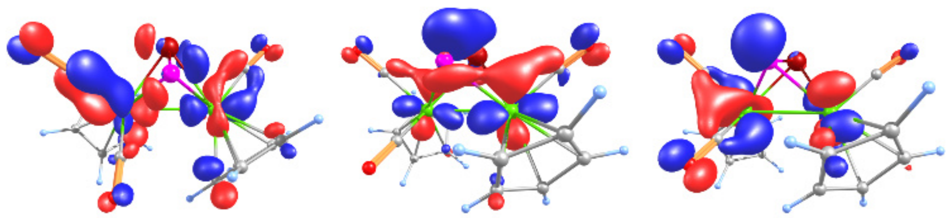

Figure 3: Frontier molecular orbitals (α spin) in [**B**]$^{\cdot+}$, calculated at the TPSSh/def2-TZVP level of theory.

Spectroscopic investigations

The ^{1}H NMR spectra of **1**–**5** in CD_2Cl_2 solution only feature one sharp singlet at δ = 5.66 ppm (**1**), 5.61 ppm (**2**), 5.68 ppm (**3a**), 5.69 ppm (**4a**) and 5.72 ppm (**5**), respectively, for the Cp ligands. In the case of **5**, also small singlets at δ = 5.64 and 5.78 ppm are detected, which can be attributed to trace impurities of **VIII** and **IX**. The latter are received by oxidation of **IV** and **V**, which are formed in the synthesis of **E**, and cannot be completely separated from each other. Likewise, one singlet is observed in the ^{13}C{^{1}H} NMR spectra for the Cp ligands indicating a highly dynamic behaviour of the Cp ligands in solution, which cannot be resolved on the NMR timescale. Characteristic signals for the [TEF]$^-$ anion and the CO ligands are observed in the ^{19}F{^{1}H} as well as the ^{13}C{^{1}H} NMR spectra.

The ^{31}P{^{1}H} NMR spectrum of **1** at room temperature shows only one relatively sharp signal at δ = –28.8 ppm ($\omega_{1/2}$ = 11 Hz), which is shifted to higher field by 60 ppm compared to the starting material **A** (δ = 30.1 ppm).[29] Upon cooling to 193 K, the signal moves farther to higher field

(δ = –39.4 ppm) and undergoes broadening ($\omega_{1/2}$ ~ 1700 Hz) suggesting that the fast dynamic processes in **1**, which render all P atoms as well as Cp and CO ligands chemically equivalent on the NMR timescale, are constrained at lower temperatures. Below 253 K, two new signals at δ = –119.7 ppm and 21.4 ppm arise in addition to the broad singlet indicating the formation of a new, unidentified species. The $^{31}P\{^1H\}$ NMR spectrum of **2** also reveals a sole singlet at δ = 35.0 ppm, which again is shifted to higher field by 60 ppm in comparison to the starting material **B** (δ = 98.8 ppm).[18] This verifies the suggestion that, analogously to **1**, a P–P coupled dicationic product is formed (Scheme 2).

Solutions of **1**, **2**, **4a** and **5** in CD_2Cl_2 or CH_2Cl_2 are all silent in the X-band EPR spectra at room temperature and at 77 K. This indicates that no dissociation of the dicationic species occurs, which is in good agreement with the calculated dissociation energies (*vide supra*). Likewise, **3a** is EPR-silent at room temperature as well, but shows a very weak axial signal (g_{iso} = 1.954) upon cooling to 77 K. This suggests that very small amounts of the radical monocation $[\mathbf{C}]^{\cdot+}$ might be present in frozen solution at very low temperatures. In contrast, no dimeric products can be observed in the ESI mass spectra of **1**–**5** suggesting that solely the monocations $[\mathbf{Mo_2EE'}]^+$ are present in the gas phase (only $[\mathbf{Mo_2PAs}]_2^{2+}$ could be observed in very concentrated solutions of **1** in a minor ratio).

$^{31}P\{^1H\}$ MAS NMR and IR spectra show that, in contrast to its lighter congener **VI**, **1** does not undergo reversible isomerisation.[11] Furthermore, at least five CO bands are observed in the IR spectra supporting the asymmetrical molecular structure (Figure 2a).

Influence of the counter ion on the solid-state structure of 3 and 4

The $[TEF]^-$ anion causes major problems during the refinement and solution of single crystal X-ray diffraction experiments (*e.g.*, in **2** or **VII**)[11] due to its high symmetry, weak coordination properties and the free rotation of the perfluorinated *tert*-butoxy groups, which can lead to a severe disorder. However, without the $[TEF]^-$ anion, the dicationic products are insoluble in all common solvents except for MeCN, $MeNO_2$ and acetone, in which fast decomposition occurs even at low temperatures,[11] or in liquid SO_2, which complicates crystallization (due to its low boiling point (−10 °C) and its toxicity)[30] or crystal mounting (due to gas evolution probably caused by embedded SO_2 molecules).

Therefore, we introduced a similar perhalogenated alkoxyaluminate anion $[Al\{OC(CCl_3)(CF_3)_2\}_4]^-$ (= $[TEF^{Cl}]^-$), where one CF_3 group on every *tert*-butoxy ligand is replaced by a CCl_3 substituent.[31] This lowers the symmetry of the anion and can lead to a decrease in disorder. Moreover, it was of interest to determine if small changes in the structure of the counterion can influence the outcome of the solid-state structure. However, the strong one-electron oxidant $[Thia]^+$ is unknown with this counterion. Hence, a route for a high-yielding synthesis of $[Thia][TEF^{Cl}]$ had to be developed. A simple one-step reaction of $Li[TEF^{Cl}]$, $NO[SbF_6]$ and thianthrene gives the deep purple $[Thia][TEF^{Cl}]$ in 89 % yield (Equation 1). The reaction is performed in liquid SO_2 to ensure that all starting materials are fully dissolved. $[Thia][TEF^{Cl}]$ is highly soluble in CH_2Cl_2 even at lower temperatures and can be crystallized

$$\mathrm{Li[TEF^{Cl}] + NO[SbF_6] + Thia \xrightarrow[\text{r.t., 24h}]{SO_2(l)} \underset{(89\ \%)}{[Thia][TEF^{Cl}]} + Li[SbF_6]\downarrow + NO\uparrow}$$

Equation 1: Synthesis of $[Thia][TEF^{Cl}]$.

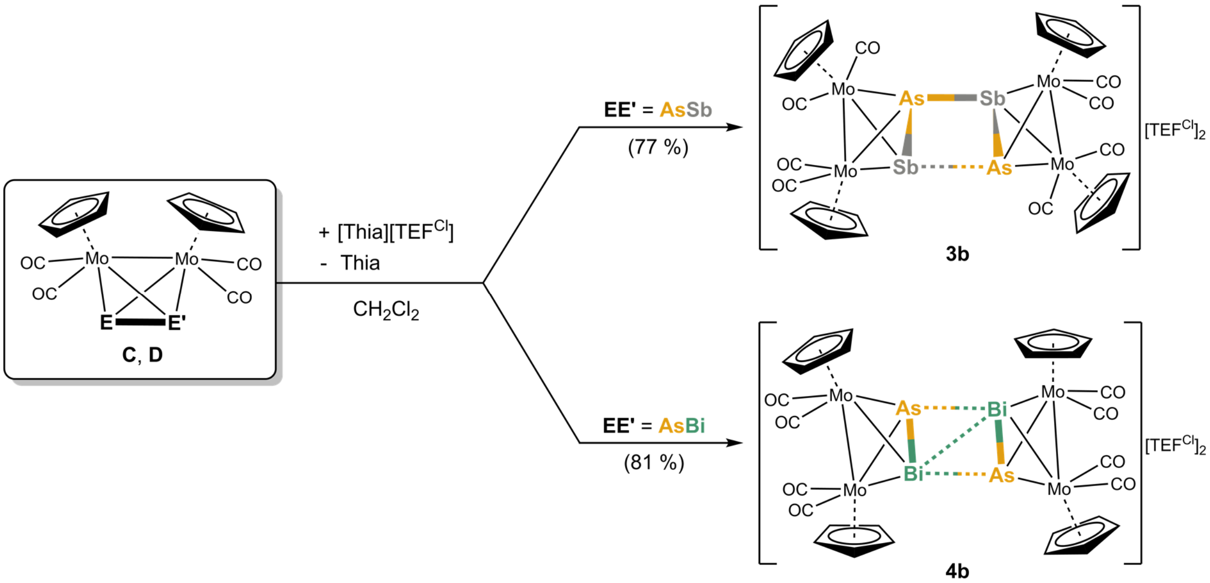

Scheme 3: Oxidation of **C** and **D** with Thia[TEF^{Cl}] resulting in dimerization reactions yielding a dicationic, cyclic As_2Sb_2 ligand (**3b**) or a planarized, distorted butterfly-like As_2Bi_2 motif (**4b**), respectively. Isolated yields are given in parentheses.

as dark purple blocks from CH_2Cl_2/*n*-hexane.[19] Furthermore, the reaction can be carried out in a multigram scale.

To gain a first insight into the influence of the counterion within the oxidation of tetrahedral dipnictogen complexes, [Thia][TEF^{Cl}] was reacted with solutions of **C**–**E**. It appears that the counter anion has no influence on the reactivity itself since again only the dimeric, dicationic E–E coupled products [{CpMo(CO)$_2$}$_4$(μ_4,η^2:η^2:η^2:η^2-$E_2E'_2$)][TEF^{Cl}]$_2$ ($E_2E'_2$ = As_2Sb_2 (**3b**), As_2Bi_2 (**4b**)) can be obtained (Scheme 3) in good crystalline yields of 77 % and 81 %, respectively. Despite several attempts, the oxidation product of **E** could not be crystallized due to the high solubility of the [TEF^{Cl}]$^-$ anion leading to oily products. However, the exchange of the counterion surprisingly has a dramatic impact on the molecular structure of **3b**, which differs significantly from its [TEF]$^-$ derivative **3a** (**4b** only shows slight deviations to **4a**).

The dication in **3b** builds up a completely unprecedented structural motif (Figure 4a). It contains a central, cyclic As_2Sb_2 ligand. It is very remarkable that the arsenic and antimony atoms within the cycle are bound in an alternating fashion.[19] The intratetrahedral As–Sb bonds are elongated compared to free **C** by 0.1 to 0.2 Å,[18] but are still in the range of a single bond. The Mo–Mo bonds are widened up in the same manner. The Mo_2AsSb tetrahedra are tilted against each other by approximately 13° leading to a dihedral angle of the As_2Sb_2 ring of 155.39(1)°. Furthermore, they are interconnected *via* two newly formed As–Sb bonds (As2–Sb1: 2.9108(1) Å; As1–Sb2: 3.0270(1) Å), with one of them being 0.11 Å longer than the other one, but even the shorter bond exceeds the sum of the covalent radii (Σ(As–Sb) = 2.62 Å)[23] by 0.29 Å. Additionally, the As_2Sb_2 cycle reveals a very long diagonal As1–As2 (4.3525(1) Å) distance which exceeds the sum of the van-der-Waals radii[25] by far excluding any further interactions. But more interestingly, it also exhibits a relatively short Sb1···Sb2 contact (3.4492(1) Å), which is 0.7 Å below the sum of the van-der-Waals radii (Sb–Sb: Σ = 4.12 Å).[25] This leads to a slight distortion within the cycle with angles between 73.09(1)° and 100.37(1)°, with the smaller angles being

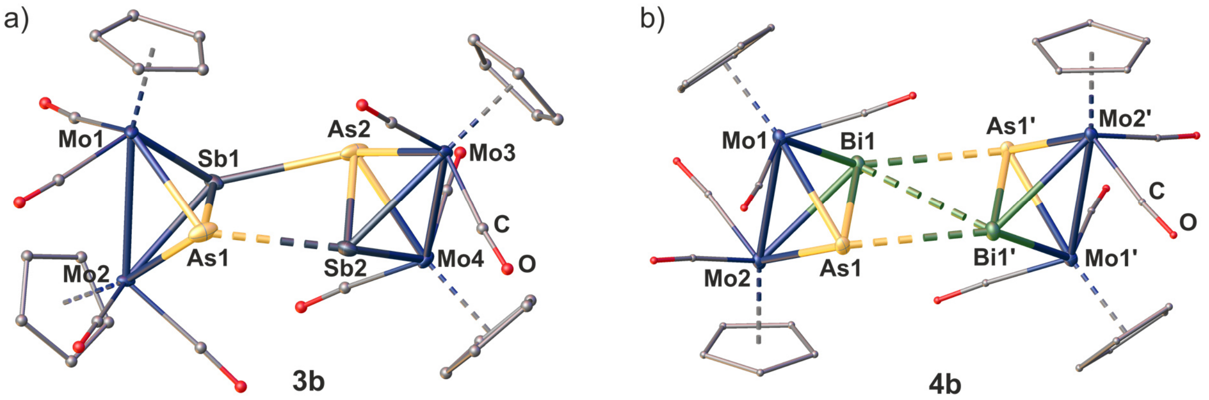

Figure 4: Molecular structure of the dicationic parts of **3b** (a) and **4b** (b). Anisotropic displacement is set to the 50% probability level. H atoms are omitted and C as well as O atoms are drawn as small spheres for clarity. Selected bond lengths [Å] and angles: **3b**: As1–Sb1 2.7540(1), Sb1–As2 2.9108(1), As2–Sb2 2.6504(1), Sb2–As1 3.0270(1), Sb1–Sb2 3.4492(1), As1-Sb1-Sb2-As2 154.39(1); **4b**: As1–Bi1 2.8377(1), Bi1–Bi1' 3.4273(1), As1–Bi1' 3.2184(1), Mo1–Mo2 3.1763(1), As1-Bi1-Bi1' 60.96(1), As1-Bi1-Bi1'-As1' 180.0(1).

at the arsenic atoms. Therefore, **3b** can be regarded as an intermediate stage between the As_2Sb_2 cage in **3a** and the As_2Bi_2 cycles in **4a** and **4b**, respectively. Overall, while cyclic As_4 units are known as the heavier dianionic *cyclo*-butadiene analogues,[32] the As_2Sb_2 cycle in **3b** is the first example of its kind.

Geometry optimizations (TPSSh/def2-TZVP level) starting from the experimental geometries of **3a** as well as **3b** lead in both cases to a "cage-like" geometry similar to **5**, indicating that the anion has a strong influence on the formed geometry in the solid state. In comparison to **3b**, the $[TEF^{Cl}]^-$ counterion has no big influence on the molecular structure of **4**. The cation in **4b** (Figure 4b) is similar to its $[TEF]^-$ congener **4a** regarding all bond lengths and angles except for the Bi–Bi bond, which is elongated by 0.15 Å in **4b** compared to **4a**.

To investigate the influence of the counter ion towards a possible dissociation of the dications in solution, X-band EPR spectra of **4b** were recorded which were silent both at room temperature and in frozen solution at 77 K. This indicates that no radical monocations $[\mathbf{D}]^{\cdot+}$ are present in solution just as in the case of **4a**.

5.3 Conclusion

In summary, we have studied the one-electron oxidation chemistry of the tetrahedral hetero-dipnictogen complexes **A**–**E**. We successfully discovered the structural diversity of the rare class of hetero-polypnictogen compounds. The unique EE' ligand complexes are readily oxidized by the organic radical cation $[Thia]^{\cdot+}$. The initially formed radical monocations $[\mathbf{A}]^{\cdot+}$, $[\mathbf{B}]^{\cdot+}$, $[\mathbf{C}]^{\cdot+}$, $[\mathbf{D}]^{\cdot+}$ and $[\mathbf{E}]^{\cdot+}$, respectively, dimerize immediately in solution *via* E–E bond formation giving the novel dicationic products $[\{CpMo(CO)_2\}_4(\mu_4,\eta^2:\eta^2:\eta^2:\eta^2\text{-E'EEE'})][TEF]_2$ (EE' = PAs (**1**), PSb (**2**), SbAs (**3a**), BiAs (**4a**), SbBi (**5**)), which reveal unprecedented four-membered hetero-pnictogen chains, free from organic substituents and are stabilized in the coordination sphere of transition metals. Remarkably, in **1**, **2** and **5**, the new bonds are formed between the respective lighter pnictogen atoms, whereas the aggregation in **3a** and **4a** takes place *via* the heavier pnictogen atoms. The products **1** and **2** bear unique, unsubstituted P_2E_2 chains in gauche conformation, while **5** exhibits a distorted “butterfly-like” (bicyclo[1.1.0]butane) Sb_2Bi_2 cage with two additional short Sb···Bi contacts. However, **3a** represents a novel and very remarkable intermediate stage between those two structural motifs, in which the additional As···Sb contacts are considerably longer and also the bond angles and the arrangement of the Cp substituents differ. **4a** even shows an entirely unprecedented structure exhibiting a planar As_2Bi_2 cycle, which can be interpreted as a planarized "butterfly-like" core. Moreover, **1** and **2** contain the first unsubstituted E_2P_2 (E = As, Sb) ligands that are only stabilized in the coordination sphere of transition metal fragments, and **3a**–**5** exhibit the first $E_2E'_2$ ligands of the heavy pnictogen elements As, Sb and Bi in general. The exchange of the counterion (using $[TEF^{Cl}]^-$) has no effect on the molecular structure of **4**. However, in **3b**, the $[TEF^{Cl}]^-$ anion causes cyclization of the As_2Sb_2 ligand yielding a unique, cyclic As_2Sb_2 ligand in which the As and Sb atoms are bound in an alternating fashion. The influence of the counterion on the molecular structure of dicationic E_4 and $E_2E'_2$ compounds will be a topic of future research. Overall, it could be proved that the oxidation of hetero-polypnictogen ligand complexes is a useful synthetic tool to gain access to the class of unsubstituted, cationic hetero-polypnictogen frameworks stabilized in the coordination sphere of transition metals, which are not obtained by other ways.

5.4 Supporting Information

5.4.1 General remarks

All manipulations were carried out under an inert atmosphere of dried nitrogen/argon using standard Schlenk and glovebox techniques. The used Schlenk flasks were heated at 550 °C for at least 15-30 minutes under reduced pressure prior to use to get rid of water traces adhered to the glass surface. The starting materials Li[TEF^{Cl}],[33] [Thia][TEF],[34] and [{CpMo(CO)$_2$}$_2$(μ,η^2:η^2-EE')] (EE' = PAs (**A**), PSb (**B**), AsSb (**C**), AsBi (**D**), SbBi(**E**))[35] were synthesized *via* the respective literature procedures. The reagents thianthrene and [NO][SbF_6] are commercially available and were used without further purification. Solvents were freshly distilled under nitrogen after drying over CaH_2 (CH_2Cl_2, CD_2Cl_2), K or Na/K alloy (alkanes), P_4O_{10} (*ortho*-difluorobenzene = *o*-DFB) or NaH (toluene). Dried solvents were also taken from a solvent purification system from MBraun. For reactions in liquid SO_2, SO_2 gas cylinders were bought from Linde and SO_2 was condensed into Schlenk flasks with a Young valve at −196 °C under reduced pressure. Diatomaceous earth used for filtrations was stored at 130 °C for at least 24 h prior to use. NMR spectra were recorded at 300 K (if not stated otherwise) on a Bruker Avance 300 MHz NMR spectrometer (^{1}H: 300.132 MHz, ^{31}P: 121.495 MHz, ^{13}C: 75.468 MHz, ^{19}F: 282.404 MHz) or a Bruker Avance 400 MHz NMR spectrometer (^{1}H: 400.130 MHz, ^{31}P: 161.976 MHz, ^{13}C: 100.613 MHz, ^{19}F: 376.498 MHz) with external references of $SiMe_4$ (^{1}H, ^{13}C), CCl_3F (^{19}F) and H_3PO_4 (85%, ^{31}P). The chemical shifts δ are presented in parts per million (ppm) and coupling constants J in Hz. X-Band EPR spectra were recorded on a MiniScope MS400 device from Magnettech GmbH with a frequency of 9.5 GHz equipped with a rectangular resonator TE102. Cyclic voltammetry (CV) measurements were performed in CH_2Cl_2 solution containing [NBu_4][PF_6] (c = 0.1 mol·L^{-1}) as supporting electrolyte. Ferrocene (Cp_2Fe) was added to the samples after the complete measurements and Cp_2Fe was used as an internal reference (E($Cp_2Fe^{0/+}$) = 0 V). ESI-MS spectra were either measured on a Finnigan Thermoquest TSQ 7000 mass-spectrometer by the MS department of the University of Regensburg or on a Waters Micromass LCT ESI-TOF mass-spectrometer by the first author. IR spectra were recorded either as solids using a ThermoFisher Nicolet iS5 FT-IR spectrometer with an iD7 ATR module and an ITX Germanium or ITX Diamond crystal, or grinded together with dried KBr and pressed to pellets and measured on a VARIAN FTS-800 FT-IR spectrometer. Elemental analyses (EA) were performed by the micro analytical laboratory of the University of Regensburg.

5.4.2 Experimental details

Synthesis of [Thia]$^{\cdot+}$ with [TEF^{Cl}]$^-$ as counterion

In order to vary the weakly coordinating anion (= WCA) of the desired products and to investigate their influence on the solid-state structures, the used strong one-electron oxidant thianthrenium [$C_{12}H_8S_2$]$^{\cdot+}$ (= [Thia]$^+$, E^0 = 0.86 V vs $Cp_2Fe^{0/+}$)[36] was synthesized with the WCA [Al{OC(CF_3)$_2$(CCl_3)}$_4$]$^-$ (=[TEF^{Cl}]$^-$). A simple one-step synthesis starting from commercially available reagents afford the deep

$$\mathrm{Li[TEF^{Cl}] + NO[SbF_6] + Thia \xrightarrow[\text{r.t., 24h}]{SO_2(l)} \underset{(89\ \%)}{[Thia][TEF^{Cl}]} + Li[SbF_6]\downarrow + NO\uparrow}$$

Equation S1: Synthesis of [Thia][TEF^{Cl}].

purple salt [Thia][TEF^{Cl}] in excellent yields and in a multigram scale (Equation S1). The reaction is performed in liquid SO_2 to ensure the solubility of all components.

A Schlenk flask equipped with a Young valve was loaded with a stirring bar, thianthrene (1.00 g, 4.62 mmol, 1.0 eq.), NO[SbF_6] (1.22 g, 4.59 mmol, 1 eq.) and Li[TEF^{Cl}] (5.44 g, 4.65 mmol, 1.0 eq.). 60 mL SO_2 were condensed onto these solids under reduced pressure at –196 °C. The flask was closed under reduced pressure and the cooling was removed. Upon dissolution the reaction turns from light blue to dark blue and finally to dark violet. After stirring at room temperature for 24 h the SO_2 was removed. The residue was dissolved/suspended in 30 mL CH_2Cl_2 and transferred onto a frit with diatomaceous earth. The dark purple solution was filtered, and the residue washed with CH_2Cl_2 till the filtrate is colourless. The amount of solvent was reduced to 15 mL and addition of 200 mL *n*-hexane leads to precipitation of dark purple [Thia][TEF^{Cl}], which was washed twice with 60 mL of a 1:1 mixture of *n*-hexane/toluene. Recrystallization *via* layering a CH_2Cl_2 solution with *n*-hexane (1:6) affords dark purple crystals. These were washed again with 50 mL toluene and dried in vacuum for 3 hours.Yield 5.61 g (4.06 mmol = 89 %). ^{1}H NMR (400 MHz, CD_2Cl_2) no signals detectable for $[Thia]^{\cdot+}$. ^{19}F{^{1}H} NMR (282.4 MHz, CD_2Cl_2) δ/ppm = –67.4 (s). Anal. calcd. for [Thia][TEF^{Cl}]: C: 24.35, H: 0.58, S: 4.64. Found: C: 24.61, H: 0.68, S: 4.72. Positive ion ESI-MS *m/z* (%): 215.97 (100) $[Thia]^{+}$. Negative ion ESI-MS *m/z* (%): 1162.59 (100) $[TEF^{Cl}]^{-}$.

5.4.2.1 Oxidation of A–E with [Thia][TEF]

Preparation of [{CpMo(CO)$_2$}$_4$(μ_4,η^2:η^2:η^2:η^2-AsPPAs)][TEF]$_2$ (1)

A dark purple solution of [Thia][TEF] (203 mg, 0.17 mmol, 1.0 eq.) in 15 mL CH_2Cl_2 was transferred to an orange red solution of [{CpMo(CO)$_2$}$_2$(μ,η^2:η^2-PAs)] (**A**) (98 mg, 0.18 mmol, 1.05 eq.) in 10 mL CH_2Cl_2 at room temperature causing an immediate colour change to a dark greenish red solution. After stirring for 120 minutes, addition of 60 mL *n*-hexane led to precipitation of a dark green powder of crude **1**. The slightly orange supernatant solution was removed and the precipitate washed twice with 20 mL of pure toluene. The crude product was dried in vacuum. Recrystallization *via* layering a CH_2Cl_2 solution with *n*-hexane (1:5) and storage at +4 °C afforded pure **1** as dark red blocks, which were suitable for single crystal X-ray diffraction. The supernatant was removed and the crystals were dried in vacuum.

Yield 189 mg (0.062 mmol = 73 %). ^{1}H NMR (300 MHz, CD_2Cl_2) δ/ppm = 5.66 (s, Cp). ^{31}P{^{1}H} NMR (121.5 MHz, CD_2Cl_2) δ/ppm = −28.8 (s). ^{31}P NMR (121.5 MHz, CD_2Cl_2) δ/ppm = −29.1 (s); for ^{31}P{^{1}H} VT-NMR see NMR section below. ^{13}C{^{1}H} NMR (75.5 MHz, CD_2Cl_2) δ/ppm = 219.2 (small, br, CO), 121.65 (q, $^{1}J_{CF}$ = 293 Hz; CF_3), 90.98 (s, Cp). ^{19}F{^{1}H} NMR (282.4 MHz, CD_2Cl_2) δ/ppm = −75.5 (s, CF_3). Compound **1** is silent in the X-band EPR spectra in the solid-state and in CH_2Cl_2 solution at room temperature and at 77 K. Anal. calcd. for $[(C_{14}H_{10}O_4Mo_2PAs)_2][TEF]_2$: C: 23.91, H: 0.67. Found: (crystalline product **1**): C: 24.26; H: 0.82. Positive ion ESI-MS *m/z* (%): 539.63 (15) $[\mathbf{A}]^+$, 511.71 (3) $[\mathbf{A}–1·CO]^+$, 483.68 (37) $[\mathbf{A}–2·CO]^+$, 455.68 (100) $[\mathbf{A}–3·CO]^+$, 427.69 (70) $[\mathbf{A}–4·CO]^+$; in very concentrated solutions: 511,71 (5) $[\mathbf{A}\text{-}1·CO]_2^{2+}$. Negative ion ESI-MS *m/z* (%): 966.9 (100) $[TEF]^–$. **1** (crystalline): IR(KBr) $\tilde{\nu}/cm^{-1}$ = 3136 (w), 2344 (vw), 2062(s), 2050 (s), 2032 (vs), 1991 (s), 1955 (m), 1624 (vw), 1426 (w), 1354 (s), 1302 (vs), 1277 (vs), 1243 (vs), 1219 (vs), 1172 (m), 973 (vs), 841 (m), 727 (s). **1** (precipitate): IR(KBr) $\tilde{\nu}/cm^{-1}$ = 3133 (w), 2960 (vw), 2925 (w), 2854 (vw), 2360 (w), 2343 (w), 2062 (s), 2051 (vs), 2037 (vs), 2023 (vs), 1995 (s, br), 1955 (m, br), 1627 (w), 1426 (w), 1384 (w), 1353 (m), 1302 (vs), 1277 (vs), 1244 (vs), 1220 (vs), 1173 (m), 974 (vs), 841 (m), 728 (s).

Preparation of $[\{CpMo(CO)_2\}_4(\mu_4,\eta^2:\eta^2:\eta^2:\eta^2\text{-SbPPSb})][TEF]_2$ (2)

A dark purple solution of [Thia][TEF] (121 mg, 0.10 mmol, 1.0 eq.) in 7 mL CH_2Cl_2 was transferred to an orange red solution of $[\{CpMo(CO)_2\}_2(\mu,\eta^2:\eta^2\text{-PSb})]$ (**B**) (60 mg, 0.10 mmol, 1.0 eq.) in 3 mL CH_2Cl_2 at room temperature causing an immediate colour change to a dark orange brown solution. After stirring for 30 minutes, addition of 40 mL *n*-hexane led to precipitation of a brown, fluffy powder of crude **2**. The slightly orange supernatant solution was removed and the precipitate washed twice with 20 mL of pure toluene leading to an oily solid. The crude product was dried in vacuum, redissolved in 5 mL CH_2Cl_2 and precipitated with 30 mL *n*-hexane yielding again a fluffy, brown powder. Recrystallization *via* layering a CH_2Cl_2 solution with *n*-hexane (1:5) and storage at +4 °C afforded pure **2** as thin orange red plates, which were not suitable for good single crystal X-ray diffraction (several attempts to get suitable crystals by changing the solvents, crystallization methods or crystallization temperatures were unsuccessful). The supernatant was removed and the crystals were dried in vacuum.

Yield 137 mg (0.044 mmol = 88 %). ^1H NMR (400 MHz, CD_2Cl_2) δ/ppm = 5.61 (s, Cp). $^{31}P\{^1H\}$ NMR (162.0 MHz, CD_2Cl_2) δ/ppm = 34.7 (s). ^{31}P NMR (162.0 MHz, CD_2Cl_2) δ/ppm = 34.6 (s). $^{19}F\{^1H\}$ NMR (376.6 MHz, CD_2Cl_2) δ/ppm = −75.5 (s). $^{31}P\{^1H\}$ NMR of crude solution of **2** (162.0 MHz, CH_2Cl_2/C_6D_6) δ/ppm = 35.0 (s). ^{31}P NMR of crude solution of **2** (162.0 MHz, CH_2Cl_2/C_6D_6) δ/ppm = 35.0 (s); for $^{31}P\{^1H\}$ VT-NMR see NMR section below. Compound **2** is silent in the X-band EPR spectra in CH_2Cl_2 solution at room temperature and at 77 K. Anal. calcd. for $[(C_{14}H_{10}O_4Mo_2PSb)_2][TEF]_2·(toluene)_{0.7}$: C: 24.57, H: 0.81. Found: C: 24.55, H: 0.60. Mass spectrometric investigations were unsuccessful due to decomposition of **2** during the measurement.

Preparation of $[\{CpMo(CO)_2\}_4(\mu_4,\eta^2:\eta^2:\eta^2:\eta^2\text{-AsSbSbAs})][TEF]_2$ (3a)

A dark purple solution of [Thia][TEF] (56 mg, 0.048 mmol, 1.0 eq.) in 7 mL CH_2Cl_2 was transferred to a red solution of $[\{CpMo(CO)_2\}_2(\mu,\eta^2:\eta^2\text{-AsSb})]$ (**C**) (41 mg, 0.048 mmol, 1.0 eq.) in 5 mL CH_2Cl_2 at room temperature causing an immediate colour change to a dark greenish brown solution. After stirring for 15 minutes, addition of 50 mL *n*-hexane led to precipitation of a green to black powder. The slightly orange supernatant solution was removed and the precipitate washed twice with 30 mL of pure toluene. Recrystallization *via* layering a CH_2Cl_2 solution with *n*-hexane (1:5) and storage at +4 °C

afforded pure **3a** as dark red to black blocks, which were suitable for single crystal X-ray diffraction. The supernatant was removed and the crystals were dried in vacuum.
Yield 70 mg (0.022 mmol = 92 %). ^{1}H NMR (400 MHz, CD_2Cl_2) δ/ppm = 5.68 (s, Cp). ^{19}F{^{1}H} NMR (376.5 MHz, CD_2Cl_2) δ/ppm = −75.5 (s, CF_3). Compound **3a** is silent in the X-band EPR spectra in CH_2Cl_2 solution at room temperature, but shows a very weak axial signal (g_{iso} = 1.954) at 77 K. Anal. calcd. for [($C_{14}H_{10}O_4Mo_2AsSb)_2$][TEF]$_2$: C: 22.55, H: 0.63. Found: C: 22.94, H: 0.72. Positive ion ESI-MS *m/z* (%): 629.63 (80) [**C**]$^+$, 601.67 (3) [**C**–CO]$^+$, 573.68 (20) [**C**–2·CO]$^+$, 545.67 (100) [**C**–3·CO]$^+$, 517.68 (50) [**C**–4 CO]$^+$. IR (ATR) $\tilde{\nu}$/cm^{-1} = 2055 (w), 2048 (w), 2038 (w), 1999 (m), 1988 (m), 1961 (w), 1934 (vw), 1352 (w), 1297 (m), 1274 (s), 1240 (s), 1213 (vs), 1173 (w), 971 (vs), 841 (w), 727 (s); C-H around 3000 not observed (too small).

Preparation of [{CpMo(CO)$_2$}$_4$(μ_4,η^2:η^2:η^2:η^2-AsBiBiAs)][TEF]$_2$ (4a)

A dark purple solution of [Thia][TEF] (118 mg, 0.10 mmol, 1.0 eq.) in 5 mL CH_2Cl_2 was transferred to a dark red solution of [{CpMo(CO)$_2$}$_2$(μ,η^2:η^2-AsBi)] (**D**) (72 mg, 0.10 mmol, 1.0 eq.) in 3 mL CH_2Cl_2 at room temperature causing an immediate colour change to a dark brown solution. After stirring for 30 minutes, addition of 40 mL *n*-pentane led to precipitation of a brown to black powder. The slightly orange supernatant solution was removed and the precipitate washed twice with 20 mL of pure toluene and twice with 20 mL *n*-pentane. The crude product was dried in vacuum and recrystallization *via* layering a CH_2Cl_2 solution with *n*-hexane (1:5) and storage at room temperature under exclusion of light afforded pure **4a** as black blocks, which were suitable for single crystal X-ray diffraction. The supernatant was removed and the crystals were dried in vacuum.
Yield 150 mg (0.0445 mmol = 89 %). ^{1}H NMR (400 MHz, CD_2Cl_2) δ/ppm = 5.69 (s, Cp). ^{13}C{^{1}H} NMR (100.6 MHz, CD_2Cl_2) δ/ppm = 89.80 (s, Cp), 121.25 (q, $^1J_{CF}$ = 291 Hz; CF_3), 214.33 (s, CO), 215.65 (s, CO). ^{19}F{^{1}H} NMR (376.6 MHz, CD_2Cl_2) δ/ppm = −75.5 (s, CF_3). Compound **4a** is silent in the X-band EPR spectra in CH_2Cl_2 solution at room temperature and at 77 K. Anal. calcd. for [($C_{14}H_{10}O_4Mo_2AsBi)_2$][TEF]$_2$: C: 21.38, H: 0.60. Found: C: 21.82, H: 0.56. Positive ion ESI-MS *m/z* (%): 717.77 (100) [**D**]$^+$, 734.77 (15) [**D**+O]$^+$. Negative ion ESI-MS *m/z* (%): 966.91 (100) [TEF]$^-$.

Preparation of [{CpMo(CO)$_2$}$_4$(μ_4,η^2:η^2:η^2:η^2-BiSbSbBi)][TEF]$_2$ (5)

A dark purple solution of [Thia][TEF] (59 mg, 0.05 mmol, 1.0 eq.) in 10 mL *o*-DFB was transferred to a dark bordeaux red solution of [{CpMo(CO)$_2$}$_2$(μ,η^2:η^2-SbBi)] (**E**) (38 mg, 0.05 mmol, 1.0 eq.) in a mixture of 10 mL *o*-DFB and 1 mL CH_2Cl_2 at −20 °C causing an immediate colour change to a dark brown to black solution. After stirring for 60 minutes at −20 °C, addition of 80 mL *n*-hexane led to precipitation of a dark green to black powder. The slightly red supernatant solution was removed and the precipitate washed twice with 20 mL of pure toluene. The crude product was dried in vacuum and recrystallization *via* layering an *o*-DFB solution with *n*-hexane (1:4) and storage at +4 °C afforded pure **5** as black blocks, which were suitable for single crystal X-ray diffraction. The supernatant was removed and the crystals were dried in vacuum.
Yield 73 mg (0.021 mmol = 84 %). ^{1}H NMR (400 MHz, CD_2Cl_2) δ/ppm = 5.64 (s, Cp, traces of **XI**), 5.72 (s, Cp of **5**), 5.78 (s, Cp, traces of **XII**). ^{19}F{^{1}H} NMR (376.6 MHz, CD_2Cl_2) δ/ppm = −75.5 (s, CF_3). Compound **5** is silent in the X-band EPR spectra in CH_2Cl_2 solution at room temperature and at 77 K. Anal. calcd.

for $[(C_{14}H_{10}O_4Mo_2SbBi)_2][TEF]_2$: C: 20.80, H: 0.58. Found: C: 21.38, H: 0.45. Mass spectrometric investigations were unsuccessful due to decomposition of **5** during the measurement.

5.4.2.2 Oxidation of C and D with [Thia][TEF^{Cl}]

Preparation of [{CpMo(CO)$_2$}$_4$(μ$_4$,η^2:η^2:η^2:η^2-AsSbAsSb)][TEF^{Cl}]$_2$ (3b)

A dark purple solution of [Thia][TEF^{Cl}] (89 mg, 0.065 mmol, 1.0 eq.) in 5 mL CH_2Cl_2 was transferred to a red solution of [{CpMo(CO)$_2$}$_2$(μ,η^2:η^2-AsSb)] (**C**) (41 mg, 0.065 mmol, 1.0 eq.) in 5 mL CH_2Cl_2 at room temperature causing an immediate colour change to a dark brown solution. After stirring for 15 minutes, addition of 40 mL toluene led to precipitation of a dark greenish brown powder. The slightly brown supernatant solution was removed and the precipitate dried in vacuum. Recrystallization *via* layering a CH_2Cl_2 solution with *n*-hexane (1:5) and storage at +4 °C afforded pure **3b** as dark red blocks, which were suitable for single crystal X-ray diffraction. The supernatant was removed and the crystals were dried in vacuum.

Yield 89 mg (0.025 mmol = 77 %). ^{1}H NMR (400 MHz, CD_2Cl_2) δ/ppm = 5.70 (s, Cp). ^{19}F{^{1}H} NMR (376.6 MHz, CD_2Cl_2) δ/ppm = −68.5 (s, CF_3). Anal. calcd. for $[(C_{14}H_{10}O_4Mo_2AsSb)_2][TEF^{Cl}]_2$: C: 20.07, H: 0.56. Found: C: 20.31, H: 0.74. Positive ion ESI-MS *m/z* (%): 629.65 (100) [**C**]$^+$, 584.7 (37) [**VI**]$^+$, 573.7 (8) [**C**–2·CO]$^+$, 556.7 (8) [**VI**–CO]$^+$, 545.7 (18) [**C**–3·CO]$^+$, 528.7 (10) [**VI**–2·CO]$^+$, 517.7 (6) [**C**–4·CO]$^+$, 500.7 (7) [**VI**–3·CO]$^+$, 472.7 (4) [**VI**–4·CO]$^+$. Negative ion ESI-MS *m/z* (%): 1162.64 (100) [TEF^{Cl}]$^-$. IR (ATR) $\tilde{\nu}$/cm^{-1} = 3145 (vw), 3138 (vw), 3122 (vw), 2360 (w), 2344 (w), 2053 (w), 2032 (w), 1998 (m), 1983 (m), 1970 (w), 1954 (w), 1943 (w), 1310 (w), 1243 (m), 1194 (vs), 1145 (w), 1010 (w), 964 (w), 858 (m), 787 (m), 725 (m), 712 (s).

Preparation of [{CpMo(CO)$_2$}$_4$(μ$_4$,η^2:η^2:η^2:η^2-AsBiBiAs)][TEF^{Cl}]$_2$ (4b)

A dark purple solution of [Thia][TEF^{Cl}] (58 mg, 0.042 mmol, 1.0 eq.) in 3 mL CH_2Cl_2 was transferred to a dark red solution of [{CpMo(CO)$_2$}$_2$(μ,η^2:η^2-AsBi)] (**D**) (30 mg, 0.042 mmol, 1.0 eq.) in 5 mL CH_2Cl_2 at −50 °C causing an immediate colour change to a dark greenish brown solution. After stirring for 60 minutes, addition of 40 mL *n*-hexane led to precipitation of a dark green to black powder. The slightly brown supernatant solution was removed and washed twice with pure toluene. The crude product was dried in vacuum and recrystallization *via* layering a CH_2Cl_2 solution with *n*-hexane (1:4) and storage at +4 °C afforded pure **4b** as dark red blocks, which were suitable for single crystal X-ray diffraction. The supernatant was removed and the crystals were dried in vacuum.

Yield 64 mg (0.017 mmol = 81 %). Compound **4b** is silent in the X-band EPR spectra in CH_2Cl_2 solution at room temperature and at 77 K. Anal. calcd. for $[(C_{14}H_{10}O_4Mo_2AsBi)_2][TEF^{Cl}]_2$: C: 19.14, H: 0.54. Found: C: 19.30, H: 0.40. Mass spectrometric investigations were unsuccessful due to decomposition of **4b** during the measurement.

5.4.3 Cyclovoltammetry

CV of A

The CV of **A** in CH_2Cl_2 solution is depicted in Figure S1. The complex undergoes a pseudo-reversible oxidation with the peak of the anodic wave at +0.19 V vs. $Cp_2Fe^{0/+}$, while the corresponding cathodic wave is significantly shifted to –0.31 V vs. $Cp_2Fe^{0/+}$. This suggests that after the first oxidation of **A**, the shifted peak for the reduction corresponds to the dication of [**A-A**]$^{2+}$. During this study, no decline of the cathodic wave of [**A-A**]$^{2+}$ or the observation of any reduction assignable to the monocation [**A**]$^+$ could be observed in the CV regardless of the scan rates, the temperature and the concentration of **A**. This points to a rapid dimerization to the dication. The full CV of **A** (Figure S2) reveals also a second (+0.45 V vs. $Cp_2Fe^{0/+}$) and a third oxidation (+0.71 V vs. $Cp_2Fe^{0/+}$), which are irreversible.

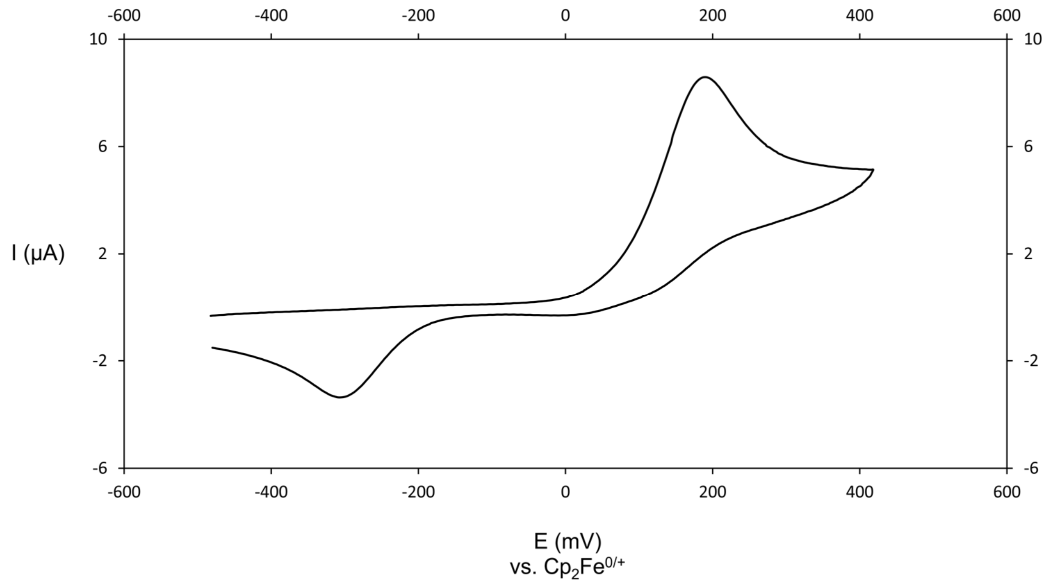

Figure S1. CV of **A** showing only the first (pseudo-reversible) oxidation.

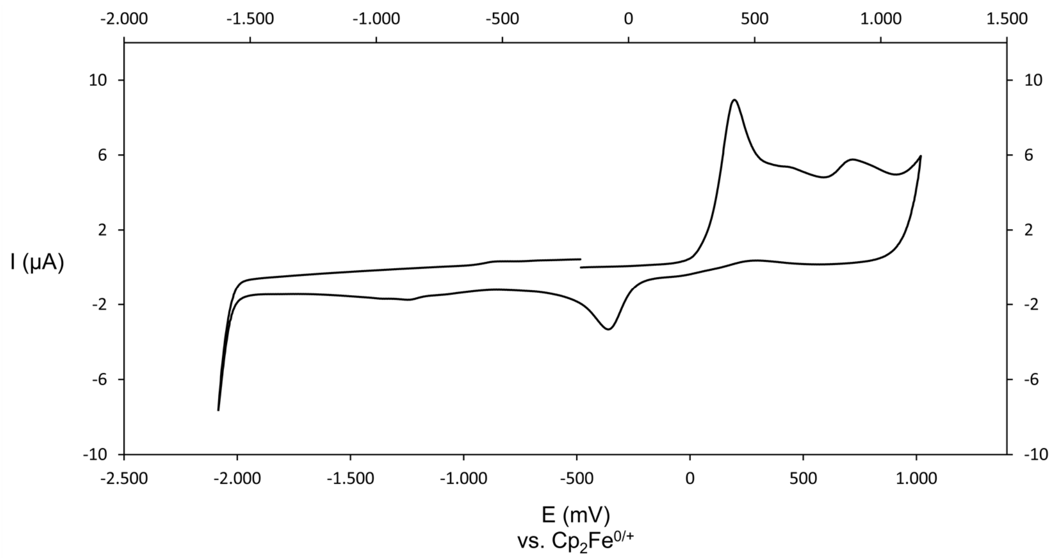

Figure S2. Full CV of **A**.

CV of B

The CV of **B** in CH_2Cl_2 solution is depicted in Figure S3. The complex undergoes a pseudo-reversible oxidation with the peak of the anodic wave at +0.08 V vs. $Cp_2Fe^{0/+}$, while the corresponding cathodic wave is significantly shifted to –0.43 V vs. $Cp_2Fe^{0/+}$. This suggests that after the first oxidation of **B**, the shifted peak for the reduction corresponds to the dication of [**B-B**]$^{2+}$. During this study, no decline of the cathodic wave of [**B-B**]$^{2+}$ or the observation of any reduction assignable to the monocation [**B**]$^+$ could be observed in the CV regardless of the scan rates, the temperature and the concentration of **B**. This points to a rapid dimerization to the dication. The full CV of **B** (Figure S4) reveals also a second oxidation (+0.56 V vs. $Cp_2Fe^{0/+}$) and a reduction (−2.16 V vs. $Cp_2Fe^{0/+}$), which are irreversible.

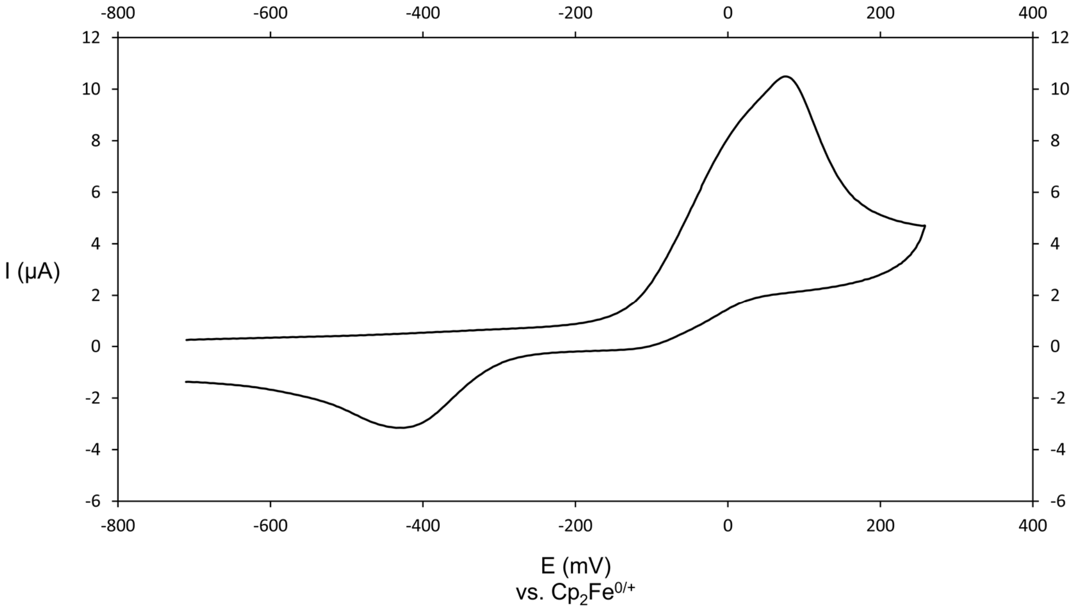

Figure S3. CV of **B** showing only the first (pseudo-reversible) oxidation.

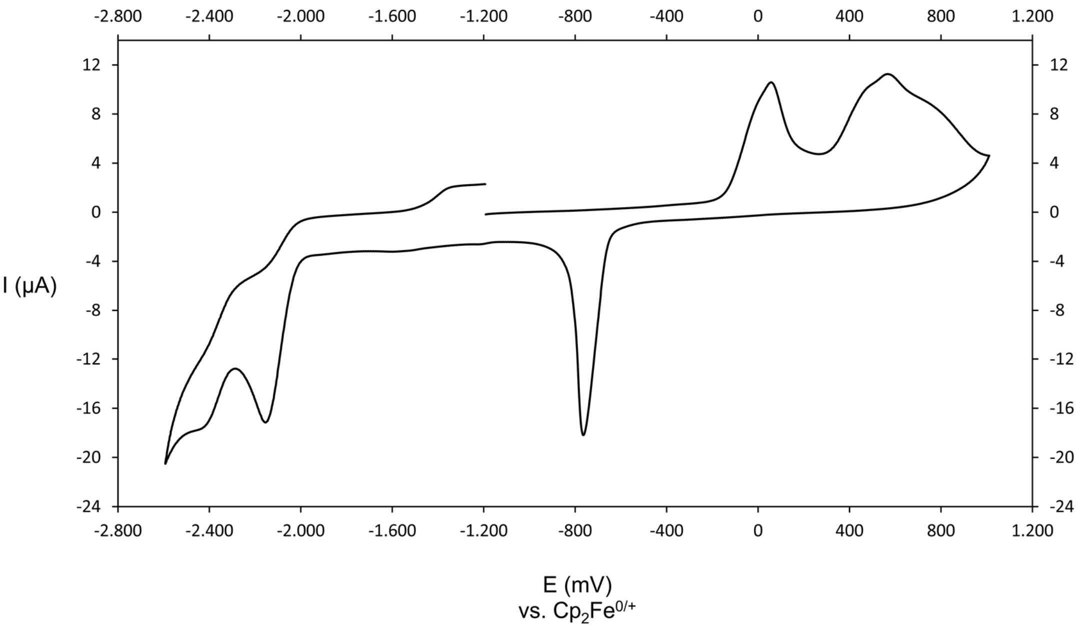

Figure S4. Full CV of **B**.

CV of C

The CV of **C** in CH_2Cl_2 solution is depicted in Figure S5. The complex undergoes a pseudo-reversible oxidation with the peak of the anodic wave at +0.12 V vs. $Cp_2Fe^{0/+}$, while the corresponding cathodic wave is significantly shifted to –0.20 V vs. $Cp_2Fe^{0/+}$. This suggests that after the first oxidation of **C**, the shifted peak for the reduction corresponds to the dication of [**C-C**]$^{2+}$. During this study, no decline of the cathodic wave of [**C-C**]$^{2+}$ or the observation of any reduction assignable to the monocation [**C**]$^{+}$ could be observed in the CV regardless of the scan rates, the temperature and the concentration of **C**. This points to a rapid dimerization to the dication. The full CV of **C** (Figure S6) reveals also a second (+0.55 V vs. $Cp_2Fe^{0/+}$) and a third oxidation (+1.26 V vs. $Cp_2Fe^{0/+}$) as well as a reduction (−2.17 V vs. $Cp_2Fe^{0/+}$), which are irreversible.

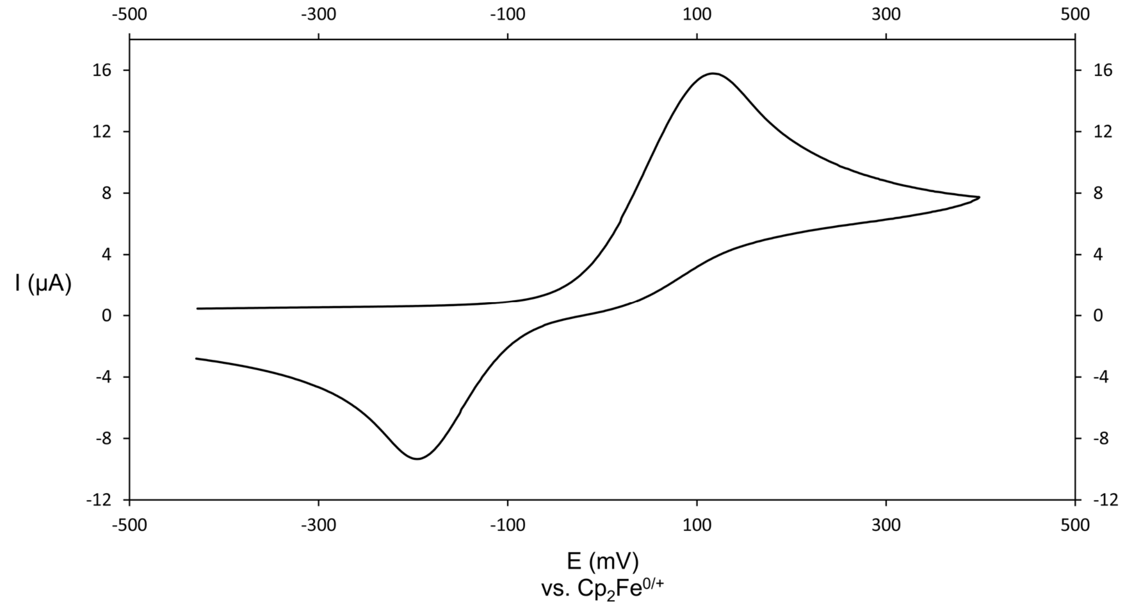

Figure S5. CV of **C** showing only the first (pseudo-reversible) oxidation.

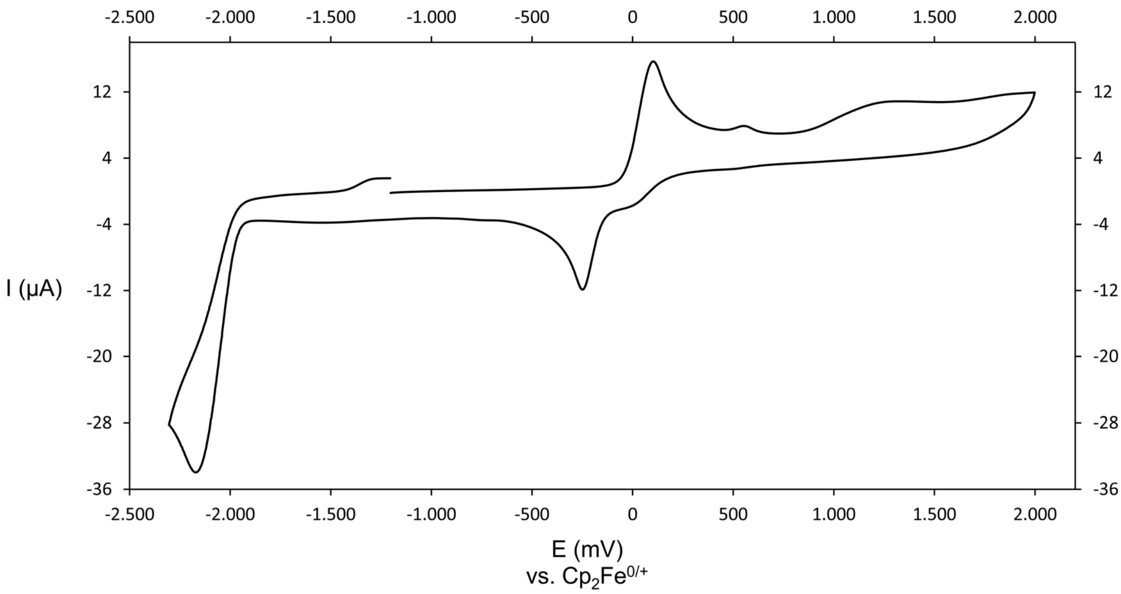

Figure S6. Full CV of **C**.

CV of D

The CV of **D** in CH_2Cl_2 solution is depicted in Figure S7. The complex undergoes a pseudo-reversible oxidation with the peak of the anodic wave at –0.10 V vs. $Cp_2Fe^{0/+}$, while the corresponding cathodic wave is significantly shifted to –0.36 V vs. $Cp_2Fe^{0/+}$. This suggests that after the first oxidation of **D**, the shifted peak for the reduction corresponds to the dication of [**D-D**]$^{2+}$. During this study, no decline of the cathodic wave of [**D-D**]$^{2+}$ or the observation of any reduction assignable to the monocation [**D**]$^{+}$ could be observed in the CV regardless of the scan rates, the temperature and the concentration of **D**. This points to a rapid dimerization to the dication. The full CV of **D** (Figure S8) reveals also a second (+0.19 V vs. $Cp_2Fe^{0/+}$) and a third oxidation (+0.88 V vs. $Cp_2Fe^{0/+}$) as well as a reduction (−2.26 V vs. $Cp_2Fe^{0/+}$), which are irreversible.

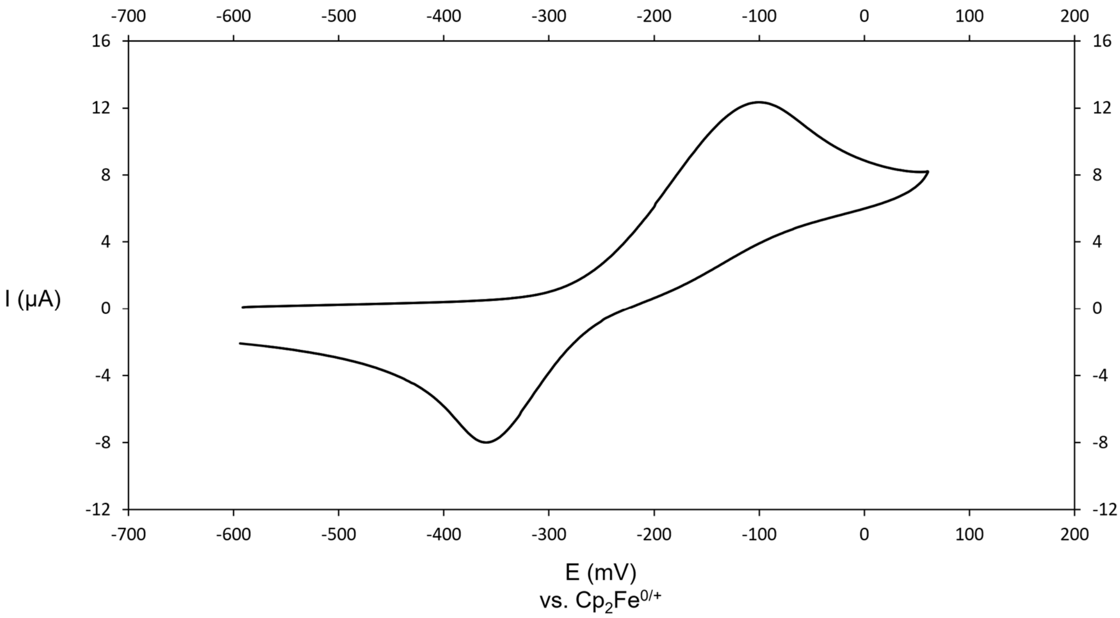

Figure S7. CV of **D** showing only the first (pseudo-reversible) oxidation.

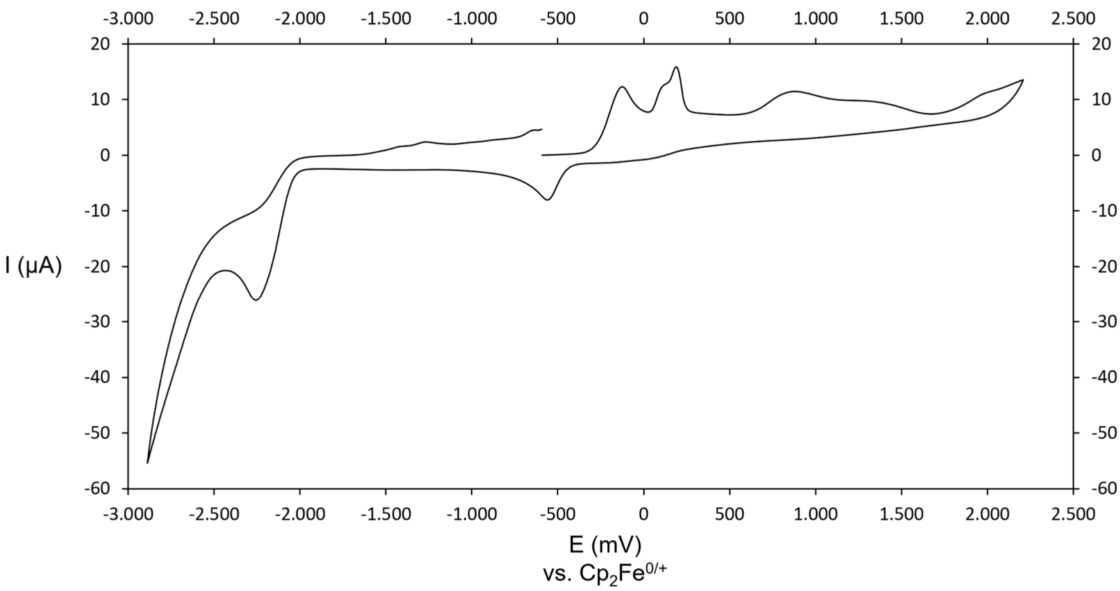

Figure S8. Full CV of **D**.

CV of E

The CV of **E** in CH_2Cl_2 solution is depicted in Figure S9. The complex undergoes a pseudo-reversible oxidation with the peak of the anodic wave at −0.07 V vs. $Cp_2Fe^{0/+}$, while the corresponding cathodic wave is significantly shifted to –0.44 V vs. $Cp_2Fe^{0/+}$. This suggests that after the first oxidation of **E**, the shifted peak for the reduction corresponds to the dication of [**E-E**]$^{2+}$. During this study, no decline of the cathodic wave of [**E-E**]$^{2+}$ or the observation of any reduction assignable to the monocation [**E**]$^{+}$ could be observed in the CV regardless of the scan rates, the temperature and the concentration of **E**. This points to a rapid dimerization to the dication. Besides the oxidation, also a small shoulder at (+0.05 V vs. $Cp_2Fe^{0/+}$), which can be attributed to small trace impurities of **VI**, which are formed during its synthesis.[2] The full CV of **E** (Figure S10) reveals also a second (+0.48 V vs. $Cp_2Fe^{0/+}$) and a third oxidation (+0.89 V vs. $Cp_2Fe^{0/+}$) as well as a reduction (−2.11 V vs. $Cp_2Fe^{0/+}$), which are irreversible.

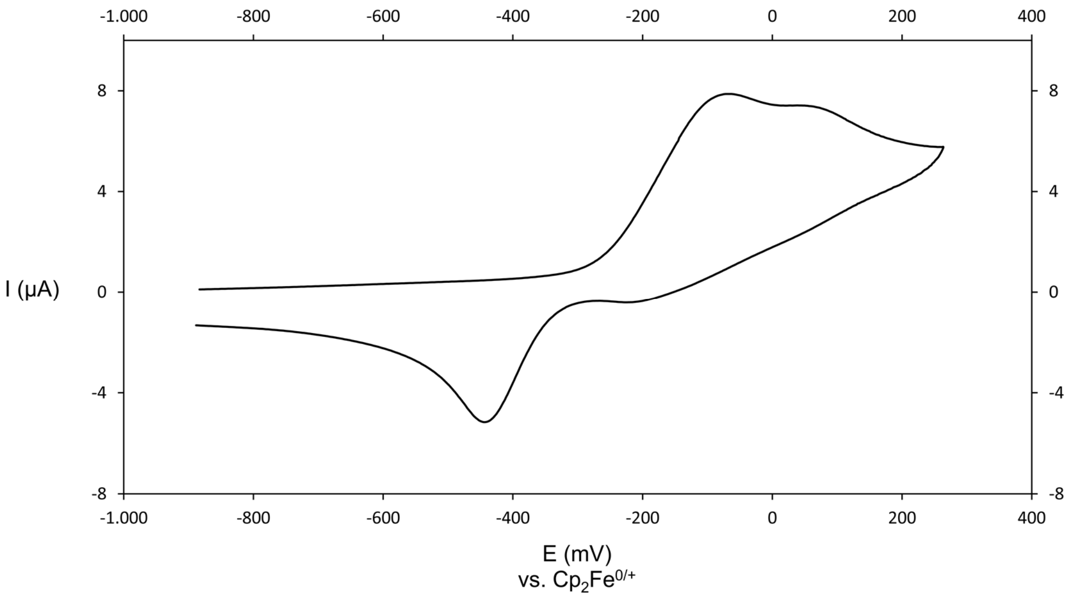

Figure S9. CV of **E** showing only the first (pseudo-reversible) oxidation.

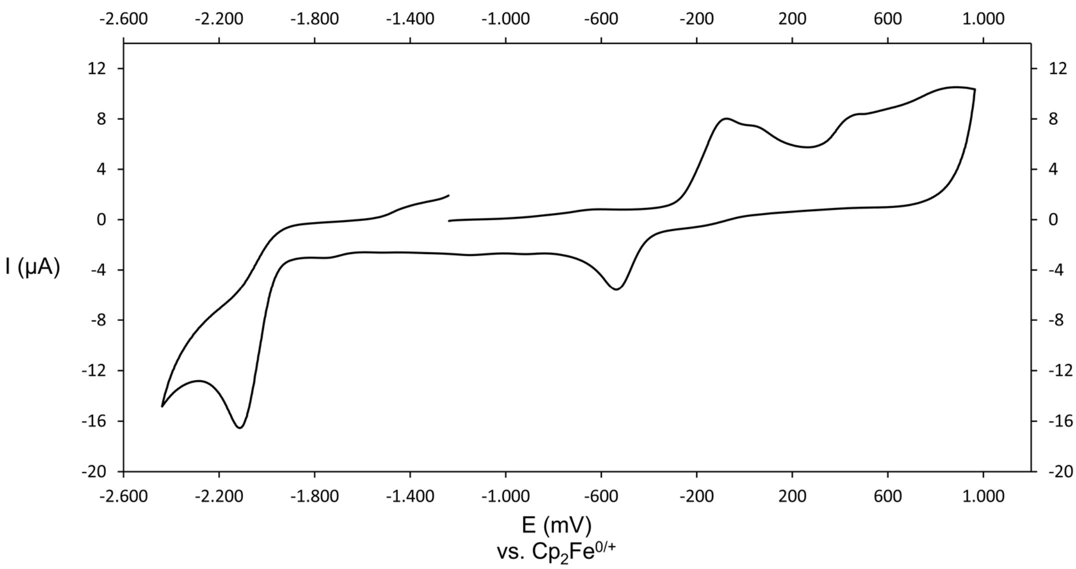

Figure S10. Full CV of **E**.

5.4.4 NMR spectra

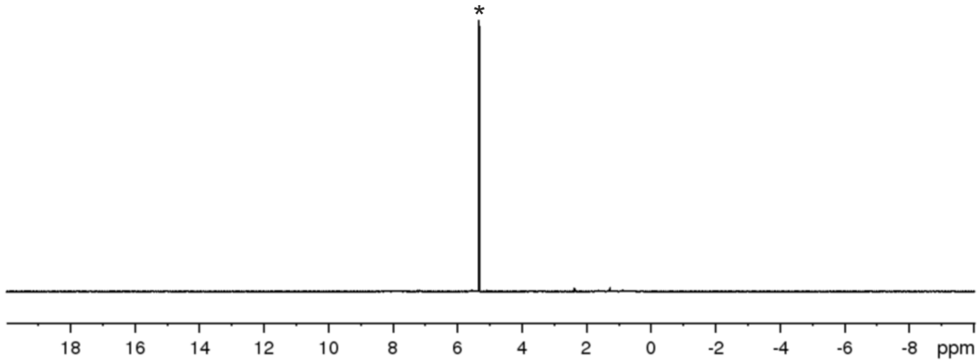

Figure S11: ^1H NMR spectrum of [Thia][TEF^{Cl}] in CD_2Cl_2; * = CD_2Cl_2.

The ^1H NMR spectrum of [Thia][TEF^{Cl}] reveals no signals for $[Thia]^{\cdot+}$ affirming the paramagnetic character of the radical cation.

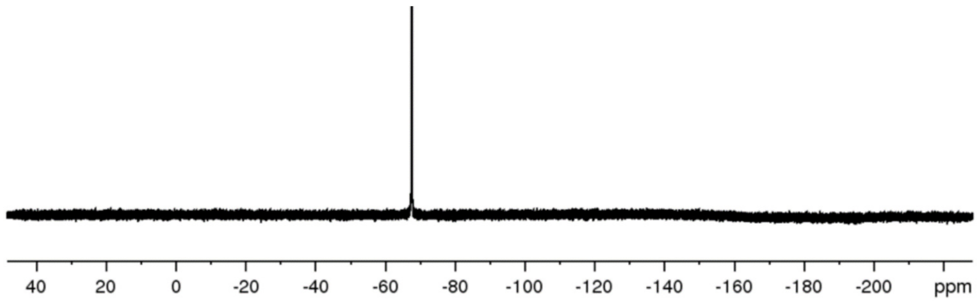

Figure S12: $^{19}F\{^1H\}$ NMR spectrum of [Thia][TEF^{Cl}] in CD_2Cl_2.

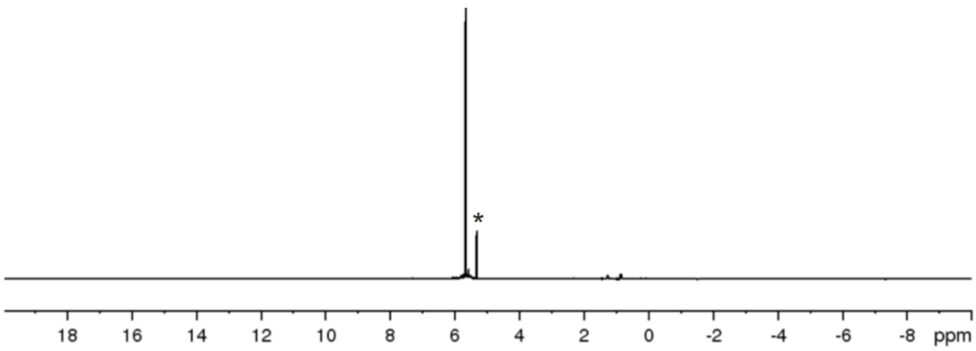

Figure S13: ^1H NMR spectrum of [$\{CpMo(CO)_2\}_4(\mu_4,\eta^2:\eta^2:\eta^2:\eta^2$-AsPPAs)][TEF]$_2$ (**1**) in CD_2Cl_2; * = CD_2Cl_2.

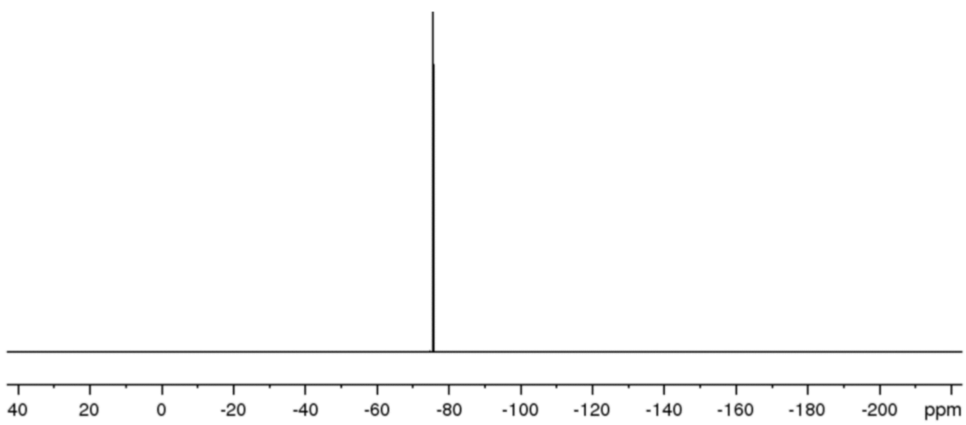

Figure S14: $^{19}F\{^1H\}$ NMR spectrum of [$\{CpMo(CO)_2\}_4(\mu_4,\eta^2:\eta^2:\eta^2:\eta^2$-AsPPAs)][TEF]$_2$ (**1**) in CD_2Cl_2.

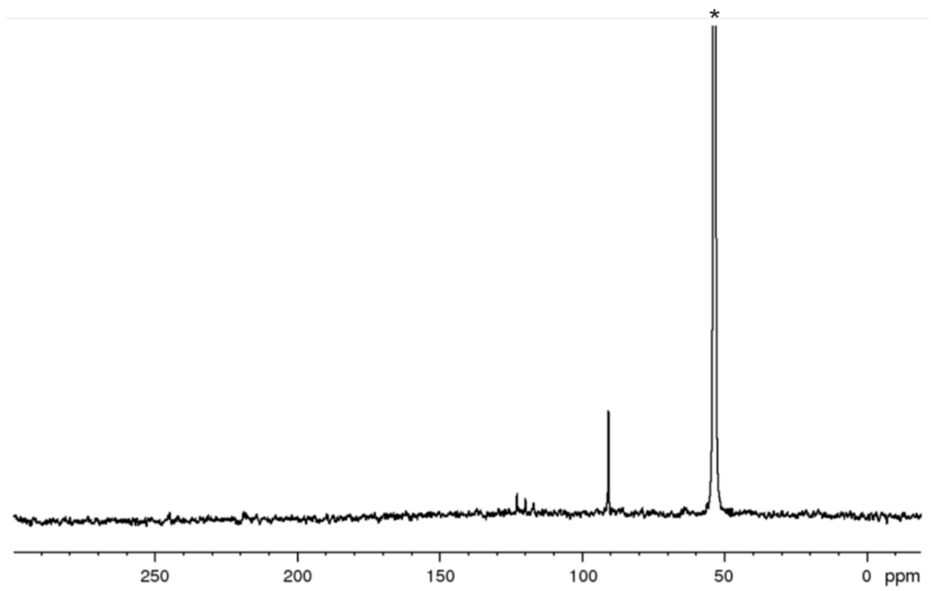

Figure S15: $^{13}C\{^1H\}$ NMR spectrum of $[\{CpMo(CO)_2\}_4(\mu_4,\eta^2:\eta^2:\eta^2:\eta^2\text{-AsPPAs})][TEF]_2$ (**1**) in CD_2Cl_2; * = CD_2Cl_2.

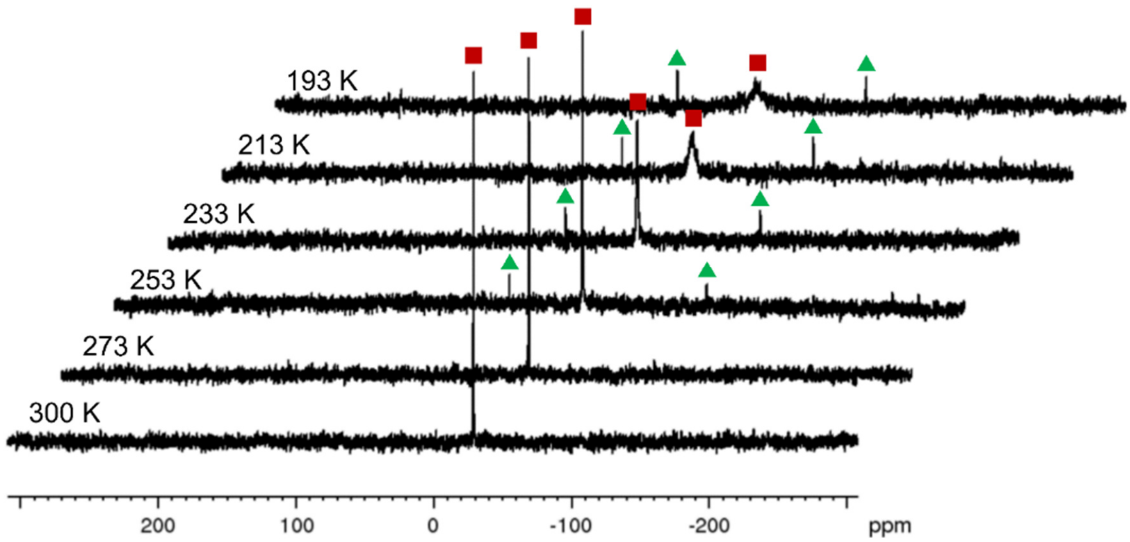

Figure S16: $^{31}P\{^1H\}$ VT-NMR spectrum of $[\{CpMo(CO)_2\}_4(\mu_4,\eta^2:\eta^2:\eta^2:\eta^2\text{-AsPPAs})][TEF]_2$ (**1**) in CD_2Cl_2.

In Figure S16 the $^{31}P\{^1H\}$ variable temperature (VT) NMR spectrum of **1** from 300 K to 193 K is shown. At room temperature a relatively sharp singlet at $\delta = -28.8$ ppm ($\omega_{1/2} = 11$ Hz) is observed, which is shifted to lower frequencies by 60 ppm compared to the starting material **A** ($\delta = 30.1$ ppm).[3] Upon cooling to 193 K, the signal (■) moves farther to lower frequencies ($\delta = -39.4$ ppm) and undergoes broadening ($\omega_{1/2} \sim 1700$ Hz). Additionally, two new signals (▲) at $\delta = -119.7$ ppm and 21.4 ppm arise below 253 K indicating the formation of a new, unidentified species.

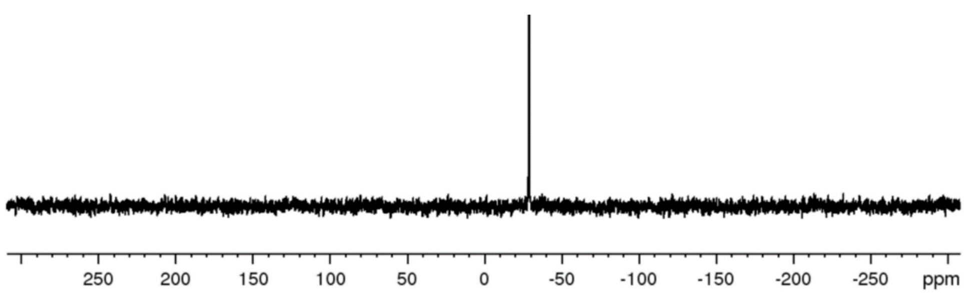

Figure S17: $^{31}P\{^1H\}$ NMR spectrum of $[\{CpMo(CO)_2\}_4(\mu_4,\eta^2:\eta^2:\eta^2:\eta^2\text{-AsPPAs})][TEF]_2$ (**1**) in CD_2Cl_2.

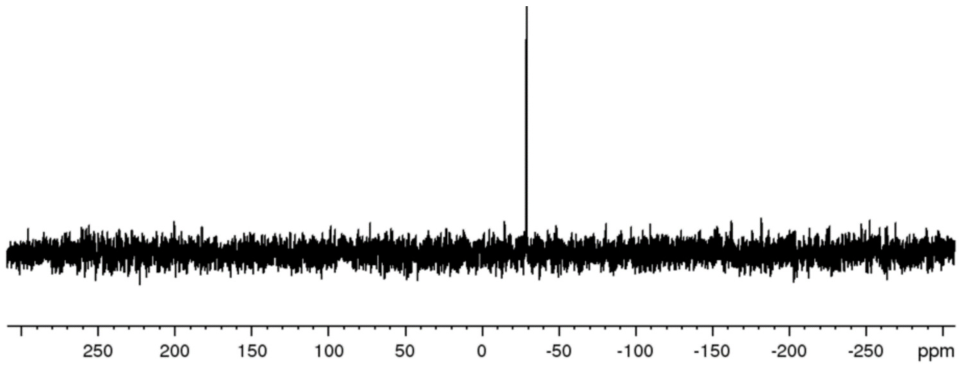

Figure S18: ^{31}P NMR spectrum of [{CpMo(CO)$_2$}$_4$(μ$_4$,η^2:η^2:η^2:η^2-AsPPAs)][TEF]$_2$ (**1**) in CD_2Cl_2.

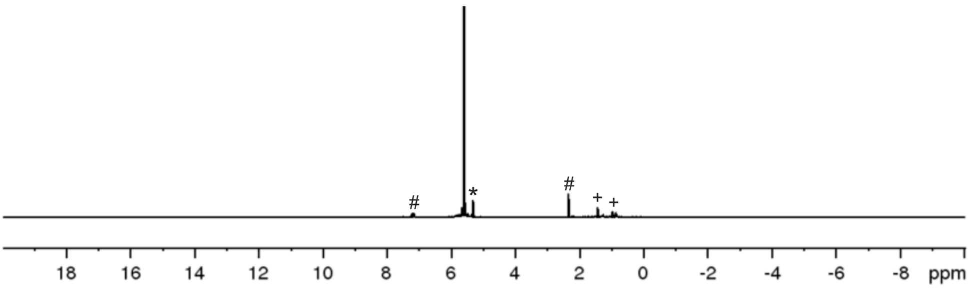

Figure S19: ^{1}H NMR spectrum of [{CpMo(CO)$_2$}$_4$(μ$_4$,η^2:η^2:η^2:η^2-SbPPSb)][TEF]$_2$ (**2**) in CD_2Cl_2; + = H grease, # = toluene, * = CD_2Cl_2.

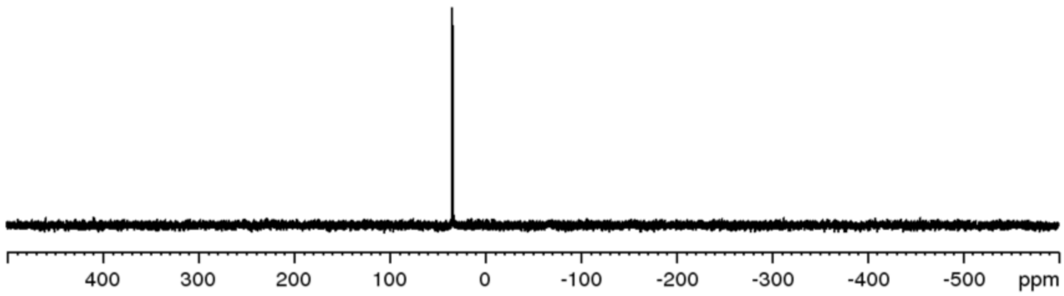

Figure S20: ^{31}P{^{1}H} NMR spectrum of [{CpMo(CO)$_2$}$_4$(μ$_4$,η^2:η^2:η^2:η^2-SbPPSb)][TEF]$_2$ (**2**) in CD_2Cl_2.

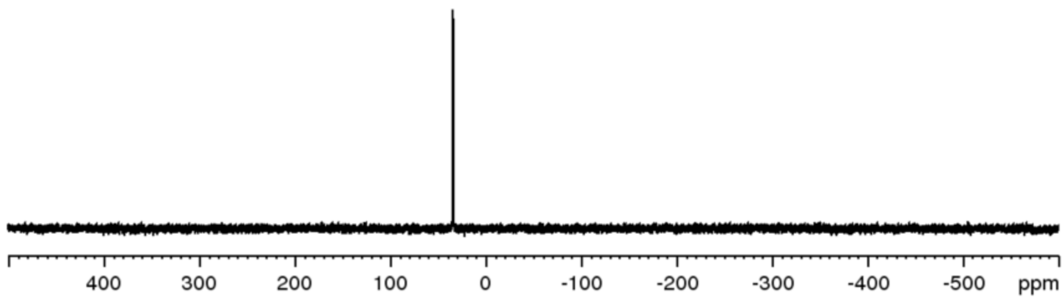

Figure S21: ^{31}P NMR spectrum of [{CpMo(CO)$_2$}$_4$(μ$_4$,η^2:η^2:η^2:η^2-SbPPSb)][TEF]$_2$ (**2**) in CD_2Cl_2.

The ^{31}P{^{1}H} and ^{31}P NMR spectra of **2** (Figure S20 and Figure S21) reveal a sole singlet at δ = 35.0 ppm, which again is shifted to lower frequencies by 55 ppm in comparison to the starting material **B** (δ = 90.7 ppm).[3] This affirms the suggestion that analogue to **1** a P–P coupled dicationic product is formed.

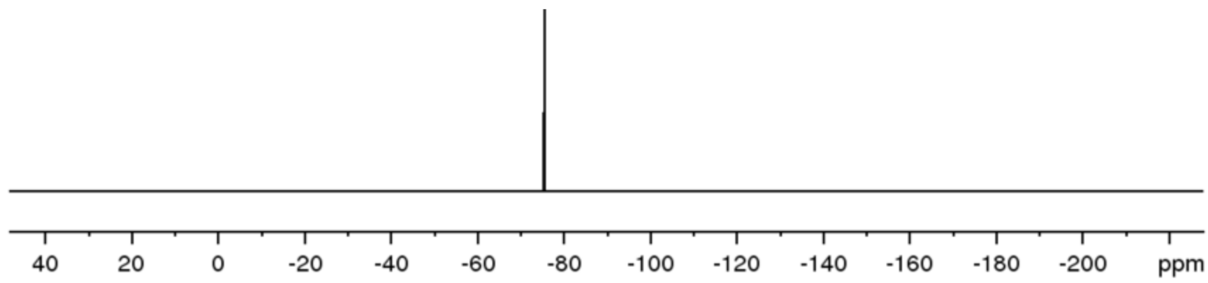

Figure S22: $^{19}F\{^1H\}$ NMR spectrum of [{CpMo(CO)$_2$}$_4$(μ$_4$,η^2:η^2:η^2:η^2-SbPPSb)][TEF]$_2$ (**2a**) in CD_2Cl_2.

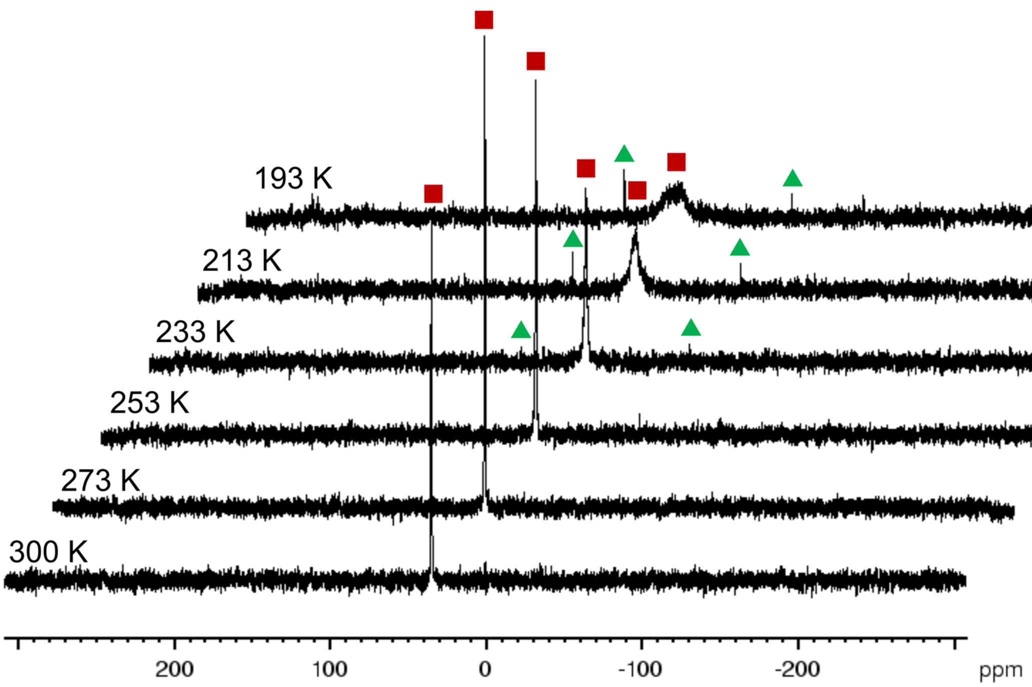

Figure S23: $^{31}P\{^1H\}$ VT-NMR spectrum of [{CpMo(CO)$_2$}$_4$(μ$_4$,η^2:η^2:η^2:η^2-SbPPSb)][TEF]$_2$ (**2**) in CD_2Cl_2.

In Figure S23 the $^{31}P\{^1H\}$ variable temperature (VT) NMR spectrum of **2** from 300 K to 193 K is shown. At room temperature a relatively sharp singlet at δ = 35.0 ppm ($\omega_{1/2}$ = 72 Hz), which is shifted to lower frequencies by 55 ppm compared to the starting material **B** (δ = 90.7 ppm).[3] The same behaviour was also observed for **1**. Upon cooling to 193 K, the signal (■) moves farther to lower frequencies (δ = 28.4 ppm) and undergoes broadening ($\omega_{1/2}$ ~ 17000 Hz). Additionally, two new signals (▲) at δ = –40.9 ppm and 66.5 ppm arise below 233 K indicating the formation of a new, unidentified species, like it was described for **1**.

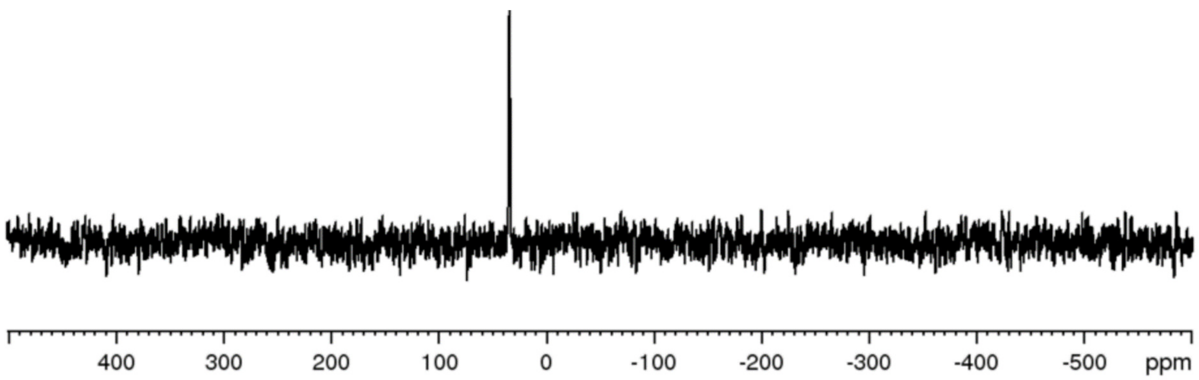

Figure S24: $^{31}P\{^1H\}$ NMR spectrum of the crude solution of [{CpMo(CO)$_2$}$_4$(μ$_4$,η^2:η^2:η^2:η^2-SbPPSb)][TEF]$_2$ (**2**) in CH_2Cl_2/C_6D_6.

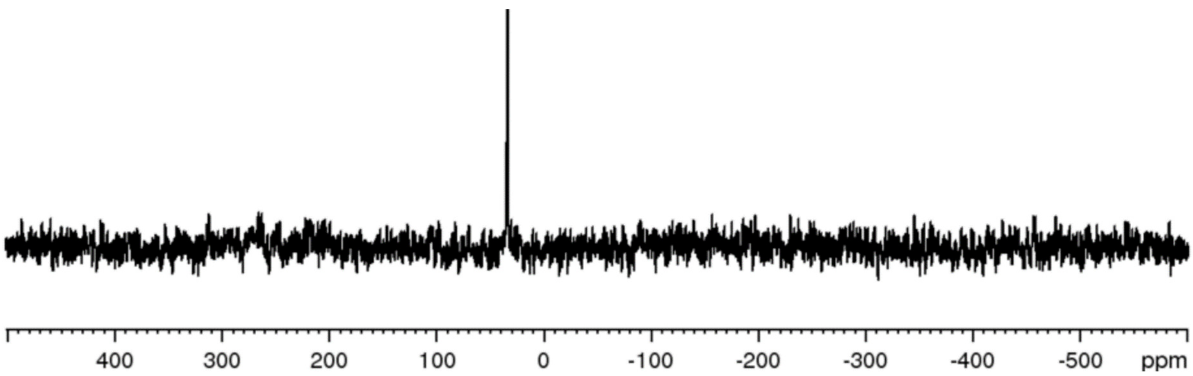

Figure S25: $^{31}P\{^1H\}$ NMR spectrum of the crude solution of [{CpMo(CO)$_2$}$_4$(μ_4,η^2:η^2:η^2:η^2-SbPPSb)][TEF]$_2$ (**2**) in CH_2Cl_2/C_6D_6.

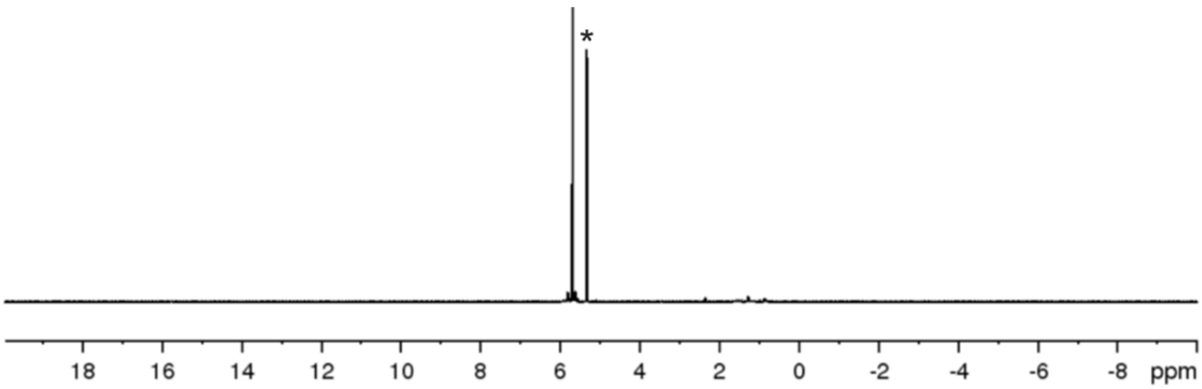

Figure S26: ^1H NMR spectrum of [{CpMo(CO)$_2$}$_4$(μ_4,η^2:η^2:η^2:η^2-AsSbSbAs)][TEF]$_2$ (**3a**) in CD_2Cl_2; * = CD_2Cl_2.

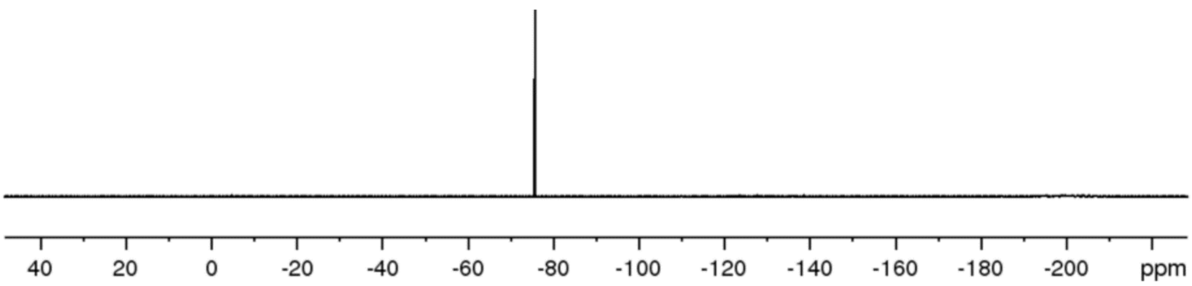

Figure S27: $^{19}F\{^1H\}$ spectrum of [{CpMo(CO)$_2$}$_4$(μ_4,η^2:η^2:η^2:η^2-AsSbSbAs)][TEF]$_2$ (**3a**) in CD_2Cl_2.

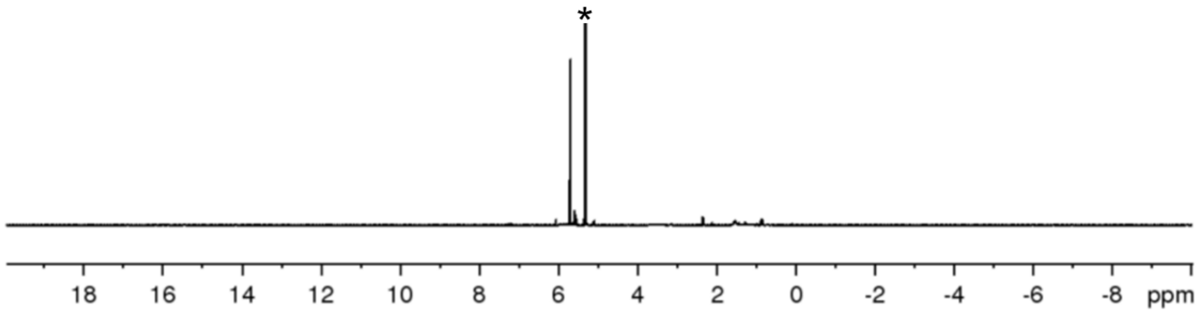

Figure S28: ^1H NMR spectrum of [{CpMo(CO)$_2$}$_4$(μ_4,η^2:η^2:η^2:η^2-AsSbAsSb)][TEF^{Cl}]$_2$ (**3b**) in CD_2Cl_2, * = CD_2Cl_2.

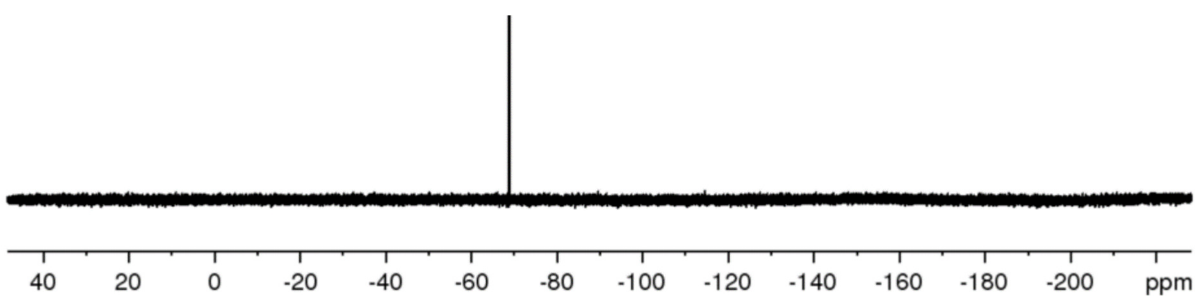

Figure S29: $^{19}F\{^1H\}$ NMR spectrum of [{CpMo(CO)$_2$}$_4$(μ_4,η^2:η^2:η^2:η^2-AsSbAsSb)][TEF^{Cl}]$_2$ (**3b**) in CD_2Cl_2.

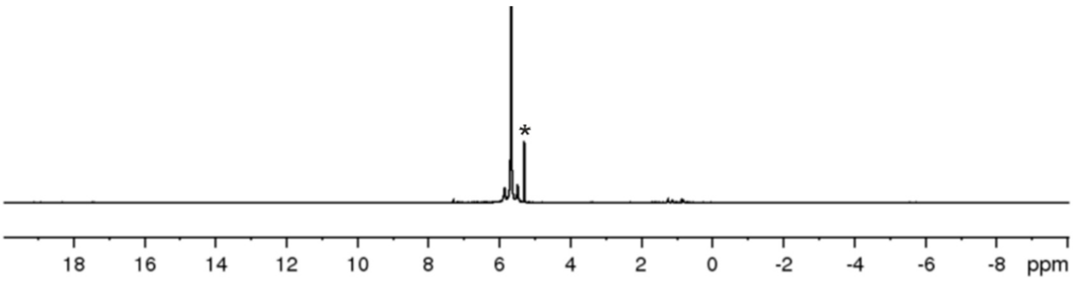

Figure S30: ^{1}H NMR spectrum of [{CpMo(CO)$_2$}$_4$(μ$_4$,η^2:η^2:η^2:η^2-AsBiBiAs)][TEF]$_2$ (**4a**) in CD_2Cl_2; * = CD_2Cl_2.

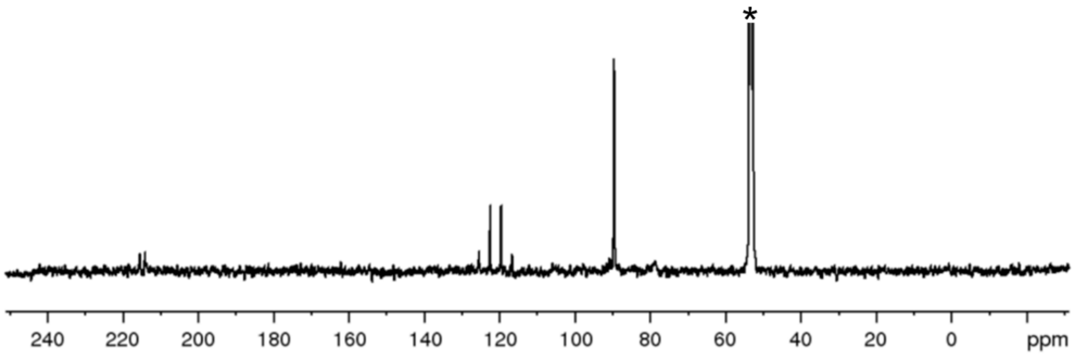

Figure S31: ^{13}C{^{1}H} NMR spectrum of [{CpMo(CO)$_2$}$_4$(μ$_4$,η^2:η^2:η^2:η^2-AsBiBiAs)][TEF]$_2$ (**4a**) in CD_2Cl_2; * = CD_2Cl_2.

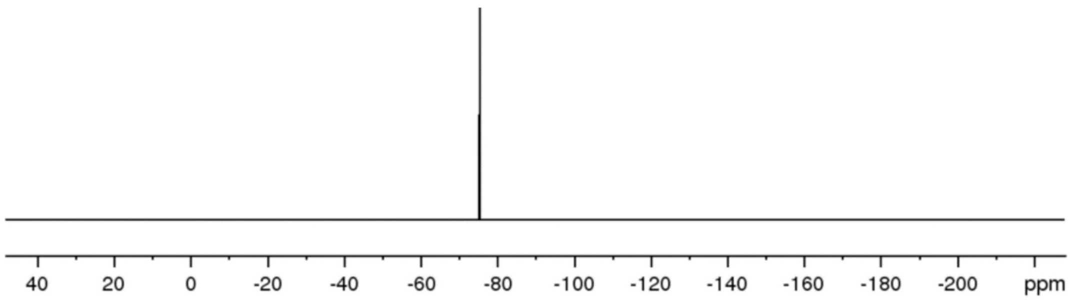

Figure S32: ^{19}F{^{1}H} NMR spectrum of [{CpMo(CO)$_2$}$_4$(μ$_4$,η^2:η^2:η^2:η^2-AsBiBiAs)][TEF]$_2$ (**4a**) in CD_2Cl_2.

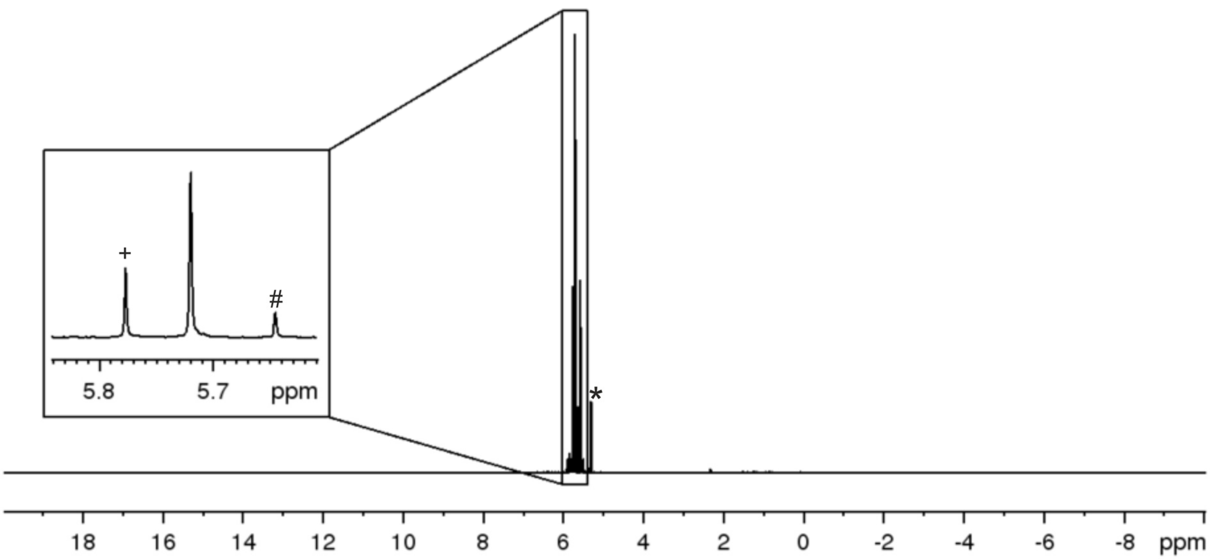

Figure S33: ^{1}H NMR spectrum of [{CpMo(CO)$_2$}$_4$(μ$_4$,η^2:η^2:η^2:η^2-BiSbSbBi)][TEF]$_2$ (**5**) in CD_2Cl_2; * = CD_2Cl_2, # = **XI**, + = **XII**.

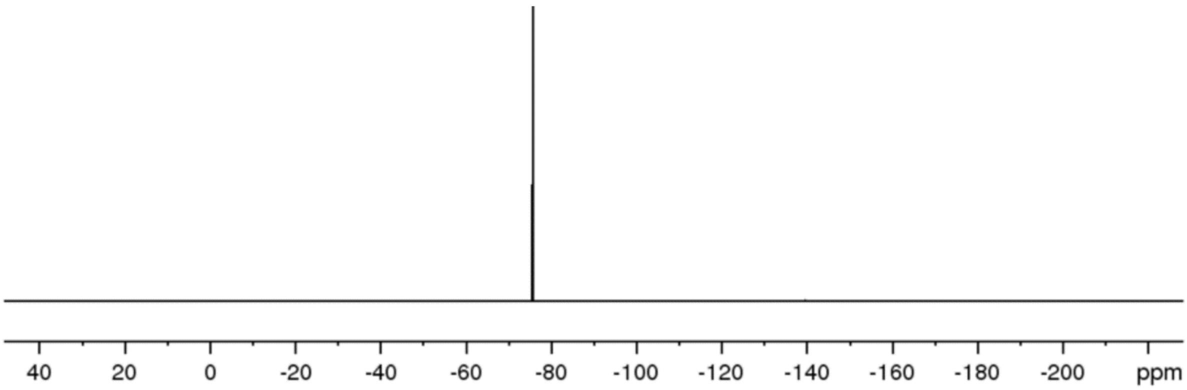

Figure S34: $^{19}F\{^1H\}$ NMR spectrum of [{CpMo(CO)$_2$}$_4$(μ_4,η^2:η^2:η^2:η^2-BiSbSbBi)][TEF]$_2$ (**5**) in CD_2Cl_2.

5.4.5 Mass spectrometry

The mass spectra, which were recorded by the mass spectrometry department of the University of Regensburg, are not available to the authors in a digital format and, therefore, could not be displayed in the following.

ESI mass spectrometry of [Thia][TEF^{Cl}]

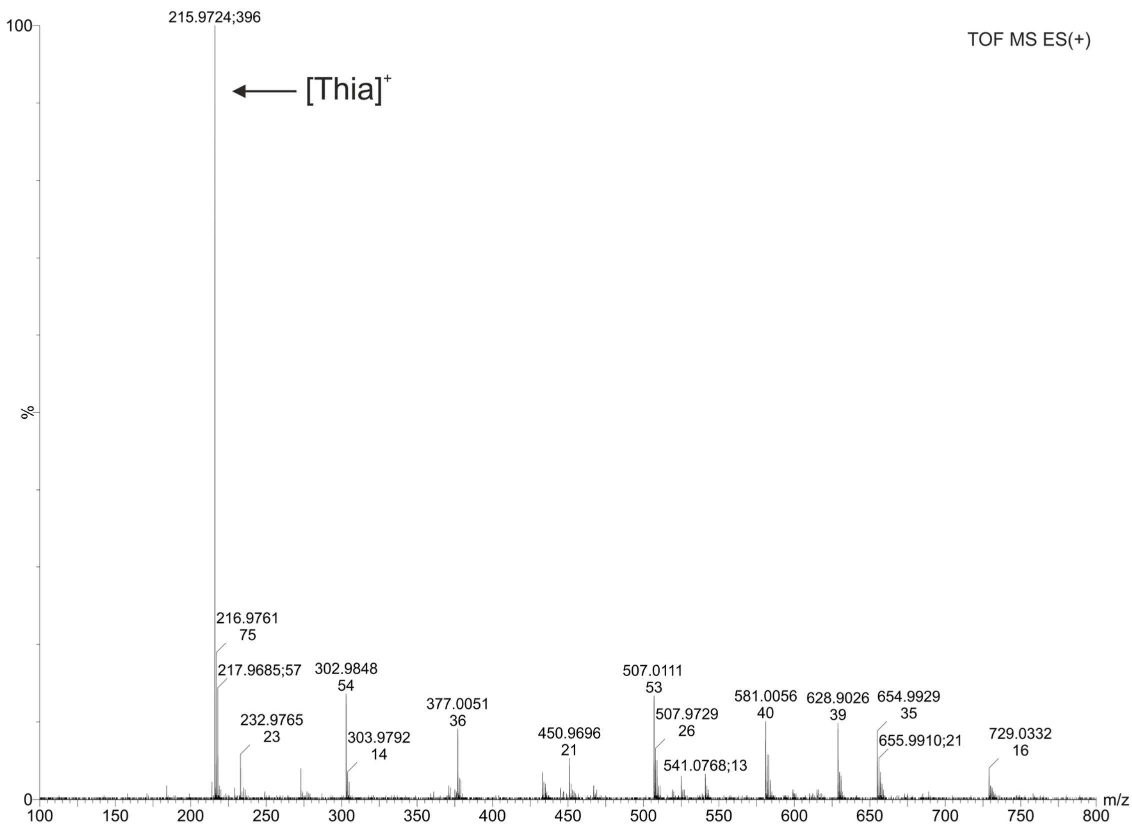

Figure S35: ESI(+) MS spectrum of [Thia][TEF^{Cl}].

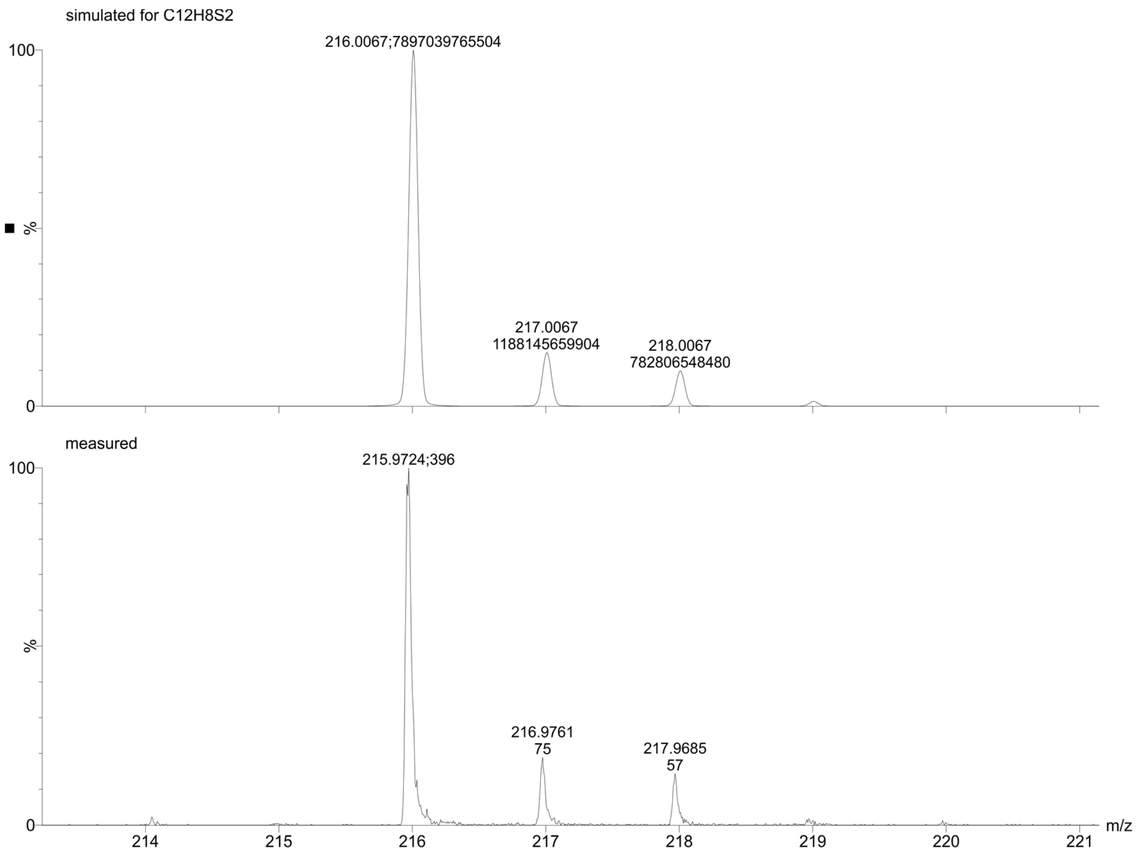

Figure S36: Molecular ion peak of [Thia]$^+$. Bottom: measured spectrum, top: simulated spectrum.

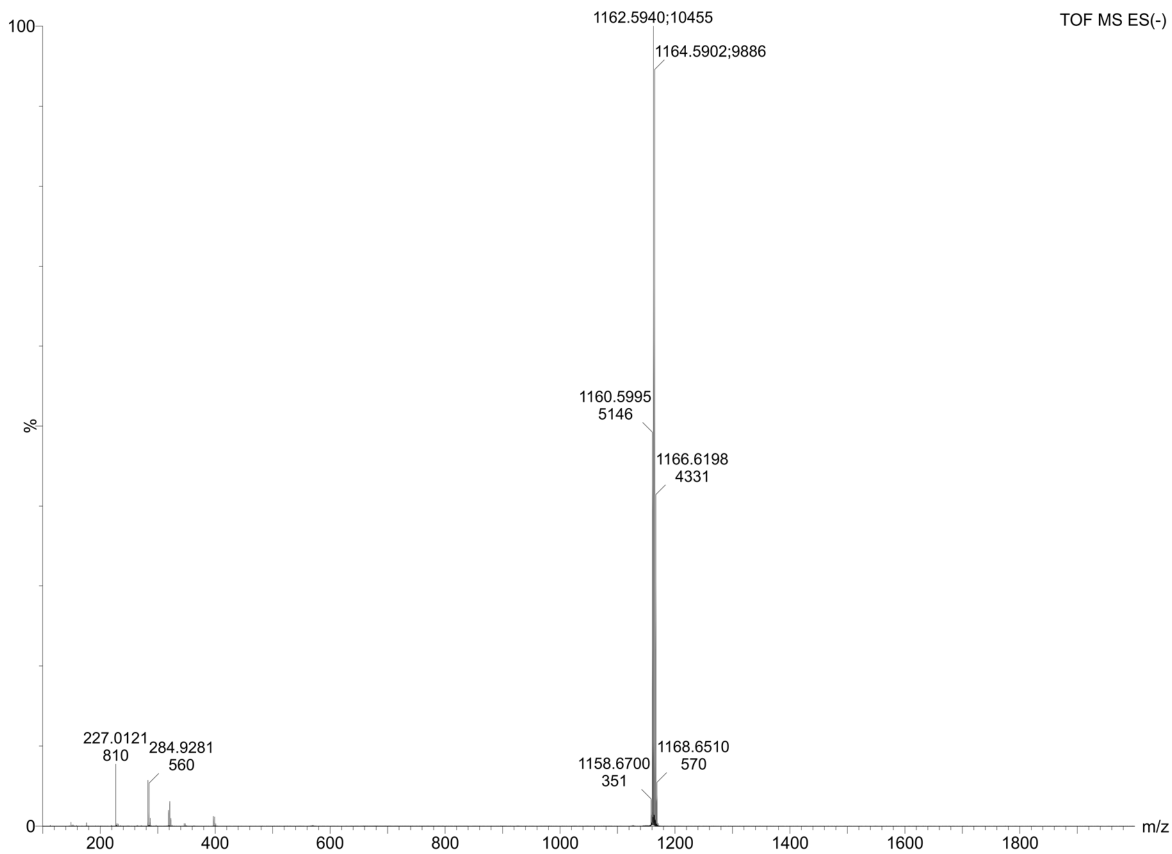

Figure S37: ESI(−) MS spectrum of [Thia][TEF^{Cl}].

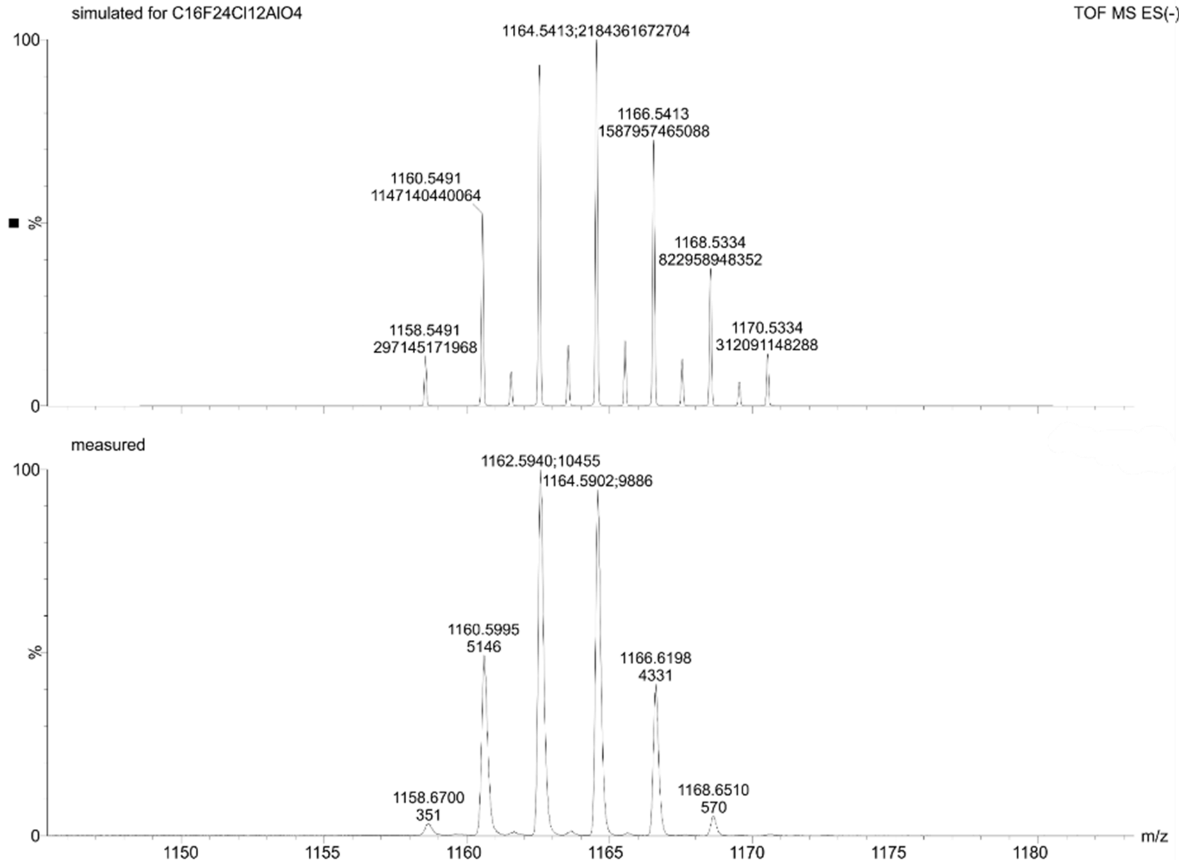

Figure S38: Molecular ion peak of [TEF^{Cl}]$^-$. Bottom: measured spectrum, top: simulated spectrum.

ESI mass spectrometry of 1:

The ESI mass spectrum of a CH_2Cl_2 solution of crystalline **1** (Figure S39) clearly shows signals assignable to the monocationic species [**A**]$^+$, [**A**–1(CO)]$^+$, [**A**–2(CO)]$^+$, [**A**–3(CO)]$^+$ and [**A**–4(CO)]$^+$. However, by varying the extraction cone voltages one can also record signals for a dicationic species, which can be assigned to [$\mathbf{A_2}$-2(CO)]$^{2+}$ (Figure S40). Additionally, some small peaks (≈7:1 intensity, shifted by ≈0.5 Da) are detected in the *m/z* regions for signals, which may be assigned to [**A**–CO–O]$^+$ and [**A**–2(CO)]$^+$. The overlay of the latter signals with monocationic species though does not allow a reliable assignment by isotopic distribution modelling of these species and the reported formulas in Figure S40 should be regarded as suggested species.

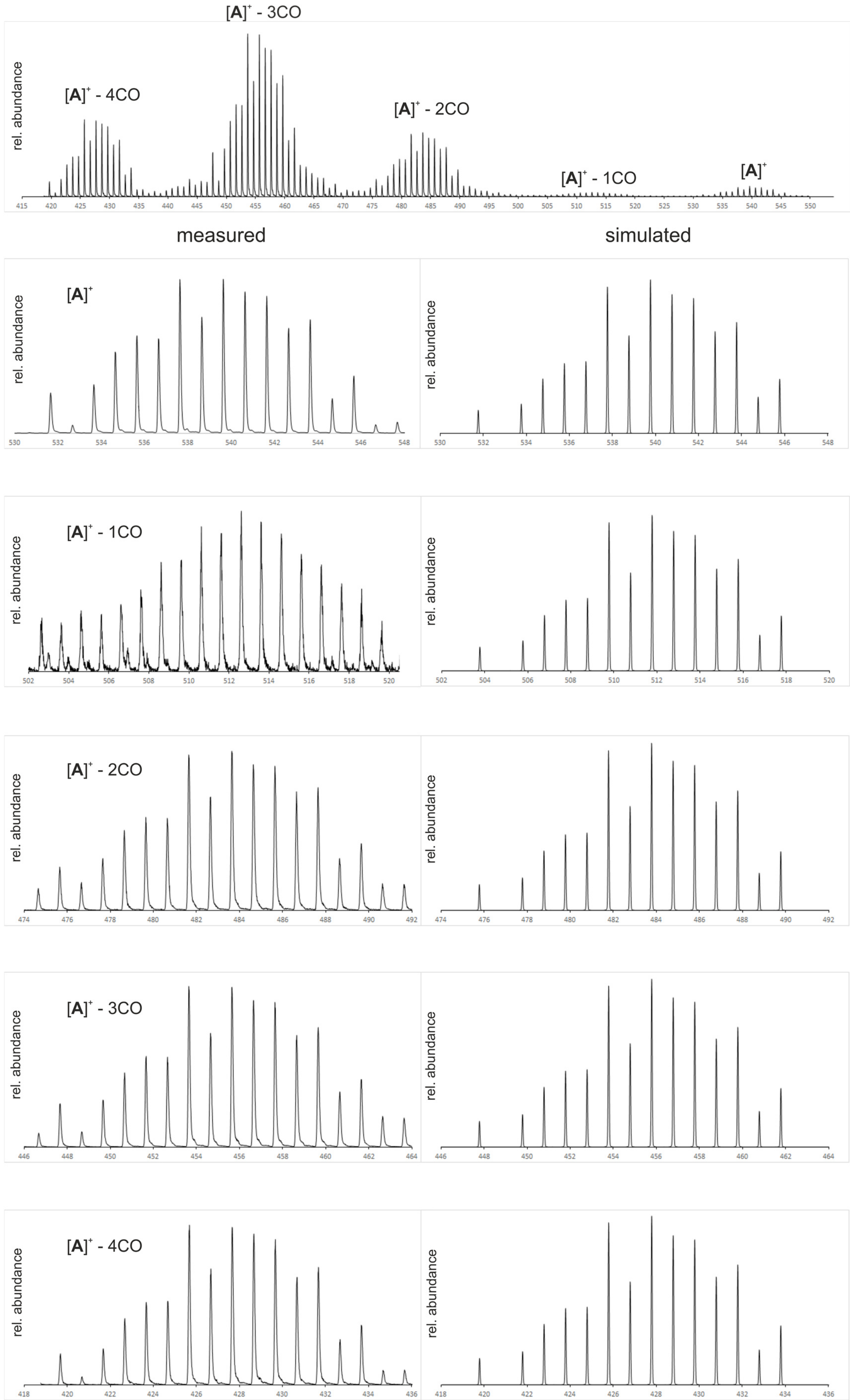

Figure S39: (top) ESI MS spectrum of **1** from CH_2Cl_2. Measured (left) and simulated (right) isotopic distribution for the assignable peaks.

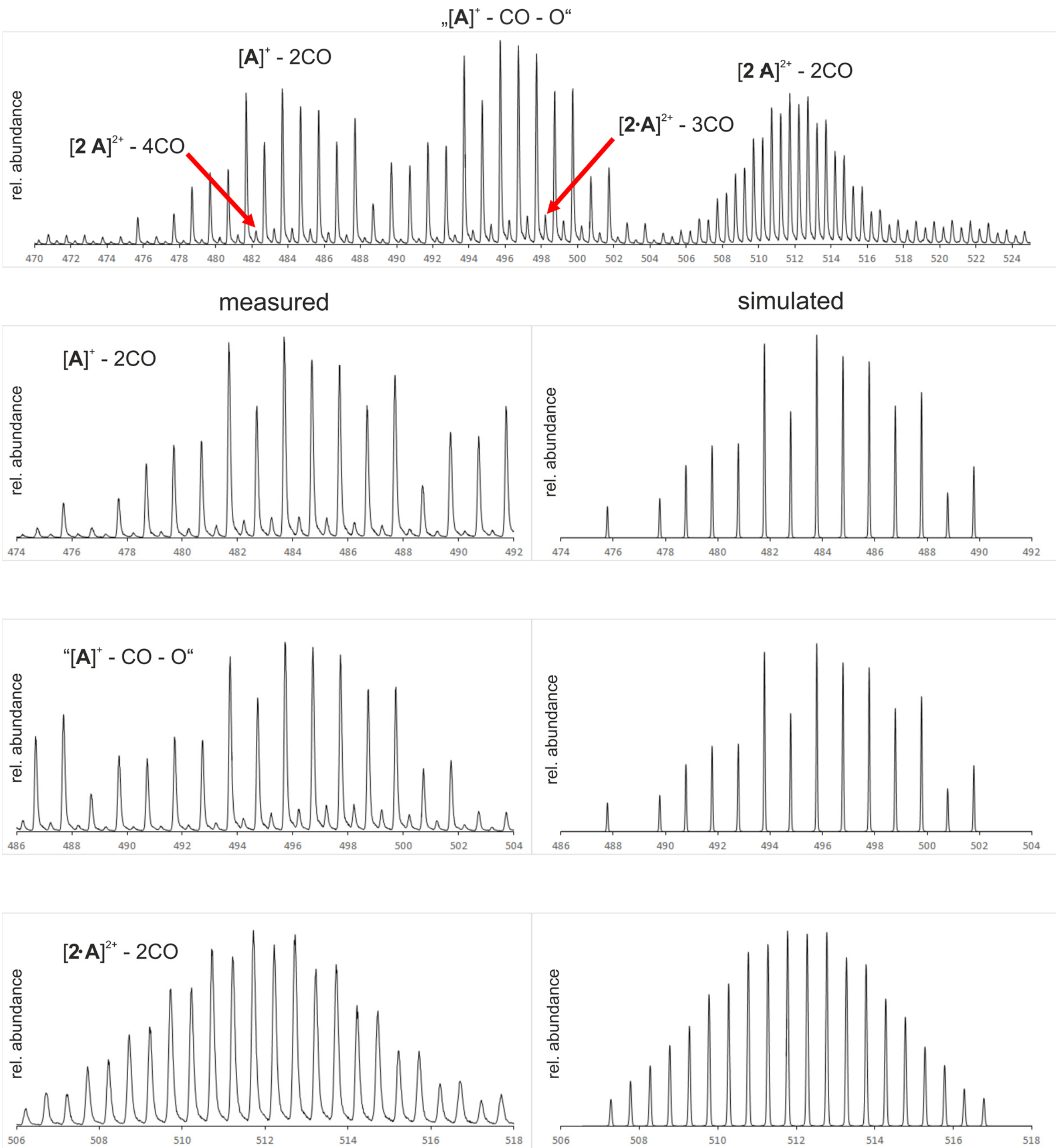

Figure S40: (top) ESI MS spectrum of **1** from CH_2Cl_2 after varying the extraction cone voltage. Measured (left) and simulated (right) isotopic distribution for the assignable peaks.

ESI mass spectrometry of 3a:

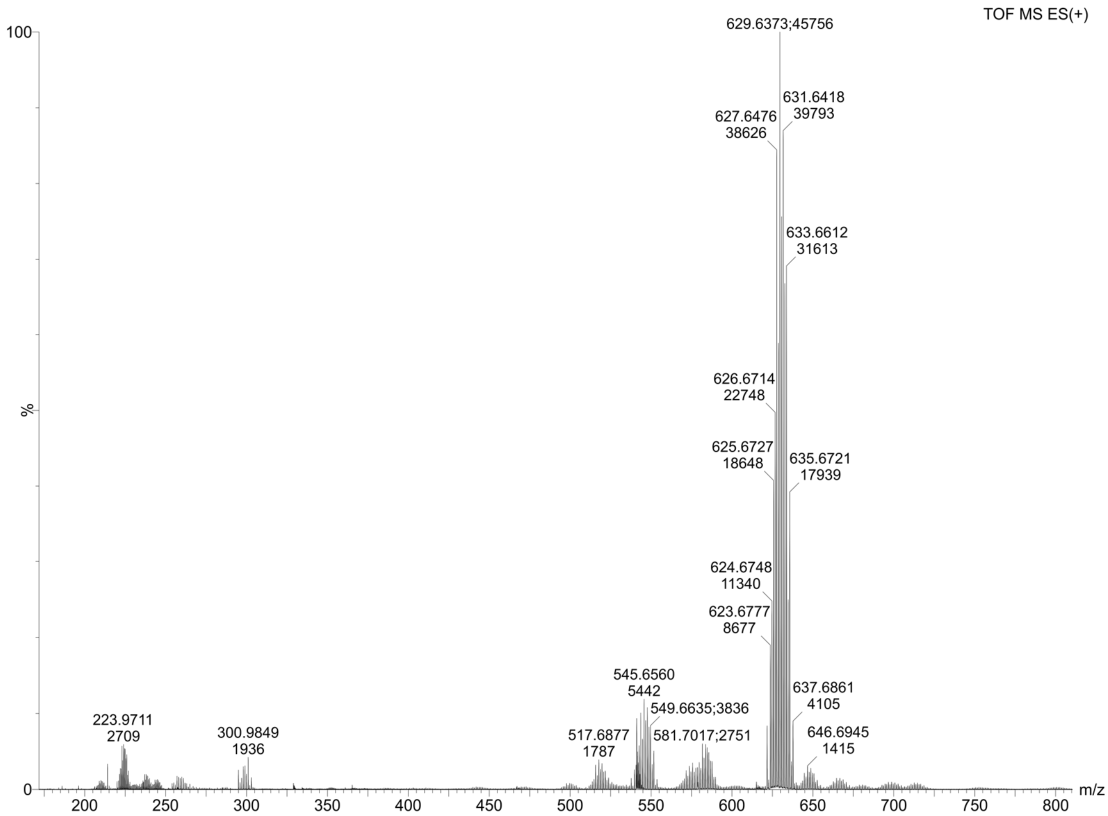

Figure S41: ESI(+) MS spectrum of **3a**.

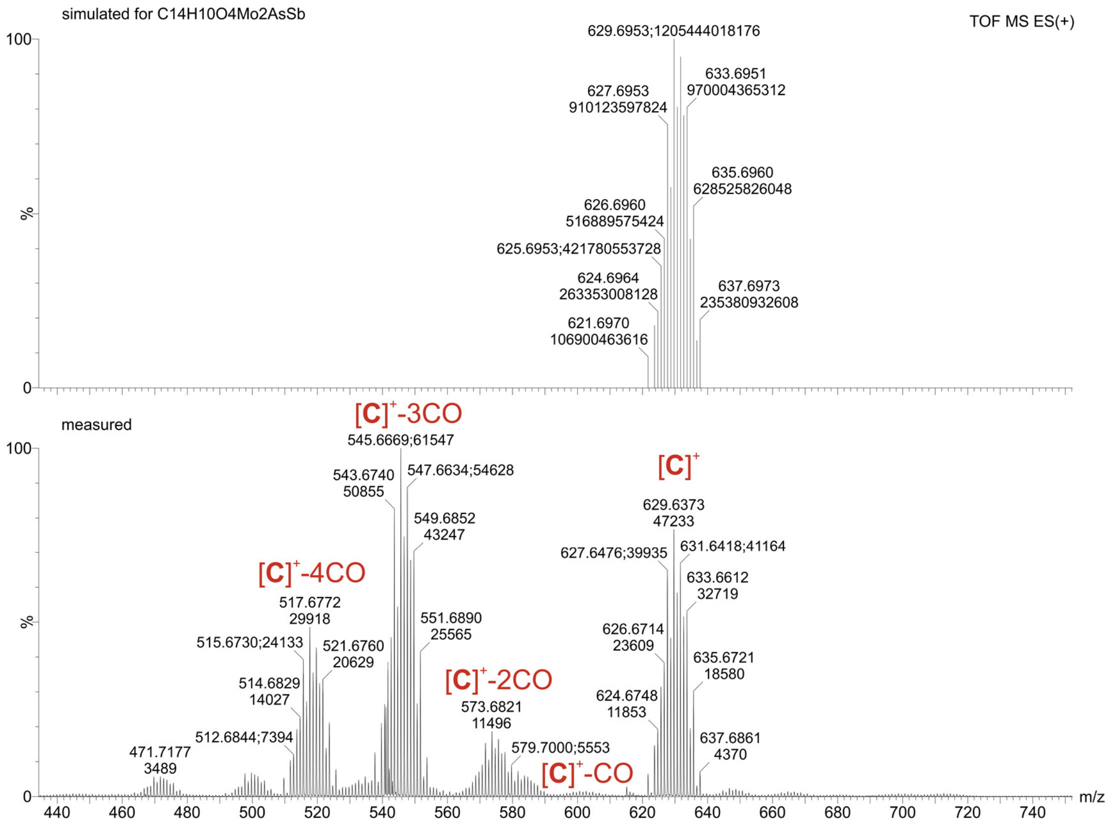

Figure S42: Assignable signals in the ESI(+) MS spectrum of **3a**. Bottom: measured spectrum, top: simulated molecular ion peak [**C**]$^+$.

ESI mass spectrometry of 3b:

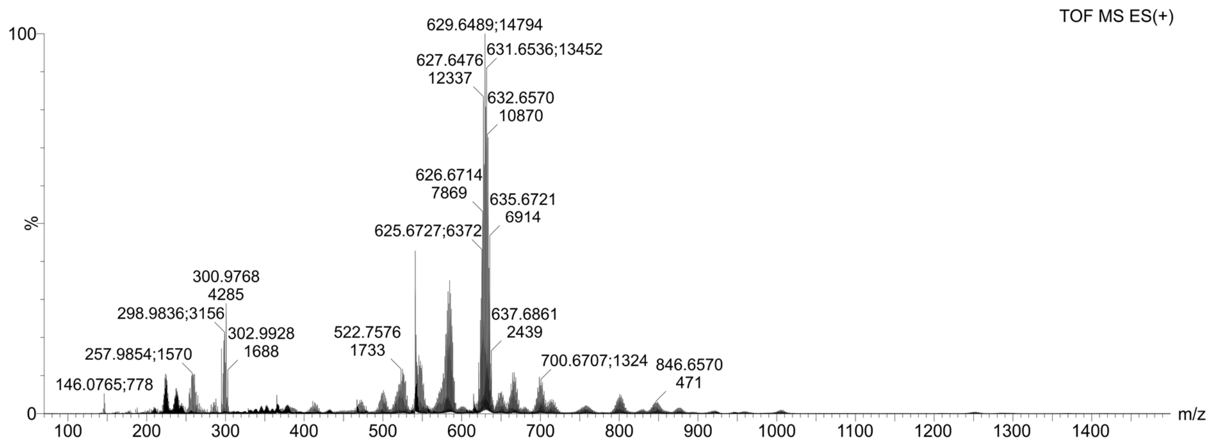

Figure S43: ESI(+) MS spectrum of **3b**.

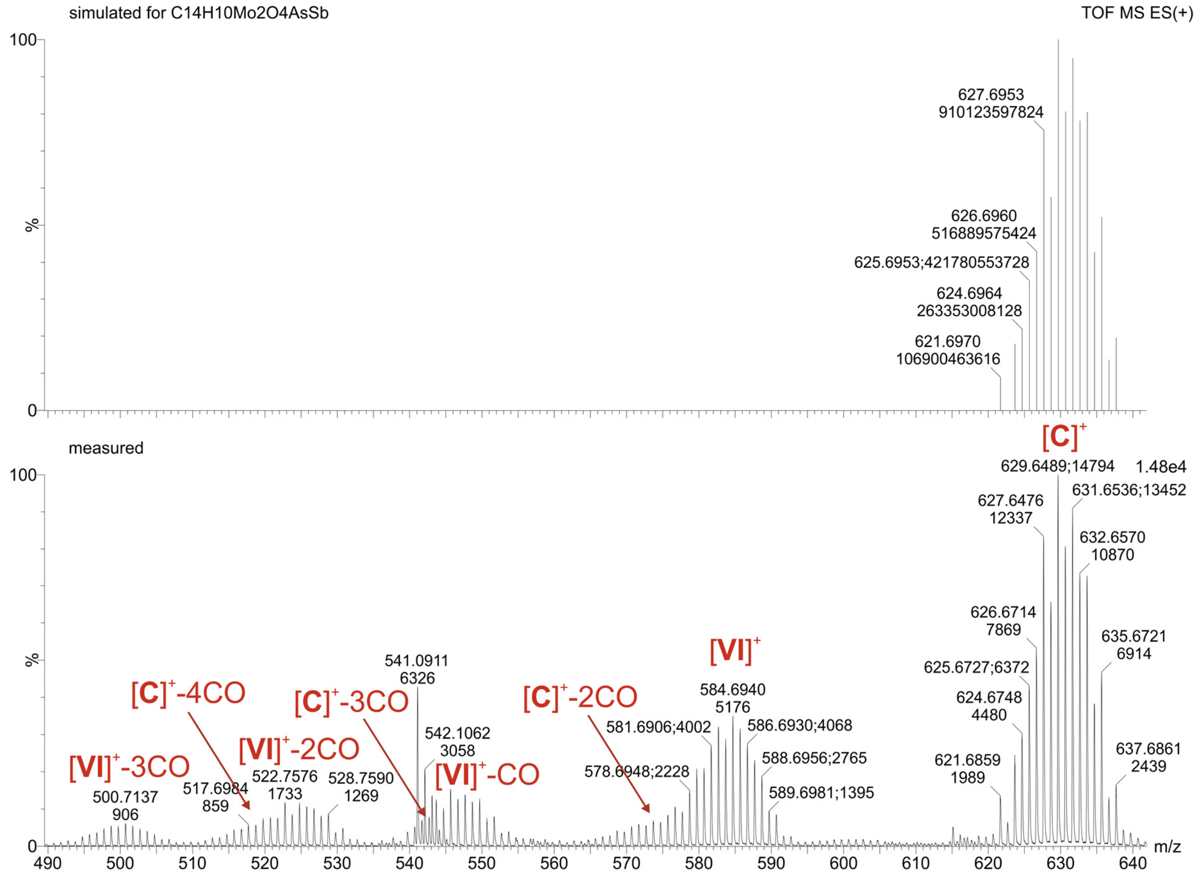

Figure S44: Assignable signals in the ESI(+) MS spectrum of **3b**. Bottom: measured spectrum, top: simulated molecular ion peak of [**C**]$^+$.

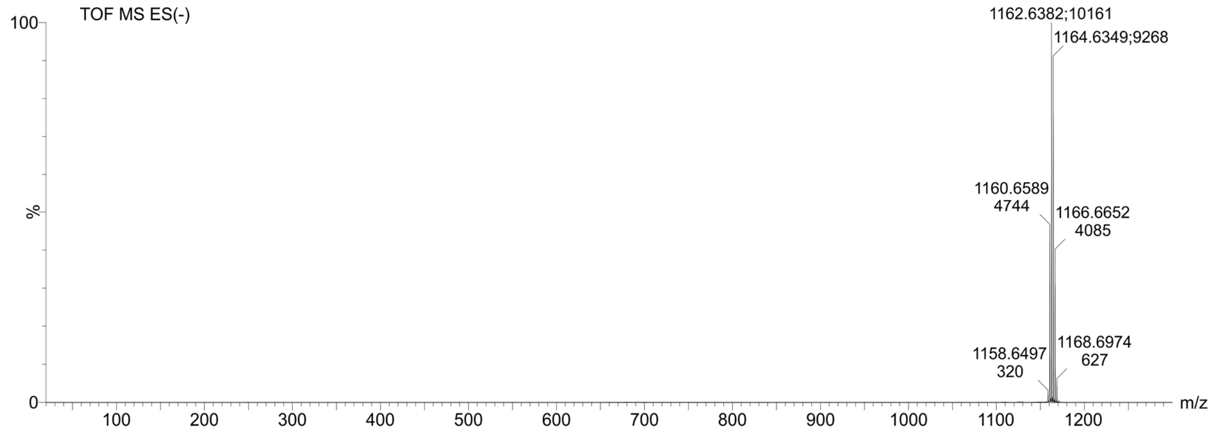

Figure S45: ESI(−) MS spectrum of **3b**.

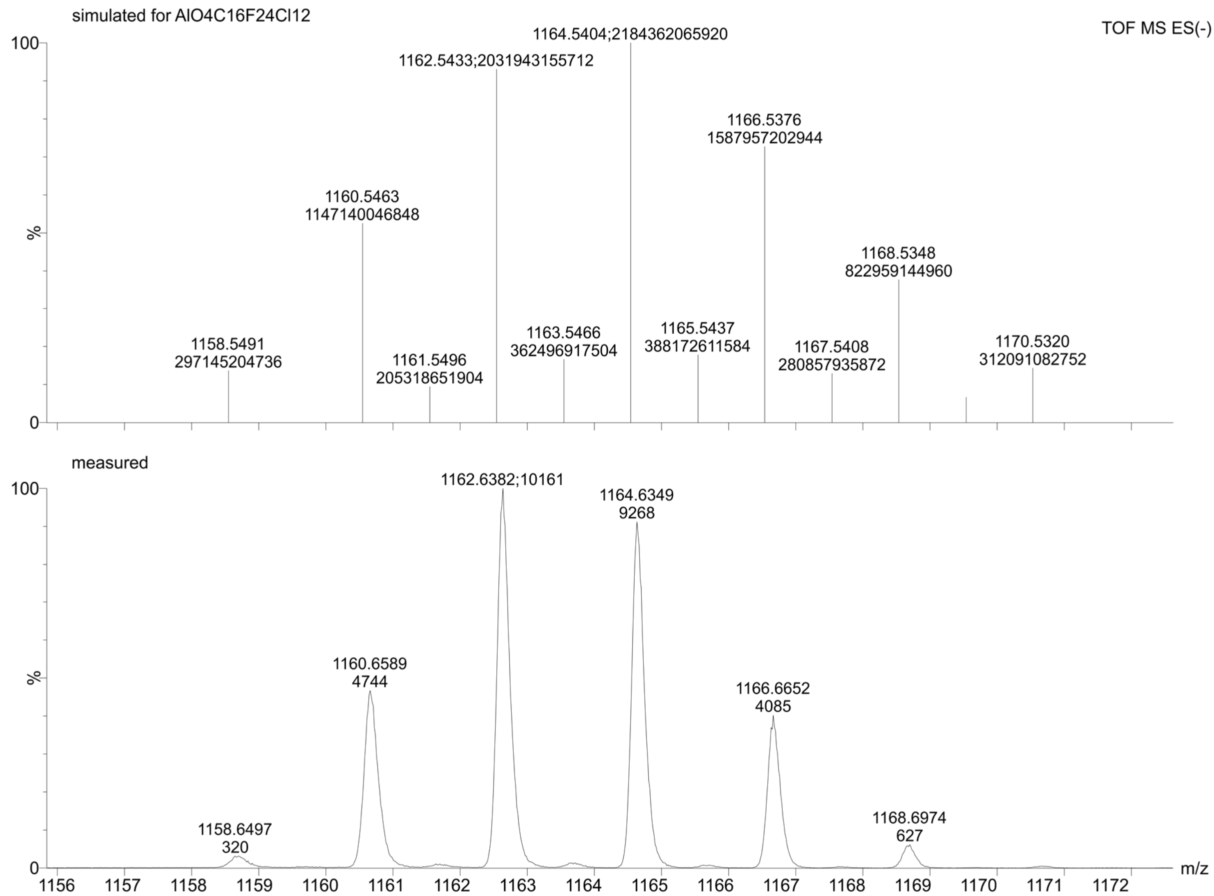

Figure S46: Molecular ion peak of $[TEF^{Cl}]^-$ in the ESI(−) MS spectrum of **3b**. Bottom: measured spectrum, top: simulated spectrum.

5.4.6 EPR spectra

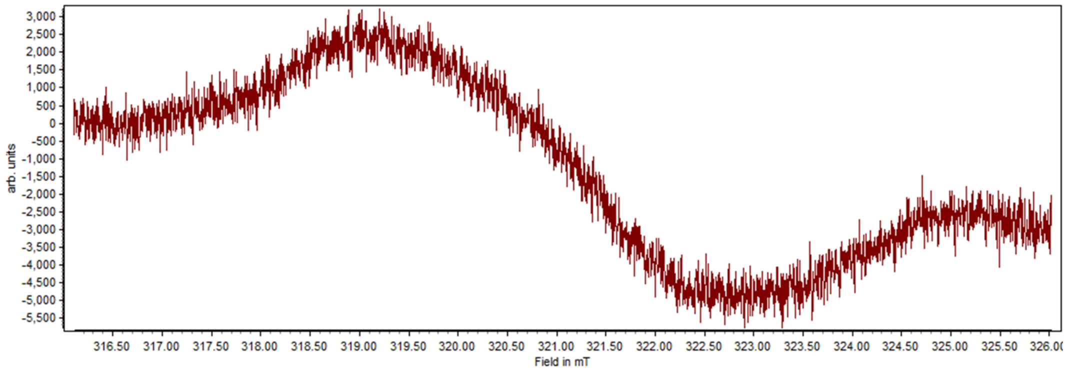

Figure S47: X-Band EPR spectrum of **1** at room temperature showing no signal.

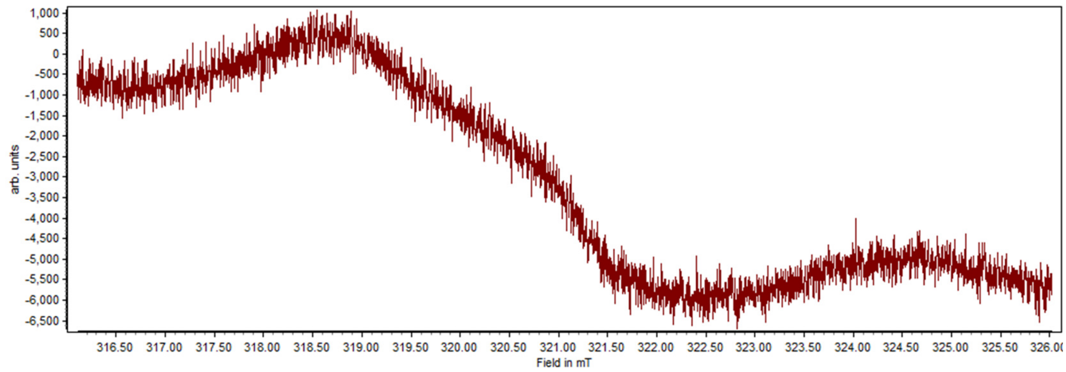

Figure S48: X-Band EPR spectrum of **1** at 77 K showing no signal.

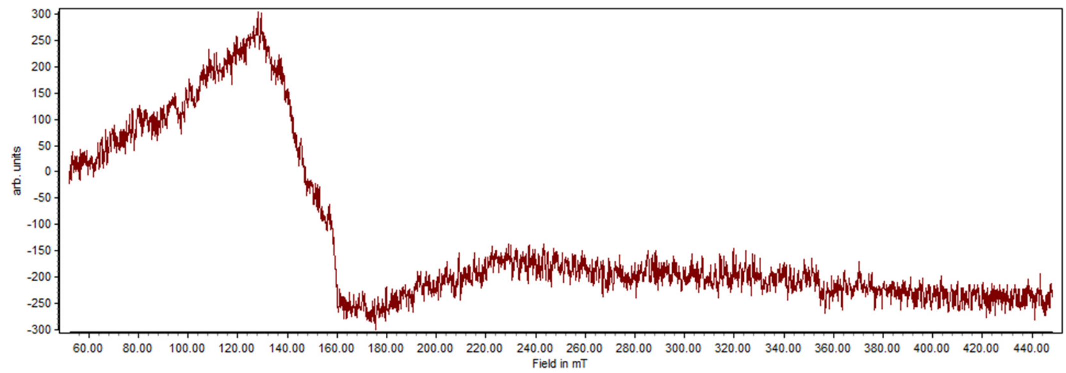

Figure S49: X-Band EPR spectrum of **2** at room temperature showing no signal. The "signal" at ~145 mT arises from the glas measuring apparatus, which was used and contains Fe.

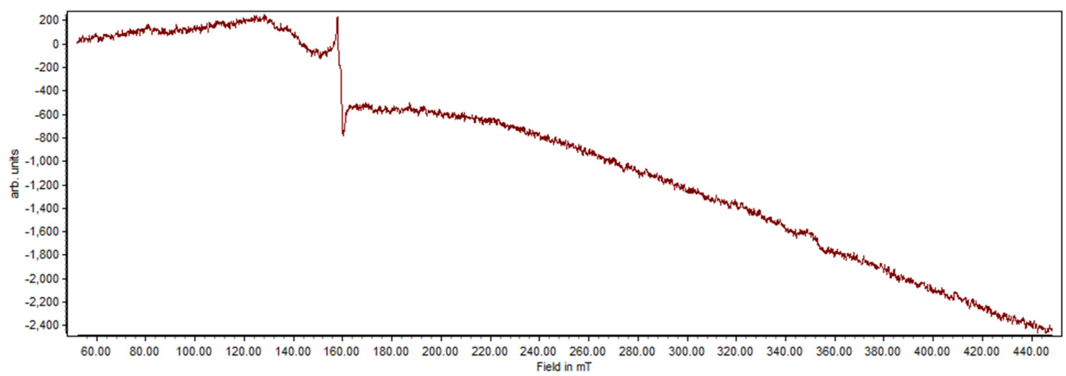

Figure S50: X-Band EPR spectrum of **2** at 77 K showing no signal. The "signal" at ~145 mT arises from the glas measuring apparatus, which was used and contains Fe.

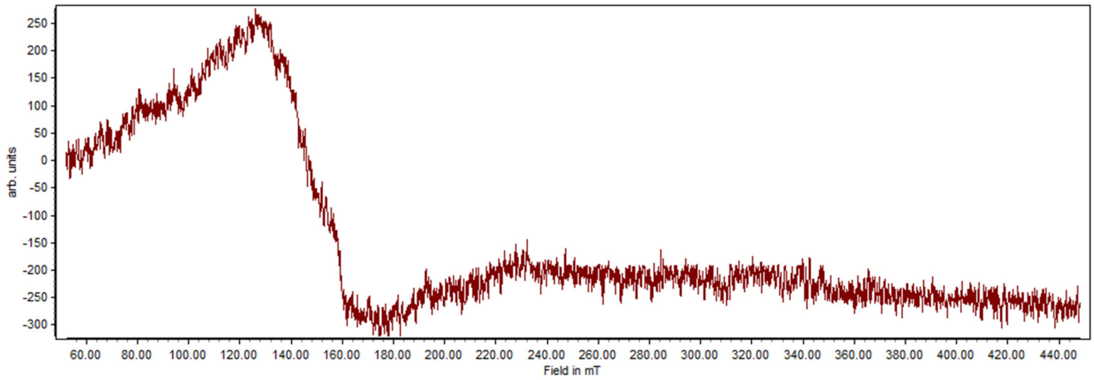

Figure S51: X-Band EPR spectrum of **3a** at room temperature showing no signal. The "signal" at ~145 mT arises from the glas measuring apparatus, which was used and contains Fe.

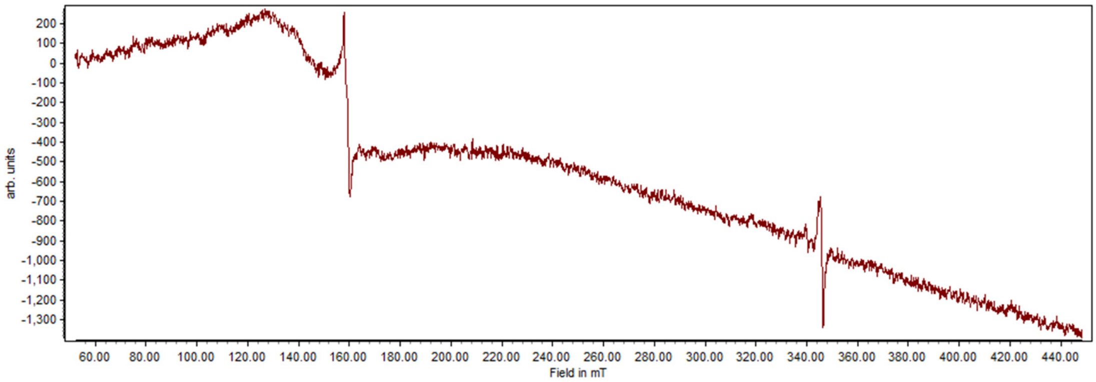

Figure S52: X-Band EPR spectrum of **3a** at 77 K showing a very weak axial signal (g_{iso} = 1.954). The "signal" at ~145 mT arises from the glas measuring apparatus, which was used and contains Fe.

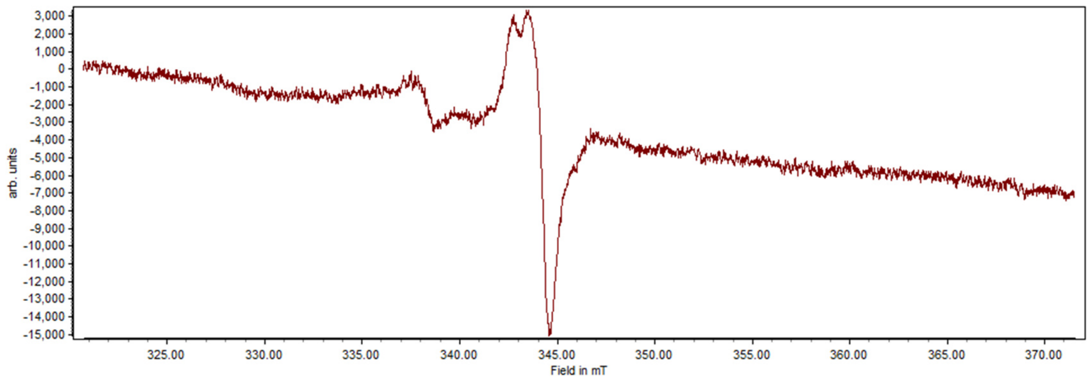

Figure S53: X-Band EPR spectrum of **3a** at 77 K from 320–370 mT showing a very weak axial signal (g_{iso} = 1.954).

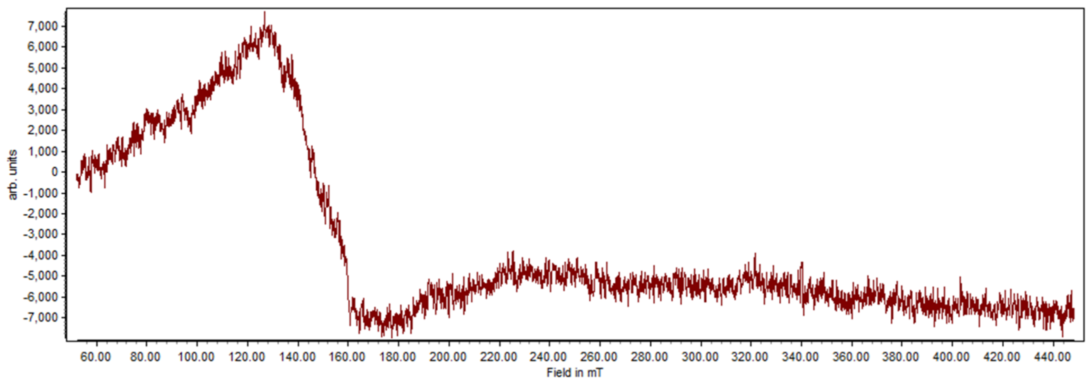

Figure S54: X-Band EPR spectrum of **4a** at room temperature showing no signal. The "signal" at ~145 mT arises from the glas measuring apparatus, which was used and contains Fe.

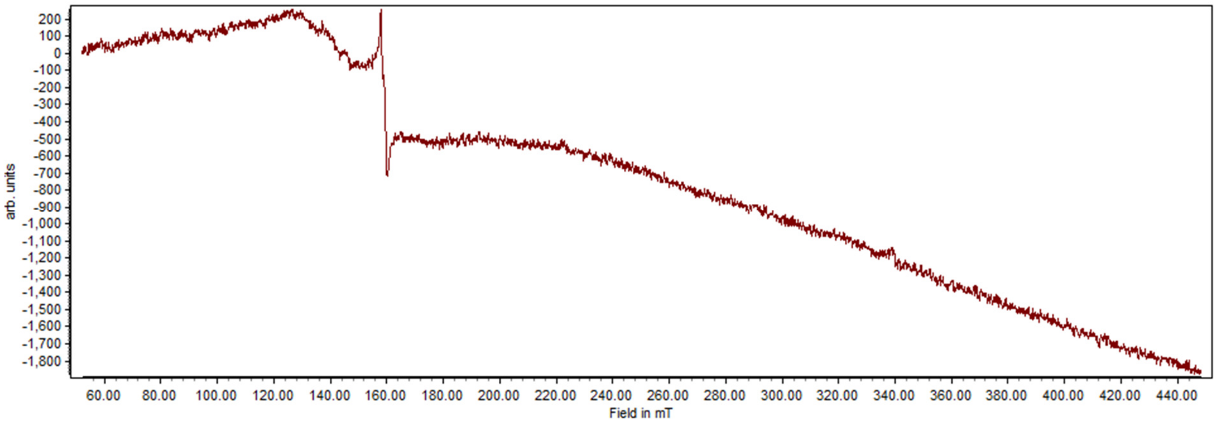

Figure S55: X-Band EPR spectrum of **4a** at 77 K showing no signal. The "signal" at ~145 mT arises from the glas measuring apparatus, which was used and contains Fe.

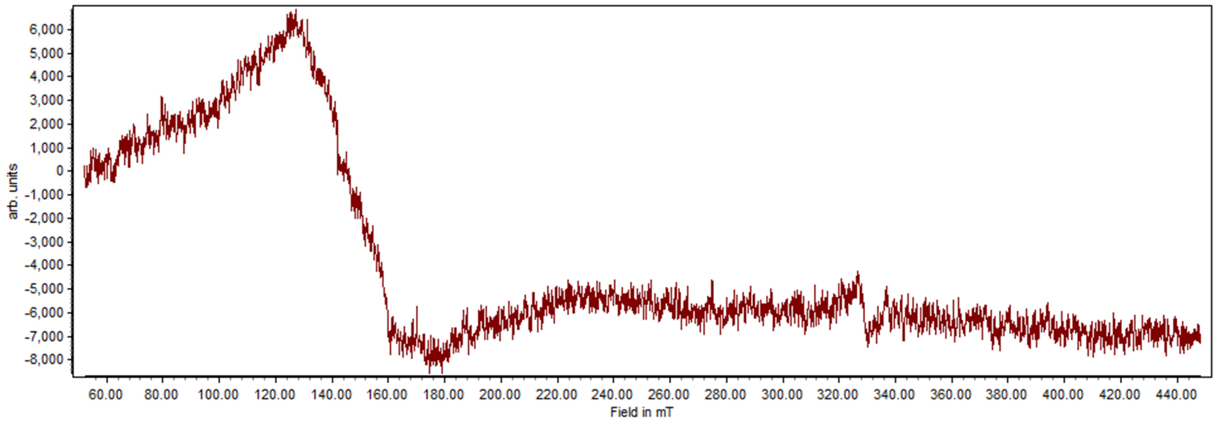

Figure S56: X-Band EPR spectrum of **4b** at room temperature showing no signal. The "signal" at ~145 mT arises from the glas measuring apparatus, which was used and contains Fe.

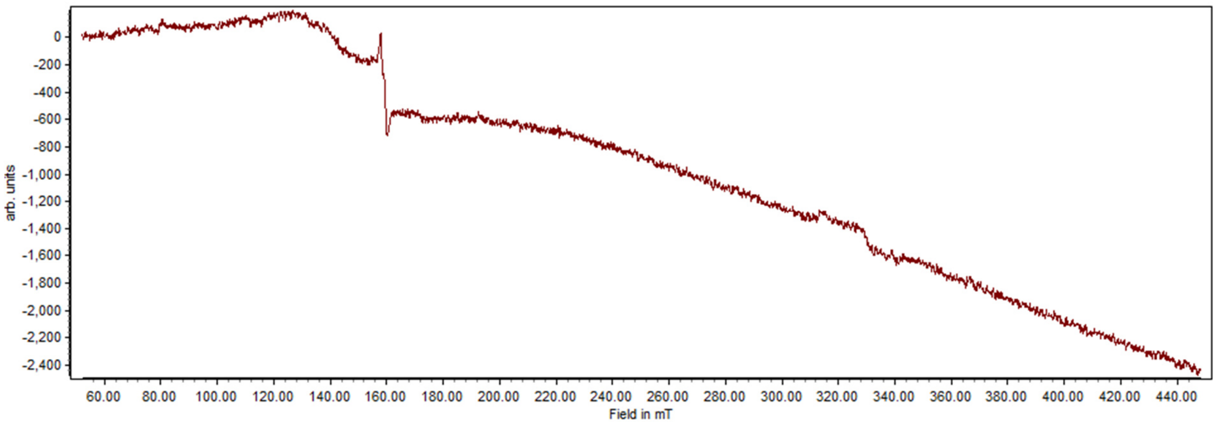

Figure S57: X-Band EPR spectrum of **4b** at 77 K showing no signal. The "signal" at ~145 mT arises from the glas measuring apparatus, which was used and contains Fe.

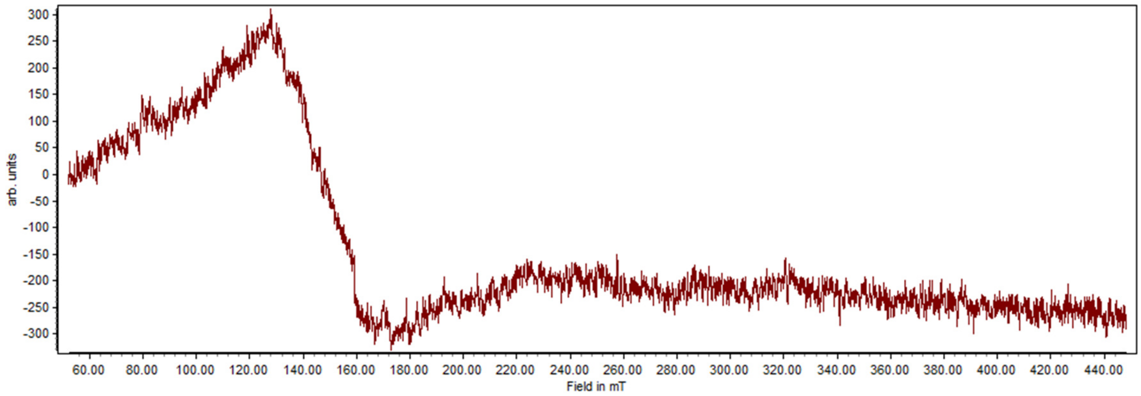

Figure S58: X-Band EPR spectrum of **5** at room temperature showing no signal. The "signal" at ~145 mT arises from the glas measuring apparatus, which was used and contains Fe.

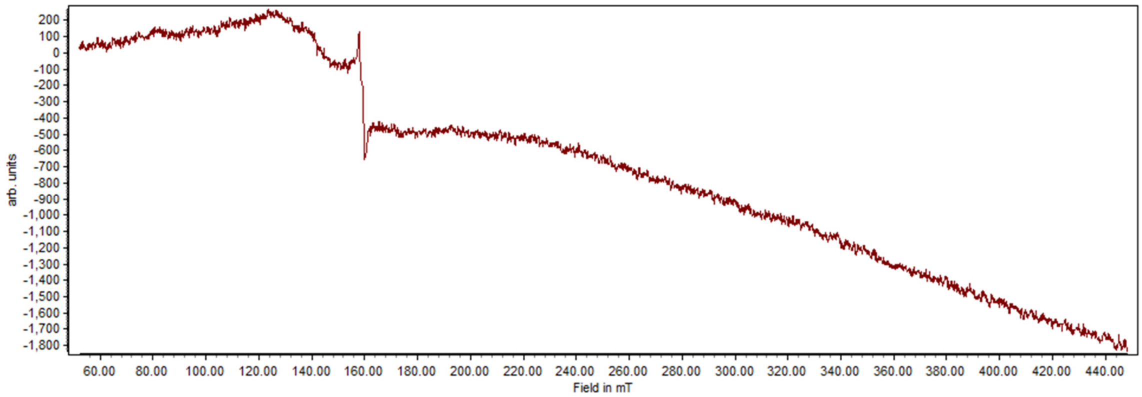

Figure S59: X-Band EPR spectrum of **5** at 77 K showing no signal. The "signal" at ~145 mT arises from the glas measuring apparatus, which was used and contains Fe.

5.4.7 X-ray crystallography

All crystal manipulations were performed under mineral oil. The diffraction experiments were performed at 123 K (if not stated otherwise) either on a Rigaku (former Agilent Technologies or Oxford Diffraction) SuperNova Single Source with an Atlas detector, a Gemini Ultra with an AtlasS2 detector, on a GV50 diffractometer with a TitanS2 detector or on a XtaLAB Synergy R DW system with a HyPix-Arc 150 detector using Cu-K_α, Cu-K_β or Mo-K_α radiation. Crystallographic data together with the details of the experiments are given in Table S1 and Table S2. The cell determination, data reduction and absorption correction for all compounds were performed with the help of the CrysAlis PRO software.[37] All structures were solved by using the programs SHELXT[38] and Olex2.[39] The full-matrix least-squares refinement against F^2 was done using SHELXL[40] and Olex2.[39] If not stated otherwise, all atoms except hydrogen atoms were refined anisotropically. The H atoms were calculated geometrically and a riding model was used during the refinement process.

CCDC-2105248 (**1**), CCDC-2105249 (**3a**), CCDC-2105250 (**3b**), CCDC-2105251 (**4a**), CCDC-2105252 (**4b**) and CCDC-2105253 (**5**), contain the supplementary crystallographic data for this paper. These data can be obtained free of charge at www.ccdc.cam.ac.uk/conts/retrieving.html (or from the Cambridge Crystallographic Data Centre, 12 Union Road, Cambridge CB2 1EZ, UK; Fax: + 44-1223-336-033; e-mail: deposit@ccdc.cam.ac.uk).

Table S1: Crystallographic details for the compounds **1**, **2**, **3a** and **4a**.

	1	**2**	**3a**	**4a**
formula	$C_{60}H_{20}Al_2As_2F_{72}Mo_4O_{16}P_2$	$C_{60}H_{20}Al_2F_{72}Mo_4O_{16}P_2Sb_2$	$C_{60}H_{20}Al_2F_{72}Mo_4O_{16}As_2Sb_2$	$C_{60.1}H_{19.2}Al_2As_{2.12}Bi_{1.88}Cl_{0.2}F_{72}Mo_4O_{16}$
weight [g·mol^{-1}]	3014.26	3277.77	3195.82	3361.68
Temperature [K]	123.0(1)	123.0(1)	100.01(10)	123.0(1)
crystal system	monoclinic	monoclinic	orthorhombic	triclinic
space group	$P2_1/n$	$P2_1/m$	$Pbca$	$P\bar{1}$
a [Å]	15.48296(15)	16.5312(16)	27.8964(2)	14.9100(3)
b [Å]	21.4711(2)	14.7868(11)	22.20040(10)	15.9359(6)
c [Å]	26.9785(3)	20.505(2)	29.7016(2)	20.4158(7)
α [°]	90	90	90	80.965(3)
β [°]	90.8706(9)	105.272(12)	90	82.393(2)
γ [°]	90	90	90	75.244(2)
Volume [Å^3]	8967.59(15)	4835.3(8)	18394.5.5(2)	4611.0(3)
Z	4	4	8	2
ρ_{calc} [g·cm^{-3}]	2.233		2.308	2.421
μ [mm^{-1}]	7.820		2.047	5.088
F(000)	5784.0		12144	3158
crystal size [mm^3]	0.260 × 0.144 × 0.100		0.174 × 0.119 × 0.109	0.606 × 0.135 × 0.13
diffractometer	SuperNova	GV50	XtaLAB Synergy R, DW system	Gemini Ultra
absorption correction	gaussian		gaussian	gaussian
T_{min} / T_{max}	0.349 / 0.602		0.727 / 1.000	0.354 / 0.760
radiation [Å]	Cu-Kα (λ = 1.54184)	Cu-Kα (λ = 1.54184)	Mo-Kα (λ = 0.71073)	Mo-Kα (λ = 0.71073)
2Θ range [°]	6.996 to 147.820		3.670 to 65.154	6.732 to 61.016
completeness [%]	99.3		100	99.2
reflns collected / unique	42829 / 17600		437712 / 33485	48635 / 27938
R_{int} / R_{sigma}	0.0239 / 0.0264		0.0704 / 0.0288	0.0396 / 0.0744
data / restraints / parameters	15039 / 587 / 1896		27529 / 1404 / 2548	20441 / 1724 / 2440
GOF on F^2	1.063		1.031	1.013
R_1 / wR_2 [$I \geq 2\sigma(I)$]	0.0349 / 0.0964		0.0325 / 0.0786	0.0437 / 0.0814
R_1 / wR_2 [all data]	0.0408 / 0.0985		0.0436 / 0.0831	0.0721 / 0.0920
max / min $\Delta\rho$ [e·Å^{-3}]	1.851 / –0.738		1.461 / –0.784	1.387 / –1.053
Identification code	LD106_new_abs_error_model_off	LD202	LD461_oP_abs_gaus	CR500_Moa

Table S2: Crystallographic details for the compounds **5**, **3b** and **4b**.

	5	**3b**	**4b**
formula	$C_{60}H_{20}Al_2Bi_2F_{72}Mo_4O_{16}Sb_2$	$C_{60}H_{20}Al_2As_2Cl_{24}F_{48}Mo_4O_{16}Sb_2$	$C_{62}H_{24}O_{16}F_{48}Al_2Cl_{28}As_{2.07}Mo_4Bi_{1.93}$
weight [g·mol^{-1}]	3463.94	3590.62	3925.55
Temperature [K]	110.0(1)	123.0(1)	123.0(1)
crystal system	monoclinic	monoclinic	monoclinic
space group	$P2_1/n$	$P2_1/c$	$P2_1/n$
a [Å]	15.58570(10)	20.6398(2)	13.3028(2)
b [Å]	22.6461(2)	23.2138(2)	27.6708(4)
c [Å]	25.9891(2)	23.1270(2)	14.6789(3)
α [°]	90	90	90
β [°]	90.5190(10)	112.9690(10)	96.234(2)
γ [°]	90	90	90
Volume [Å^3]	9172.61(12)	10202.27(17)	5371.34(16)
Z	4	4	2
ρ_{calc} [g·cm^{-3}]	2.508	2.338	2.427
μ [mm^{-1}]	13.899	16.089	5.090
F(000)	6472.0	6840.0	3709.0
crystal size [mm^3]	0.373 × 0.109 × 0.086	0.275 × 0.122 × 0.11	0.984 × 0.237 × 0.128
diffractometer	GV50	GV50	SuperNova
absorption correction	gaussian	gaussian	gaussian
T_{min} / T_{max}	0.079 / 0.642	0.477 / 0.719	0.106 / 1.000
radiation [Å]	Cu-Kβ (λ = 1.39222)	Cu-Kα (λ = 1.54184)	Mo-Kα (λ = 0.71073)
2Θ range [°]	4.674 to 148.256	7.616 to 148.062	5.89 to 69.18
completeness [%]	99.6	99.6	99.8
reflns collected / unique	84463 / 24730	58041 / 20043	51984 / 21333
R_{int} / R_{sigma}	0.0457 / 0.0333	0.0525 / 0.0453	0.0391 / 0.0513
data / restraints / parameters	23965 / 656 / 1694	18107 / 587 / 1675	18316 / 0 / 743
GOF on F^2	1.165	1.033	1.068
R_1 / wR_2 [$I \geq 2\sigma(I)$]	0.0577 / 0.1524	0.0458 / 0.1181	0.0378 / 0.0816
R_1 / wR_2 [all data]	0.0589 / 0.1531	0.0523 / 0.1233	0.0484 / 0.0856
max / min $\Delta\rho$ [e·Å^{-3}]	2.412 / −1.793	1.903 / −1.166	1.920 / −1.979
Identification code	LD364_mP_abs_gaus	LD196_CR014_abs	LD448_abs

Refinement details for 1

Compound **1** can be regarded as isostructural to compound **2**, **IX** and **X**. It crystallizes in the monoclinic space group $P2_1/n$ with one dicationic complex exhibiting a central AsPPAs zigzag chain and two independent WCAs $[TEF]^-$ in the asymmetric unit. The refinement of the cationic part could be performed without any difficulty. For one $[TEF]^-$ anion (including Al1) a positional disorder for the fragment $Al\{OC(CF_3)_3\}_2$ is observed with a ratio of 90:10. Due to the low occupancy of the minor part was only the Al11 atom anisotropically refined and the U_{iso} of the O, C and F atoms was set to 0.3. The other $[TEF]^-$ anion (including Al2) shows a rotational or positional disorder of the -$OC(CF_3)_3$ groups with ratios of 88:12, 86:14, 81:19 and 60:40, respectively. The disordered groups were partially restrained with DFIX, SADI and SIMU commands during the refinement process.

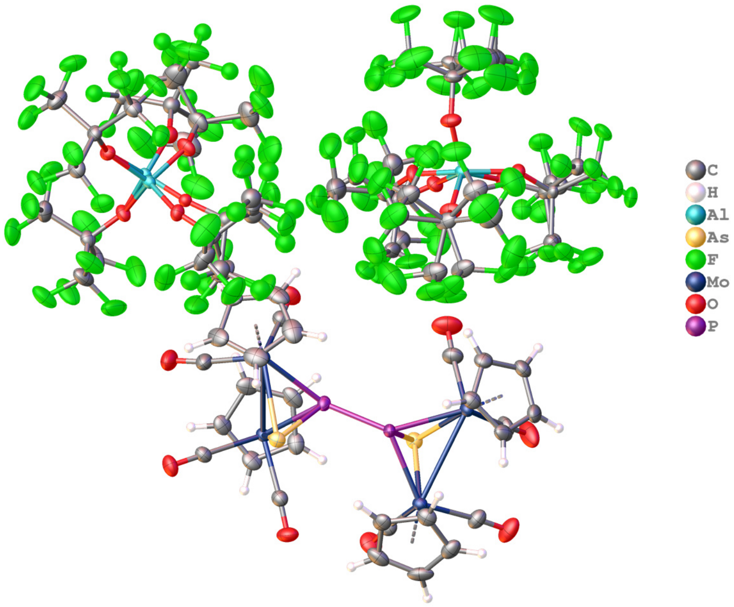

Figure S60: Molecular structure of **1**. The asymmetric unit is shown containing one dication and two $[TEF]^-$ anions, which both show disorder of several –$OC(CF_3)_3$ groups.

Refinement details for 2

The X-ray dataset of **2** is very weak and, therefore, a proper refinement of the molecular structure was not possible. Only the heavy atom framework of the dicationic part can be identified, which suggests in combination with the spectroscopical data of **2** (*vide supra*) and the unit cell parameters that **2** also forms a dicationic SbPPSb zigzag chain upon P–P bond formation being isostructural to **1**, **IX** and **X**. The heavy atom framework of **2** is shown in Figure S61.

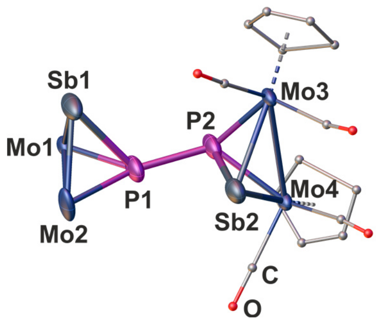

Figure S61: Heavy atom framework of the dicationic part of **2**. H atoms as well as the Cp and CO ligands of one Mo_2PSb unit are omitted for clarity. Additionally, Cp and CO ligands are drawn as small spheres.

Refinement details for 3a

Compound **3a** crystallizes in the orthorhombic space group *Pbca* with one dication exhibiting a central AsSbSbAs chain/cage and two independent WCAs $[TEF]^-$ in the asymmetric unit. The cationic unit shows a positional disorder of the $(Mo_2AsSB)_2$ unit with a ratio of 80:20. For one $[TEF]^-$ anion (including Al1) a positional disorder for three -$OC(CF_3)_3$ groups is observed with a ratio of 60:40, 51:49 and 50:50, respectively. The other $[TEF]^-$ anion (including Al2) shows a positional disorder of two -$OC(CF_3)_3$ groups over two positions with a ratio of 70:30 and of two -$OC(CF_3)_3$ group over three positions with ratios of 50:25:25 and 47:29:24, respectively. The disordered groups were partially restrained with DFIX, SADI and SIMU commands during the refinement process. An interesting feature of the molecular structure in **3a** is the arrangement of the Cp substituents. While the arrangement at one of the Mo_2AsSb units resembles the respective arrangement of chain-type structures (see Figure 2b (chapter 5.2), right Mo_2AsSb unit), like in **1**, the arrangement at the other Mo_2AsSb unit is similar to those in cage-type structures (see Figure 2b (chapter 5.2), left Mo_2AsSb unit), like, *e.g.*, in **5**. This again shows that the structure of **3a** represents an intermediate stage between the chain-type structures in **1**, **2**, **VI** and **VII**, and the cage-type structures in **5**, **VIII** and **IX**.

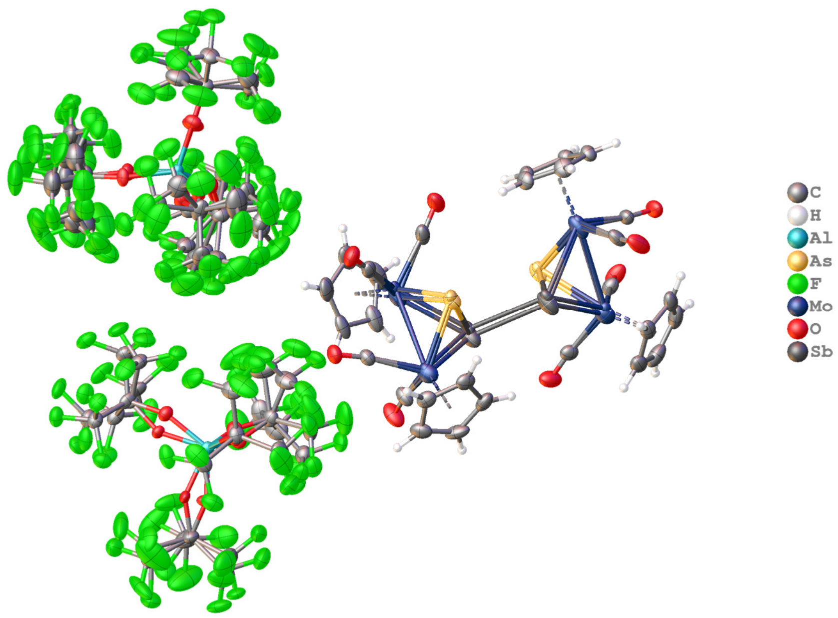

Figure S62: Molecular structure of **3a**. The asymmetric unit is shown containing one disordered dication and two disordered $[TEF]^-$ anions.

Refinement details for 3b

Compound **3b** crystallizes in the monoclinic space group $P2_1/c$ with one dication exhibiting a central AsSbAsSb cycle and two independent WCAs $[TEF^{Cl}]^-$ in the asymmetric unit. The cationic unit shows a disorder of the As_2Sb_2 cycle in a ratio of 84:16. Further shows one of the $[TEF^{Cl}]^-$ anions (including Al1) a rotational and a positional disorder of two -$OC(CF_3)_2(CCl_3)$ groups in a ratio of 85:15. The second $[TEF^{Cl}]^-$ anion (including Al2) shows a disorder of the two oxygen atoms O14 and O15 in ratios of 60:40 and 50:50, respectively. Further is the Cl atom Cl21 disordered over two positions with the ratio 70:30. The disordered groups were partially restrained with SADI, ISOR and SIMU commands during the refinement process.

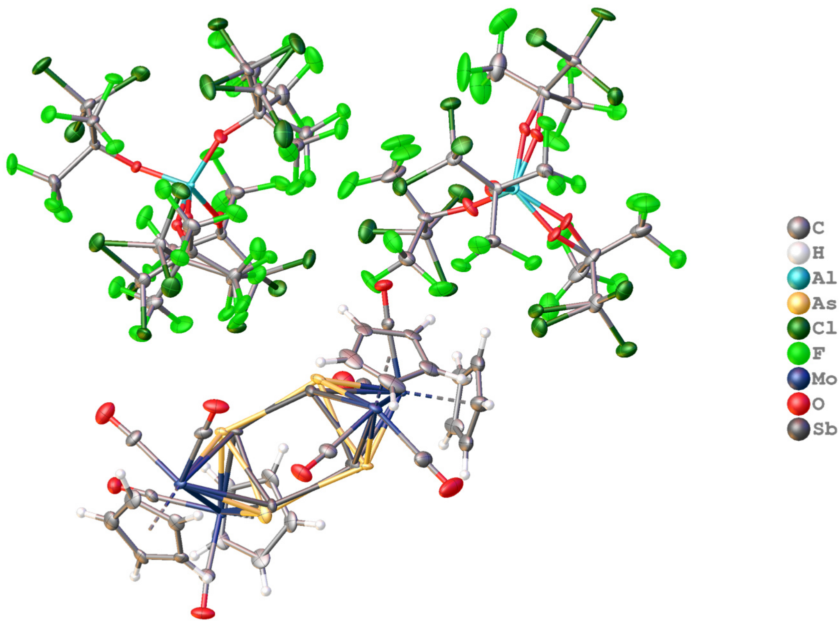

Figure S63: Molecular structure of **3b**. The asymmetric unit is shown containing one disordered dication and two disordered $[TEF^{Cl}]^-$ anions.

Refinement details for 4a

Compound **4a** crystallizes in the triclinic space group $P\bar{1}$ with two half dications exhibiting a central AsBiBiAs ring and two independent WCAs $[TEF]^-$ as well as 0.1 molecules CH_2Cl_2 in the asymmetric unit. One of these dications co-crystallizes with the dicationic As_4 chain-type compound **X** in a ratio of 88:12. One Cp ligand exhibits rotational disorder. One $[TEF]^-$ anion (including Al2) shows rotational and positional disorder of all four perfluorinated *tert*-butoxy groups in a ratio of 50:50, 50:50, 63:37 and 58:42. The second $[TEF]^-$ anion (including Al1) shows also a rotational and positional disorder of all four -$OC(CF_3)_3$ groups, whereat three of these groups are disordered over two positions (88:12; 86:14; 74:26) and the third one shows a disorder over three positions (55:31:14). The disordered groups were partially restrained with DFIX, SADI and SIMU commands during the refinement process.

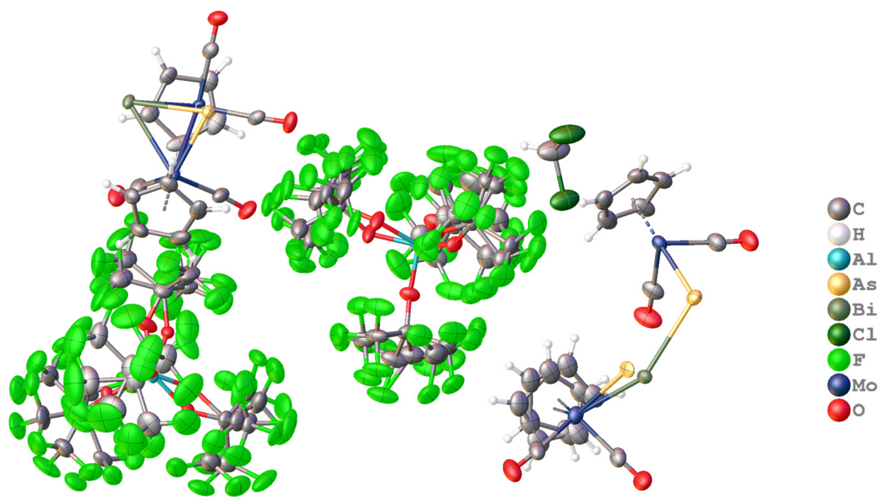

Figure S64: Molecular structure of **4a**. The asymmetric unit is shown containing two half molecules of the dication, two disordered $[TEF]^-$ anions and one solvent molecule CH_2Cl_2. One of the dications co-crystallizes with the dicationic As_4 chain-type compound **X** in a ratio of 88:12 and exhibits rotational disorder of one of its Cp ligands.

Refinement details for 4b

Compound **4b** crystallizes in the monoclinic space group $P2_1/n$ with one half dication exhibiting a central AsBiBiAs cycle, one WCA $[TEF^{Cl}]^-$ and one solvent molecule CH_2Cl_2 in the asymmetric unit. The cyclic dication $[\{CpMo(CO)_2\}_2(\mu,\eta^2{:}\eta^2\text{-BiAs})]_2^{2+}$ co-crystallizes with the dicationic As_4 chain-type compound **X** in a ratio of 97:3. The anion $[TEF^{Cl}]^-$ shows no sign of disorder.

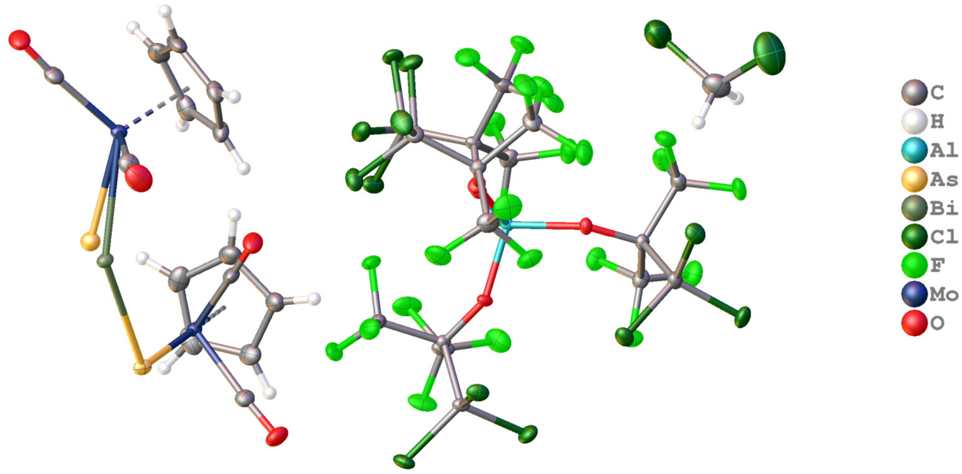

Figure S65: Molecular structure of **4b**. The asymmetric unit is shown containing one half dication, one $[TEF^{Cl}]^-$ anion and one solvent molecule CH_2Cl_2. The dication co-crystalizes with the dicationic As_4 chain **X** in a ratio of 97:3.

Refinement details for 5

Compound **5** crystallizes in the monoclinic space group $P2_1/n$ with one dication exhibiting a central BiSbSbBi cage and two independent WCAs $[TEF]^-$ in the asymmetric unit. The dication $[\{CpMo(CO)_2\}_2(\mu,\eta^2{:}\eta^2\text{-BiSb})]_2^{2+}$ features a disorder over two positions of both BiSb dumbbells (76:24) and one Cp ligand (59:41). It could, however, also be a co-crystallization with the dicationic Sb_4 and/or Bi_4 cages **XI** and **XII**, respectively, which were also detected in the NMR spectra (*vide supra*). One $[TEF]^-$ anion (including Al2) shows rotational disorder of two perfluorinated *tert*-butoxy groups in a ratio of 52:48 and 72:28. The disordered groups were partially restrained with SADI and SIMU commands during the refinement process.

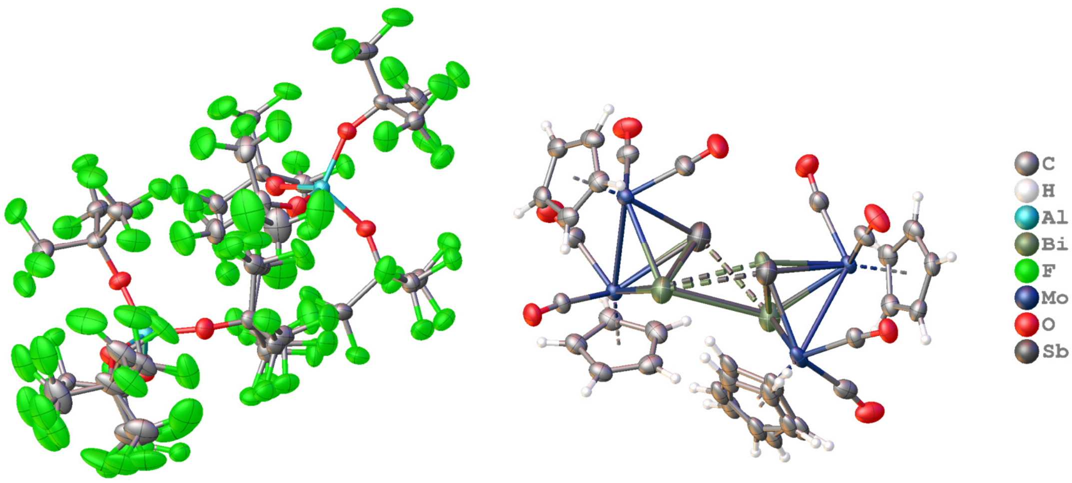

Figure S66: Molecular structure of **5**. The asymmetric unit is shown containing one disordered dication and two disordered $[TEF]^-$ anions.

5.4.8 Details of DFT Calculations

The DFT calculations have been performed with the ORCA program.[41] The geometries have been optimized with the TPSSh[42] functional together with the def2-TZVP[43] basis set. The starting point for the geometry optimizations were the coordinates obtained from the X-ray diffractions. To speed up the calculations in a first step the geometries has been optimized at the BP86[44]/def2-SVP level, than at the BP86/def2-TZVP, TPSSh/def2-TZVP (using the RIJCOSX[45] approximation) and finally at the TPSSh/def2-TZVP level (the latter without the RIJCOSX approximation). The dispersion effects have been incorporated by using the charge dependent atom-pairwise dispersion correction model (D4).[46] For the solvent effects has been accounted *via* the Conductor-like Polarizable Continuum Model (CPCM)[47] as implemented in Orca, using the dielectric constant of dichloromethane. The atomic orbital contribution to the frontier molecular orbitals of compounds **A**–**E** has been determined at the B3LYP[44a,48]/def2-TZVP level using Loewdin orbital population analysis. For the calculation of the reaction energies, the total SCF energies (TPSSh/def2-TZVP) have been used without further corrections.

Table S3: Total SCF energies calculated at the TPSSh/def2-TZVP level.

Compound	Total energy (ha)
$[(CpMo(CO)_2\}_2(PAs)]^+$ (**A**$^+$)	-3554.5933
$[(CpMo(CO)_2\}_2(PSb)]^+$ (**B**$^+$)	-1558.9503
$[(CpMo(CO)_2\}_2(PBi)]^+$	-1533.3556
$[(CpMo(CO)_2\}_2(AsSb)]^+$ (**C**$^+$)	-3453.4141
$[(CpMo(CO)_2\}_2(AsBi)]^+$ (**D**$^+$)	-3427.8200
$[(CpMo(CO)_2\}_2(SbBi)]^+$ (**E**$^+$)	-1432.1813
$[(CpMo(CO)_2\}_2(PAs)]_2^{2+}$ (**1**)	-7109.2427
$[(CpMo(CO)_2\}_2(PSb)]_2^{2+}$ (**2**)	-3117.9608
$[(CpMo(CO)_2\}_2(AsSb)]_2^{2+}$ (**3a**)	-6906.8826
$[(CpMo(CO)_2\}_2(AsBi)]_2^{2+}$ (**4a**)	-6855.6950
$[(CpMo(CO)_2\}_2(SbBi)]_2^{2+}$ (**5**)	-2864.4257

Table S4: Mulliken spin densities calculated at the TPSSh/def2-TZVP level.

$[(CpMo(CO)_2\}_2(PAs)]^+$ (**A**$^+$)			
As	P	Mo	Mo
0.022	0.016	0.423	0.397
$[(CpMo(CO)_2\}_2(PSb)]^+$ (**B**$^+$)			
Sb	P	Mo	Mo
0.157	0.138	0.238	0.402
$[(CpMo(CO)_2\}_2(PBi)]^+$			
Bi	P	Mo	Mo
0.206	0.155	0.211	0.370
$[(CpMo(CO)_2\}_2(AsSb)]^+$ (**C**$^+$)			
Sb	As	Mo	Mo
0.167	0.154	0.254	0.367
$[(CpMo(CO)_2\}_2(AsBi)]^+$ (**D**$^+$)			
Bi	As	Mo	Mo
0.2133	0.1724	0.22449	0.3381
$[(CpMo(CO)_2\}_2(SbBi)]^+$ (**E**$^+$)			
Bi	Sb	Mo	Mo
0.257	0.226	0.247	0.231

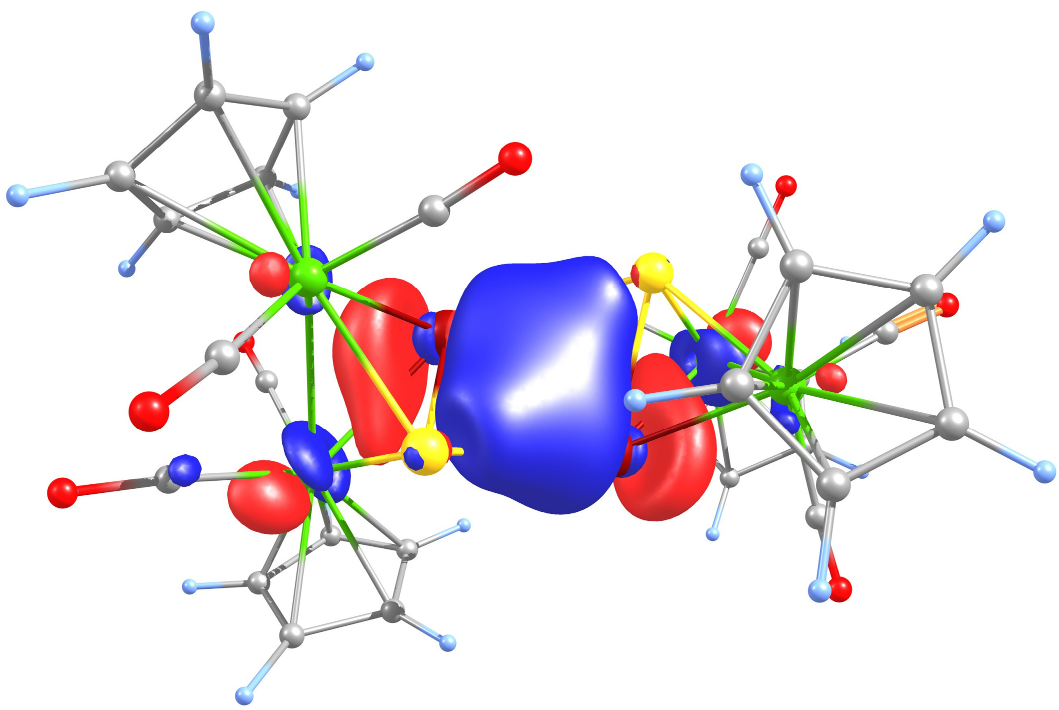

Figure S67: Intrinsic bonding orbital[49] representing a 2e4c bond in $[(CpMo(CO)_2\}_2(AsSb)]_2^{2+}$ (**3a**) (TPSSh/def2-TZVP level).

Table S5: Cartesian coordinates of the optimized geometry of $[(CpMo(CO)_2)_2(PAs)]^+$ (**A**$^+$) (TPSSh/def2-TZVP level).

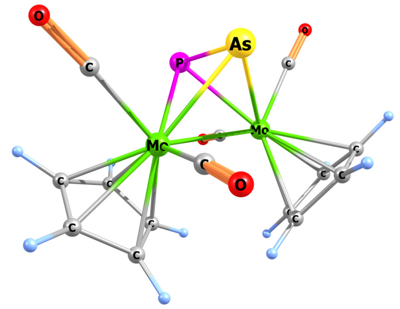

Atom	X	Y	Z
As	-0.610966	-2.460618	-0.910819
P	-1.738249	-1.693525	0.839316
Mo	0.696782	-1.060954	0.887756
Mo	-1.269650	0.067632	-0.902140
C	-0.736118	2.029106	0.277819
H	0.093540	2.139065	0.955724
C	-2.868398	1.720693	-0.520259
H	-3.926207	1.510736	-0.564317
C	-2.043460	2.102696	-1.619976
H	-2.369461	2.250644	-2.637558
C	-0.721155	2.298408	-1.118548
H	0.127950	2.630745	-1.695596
C	-2.064790	1.670979	0.645800
H	-2.406099	1.417388	1.637066
C	-2.895926	-0.819607	-1.669453
C	-0.311624	-0.233474	-2.647801
O	-3.854636	-1.264780	-2.109284
O	0.226998	-0.334750	-3.656166
C	2.141380	0.373218	-0.284312
H	1.825427	1.140439	-0.971111
C	2.931888	-1.621741	0.538610
H	3.279795	-2.641984	0.593749
C	2.836340	-0.709105	1.630432
H	3.117111	-0.908581	2.652686
C	2.348660	0.529899	1.114140
H	2.205649	1.435221	1.683624
C	2.502476	-0.958189	-0.638294
H	2.470953	-1.385225	-1.628248
C	0.714301	-2.901218	1.687443
C	-0.054321	-0.389476	2.633019
O	0.784372	-3.942300	2.157768
O	-0.432561	0.008657	3.638929

Selected Mayer bond orders larger than 0.100:

B (0-As, 1-P): 1.0872 B (0-As, 2-Mo): 0.8196 B (0-As, 3-Mo): 0.8466 B (1-P, 2-Mo): 0.8847
B (1-P, 3-Mo): 0.8635 B (2-Mo, 3-Mo): 0.5894

Table S6: Cartesian coordinates of the optimized geometry of $[(CpMo(CO)_2)_2(PSb)]^+$ (**B**$^+$) (TPSSh/def2-TZVP level).

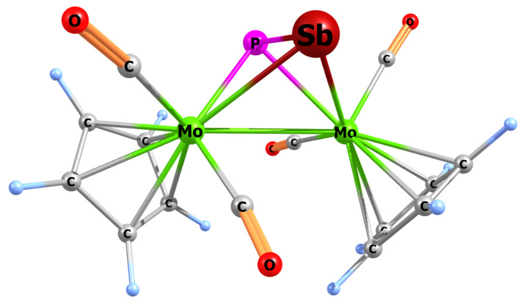

Atom	X	Y	Z
Sb	-0.646814	-2.509003	-0.993646
P	-1.626806	-1.422281	1.012484
Mo	0.854833	-1.113182	0.836797
Mo	-1.467061	0.156972	-0.851129
C	-1.161050	2.203875	0.262654
H	-0.280476	2.439496	0.837805
C	-3.276506	1.508541	-0.329638
H	-4.278372	1.110190	-0.283577
C	-2.640350	2.050167	-1.490277
H	-3.077465	2.133987	-2.473282
C	-1.340505	2.478097	-1.119550
H	-0.612742	2.934229	-1.772867
C	-2.362048	1.606572	0.752508
H	-2.558429	1.315752	1.771996
C	-2.548486	-0.671885	-2.317019
C	0.046022	0.150824	-2.143744
O	-3.213157	-1.052937	-3.173724
O	0.856322	0.255282	-2.958695
C	2.521566	0.100683	-0.299167
H	2.313923	0.957769	-0.918516
C	2.911148	-2.057677	0.402876
H	3.059127	-3.126348	0.404599
C	3.049345	-1.187524	1.531585
H	3.321540	-1.480579	2.533497
C	2.809236	0.141702	1.087087
H	2.848071	1.030112	1.698340
C	2.581413	-1.261010	-0.727669
H	2.460346	-1.614168	-1.738826
C	0.693822	-2.591214	2.164300
C	0.203045	0.121053	2.255930
O	0.657216	-3.442667	2.931845
O	-0.096709	0.835168	3.107023

Selected Mayer bond orders larger than 0.100:

B (0-Sb, 1-P): 0.9265 B (0-Sb, 2-Mo): 0.8113 B (0-Sb, 3-Mo): 0.8238 B (1-P, 2-Mo): 0.9512
B (1-P, 3-Mo): 0.9418 B (2-Mo, 3-Mo): 0.3914

Table S7: Cartesian coordinates of the optimized geometry of $[(CpMo(CO)_2)_2(PBi)]^+$ (TPSSh/def2-TZVP level).

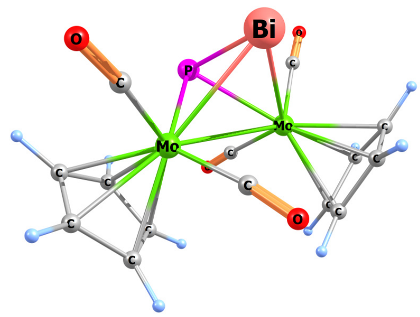

Atom	X	Y	Z
Bi	-0.6625821	-2.6088159	-1.0549283
P	-1.6344873	-1.4073746	1.0215391
Mo	0.8428148	-1.1220357	0.8376144
Mo	-1.4699544	0.1455159	-0.8582134
C	-1.1215365	2.1757054	0.2801934
H	-0.2442382	2.3820982	0.8715215
C	-3.2452086	1.5427336	-0.3503658
H	-4.2592149	1.1748957	-0.3209682
C	-2.5762029	2.0738774	-1.4977752
H	-2.9954029	2.1774480	-2.4866242
C	-1.2708829	2.4631442	-1.1028905
H	-0.5201973	2.9037411	-1.7407270
C	-2.3456105	1.6090268	0.7465628
H	-2.5646312	1.3174937	1.7612614
C	-2.6078876	-0.6730147	-2.2834782
C	0.0244885	0.1023473	-2.1689436
O	-3.3143641	-1.0350166	-3.1169998
O	0.8281959	0.2006131	-2.9936759
C	2.4805287	0.1214283	-0.3178486
H	2.2548170	0.9576198	-0.9589511
C	2.9300713	-2.0070762	0.4361244
H	3.1135013	-3.0699284	0.4618031
C	3.0261564	-1.1101259	1.5481214
H	3.2983184	-1.3726273	2.5583544
C	2.7474832	0.2018435	1.0704583
H	2.7525478	1.1049685	1.6610751
C	2.5876807	-1.2459933	-0.7154449
H	2.4941225	-1.6230447	-1.7209923
C	0.6987606	-2.6478808	2.1081456
C	0.1869409	0.0525583	2.2994442
O	0.6776055	-3.5223044	2.8513561
O	-0.1116317	0.7381791	3.1752512

Selected Mayer bond orders larger than 0.100:

B (0-Bi, 1-P): 0.8614 B (0-Bi, 2-Mo): 0.7541 B (0-Bi, 3-Mo): 0.7880 B (0-Bi, 14-C): 0.1081
B (1-P, 2-Mo): 0.9677 B (1-P, 3-Mo): 0.9641 B (2-Mo, 3-Mo): 0.3897 B (2-Mo, 18-C): 0.4194
B (2-Mo, 20-C): 0.4489

Table S8: Cartesian coordinates of the optimized geometry of $[(CpMo(CO)_2)_2(AsSb)]^+$ (**C**$^+$) (TPSSh/def2-TZVP level).

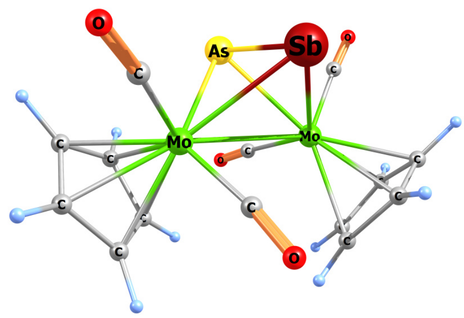

Atom	X	Y	Z
Sb	-0.5965984	-2.4985963	-1.047114
As	-1.7203446	-1.5105099	1.066838
Mo	0.8604917	-1.1386282	0.846772
Mo	-1.4665777	0.1570589	-0.854185
C	-1.1528209	2.1893921	0.289948
H	-0.2869097	2.4061341	0.893930
C	-3.2597377	1.5325985	-0.371902
H	-4.2708059	1.1559192	-0.357322
C	-2.5792911	2.0702246	-1.509812
H	-2.9852043	2.1718917	-2.504339
C	-1.2837880	2.4738212	-1.094497
H	-0.5289867	2.9244407	-1.720285
C	-2.3771120	1.6075757	0.739179
H	-2.6111144	1.3232586	1.752686
C	-2.6068874	-0.6705884	-2.271143
C	0.0147336	0.1443785	-2.179186
O	-3.3101129	-1.0548157	-3.095208
O	0.8155767	0.2489923	-3.004108
C	2.4920348	0.1059768	-0.307902
H	2.2638492	0.9543831	-0.931852
C	2.9342409	-2.0382944	0.406051
H	3.1057760	-3.1034195	0.413877
C	3.0564657	-1.1584614	1.528746
H	3.3381880	-1.4396818	2.531381
C	2.7835593	0.1618923	1.077338
H	2.8041171	1.0551292	1.682465
C	2.5821186	-1.2564293	-0.728141
H	2.4700237	-1.6178016	-1.737552
C	0.7259404	-2.6192988	2.174184
C	0.1831404	0.0876488	2.257321
O	0.7197797	-3.4695914	2.945273
O	-0.1137441	0.8053995	3.108560

Selected Mayer bond orders larger than 0.100:

B (0-Sb, 1-As): 0.9199 B (0-Sb, 2-Mo): 0.8233 B (0-Sb, 3-Mo): 0.8456 B (1-As, 2-Mo): 0.9303
B (1-As, 3-Mo): 0.9291 B (2-Mo, 3-Mo): 0.3867

Table S9: Cartesian coordinates of the optimized geometry of $[(CpMo(CO)_2\}_2(AsBi)]^+$ (**D⁺**) (TPSSh/def2-TZVP level).

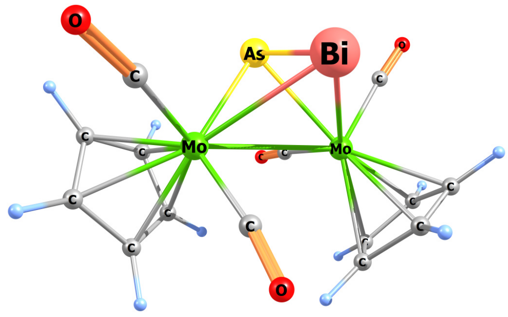

Atom	X	Y	Z
Bi	-0.603918	-2.589742	-1.107583
As	-1.722326	-1.493966	1.075422
Mo	0.856004	-1.141906	0.848845
Mo	-1.469296	0.151633	-0.859932
C	-1.130392	2.177833	0.289581
H	-0.262195	2.382720	0.894444
C	-3.245142	1.548127	-0.373767
H	-4.261235	1.185371	-0.358769
C	-2.557687	2.077852	-1.511259
H	-2.962054	2.185756	-2.505699
C	-1.257258	2.464817	-1.094902
H	-0.496750	2.906568	-1.720139
C	-2.361984	1.611494	0.737556
H	-2.599716	1.329532	1.750927
C	-2.638550	-0.671481	-2.251630
C	0.006503	0.121721	-2.187642
O	-3.367329	-1.037762	-3.064310
O	0.806388	0.232120	-3.015353
C	2.474527	0.116157	-0.314757
H	2.239083	0.953871	-0.950081
C	2.943623	-2.013251	0.426773
H	3.132358	-3.075294	0.4466910
C	3.044501	-1.120201	1.540841
H	3.324994	-1.385609	2.548042
C	2.753752	0.191433	1.071879
H	2.758868	1.091948	1.666482
C	2.587791	-1.248885	-0.719053
H	2.493293	-1.620865	-1.726441
C	0.722997	-2.647213	2.144507
C	0.180066	0.058435	2.278482
O	0.723186	-3.510398	2.902636
O	-0.112102	0.769179	3.138202

Selected Mayer bond orders larger than 0.100:

B (0-Bi, 1-As): 0.8587 B (0-Bi, 2-Mo): 0.7675 B (0-Bi, 3-Mo): 0.8031 B (1-As, 2-Mo): 0.9447
B (1-As, 3-Mo): 0.9533 B (2-Mo, 3-Mo): 0.3837

Table S10: Cartesian coordinates of the optimized geometry of $[(CpMo(CO)_2\}_2(SbBi)]^+$ (**E⁺**) (TPSSh/def2-TZVP level).

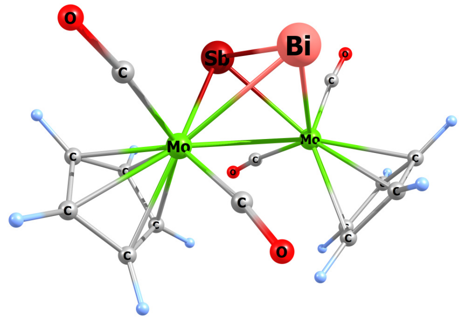

Atom	X	Y	Z
Bi	0.442370	5.922866	7.856550
Sb	1.502950	5.823532	5.190276
Mo	-0.481483	4.043711	5.858225
Mo	2.446205	4.041462	7.137506
O	-1.265329	2.819391	8.633455
O	-2.864302	6.069579	6.101510
C	-0.915092	3.328204	7.654623
C	-1.949739	5.368853	6.064337
O	3.265132	2.818340	4.373432
O	4.807131	6.087872	6.869914
C	2.906828	3.321731	5.350780
C	3.902366	5.376883	6.923360
C	1.882128	2.129192	8.393628
H	1.010716	1.523835	8.206782
C	3.160723	1.931421	7.814368
H	3.420541	1.159235	7.106848
C	4.045553	2.913208	8.338159
H	5.095447	3.006570	8.108777
C	3.304350	3.725944	9.252236
H	3.697926	4.543511	9.835940
C	1.966434	3.241724	9.284936
H	1.179021	3.595693	9.930958
C	0.086532	2.118151	4.629259
H	0.949502	1.507809	4.838768
C	-1.205516	1.934681	5.184531
H	-1.484529	1.171941	5.894956
C	-2.070915	2.918437	4.635249
H	-3.123708	3.023879	4.845715
C	-1.306166	3.717637	3.728497
H	-1.680964	4.534462	3.131552
C	0.027277	3.222841	3.726041
H	0.831212	3.571607	3.097631

Selected Mayer bond orders larger than 0.100:

B (0-Bi, 1-Sb): 0.8384 B (0-Bi, 2-Mo): 0.8133 B (0-Bi, 3-Mo): 0.7789 B (1-Sb, 2-Mo): 0.8574
B (1-Sb, 3-Mo): 0.8735 B (2-Mo, 3-Mo): 0.3761

Table S11: Cartesian coordinates of the optimized geometry of $[(CpMo(CO)_2\}_2(PAs)]_2^{2+}$ (**1**) (TPSSh/def2-TZVP level).

Atom	X	Y	Z
Mo	14.252187	4.366093	33.879736
Mo	12.719242	1.673549	33.423942
Mo	11.032047	3.240545	28.431425
Mo	12.332175	6.115833	28.691846
As	11.648135	3.974739	34.097143
P	12.686417	3.741846	32.142838
P	11.606853	4.533892	30.400086
As	13.435361	3.831699	29.131267
O	14.840631	7.080647	30.297906
O	14.993249	0.950344	31.380525
C	14.196707	1.245460	32.154963
O	12.453558	3.218794	25.614419
O	14.278376	5.706785	26.246252
C	11.972606	3.245096	26.652778
C	13.939620	6.679553	29.711953
C	16.380610	3.936293	34.671673
H	16.559534	3.533863	35.656611
C	16.048519	4.081486	32.397461
H	15.931075	3.812291	31.359458
O	12.359467	0.473980	29.064902
C	10.341617	7.256227	29.124026
H	9.6108203	6.912545	29.839277
C	13.565593	5.807980	27.137671
O	13.597906	4.412470	36.965347
C	16.261809	3.181323	33.474921
H	16.343097	2.109432	33.404327
C	11.920959	1.513075	28.843442
C	9.1528092	3.620955	27.151152
H	9.1862893	4.169072	26.222431
C	11.451045	8.097754	29.422259
H	11.693673	8.509372	30.389421
C	8.8716308	3.082920	29.372183
H	8.6729191	3.169262	30.428972
O	14.727282	1.272457	35.797546
C	10.351605	6.985164	27.727457
H	9.6272392	6.414802	27.171521
C	16.272688	5.319233	34.335559

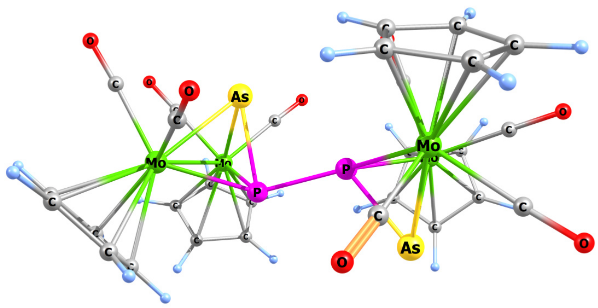

Atom	X	Y	Z
H	16.365719	6.150302	35.016808
C	16.059570	5.404150	32.923385
H	15.967224	6.314935	32.354976
C	9.1603366	1.885069	28.670287
H	9.2138725	0.895163	29.096558
C	9.3319018	2.207789	27.292808
H	9.5271744	1.505549	26.497588
C	14.023937	1.525540	34.916120
C	13.551649	6.234159	33.818338
C	8.8690024	4.154784	28.437865
H	8.6301552	5.177635	28.671785
C	12.206782	-0.51555	33.779131
H	12.964776	-1.24955	34.002723
C	11.469377	7.649105	27.161166
H	11.739957	7.644303	26.116475
C	13.791157	4.378517	35.835359
C	10.697359	0.793683	32.631002
H	10.132625	1.252921	31.835055
C	11.730437	-0.17005	32.477336
H	12.070329	-0.59505	31.546265
C	12.152884	8.344545	28.199562
H	13.022133	8.971660	28.077515
O	13.203219	7.324472	33.760787
C	10.522262	1.043252	34.021699
H	9.7773984	1.688366	34.459436
C	11.459784	0.247125	34.732303
H	11.561305	0.198034	35.805041

Selected Mayer bond orders larger than 0.100:

B (0-Mo, 1-Mo): 0.4639; B (0-Mo, 4-As): 0.9126; B (0-Mo, 5-P): 0.7025
B (0-Mo, 15-C): 0.4683; B (0-Mo, 17-C): 0.4385; B (0-Mo, 23-O): 0.1064
B (0-Mo, 24-C): 0.4137; B (0-Mo, 36-C): 0.4923; B (0-Mo, 38-C): 0.4706
B (0-Mo, 44-C): 0.1611; B (0-Mo, 45-C): 1.1261; B (0-Mo, 52-C): 1.1123
B (0-Mo, 59-O): 0.1049; B (1-Mo, 4-As): 0.7679; B (1-Mo, 5-P): 0.7405
B (1-Mo, 9-O): 0.1056; B (1-Mo, 10-C): 1.1022; B (1-Mo, 33-O): 0.1029
B (1-Mo, 44-C): 1.1495; B (1-Mo, 48-C): 0.5140; B (1-Mo, 53-C): 0.4387
B (1-Mo, 55-C): 0.4196; B (1-Mo, 60-C): 0.3806; B (1-Mo, 62-C): 0.4601
B (2-Mo, 3-Mo): 0.3970; B (2-Mo, 6-P): 0.6984; B (2-Mo, 7-As): 0.8701
B (2-Mo, 13-C): 1.0731; B (2-Mo,19-O): 0.1111; B (2-Mo, 26-C): 1.1755
B (2-Mo, 27-C): 0.4806; B (2-Mo, 31-C): 0.4223; B (2-Mo, 40-C): 0.4536
B (2-Mo, 42-C): 0.4787; B (2-Mo, 46-C): 0.4246; B (3-Mo, 6-P): 0.7604
B (3-Mo, 7-As): 0.8495; B (3-Mo, 8-O): 0.1037; B (3-Mo, 12-O): 0.1001
B (3-Mo, 14-C): 1.1852; B (3-Mo, 20-C): 0.4461; B (3-Mo, 22-C): 1.0967
B (3-Mo, 29-C): 0.4651; B (3-Mo, 34-C): 0.4056; B (3-Mo, 50-C): 0.4380
B (3-Mo, 57-C): 0.5006; B (4-As, 5-P): 0.9632; B (5-P, 6-P): 0.7926
B (6-P, 7-As): 0.9394; B (8-O, 14-C): 2.2029; B (9-O, 10-C): 2.1706

Table S12: Cartesian coordinates of the optimized geometry of $[(CpMo(CO)_2\}_2(PSb)]_2^{2+}$ (**2**) (TPSSh/def2-TZVP level).

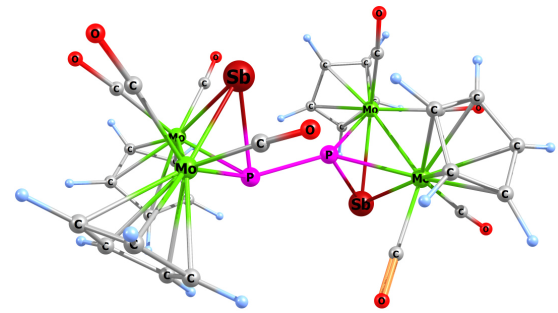

Atom	X	Y	Z
Mo	13.573928	4.550532	34.16769
Mo	12.683932	1.589743	33.52156
Mo	10.690541	3.283582	28.50550
Mo	12.683251	5.758249	28.59835
Sb	10.883815	3.667027	34.18097
P	12.362527	3.645245	32.25152
P	11.550433	4.534063	30.40876
Sb	13.352255	3.162056	29.23563
O	15.376165	6.227144	30.11666
O	15.423291	1.369806	32.01379
C	14.440049	1.503871	32.59843
O	11.923475	3.030227	25.61507
O	14.444388	4.796841	26.17638
C	11.534868	3.136094	26.68881
C	14.388965	5.994574	29.57475
C	15.611935	4.611073	35.27653
H	15.717003	4.318837	36.30991
C	15.591228	4.536699	32.97597
H	15.689558	4.181603	31.96328
O	11.293588	0.253941	28.97810
C	11.024567	7.370122	28.96930
H	10.251261	7.259551	29.71308
C	13.788211	5.078866	27.07677
O	12.591968	4.580626	37.15551
C	15.813181	3.770789	34.15326
H	16.105927	2.735002	34.19547
C	11.154955	1.390835	28.83269
C	8.8834853	4.034870	27.27969
H	8.9929641	4.513324	26.31875
C	12.308724	7.938754	29.19605
H	12.668374	8.345238	30.12836
C	8.6065040	3.689722	29.53939
H	8.4881937	3.868971	30.59644
O	14.209905	1.593338	36.26556
C	10.933668	7.007418	27.59684
H	10.078365	6.591218	27.09275
C	15.286604	5.916594	34.80156
H	15.118198	6.791267	35.40984
C	15.274133	5.865424	33.37110
H	15.096505	6.699615	32.71212
C	8.5752454	2.424077	28.90186
H	8.4220178	1.472949	29.38764
C	8.7431779	2.628083	27.49973
H	8.7298207	1.861158	26.74124
C	13.663233	1.696450	35.25287
C	12.562848	6.245225	33.91315
C	8.7996009	4.684494	28.53955
H	8.8217750	5.745766	28.71805
C	12.624472	-0.682958	33.58912
H	13.497932	-1.271521	33.82126
C	12.162147	7.345061	26.97354
H	12.396535	7.206439	25.92933
C	12.875681	4.525644	36.04049
C	10.976616	0.428219	32.41915
H	10.394137	0.857742	31.62028
C	12.205557	-0.272128	32.28251
H	12.711690	-0.495617	31.35681
C	13.017988	7.926202	27.95271
H	14.007262	8.319249	27.77825
O	12.049073	7.258880	33.74776
C	10.623127	0.448631	33.79908
H	9.704668	0.833746	34.21242
C	11.646563	-0.222672	34.52084
H	11.662079	-0.384559	35.58738

Selected Mayer bond orders larger than 0.100:

B (0-Mo, 1-Mo): 0.4478 B (0-Mo, 4-Sb): 0.8107 B (0-Mo, 5-P): 0.7395 B (0-Mo, 15-C): 0.4550
B (0-Mo, 17-C): 0.4455 B (0-Mo, 23-O): 0.1247 B (0-Mo, 24-C): 0.4070 B (0-Mo, 36-C): 0.4779
B (0-Mo, 38-C): 0.4686 B (0-Mo, 44-C): 0.1478 B (0-Mo, 45-C): 1.1633 B (0-Mo, 52-C): 1.1713
B (0-Mo, 59-O): 0.1121 B (1-Mo, 4-Sb): 0.7059 B (1-Mo, 5-P): 0.7256 B (1-Mo, 9-O): 0.1079
B (1-Mo, 10-C): 1.1350 B (1-Mo, 33-O): 0.1008 B (1-Mo, 44-C): 1.1210 B (1-Mo, 48-C): 0.4983
B (1-Mo, 53-C): 0.4303 B (1-Mo, 55-C): 0.4561 B (1-Mo, 60-C): 0.3844 B (1-Mo, 62-C): 0.4600
B (2-Mo, 3-Mo): 0.3905 B (2-Mo, 6-P): 0.7275 B (2-Mo, 7-Sb): 0.7968 B (2-Mo, 42-C): 0.4836
B (2-Mo, 11-O): 0.1035 B (2-Mo, 34-C): 0.1064 B (3-Mo, 12-O): 0.1128 B (3-Mo, 7-Sb): 0.8156
B (2-Mo, 26-C): 1.2287 B (2-Mo, 46-C): 0.4375 B (3-Mo, 22-C): 1.1425 B (3-Mo, 14-C): 1.2217
B (3-Mo, 8-O): 0.1114 B (3-Mo, 20-C): 0.4344 B (3-Mo, 50-C): 0.4261 B (3-Mo, 29-C): 0.4641
B (3-Mo, 34-C): 0.4157 B (2-Mo, 27-C): 0.4660 B (4-Sb, 52-C): 0.1474 B (3-Mo, 57-C): 0.5000
B (4-Sb, 5-P): 0.8695 B (2-Mo, 19-O): 0.1287 B (5-P, 7-Sb): 0.1198 B (4-Sb, 60-C): 0.1551
B (5-P, 6-P): 0.8140 B (2-Mo, 40-C): 0.4500 B (2-Mo, 31-C): 0.4157 B (6-P, 7-Sb): 0.8336
B (2-Mo, 13-C): 1.1107 B (3-Mo, 6-P): 0.7250

Table S13: Cartesian coordinates of the optimized geometry of $[(CpMo(CO)_2\}_2(AsSb)]_2^{2+}$ (**3a/b**) (TPSSh/def2-TZVP level).

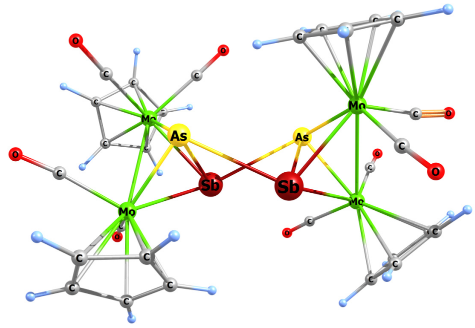

Atom	X	Y	Z
Mo	6.14298	13.59361	16.0940
Mo	3.13427	12.71872	16.2181
Mo	3.03839	18.87210	13.5149
Mo	1.74111	18.78616	16.3817
Sb	4.08114	14.77177	14.5904
As	4.17698	14.76768	17.2847
Sb	4.17330	17.60695	15.7421
As	1.81696	16.94179	14.5791
O	4.72197	21.19788	14.7827
O	0.53985	20.77705	13.4112
O	-1.17240	18.62299	15.2123
O	3.78024	11.26040	13.5167
O	6.58153	12.99609	19.1488
O	1.00952	16.32968	18.1734
C	4.32223	11.41008	17.1406
O	4.86916	10.55464	17.6886
C	3.10006	20.34170	17.4772
C	3.61082	11.82093	14.5089
C	2.18492	21.09034	16.6817
H	2.43692	21.77247	15.8869
C	7.77233	13.62179	14.4824
H	8.09321	14.53528	14.0066
C	1.28132	17.19737	17.4724
C	4.06304	20.33946	14.3869
C	6.76517	12.73681	14.0022
H	6.19986	12.85479	13.0913
C	1.42994	20.05425	13.5258
C	7.64477	11.82838	15.9268
H	7.83652	11.15281	16.7462
C	-0.08838	18.65746	15.5871
C	2.34618	19.60551	18.4352
H	2.75174	18.97335	19.2096
O	7.37051	16.42040	16.6440
C	8.32320	13.05780	15.6785
H	9.13180	13.46607	16.2640
C	2.52817	18.55851	11.2902
H	1.51890	18.62884	10.9156
C	6.69518	11.62937	14.8940
H	6.04951	10.77224	14.7966
C	0.87236	20.81274	17.1355
C	0.95979	19.89677	18.2236
H	0.13252	19.52470	18.8072
C	6.88841	15.39344	16.4643
C	3.17620	17.36731	11.7188
H	2.74760	16.37749	11.7098
C	1.33459	13.19860	17.6655
H	1.38914	13.86601	18.5091
C	3.46216	19.63630	11.4037
H	3.28707	20.66315	11.1236
C	4.68234	19.09972	11.9105
H	5.59162	19.65088	12.0937
C	4.50586	17.70319	12.1026
H	5.25857	17.01663	12.4587
C	6.36210	13.22089	18.0453
C	1.59516	11.80328	17.6948
H	1.89351	11.23778	18.5640
C	1.36742	11.27544	16.3901
H	1.45059	10.23958	16.1006
C	0.95491	13.54263	16.3372
H	0.68653	14.52640	15.9854
C	0.97385	12.36013	15.5458
H	0.70128	12.29055	14.5043
H	-0.03552	21.24021	16.7382
H	4.17605	20.37547	17.4102

Selected Mayer bond orders larger than 0.100:

B (0-Mo, 1-Mo): 0.4179 B (0-Mo, 4-Sb): 0.6313 B (0-Mo, 5-As): 0.9770
B (0-Mo, 12-O): 0.1104 B (0-Mo, 14-C): 0.1529 B (0-Mo, 20-C): 0.4710
B (0-Mo, 24-C): 0.4433 B (0-Mo, 27-C): 0.4422 B (0-Mo, 32-O): 0.1020
B (0-Mo, 33-C): 0.4902 B (0-Mo, 37-C): 0.4249 B (0-Mo, 42-C): 1.1453
B (0-Mo, 53-C): 1.1299 B (1-Mo, 4-Sb): 0.7173 B (1-Mo, 5-As): 0.8696
B (1-Mo, 11-O): 0.1132 B (1-Mo, 14-C): 1.1338 B (1-Mo, 17-C): 1.1708
B (1-Mo, 45-C): 0.3930 B (1-Mo, 54-C): 0.4391 B (1-Mo, 56-C): 0.5086
B (1-Mo, 58-C): 0.4320 B (1-Mo, 60-C): 0.4435 B (2-Mo, 3-Mo): 0.4229
B (2-Mo, 6-Sb): 0.6956 B (2-Mo, 7-As): 0.9153 B (2-Mo, 8-O): 0.1082
B (2-Mo, 23-C): 1.1452 B (2-Mo, 26-C): 1.1408 B (2-Mo, 35-C): 0.4523
B (2-Mo, 43-C): 0.4016 B (2-Mo, 47-C): 0.5084 B (2-Mo, 49-C): 0.4394
B (2-Mo, 51-C): 0.4049 B (3-Mo, 6-Sb): 0.6826 B (3-Mo, 7-As): 0.9160
B (3-Mo, 10-O): 0.1147 B (3-Mo, 13-O): 0.1000 B (3-Mo, 16-C): 0.4521
B (3-Mo, 18-C): 0.4323 B (3-Mo, 22-C): 1.1602 B (3-Mo, 26-C): 0.1146
B (3-Mo, 29-C): 1.1252 B (3-Mo, 30-C): 0.4650 B (3-Mo, 39-C): 0.4374
B (3-Mo, 40-C): 0.4915 B (4-Sb, 5-As): 0.6726 B (4-Sb, 6-Sb): 0.5246
B (4-Sb, 7-As): 0.2447 B (5-As, 6-Sb): 0.2145 B (6-Sb, 7-As): 0.6481

Table S14: Cartesian coordinates of the optimized geometry of $[(CpMo(CO)_2\}_2(AsBi)]_2^{2+}$ (**4a/b**) (TPSSh/def2-TZVP level).

Atom	X	Y	Z
Bi	9.88186	-0.24595	9.99719
Mo	12.3478	1.21759	9.54352
Mo	10.5162	0.14794	7.22244
As	10.2024	2.22982	8.71108
O	11.0996	2.61330	5.36562
O	13.2846	-1.77690	9.64596
O	13.9202	1.60093	6.85341
C	10.8973	1.75081	6.09642
C	12.8894	-0.69754	9.54813
C	12.3302	3.11676	10.9253
H	11.5752	3.88704	10.9064
C	13.2709	1.43133	7.79182
C	9.87657	-1.93250	6.50064
H	8.88862	-2.32675	6.68046
C	11.0197	-2.13693	7.32524
H	11.0534	-2.73165	8.22454
C	12.3449	1.97139	11.7713
H	11.5929	1.70375	12.4977
C	13.5216	3.10568	10.1488
H	13.8140	3.85555	9.43051
C	12.1300	-1.50122	6.69760
H	13.1474	-1.49628	7.05185
C	11.6774	-0.89668	5.49974
H	12.2898	-0.35111	4.7982
C	14.2805	1.95115	10.5190
H	15.2504	1.67638	10.1351
C	10.2824	-1.16071	5.36477
H	9.65860	-0.86779	4.53509
C	13.5443	1.25174	11.5191
H	13.8528	0.34681	12.0191
O	7.47538	0.63666	6.68457
C	8.59129	0.50169	6.92182
Bi	8.45991	2.33725	11.3780
Mo	5.79933	2.81205	10.4148
Mo	6.39932	0.82408	12.7639
As	6.72431	0.46832	10.2240
O	4.11280	-1.16158	11.9301

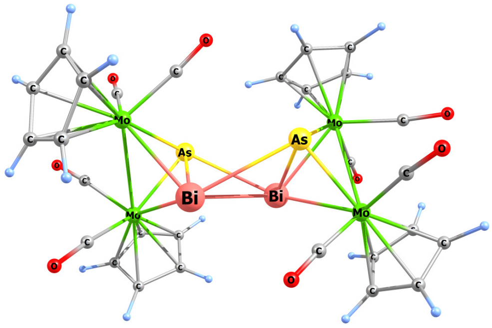

Atom	X	Y	Z
O	6.20528	5.00271	12.6224
O	3.09667	2.01982	11.7995
C	4.95079	-0.41574	12.1739
C	6.07871	4.14323	11.8633
C	5.37829	2.57597	8.10702
H	5.36887	1.63582	7.58161
C	4.14026	2.23558	11.3554
C	7.27818	1.01206	14.8723
H	8.27571	0.67864	15.1125
C	6.90933	2.33271	14.4854
H	7.57420	3.17842	14.4046
C	6.49844	3.43808	8.28029
H	7.50016	3.26208	7.92063
C	4.25657	3.19374	8.71974
H	3.25571	2.79126	8.74911
C	5.49477	2.35973	14.3218
H	4.89953	3.21875	14.0593
C	4.98990	1.06409	14.5931
H	3.95100	0.77341	14.5650
C	4.67150	4.44299	9.26375
H	4.03898	5.15785	9.76636
C	6.08655	0.22118	14.9423
H	6.02239	-0.81225	15.2443
C	6.06757	4.59183	8.99439
H	6.67830	5.44339	9.25059
O	8.31874	-1.64634	12.7604
C	7.61200	-0.73952	12.7199

Selected Mayer bond orders larger than 0.100:

B (0-Bi, 1-Mo): 0.6362 B (0-Bi, 2-Mo): 0.6487 B (0-Bi, 3-As): 0.5781 B (0-Bi, 32-Bi): 0.4243
B (0-Bi, 35-As): 0.2528 B (1-Mo, 2-Mo): 0.4266 B (1-Mo, 3-As): 0.9562 B (1-Mo, 5-O): 0.1099
B (1-Mo, 8-C): 1.1449 B (1-Mo, 9-C): 0.3956 B (1-Mo, 11-C): 1.1541 B (1-Mo, 16-C): 0.4100
B (1-Mo, 18-C): 0.4487 B (1-Mo, 24-C): 0.4985 B (1-Mo, 28-C): 0.4308 B (2-Mo, 3-As): 0.9279
B (2-Mo, 4-O): 0.1197 B (2-Mo, 7-C): 1.1412 B (2-Mo, 11-C): 0.1223 B (2-Mo, 12-C): 0.4646
B (2-Mo, 14-C): 0.4524 B (2-Mo, 20-C): 0.4275 B (2-Mo, 22-C): 0.4397 B (2-Mo, 26-C): 0.4860
B (2-Mo, 30-O): 0.1009 B (2-Mo, 31-C): 1.1651 B (3-As, 32-Bi): 0.2583 B (4-O, 7-C): 2.2021
B (5-O, 8-C): 2.1529 B (6-O, 11-C): 2.1628 B (9-C, 10-H): 0.9541 B (9-C, 16-C): 1.1391
B (9-C, 18-C): 1.1960 B (2-C, 13-H): 0.9451 B (12-C, 14-C): 1.1330 B (12-C, 26-C): 1.0903
B (14-C, 15-H): 0.9654 B (14-C, 20-C): 1.1149 B (16-C, 17-H): 0.9564 B (16-C, 28-C): 1.1768
B (18-C, 19-H): 0.9370 B (18-C, 24-C): 1.1200 B (20-C, 21-H): 0.9522 B (20-C, 22-C): 1.1983
B (22-C, 23-H): 0.9351 B (22-C, 26-C): 1.1431 B (24-C, 25-H): 0.9427 B (24-C, 28-C): 1.1780
B (26-C, 27-H): 0.9466 B (28-C, 29-H): 0.9378 B (30-O, 31-C): 2.1823 B (32-Bi, 33-Mo): 0.6822
B (32-Bi, 34-Mo): 0.5968 B (32-Bi, 35-As): 0.5872 B (33-Mo, 34-Mo): 0.424 B (33-Mo, 35-As): 0.9175
B (33-Mo, 37-O): 0.1159 B (33-Mo, 40-C): 1.1766 B (33-Mo, 41-C): 0.3908 B (33-Mo, 43-C): 1.1372
B (33-Mo, 48-C): 0.4356 B (33-Mo, 50-C): 0.4398 B (33-Mo, 56-C): 0.4936 B (33-Mo, 60-C): 0.4423
B (34-Mo, 35-As): 0.9741 B (34-Mo, 36-O): 0.1140

Table S15: Cartesian coordinates of the optimized geometry of $[(CpMo(CO)_2\}_2(SbBi)]_2^{2+}$ (**5**) (TPSSh/def2-TZVP level).

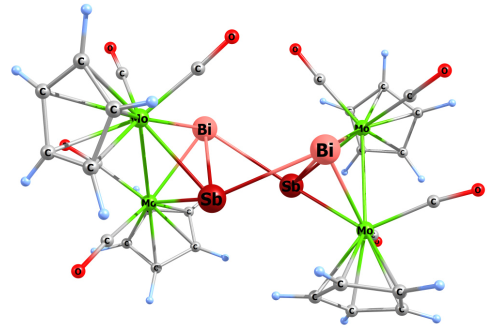

Atom	X	Y	Z
Mo	12.4376	1.92066	16.08707
Mo	9.36569	2.76006	15.80759
Mo	11.7782	7.96999	12.92952
Mo	13.0819	8.51122	15.79854
Sb	11.4338	3.80009	14.28125
Bi	11.2609	4.28687	17.23250
Sb	10.8977	6.84591	15.30444
Bi	13.5907	6.19478	14.16250
O	12.3836	1.46782	19.19143
O	9.42652	0.65364	13.48997
O	9.54836	0.42449	17.89323
O	14.0085	10.1478	12.57695
O	16.0323	8.79302	14.76670
O	14.1041	6.45481	17.91636
O	14.9539	3.72811	16.48860
O	9.79838	10.2051	13.87337
C	10.5722	9.39207	13.60716
C	13.5391	10.7321	16.31909
H	14.3814	11.2639	15.90404
C	13.5477	9.95015	17.50995
H	14.3922	9.79945	18.16365
C	12.3441	1.69996	18.06361
C	9.49241	1.41081	14.35773
C	9.59207	1.28896	17.12787
C	13.2252	9.33087	12.80828
C	14.9362	8.63043	15.08167
C	13.7413	7.16247	17.08136
C	13.9839	3.11673	16.36826
C	12.2235	9.44394	17.70621
H	11.8896	8.84295	18.53750
C	11.4104	9.91620	16.63628
H	10.3497	9.75260	16.52948
C	12.2272	10.7174	15.78643
H	11.9101	11.2427	14.90087
C	11.9488	-0.19925	15.15533
H	10.9634	-0.63170	15.10557
C	12.8584	-0.36266	16.22813
H	12.6763	-0.93194	17.12662
C	14.0621	0.32720	15.90325
H	14.9574	0.35825	16.50389
C	13.8844	0.92651	14.61570
H	14.6243	1.49080	14.06995
C	12.5748	0.60404	14.15821
H	12.1596	0.86345	13.19722
C	11.8906	6.30028	11.27253
H	12.4856	5.40091	11.29694
C	12.2906	7.55266	10.72428
H	13.2593	7.77562	10.30492
C	11.1759	8.44244	10.78427
H	11.1464	9.45374	10.41059
C	10.0904	7.73363	11.38541
H	9.09637	8.11754	11.55414
C	10.5320	6.41756	11.68259
H	9.93289	5.63402	12.12033
C	7.10797	2.47837	15.91974
H	6.65777	1.49908	15.95793
C	7.49130	3.27569	17.04020
H	7.39056	3.00166	18.07880
C	7.98857	4.51868	16.55305
H	8.28281	5.36318	17.15644
C	7.92398	4.48691	15.13093
H	8.21179	5.28652	14.46592
C	7.38490	3.23358	14.73877
H	7.18742	2.92261	13.72465

Selected Mayer bond orders larger than 0.100:

B (0-Mo, 1-Mo): 0.3910 B (0-Mo, 4-Sb): 0.7379 B (0-Mo, 5-Bi): 0.7715 B (0-Mo, 8-O): 0.1249
B (0-Mo, 14-O): 0.1146 B (0-Mo, 21-C): 1.1933 B (0-Mo, 23-C): 0.1294 B (0-Mo, 27-C): 1.2087
B (0-Mo, 34-C): 0.4272 B (0-Mo, 36-C): 0.4349 B (0-Mo, 38-C): 0.4924 B (0-Mo, 40-C): 0.4545
B (0-Mo, 42-C): 0.4564 B (1-Mo, 4-Sb): 0.7364 B (1-Mo, 5-Bi): 0.7569 B (1-Mo, 9-O): 0.1146
B (1-Mo, 10-O): 0.1074 B (1-Mo, 22-C): 1.1817 B (1-Mo, 23-C): 1.1591 B (1-Mo, 54-C): 0.5044
B (1-Mo, 56-C): 0.4556 B (1-Mo, 58-C): 0.4181 B (1-Mo, 60-C): 0.3996 B (1-Mo, 62-C): 0.4469
B (2-Mo, 3-Mo): 0.3909 B (2-Mo, 6-Sb): 0.7371 B (2-Mo, 7-Bi): 0.7560 B (2-Mo, 11-O): 0.1069
B (2-Mo, 15-O): 0.1152 B (2-Mo, 16-C): 1.1849 B (2-Mo, 24-C): 1.1570 B (2-Mo, 44-C): 0.4177
B (2-Mo, 46-C): 0.4557 B (2-Mo, 48-C): 0.5053 B (2-Mo, 50-C): 0.4462 B (2-Mo, 52-C): 0.4002
B (3-Mo, 6-Sb): 0.7401 B (3-Mo, 7-Bi): 0.7723 B (3-Mo, 12-O): 0.1240 B (3-Mo, 13-O): 0.1148
B (3-Mo, 17-C): 0.4348 B (3-Mo, 19-C): 0.4915 B (3-Mo, 24-C): 0.1270 B (3-Mo, 25-C): 1.1902
B (3-Mo, 26-C): 1.2110 B (3-Mo, 28-C): 0.4542 B (3-Mo, 30-C): 0.4573 B (3-Mo, 32-C): 0.4264
B (4-Sb, 5-Bi): 0.5389 B (4-Sb, 6-Sb): 0.4557 B (4-Sb, 7-Bi): 0.3460 B (5-Bi, 6-Sb): 0.3451
B (5-Bi, 21-C): 0.1037 B (5-Bi, 58-C): 0.1143 B (6-Sb, 7-Bi): 0.5374 B (7-Bi, 25-C): 0.1020
B (7-Bi, 44-C): 0.1149

Table S16: Natural charge distribution of the $E_2E'_2$ cores in **1**-**5**, calculated at the TPSSh/def2-TZVP level.

$[(CpMo(CO)_2\}_2(PAs)]_2^{2+}$ (**1**)		$[(CpMo(CO)_2\}_2(PSb)]_2^{2+}$ (**2**)		$[(CpMo(CO)_2\}_2(AsSb)]_2^{2+}$ (**3a**)	
Atom	Nat. charge	Atom	Nat. charge	Atom	Nat. charge
As1	0.434	Sb1	0.736	Sb1	0.565
P1	0.159	P1	0.037	As1	0.358
P2	0.257	P2	0.174	Sb2	0.628
As1	0.562	Sb2	0.938	As2	0.330
SUM	1.412	SUM	1.885	SUM	1.882

$[(CpMo(CO)_2\}_2(AsBi)]_2^{2+}$ (**4a**)		$[(CpMo(CO)_2\}_2(SbBi)]_2^{2+}$ (**5**)	
Atom	Nat. charge	Atom	Nat. charge
Bi1	0.720	Sb1	0.408
As1	0.286	Bi1	0.857
Bi2	0.680	Sb2	0.412
As2	0.318	Bi2	0.856
SUM	2.004	SUM	2.533

5.5 References

[1] A. F. Holleman and E. Wiberg, *Inorganic Chemistry, Vol. 101*, Walter de Gruyter, Berlin, 2001, p. 778.
[2] M. Eggersdorfer, *Ullmann's Encyclopedia of Industrial Chemistry, Vol. 36*, Wiley-VCH, Weinheim, 2000, pp. 29-45.
[3] R. Hoffmann, *Angew. Chem. Int. Ed.* 1982, **21**, 711-724.
[4] a) M. Baudler and K. Glinka, *Chem. Rev.* 1993, **93**, 1623-1667; b) M. Baudler and K. Glinka, *Chem. Rev.* 1994, **94**, 1273-1297.
[5] a) C. A. Dyker and N. Burford, *Chem. Asian J.* 2008, **3**, 28-36; b) A. P. M. Robertson, P. A. Gray and N. Burford, *Angew. Chem. Int. Ed.* 2014, **53**, 6050-6069; c) M. Donath, F. Hennersdorf and J. J. Weigand, *Chem. Soc. Rev.* 2016, **45**, 1145-1172.
[6] O. J. Scherer, H. Sitzmann and G. Wolmershäuser, *Angew. Chem. Int. Ed.* 1985, **24**, 351-353.
[7] M. Fleischmann, F. Dielmann, L. J. Gregoriades, E. V. Peresypkina, A. V. Virovets, S. Huber, A. Y. Timoshkin, G. Balázs and M. Scheer, *Angew. Chem. Int. Ed.* 2015, **54**, 13110-13115.
[8] a) R. F. Winter and W. E. Geiger, *Organometallics* 1999, **18**, 1827-1833; b) M. V. Butovskiy, G. Balázs, M. Bodensteiner, E. V. Peresypkina, A. V. Virovets, J. Sutter and M. Scheer, *Angew. Chem. Int. Ed.* 2013, **52**, 2972-2976.
[9] a) T. Köchner, T. A. Engesser, H. Scherer, D. A. Plattner, A. Steffani and I. Krossing, *Angew. Chem. Int. Ed.* 2012, **51**, 6529-6531; b) T. Köchner, S. Riedel, A. J. Lehner, H. Scherer, I. Raabe, T. A. Engesser, F. W. Scholz, U. Gellrich, P. Eiden, R. A. Paz Schmidt, D. A. Plattner and I. Krossing, *Angew. Chem. Int. Ed.* 2010, **49**, 8139-8143.
[10] I. Krossing and I. Raabe, *Angew. Chem. Int. Ed.* 2004, **43**, 2066-2090.
[11] L. Dütsch, M. Fleischmann, S. Welsch, G. Balázs, W. Kremer and M. Scheer, *Angew. Chem. Int. Ed.* 2018, **57**, 3256-3261.
[12] a) A. J. Ashe and E. G. Ludwig, *J. Organomet. Chem.* 1986, **303**, 197-204; b) D. Nikolova and C. von Hänisch, *Eur. J. Inorg. Chem.* 2005, 378-382; c) J. G. Stevens, J. M. Trooster, H. F. Martens and H. A. Meinema, *Inorg. Chim. Acta* 1986, **115**, 197-201.

[13] S. Traut, A. P. Hähnel and C. von Hänisch, *Dalton Trans.* 2011, **40**, 1365-1371.
[14] a) K. M. Marczenko and S. S. Chitnis, *Chem. Commun.* 2020, **56**, 8015-8018; b) T. Sasamori, N. Takeda and N. Tokitoh, *Chem. Commun.* 2000, 1353-1354.
[15] B. Ringler, M. Müller and C. von Hänisch, *Eur. J. Inorg. Chem.* 2018, 640-646.
[16] C. Ritter, N. Michel, A. Rinow, B. Ringler and C. von Hänisch, *Eur. J. Inorg. Chem.* 2021, 2514-2522.
[17] M. Donath, E. Conrad, P. Jerabek, G. Frenking, R. Fröhlich, N. Burford and J. J. Weigand, *Angew. Chem. Int. Ed.* 2012, **51**, 2964-2967.
[18] L. Dütsch, C. Riesinger, G. Balázs and M. Scheer, *Chem. Eur. J.* 2021, **27**, 8804-8810.
[19] For details see Supporting Information.
[20] N. G. Connelly and W. E. Geiger, *Chem. Rev.* 1996, **96**, 877-910.
[21] Independent on numerous attempts the obtained datasets of the single crystal X-ray diffraction experiments of **2** are very weak since **2** only crystallizes as thin plates or forms an oil. Therefore, only a first insight into the geometry of the heavy-atom framework of the molecular structure can be given revealing a P-P coupled SbPPSb chain as central unit. No bond lengths or angles can be discussed. The presence of a P-P coupled product containing an SbPPSb chain is supported by ^{31}P NMR. For further details, see the Supporting Information.
[22] a) J. E. Davies, L. C. Kerr, M. J. Mays, P. R. Raithby, P. K. Tompkin and A. D. Woods, *Angew. Chem. Int. Ed.* 1998, **37**, 1428-1429; b) J. E. Davies, M. J. Mays, P. R. Raithby, G. P. Shields, P. K. Tompkin and A. D. Woods, *J. Chem. Soc., Dalton Trans.* 2000, 1925-1930.
[23] P. Pyykkö, *J. Phys. Chem. A* 2015, **119**, 2326-2337.
[24] Two independent molecules in the asymmetric unit of **4a** are observed. The given bond lengths and angles are the ones of one dication. The second molecule is very similar.
[25] M. Mantina, A. C. Chamberlin, R. Valero, C. J. Cramer and D. G. Truhlar, *J. Phys. Chem. A* 2009, **113**, 5806-5812.
[26] a) L. Tuscher, C. Ganesamoorthy, D. Bläser, C. Wölper, S. Schulz, *Angew. Chem. Int. Ed.* **2015**, *54*, 10657-10661; b) L. Tuscher, C. Helling, C. Ganesamoorthy, J. Krüger, C. Wölper, W. Frank, A. Nizovtsev, S. Schulz, *Chem. Eur. J.* **2017**, *23*, 12297-12304; c) J. Krüger, C. Wölper, S. Schulz, *Inorg. Chem.* **2020**, *59*, 11142-11151.
[27] a) E. Conrad, N. Burford, R. McDonald and M. J. Ferguson, *J. Am. Chem. Soc.* 2009, **131**, 5066-5067; b) M. Mehta, J. E. McGrady and J. M. Goicoechea, *Chem. Eur. J.* 2019, **25**, 5445-5450; c) J. Bresien, A. Hinz, A. Schulz and A. Villinger, *Eur. J. Inorg. Chem.* 2018, 1679-1682; d) L. Weber, D. Bungardt and R. Boese, *Z. Anorg. Allg. Chem.* 1989, **578**, 205-224.
[28] C. Schwarzmaier, M. Bodensteiner, A. Y. Timoshkin and M. Scheer, *Angew. Chem. Int. Ed.* 2014, **53**, 290-293.
[29] P. W. Roesky, N. Reinfandt, C. Schoo, L. Dütsch, R. Köppe, S. N. Konchenko and M. Scheer, *Chem. Eur. J.* 2021, **27**, 3974-3978.
[30] A. F. Holleman and E. Wiberg, *Inorganic Chemistry, Vol. 101*, Walter de Gruyter, Berlin, 2001, pp. 531-532.
[31] X. Zheng, Z. Zhang, G. Tan and X. Wang, *Inorg. Chem.* 2016, **55**, 1008-1010.
[32] a) N. Reinfandt, C. Schoo, L. Dütsch, R. Köppe, S. N. Konchenko, M. Scheer and P. W. Roesky, *Chem. Eur. J.* 2021, **27**, 3974-3978; b) F. Spitzer, G. Balázs, C. Graßl and M. Scheer, *Chem. Commun.* 2020, **56**, 13209-13212; c) F. Spitzer, G. Balázs, C. Graßl, M. Keilwerth, K. Meyer and M. Scheer, *Angew. Chem. Int. Ed.* 2018, **57**, 8760-8764; d) O. J. Scherer, J. Vondung and G. Wolmershäuser, *J. Organomet. Chem.* 1989, **376**, C35-C38.
[33] X. Zheng, Z. Zhang, G. Tan and X. Wang, *Inorg. Chem.* 2016, **55**, 1008-1010.
[34] L. Dütsch, M. Fleischmann, S. Welsch, G. Balázs, W. Kremer and M. Scheer, *Angew. Chem. Int. Ed.* 2018, **57**, 3256-3261.
[35] L. Dütsch, C. Riesinger, G. Balázs and M. Scheer, *Chem. Eur. J.* 2021, **27**, 8804-8810.
[36] N. G. Connelly and W. E. Geiger, *Chem. Rev.* 1996, **96**, 877-910.
[37] Agilent (2014). CrysAlis PRO. Agilent Technologies Ltd., Yarnton, Oxfordshire, England.
[38] G. Sheldrick, Acta Crystallographica Section A **2015**, 71, 3-8.
[39] O. V. Dolomanov, L. J. Bourhis, R. J. Gildea, J. A. K. Howard and H. Puschmann, *J. Appl. Cryst.* 2009, **42**, 339-341.
[40] G. Sheldrick, *Acta Crystallographica Section C* 2015, **71**, 3-8.
[41] F. Neese, *WIREs Comput. Mol. Sci.* 2018, **8**, e1327.
[42] a) J. Tao, J. P. Perdew, V. N. Staroverov, G. E. Scuseria, *Phys. Rev. Lett.* **2003**, *91*, 146401; b) V. N. Staroverov, G. E. Scuseria, J. Tao and J. P. Perdew, *J. Chem. Phys.* 2003, **119**, 12129-12137; Erratum: *J. Chem. Phys.* 2004, **121**, 11507.
[43] a) F. Weigend, M. Häser, H. Patzelt and R. Ahlrichs, *Chem. Phys. Lett.* 1998, **294**, 143; b) F. Weigend and R. Ahlrichs, *PCCP* 2005, **7**, 3297-3305.
[44] a) A. D. Becke, *Physical Review A* 1988, **38**, 3098-3100; b) J. P. Perdew, *Physical Review B* 1986, **33**, 8822-8824; Erratum: *Physical Review B* 1986, **8834**, 7406.
[45] F. Neese, F. Wennmohs, A. Hansen and U. Becker, *Chem. Phys.* 2009, **356**, 98.
[46] E. Caldeweyher, S. Ehlert, A. Hansen, H. Neugebauer, S. Spicher, C. Bannwarth and S. Grimme, *J. Chem. Phys.* 2019, **150**, 154122.
[47] V. Barone and M. Cossi, *J. Phys. Chem. A* 1998, **102**, 1995-2001.
[48] a) P. J. Stephens, F. J. Devlin, C. F. Chabalowski and M. J. Frisch, *J. Phys. Chem.* 1994, **98**, 11623-11627; b) C. Lee, W. Yang and R. G. Parr, *Physical Review B* 1988, **37**, 785-789.
[49] G. Knizia, *J. Chem. Theory Comput.* 2013, **9**, 4834-4843.

Preface

The following chapter has not been published until the submission of this thesis. It directly adjoins the topic of the previous chapter. Thus, some results are addressed in both chapters. Additionally, some results are preliminary and have to be corroborated by further studies and computations, which have not been finished until the end of this thesis.

Authors

Luis Dütsch, Christoph Riesinger, Martin Fleischmann and Manfred Scheer

Author Contributions

The main part (conceptualization, preparation of the compounds [Thia][FAl], **1**$[TEF^{Cl}]_2$, **2**$[TEF^{Cl}]_2$, **5**$[TEF^{Cl}]_2$, **6**$[TEF^{Cl}]_2$, **7**$[TEF^{Cl}]_2$, **8**$[TEF^{Cl}]_2$, **10**$[TEF]_2$, **10**$[TEF^{Cl}]_2$, **11**$[TEF]_2$, **11**$[FAl]_2$, **13**$[TEF^{Cl}]_2$ and **15**$[TEF]_2$, writing, visualization, and execution and evaluation of measurements) of this work was done by the first author (Luis Dütsch). Christoph Riesinger assisted in the synthesis and characterization of **7**$[TEF^{Cl}]_2$ in the course of his Bachelor thesis. [Thia][FAl] was synthesized by Martin Fleischmann and was also part of his PhD thesis. Manfred Scheer supervised the research and revised the manuscript.

Acknowledgements

This work was supported by the Deutsche Forschungsgemeinschaft within the project Sche 384/36-1.

6 Manipulating the Structure of Dicationic E_4 and E_2E' Ligands (E, E' = P, As, Sb, Bi): Influence of Metal Atoms, Cp Ligands and Counter Ions

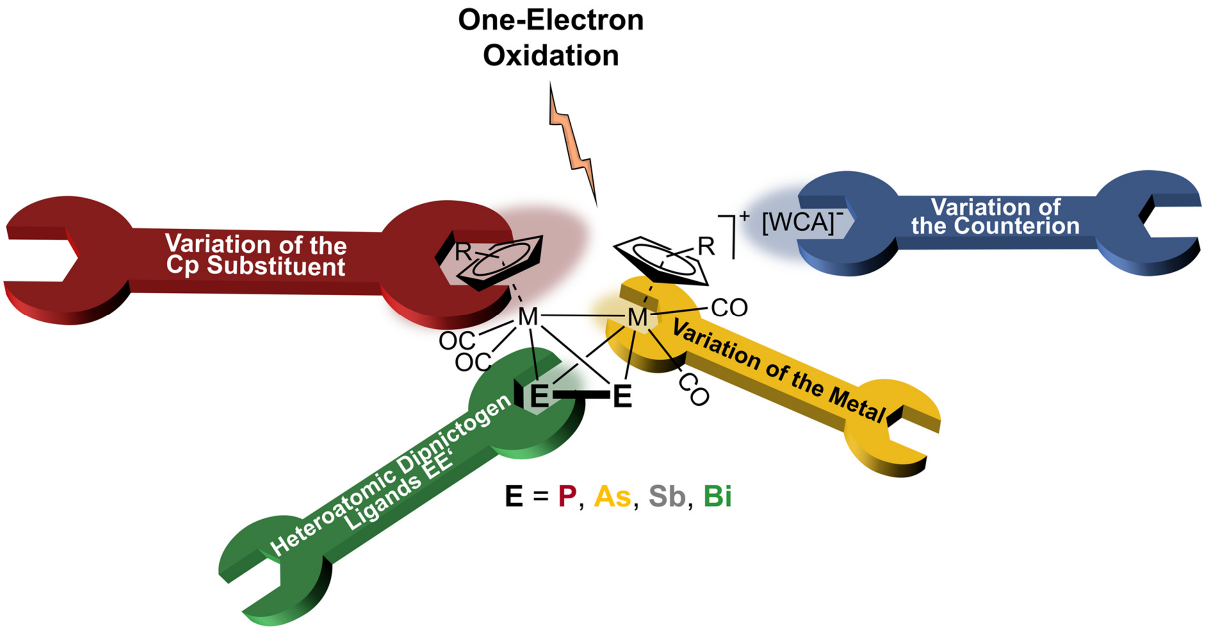

Abstract: *The influence of the metal atom, the Cp ligand and the counterion on the reactivity of the tetrahedral complexes [{Cp^{R}M(CO)$_2$}$_2$(μ,η^2:η^2-EE')] (Cp^R = Cp, Cp*; M = Mo, W; E and E' = P, As, Sb, Bi; "**M$_2$EE'**") towards the strong one-electron oxidant [C$_{12}$H$_8$S$_2$]$^{\cdot+}$ (=[Thia]$^{\cdot+}$) containing the weakly coordinating anions [Al{OC(CF$_3$)$_2$(CX$_3$)}$_4$]$^-$ (X = F ([TEF]$^-$), Cl ([TEF^{Cl}]$^-$) and [FAl{O(C$_6$F$_{10}$)(C$_6$F$_5$)}$_3$]$^-$ (= [FAl]$^-$) is reported. Additionally, the influence of the counterions on the solid-state structure of the resulting products was investigated as well. In each case of these reactions the radical monocations [**M$_2$EE'**]$^{\cdot+}$ are formed first selectively, which immediately dimerize via E–E bond formation giving the compounds [{CpMo(CO)$_2$}$_4$(μ$_4$,η^2:η^2:η^2:η^2-E'EEE')][TEF^{Cl}]$_2$ (EE' = P$_2$ (**1**[TEF^{Cl}]$_2$, As$_2$ (**2**[TEF^{Cl}]$_2$), PAs (**5**[TEF^{Cl}]$_2$), PSb (**6**[TEF^{Cl}]$_2$), AsSb (**7**[TEF^{Cl}]$_2$), AsBi (**8**[TEF^{Cl}]$_2$)), [{CpW(CO)$_2$}$_4$(μ$_4$,η^2:η^2:η^2:η^2-P$_4$)][X]$_2$ (X = TEF (**10**[TEF]$_2$), TEF^{Cl} (**10**[TEF^{Cl}]$_2$)) and [{Cp*Mo(CO)$_2$}$_4$(μ$_4$,η^2:η^2:η^2:η^2-As$_4$)][X]$_2$ (X = TEF (**11**[TEF]$_2$), FAl (**11**[FAl]$_2$)), which contain dicationic, unsubstituted E$_4$ and E$_2$E'$_2$ ligands stabilized in the coordination sphere of transition metal fragments. In contrast, ^{Cp*}**Mo$_2$As$_2$** forms the dicationic compound [{Cp*Mo(CO)$_2$}$_3$(μ$_3$,η^3:η^2:η^1-As$_3$)][TEF^{Cl}]$_2$, which contains an unprecedented Mo$_3$As$_3$ unit, via formal elimination of a [Cp*Mo(CO)$_2$As] fragment in the reaction with [Thia][TEF^{Cl}]. In general, the Cp substituent or the metal atom, respectively, only have marginal influence on the solid-state structure, whereas the use of different WCAs causes planarization or cyclization of the dicationic E$_4$ and E$_2$E'$_2$ ligands. Additionally, two different **Mo$_2$E$_2$** units (**Mo$_2$P$_2$** + **Mo$_2$As$_2$**) can be linked together via an oxidative dimerization to give a stochastic mixture of **1**, **2** and [{CpMo(CO)$_2$}$_4$(μ$_4$,η^2:η^2:η^2:η^2-PPAsAs)] (**15**).*

6.1 Introduction

Transition metal complexes bearing substituent-free polypnictogen ligands (E_n ligand complexes) can be used as precursors for the formation of new, extended polypnictogen scaffolds. While the reduction of E_n ligand complexes[1] as well as their functionalization with nucleophiles[1c, 2] has been shown to afford anionic polypnictogen units in many cases, their oxidation behaviour has been studied far less.[1f, 1i] To address the oxidation behaviour of such complexes we could show (*cf.* chapter 4) that the tetrahedrane derivatives [{CpMo(CO)$_2$}$_2$(μ,η^2:η^2-E$_2$)] (E = P, As, Sb, Bi; "**Mo$_2$E$_2$**"), which are isolobal to P_4 and As_4, are excellent starting materials to build up dicationic P_4 (**1**[TEF]$_2$) and As_4 (**2**[TEF]$_2$) chains as well as Sb_4 (**3**[TEF]$_2$) and Bi_4 (**4**[TEF]$_2$) cages, respectively, *via* dimerization reactions upon one-electron oxidation with the strong radical oxidant [$C_{12}H_8S_2$]$^{\cdot+}$ ([Thia]$^{\cdot+}$ = "thianthrenium") (Scheme 1).[3] Thereby, the E_4 ligands in **1**[TEF]$_2$ and **2**[TEF]$_2$ show an unusual gauche conformation, whereas in **3**[TEF]$_2$ and **4**[TEF]$_2$ distorted "butterfly-like" (bicyclo[1.1.0]butane) structural motifs are observed in the solid state, which do not bear any organic substituents. These dications are further stabilized by the weakly coordinating anion (WCA) [Al{OC(CF$_3$)$_3$}$_4$] (= [TEF]$^-$).

The tetrahedral compounds **Mo$_2$E$_2$** exhibit multiple adjusting screws to vary the steric and electronic properties as well as the elemental composition in order to manipulate their reactivity towards oxidation and to control the outcoming products (Scheme 2). The exchange of one of the pnictogen atoms is possible leading to tetrahedral complexes [{CpMo(CO)$_2$}$_2$(μ,η^2:η^2-PE)] (E = As (**Mo$_2$PAs**), Sb (**Mo$_2$PSb**)) containing a hetero-dipnictogen **PE** ligand.[4] Recently, we developed a new synthetic approach for these complexes (*cf.* chapter 3)[5], which not only increased their yield considerably, but also made the heavier congeners [{CpMo(CO)$_2$}$_2$(μ,η^2:η^2-AsSb)] (**Mo$_2$AsSb**), [{CpMo(CO)$_2$}$_2$(μ,η^2:η^2-AsBi)] (**Mo$_2$AsBi**) and [{CpMo(CO)$_2$}$_2$(μ,η^2:η^2-SbBi)] (**Mo$_2$SbBi**) accessible

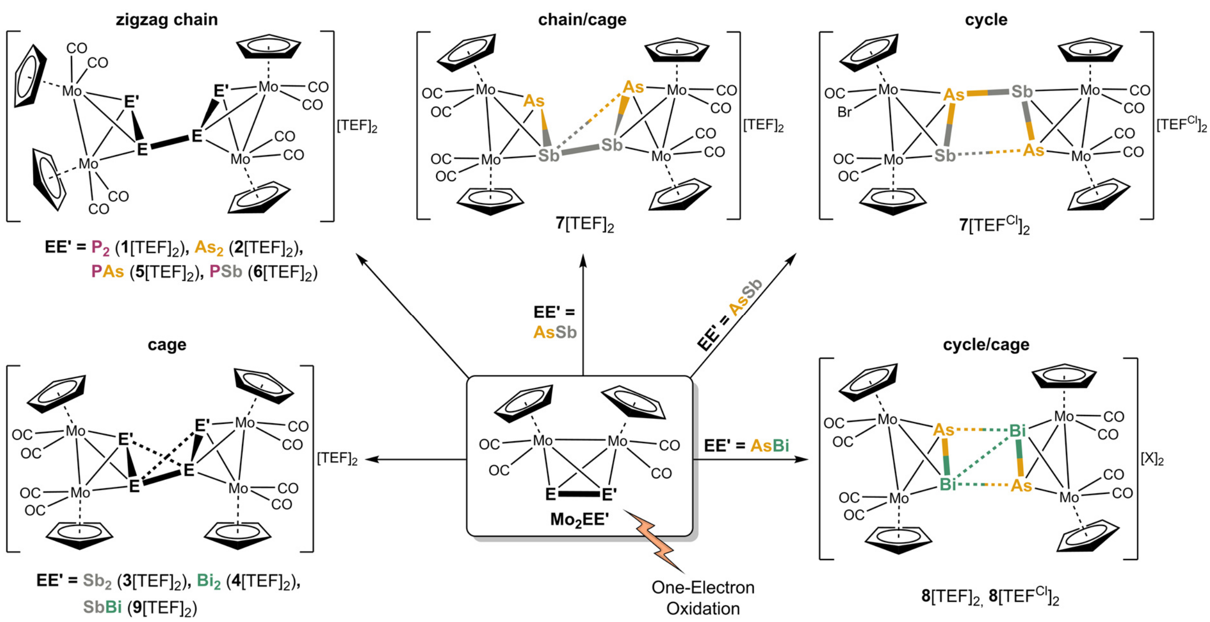

Scheme 1: One-electron oxidation of the complexes [{CpMo(CO)$_2$}$_2$(μ,η^2:η^2-E$_2$)] (E = P, As, Sb, Bi; "**Mo$_2$E$_2$**") and [{CpMo(CO)$_2$}$_2$(μ,η^2:η^2-EE')] (EE' = PAs, PSb, AsSb, AsBi, SbBi; "**Mo$_2$EE'**") leading to dicationic E_4 chains and cages as well as $E_2E'_2$ chains, cages and rings.

allowing their further investigation. These complexes **Mo_2EE'** bear the potential to assemble manifold E_n ligand geometries in the solid state upon oxidation compared to **Mo_2E_2** due to their different pnictogen atoms. And indeed, here we could show that one-electron oxidation of **Mo_2PAs–Mo_2SbBi** (*cf.* chapter 5) forms unique hetero-tetrapnictogen ligand complexes, which feature either dicationic AsPPAs (**5**[TEF]$_2$) as well as SbPPSb (**6**[TEF]$_2$) zigzag chains, AsSbSbAs (**7**[TEF]$_2$) as well as BiSbSbBi (**9**[TEF]$_2$) cage-like compounds or a planar AsBiBiAs (**8**[TEF]$_2$) cage/cycle (Scheme 1).[6]

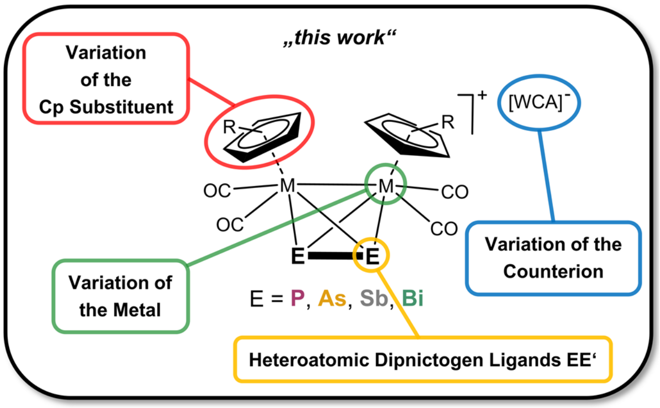

Scheme 2: *This work*: Tuning the properties of the tetrahedral complexes **Mo_2E_2** by varying the metal atoms, Cp substituents or the E_2 ligand (exchanging one of the pnictogen atoms with a different one), respectively, and investigation on their reactivity towards one-electron oxidants with different weakly coordinating anions (WCAs).

Therefore, the question arose if further tuning of the reactivity of the starting materials could influence the reaction outcomes and if the solid-state structures will also be affected. Hence, we report on the oxidation of the tetrahedral complexes **$^{CpR}M_2EE'$**, which incorporate different Cp^R ligands (*e.g.*, Cp* = C_5Me_5, Cp' = $C_5H_4{}^tBu$)[7] or metal atoms (W and Cr)[7e, 8]. Additionally, the impact of the used counterion (WCA) on the molecular structure in the solid state was investigated (Scheme 2) since we observed cyclization of the As_2Sb_2 ligand in **7** in preliminary work (*cf.* chapter 5) when switching from $[TEF]^-$ to the similar WCA $[Al\{OC(CF_3)_2(CCl_3)\}_4]$ (= $[TEF^{Cl}]^-$) (Scheme 1).

6.2 Results and Discussion

Influence of the Cp ligand and the metal atom

As mentioned before, the metal atom and Cp^R ligand in the starting material can easily be exchanged. Thus, the one-electron oxidation of the tungsten derivative $[\{CpW(CO)_2\}_2(\mu,\eta^2:\eta^2\text{-}P_2)]$ (**W_2P_2**)[9] and the Cp* derivative $[\{Cp^*Mo(CO)_2\}_2(\mu,\eta^2:\eta^2\text{-}As_2)]$ (**$^{Cp*}Mo_2As_2$**); Cp* = C_5Me_5)[7b] with [Thia][TEF] leads to $[\{CpW(CO)_2\}_4(\mu_4,\eta^2:\eta^2:\eta^2:\eta^2\text{-}P_4)][TEF]_2$ (**10**[TEF]$_2$) and $[\{Cp^*Mo(CO)_2\}_4(\mu_4,\eta^2:\eta^2:\eta^2:\eta^2\text{-}As_4)][TEF]_2$ (**11**[TEF]$_2$) in 87 and 67% yield (Figure 1a), respectively, which, however, show only minor structural deviations from their Cp or Mo counterparts. The molecular structures of **10**[TEF]$_2$ and **11**[TEF]$_2$ as well as selected bond lengths and angles are depicted in Figure 1b/c.

The ^1H NMR spectrum of **11**[TEF]$_2$ in CD_2Cl_2 solution shows only one singlet at δ = 2.08 ppm for the methyl groups of the Cp* ligands and the characteristic singlet for the $[TEF]^-$ anion is observed in the $^{19}F\{^1H\}$ NMR spectrum. In the ESI(+) mass spectra of **10**[TEF]$_2$ and **11**[TEF]$_2$ only the monomeric species $[\mathbf{W_2P_2}]^{\cdot+}$ and $[\mathbf{^{Cp*}Mo_2As_2}]^{\cdot+}$ can be detected, suggesting a dissociation in the gas-phase as it was found for **1**[TEF]$_2$ and **2**[TEF]$_2$.[3]

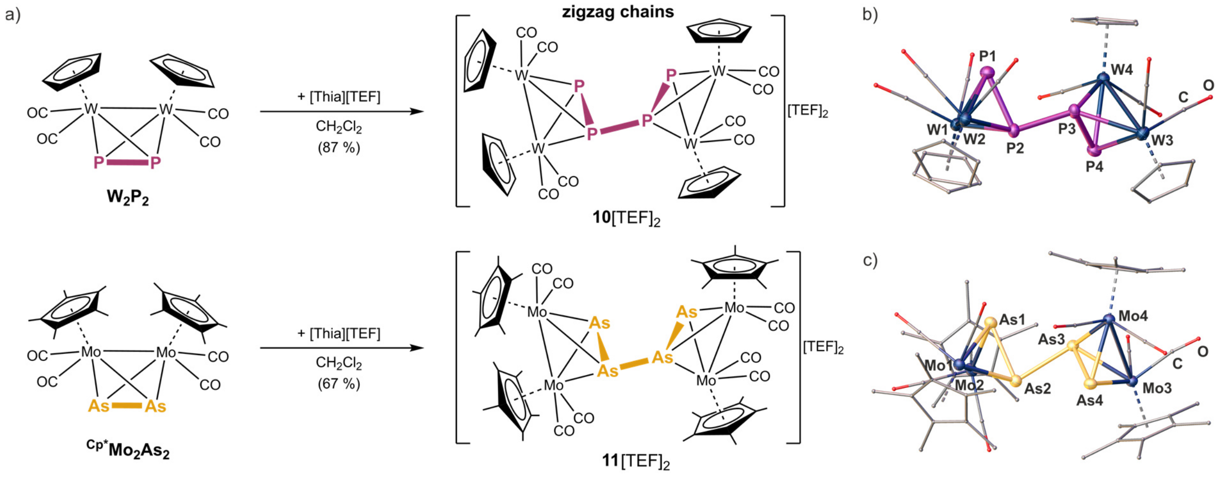

Figure 1: a) Oxidation of the tungsten derivative [{CpW(CO)$_2$}$_2$(μ,η^2:η^2-P$_2$)] (**W$_2$P$_2$**) and the Cp* derivative [{Cp*Mo(CO)$_2$}$_2$(μ,η^2:η^2-As$_2$)] (**^{Cp*}Mo$_2$As$_2$**) (yields are given in parentheses); b) Molecular structure of **10**[TEF]$_2$; c) Molecular structure of **11**[TEF]$_2$. Anisotropic displacement is set to the 50% probability level. H atoms are omitted and C as well as O atoms are drawn as small spheres for clarity. Selected bond lengths [Å] and angles [°]: **10**[TEF]$_2$: P1–P2 2.1888(1), P2–P3 2.2193(1), P3–P4 2.1458(1), W1–W2 3.1494(1), W3–W4 3.1250(1), P1-P2-P3 96.67(1), P2-P3-P4 103.11(1), P1-P2-P3-P4 133.76(1); **11**[TEF]$_2$: As1–As2 2.435(1), As2–As3 2.574(1), As3–As4 2.440(1), Mo1–Mo2 3.227(1), Mo3–Mo4 3.222(1), As1-As2-As3 82.89(4), As2-As3-As4 81.23(4), As1-As2-As3-As4 139.54(4).

Influence of the counterion (WCA)

Moreover, it was of special interest to investigate the impact of the counterion on both the reactivity towards one-electron oxidants as well as its influence on the molecular structure of the resulting products. Hence, we exchanged the [TEF]$^-$ anion with [TEF^{Cl}]$^-$ by reacting solutions of **Mo$_2$E$_2$** (E = P–Bi), **Mo$_2$EE'** (E ≠ E' = P–Bi) and **W$_2$P$_2$** with [Thia][TEF^{Cl}] (Scheme 3). It appears that in all of these reactions the counter anion has no influence on the reactivity itself since again the dimeric, dicationic E–E coupled products [{CpMo(CO)$_2$}$_4$(μ$_4$,η^2:η^2:η^2:η^2-E$_4$)][TEF^{Cl}]$_2$ (E = P (**1**[TEF^{Cl}]$_2$, As (**2**[TEF^{Cl}]$_2$)), [{CpMo(CO)$_2$}$_4$(μ$_4$,η^2:η^2:η^2:η^2-E$_2$E'$_2$)][TEF^{Cl}]$_2$ (E$_2$E'$_2$ = P$_2$As$_2$ (**5**[TEF^{Cl}]$_2$), P$_2$Sb$_2$ (**6**[TEF^{Cl}]$_2$), As$_2$Sb$_2$ (**7**[TEF^{Cl}]$_2$), As$_2$Bi$_2$ (**8**[TEF^{Cl}]$_2$)) and [{CpW(CO)$_2$}$_4$(μ$_4$,η^2:η^2:η^2:η^2-P$_4$)][TEF^{Cl}]$_2$ (**10**[TEF^{Cl}]$_2$) can be obtained selectively in good crystalline yields ranging from 77 % to 96 % (regardless of several attempts, the oxidation products of **Mo$_2$Sb$_2$**, **Mo$_2$Bi$_2$** and **Mo$_2$SbBi** could not be crystallized due to the high solubility of the [TEF^{Cl}]$^-$ anion leading to oily products). However, the exchange of the counterion has a dramatic influence on the solid-state structures of the [TEF^{Cl}] salts of **1**, **2**, **5**, **6**, **7**, **8** and **10** (Figure 3).

The dications in **1**[TEF^{Cl}]$_2$, **5**[TEF^{Cl}]$_2$ and **10**[TEF^{Cl}]$_2$ contain zigzag P$_4$ and AsPPAs chains (Figure 3a-c) similar to their analogues stabilized by the [TEF]$^-$ anion regarding P–P, P–As, Mo–Mo and W–W bond lengths, respectively (*vide supra*).[3] However, the respective P$_4$ and P$_2$As$_2$ chains in **1**[TEF^{Cl}]$_2$ and **5**[TEF^{Cl}]$_2$ reveal a drastic planarization compared to their [TEF]$^-$ salts since the dihedral angles approach 180° (173.4(2)° (**1**[TEF^{Cl}]$_2$) and 172.8(2)° (**5**[TEF^{Cl}]$_2$)) and, thus, approach the optimized structure obtained DFT computations, which predict symmetric, planar E$_4$ chains.[3] Furthermore, in the tungsten complex **10**[TEF^{Cl}]$_2$ a perfectly planar P$_4$ chain with a dihedral angle of 180.0(1)° is observed, which resembles the dicationic P$_4$ chain stabilized by [SbF$_6$]$^-$ anions (*cf.* chapter 4).[3]

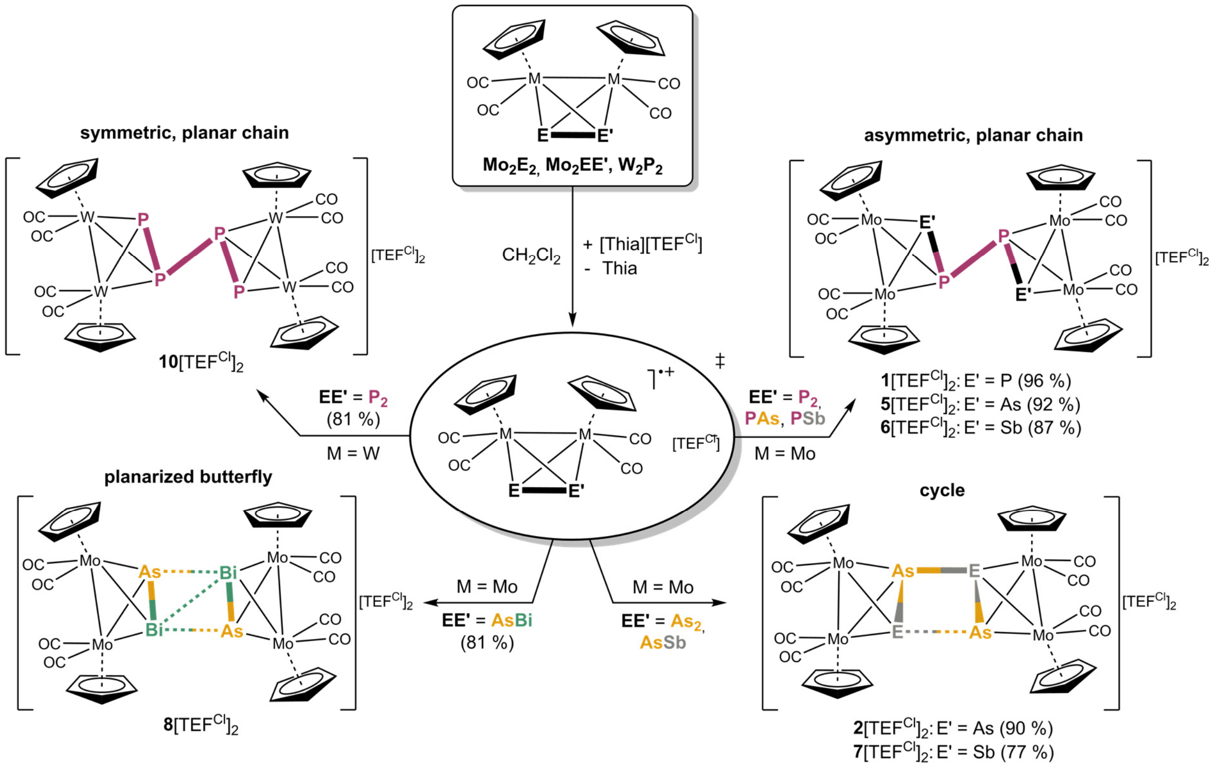

Scheme 3: Oxidation of **Mo_2E_2**, **Mo_2EE'** and **W_2P_2** with Thia[TEF^{Cl}] leading to dimeric, dicationic products possessing E_4 and $E_2E'_2$ ligands, which exhibit asymmetric (**1**[TEF^{Cl}]$_2$, **5**[TEF^{Cl}]$_2$ and **6**[TEF^{Cl}]$_2$) or symmetric planar chains (**10**[TEF^{Cl}]$_2$), cycles (**2**[TEF^{Cl}]$_2$ and **7**[TEF^{Cl}]$_2$) or a planarized, distorted butterfly unit (**8**[TEF^{Cl}]$_2$), respectively. Yields are given in parentheses.

The molecular structure of **6**[TEF^{Cl}]$_2$ could, regardless of numerous attempts, not be determined due to the limited crystal quality. However, it was possible to determine the unit cell, whose parameters are similar to those of **1**[TEF^{Cl}]$_2$, **5**[TEF^{Cl}]$_2$ and **10**[TEF^{Cl}]$_2$. Therefore, it can be assumed that the solid-state structure of **6**[TEF^{Cl}]$_2$ is similar to the ones of **1**[TEF^{Cl}]$_2$, **5**[TEF^{Cl}]$_2$ and **10**[TEF^{Cl}]$_2$. This assumption is supported by ^{31}P NMR spectroscopy, which shows a signal at $\delta = 35.3$ ppm in *o*-DFB/C_6D_6, which is in accordance with the signal of **6**[TEF]$_2$ ($\delta = 34.7$ ppm). Furthermore, after prolonged storage some crystals of the decomposition product [{CpMo(CO)$_2$}$_4$(μ-SbCl)(μ_4,η^1:η^2:η^2-P(PCl)Sb)][TEF^{Cl}]$_2$ (**12**[TEF^{Cl}]$_2$) could be isolated and subjected to X-ray diffraction analysis revealing a P-P coupled dicationic structure (Figure 2), which corroborates the assumption of the formation of a dicationic SbPPSb chain upon oxidation of **Mo_2PSb**. Compound **12**[TEF^{Cl}]$_2$ consists of two Mo_2PSb cores, which are linked together *via* newly formed P–P and P–Sb bonds. The former (2.2028(1) Å) is a classical single bond, while the latter (2.6345(1) Å) is elongated by 0.1 Å

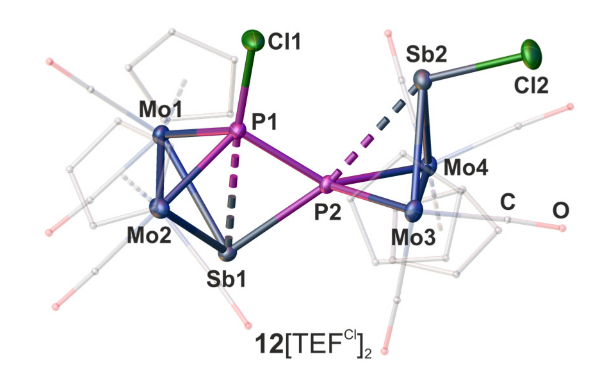

Figure 2: Molecular structure of **12**[TEF^{Cl}]$_2$. Anisotropic displacement is set to the 50% probability level. H atoms as well as counterions are omitted, and C as well as O atoms are drawn translucent and as small spheres for clarity. Selected bond lengths [Å] and angles [°]: Sb1–P1 2.86157(2), Sb1–P2 2.63445(2), P1–P2 2.20283(3), P2–Sb2 3.01221(3), Mo1–Mo2 3.14914(4), Mo3–Mo4 3.13602(4), P1–Cl1 2.08466(1), Sb2–Cl2 2.42339(1), Sb2-P1-P2-Sb2 172.82(1).

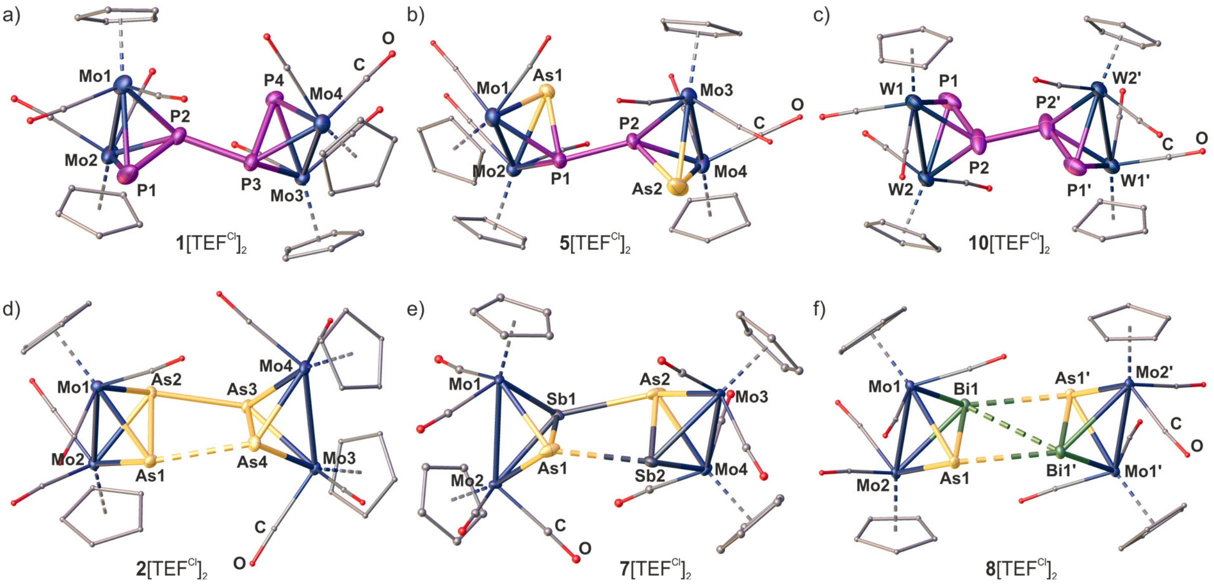

Figure 3: Molecular structure of the dicationic parts of **1**[TEF^{Cl}]$_2$ (a), **5**[TEF^{Cl}]$_2$ (b), **10**[TEF^{Cl}]$_2$ (c), **2**[TEF^{Cl}]$_2$ (d), **7**[TEF^{Cl}]$_2$ (e) and **8**[TEF^{Cl}]$_2$ (f). Anisotropic displacement is set to the 50% probability level. H atoms are omitted and C as well as O atoms are drawn as small spheres for clarity. Selected bond lengths [Å] and angles [°]: **1**[TEF^{Cl}]$_2$: P1–P2 2.199(3), P2–P3 2.190(3), P3–P4 2.097(4), Mo1–Mo2 3.181(1), Mo3–Mo4 3.138(1), As1-P1-P2 88.6(1), P1-P2-As2 115.9(1), As1-P1-P2-As2 173.4(2); **5**[TEF^{Cl}]$_2$: P1–As1 2.322(4), P1–P2 2.197(5), P2–As2 2.214(4), Mo1–Mo2 3.196(2), Mo3–Mo4 3.140(2), As1-P1-P2 87.33(2), P1-P2-As2 115.0(2), As1-P1-P2-As2 172.8(2); **10**[TEF^{Cl}]$_2$: P1–P2 2.143(2), P2–P2' 2.183(2), W1–W2 3.130(2), P1-P2-P2' 102.3(9), P1-P2-P2'-P1' 180.0(1); **2**[TEF^{Cl}]$_2$: As1–As2 2.4416(5), As2–As3 2.7121(5), As3–As4 2.5465(6), As4–As1 2.9049(6), As1-As2-As4-As3 148.86(2); **7**[TEF^{Cl}]$_2$: As1–Sb1 2.7297(7), Sb1–As2 2.8699(8), As2–Sb2 2.6225(7), Sb2–As1 2.9833(8), Sb1–Sb2 3.49065(2), As1-Sb1-Sb2-As2 148.33(2); **8**[TEF^{Cl}]$_2$: As1–Bi1 2.8372(4), Bi1–Bi1' 3.4264(3), As1–Bi1' 3.2187(3), Mo1–Mo2 3.1765(4), As1-Bi1-Bi1' 60.99(1), As1-Bi1-Bi1'-As1' 180.0(1).

compared to the sum of the covalent radii.[10] The original intratetrahedral P–Sb bonds exceed a classical single bond even more (P1–Sb1: 2.8616(1) Å, P2–Sb2: 3.0122(1) Å). This is probably caused by the additionally bound chlorine atoms on P1 and Sb2 as it was also observed for, *e.g.*, halogenation reactions of **Mo_2P_2**.[11] Moreover, the elongation of the P1–Sb1 bond can be explained by the partial insertion of the formally cationic P2 atom into the P1–Sb1 bond (*cf.* the insertion of phosphenium ions in P_4).[12] Furthermore, the Sb2 atom in **12**[TEF^{Cl}]$_2$ can be regarded as a chlorostibinidene, which donates to the P_2Sb cyclic unit, and is stabilized by two [CpMo(CO)$_2$] fragments. Since only few crystals of **12**[TEF^{Cl}]$_2$ could be isolated, no further investigations were carried out to determine the chlorine source. It can either originate from the solvent (CH_2Cl_2) or less likely from the counter ion [TEF^{Cl}]$^-$. Elemental analysis and mass spectrometric measurements of the isolated crystals perfectly fit to the composition of compound **12**[TEF^{Cl}]$_2$.

While the [TEF^{Cl}]$^-$ anion causes planarization of the E_4 chains in **1**, **5** and **10**, respectively, the molecular structures of **2**[TEF^{Cl}]$_2$ and **7**[TEF^{Cl}]$_2$ differ significantly from their [TEF]$^-$ congeners **2**[TEF]$_2$ and **7**[TEF]$_2$ and build up unprecedented structural motifs (Figure 3d-e). The compounds **2**[TEF^{Cl}]$_2$ and **7**[TEF^{Cl}]$_2$ contain a central, cyclic As_4 or As_2Sb_2 ligand, respectively. Interestingly, in the latter case the arsenic and antimony atoms within the cycle are bound in an alternating fashion (for a detailed description of the molecular structure of **7**[TEF^{Cl}]$_2$ see chapter 5).[13] The intratetrahedral As–As bonds in **2**[TEF^{Cl}]$_2$ are elongated compared to free **Mo_2As_2** by 0.1 to 0.2 Å,[8f] but are still in the range of a single bond. The Mo–Mo bonds are widened up in the same manner. The Mo_2As_2 tetrahedra are tilted against each other by approximately 15° leading to a dihedral angle of the As_4 ring of 148.86(2)°.

Furthermore, they are interconnected *via* two newly formed As–As bonds, where one of them is 0.19 Å longer than the other, but even the shorter bond exceeds the sum of the covalent radii (Σ(As–As) = 1.42 Å)[10] by 0.29 Å. The angles within the As_4 cycle in **2**[TEF^{Cl}]$_2$ are all around 90° (83.28(2)°–90.63(2)°) and the diagonal As–As distances (3.6319(5) and 3.7407(6) Å) are exceeding the sum of the van-der-Waals radii[14] excluding any further interactions. Overall, while cyclic As_4 units are known as heavier dianionic analogues of *cyclo*-butadiene,[1h, 15] compound **2**[TEF^{Cl}]$_2$ depicts the first cationic cyclic As_4 moiety, which additionally is stabilized without any organic substituents. Furthermore, **7**[TEF^{Cl}]$_2$ contains the first cyclic As_2Sb_2 ligand in general.

In comparison to **5**[TEF^{Cl}]$_2$–**7**[TEF^{Cl}]$_2$, the [TEF^{Cl}]$^-$ derivative **8**[TEF^{Cl}]$_2$ (Figure 3f) shows close similarity to its [TEF]$^-$ congener **8**[TEF]$_2$ regarding the bond lengths and angles except for the Bi–Bi bond, which is elongated by 0.14 Å in **8**[TEF^{Cl}]$_2$ compared to **8**[TEF]$_2$.

Also, the Cp* derivative ^{Cp*}**Mo$_2$As$_2$** was oxidized with [Thia]$^+$ salts containing different counterions. Therefore, the thianthrenium salt with the WCA [FAl]$^-$ (= [FAl{O(C_6F_{10})(C_6F_5)}$_3$]$^-$) was synthesized in an analogous procedure as [Thia][TEF^{Cl}] (*cf.* chapter 5).[13] Due to enhanced solubility of the Cp* substituents the product of the reaction of [Thia][FAl] is already soluble in *ortho*-difluorobenzene. The oxidation leads again to a dimerized, dicationic product [{Cp*Mo(CO)$_2$}$_4$(μ_4,η^2:η^2:η^2:η^2-As_4)][FAl]$_2$ (**11**[FAl]$_2$), which resembles its [TEF]$^-$ analogue **11**[TEF]$_2$ (Figure 1c). In contrast, the reaction of ^{Cp*}**Mo$_2$As$_2$** with [Thia][TEF^{Cl}] in CH_2Cl_2 leads to the unprecedented product [{Cp*Mo(CO)$_2$}$_3$(μ_3,η^3:$\eta^{1:1}$:η^1-As_3)][TEF^{Cl}]$_2$ (**13**[TEF^{Cl}]$_2$) in 83 % yield, where one [Cp*Mo(CO)$_2$As] fragment is eliminated during the reaction (Scheme 4). Compound **13**[TEF^{Cl}]$_2$ crystallizes as thin red needles from *o*-DFB/*n*-pentane.[16] Single crystal X-ray diffraction of **13**[TEF^{Cl}]$_2$ (Figure 4) reveals an As_3 ligand, which is stabilized by a bridging dimolybdenum fragment [Cp*Mo(CO)$_2$]$_2$ in an η^3:$\eta^{1:1}$ coordination mode. The As1–As2 (2.369(1) Å) and As2–As3 (2.380(1) Å) bond lengths within the As_3 chain are between an As–As single (2.42 Å) and double bond (2.28 Å).[10] Therefore, the As_3 ligand can be described as an all-arsenic analogue of an allylic system. Additionally, another [Cp*Mo(CO)$_2$] fragment is bound to the As3 atom in an η^1 fashion with a very short Mo3–As3 bond length of 2.365(1) Å, which matches a Mo–As double bond. This hints to a possible arsinidene character of the As3 moiety, which has to be further comfirmed by theoretical calculations (not finished till the end of this thesis).

Overall, the structure can be described as a distorted, square pyramidal Mo_2As_3 core, which incorporates an allylic As_3 ligand and is additionally bound to a [Cp*Mo(CO)$_2$] fragment. Thereby, **13**[TEF^{Cl}]$_2$ contains a very rare example of an allylic As_3 ligand, which is stabilized without bulky, organic

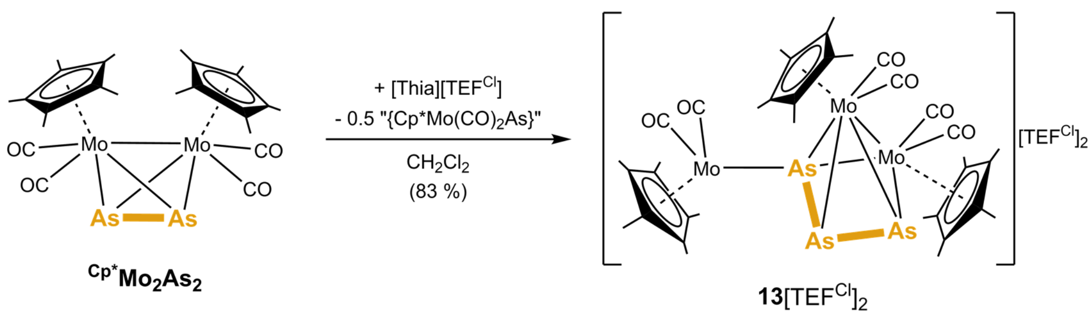

Scheme 4: Oxidation of ^{Cp*}Mo$_2$As$_2$ with [Thia][TEF^{Cl}].

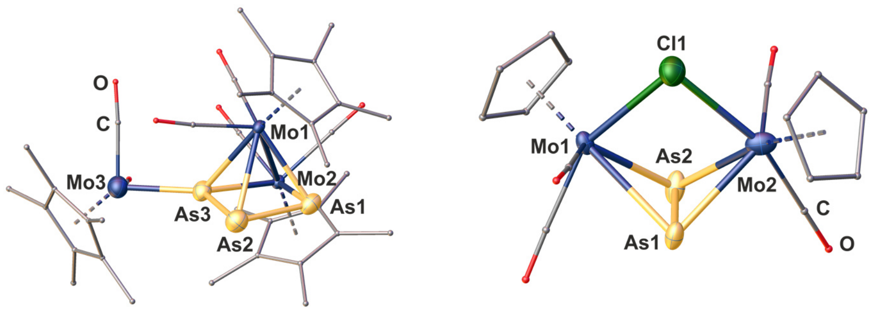

13[TEF^{Cl}]$_2$ **14**[TEF^{Cl}]

Figure 4: Left: Molecular structure of the cation in **13**[TEF^{Cl}]$_2$; Right: Molecular structure of the cation in **14**[TEF^{Cl}]. Anisotropic displacement is set to the 50% probability level. H atoms as well as counterions are omitted, and C as well as O atoms are drawn as small spheres for clarity. Selected bond-lengths [Å]: **13**[TEF^{Cl}]$_2$: As1–As2 2.369(1), As2–As3 2.380(1), As3–As1 3.150(1), Mo1–Mo2 3.2273(8), Mo3–As3 2.365(1), Mo1–As 2.602(1)-2.742(1); Mo2–As 2.558(1)-2.578(1); **14**[TEF^{Cl}]: As1–As2 2.316(1), Mo–Mo 3.6636(8), Mo1/Mo2–Cl1 2.582(2)/2.477(2).

ligands.[1i, 17] Moreover, the bonding situation in the dication in **13**[TEF^{Cl}]$_2$ may be also elucidated by describing the central Mo_2As_3 core by the *Wade´s* rules.[18] According to these, the Mo_2As_3 core has 14 (= 2n+4) skeletal electrons resulting in a *nido*-type cluster, which corresponds to a square pyramid for n = 5.

As the cyclic voltammograms of $\mathbf{Mo_2E_2}$[3] and **Mo₂EE'**[13] also show a second irreversible oxidation below the oxidation potential of [Thia]$^+$ it should be generally possible to achieve a double oxidation of these complexes. However, such a behaviour was never observed not even when an excess of the oxidation agent was used. Solely in the reaction of $\mathbf{Mo_2As_2}$ with Thia[TEF^{Cl}] one single crystal of a side product ([{CpMo(CO)$_2$}$_2$(μ,η^2:η^2-As$_2$)(*μ*-Cl)][TEF^{Cl}] (**14**[TEF^{Cl}])) could be found, which indicates the possibility of a double oxidized product. Compound **14**[TEF^{Cl}] (Figure 4) consists of a formally double oxidized, dicationic tetrahedra $\mathbf{Mo_2As_2}$, which is stabilized by one [TEF^{Cl}]$^-$ anion on the one hand, and a Cl^- anion on the other hand. The latter is inserted into to Mo–Mo bond, which is opened and elongated to 3.664(1) Å. The Mo–Cl bonds are 0.1 and 0.2 Å longer than a calculated single bond (Mo–Cl: 2.37 Å)[10] rather suggesting a donating bond character. The As–As bond length instead remains basically unchanged as it is the same as in free $\mathbf{Mo_2As_2}$.[8f]

Linking of two different Mo_2E_2 units

Moreover, it was of interest to investigate if it is possible to link two different Mo_2E_2 moieties *via* oxidative dimerization. Hence, we reacted 1:1 solutions of $\mathbf{Mo_2P_2}$ and $\mathbf{Mo_2As_2}$ in CH_2Cl_2 with an equimolar amount of Thia[TEF] (Figure 5). Generally, three possible products can be formed upon dimerization during this reaction, either by combining $\mathbf{Mo_2P_2}$ or $\mathbf{Mo_2As_2}$, respectively, with themselves ($\mathbf{Mo_2P_2}$+$\mathbf{Mo_2P_2}$ resulting in **1**[TEF]$_2$ or $\mathbf{Mo_2As_2}$+$\mathbf{Mo_2As_2}$ resulting in **2**[TEF]$_2$) or combining $\mathbf{Mo_2P_2}$ with $\mathbf{Mo_2As_2}$, which would lead to the unprecedented product [{CpMo(CO)$_2$}$_4$(μ$_4$,η^2:η^2:η^2:η^2-PPAsAs)][TEF]$_2$ (**15**[TEF]$_2$). The reaction mixture was precipitated with *n*-hexane and, after washing with toluene, crystalline samples could be obtained from CH_2Cl_2/*n*-hexane. These crystals were subjected to single crystal X-ray diffraction and NMR spectroscopy. In the ^{31}P and ^{31}P{^{1}H} NMR spectra in CD_2Cl_2 one broad (*δ* = −0.2 ppm, $\omega_{1/2}$ = 491 Hz) and one sharp singlet (*δ* = −85.1 ppm) in a ratio of

1:1 can be detected (the same was observed in the ^{31}P and $^{31}P\{^1H\}$ NMR spectra of the crude solution). While the former signal can be unambiguously assigned to the formation of **1**[TEF]$_2$, the latter arises from an unknown product and might indicate the presence of **15**[TEF]$_2$. Furthermore, the ^1H NMR spectrum reveals three singlets in a 1:1:1 ratio at δ = 5.68, 5.75 and 5.82 ppm. Here, the former two can be assigned to **2**[TEF]$_2$ and **1**[TEF]$_2$, respectively, whereas the latter again originates from an unknown compound. Hence, these spectra indicate that the three predicted products **1**[TEF]$_2$, **2**[TEF]$_2$ and **15**[TEF]$_2$ are formed in equimolar amounts. Additionally, it was also possible to get single crystals of **15**[TEF]$_2$ (the molecular structures of **1**[TEF]$_2$ and **2**[TEF]$_2$ are described in chapter 4).[3] One should consider that the shape and colour of the crystals within the mixture are similar. The crystals of the different products can only be distinguished by measuring the cell parameters. **15**[TEF]$_2$ crystallizes in the monoclinic space group $P2_1/c$ with two dications and four [TEF]$^-$ anions in the asymmetric unit. The dication (Figure 5) consists of an Mo_2P_2 and an Mo_2As_2 tetrahedron, which are linked together *via* a newly formed P–As bond resulting in a four-membered, zigzag PPAsAs chain. The P1–P2 (2.148(7) Å) bond length is similar to those in **1**[TEF]$_2$. However, the As1–As2 (2.532(3) Å) bond length is elongated by 0.1 Å compared to **2**[TEF]$_2$. The new P1–As1 (2.444(5) Å) bond is also only 0.1 Å longer than a P–As single bond (2.32 Å).[10] Interestingly, in contrast to **1**[TEF]$_2$ and **2**[TEF]$_2$, an additional short P1···As2 (2.897(5) Å) contact can be observed leading to a distortion of the P_2As_2 chain. Therefore, the formally cationic P1 atom partially inserts into the As–As bond, which was also observed for **12**[TEF^{Cl}]$_2$ in a similar fashion (*vide supra*). The distortion of the P_2As_2 chain can also be seen within the angles of the chain. While the As2-As1-P1 angle is shortened to 71.2(1)° in comparison to **1**[TEF]$_2$ or **2**[TEF]$_2$, respectively, the As1-P1-P2 angle is widened up to 124.3(3)°. The former is caused by a short P1···As2

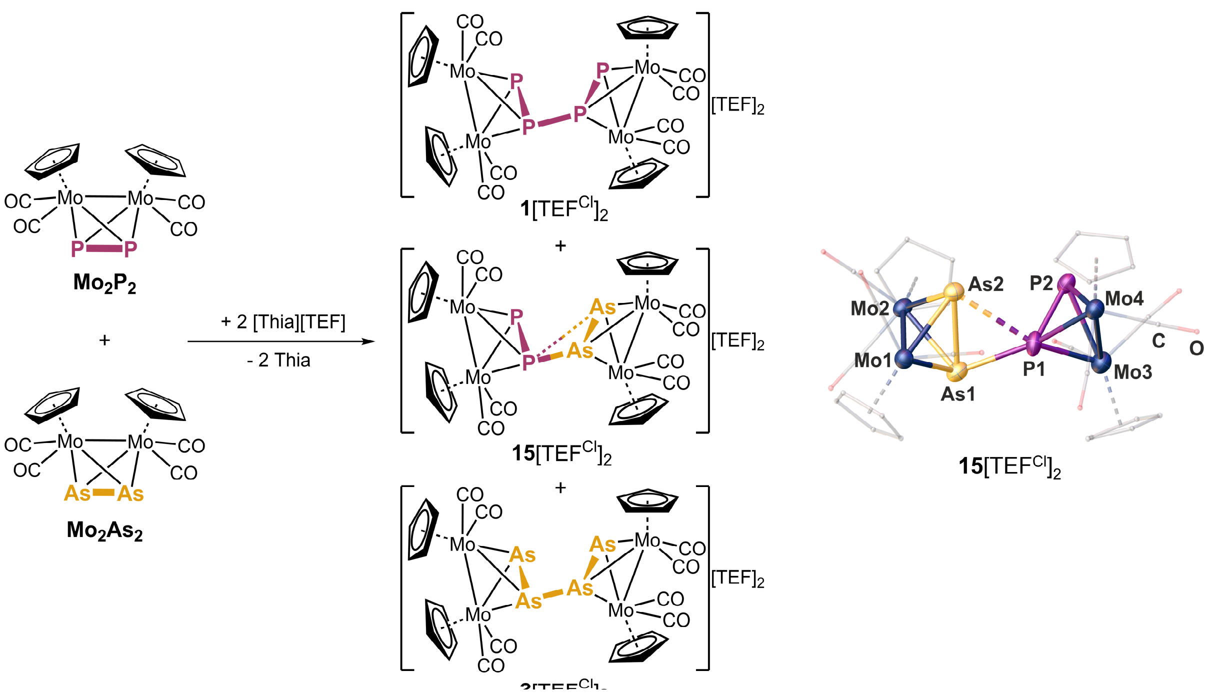

Figure 5: Left: Oxidation of a 1:1 solution of **Mo_2P_2** and **Mo_2As_2** with [Thia][TEF]; right: Molecular structure of **15**[TEF]$_2$. Anisotropic displacement is set to the 50% probability level. H atoms as well as counterions are omitted, and C as well as O atoms are drawn translucent and as small spheres for clarity. Selected bond-lengths [Å] and angles [°]: As1–As2 2.532(3), As1–P1 2.444(5), P1–P2 2.148(7), P1–As2 2.897(5), Mo1–Mo2 3.154(2), Mo3–Mo4 3.125(2), As2-As1-P1 71.2(1), As1-P1-P2 124.3(3), As2-As1-P1-P2 135.6(2).

contact. The dihedral angle (135.6(2)°) is similar to those of **1**[TEF]$_2$ and **2**[TEF]$_2$. Overall, the presence of compound **15**[TEF]$_2$ shows that it is possible to link two different tetrahedral **Mo₂E₂** complexes *via* oxidation.

6.3 Conclusion

In summary, we have tuned the electronic and steric properties of the complexes **Mo_2E_2** (E = P–Bi) by exchanging the metal atom (using W instead of Mo), the Cp^R ligand (using Cp* instead of Cp) or the E_2 ligand (using the respective hetero-dipnictogen complexes **Mo_2EE'** (E ≠ E' = P–Bi)) and investigated the influence of these factors on the reactivity towards one-electron oxidants with different WCAs. The reactions of **Mo_2EE'** with [Thia][TEF] leads to dimerization reaction *via* E–E bond formation yielding P_2As_2 and P_2Sb_2 chains in gauche conformation, As_2Sb_2 and Sb_2Bi_2 cage-type units as well as a planar As_2Bi_2 cyclic moiety. These $E_2E'_2$ ligands are free from any organic substituents and are only stabilized in the coordination sphere of dimolybdenum fragments (*cf.* chapter 5) Using the W or Cp* derivatives **W_2P_2** and **$^{Cp*}Mo_2As_2$**, respectively, as starting materials has no effect on the reactivity itself and only results in very small changes regarding the bond lenghts and angles within the molecular structures of the products. In contrast, the use of other counterions, like [TEF^{Cl}]$^-$, has a bigger impact on the product structures. The [TEF^{Cl}]$^-$ anion causes planarization of the initially gauche-conformed chains and, moreover, in **2**[TEF^{Cl}]$_2$ and **7**[TEF^{Cl}]$_2$ an interesting cyclization of the As_4 chain and the As_2Sb_2 cage-type ligand occurs yielding a novel As_4 ring and an unprecedented As_2Sb_2 cycle. In **8**[TEF^{Cl}]$_2$ though, the As_2Bi_2 cycle remains mostly the same like in **8**[TEF]$_2$. Within the oxidation of **$^{Cp*}Mo_2As_2$** with [Thia][TEF^{Cl}] a different reactivity was observed, where formally a [Cp*Mo(CO)$_2$As] fragment was eliminated resulting in a dicationic Mo_3As_3 unit. The latter contains a square pyramidal Mo_2As_3 *nido*-type unit with an unprecedented allylic As_3 ligand, and a Mo–As bond with multiple bond character. A possible, irreversible double oxidation of the tetrahedral dipnictogen complexes, as it is predicted by CV studies, could not be observed in general. Only in the reaction of **Mo_2As_2** with [Thia][TEF^{Cl}] some crystals of the side product **14**[TEF^{Cl}] could be isolated revealing a formally double oxidized complex **Mo_2As_2** stabilized by a [TEF^{Cl}]$^-$ and a Cl^- counterion, which inserted into the Mo–Mo bond. However, it was possible to interlink two different tetrahedra *via* oxidative dimerization by reacting a 1:1 mixture of **Mo_2P_2** and **Mo_2As_2** with equimolar amounts of [Thia][TEF]. This leads to the formation of the three possible products **1**[TEF]$_2$, **2**[TEF]$_2$ and **15**[TEF]$_2$ in a stochastic ratio of 1:1:1. Overall, it could be shown that the oxidation of hetero-polypnictogen ligand complexes is a useful synthetic tool to easily connect them and form larger unsubstituted, cationic hetero-polypnictogen frameworks, which are not accessible by other ways.

6.4 Supporting Information

6.4.1 General remarks

All manipulations were carried out under an inert atmosphere of dried nitrogen/argon using standard Schlenk and glovebox techniques. The used Schlenk flasks were heated at 550 °C for at least 15-30 minutes under reduced pressure prior to use to get rid of water traces adhered to the glass surface. The starting materials Li[FAl],[19] [Thia][SbF_6],[20] [Thia][TEF],[3] [Thia][TEF^{Cl}] (*cf.* chapter 5), [{CpMo(CO)$_2$}$_2$(μ,η^2:η^2-EE')] (EE' = PAs (**Mo₂PAs**), PSb (**Mo₂PSb**), AsSb (**Mo₂AsSb**), AsBi (**Mo₂AsBi**), SbBi(**Mo₂SbBi**)),[5] [{CpMo(CO)$_2$}$_2$(μ,η^2:η^2-E_2)] (E = P (**Mo₂P₂**),[5,21] As (**Mo₂As₂**)[5,8f]), [{CpW(CO)$_2$}$_2$(μ,η^2:η^2-P_2)] (**W₂P₂**)[9] and [{Cp*Mo(CO)$_2$}$_2$(μ,η^2:η^2-As_2)] (^{Cp*}**Mo₂As₂**)[7b] were synthesized *via* the respective literature procedures. The reagents thianthrene and [NO][SbF_6] are commercially available and were used without further purification. Solvents were freshly distilled under nitrogen after drying over CaH_2 (CH_2Cl_2, CD_2Cl_2), K or Na/K alloy (alkanes), P_4O_{10} (*ortho*-difluorobenzene = *o*-DFB) or NaH (toluene, C_6D_6). Dried solvents were also taken from a solvent purification system from MBraun. For reactions in liquid SO_2, SO_2 gas cylinders were bought from Linde and SO_2 was condensed into Schlenk flasks with a Young valve at −196 °C under reduced pressure. Diatomaceous earth used for filtrations was stored at 130 °C for at least 24 h prior to use. NMR spectra were recorded at 300 K (if not stated otherwise) on a Bruker Avance 300 MHz NMR spectrometer (^{1}H: 300.132 MHz, ^{31}P: 121.495 MHz, ^{13}C: 75.468 MHz, ^{19}F: 282.404 MHz) or a Bruker Avance 400 MHz NMR spectrometer (^{1}H: 400.130 MHz, ^{31}P: 161.976 MHz, ^{13}C: 100.613 MHz, ^{19}F: 376.498 MHz) with external references of $SiMe_4$ (^{1}H, ^{13}C), CCl_3F (^{19}F) and H_3PO_4 (85%, ^{31}P). The chemical shifts δ are presented in parts per million (ppm) and coupling constants J in Hz. X-Band EPR spectra were recorded on a MiniScope MS400 device from Magnettech GmbH with a frequency of 9.5 GHz equipped with a rectangular resonator TE102. ESI-MS spectra were either measured on a Finnigan Thermoquest TSQ 7000 mass-spectrometer by the MS department of the University of Regensburg or on a Waters Micromass LCT ESI-TOF mass-spectrometer by the first author. IR spectra were recorded either as solids using a ThermoFisher Nicolet iS5 FT-IR spectrometer with an iD7 ATR module and an ITX Germanium or ITX Diamond crystal, or grinded together with dried KBr and pressed to pellets and measured on a VARIAN FTS-800 FT-IR spectrometer. Elemental analyses (EA) were performed by the micro analytical laboratory of the University of Regensburg.

6.4.2 Experimental details

6.4.2.1 Synthesis of [Thia][FAl]

In order to vary the weakly coordinating anion (= WCA) of the desired products and to investigate their influence on the solid-state structures, the used strong one-electron oxidant thianthrenium $[C_{12}H_8S_2]^{\cdot+}$ (= $[Thia]^+$, E^0 = 0.86 V vs $Cp_2Fe^{0/+}$)[22] was synthesized with the WCA $[FAl\{O(C_6F_{10})(C_6F_5)\}_3]^-$ (= $[FAl]^-$).[23]

For [Thia][FAl] two synthetic procedures were developed affording the deep purple salt [Thia][FAl] in good yield (Scheme S1). Hereby, method 2 represents a simple one-step synthesis starting from commercially available reagents.

method 1: $\mathrm{Li[FAl] + [Thia][SbF_6] \xrightarrow[\text{ultrasonic activation}]{CH_2Cl_2,\ 20\ h} [Thia][FAl] + Li[SbF_6]\downarrow}$

method 2: $\mathrm{Li[FAl] + NO[SbF_6] + Thia \xrightarrow[\text{r.t., 24h}]{SO_2(l)} [Thia][FAl] + Li[SbF_6]\downarrow + NO\uparrow}$ (72 %)

Scheme S1: Two synthetic procedures for [Thia][FAl].

Method 1: [Thia][SbF_6] (135 mg, 0.30 mmol, 1 eq.) and Li[FAl] (450 mg, 0.32 mmol, 1.1 eq.) were placed in a Schlenk flask equipped with a Young valve. Subsequently 20 mL of CH_2Cl_2 were condensed onto the solids at –196 °C. The flask was closed under reduced pressure. Upon dissolution of the compounds the formation of a deep violet solution could be observed. The flask was sonicated for 20 h. In order to precipitate the ionic product the reaction mixture was filtered over diatomaceous earth directly into 100 mL of stirred *n*-hexane. Thereby, the formation of a small amount of pink precipitate could be observed. The supernatant solution was decanted off, the solid was washed with 100 mL of *n*-hexane and dried in vacuum. The solid was dissolved in 20 mL of CH_2Cl_2 and the cloudy light pink solution was filtered and carefully layered with 80 mL of *n*-hexane. After storage at +4 °C [Thia][FAl] was obtained as very thin pink needles in the course of several days. From these crystals we were able to determine the solid-state structure of [Thia][FAl], but the yield was very low since a large percentage of the product was lost during the filtration because of its low solubility in CH_2Cl_2. Therefore, no yield was determined for this preparation method.

Method 2: A double Schlenk flask equipped with two Young valves and a G4 frit plate in the middle was loaded on one side with a stirring bar, thianthrene (151 mg, 0.7 mmol, 1.2 eq.), NO[SbF_6] (160 mg, 0.6 mmol, 1 eq.) and Li[FAl] (1 g, 0.72 mmol, 1.2 eq.). SO_2 (10 mL) was condensed onto these solids under reduced pressure at –196 °C. The flask was closed under reduced pressure and the cooling was removed. Upon dissolution the reaction turns from light blue to dark blue and finally to dark violet. After stirring at room temperature for 24 h the dark violet solution was filtered over the G4 frit to the other side. SO_2 was condensed back onto the remaining dark purple residue by cooling to –196 °C and subsequently filtered again to the other side after stirring at room temperature for 10 min. This procedure was repeated four times until the stirred solution had only a light purple colour. Finally, the SO_2 was removed and the remaining solid was dissolved in 20 mL MeCN to form a deep violet solution. This solution was transferred into 200 mL of pure toluene resulting in a clear purple solution. The amount of solvent was reduced under reduced pressure until a dark precipitate formed and a light pink solution remained. The supernatant solution was decanted off and the residue washed two times with 50 mL of toluene and one time with Et_2O and subsequently dried in vacuum to afford a pink to violet fine powder.

Yield 683 mg (72%). ^{1}H NMR (400 MHz, CD_2Cl_2, 300 K) no signals detectable for [Thia]$^{+}$. ^{19}F{^{1}H} NMR (282.4 MHz, CD_3CN, 300 K) δ/ppm = –111.6 (d, $J_{F,F}$ = 277 Hz, 2F), –116.1 (d, $J_{F,F}$ = 279 Hz, 2F), –120.9 (d, $J_{F,F}$ = 278 Hz, 2F), –127.7 (s, 2F), –129.7 (d, $J_{F,F}$ = 275 Hz, 2F), –136.4 (d, $J_{F,F}$ = 277 Hz, 2F), –140.7 (d, $J_{F,F}$ = 277 Hz, 1F), –153.8 (t, $J_{F,F}$ = 22 Hz, 1F), –164.5 (t, $J_{F,F}$ = 18 Hz, 1F), –170.5 (s, AlF). Elemental analysis shows a possible impurity with thianthrene (11%). Anal. calcd. for [Thia][FAl]: C: 36.09, H: 0.50, S: 4.01. Anal. calcd. for [Thia][FAl]·(thianthrene)$_{0.11}$: C: 36.53, H: 0.55, S: 4.39. Found: C: 36.54, H: 0.71, S: 4.49. Positive ion ESI-MS *m/z* (%): 215.9 (100) [Thia]$^{+}$. Negative ion ESI-MS *m/z* (%): 1381.2 (100) [FAl]$^{-}$. IR(KBr) $\tilde{\nu}$/cm^{-1} = 3620 (vw), 3165 (vw), 3089 (vw), 3039 (vw), 3005 (vw), 2967 (vw), 2928 (vw), 2850 (vw), 2866 (vw), 2537 (vw), 2490 (vw), 2411 (vw), 1653 (m), 1534 (m), 1522 (w), 1484 (vs), 1436 (vw), 1422 (vw), 1324 (m), 1307 (m), 1264 (s), 1244 (s), 1205 (vs), 1185 (s), 1155 (s), 1134 (m), 1105 (s), 1033 (m), 1019 (s), 1005 (m), 954 (vs), 910 (m), 850 (w), 810 (w), 766 (m), 748 (s), 730 (m), 666 (w), 648 (w), 635 (w), 625 (w), 600 (w), 536 (w), 525 (w), 498 (w), 428 (vw).

6.4.2.2 Oxidation of W_2P_2 and $^{Cp*}Mo_2As_2$ with [Thia][TEF]

Preparation of [{CpW(CO)$_2$}$_4$(μ$_4$,η^2:η^2:η^2:η^2-P$_4$)][TEF]$_2$ (10[TEF]$_2$)

A dark purple solution of [Thia][TEF] (36 mg, 0.03 mmol, 1.0 eq.) in 8 mL CH_2Cl_2 was transferred to an orange solution of [{CpW(CO)$_2$}$_2$(μ,η^2:η^2-P$_2$)] (**W_2P_2**) (20 mg, 0.03 mmol, 1.0 eq.) in 5 mL CH_2Cl_2 at room temperature causing an immediate colour change to a brown solution. After stirring for 60 minutes, addition of 40 mL *n*-hexane led to precipitation of a dark green powder. The slightly red supernatant solution was removed and the precipitate washed twice with 20 mL of pure toluene. The crude product was dried in vacuum and recrystallization *via* layering a CH_2Cl_2 solution with *n*-hexane (1:5) and storage at +4 °C afforded pure **10**[TEF]$_2$ as dark red blocks, which were suitable for single crystal X-ray diffraction. The supernatant was removed and the crystals were dried in vacuum.
Yield 43 mg (0.013 mmol = 87 %). Anal. calcd. for [($C_{14}H_{10}O_4W_2P_2$)$_2$][TEF]$_2$: C: 21.98, H: 0.61. Found: C: 22.30, H: 0.74. Positive ion MS *m/z* (%): 672.92 (100) [**W_2P_2**]$^{+}$, 688.91 (91) [**W_2P_2**+O]$^{+}$.

Preparation of [{Cp*Mo(CO)$_2$}$_4$(μ$_4$,η^2:η^2:η^2:η^2-As$_4$)][TEF]$_2$ (11[TEF]$_2$)

A dark purple solution of [Thia][TEF] (69 mg, 0.058 mmol, 1.0 eq.) in 10 mL CH_2Cl_2 was transferred to a red solution of [{Cp*Mo(CO)$_2$}$_2$(μ,η^2:η^2-As$_2$)] (**$^{Cp*}Mo_2As_2$**) (42 mg, 0.058 mmol, 1.0 eq.) in 10 mL CH_2Cl_2 at room temperature causing an immediate colour change to dark red to black solution. After stirring for 40 minutes, addition of 50 mL *n*-hexane led to precipitation of a dark red powder. The slightly red supernatant solution was removed and the precipitate dried in vacuum. Recrystallization *via* layering a CH_2Cl_2 solution with *n*-hexane (1:4) and storage at +4 °C afforded pure **11**[TEF]$_2$ as dark red blocks, which were suitable for single crystal X-ray diffraction. The supernatant was removed and the crystals were dried in vacuum.
Yield 66 mg (0.020 mmol = 67 %). ^{1}H NMR (300 MHz, CD_2Cl_2) δ/ppm = 2.08 (s, Cp*). ^{19}F{^{1}H} NMR (282.4 MHz, CD_2Cl_2) δ/ppm = −75.6 (s, CF_3). Anal. calcd. for [($C_{24}H_{30}O_4Mo_2As_2$)$_2$][TEF]$_2$: C: 28.41, H: 1.79. Found: C: 28.62, H: 1.99. Positive ion ESI-MS *m/z* (%): 725.0 (100) [**$^{Cp*}Mo_2As_2$**]$^{+}$. Negative ion ESI-MS *m/z* (%): 967.2 (100) [TEF]$^{-}$.

6.4.2.3 Oxidation of $^{CpR}Mo_2E_2$, Mo_2EE' and W_2P_2 with [Thia][TEF^{Cl}]

Preparation of [{CpMo(CO)$_2$}$_4$(μ_4,η^2:η^2:η^2:η^2-P_4)][TEF^{Cl}]$_2$ (1[TEF^{Cl}]$_2$)

A dark purple solution of [Thia][TEF^{Cl}] (138 mg, 0.10 mmol, 1.0 eq.) in 8 mL CH_2Cl_2 was transferred to an orange solution of [{CpMo(CO)$_2$}$_2$(μ,η^2:η^2-P_2)] (**Mo_2P_2**) (50 mg, 0.10 mmol, 1.0 eq.) in 10 mL CH_2Cl_2 at room temperature causing an immediate colour change to a dark greenish red solution. After stirring for 60 minutes, addition of 70 mL *n*-hexane led to precipitation of a dark green powder. The slightly brown supernatant solution was removed and the precipitate washed twice with 30 mL of pure toluene. The crude product was dried in vacuum and recrystallization *via* layering a CH_2Cl_2 solution with *n*-pentane (1:4) and storage at +4 °C afforded pure **1**[TEF^{Cl}]$_2$ as dark red blocks, which were suitable for single crystal X-ray diffraction. The supernatant was removed and the crystals were dried in vacuum.
Yield 145 mg (0.048 mmol = 96 %). ^{1}H NMR (300 MHz, CD_2Cl_2) δ/ppm = 5.77 (s, Cp). ^{31}P{^{1}H} NMR (121.5 MHz, CD_2Cl_2) δ/ppm = −0.2 (s, $\omega_{1/2}$ = 245 Hz). ^{31}P NMR (121.5 MHz, CD_2Cl_2) δ/ppm = −0.2 (s, $\omega_{1/2}$ = 245 Hz). ^{19}F{^{1}H} NMR (282.4 MHz, CD_2Cl_2) δ/ppm = −68.5 (s, CF_3). Anal. calcd. for [($C_{14}H_{10}O_4Mo_2P_2$)$_2$][TEF^{Cl}]$_2$: C: 21.70, H: 0.61. Found: C: 20.83, H: 0.94.

Preparation of [{CpMo(CO)$_2$}$_4$(μ_4,η^2:η^2:η^2:η^2-As_4)][TEF^{Cl}]$_2$ (2[TEF^{Cl}]$_2$)

A dark purple solution of [Thia][TEF^{Cl}] (69 mg, 0.05 mmol, 1.0 eq.) in 10 mL CH_2Cl_2 was transferred to an orange red solution of [{CpMo(CO)$_2$}$_2$(μ,η^2:η^2-As_2)] (**Mo_2As_2**) (30 mg, 0.05 mmol, 1.0 eq.) in 10 mL CH_2Cl_2 at room temperature causing an immediate colour change to a dark greenish red solution. After stirring for 120 minutes, addition of 70 mL *n*-hexane led to precipitation of a dark green powder. The slightly brown supernatant solution was removed and the precipitate washed twice with 20 mL of pure toluene. The crude product was dried in vacuum and recrystallization *via* layering a CH_2Cl_2 solution with *n*-hexane (1:4) and storage at +4 °C afforded pure **2**[TEF^{Cl}]$_2$ as dark red blocks, which were suitable for single crystal X-ray diffraction. The supernatant was removed and the crystals were dried in vacuum.
Yield 79 mg (0.023 mmol = 90 %). ^{1}H NMR (300 MHz, CD_2Cl_2) δ/ppm = 5.78 (s, Cp), 5.58 (s). ^{19}F{^{1}H} NMR (282.4 MHz, CD_2Cl_2) δ/ppm = −68.5 (s, CF_3). Anal. calcd. for [($C_{14}H_{10}O_4Mo_2As_2$)$_2$][TEF^{Cl}]$_2$: C: 20.61, H: 0.58. Found: C: 20.33, H: 0.80.

Preparation of [{CpMo(CO)$_2$}$_4$(μ_4,η^2:η^2:η^2:η^2-AsPPAs)][TEF^{Cl}]$_2$ (5[TEF^{Cl}]$_2$)

A dark purple solution of [Thia][TEF^{Cl}] (70 mg, 0.05 mmol, 1.0 eq.) in 10 mL CH_2Cl_2 was transferred to an orange red solution of [{CpMo(CO)$_2$}$_2$(μ,η^2:η^2-PAs)] (**Mo_2PAs**) (27 mg, 0.05 mmol, 1.0 eq.) in 10 mL CH_2Cl_2 at room temperature causing an immediate colour change to a dark red solution. After stirring for 90 minutes, addition of 60 mL *n*-pentane led to precipitation of a dark green to black powder. The slightly brown supernatant solution was removed and the precipitate washed twice with 20 mL of pure toluene. The crude product was dried in vacuum and recrystallization *via* layering a CH_2Cl_2 solution with *n*-hexane (1:4) and storage at +4 °C afforded pure **5**[TEF^{Cl}]$_2$ as dark red blocks, which were suitable for single crystal X-ray diffraction. The supernatant was removed and the crystals were dried in vacuum.

Yield 78 mg (0.023 mmol = 92 %). ^{1}H NMR (400 MHz, CD_2Cl_2) δ/ppm = 5.69 (s, Cp). $^{31}P\{^1H\}$ NMR (162.0 MHz, CD_2Cl_2) δ/ppm = −28.6 (s). ^{31}P NMR (162.0 MHz, CD_2Cl_2) δ/ppm = −28.6 (s). $^{13}C\{^1H\}$ NMR (100.6 MHz, CD_2Cl_2) δ/ppm = 90.63 (s, Cp), 97.24 (s, CCl_3), 122.10 (q, $^1J_{CF}$ = 297 Hz; CF_3), 218.16 (s, CO). $^{19}F\{^1H\}$ NMR (376.6 MHz, CD_2Cl_2) δ/ppm = −68.5 (s, CF_3). Anal. calcd. for $[(C_{14}H_{10}O_4Mo_2PAs)_2][TEF^{Cl}]_2$: C: 21.14, H: 0.59. Found: C: 20.72, H: 0.73.

Preparation of [{CpMo(CO)$_2$}$_4$(μ_4,η^2:η^2:η^2:η^2-SbPPSb)][TEF^{Cl}]$_2$ (6[TEF^{Cl}]$_2$)

A dark purple solution of [Thia][TEF^{Cl}] (177 mg, 0.13 mmol, 1.0 eq.) in 5 mL CH_2Cl_2 was transferred to an orange red solution of [{CpMo(CO)$_2$}$_2$(μ,η^2:η^2-PSb)] (**Mo$_2$PSb**) (75 mg, 0.13 mmol, 1.0 eq.) in 5 mL CH_2Cl_2 at room temperature causing an immediate colour change to a dark orange brown solution. After stirring for 30 minutes, addition of 40 mL *n*-hexane led to precipitation of a brown, fluffy powder. The slightly orange supernatant solution was removed and the precipitate washed twice with 20 mL of pure toluene leading to an oily solid. The crude product was dried in vacuum, redissolved in 5 mL CH_2Cl_2 and precipitated with 30 mL *n*-hexane yielding again a fluffy, brown powder. The precipitate was dissolved in 4 mL CH_2Cl_2 and 0.5 mL *n*-hexane were added. Storage at −30 °C for 24 hours afforded **6**[TEF^{Cl}]$_2$ as thin orange plates, which were not suitable for single crystal X-ray diffraction and, therefore, only a unit cell could be determined. After 7 days of storage orange rods of the side product [{CpMo(CO)$_2$}$_4$(μ-SbCl)(μ_4,η^1:η^2:η^2-P(PCl)Sb)][TEF^{Cl}]$_2$ (**12**[TEF^{Cl}]$_2$) could be obtained, which were suitable for single crystal X-ray diffraction. The crystals of **12**[TEF^{Cl}]$_2$ were isolated, dried in vacuum and subjected to mass spectrometry and elemental analysis.

6[TEF^{Cl}]$_2$: Yield 107 mg (0.0305 mmol = 87 %). $^{31}P\{^1H\}$ NMR of the crude solution of **6**[TEF^{Cl}]$_2$ (162.0 MHz, C_6D_6/*o*-DFB) δ/ppm = 35.4 (s). ^{31}P NMR of the crude solution of **6**[TEF^{Cl}]$_2$ (162.0 MHz, C_6D_6/*o*-DFB) δ/ppm = 35.3 (s).

12[TEF^{Cl}]$_2$: Yield 7 mg (0.002 mmol = 8 %). Anal. calcd. for $[(C_{14}H_{10}O_4Mo_2PSbCl)_2][TEF^{Cl}]_2(CH_2Cl_2)_2$: C: 19.89, H: 0.65. Found: C: 19.83, H: 0.75. Positive ion ESI-MS *m/z* (%): 622.72 (100) [**12**]$^{2+}$, 1142.51 (4) [**12**$^{2+}$+Cl$^-$-5·CO]$^+$, 1281.40 (6) [**12**$^{2+}$+Cl$^-$]$^+$.

Preparation of [{CpMo(CO)$_2$}$_4$(μ_4,η^2:η^2:η^2:η^2-AsSbAsSb)][TEF^{Cl}]$_2$ (7[TEF^{Cl}]$_2$)

A dark purple solution of [Thia][TEF^{Cl}] (89 mg, 0.065 mmol, 1.0 eq.) in 5 mL CH_2Cl_2 was transferred to a red solution of [{CpMo(CO)$_2$}$_2$(μ,η^2:η^2-AsSb)] (**Mo$_2$AsSb**) (41 mg, 0.065 mmol, 1.0 eq.) in 5 mL CH_2Cl_2 at room temperature causing an immediate colour change to a dark brown solution. After stirring for 15 minutes, addition of 40 mL toluene led to precipitation of a dark greenish brown powder. The slightly brown supernatant solution was removed and the precipitate dried in vacuum. Recrystallization *via* layering a CH_2Cl_2 solution with *n*-hexane (1:5) and storage at +4 °C afforded pure **7**[TEF^{Cl}]$_2$ as dark red blocks, which were suitable for single crystal X-ray diffraction. The supernatant was removed and the crystals were dried in vacuum.

Yield 89 mg (0.025 mmol = 77 %). ^{1}H NMR (400 MHz, CD_2Cl_2) δ/ppm = 5.70 (s, Cp). $^{19}F\{^1H\}$ NMR (376.6 MHz, CD_2Cl_2) δ/ppm = −68.5 (s, CF_3). Anal. calcd. for $[(C_{14}H_{10}O_4Mo_2AsSb)_2][TEF^{Cl}]_2$: C: 20.07, H: 0.56. Found: C: 20.31, H: 0.74. Positive ion ESI-MS *m/z* (%): 629.65 (100) [**Mo_2AsSb**]$^+$, 584.7 (37) [**Mo_2As_2**]$^+$, 573.7 (8) [**Mo_2AsSb**–2·CO]$^+$, 556.7 (8) [**Mo_2As_2**–CO]$^+$, 545.7 (18) [**Mo_2AsSb**–3·CO]$^+$, 528.7 (10) [**Mo_2As_2**–2·CO]$^+$, 517.7 (6) [**Mo_2AsSb**–4·CO]$^+$, 500.7 (7) [**Mo_2As_2**–3·CO]$^+$, 472.7 (4) [**Mo_2As_2**–4·CO]$^+$. Negative ion ESI-MS *m/z* (%): 1162.64 (100) [TEF^{Cl}]$^-$. IR (ATR) $\tilde{\nu}$/cm^{-1} = 3145 (vw), 3138 (vw), 3122 (vw), 2360 (w), 2344 (w), 2053 (w), 2032 (w), 1998 (m), 1983 (m), 1970 (w), 1954 (w), 1943 (w), 1310 (w), 1243 (m), 1194 (vs), 1145 (w), 1010 (w), 964 (w), 858 (m), 787 (m), 725 (m), 712 (s).

Preparation of [{CpMo(CO)$_2$}$_4$(μ_4,η^2:η^2:η^2:η^2-AsBiBiAs)][TEF^{Cl}]$_2$ (8[TEF^{Cl}]$_2$)

A dark purple solution of [Thia][TEF^{Cl}] (58 mg, 0.042 mmol, 1.0 eq.) in 3 mL CH_2Cl_2 was transferred to a dark red solution of [{CpMo(CO)$_2$}$_2$(μ,η^2:η^2-AsBi)] (**Mo_2AsBi**) (30 mg, 0.042 mmol, 1.0 eq.) in 5 mL CH_2Cl_2 at −50 °C causing an immediate colour change to a dark greenish brown solution. After stirring for 60 minutes, addition of 40 mL *n*-hexane led to precipitation of a dark green to black powder. The slightly brown supernatant solution was removed and washed twice with pure toluene. The crude product was dried in vacuum and recrystallization *via* layering a CH_2Cl_2 solution with *n*-hexane (1:4) and storage at +4 °C afforded pure **8**[TEF^{Cl}]$_2$ as dark red blocks, which were suitable for single crystal X-ray diffraction. The supernatant was removed and the crystals were dried in vacuum.

Yield 64 mg (0.017 mmol = 81 %). Compound **8**[TEF^{Cl}]$_2$ is silent in the X-band EPR spectra in CH_2Cl_2 solution at room temperature and at 77 K. Anal. calcd. for [($C_{14}H_{10}O_4Mo_2AsBi$)$_2$][TEF^{Cl}]$_2$: C: 19.14, H: 0.54. Found: C: 19.30, H: 0.40.

Preparation of [{CpW(CO)$_2$}$_4$(μ_4,η^2:η^2:η^2:η^2-P_4)][TEF^{Cl}]$_2$ (10[TEF^{Cl}]$_2$)

A dark purple solution of [Thia][TEF^{Cl}] (43 mg, 0.03 mmol, 1.0 eq.) in 3 mL *o*-DFB was transferred to an orange solution of [{CpW(CO)$_2$}$_2$(μ,η^2:η^2-P_2)] (**W_2P_2**) (21 mg, 0.03 mmol, 1.0 eq.) in 7 mL *o*-DFB at room temperature causing an immediate colour change to a dark brown solution. After stirring for 40 minutes, addition of 40 mL *n*-hexane led to precipitation of a dark greenish brown, fluffy powder. The slightly red supernatant solution was removed and the precipitate washed twice with 20 mL of pure toluene. The crude product was dried in vacuum and recrystallization *via* layering an *o*-DFB solution with *n*-hexane (1:4) and storage at room temperature afforded pure **10**[TEF^{Cl}]$_2$ as dark brown rods, which were suitable for single crystal X-ray diffraction. The supernatant was removed and the crystals were dried in vacuum.

Yield 46 mg (0.013 mmol = 81 %).

Preparation of [{Cp*Mo(CO)$_2$}$_3$(μ_3,η^3:η^2:η^1-As_3)][TEF^{Cl}]$_2$ (13[TEF^{Cl}]$_2$)

A dark purple solution of [Thia][TEF^{Cl}] (138 mg, 0.10 mmol, 1.0 eq.) in 7 mL *o*-DFB was transferred to a red solution of [{Cp*Mo(CO)$_2$}$_2$(μ,η^2:η^2-As_2)] (**$^{Cp*}Mo_2As_2$**) (72 mg, 0.10 mmol, 1.0 eq.) in 7 mL *o*-DFB at room temperature causing an immediate colour change to a dark bordeaux red solution. After stirring for 60 minutes, addition of 60 mL *n*-pentane led to precipitation of a dark red powder. The slightly brown supernatant solution was removed and recrystallization *via* layering an *o*-DFB solution

with *n*-pentane (1:5) and storage at room temperature afforded red oil and powder as well as red plates, which were suitable for single crystal X-ray diffraction revealing **13**[TEF^{Cl}]$_2$. The supernatant was removed and the residue dried in vacuum.
Yield 142 mg (0.042 mmol = 83 %). Anal. calcd. for [($C_{36}H_{45}O_6Mo_3As_3$)][TEF^{Cl}]$_2$(*o*-DFB)$_{1.65}$ (= **13**[TEF^{Cl}]$_2$): C: 25.96, H: 1.44. Anal. calcd. for [($C_{24}H_{30}O_4Mo_2As_2$)$_2$][TEF^{Cl}]$_2$ (= TEF^{Cl} derivative of **11**[TEF]$_2$ and **11**[FAl]$_2$): C: 25.44, H: 1.60. Found: C: 25.94, H: 1.41.

6.4.2.4 Preparation of [{Cp*Mo(CO)$_2$}$_4$(μ_4,η^2:η^2:η^2:η^2-As$_4$)][FAl]$_2$ (11[FAl]$_2$)

A dark purple solution of [Thia][FAl] (80 mg, 0.05 mmol, 1.0 eq.) in 25 mL *o*-DFB was transferred to an orange solution of [{Cp*Mo(CO)$_2$}$_2$(μ,η^2:η^2-As$_2$)] (**^{Cp*}Mo$_2$As$_2$**) (36 mg, 0.05 mmol, 1.0 eq.) in 7 mL *o*-DFB at room temperature causing an immediate colour change to a dark bordeaux red solution. After stirring for 40 minutes, the solvent was reduced to 5 mL and addition of 40 mL *n*-pentane led to precipitation of a dark red powder. The slightly red supernatant solution was removed and the precipitate washed twice with 20 mL of pure toluene. The crude product was dried in vacuum and recrystallization *via* layering an *o*-DFB solution with *n*-pentane (1:4) and storage at +4 °C afforded pure **11**[FAl]$_2$ as dark red blocks, which were suitable for single crystal X-ray diffraction. The supernatant was removed and the crystals were dried in vacuum.
Yield 79 mg (0.019 mmol = 76 %). Anal. calcd. for [($C_{24}H_{30}O_4Mo_2As_2$)$_2$][FAl]$_2$(*o*-DFB)$_{1.5}$: C: 35.36, H: 1.51. Found: C: 35.30, H: 1.16.

6.4.2.5 Oxidation of a 1:1 mixture of [{CpMo(CO)$_2$}$_2$(μ,η^2:η^2-P$_2$)] and [{CpMo(CO)$_2$}$_2$ (μ,η^2:η^2-As$_2$)] with equimolar amounts of [Thia][TEF]

A dark purple solution of [Thia][TEF] (62 mg, 0.052 mmol, 1.0 eq.) in 7 mL CH_2Cl_2 was transferred to an orange red solution of a 1:1 mixture of [{CpMo(CO)$_2$}$_2$(μ,η^2:η^2-P$_2$)] (**Mo$_2$P$_2$**) (13 mg, 0.026 mmol, 0.5 eq.) and [{CpMo(CO)$_2$}$_2$(μ,η^2:η^2-As$_2$)] (**Mo$_2$As$_2$**) (15 mg, 0.026 mmol, 0.5 eq.) in 7 mL CH_2Cl_2 at room temperature causing an immediate colour change to a dark brown solution. After stirring for 15 minutes, addition of 60 mL *n*-hexane led to precipitation of a dark brown powder. The slightly brown supernatant solution was removed and the precipitate washed twice with 20 mL of pure toluene. The crude product was dried in vacuum and recrystallization *via* layering a CH_2Cl_2 solution with *n*-hexane (1:4) and storage at +4 °C afforded orange to dark red blocks, which were suitable for single crystal X-ray diffraction revealing a mixture of [{CpMo(CO)$_2$}$_4$(μ_4,η^2:η^2:η^2:η^2-P$_4$)][TEF]$_2$ (**1**[TEF]$_2$), [{CpMo(CO)$_2$}$_4$(μ_4,η^2:η^2:η^2:η^2-As$_4$)][TEF]$_2$ (**2**[TEF]$_2$) and [{CpMo(CO)$_2$}$_4$(μ_4,η^2:η^2:η^2:η^2-PPAsAs)][TEF]$_2$ (**15**[TEF]$_2$). The supernatant was removed and the crystals dried in vacuum. The different product could not be separated.
Yield 63 mg (0.021 mmol = 81 %). ^{1}H NMR (400 MHz, CD_2Cl_2) δ/ppm = 5.67 (s, Cp of **2**[TEF]$_2$),[3] 5.74 (s, Cp of **1**[TEF]$_2$),[3] 5.82 (s, Cp of **15**[TEF]$_2$). ^{31}P{^{1}H} NMR (162.0 MHz, CD_2Cl_2) δ/ppm = 0.0 (s, $\omega_{1/2}$ = 475 Hz, **1**[TEF]$_2$), −84.8 (s, **15**[TEF]$_2$). ^{31}P NMR (162.0 MHz, CD_2Cl_2) δ/ppm = −0.2 (s, $\omega_{1/2}$ = 493 Hz; **1**[TEF]$_2$), −85.1 (s, **15**[TEF]$_2$). ^{19}F{^{1}H} NMR (376.5 MHz, CD_2Cl_2) δ/ppm = −75.5 (s, CF_3).

6.4.3 NMR spectra

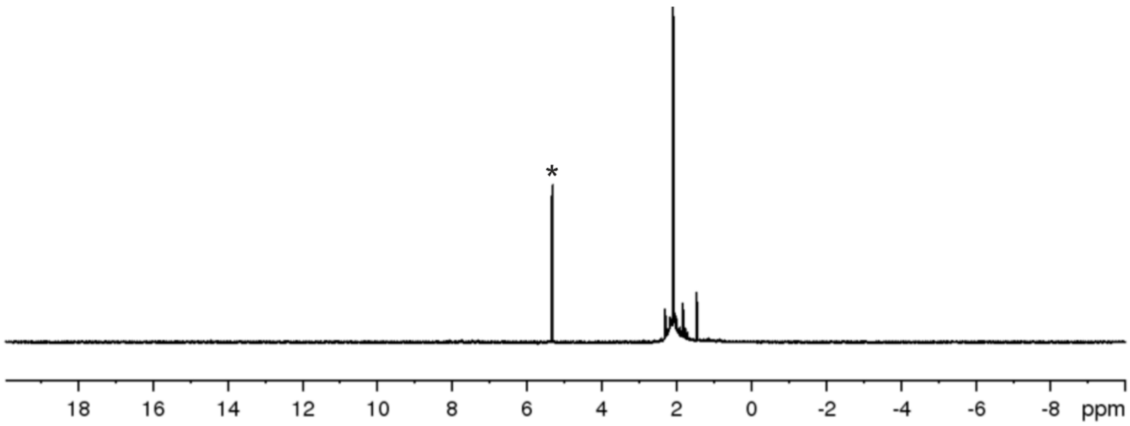

Figure S1: ^{1}H NMR spectrum of $[\{Cp^*Mo(CO)_2\}_4(\mu_4,\eta^2{:}\eta^2{:}\eta^2{:}\eta^2\text{-}As_4)][TEF]_2$ (**11**[TEF]$_2$) in CD_2Cl_2; * = CD_2Cl_2.

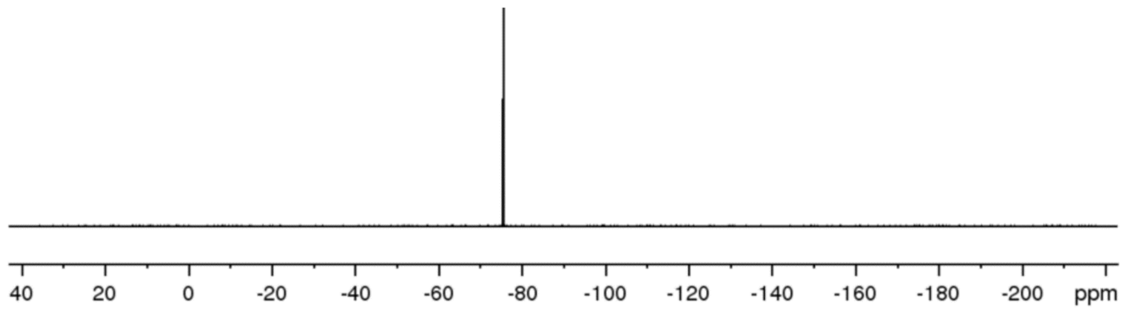

Figure S2: ^{19}F{^{1}H} NMR spectrum of $[\{Cp^*Mo(CO)_2\}_4(\mu_4,\eta^2{:}\eta^2{:}\eta^2{:}\eta^2\text{-}As_4)][TEF]_2$ (**11**[TEF]$_2$) in CD_2Cl_2.

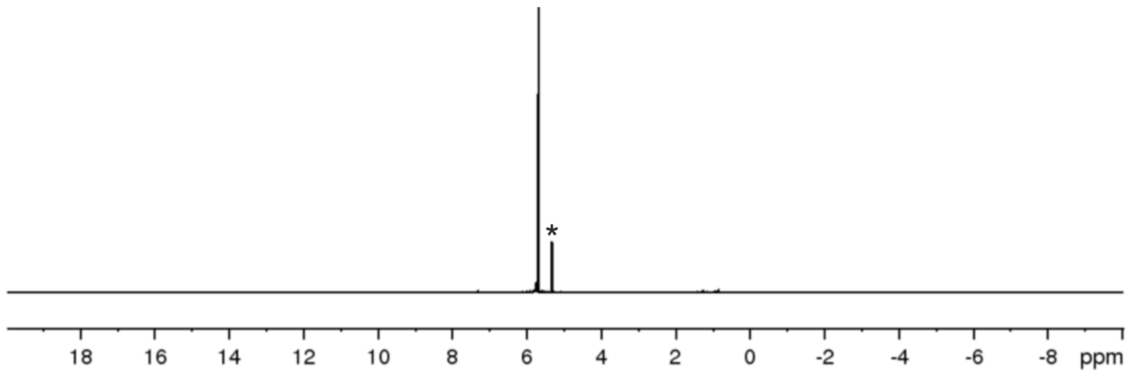

Figure S3: ^{1}H NMR spectrum of $[\{CpMo(CO)_2\}_4(\mu_4,\eta^2{:}\eta^2{:}\eta^2{:}\eta^2\text{-}AsPPAs)][TEF^{Cl}]_2$ (**5**[TEF^{Cl}]$_2$) in CD_2Cl_2; * = CD_2Cl_2.

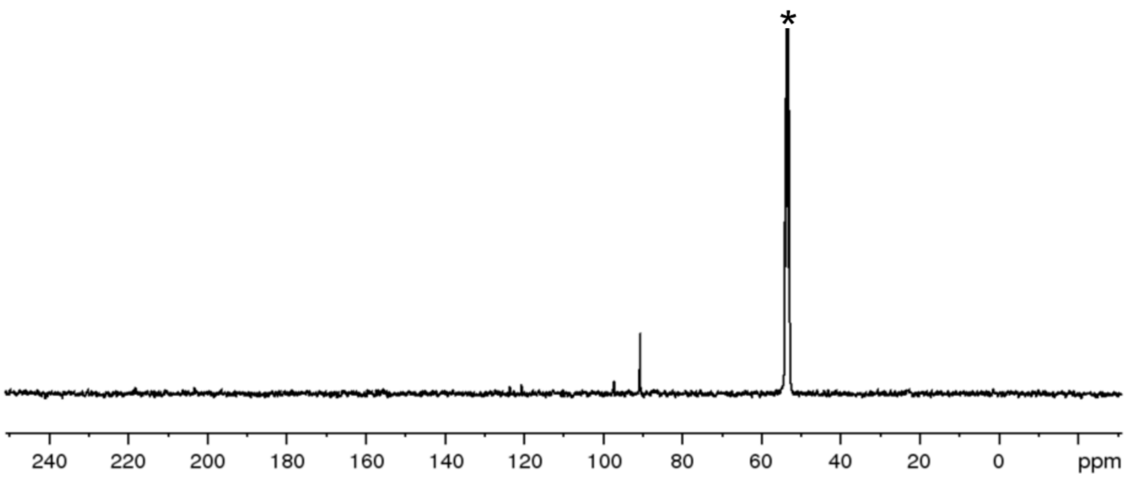

Figure S4: ^{13}C{^{1}H} NMR spectrum of $[\{CpMo(CO)_2\}_4(\mu_4,\eta^2{:}\eta^2{:}\eta^2{:}\eta^2\text{-}AsPPAs)][TEF^{Cl}]_2$ (**5**[TEF^{Cl}]$_2$) in CD_2Cl_2; * = CD_2Cl_2.

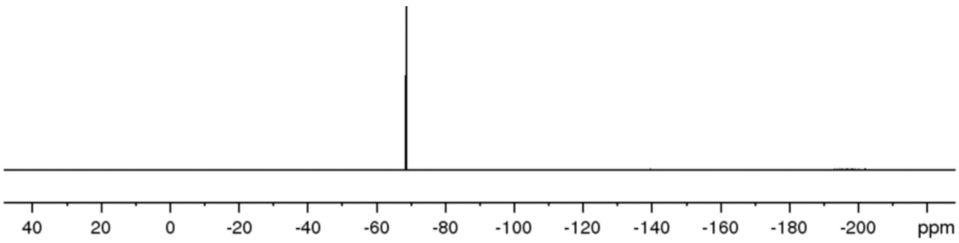

Figure S5: $^{19}F\{^1H\}$ NMR spectrum of [{CpMo(CO)$_2$}$_4$(μ_4,η^2:η^2:η^2:η^2-AsPPAs)][TEF^{Cl}]$_2$ (**5**[TEF^{Cl}]$_2$) in CD_2Cl_2.

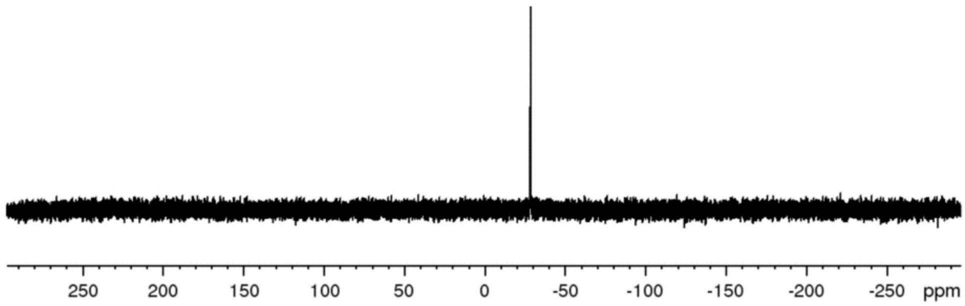

Figure S6: $^{31}P\{^1H\}$ NMR spectrum of [{CpMo(CO)$_2$}$_4$(μ_4,η^2:η^2:η^2:η^2-AsPPAs)][TEF^{Cl}]$_2$ (**5**[TEF^{Cl}]$_2$) in CD_2Cl_2.

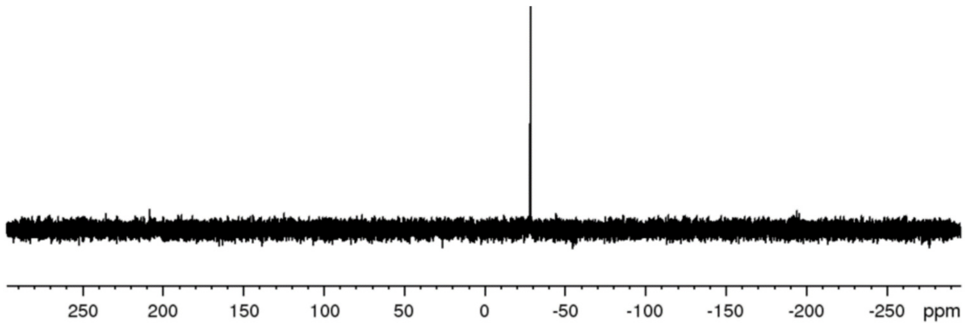

Figure S7: ^{31}P NMR spectrum of [{CpMo(CO)$_2$}$_4$(μ_4,η^2:η^2:η^2:η^2-AsPPAs)][TEF^{Cl}]$_2$ (**5**[TEF^{Cl}]$_2$) in CD_2Cl_2.

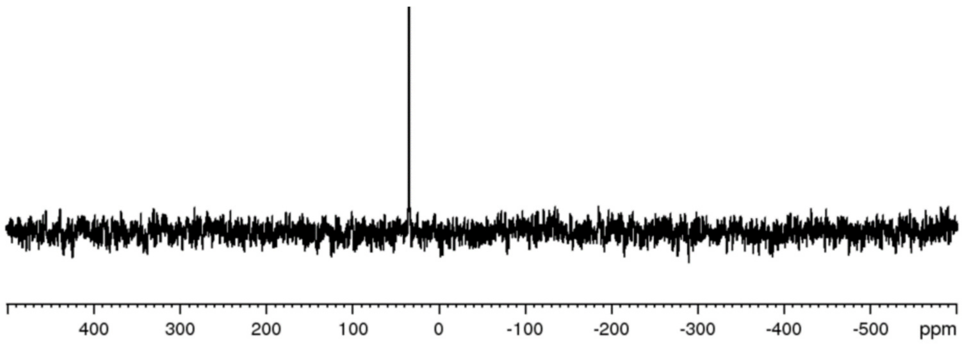

Figure S8: $^{31}P\{^1H\}$ NMR spectrum of a crude solution of [{CpMo(CO)$_2$}$_4$(μ_4,η^2:η^2:η^2:η^2-SbPPSb)][TEF^{Cl}]$_2$ (**6**[TEF^{Cl}]$_2$) in *o*-DFB/C_6D_6.

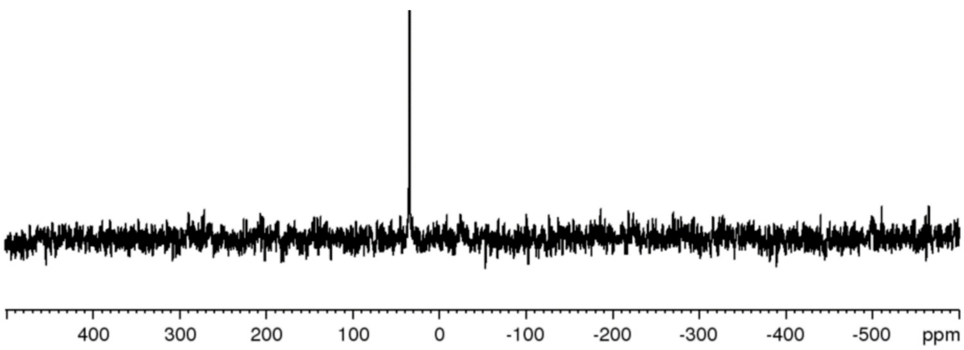

Figure S9: ^{31}P NMR spectrum of a crude solution of [{CpMo(CO)$_2$}$_4$(μ_4,η^2:η^2:η^2:η^2-SbPPSb)][TEF^{Cl}]$_2$ (**6**[TEF^{Cl}]$_2$) in *o*-DFB/C_6D_6.

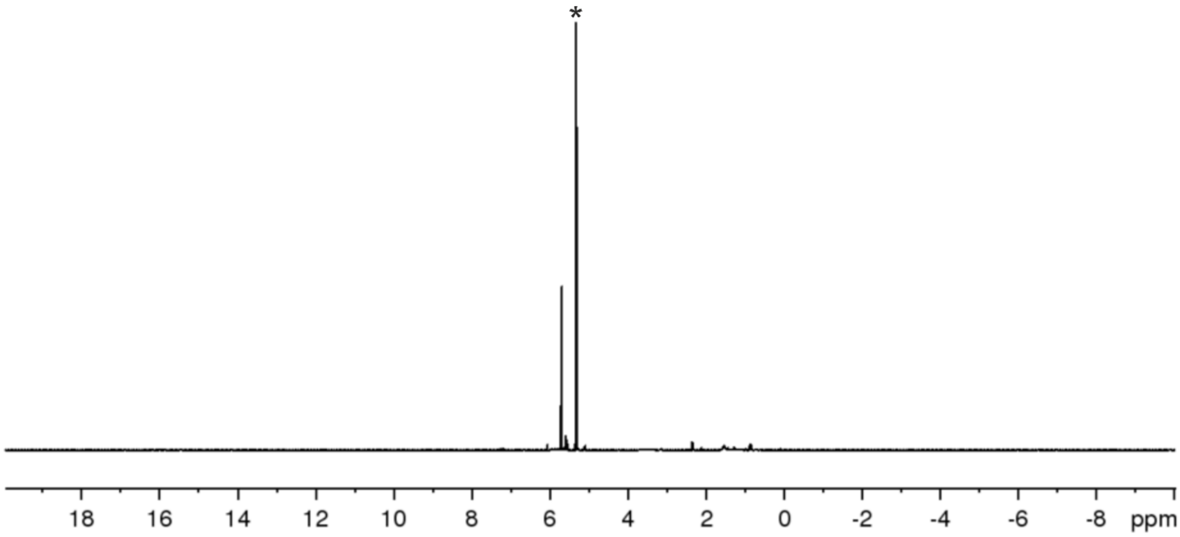

Figure S10: ^{1}H NMR spectrum of $[\{CpMo(CO)_2\}_4(\mu_4,\eta^2:\eta^2:\eta^2:\eta^2\text{-}AsSbAsSb)][TEF^{Cl}]_2$ (**7**$[TEF^{Cl}]_2$) in CD_2Cl_2, * = CD_2Cl_2.

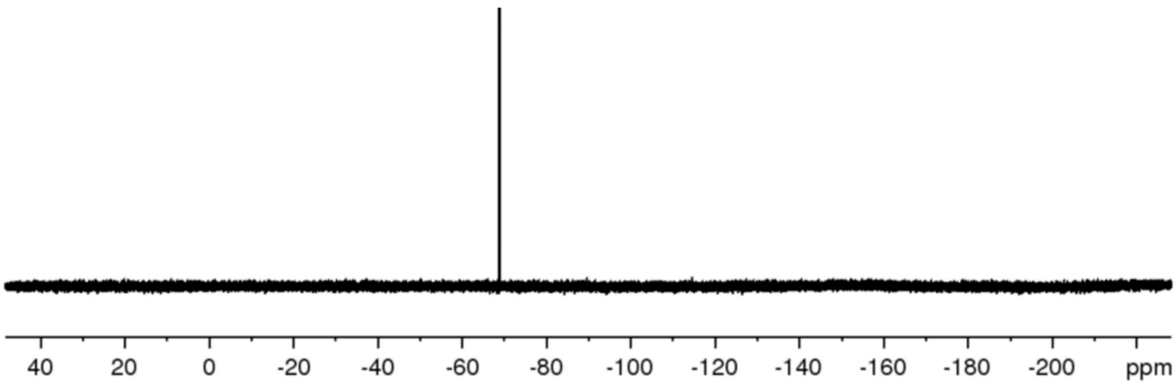

Figure S11: $^{19}F\{^{1}H\}$ NMR spectrum of $[\{CpMo(CO)_2\}_4(\mu_4,\eta^2:\eta^2:\eta^2:\eta^2\text{-}AsSbAsSb)][TEF^{Cl}]_2$ (**7**$[TEF^{Cl}]_2$) in CD_2Cl_2.

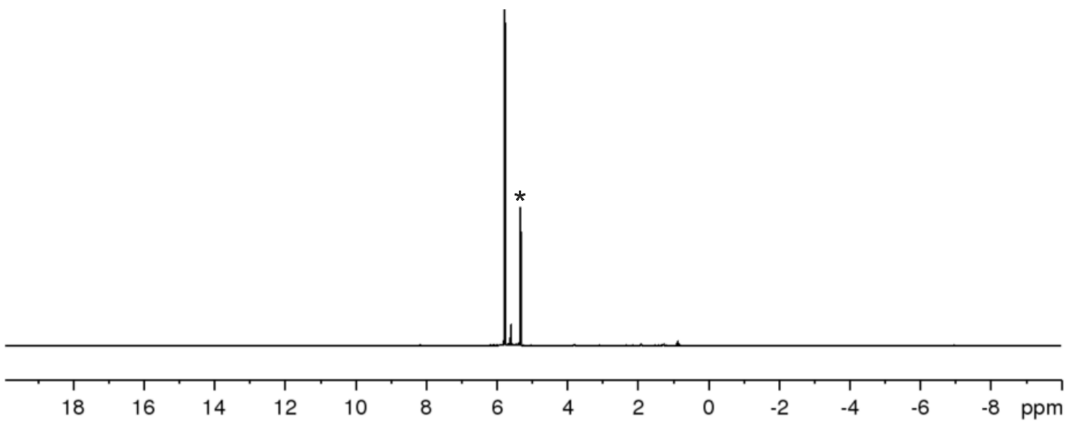

Figure S12: ^{1}H NMR spectrum of $[\{CpMo(CO)_2\}_4(\mu_4,\eta^2:\eta^2:\eta^2:\eta^2\text{-}P_4)][TEF^{Cl}]_2$ (**1**$[TEF^{Cl}]_2$) in CD_2Cl_2, * = CD_2Cl_2.

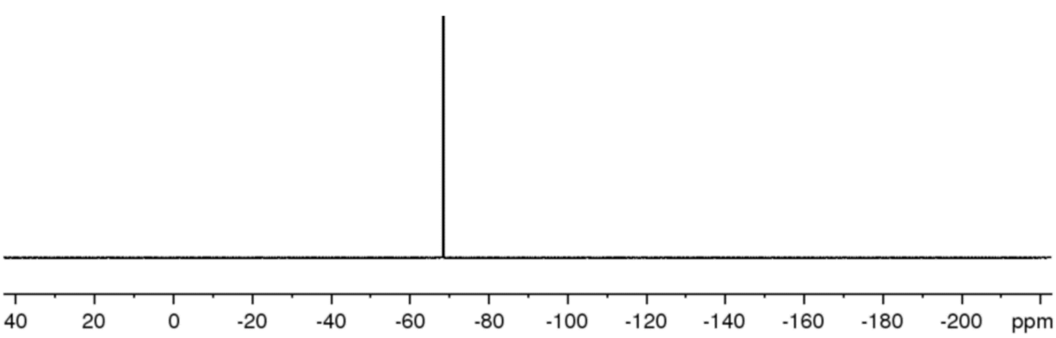

Figure S13: $^{19}F\{^{1}H\}$ NMR spectrum of $[\{CpMo(CO)_2\}_4(\mu_4,\eta^2:\eta^2:\eta^2:\eta^2\text{-}P_4)][TEF^{Cl}]_2$ (**1**$[TEF^{Cl}]_2$) in CD_2Cl_2.

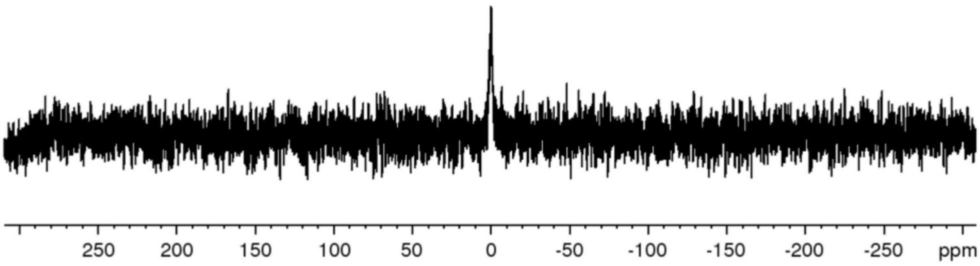

Figure S14: $^{31}P\{^{1}H\}$ NMR spectrum of $[\{CpMo(CO)_2\}_4(\mu_4,\eta^2{:}\eta^2{:}\eta^2{:}\eta^2\text{-}P_4)][TEF^{Cl}]_2$ (**1**$[TEF^{Cl}]_2$) in CD_2Cl_2.

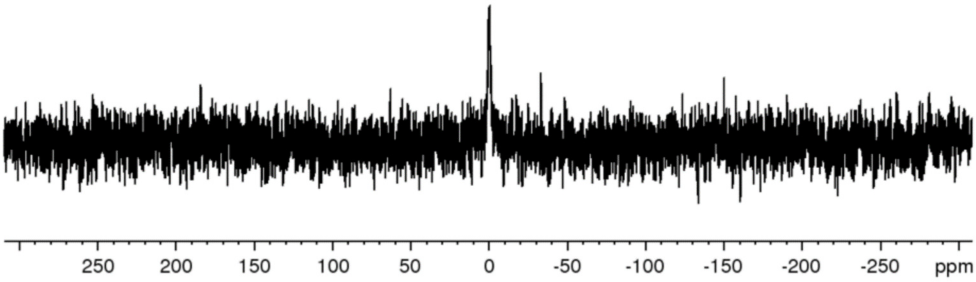

Figure S15: ^{31}P NMR spectrum of $[\{CpMo(CO)_2\}_4(\mu_4,\eta^2{:}\eta^2{:}\eta^2{:}\eta^2\text{-}P_4)][TEF^{Cl}]_2$ (**1**$[TEF^{Cl}]_2$) in CD_2Cl_2.

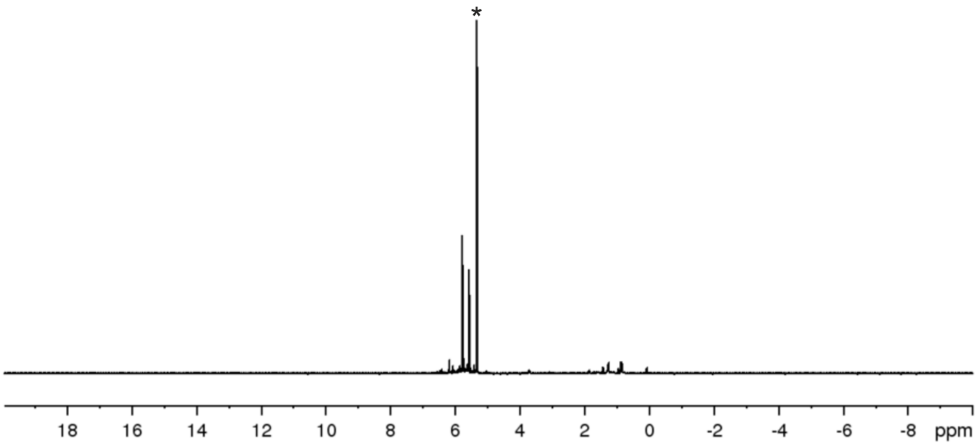

Figure S16: ^{1}H NMR spectrum of $[\{CpMo(CO)_2\}_4(\mu_4,\eta^2{:}\eta^2{:}\eta^2{:}\eta^2\text{-}As_4)][TEF^{Cl}]_2$ (**2**$[TEF^{Cl}]_2$) in CD_2Cl_2, * = CD_2Cl_2.

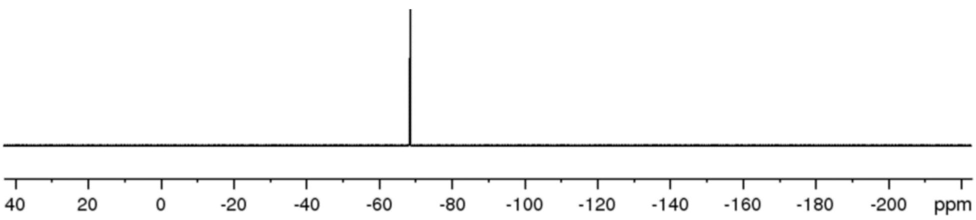

Figure S17: $^{19}F\{^{1}H\}$ NMR spectrum of $[\{CpMo(CO)_2\}_4(\mu_4,\eta^2{:}\eta^2{:}\eta^2{:}\eta^2\text{-}As_4)][TEF^{Cl}]_2$ (**2**$[TEF^{Cl}]_2$) in CD_2Cl_2.

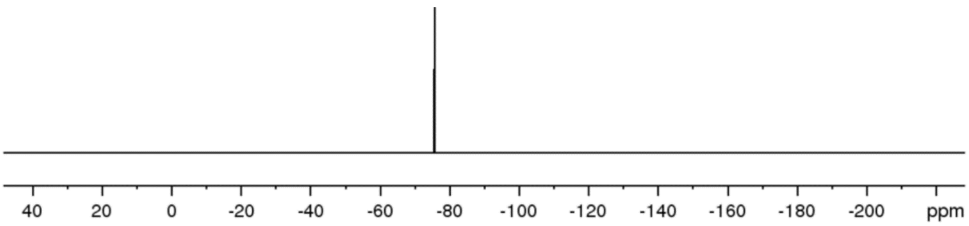

Figure S18: $^{19}F\{^{1}H\}$ NMR spectrum of the oxidation of a 1:1 mixture of **Mo_2P_2** and **Mo_2As_2** with equimolar amounts of [Thia][TEF] in CD_2Cl_2.

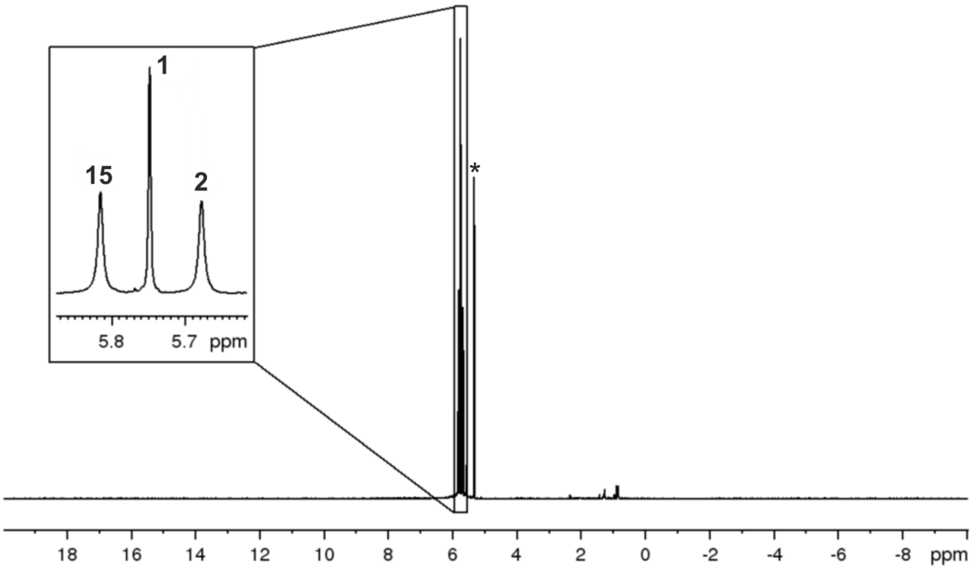

Figure S19: ^{1}H NMR spectrum of the oxidation of a 1:1 mixture of **Mo_2P_2** and **Mo_2As_2** with equimolar amounts of [Thia][TEF] in CD_2Cl_2, * = CD_2Cl_2.

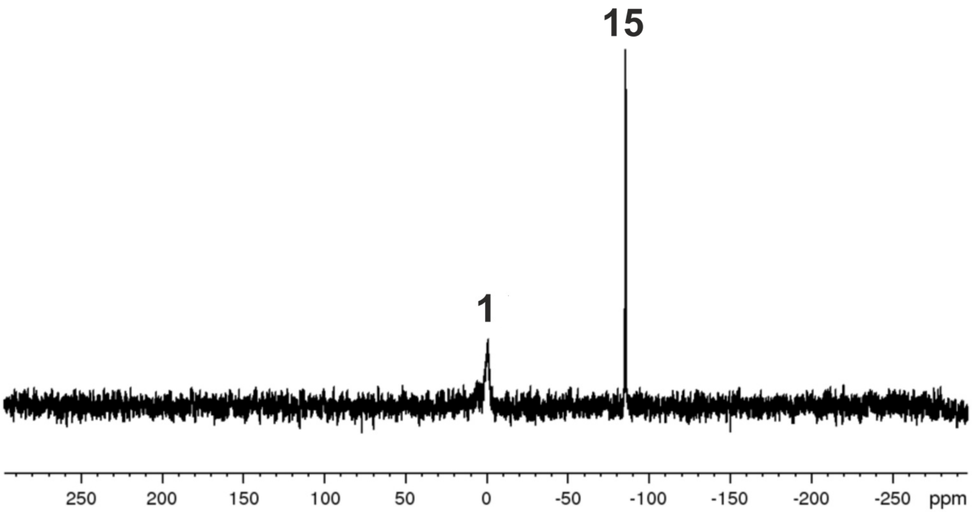

Figure S20: $^{31}P\{^{1}H\}$ NMR spectrum of the oxidation of a 1:1 mixture of **Mo_2P_2** and **Mo_2As_2** with equimolar amounts of [Thia][TEF] in CD_2Cl_2.

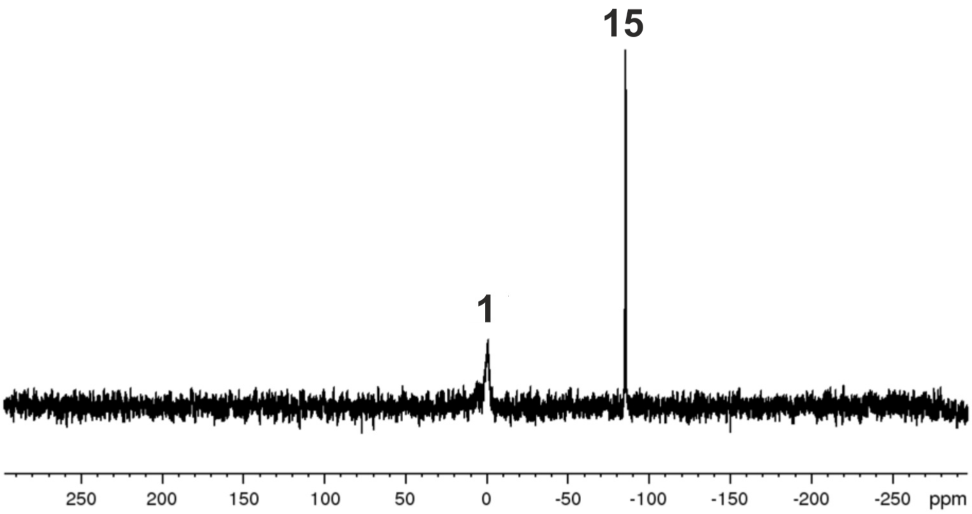

Figure S21: ^{31}P NMR spectrum of the oxidation of a 1:1 mixture of **Mo_2P_2** and **Mo_2As_2** with equimolar amounts of [Thia][TEF] in CD_2Cl_2.

6.4.4 Mass spectrometry

The mass spectra, which were recorded by the mass spectrometry department of the University of Regensburg, are not available to the authors in a digital format and, therefore, could not be displayed in the following.

ESI mass spectrometry of 7[TEF^{Cl}]$_2$:

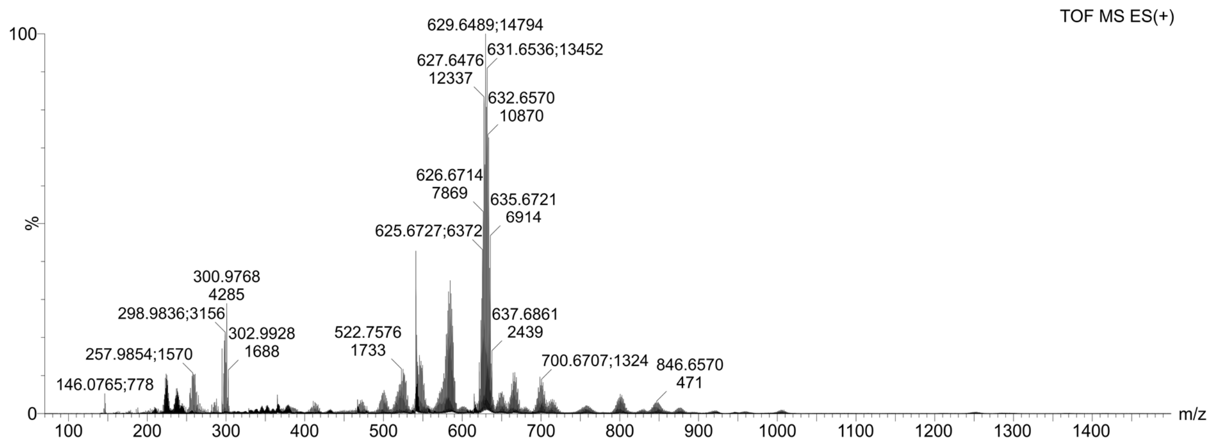

Figure S22: ESI(+) MS spectrum of **7**[TEF^{Cl}]$_2$.

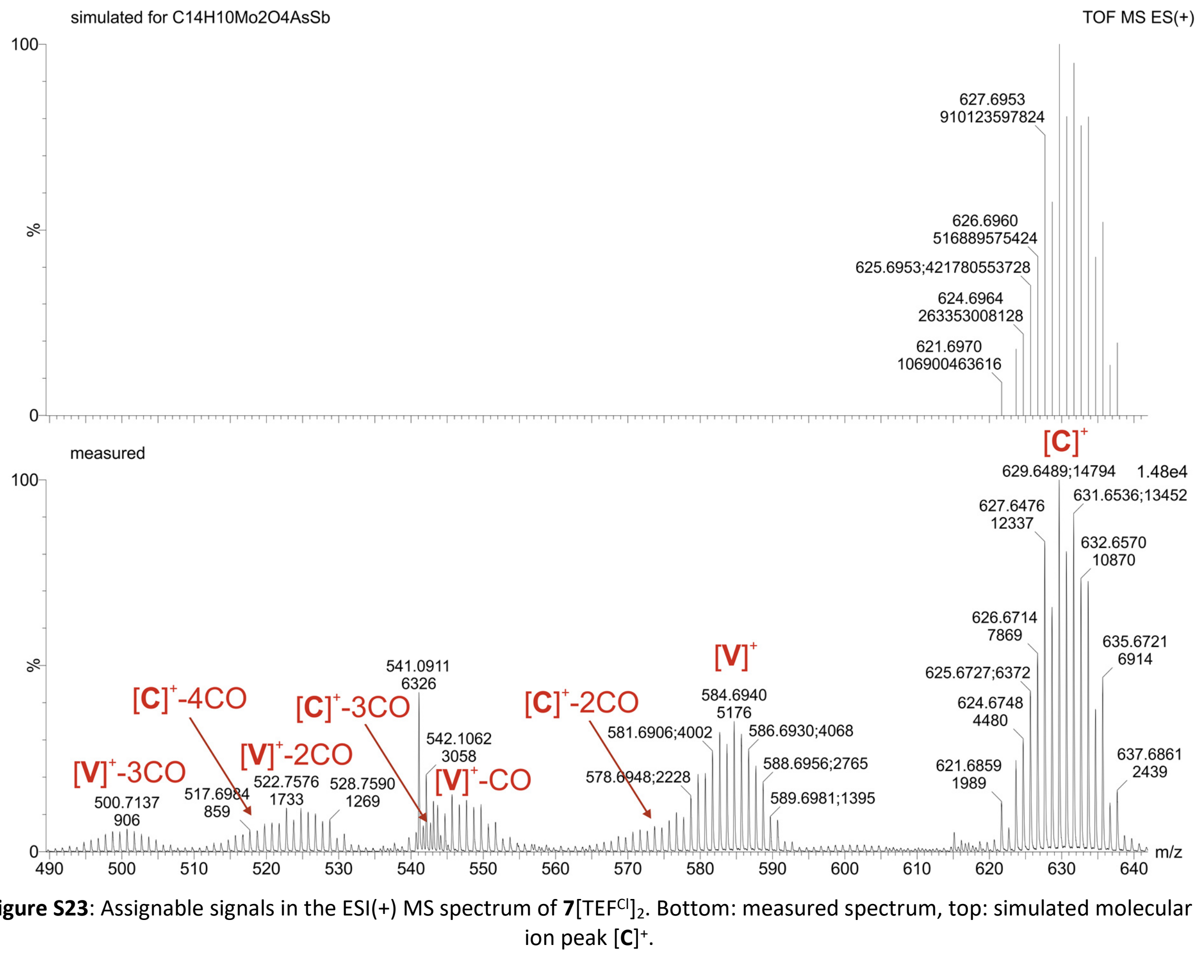

Figure S23: Assignable signals in the ESI(+) MS spectrum of **7**[TEF^{Cl}]$_2$. Bottom: measured spectrum, top: simulated molecular ion peak [**C**]$^+$.

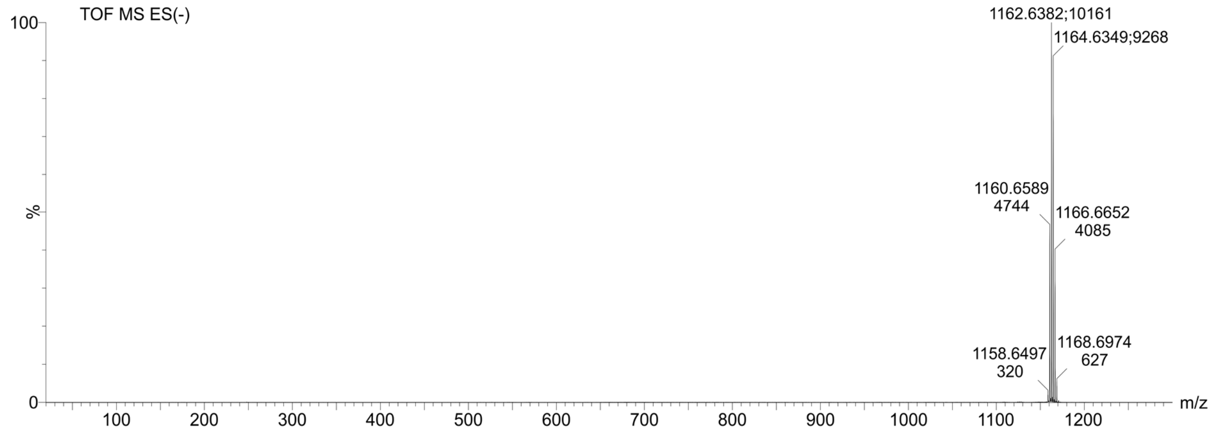

Figure S24: ESI(−) MS spectrum of **7**[TEF^{Cl}]$_2$.

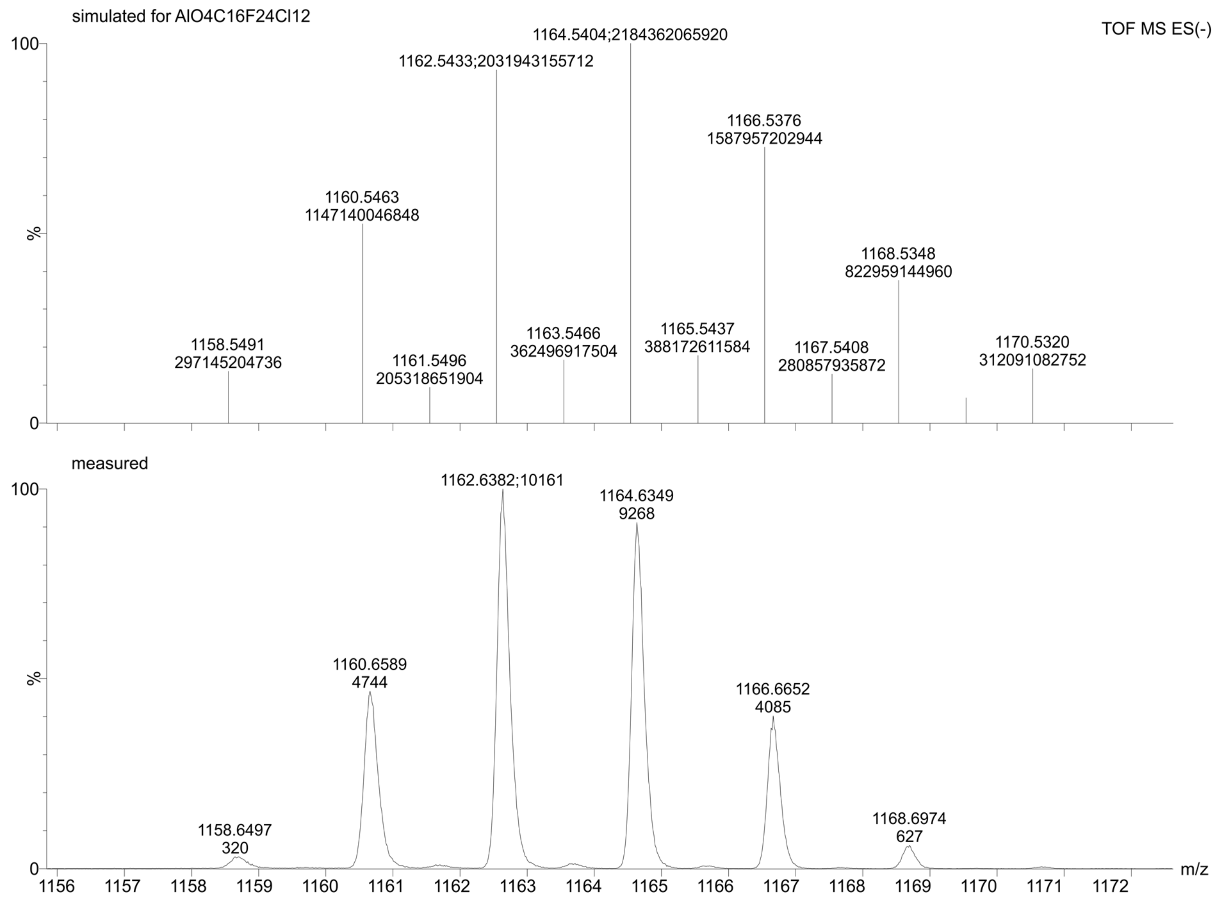

Figure S25: Molecular ion peak of [TEF^{Cl}]$^-$ in the ESI(−) MS spectrum of **7**[TEF^{Cl}]$_2$. Bottom: measured spectrum, top: simulated spectrum.

6.4.5 EPR spectra

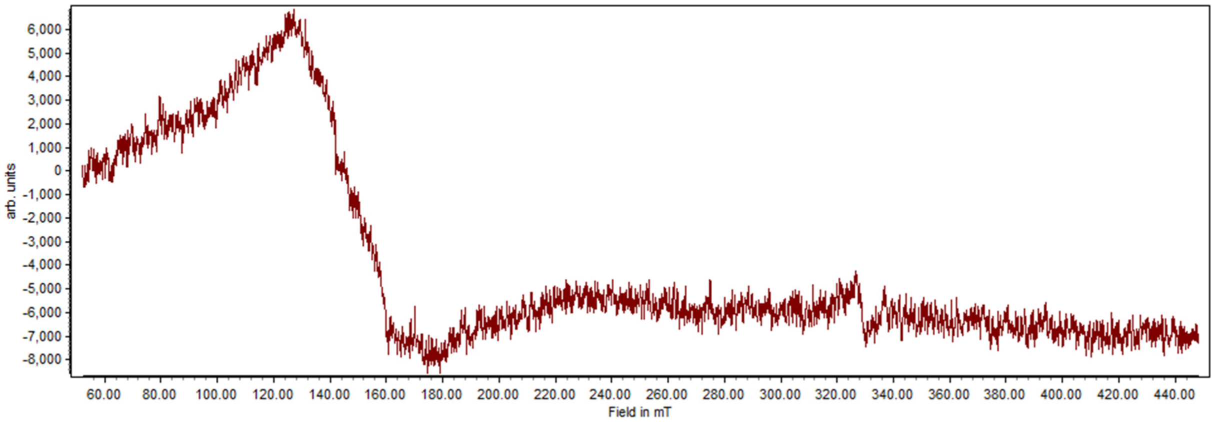

Figure S26: X-Band EPR spectrum of **8**[TEF^{Cl}]$_2$ at room temperature showing no signal.

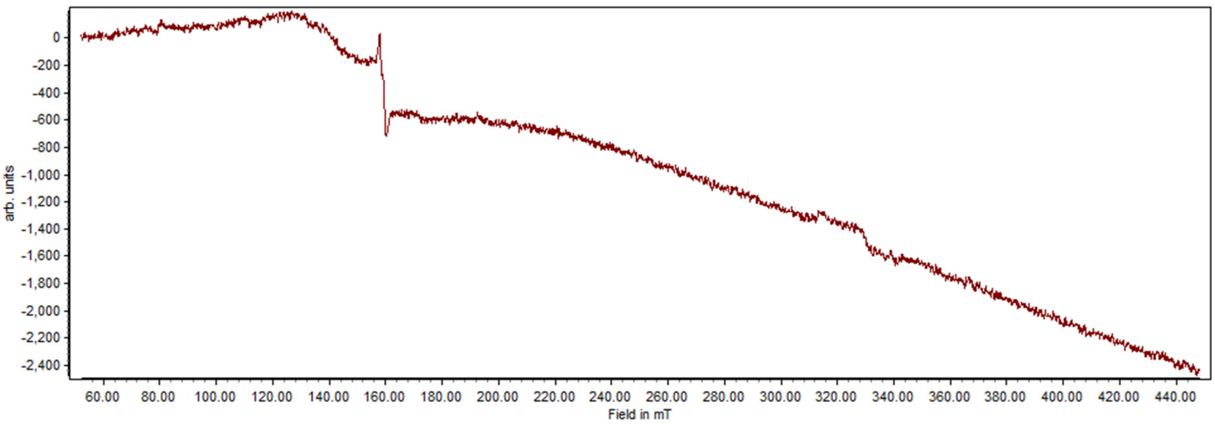

Figure S27: X-Band EPR spectrum of **8**[TEF^{Cl}]$_2$ at 77 K showing no signal.

6.4.6 X-ray crystallography

All crystal manipulations were performed under mineral oil. The diffraction experiments were performed at 123 K (if not stated otherwise) either on a Rigaku (former Agilent Technologies or Oxford Diffraction) SuperNova SingleSource with an Atlas detector, a Gemini Ultra with an AtlasS2 detector or on a GV50 diffractometer with a TitanS2 detector using Cu-K_α, Cu-K_β or Mo-K_α radiation. Crystallographic data together with the details of the experiments are given in Table S1 and Table S2. The cell determination, data reduction and absorption correction for all compounds were performed with the help of the CrysAlis PRO software.[24] All structures were solved by using the programs SHELXT[25] and Olex2.[26] The full-matrix least-squares refinement against F^2 was done using SHELXL[27] and Olex2.[26] If not stated otherwise, all atoms except hydrogen atoms were refined anisotropically. The H atoms were calculated geometrically and a riding model was used during the refinement process.

Table S1: Crystallographic details for the compounds **1**[TEF^{Cl}]$_2$, **2**[TEF^{Cl}]$_2$, **5**[TEF^{Cl}]$_2$, **6**[TEF^{Cl}]$_2$ and **7**[TEF^{Cl}]$_2$.

	1[TEF^{Cl}]$_2$	**2**[TEF^{Cl}]$_2$	**5**[TEF^{Cl}]$_2$	**6**[TEF^{Cl}]$_2$	**7**[TEF^{Cl}]$_2$
formula	$C_{61.5}H_{23}Al_2Cl_{27}F_{48}Mo_4O_{16}P_4$	$C_{60}H_{20}Al_2As_4Cl_{24}F_{48}Mo_4O_{16}$	$C_{60.75}H_{21.5}Al_2As_2Cl_{26}F_{48}Mo_4O_{16}P_2$		$C_{60}H_{20}Al_2As_2Cl_{24}F_{48}Mo_4O_{16}Sb_2$
weight [g·mol^{-1}]	3448.55	3496.96	3490.48		3590.62
Temperature [K]	89.9(4)	123.0(1)	128.21(10)		123.0(1)
crystal system	monoclinic	monoclinic	monoclinic	monoclinic	monoclinic
space group	I2/a	$P2_1/c$	I2/a		$P2_1/c$
a [Å]	25.8354(3)	20.5035(2)	25.8966(6)	25.1	20.6398(2)
b [Å]	16.6959(2)	23.1664(2)	16.7776(3)	17.3	23.2138(2)
c [Å]	49.9851(6)	23.1057(3)	50.0842(10)	50.0	23.1270(2)
α [°]	90	90	90	90	90
β [°]	102.0970(10)	113.4590(10)	102.059(2)	99.0	112.9690(10)
γ [°]	90	90	90	90	90
Volume [Å^3]	21082.1(4)	10067.9(2)	21280.5(8)	21590	10202.27(17)
Z	8	4	8		4
ρ_{calc} [g·cm^{-3}]	2.173	2.307	2.179		2.338
μ [mm^{-1}]	12.187	12.870	12.243		16.089
F(000)	13320.0	6696.0	13424.0		6840.0
crystal size [mm^3]	0.153 × 0.151 × 0.1	0.302 × 0.125 × 0.095	---		0.275 × 0.122 × 0.11
diffractometer	GV50	GV50	GV50		GV50
absorption correction	gaussian	gaussian	multi-scan		gaussian
T_{min} / T_{max}	0.894 / 0.993	0.131 / 0.397	0.378 / 1.000		0.477 / 0.719
radiation [Å]	Cu-Kα (λ = 1.54184)	Cu-Kα (λ = 1.54184)	Cu-Kα (λ = 1.54184)		Cu-Kα (λ = 1.54184)
2Θ range [°]	6.346 to 149.97	7.632 to 148.014	5.568 to 155.304		7.616 to 148.062
completeness [%]	99.5	99.7	99.8		99.7
reflns collected / unique	61185 / 20802	57933 / 19858	109564 / 21386		58050 / 20051
R_{int} / R_{sigma}	0.0562 / 0.0446]	0.0367 / 0.0314	0.3059 / 0.1352		0.0525 / 0.0453
data / restraints / parameters	20802 / 52 / 1571	19858 / 84 / 1588	21386 / 0 / 1337		20051 / 336 / 1528
GOF on F^2	1.023	1.042	1.602		1.025
R_1 / wR_2 [$I \geq 2\sigma(I)$]	0.0726 / 0.1960	0.0341 / 0.0896	0.1663 / 0.3964		0.0518 / 0.1317
R_1 / wR_2 [all data]	0.0798 / 0.2054	0.0373 / 0.0961	0.2046 / 0.4460		0.0586 / 0.1381
max / min $\Delta\rho$ [e·Å^{-3}]	2.17 / −1.93	1.45 / −1.70	5.66 / −1.46		2.48 / −2.72
Identification code	LD172_abs	LD152_2.Messung_abs	LD176	LD297	LD196_CR014_abs

Table S2: Crystallographic details for the compounds **8**[TEF^{Cl}]$_2$, **10**[TEF]$_2$, **10**[TEF^{Cl}]$_2$, **11**[TEF]$_2$ and **11**[FAl]$_2$.

	8[TEF^{Cl}]$_2$	**10**[TEF]$_2$	**10**[TEF^{Cl}]$_2$	**11**[TEF]$_2$	**11**[FAl]$_2$
formula	$C_{62}H_{24}O_{16}F_{48}Al_2Cl_{28}As_2Mo_4Bi_2$	$C_{60}H_{20}O_{16}F_{72}Al_2P_4W_4$	$C_{72}H_{28}Al_2Cl_{24}F_{52}O_{16}P_4W_4$	$C_{81.5}H_{63}Al_2As_4Cl_3F_{72}Mo_4O_{16}$	$C_{131}H_{66.5}Al_2As_4F_{95}Mo_4O_{14}$
weight [g·mol^{-1}]	3934.93	3278.00	3900.98	3510.07	4406.74
Temperature [K]	123.0(1)	123.0(1)	123.0(1)	123.0(1)	123.0(1)
crystal system	monoclinic	monoclinic	monoclinic	monoclinic	triclinic
space group	P2$_1$/n	P2$_1$/n	P2$_1$/n	P2$_1$/c	P-1
a [Å]	13.3028(2)	15.43760(10)	12.4131(3)	12.03932(14)	18.4686(4)
b [Å]	27.6708(4)	21.4962(2)	17.3376(4)	33.7292(4)	26.8610(5)
c [Å]	14.6789(3)	26.9795(2)	26.3726(7)	28.9130(4)	32.9852(6)
α [°]	90	90	90	90	112.322(2)
β [°]	96.234(2)	90.7910(10)	102.520(3)	90.4771(10)	94.884(2)
γ [°]	90	90	90	90	91.095(2)
Volume [Å^3]	5371.34(16)	8952.29(12)	5540.8(2)	11740.5(3)	15058.8(5)
Z	2	4	2	4	4
ρ_{calc} [g·cm^{-3}]	2.433	2.432	2.338	1.986	1.944
μ [mm^{-1}]	5.183	9.331	11.282	7.046	3.966
F(000)	3716.0	6152.0	3692.0	6820.0	8582.0
crystal size [mm^3]	0.984 × 0.237 × 0.128	0.347 × 0.082 × 0.072	0.372 × 0.112 × 0.089	0.222 × 0.132 × 0.053	0.39 × 0.123 × 0.077
diffractometer	SuperNova	GV50	GV50	GV50	GV50
absorption correction	gaussian	gaussian	gaussian	gaussian	gaussian
T_{min} / T_{max}	0.106 / 1.000	0.210 / 0.906	0.135 / 0.718	0.430 / 0.880	0.1259 / 1.000
radiation [Å]	Mo-Kα (λ = 0.71073)	Cu-Kβ (λ = 1.39222)	Cu-Kβ (λ = 1.39222)	Cu-Kα (λ = 1.54184)	Cu-Kβ (λ = 1.39222)
2Θ range [°]	5.89 to 69.18	4.746 to 148.22	5.55 to 149.574	6.068 to 148.648	4.846 to 139.704
completeness [%]	99.7	95.9	98.8	99.9	99.0
reflns collected / unique	51989 / 21334	62492 / 22672	44732 / 14967	90799 / 23373	128372 / 73164
R_{int} / R_{sigma}	0.0391 / 0.0513	0.0380 / 0.0344	0.0584 / 0.0538	0.0499 / 0.0399	0.0445 / 0.0622
data / restraints / parameters	21334 / 0 / 739	22672 / 0 / 1423	14967 / 132 / 670	23373 / 134 / 1878	73164 / 0 / 4442
GOF on F^2	1.051	1.034	1.542	1.101	1.021
R_1 / wR_2 [$I \geq 2\sigma(I)$]	0.0411 / 0.0933	0.0450 / 0.1233	0.1326 / 0.3702	0.0678 / 0.1569	0.0647 / 0.1698
R_1 / wR_2 [all data]	0.0514 / 0.0979	0.0478 / 0.1259	0.1495 / 0.4007	0.0758 / 0.1617	0.0892 /.1927
max / min $\Delta\rho$ [e·Å^{-3}]	2.69 / −3.22	5.26 / −2.03	4.76 / −2.23	1.41 / −1.23	2.75 / −2.28
Identification code	LD448_abs	LD303_abs	LD304_KBeta_abs	LD117_2_abs	LD413_Cub_abs

Table S3: Crystallographic details for the compounds **12**[TEF^{Cl}]$_2$, **13**[TEF^{Cl}]$_2$, **14**[TEF^{Cl}] and **15**[TEF]$_2$.

	12[TEF^{Cl}]$_2$	**13**[TEF^{Cl}]$_2$	**14**[TEF^{Cl}]	**15**[TEF^{Cl}]$_2$
formula	$C_{62}H_{24}Al_2Cl_{30}F_{48}Mo_4O_{16}P_2Sb_2$	$C_{86}H_{54}Al_2As_3Cl_{24}F_{54}Mo_3O_{14}$	$C_{30}H_{10}O_8F_{24}AlCl_{13}As_2Mo_2$	$C_{60}H_{20}O_{16}F_{72}Al_2P_2As_2Mo_4$
weight [g·mol^{-1}]	14957.75	3754.63	1783.93	3014.26
Temperature [K]	123.0(1)	123.0(1)	123.0(1)	123.0(1)
crystal system	orthorhombic	monoclinic	monoclinic	monoclinic
space group	$P2_12_12_1$	$P2_1/c$	$P2_1/c$	$P2_1/c$
a [Å]	11.43170(10)	31.9685(5)	12.48870(10)	30.9891(7)
b [Å]	28.3661(4)	12.8983(2)	16.9303(2)	27.3473(5)
c [Å]	33.3185(5)	30.9613(5)	24.7286(2)	21.5247(5)
α [°]	90	90	90	90
β [°]	90	105.052(2)	101.0640(10)	95.765(2)
γ [°]	90	90	90	90
Volume [Å^3]	10804.3(2)	12328.5(4)	5131.37(9)	18149.2(7)
Z	4	4	4	8
ρ_{calc} [g·cm^{-3}]	2.299	2.023	2.309	2.206
μ [mm^{-1}]	1.872	9.564	13.112	7.727
F(000)	7152.0	7308.0	3416.0	11568.0
crystal size [mm^3]	0.907 × 0.23 × 0.073	0.569 × 0.221 × 0.043	0.365 × 0.122 × 0.07	0.117 × 0.086 × 0.033
diffractometer	Gemini Ultra	GV50	GV50	GV50
absorption correction	gaussian	gaussian	gaussian	gaussian
T_{min} / T_{max}	0.473 / 0.890	0.059 / 1.000	0.104 / 0.719	0.641 / 0.931
radiation [Å]	Mo-Kα (λ = 0.71073)	Cu-Kα (λ = 1.54184)	Cu-Kα (λ = 1.54184)	Cu-Kα (λ = 1.54184)
2Θ range [°]	6.688 to 65.574	7.208 to 148.016	7.212 to 147.704	13.186 to 102.394
completeness [%]	99.8	99.6	99.1	99.1
reflns collected / unique	103575 / 36553	83857 / 24280	28907 / 9917	57989 / 19276
R_{int} / R_{sigma}	0.0550 / 0.0849	0.0898 / 0.0556	0.0253 / 0.0225	0.0775 / 0.0873
data / restraints / parameters	36553 / 984 / 2377	24280 / 0 / 1651	9917 / 0 / 721	19276 / 408 / 2522
GOF on F^2	1.051	1.470	1.065	1.028
R_1 / wR_2 [$I \geq 2\sigma(I)$]	0.0610 / 0.1149	0.1113 / 0.3320	0.0615 / 0.1500	0.0998 / 0.2583
R_1 / wR_2 [all data]	0.0849 / 0.1254	0.1197 / 0.3461	0.0628 / 0.1519	0.1311 / 0.2916
max / min $\Delta\rho$ [e·Å^{-3}]	1.33 / −2.13	4.92 / −4.96	4.28 / −3.59	2.06 / −1.42
Identification code	LD297_Gemini_abs	LD412_abs	LD152_abs	LD181_abs

Refinement details for 1[TEF^{Cl}]$_2$

Compound **1**[TEF^{Cl}]$_2$ crystallizes in the monoclinic space group *I*2/*a* with one dication exhibiting a nearly planar, central P_4 chain, two independent WCAs [TEF^{Cl}]$^-$ and 1 ½ solvent molecules CH_2Cl_2 in the asymmetric unit. The refinement could be done without any difficulty. One [TEF^{Cl}]$^-$ anion (including Al1) shows rotational disorder of one $OC(CF_3)_2(CCl_3)$ group in a ratio of 73:27. The disordered parts were partially constrained with DANG, SADI and DFIX commands and the ADPs with EADP commands during the refinement process.

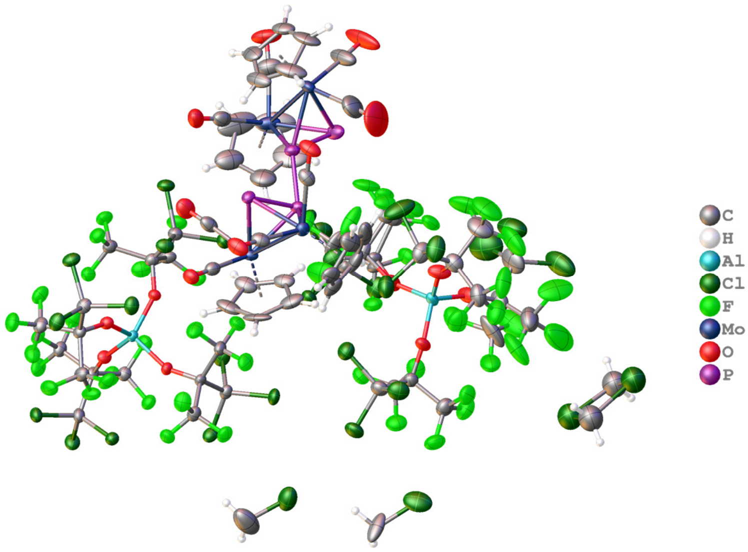

Figure S28: Molecular structure of **1**[TEF^{Cl}]$_2$. The asymmetric unit is shown containing one dication, two [TEF^{Cl}]$^-$ anions and 1 ½ solvent molecules CH_2Cl_2.

Refinement details for 2[TEF^{Cl}]$_2$

Compound **2**[TEF^{Cl}]$_2$ crystallizes in the monoclinic space group *P*2$_1$/*c* with one dication exhibiting a central As_4 ring and two independent WCAs [TEF^{Cl}]$^-$ in the asymmetric unit. The refinement could be done without any difficulty. One [TEF^{Cl}]$^-$ anion (including Al1) shows rotational disorder of two $OC(CF_3)_2(CCl_3)$ groups in a ratio of 75:25 and 89:11. The disordered parts were partially constrained with DANG and DFIX commands and the ADPs with EADP commands during the refinement process.

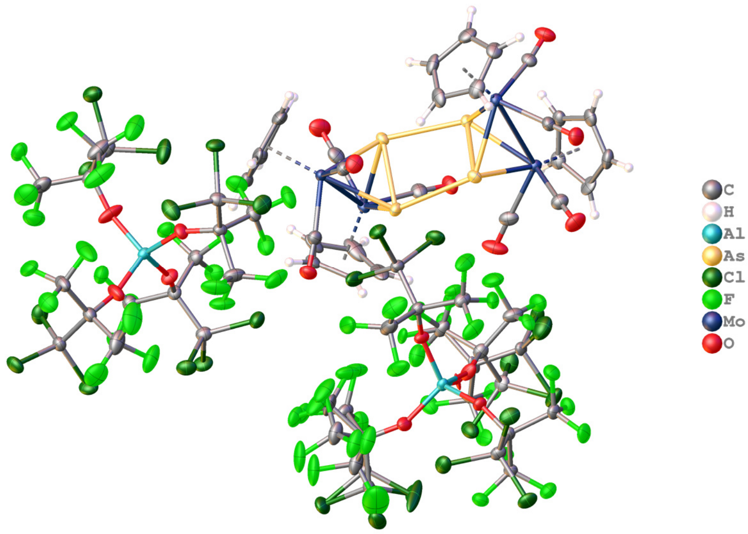

Figure S29: Molecular structure of **2**[TEF^{Cl}]$_2$. The asymmetric unit is shown containing one dication and two [TEF^{Cl}]$^-$ anions.

Refinement details for 5[TEF^{Cl}]$_2$

Compound **5**[TEF^{Cl}]$_2$ crystallizes in the monoclinic space group *I*2/*a* with one dication exhibiting a nearly planar, central AsPPAs chain, two independent WCAs [TEF^{Cl}]$^-$ and two half solvent molecules CH_2Cl_2 (with in occupancy of 0.5 and 0.25) in the asymmetric unit. The data set of the X-ray diffraction experiment is weak and, therefore, the refinement was hampered. Thus, the reported bond lengths and angles should be considered carefully. Additionally, one [TEF^{Cl}]$^-$ anion shows severe disorder, which could not be resolved until the end of this thesis.

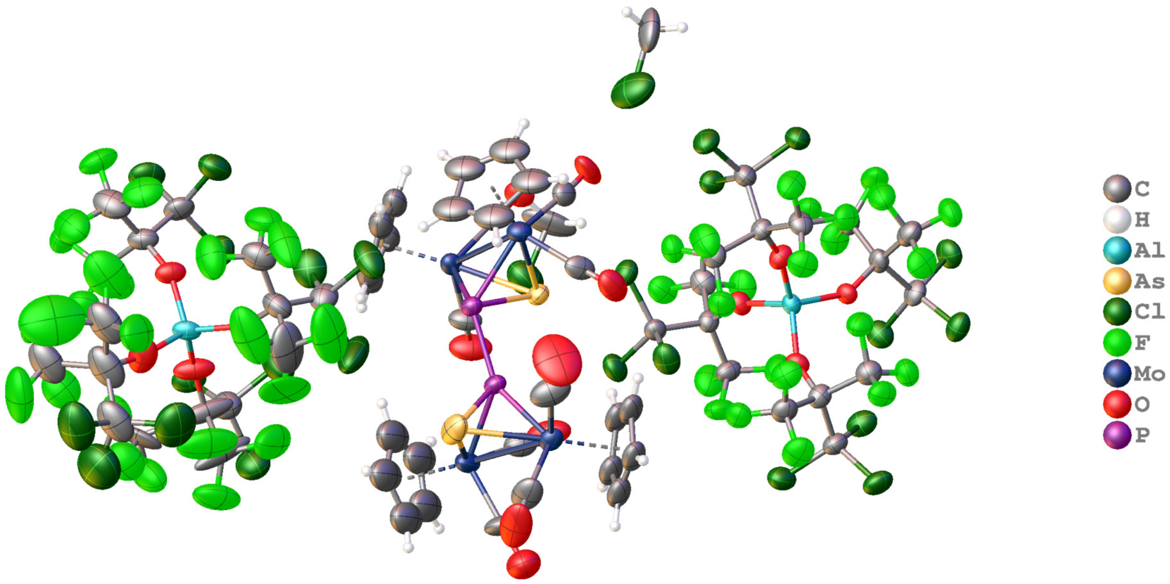

Figure S30: Molecular structure of **5**[TEF^{Cl}]$_2$. The asymmetric unit is shown containing one dication, two [TEF^{Cl}]$^-$ anions and two half solvent molecules CH_2Cl_2.

Refinement details for 6[TEF^{Cl}]$_2$

Compound **6**[TEF^{Cl}]$_2$ crystallizes as very thin orange plates, which could not be characterized crystallographically. However, a unit cell could be determined (Table S1), which is similar to those of **1**[TEF^{Cl}]$_2$, **5**[TEF^{Cl}]$_2$ and **10**[TEF^{Cl}]$_2$ suggesting the formation of a similar dicationic product with an SbPPSb ligand. This assumption is corroborated by the isolation and characterization of **12**[TEF^{Cl}]$_2$, which is a decomposition product of **6**[TEF^{Cl}]$_2$ and exhibits a SbPPSb chain (*vide infra*).

Refinement details for 7[TEF^{Cl}]$_2$

Compound **7**[TEF^{Cl}]$_2$ crystallizes in the monoclinic space group $P2_1/c$ with one dication exhibiting a central AsSbAsSb cycle and two independent WCAs [TEF^{Cl}]$^-$ in the asymmetric unit. The refinement could be performed without any difficulty. One [TEF^{Cl}]$^-$ anion (including Al1) shows rotational disorder of two $OC(CF_3)_2(CCl_3)$ groups in a ratio of 83:17 and 89:11. The disordered parts were partially constrained with DANG and DFIX commands and the ADPs with EADP and SIMU commands during the refinement process. In the four-membered pnictogen ring every position is occupied by both arsenic and antimony in the following ratios: Sb1 (84 % Sb and 16 % As), As1 (84 % As and 16 % Sb), Sb2 (81 % Sb and 19 % As) and As2 (81 % Sb and 19 % As).

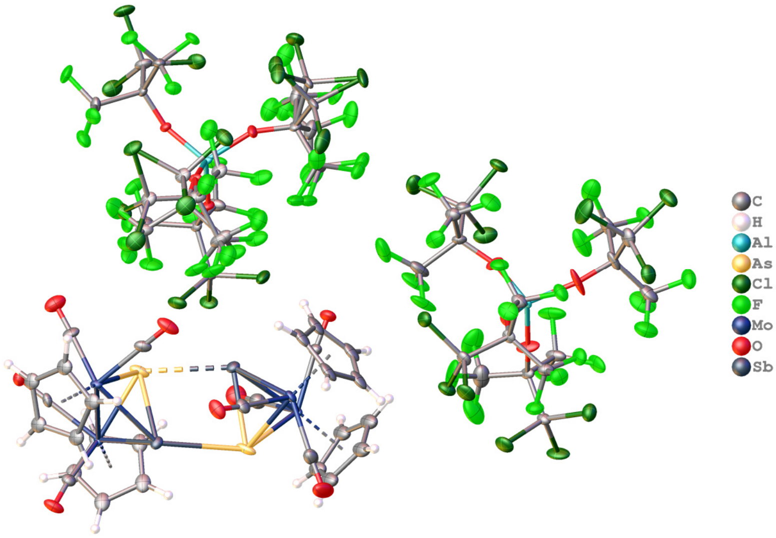

Figure S31: Molecular structure of **7**[TEF^{Cl}]$_2$. The asymmetric unit is shown containing one dication and two [TEF^{Cl}]$^-$ anions, of which one shows rotational disorder of two -$OC(CF_3)_2(CCl_3)$ groups.

Refinement details for 8[TEF^{Cl}]$_2$

Compound **8**[TEF^{Cl}]$_2$ crystallizes in the monoclinic space group $P2_1/n$ with one half dication exhibiting a central AsBiBiAs cycle, one WCA [TEF^{Cl}]$^-$ and one solvent molecule CH_2Cl_2 in the asymmetric unit. The refinement could be performed without any difficulty.

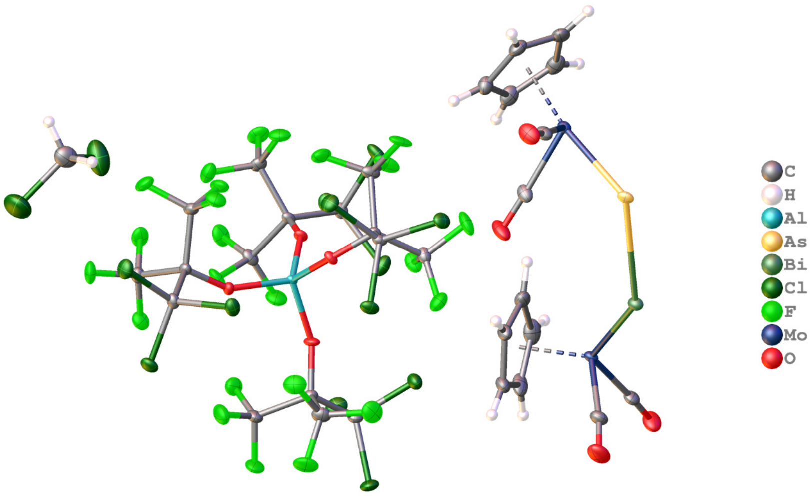

Figure S32: Molecular structure of **8**[TEF^{Cl}]$_2$. The asymmetric unit is shown containing one half dication, one [TEF^{Cl}]$^-$ anion and one CH_2Cl_2 molecule.

Refinement details for 10[TEF]$_2$

Compound **10**[TEF]$_2$ crystallizes in the monoclinic space group $P2_1/n$ with one dication exhibiting a central P_4 chain in gauche conformation and two independent WCAs [TEF]$^-$ in the asymmetric unit. The refinement could be performed without any difficulty. The completeness is only 95.9 % due to the orientation of the crystal in relation to the primary beam stop.

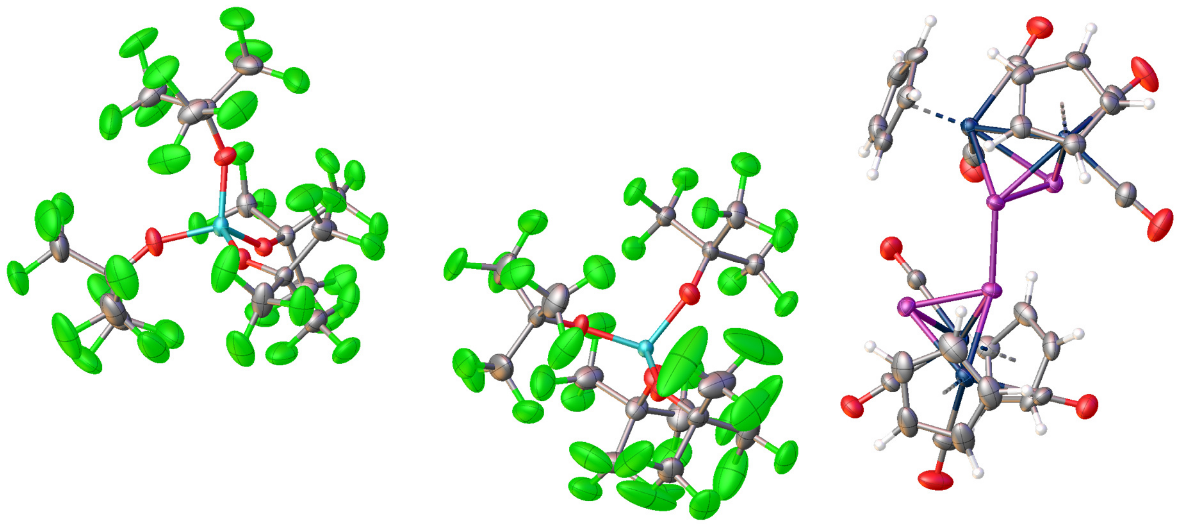

Figure S33: Molecular structure of **10**[TEF]$_2$. The asymmetric unit is shown containing one dication and two [TEF]$^-$ anions.

Refinement details for 10[TEF^{Cl}]$_2$

Compound **10**[TEF^{Cl}]$_2$ crystallizes in the monoclinic space group $P2_1/n$ with one half dication exhibiting a central, symmetric and planar P_4 chain, one WCA [TEF^{Cl}]$^-$ and one solvent molecule *o*-DFB in the asymmetric unit. The [TEF^{Cl}]$^-$ anion exhibits rotation disorder of its perhalogenated *tert*-butoxy groups, which could not be resolved till the end of this thesis. Thus, the reported bond lengths should be considered carefully.

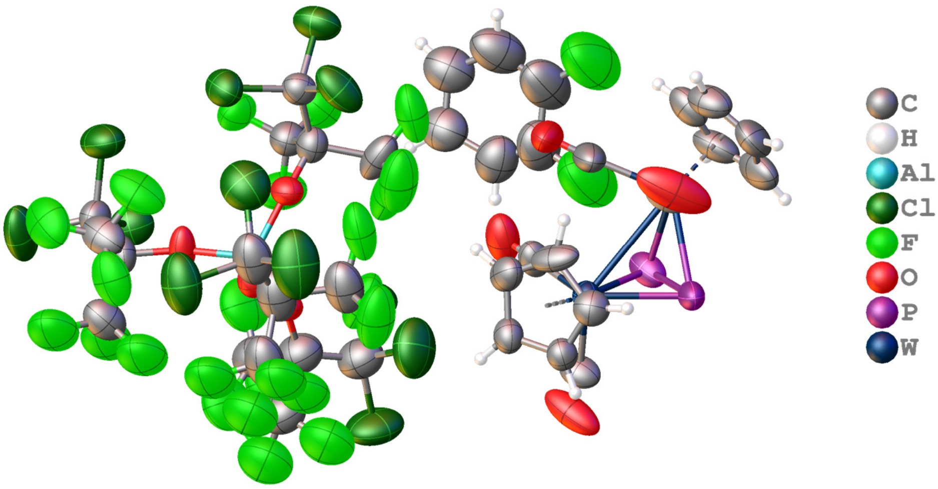

Figure S34: Molecular structure of **10**[TEF^{Cl}]$_2$. The asymmetric unit is shown containing one half dication, one [TEF^{Cl}]$^-$ anion and one solvent molecule *o*-DFB.

Refinement details for 11[TEF]₂

Compound **11**$[TEF]_2$ crystallizes in the monoclinic space group $P2_1/c$ with one dication exhibiting a central As_4 chain in gauche conformation, two independent WCAs $[TEF]^-$ and two solvent molecules CH_2Cl_2 in the asymmetric unit. The refinement could be performed without any difficulty. The $[TEF]^-$ anion including Al1 shows rotational disorder of two perfluorinated *tert*-butoxy groups in a ratio of 57:43 and 82:18. The second $[TEF]^-$ anion including Al2 shows rotational disorder of one $OC(CF_3)_3$ group in a ratio of 52:48. The disordered parts were partially constrained with DANG and DFIX commands and the anisotropic displacement parameters (ADPs) with EADP commands during the refinement process.

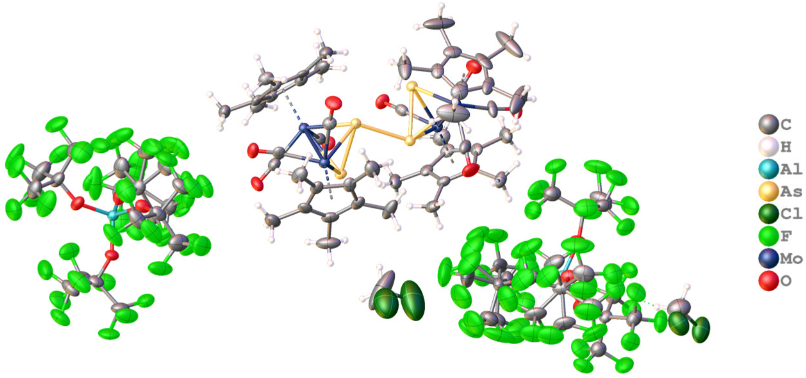

Figure S35: Molecular structure of **11**$[TEF]_2$. The asymmetric unit is shown containing one dication, two disordered $[TEF^{Cl}]^-$ anions and two solvent molecules CH_2Cl_2.

Refinement details for 11[FAl]₂

Compound **11**$[FAl]_2$ crystallizes in the triclinic space group *P*-1 with two dications exhibiting a central As_4 chain in gauche conformation, four independent WCAs $[FAl]^-$ and three solvent molecules *o*-DFB in the asymmetric unit. The refinement could be performed without any difficulty. The ADPs of the C atoms of two Cp* ligands were constrained by EADP commands during the refinement process.

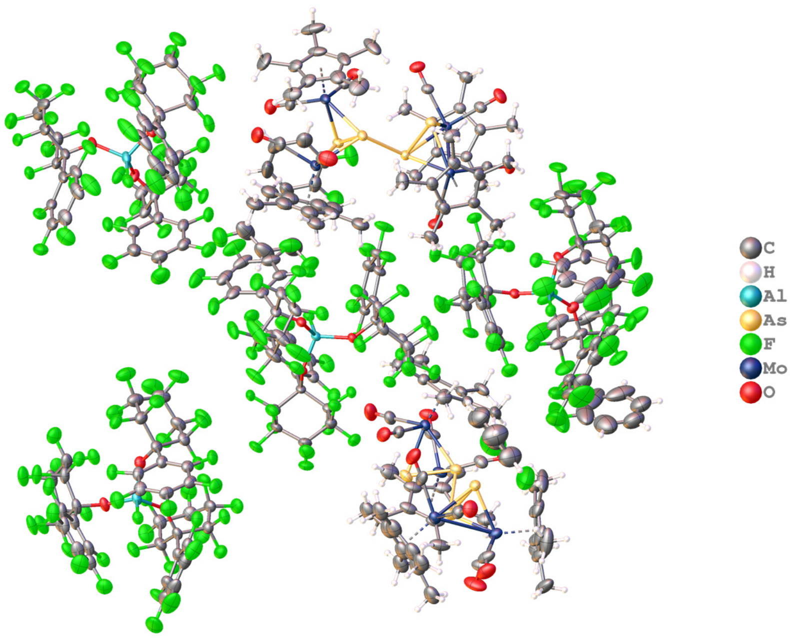

Figure S36: Molecular structure of **11**$[FAl]_2$. The asymmetric unit is shown containing two dications, four $[FAl]^-$ anions and three solvent molecules *o*-DFB.

Refinement details for 12[TEF^{Cl}]$_2$

Compound **12**[TEF^{Cl}]$_2$ crystallizes in the orthorhombic space group $P2_12_12_1$ with one dication two independent WCAs [TEF^{Cl}]$^-$ and two solvent molecules CH_2Cl_2 in the asymmetric unit. Both [TEF^{Cl}]$^-$ anions show rotational disorder of all four $OC(CF_3)_2(CCl_3)$ groups in a ratio of 60:40, 70:30, 80:20 and 67:33 within [TEF^{Cl}]$^-$ containing Al1 and 89:11, 88:12, 91:9 and 68:32 within [TEF^{Cl}]$^-$ containing Al2. The disordered parts were partially constrained with DANG, DFIX, SADI and EXYZ commands and the ADPs with EADP and SIMU commands during the refinement process.

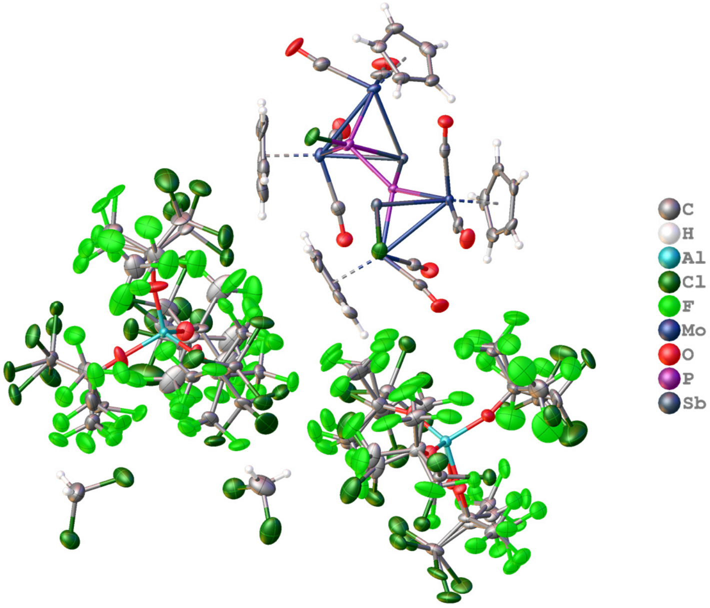

Figure S37: Molecular structure of **12**[TEF^{Cl}]$_2$. The asymmetric unit is shown containing one dication, two [TEF^{Cl}]$^-$ anions and two solvent molecules CH_2Cl_2.

Refinement details for 13[TEF^{Cl}]$_2$

Compound **13**[TEF^{Cl}]$_2$ crystallizes in the monoclinic space group $P2_1/c$ with one dication exhibiting a square pyramidal Mo_2As_3 unit, two independent WCAs [TEF^{Cl}]$^-$ and three solvent molecules *o*-DFB in the asymmetric unit. Two *o*-DFB molecules show a rotational disorder in a ratio of 50:50. The ADPs of the disordered parts were partially constrained with EADP commands during the refinement process.

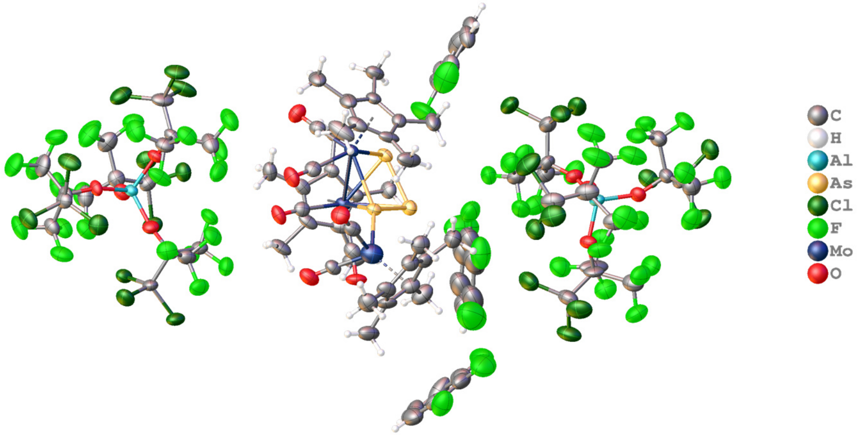

Figure S38: Molecular structure of **13**[TEF^{Cl}]$_2$. The asymmetric unit is shown containing one dication, two [TEF^{Cl}]$^-$ anions and three solvent molecules *o*-DFB.

Refinement details for 14[TEF^{Cl}]

Compound **14**[TEF^{Cl}] crystallizes in the monoclinic space group $P2_1/c$ with one cation and one WCA [TEF^{Cl}]$^-$ in the asymmetric unit. The refinement could be done without any difficulty.

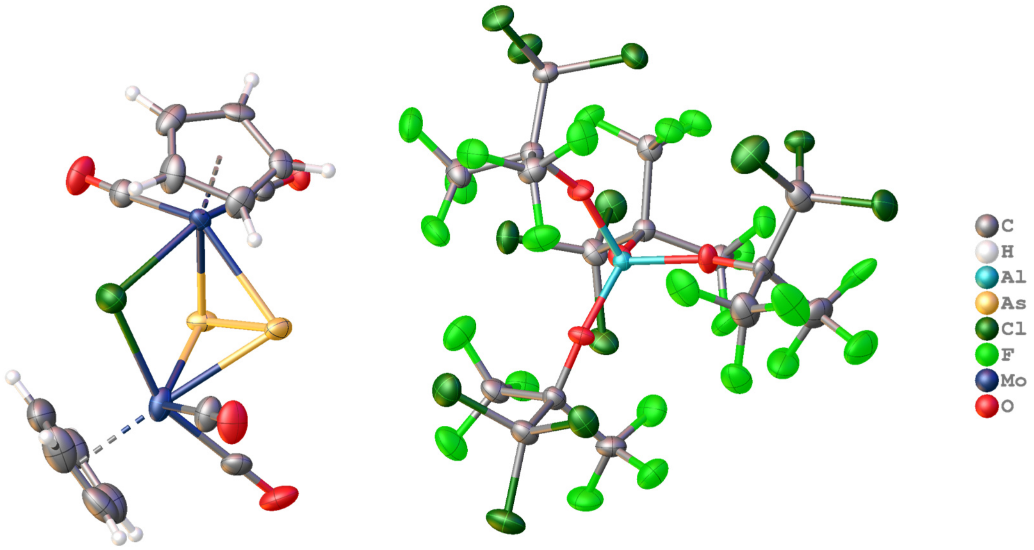

Figure S39: Molecular structure of **14**[TEF^{Cl}]. The asymmetric unit is shown containing one cation and one [TEF^{Cl}]$^-$ anion.

Refinement details for 15[TEF]$_2$

Compound **15**[TEF]$_2$ crystallizes in the monoclinic space group $P2_1/c$ with two dications exhibiting a central P_2As_2 cage and four independent WCAs [TEF]$^-$ in the asymmetric unit. All four [TEF]$^-$ anions show severe disorder of the perfluorinated *tert*-butoxy groups, which could not be completely resolved until the end of this thesis. However, the heavy atom framework of the dications could be described very well, but nonetheless, the bond lengths and angles should be considered carefully.

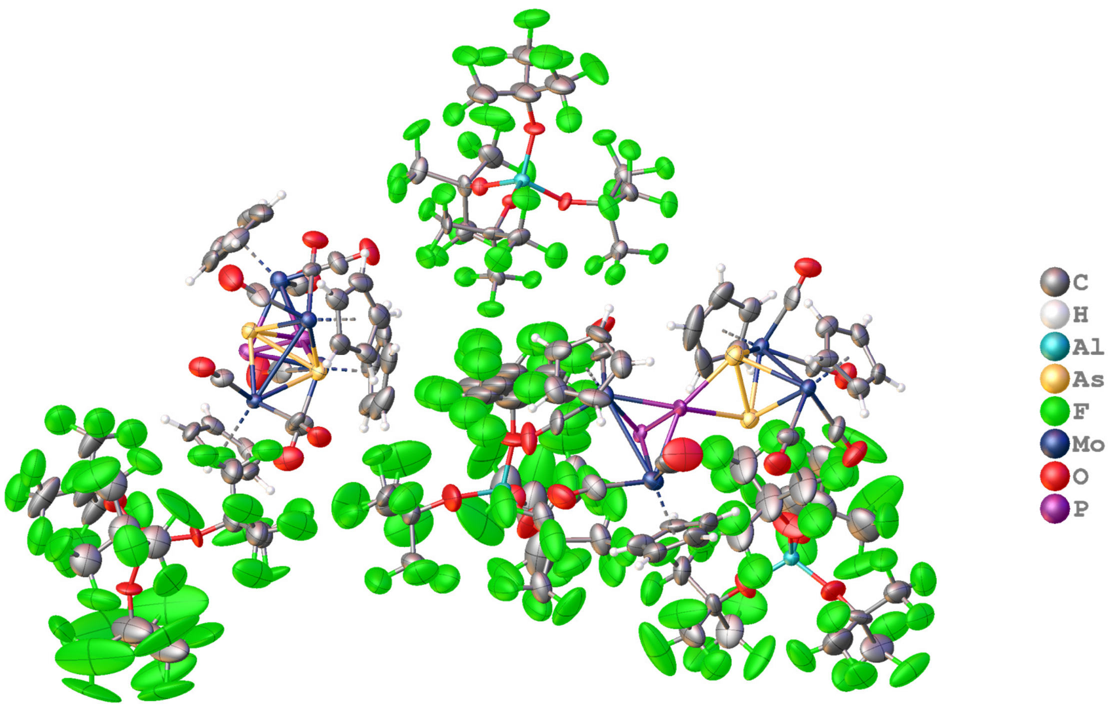

Figure S40: Molecular structure of **15**[TEF]$_2$. The asymmetric unit is shown containing two dications and four [TEF]$^-$ anions, which all show severe disorder of the -OC(CF_3)$_3$ groups.

6.5 References

[1] a) M. Schmidt, D. Konieczny, E. V. Peresypkina, A. V. Virovets, G. Balázs, M. Bodensteiner, F. Riedlberger, H. Krauss, M. Scheer, *Angew. Chem. Int. Ed.* **2017**, *56*, 7307-7311; b) C. Schoo, S. Bestgen, M. Schmidt, S. N. Konchenko, M. Scheer, P. W. Roesky, *Chem. Commun.* **2016**, *52*, 13217-13220; c) E. Mädl, G. Balázs, E. V. Peresypkina, M. Scheer, *Angew. Chem. Int. Ed.* **2016**, *55*, 7702-7707; d) N. Arleth, M. T. Gamer, R. Köppe, S. N. Konchenko, M. Fleischmann, M. Scheer, P. W. Roesky, *Angew. Chem. Int. Ed.* **2016**, *55*, 1557-1560; e) N. Arleth, M. T. Gamer, R. Koppe, N. A. Pushkarevsky, S. N. Konchenko, M. Fleischmann, M. Bodensteiner, M. Scheer, P. W. Roesky, *Chem. Sci.* **2015**, *6*, 7179-7184; f) M. V. Butovskiy, G. Balázs, M. Bodensteiner, E. V. Peresypkina, A. V. Virovets, J. Sutter, M. Scheer, *Angew. Chem. Int. Ed.* **2013**, *52*, 2972-2976; g) T. Li, M. T. Gamer, M. Scheer, S. N. Konchenko, P. W. Roesky, *Chem. Commun.* **2013**, *49*, 2183-2185; h) N. Reinfandt, C. Schoo, L. Dütsch, R. Köppe, S. N. Konchenko, M. Scheer, P. W. Roesky, *Chem. Eur. J.* **2021**, *27*, 3974-3978; i) M. Piesch, C. Graßl, M. Scheer, *Angew. Chem. Int. Ed.* **2020**, *59*, 7154-7160.

[2] E. Mädl, M. V. Butovskii, G. Balázs, E. V. Peresypkina, A. V. Virovets, M. Seidl, M. Scheer, *Angew. Chem. Int. Ed.* **2014**, *53*, 7643-7646.

[3] L. Dütsch, M. Fleischmann, S. Welsch, G. Balázs, W. Kremer, M. Scheer, *Angew. Chem. Int. Ed.* **2018**, *57*, 3256-3261.

[4] a) J. E. Davies, L. C. Kerr, M. J. Mays, P. R. Raithby, P. K. Tompkin, A. D. Woods, *Angew. Chem. Int. Ed.* **1998**, *37*, 1428-1429; b) J. E. Davies, M. J. Mays, P. R. Raithby, G. P. Shields, P. K. Tompkin, A. D. Woods, *J. Chem. Soc., Dalton Trans.* **2000**, 1925-1930.

[5] L. Dütsch, C. Riesinger, G. Balázs, M. Scheer, *Chem. Eur. J.* **2021**, *27*, 8804-8810.

[6] L. Dütsch, C. Riesinger, G. Balázs, M. Seidl, M. Scheer, *Chem. Sci.* **2021**, *12*, 14531-14539.

[7] a) O. J. Scherer, H. Sitzmann, G. Wolmershäuser, *Angew. Chem. Int. Ed.* **1985**, *24*, 351-353; b) O. J. Scherer, H. Sitzmann, G. Wolmershäuser, *J. Organomet. Chem.* **1986**, *309*, 77-86; c) I. Bernal, H. Brunner, W. Meier, H. Pfisterer, J. Wachter, M. Ziegler, *Angew. Chem. Int. Ed.* **1984**, *23*, 438-439; d) P. W. Roesky, N. Reinfandt, C. Schoo, L. Dütsch, R. Köppe, S. N. Konchenko, M. Scheer, *Chem. Eur. J.* **2021**, *27*, proofs. https://doi.org/10.1002/chem.202003905; e) M. Scheer, K. Schuster, A. Krug, H. Hartung, *Chem. Ber.* **1997**, *130*, 1299-1304; f) L. Dütsch, C. Riesinger, G. Balazs, M. Scheer, *Chem. Eur. J.* **2021**, manuscript accepted.

[8] a) M. Elsayed Moussa, P. A. Shelyganov, B. Wegley, M. Seidl, M. Scheer, *Eur. J. Inorg. Chem.* **2019**, *2019*, 4241-4248; b) J. E. Davies, M. J. Mays, P. R. Raithby, G. P. Shields, P. K. Tompkin, A. D. Woods, *J. Chem. Soc., Dalton Trans.* **2000**, 1925-1930; c) K. V. Adams, N. Choi, G. Conole, J. E. Davies, J. D. King, M. J. Mays, M. McPartlin, P. R. Raithby, *J. Chem. Soc., Dalton Trans.* **1999**, 3679-3686; d) W. Clegg, N. A. Compton, R. J. Errington, G. A. Fisher, N. C. Norman, T. B. Marder, *J. Chem. Soc., Dalton Trans.* **1991**, 2887-2895; e) L. Y. Goh, R. C. S. Wong, W. H. Yip, T. C. W. Mak, *Organometallics* **1991**, *10*, 875-879; f) P. J. Sullivan, A. L. Rheingold, *Organometallics* **1982**, *1*, 1547-1549.

[9] J. Schwalb, PhD thesis, University of Kaiserslautern, Kaiserslautern, **1988**.

[10] P. Pyykkö, *J. Phys. Chem. A* **2015**, *119*, 2326-2337.

[11] A. Garbagnati, M. Seidl, G. Balázs, M. Scheer, *Inorg. Chem.* **2021**, *60*, 5163-5171.

[12] a) J. J. Weigand, M. Holthausen, R. Fröhlich, *Angew. Chem. Int. Ed.* **2009**, *48*, 295-298; b) I. Krossing, I. Raabe, *Angew. Chem. Int. Ed.* **2001**, *40*, 4406-4409.

[13] For details see the Supporting Information.

[14] M. Mantina, A. C. Chamberlin, R. Valero, C. J. Cramer, D. G. Truhlar, *J. Phys. Chem. A* **2009**, *113*, 5806-5812.

[15] a) F. Spitzer, G. Balázs, C. Graßl, M. Scheer, *Chem. Commun.* **2020**, *56*, 13209-13212; b) F. Spitzer, G. Balázs, C. Graßl, M. Keilwerth, K. Meyer, M. Scheer, *Angew. Chem. Int. Ed.* **2018**, *57*, 8760-8764; c) O. J. Scherer, J. Vondung, G. Wolmershäuser, *J. Organomet. Chem.* **1989**, *376*, C35-C38.

[16] Apart from the crystals (**13**[TEF^{Cl}]) also red oil and powder was obtained. Therefore, it cannot be fully excluded that **13**[TEF^{Cl}] is only a side product in this reaction. Elemental analysis fits both, compound **13**[TEF^{Cl}] and a product, which is analogue to **11**[TEF] and **11**[FAl].

[17] M. Piesch, M. Scheer, *Organometallics* **2020**, *39*, 4247-4252.

[18] a) K. Wade, in *Advances in Inorganic Chemistry and Radiochemistry, Vol. 18* (Eds.: H. J. Emeléus, A. G. Sharpe), Academic Press, **1976**, pp. 1-66; b) J. D. Corbett, in *Prog. Inorg. Chem.*, John Wiley & Sons, Inc., **2007**, pp. 129-158.

[19] T. Köchner, N. Trapp, T. A. Engesser, A. J. Lehner, C. Röhr, S. Riedel, C. Knapp, H. Scherer, I. Krossing, *Angew. Chem. Int. Ed.* **2011**, *50*, 11253-11256.

[20] W. K. Lee, B. Liu, C. W. Park, H. J. Shine, K. H. Whitmire, *The Journal of Organic Chemistry* **1999**, *64*, 9206-9210.

[21] O. J. Scherer, H. Sitzmann, G. Wolmershäuser, *J. Organomet. Chem.* **1984**, *268*, C9-C12.

[22] N. G. Connelly, W. E. Geiger, *Chem. Rev.* **1996**, *96*, 877-910.

[23] M. Fleischmann, PhD thesis, University of Regensburg, Regensburg, **2015**.

[24] Agilent (2014). CrysAlis PRO. Agilent Technologies Ltd., Yarnton, Oxfordshire, England.

[25] G. Sheldrick, Acta Crystallographica Section A **2015**, 71, 3-8.

[26] O. V. Dolomanov, L. J. Bourhis, R. J. Gildea, J. A. K. Howard, H. Puschmann, *J. Appl. Crystallogr.* **2009**, *42*, 339-341.

[27] G. Sheldrick, Acta Crystallographica Section C **2015**, 71, 3-8.

Preface

The following chapter has not been published until the submission of this thesis.

Authors

Luis Dütsch, Christoph Riesinger and Manfred Scheer

Author Contributions

The main part (conceptualization, preparation of the compounds **1**[TEF]$_2$, **1**[TEF^{Cl}]$_2$, **1**[FAl]$_2$, **1**[SbF$_6$]$_2$ and **2**[FAl], writing, visualization, and execution and evaluation of measurements) of this work was done by the first author (Luis Dütsch). Christoph Riesinger assisted in the synthesis of **1**[FAl]$_2$ and performed it X-ray structural analysis. Manfred Scheer supervised the research and revised the manuscript.

Acknowledgements

This work was supported by the Deutsche Forschungsgemeinschaft within the project Sche 384/36-1.

7 Oxidation of Naked E_3 (E = P, As) Ligands – Access to a Novel Unsubstituted Dicationic P_9 Unit

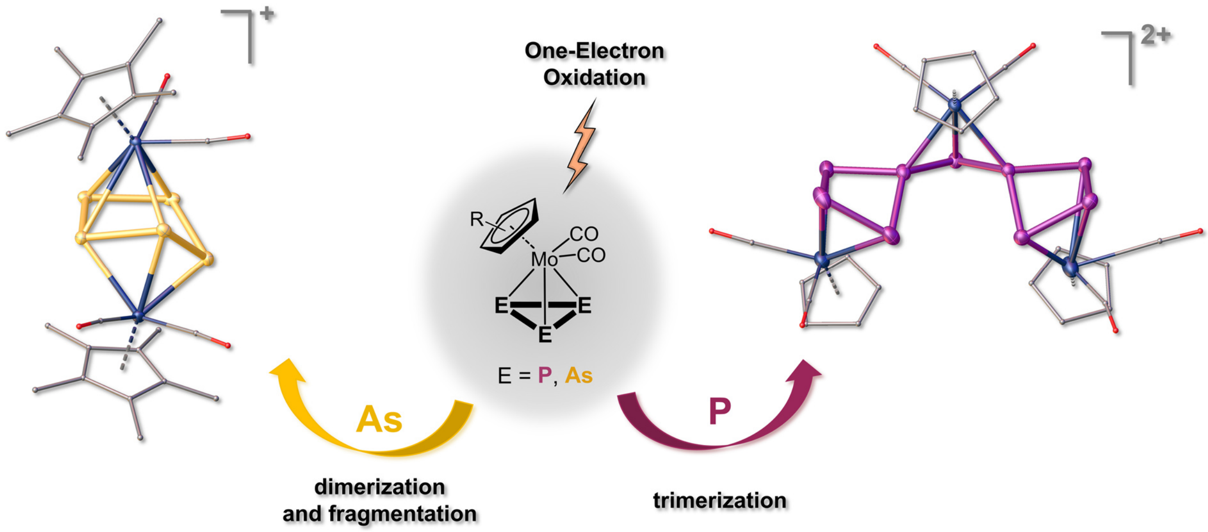

Abstract: *Herein, we report on the reactivity of tetrahedral molybdenum tripnictogen complexes $[\{Cp^RMo(CO)_2\}(\eta^3\text{-}E_3)]$ (E = P (**A**), As (**B**)) towards one-electron oxidants. Oxidation of **A** with $[Thia]^{\cdot+}$ (= $[C_{12}H_8S_2]^{\cdot+}$) leads to a trimerization reaction giving the dicationic complex $[\{CpMo(CO)_2\}_3(\mu,\eta^3:\eta^3:\eta^3\text{-}P_9)]^{2+}$ ($\mathbf{1}^{2+}$) in solution, which can be synthesized with various weakly coordinating anions. Single crystal X-ray diffraction experiments reveal that $\mathbf{1}^{2+}$ exhibits a unique, unsubstituted P_9 ligand stabilized in the coordination sphere of three $[CpMo(CO)_2]$ fragments, which is the largest dicationic polyphosphorus framework of this kind with an odd number of phosphorus atoms known so far. In contrast, oxidation of **B** leads to dimerization and fragmentation affording the monocationic triple-decker complex $[\{Cp^*Mo(CO)_2\}_2(\mu,\eta^4:\eta^3\text{-}As_5)]^+$ ($\mathbf{2}^+$) with a distorted, cyclic As_5 middle-deck.*

7.1 Introduction

Oxidation of phosphorus rich molecules has proven to be a useful tool to gain access to cationic phosphorus frameworks like the complexes [{Cp*Fe}$_2$(μ,η^5:η^5-P_{10})]$^{2+}$ and [(Cp*Mo)$_2$(μ,η^6:η^6-P_6)]$^+$.[1] Thereby, the former incorporates a substituent free, bicyclic P_{10} ligand and the latter a bis-allylic distorted P_6 middle-deck. One of the most remarkable achievements in this field is the synthesis of the only known all-phosphorus cation, namely [P_9]$^+$, which was obtained by the formal oxidation of white phosphorus with [NO]$^+$.[2] This milestone could only be accomplished with the aid of weakly coordinating anions (WCAs),[3] which are able to stabilize very labile and reactive cations due to their weakly nucleophilic properties.

In the previous chapters 4–6 we could show that the tetrahedral dimolybdenum dipnictogen complexes [{Cp^{R}Mo(CO)$_2$}$_2${μ,η^2:η^2-E_2}] (Cp^R = Cp or Cp' (^{t}BuC_5H_4); E = P, As, Sb, Bi; "**Mo$_2$E$_2$**") and [{Cp^{R}Mo(CO)$_2$}$_2${μ,η^2:η^2-EE'}] (Cp^R = Cp or Cp'; E ≠ E' = P, As, Sb, Bi; "**Mo$_2$EE'**"), which are isolobal to P_4 and As_4, are excellent precursors for the formation of extended, cationic polypnictogen structures as well. Reaction of **Mo$_2$E$_2$** and **Mo$_2$EE'** with the strong one-electron oxidant [$C_{12}H_8S_2$]$^{\cdot+}$ ("thianthrenium" = [Thia]$^{\cdot+}$] containing the WCA [Al{OC(CF$_3$)$_3$}$_4$]$^-$ ("teflonate" = [TEF]$^-$) results in dimerization reactions *via* E–E bond formation yielding unique, dicationic E_4 and $E_2E'_2$ chains (**I**, **II**, **V**, **VI**), cycles (**VIII**) and cages (**III**, **IV**, **VII**, **IX**) stabilized in the coordination sphere of transition metals (Scheme 1). Furthermore, the use of different WCAs had a remarkable impact on their molecular structure causing planarization or cyclization in some cases, whereas the exchange of the metal atom or the use of more sterically demanding Cp ligands led to very similar products.

In order to increase the amount of pnictogen atoms in the resulting cations the use of the isolobal E_3 ligand complexes [Cp^{R}Mo(CO)$_2$(η^3-E_3)] (**A**: E = P, Cp^R = Cp; **B**: E = As, Cp^R = Cp*;Scheme 1), where one [CpMo(CO)$_2$] fragment is substituted by an additional P or As atom, respectively, was the next logical step. This might enable the access to even bigger cationic pnictogen frameworks upon oxidation. Hence, in the following we report on the reaction behaviour of **A** and **B** towards one-electron oxidation agents.

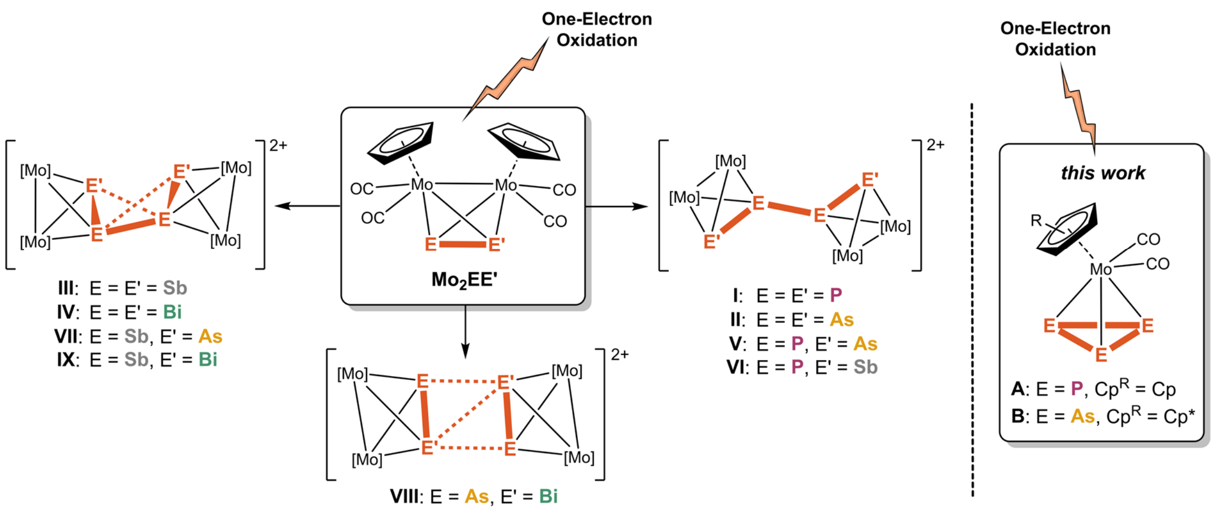

Scheme 1: One-electron oxidation of the tetrahedral dipnictogen complexes **Mo$_2$EE'** leading to dimerization reactions forming dicationic chains (**I**, **II**, **V**, **VI**), cycles (**VIII**) and cages (**III**, **IV**, **VII**, **IX**); **VII** exhibits only one short E···E' contact. *This work*: One-electron oxidation of the tetrahedral E_3 ligand complexes [Cp^{R}Mo(CO)$_2$(η^3-E_3)] (**A**: E = P, Cp^R = Cp; **B**: E = As, Cp^R = Cp*).

7.2 Results and Discussion

The cyclic voltammogram (CV) of the starting material **A** (Figure 1) in CH_2Cl_2 shows an irreversible oxidation at 0.70 V vs. $Cp_2Fe^{0/+}$. The oxidation potential of **A** is 0.42 V higher than in the analogous P_2 ligand complex **Mo_2P_2** (0.28 V vs. $Cp_2Fe^{0/+}$)[4], but [Thia][TEF] (0.86 V vs. $Cp_2Fe^{0/+}$)[5] should still be sufficient for a quantitative oxidation of **A**.

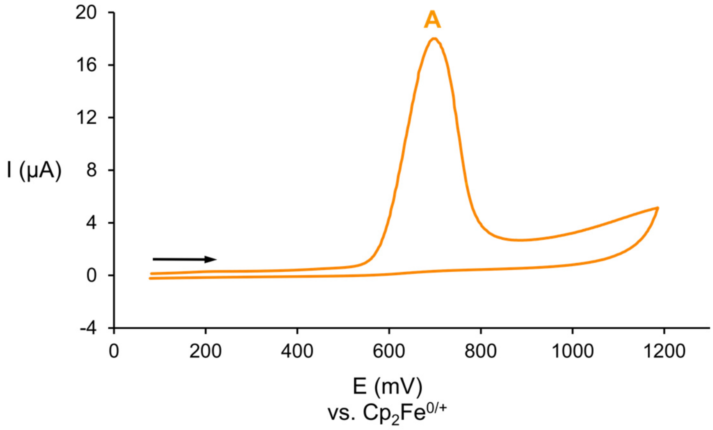

Figure 1: CV of **A** in CH_2Cl_2 showing an irreversible oxidation at 0.70 V vs $Cp_2Fe^{0/+}$; c([NBu_4][PF_6]) = 0.1 M.

When a yellow solution of **A** is reacted with dark purple [Thia][TEF] in CH_2Cl_2 an immediate colour change to dark red occurs. Against our expectations no dimerization product can be obtained, but, more interestingly, precipitation of the red solution with toluene yields orange powder of the trimeric, dicationic product [$\{CpMo(CO)_2\}_3(\mu,\eta^3:\eta^3:\eta^3-P_9)$][TEF]$_2$ (**1**[TEF]$_2$) in isolated yields of 69 % (Scheme 2). This assumes that the dark red colour originates from excess [Thia][TEF] in solution. Furthermore, when the reaction is performed in the correct stoichiometry (**A** and [Thia][TEF] in a ratio of 3:2) in either CH_2Cl_2 or *ortho*-difluorbenzene (*o*-DFB) the initially observed red solution turns orange within a minute and **1**[TEF]$_2$ is formed selectively and quantitatively in isolated yields of 87 %. Compound **1** contains a novel, dicationic P_9 ligand, which is completely free from organic substituents and only stabilized in the coordination sphere of the transition metal fragments [$CpMo(CO)_2$]. This P_9 ligand is amongst the biggest cationic and unsubstituted all-phosphorus ligands known. Moreover, it is the largest ligand with an odd number of phosphorus atoms besides the only reported homoleptic polyphosphorus cation [P_9]$^+$, which is stable in condensed phase. The latter was synthesized by *Krossing* and *co-workers* in 2012.[2b] However, $\mathbf{1}^{2+}$ is the first substituent-free P_9 dication, which is characterized crystallographically.

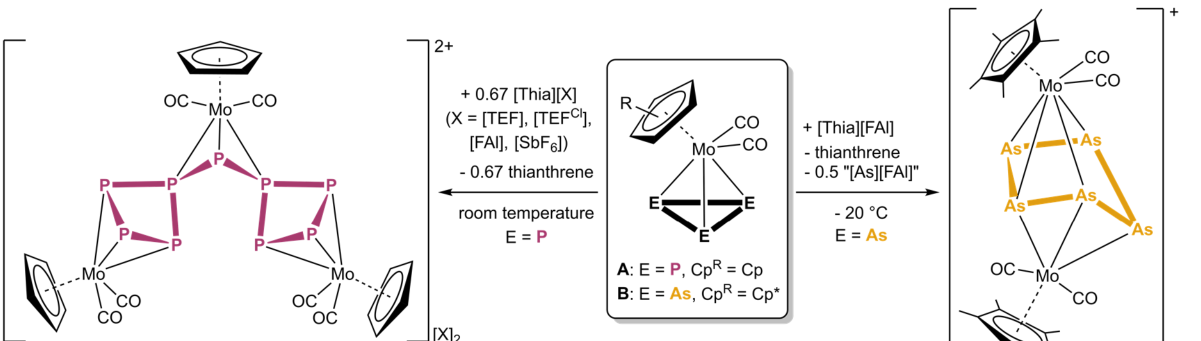

1[TEF]$_2$ (87 %)
1[TEF^{Cl}]$_2$ (70 %)
1[FAl]$_2$ (50 %)
1[SbF$_6$]$_2$ (90 %)

2[FAl] (82 %)

Scheme 2: One-electron oxidation of **A** and **B** leading to a trimeric, dicationic P_9 complex (**1**) and a distorted triple-decker complex with an As_5 middle-deck (**2**).

With these results in hand we turned our interest towards the heavier arsenic derivative **B**. Analogous reaction of a yellow solution of **B** with one equivalent [Thia][FAl] in *o*-DFB gives the monocationic, distorted triple-decker complex [{$Cp^*Mo(CO)_2$}$_2$($\mu,\eta^4:\eta^3$-As_5)][FAl] (**2**[FAl]) incorporating an unsubstituted As_5 middle-deck in isolated yields of 82 % (Scheme 2). This time dimerization of the As_3 complex occurs but appears to be followed by rapid fragmentation affording a formal equivalent of "[As][TEF]". However, the side-product could not be identified independent on numerous attempts.

It turned out to be very challenging to grow crystals of **1**[TEF]$_2$ in proper quality for single crystal X-ray diffraction. Therefore, we exchanged the counterions of **1**, which led either to insoluble precipitates in CH_2Cl_2 ([FAl{OC(C_5F_{10})(C_6F_5)}$_3$] = [FAl]$^-$) or *o*-DFB ([SbF_6]$^-$), or to oily products ([Al{OC(CF_3)$_2$(CCl_3)}$_4$]$^-$ = [TEF^{Cl}]$^-$). Interestingly, in the reaction of **A** with [Thia][SbF_6] at first a dark green precipitate is formed, which slowly turned orange over the course of 90 minutes. This may point to an initial formation of the dicationic dimerization product of **A** since the oxidation product of **Mo_2P_2** (**I**, Scheme 1) also forms a dark green powder upon precipitation.[4] However, attempts to isolate and further characterize the green powder failed as it is insoluble in most solvents and undergoes decomposition in MeCN, $MeNO_2$ and acetone. Luckily, **1**[FAl]$_2$ is at least partially soluble in *ortho*-difluorobenzene (*o*-DFB) allowing its crystallization from *o*-DFB/*n*-hexane and its crystallographic characterization. The products **1**[TEF]$_2$, **1**[FAl]$_2$ and **2**[FAl] crystallize in the orthorhombic space group *Pnma* (**1**[TEF]$_2$), the triclinic space group *P*-1 (**1**[FAl]$_2$) or the monoclinic space group *P*2$_1$/*n* (**2**[FAl]) with half a dication **1** and one [TEF]$^-$, one dication **1** and two [FAl]$^-$ or one cation **2** and one [FAl]$^-$anion, respectively, in the asymmetric unit. The cationic parts of the molecular structures of **1**[TEF]$_2$ and **1**[FAl]$_2$ (Figure 2a/b) are almost identical and, hence, only the latter is discussed. **1** features a dicationic P_9 ligand, which is free of any organic substituents and only stabilized in the coordination sphere of three [CpMo(CO)$_2$] transition metal fragments, which coordinate in an η^3-fashion. The P_9 ligand is derived from three molecules of **A**, which are trimerized by the formation of four new P–P bonds and the cleavage of three P–P bonds. Furthermore, the P_9 ligand consists of two four-membered P_4 rings,

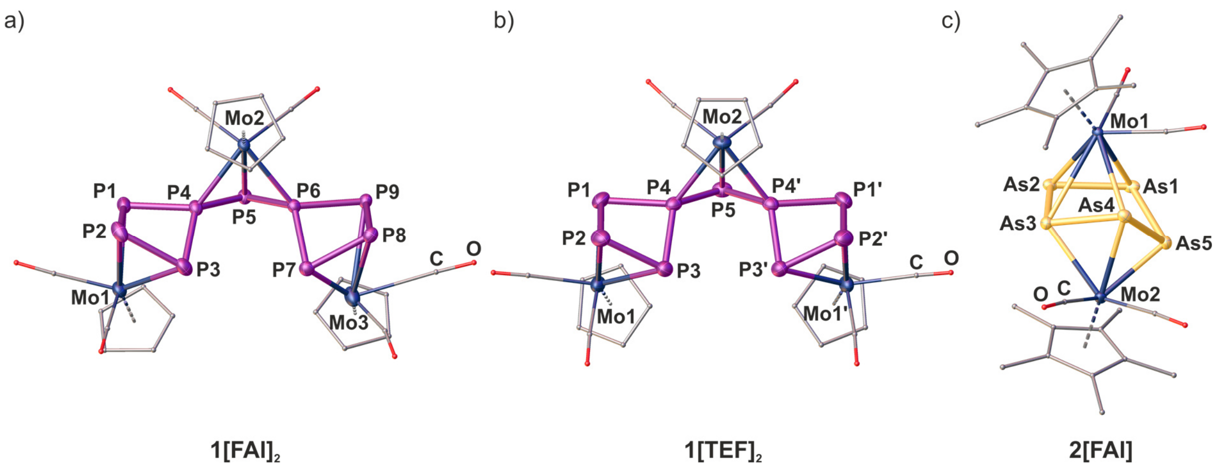

Figure 2: Molecular structures of **1**[FAl]$_2$ (a), **1**[TEF]$_2$ (b) and **2**[FAl] (c). Anisotropic displacement is set to the 50% probability level. H atoms, counterions and solvent molecules are omitted. Cp and CO ligands are drawn as small spheres for clarity. Selected bond lengths [Å] and angles [°]: **1**[FAl]$_2$: P1–P2 2.193(3), P2–P3 2.215(3), P3–P4 2.189(2), P4–P1 2.186(2), P4–P5 2.160(2), P5–P6 2.165(2), P6–P7 2.201(3), P7–P8 2.193(3), P8–P9 2.194(3), P9–P6 2.175(2), P1–P3 3.081(3), P4–P6 2.928(2), P6–P8 2.875(2), P1-P2-P3-P4 32.2(1), P7-P8-P9-P6 31.5(1); **2**[FAl]: As1–As2 2.360(1), As2–As3 2.400(1), As3–As4 2.4735(9), As4–As5 2.396(1), As5–As1 2.4495(9), As1-As2-As3-As4 20.6(1), As3-As2-As1-As5 15.9(1).

which are linked together by a single phosphorus atom (P5). In comparison, the only other P_9 cation ($[P_9]^+$) consists of two P_4 tetrahedra fused by an additional phosphonium moiety.[2b] Within the P_4 units the P atoms bound to Mo1 and Mo3 are in one plane, while the ones bound to Mo2 (P4/P6) are bend out of that plane by 32.2(1) ° and 31.5(1) °, respectively. These P_4 units resemble very well those of the insertion products of phosphenium ions into **A** (*cf.* chapter 9), which might give a hint towards the reaction mechanism (*vide infra*). All P–P bond lengths (2.160(2)–2.215(3) Å) within the P_9 ligand can be considered as P–P single bonds and they are slightly longer than in free **A**.[6] The P1–P3, P4–P6 and P7–P9 distances are significantly elongated (2.875(2)–3.081(3) Å) corroborating the cleavage of the former P–P bonds. The Mo–P distances are similar to those of free **A**[6] with Mo2–P5 (2.680(2) Å) being the longest and Mo2–P4/P6 (2.441(2)/2.445(2) Å) the shortest. The cation **2** (Figure 2c) shows a twisted triple-decker structure with two [$Cp^*Mo(CO)_2$] fragments as end-decks and a distorted, cyclic As_5 ligand as middle-deck. The Mo1 atom coordinates to the As_5 ligand in an η^4-fashion, whereas the Mo2 atom only coordinates in an η^3-mode. This might suggest that the positive charge is more located on Mo1 than on Mo2. However, to corroborate this assumption theoretical calculations have to be carried out, which are still in progress. While the Mo2–As distances are very similar (2.614(1)–2.675(1) Å) leading to a $MoAs_3$ unit, which resembles the one of **B** except of the broken As3–As5 bond (3.5966(7) Å), the Mo1–As distances differ significantly (2.622(1)–3.033(1) Å) with Mo1–As3 and Mo1–Mo4 being the longest. Within that the As3 and As4 atom are bound to both Mo atoms. The As–As distances within the As_5 ligand (2.360(1)– 2.4735(9) Å) are all in the range of As–As single bonds (2.42 Å).[7] All in all, the cyclic As_5 unit shows a distorted envelope structure.

The $^{31}P\{^1H\}$ and ^{31}P NMR spectra of the crude solutions of **1** all show four signals at $\delta = -243.2$, -17.4, 108.1 and 130.4 ppm in an $AM_2X_2Y_2Y'_2$ spin system with a signal ratio of 1:2:2:4. Signal A belongs to the central P5 atom (referred to Figure 2b) within the P_9 ligand and the signals Y/Y' to the atoms P1 and P9 as well as P3 and P7. The other two groups of signals can be assigned to the atoms P2/P8 (M) and P4/P6 (X) since the latter reveals a more complex coupling pattern due to the coupling to three different phosphorus atoms. When solutions of **A** and Thia[TEF] are reacted in ratios differing from 3:2 (2:1, 1:1 or 1:2) the formation of further products besides **1** can be observed, which could not be isolated yet (see Figures S2-S4 in the Supporting Information). The ^1H NMR spectrum of **2**[FAl] shows a singlet at $\delta = 2.01$ ppm for the Cp* ligands. The purity of **1**$[TEF]_2$ and **2**[FAl] was verified by elemental analyses.

The reaction pathway for the synthesis of **1** has not yet been clarified, but one possibility (Scheme 3, counterclockwise) is that in a first step one MoP_3 unit (including P4, P5 and P6) is formally oxidized twice leading to the cleavage of the P4–P6 bond and two positive charges, one on P4 and one on P6. These formal phosphenium ions then each insert into one P–P bond (P1–P3 and P7–P9) of a further equivalent of MoP_3 analogous to the reaction of *in situ* generated phosphenium ions with **A** (*cf.* chapter 9). A second option (Scheme 3, clockwise) is that primarily the lone pair of P4 is oxidized forming a radical cation, which then further inserts into the P1–P3 bond of a second equivalent of **A** leading to homolytic cleavage, the formation of a new P1–P4 bond and a radical centred at P3. The latter then again attacks the P4–P6 bond in the same manner giving a radical on P6. This radical is then oxidized by a second equivalent of thianthrenium yielding a formal phosphenium ion, which then

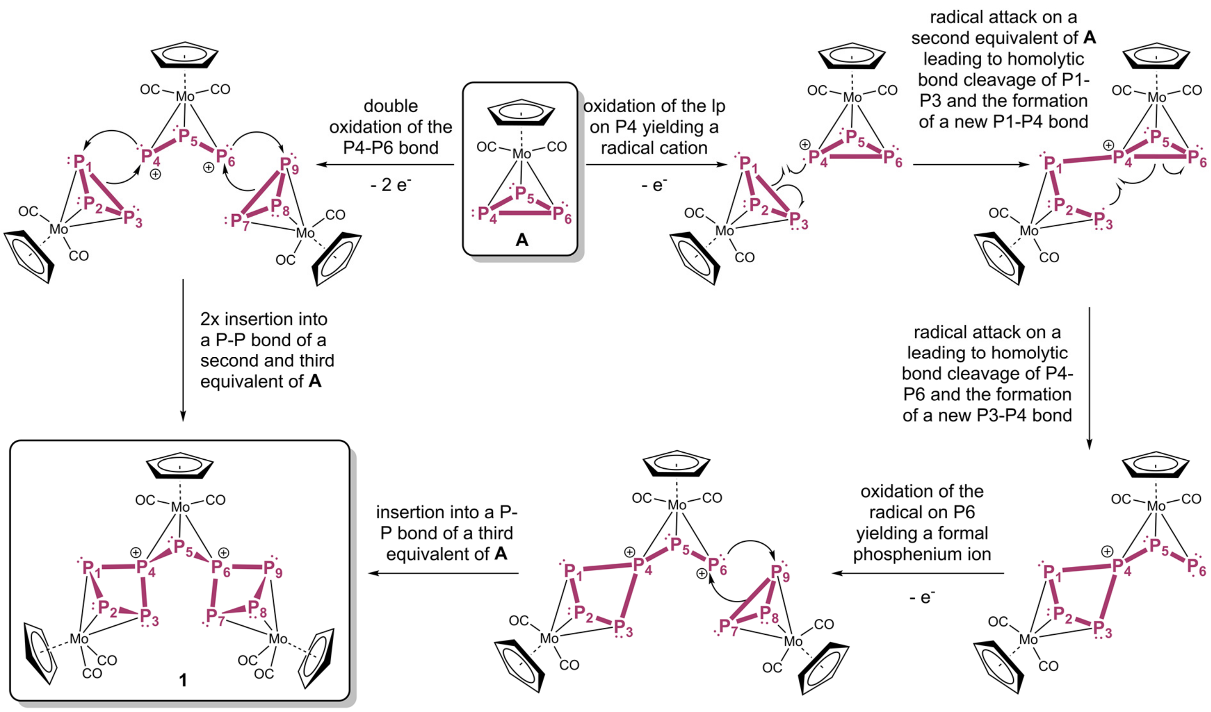

Scheme 3: Two possible reaction pathways for the formation of **1**; *counterclockwise*: double one-electron oxidation followed by insertion reactions; *clockwise*: radical mechanism.

inserts into the P7–P9 bond of a third equivalent of **A** just like in the first mechanism. However, further investigations as well as theoretical calculations have to be carried out to sort out which of these pathways takes place or if a completely different mechanism should be considered such as oxidation of **A** followed by radical dimerization and then subsequently the dimeric species reacts with another molecule **A**. Additionally, the isolation of an intermediate would shed light into the mechanism as well.

7.3 Conclusion

In summary, the one-electron oxidation of unsubstituted E_3 ligand complexes proved to be a useful tool to gain access to extended, unsubstituted, cationic polypnictogen frameworks. Thereby, the As_3 ligand complex **B** dimerizes under the loss of a formal "As^+" fragment leading to the monocationic triple-decker complex $[(Cp^*Mo(CO)_2\}_2(\mu,\eta^4:\eta^3-As_5)]^+$ (**2**) with an As_5 middle-deck in a distorted envelope geometry. More interestingly, oxidation of the analogous P_3 ligand complex **A** leads to a trimerization reaction forming the dication $[\{CpMo(CO)_2\}_3(\mu,\eta^3:\eta^3:\eta^3-P_9)]^{2+}$, which incorporates a unique, unsubstituted P_9 ligand stabilized in the coordination sphere of three [$CpMo(CO)_2$] fragments. The P_9 ligand consists of two four-membered phosphorus rings, which are bridged *via* a further phosphorus atom. This unique P_n ligand is the largest unsubstituted polyphosphorus framework with an odd number of phosphorus atoms reported to date, which carries two positiv charges and is characterized crystallographically. Moreover, since naked E_n ligands and especially cationic examples of the heavier pnictogen elements antimony and bismuth are very rare, we plan to expand this very promising approach to the heavier analogues of **A** and **B** and other E_n ligand complexes in the future.

7.4 Supporting Information

7.4.1 General remarks

All manipulations were carried out under an inert atmosphere of dried nitrogen/argon using standard Schlenk and glovebox techniques. The used Schlenk flasks were heated at 550 °C for at least 15-30 minutes under reduced pressure prior to use to get rid of water traces adhered to the glass surface. The starting materials [$CpMo(CO)_2(\eta^3-P_3)$], [$Cp^*Mo(CO)_2(\eta^3-As_3)$], [Thia][TEF], [Thia][$TEF^{Cl}$], [Thia][FAl] and [Thia][SbF_6] were synthesized according to literature procedures. Solvents were freshly distilled under nitrogen after drying over CaH_2 (CH_2Cl_2, CD_2Cl_2), K or Na/K alloy (alkanes), P_4O_{10} (*ortho*-difluorobenzene = *o*-DFB) or NaH (toluene). Dried solvents were also taken from a MB SPS-800 solvent purification system from MBraun and degassed prior to use. For NMR spectra of crude solutions a C_6D_6 capillary was used. For reactions in liquid SO_2 the gas was condensed into a flask with a Young valve at −196 °C and then warmed up to −30 °C. SO_2 gas cylinders were bought from commercial vendors. NMR spectra were recorded at 300 K (if not stated otherwise) on a Bruker Avance 300 MHz NMR spectrometer (^{1}H: 300.132 MHz, ^{31}P: 121.495 MHz, ^{19}F: 282.404 MHz) or a Bruker Avance 400 MHz NMR spectrometer (^{1}H: 400.130 MHz, ^{31}P: 161.976 MHz, ^{19}F: 376.498 MHz) with external references of $SiMe_4$ (^{1}H,), CCl_3F (^{19}F) and H_3PO_4 (85%, ^{31}P). The chemical shifts δ are presented in parts per million (ppm) and coupling constants J in Hz. The following abbreviations were used for signal assignment: s = singlet, t = triplet and m = multiplet. Elemental analyses (EA) were performed by the micro analytical laboratory of the University of Regensburg.

7.4.2 Experimental details

Synthesis of 1[TEF]$_2$

A bright yellow solution of [$CpMo(CO)_2(\eta^3-P_3)$}] (**A**; 80 mg, 0.258 mmol, 3.0 eq.) in 5 mL *o*-DFB was reacted with a dark purple solution of [Thia][TEF] (204 mg, 0.172 mmol, 2.0 eq.) in 5 mL *o*-DFB, which led to an immediate colour change to dark red. Furthermore, the solution turns orange in the course of three minutes. After stirring for 30 minutes 30 mL of toluene were added leading to precipitation of an orange powder, which was washed twice with 10 mL toluene and twice with 10 mL *n*-hexane, and dried in vacuum. Recrystallization from CH_2Cl_2/*n*-hexane at −30 °C yields pure **1**[TEF]$_2$ in form of thin orange plate, which were moderately suitable for single crystal X-ray diffraction. The solvent was removed by decanting and the crystals were dried in vacuum for 3 h.

Yield 213 mg (0.074 mmol, 87 %). ^{31}P{^{1}H} NMR of the crude solution (C_6D_6/*o*-DFB) δ/ppm = −243.2 (t, $^1J_{P5\text{-}P4/P4'}$ = 403 Hz, 1 P, P5 atom), −19.8–(−15.0) (m, $^1J_{P2/P2'\text{-}P1/P1'/P3/P3'}$ = 245 Hz, 2 P, P2/P2' atoms), 104.1–112.1 (m, 2 H, P4/P4'), 126.8–134.0 (t, $^1J_{P\text{-}P}$ = 275 Hz, 4 P, P1/P1'/P3/P3' atoms). ^{31}P NMR of the crude solution (C_6D_6/*o*-DFB) δ/ppm = −244.1 (t, $^1J_{P5\text{-}P4/P4'}$ = 404 Hz, 1 P, P5 atom), −19.8–(−15.0) (m, $^1J_{P2/P2'\text{-}P1/P1'/P3/P3'}$ = 245 Hz, 2 P, P2/P2' atoms), 104.1–112.1 (m, 2 H, P4/P4'), 126.8–134.0 (t, $^1J_{P\text{-}P}$ = 275 Hz, 4 P, P1/P1'/P3/P3' atoms). ^{19}F{^{1}H} NMR (CD_2Cl_2) δ/ppm = −75.4 (s, [TEF]$^-$). Anal. calcd. for [$C_{21}H_{15}O_6Mo_3P_9$][$AlO_4C_{16}F_{36}$]$_2$: C: 22.23, H: 0.53. Found: C: 23.14, H: 0.93.

Synthesis of 1[FAl]$_2$

Yellow [$CpMo(CO)_2(\eta^3-P_3)$] (**A**; 47 mg, 0.15 mmol, 3.0 eq.) and pink/purple [Thia][FAl] (160 mg, 0.10 mmol, 2.0 eq.) were weighed together and 15 mL *o*-DFB were added leading to red solution and some undissolved orange solid. After 30 minutes of stirring the supernatant turned bright orange and was transferred into another flask. The solution was layered with *n*-hexane and storage at room temperature yielded pure 1[FAl]$_2$ as irregular, orange blocks suitable for single crystal X-ray diffraction. The solvent was removed by decanting and the crystals were dried in vacuum for 3 h.

Yield 92 mg (0.025 mmol, 50 %). $^{31}P\{^1H\}$ NMR of the crude solution (C_6D_6/*o*-DFB) δ/ppm = −243.0 (t, $^1J_{P5\text{-}P4/P4'}$ = 400 Hz, 1 P, P5 atom), −19.8–(−15.0) (m, 2 P, P2/P8 atoms), 104.1–112.1 (m, 2 H, P4/P6), 126.8–134.0 (t, $^1J_{P\text{-}P}$ = 275 Hz, 4 P, P1/P3/P7/P9 atoms). ^{31}P NMR of the crude solution (C_6D_6/*o*-DFB) δ/ppm = −242.9 (t, $^1J_{P5\text{-}P4/P4'}$ = 400 Hz, 1 P, P5 atom), −19.8–(−15.0) (m, 2 P, P2/P8 atoms), 104.1–112.1 (m, 2 H, P4/P6), 126.8–134.0 (t, $^1J_{P\text{-}P}$ = 275 Hz, 4 P, P1/P3/P7/P9 atoms).

Synthesis of 1[TEF^{Cl}]$_2$

A bright yellow solution of [$CpMo(CO)_2(\eta^3-P_3)$] (**A**; 80 mg, 0.258 mmol, 3.0 eq.) in 5 mL *o*-DFB was reacted with a dark purple solution of [Thia][TEF^{Cl}] (238 mg, 0.172 mmol, 2.0 eq.) in 5 mL *o*-DFB, which led to an immediate colour change to dark red. Furthermore, the solution turns orange in the course of three minutes. After stirring for 30 minutes 30 mL of toluene were added leading to precipitation of an orange powder, which was washed twice with 10 mL toluene and twice with 10 mL *n*-hexane, and dried in vacuum. Recrystallization from *o*-DFB/*n*-pentane/toluene (1:1:4) at room temperature and −30 °C, respectively, only yields **1**[TEF^{Cl}]$_2$ as orange red oil. The solvent was removed by decanting and the oil dried in vacuum for 3 h.

Yield 197 mg (0.060 mmol, 70 %). $^{31}P\{^1H\}$ NMR of the crude solution (C_6D_6/*o*-DFB) δ/ppm = −243.3 (t, $^1J_{P5\text{-}P4/P4'}$ = 403 Hz, 1 P, P5 atom), −19.8–(−15.0) (m, 2 P, P2/P2' atoms), 104.1–112.1 (m, 2 H, P4/P4'), 126.8–134.0 (m, 4 P, P1/P1'/P3/P3' atoms)

Synthesis of 1[SbF$_6$]$_2$

Yellow [$CpMo(CO)_2(\eta^3-P_3)$] (**A**; 46 mg, 0.15 mmol, 3.0 eq.) and [Thia][SbF_6] (45 mg, 0.10 mmol, 2.0 eq.) were weighed together and 15 mL *o*-DFB were added leading to the formation of green solid suspended in an yellow solution. After 1 hour of stirring the supernatant bridened up and the solid turned orange. The supernatant was removed by decanting, the residue washed with 10 mL toluene and dried in vacuum. Recrystallization from liquid SO_2 at −30 °C, which was condensed onto the solid at −196 °C, and layering with *n*-hexane was unsuccessful. The solvent was evaporated and the orange powder dried in vacuum for 3 h.

Yield 63 mg (0.045 mmol, 90 %).

Synthesis of 2[FAl]

Yellow [Cp*Mo(CO)$_2$(η^3-As$_3$}] (**B**; 26 mg, 0.05 mmol, 1.0 eq.) and [Thia][FAl] (80 mg, 0.05 mmol, 1.0 eq.) each were dissolved/suspended in 10 mL *o*-DFB at −20 °C and added together yielding a red orange solution. The solution was stirred for 30 minutes and precipitated with 60 ml *n*-pentane. The red-brown residue was washed twice with 10 mL toluene and dried in vacuum. Recrystallization from *o*-DFB/*n*-pentane yielded **2**[FAl] as red crystals suitable for single crystal X-ray diffraction. The solvent was removed by decanting and the crystals dried in vacuum for 3 h.
Yield 47 mg (0.02 mmol, 82 %). ^{1}H NMR (CD$_2$Cl$_2$) *δ*/ppm = 2.01 (s, Cp*). Anal. calcd. for [$C_{24}H_{30}O_4Mo_2As_5$][$AlO_3C_{36}F_{46}$]: C: 30.93, H: 1.30. Found: C: 31.19, H: 0.91.

7.4.3 NMR spectroscopy

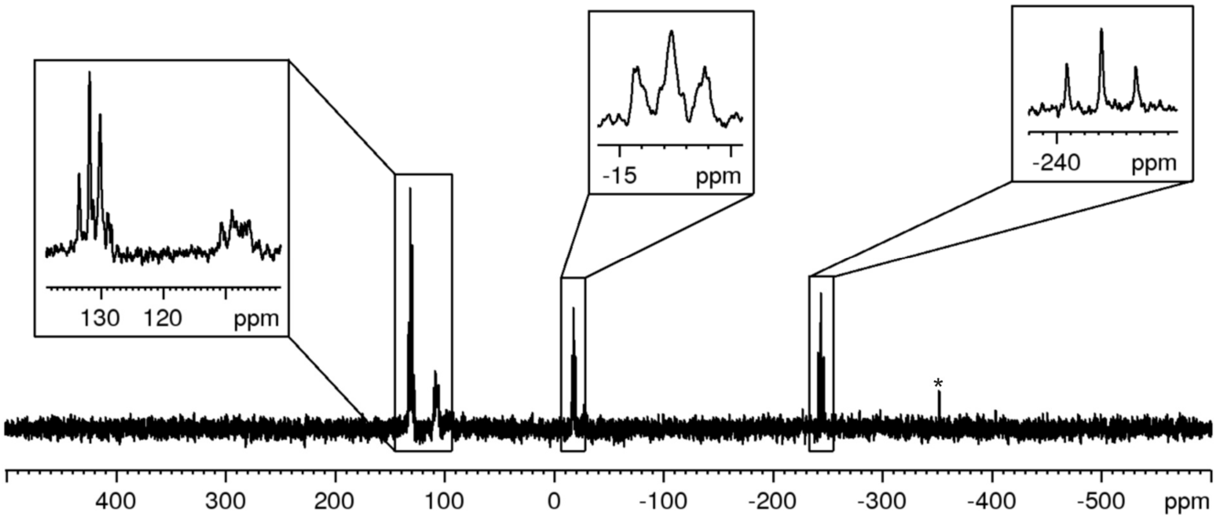

Figure S1: ^{31}P{^{1}H} NMR spectrum of the crude solution of **1**[TEF]$_2$ in C_6D_6/*o*-DFB; * = minor traces of **A**.

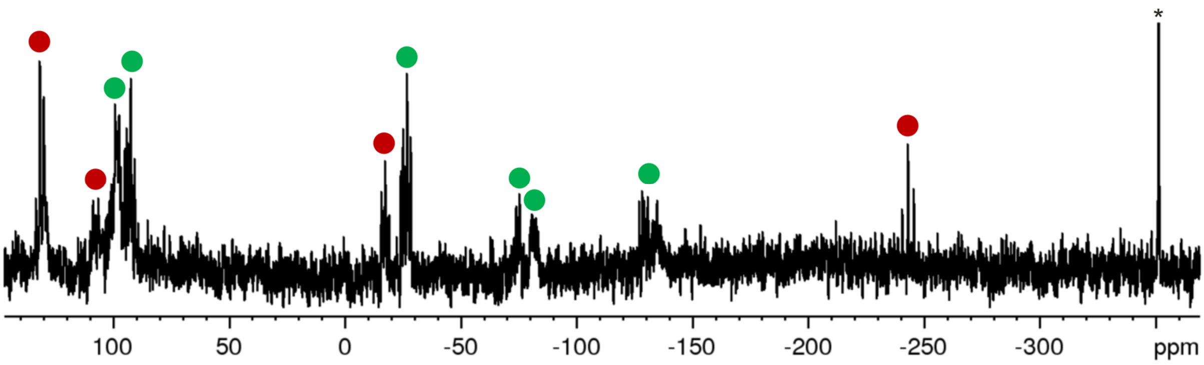

Figure S2: ^{31}P{^{1}H} NMR spectrum of the reaction of **A** with [Thia][TEF] in a ratio of 2:1; * = **A**; red = **1**[TEF]$_2$; green = unidentified side-product(s).

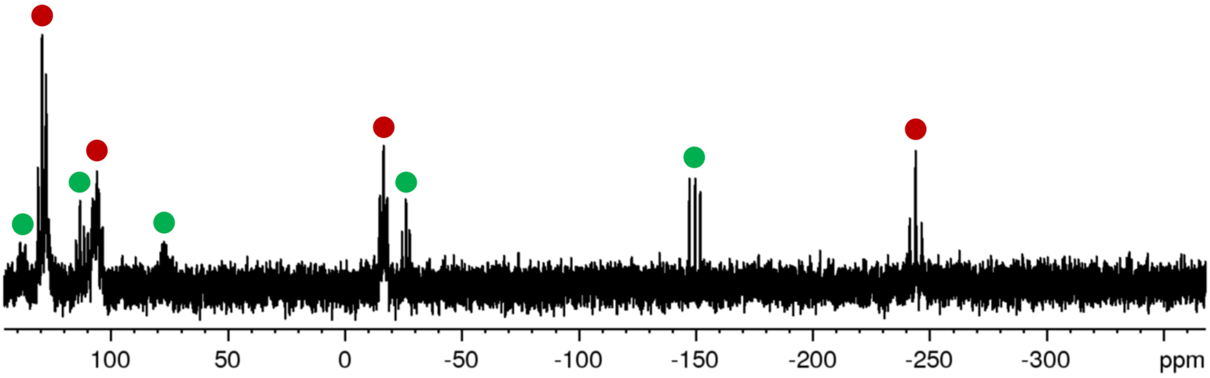

Figure S3: ^{31}P{^{1}H} NMR spectrum of the reaction of **A** with [Thia][TEF] in a ratio of 1:1; red = **1**[TEF]$_2$; green = unidentified side-product(s).

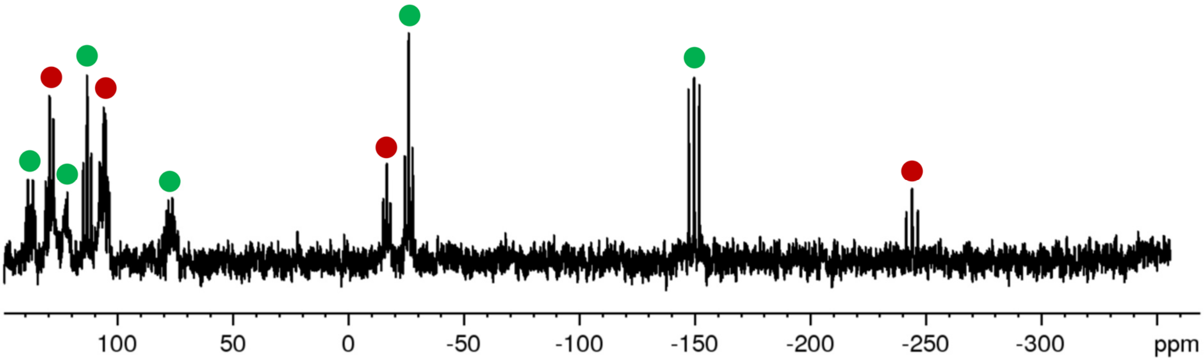

Figure S4: ^{31}P{^{1}H} NMR spectrum of the reaction of **A** with [Thia][TEF] in a ratio of 1:2; red = **1**[TEF]$_2$; green = unidentified side-product(s).

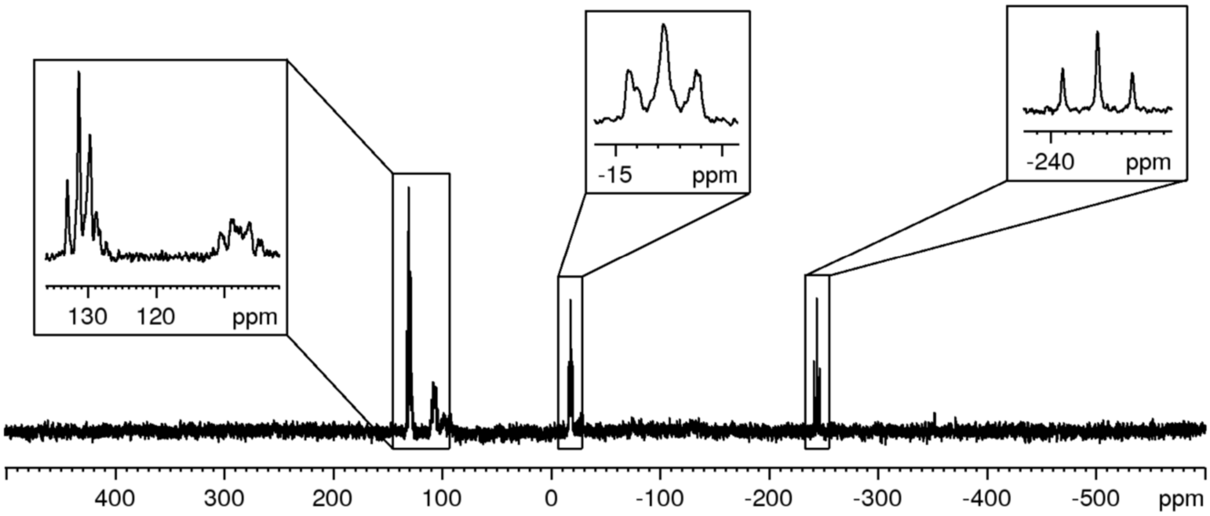

Figure S5: ^{31}P{^{1}H} NMR spectrum of the crude solution of **1**[TEF^{Cl}]$_2$ in C$_6$D$_6$/*o*-DFB.

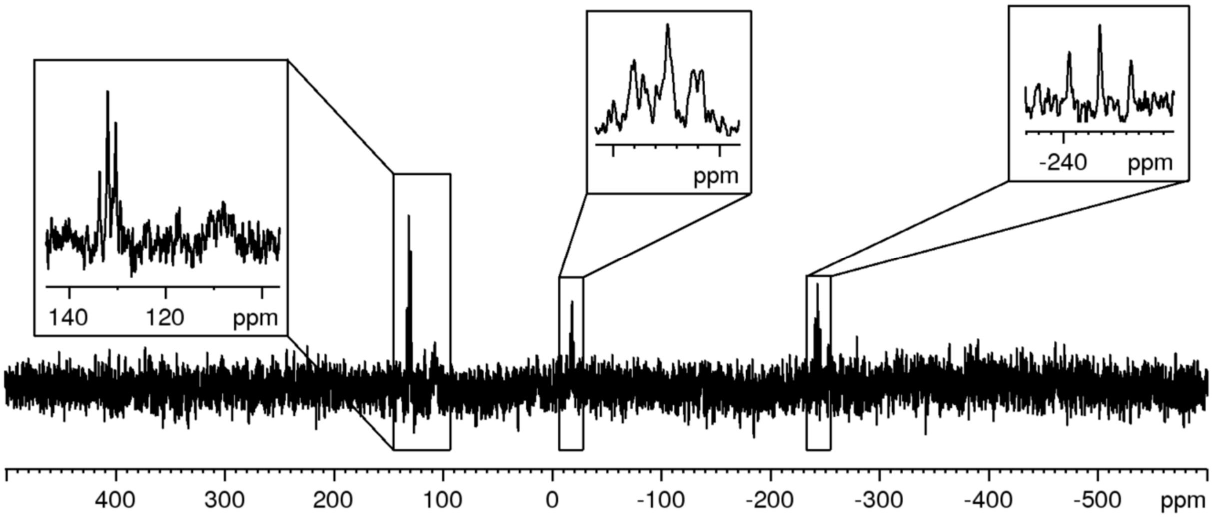

Figure S6: ^{31}P{^{1}H} NMR spectrum of the crude solution of **1**[FAl]$_2$ in C$_6$D$_6$/*o*-DFB.

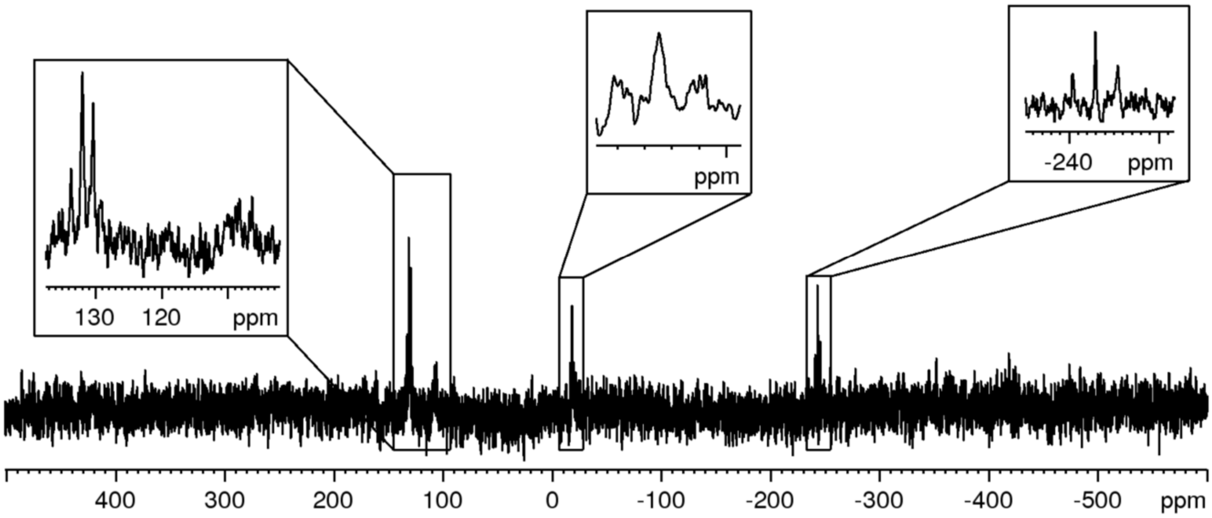

Figure S7: ^{31}P NMR spectrum of the crude solution of **1**[FAl]$_2$ in C$_6$D$_6$/*o*-DFB.

7.4.4 X-ray crystallography

All crystal manipulations were performed under mineral oil. The diffraction experiments were performed at 123 K on a Rigaku (former Agilent Technologies or Oxford Diffraction) GV50 diffractometer with a TitanS2 detector or on a XtaLAB Synergy R, DW System with a HyPix-Arc 150 detector using Cu-K_α radiation. Crystallographic data together with the details of the experiments are given in Table S1. The cell determination, data reduction and absorption correction for all compounds were performed with the help of the CrysAlis PRO software.[8] All structures were solved by using the programs SHELXT[9] and Olex2.[10] The full-matrix least-squares refinement against F^2 was done using SHELXL[11] and Olex2.[10] If not stated otherwise, all atoms except hydrogen atoms were refined anisotropically. The H atoms were calculated geometrically and a riding model was used during the refinement process.

Table S1: Crystallographic details for the compounds **1**[TEF]$_2$, **1**[FAl]$_2$ and **2**[FAl].

	1[TEF]$_2$	**1**[FAl]$_2$	**2**[FAl]
formula	$C_{53}H_{15}O_{14}F_{72}Al_2P_9Mo_3$	$C_{93}H_{15}Al_2F_{92}Mo_3O_{12}P_9$	$C_{66}H_{34}AlAs_5F_{48}Mo_2O_7$
weight [g·mol^{-1}]		3692.56	2444.39
Temperature [K]		123.0(1)	123.0(1)
crystal system	orthorhombic	triclinic	monoclinic
space group	*Pnma*	*P*-1	*P*2$_1$/*n*
a [Å]	27.1838(10)	17.6794(4)	22.5845(2)
b [Å]	16.6293(6)	19.4594(3)	13.58520(10)
c [Å]	21.0518(7)	22.6548(3)	25.3676(2)
α [°]	90	68.8570(10)	90
β [°]	90	84.7140(10)	94.3510(10)
γ [°]	90	64.257(2)	90
Volume [Å^3]	9516.4(6)	6528.5(2)	7760.73(11)
Z	4	2	4
ρ_{calc} [g·cm^{-3}]		1.878	2.092
μ [mm^{-1}]		5.238	6.693
F(000)		3568.0	4720.0
crystal size [mm^3]		0.248 × 0.214 × 0.108	0.575 × 0.156 × 0.074
diffractometer		Synergy R, DW	GV50
absorption correction		gaussian	gaussian
T_{min} / T_{max}		0.393 / 1.000	0.029 / 0.913
radiation [Å]		Cu-Kα (λ = 1.54184)	Cu-Kα (λ = 1.54184)
2Θ range [°]		4.194 to 152.09	6.99 to 148.01
completeness [%]		98.6	99.7
reflns collected / unique		109925 / 26460	47150 / 15301
R_{int} / R_{sigma}		0.0399 / 0.0271	0.0255 / 0.0200
data / restraints / parameters		26460 / 564 / 2284	15301 / 0 / 1172
GOF on F^2		1.165	1.071
R_1 / wR_2 [$I \geq 2\sigma(I)$]		0.0826 / 0.2610	0.0293 / 0.0775
R_1 / wR_2 [all data]		0.0912 / 0.2712	0.0299 / 0.0779
max / min $\Delta\rho$ [e·Å^{-3}]		1.48 / −1.62	0.75 / −0.77
Identification code	LD105_3_2_new_abs	CR621_	LD415_abs

Refinement details for 1[TEF]$_2$

Compound **1**[TEF]$_2$ crystallizes as orange plates in the orthorhombic space group *Pnma* with a half dication **1** and two half [TEF]$^-$ anions in the asymmetric unit. The refinement of the crystal structure revealed to be very difficult due to severe disorder of the [TEF]$^-$ anions over a symmetry plane. Hence, the bond lengths and angles are not discussed and only the unit cell parameters are given in Table S1.

Refinement details for 1[FAl]$_2$

Compound **1**[FAl]$_2$ crystallizes as orange blocks in the triclinic space group *P*-1 with one dication **1** and two [FAl]$^-$ anions in the asymmetric unit. The refinement of the crystal structure could be done without any difficulty. Within the cation two Cp ligands, two Mo atoms and one half of the P_9 ligand show positional disordering in ratios of 88:12 and 77:23. Additionally, one -C(C_5F_{10})(C_6F_5) group of one [FAl]$^-$ anion shows a positional disorder in a ratio of 54:46. The disordered parts were partially restrained with SADI commands and the anisotropic displacement parameters (ADPs) with SIMU commands. A solvent mask was calculated and 245 electrons were found in a volume of 1034 Å^3 in 2 voids per unit cell. This is consistent with the presence of two molecules $C_6H_4F_2$ (*o*-DFB) per asymmetric unit, which account for 232 electrons per unit cell.

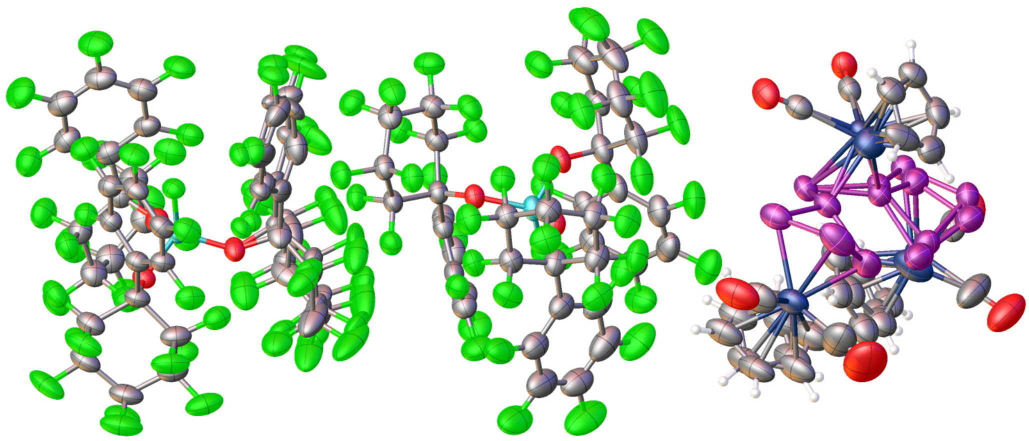

Figure S8: X-ray structure of **1**[FAl]$_2$. The asymmetric unit is shown containing one dication and two anions.

Refinement details for 2[FAl]

Compound **2**[FAl] crystallizes as dark red plates in the monoclinic space group $P2_1/n$ with one cation **2**, one [FAl]$^-$ anion and one solvent molecule (*o*-DFB) in the asymmetric unit. The refinement of the crystal structure could be done without any difficulty. No disorder was observed.

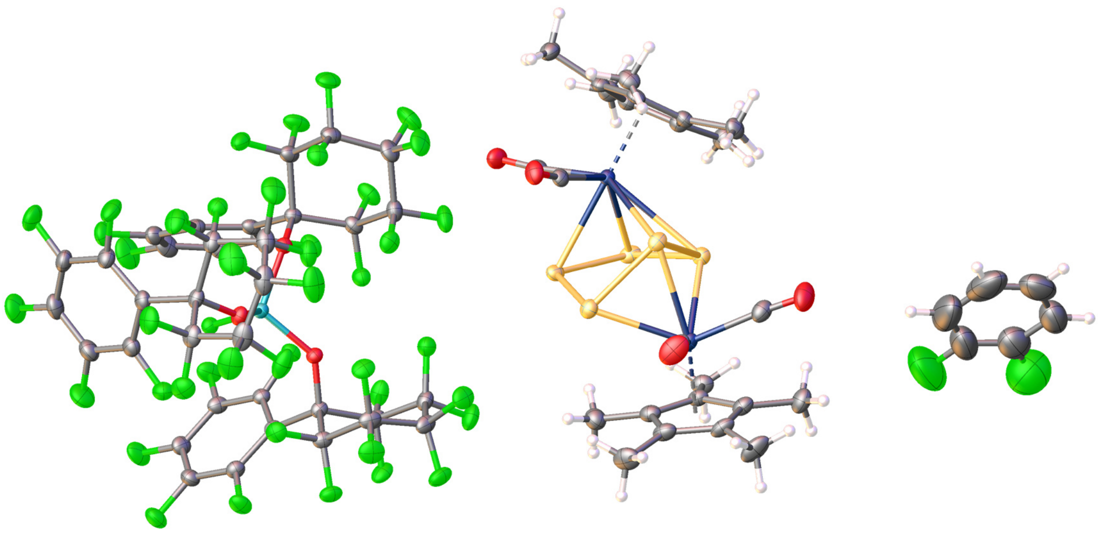

Figure S9: X-ray structure of **2**[FAl]. The asymmetric unit is shown containing one cation, one anion and one *o*-DFB molecule.

7.5 References

[1] a) M. V. Butovskiy, G. Balázs, M. Bodensteiner, E. V. Peresypkina, A. V. Virovets, J. Sutter, M. Scheer, *Angew. Chem. Int. Ed.* **2013**, *52*, 2972-2976; b) R. F. Winter, W. E. Geiger, *Organometallics* **1999**, *18*, 1827-1833; c) M. Fleischmann, F. Dielmann, L. J. Gregoriades, E. V. Peresypkina, A. V. Virovets, S. Huber, A. Y. Timoshkin, G. Balázs, M. Scheer, *Angew. Chem. Int. Ed.* **2015**, *54*, 13110-13115.

[2] a) T. Köchner, S. Riedel, A. J. Lehner, H. Scherer, I. Raabe, T. A. Engesser, F. W. Scholz, U. Gellrich, P. Eiden, R. A. Paz Schmidt, D. A. Plattner, I. Krossing, *Angew. Chem. Int. Ed.* **2010**, *49*, 8139-8143; b) T. Köchner, T. A. Engesser, H. Scherer, D. A. Plattner, A. Steffani, I. Krossing, *Angew. Chem. Int. Ed.* **2012**, *51*, 6529-6531.

[3] a) I. Krossing, I. Raabe, *Angew. Chem. Int. Ed.* **2004**, *43*, 2066-2090; b) T. A. Engesser, M. R. Lichtenthaler, M. Schleep, I. Krossing, *Chem. Soc. Rev.* **2016**, *45*, 789-899.

[4] L. Dütsch, M. Fleischmann, S. Welsch, G. Balázs, W. Kremer, M. Scheer, *Angew. Chem. Int. Ed.* **2018**, *57*, 3256-3261.

[5] N. G. Connelly, W. E. Geiger, *Chem. Rev.* **1996**, *96*, 877-910.

[6] O. J. Scherer, H. Sitzmann, G. Wolmershauser, *Acta Crystallographica Section C* **1985**, *41*, 1761-1763.

[7] P. Pyykkö, *J. Phys. Chem. A* **2015**, *119*, 2326-2337.

[8] Agilent (2014). CrysAlis PRO. Agilent Technologies Ltd., Yarnton, Oxfordshire, England.

[9] G. Sheldrick, Acta Crystallographica Section A **2015**, 71, 3-8.

[10] O. V. Dolomanov, L. J. Bourhis, R. J. Gildea, J. A. K. Howard, H. Puschmann, *J. Appl. Cryst.* **2009**, *42*, 339-341.

[11] G. Sheldrick, Acta Crystallographica Section C **2015**, 71, 3-8.

Preface

The following chapter has not been published until the submission of this thesis. Some of the results are preliminary and have to be corroborated by further studies and computations, which have not been finished until the end of this thesis.

Authors

Luis Dütsch, Christoph Riesinger and Manfred Scheer

Author Contributions

The main part (conceptualization, preparation of the compounds [Fc^{Diac}][TEF], [Fc^{Diac}][FAl], **A**, **B**, **1a**, **1b**, **2a**, **2b**, **3**, **5a**, **5b**, **6a**, **6b**, **6c**, **7a** and **8**, writing, visualization, and execution and evaluation of measurements) of this work was done by the first author (Luis Dütsch). The description of the compounds [Fc^{Diac}][TEF] and [Fc^{Diac}][FAl] was already done by Luis Dütsch in his Master thesis. Compound **8** was already synthesized before by Martin Piesch by another approach and is described in his PhD thesis. Christoph Riesinger assisted in the synthesis of **A** and **B**, and performed the spectroscopic and crystallographic analysis of **B**. Manfred Scheer supervised the research and revised the manuscript.

Acknowledgements

This work was supported by the Deutsche Forschungsgemeinschaft within the project Sche 384/36-2.

8 Synthesis of Ionic Polyarsenic Ligand Complexes and Clusters via Oxidation and Reduction

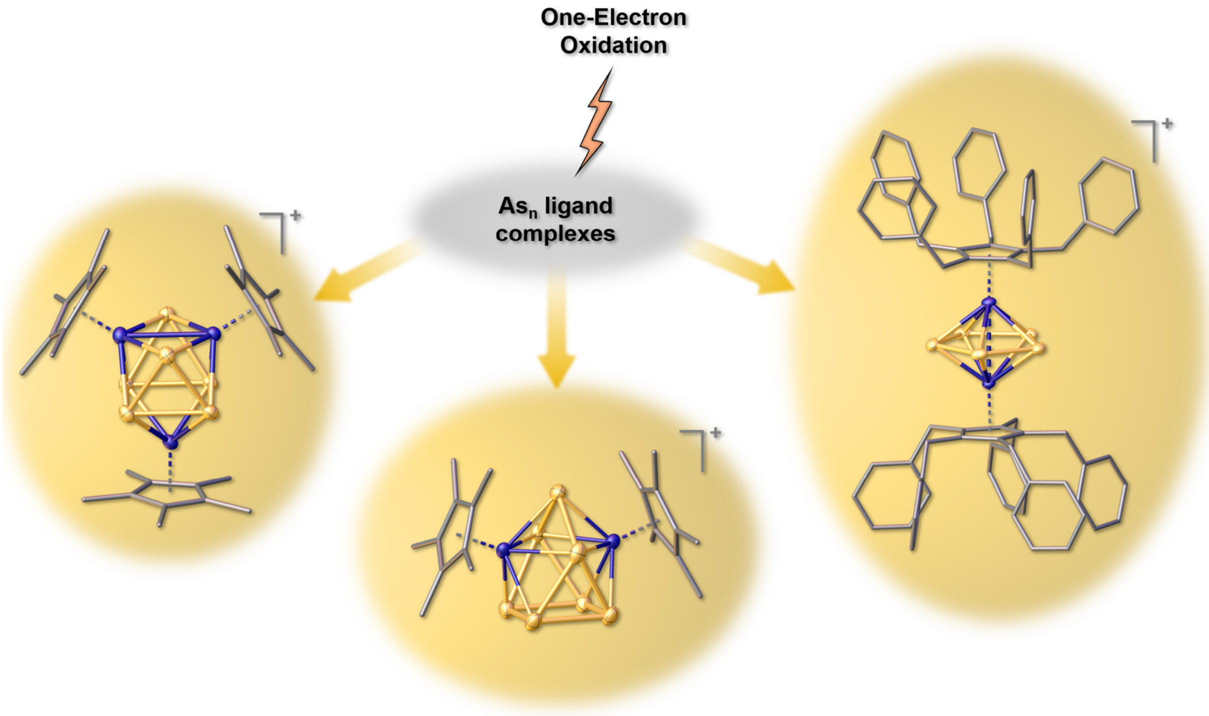

Abstract: *The formation of rare cationic polyarsenic scaffolds, which are free from organic substituents and are stabilized within the coordination sphere of transition metals, is reported. They are obtained by one-electron oxidation of naked As_n ligand complexes. Within that, various reactivities can be observed. On one hand, oxidation of $[Cp^*Fe(\eta^5\text{-}As_5)]$ (**A**) with 1,1'-diacetylferrocinium causes fragmentation and reaggregation forming the cationic complex$[(Cp^*Fe)_2(\mu,\eta^5{:}\eta^5\text{-}As_7)]^+$ (**5**), which exhibits a unique, cationic Fe_2As_7 cluster. On the other hand, oxidation of the As_5 triple-decker complexes $[(Cp^*Mo)_2(\mu,\eta^5{:}\eta^5\text{-}As_5)]$ (**C**) and $[(Cp^{Bn}Cr)_2(\mu,\eta^5{:}\eta^5\text{-}As_5)]$ (**D**) with $[Thia]^{\cdot+}$ (= $[C_{12}H_8S_2]^{\cdot+}$) leads to preservation of the original As_5 middle-decks. Furthermore, the yet uncharacterized cluster compound $[(Cp^*Fe)_3As_6]$ (**B**), which contains a central As_6 prism, could be isolated as additional product from the synthesis of **A**. Compound **B** was comprehensively studied by X-ray diffraction and cyclovoltammetry. Furthermore, its redox chemistry was investigated. Single or double oxidation with $[Thia]^{\cdot+}$ results in the complexes $[(Cp^*Fe)_3As_6]^+$ (**1**) and $[(Cp^*Fe)_3As_6]^{2+}$ (**2**), which reveal Fe–Fe bond formation, whereas reduction with KC_8 leads to As–As bond formation and the anionic compound $[(Cp^*Fe)_3As_6]^-$ (**3**). All of the cationic products were stabilized by weakly coordinating anions.*

8.1 Introduction

The stabilization of reactive p-block cations within inorganic as well as organic frameworks is not only a challenging field in fundamental research on basic chemical principles but also gives access to highly Lewis acidic species, which has been reviewed recently.[1] In particular, the investigation of cationic polypnictogen frameworks is of current interest.[2] Most catena cations exhibit pure pnictogen chains, cycles or cages, which however bear organic substituents. Remarkably, there are also reports on phosphorus-rich representatives, which are bound to non-carbon substituents,[3] and, moreover, the first substituent-free polyphosphorus cation, namely $[P_9]^+$, was obtained by Krossing *et al.* by oxidation of P_4 with $[NO]^+$.[4] This milestone in inorganic chemistry could only be accomplished with the help of weakly coordinating anions (WCAs),[5] which are able to stabilize very labile and reactive cations due to their weakly nucleophilic properties. Our research focuses on the formation and reactivity of substituent-free polypnictogen ligands (E_n ligands) in the coordination sphere of transition metals.[6] In the chapters 3–7 we have shown that one-electron oxidation of tetrahedral molybdenum complexes of the type $[(Cp^RMo(CO)_2)_2(\mu,\eta^2{:}\eta^2\text{-EE}')]$ (Cp^R = Cp, Cp*; E, E' = P, As, Sb, Bi) or $[(Cp^RMo(CO)_2)(\eta^3\text{-}E_3)]$ (Cp^R = Cp, Cp*; E = P, As) results in the formation of extended cationic polypnictogen frameworks stabilized by transition metals *via* dimerization or trimerization. In the former case dicationic $E_2E'_2$ chains, cycles and cages are obtained (*e.g.*, an As_4 chain (**I**); Scheme 1),[7] whereas the latter form a unique trimeric P_9 dication and a monocationic As_5 triple-decker complex (**II**; Scheme 1). The investigation of larger homopolypnictogen complexes towards oxidation is, however, mainly limited to phosphorus containing representatives. For example, oxidation of the hexaphosphabenzene[8] complex $[(Cp^*Mo)_2(\mu,\eta^6{:}\eta^6\text{-}P_6)]$ results in a bis-allylic distortion of the P_6 ring.[9] In contrast, oxidation of $[Cp^*Fe(\eta^5\text{-}P_5)]$ (**III**) leads to dimerization *via* P-P bond formation yielding a formally neutral, bicyclic P_{10} ligand stabilized by two $[Cp^*Fe^{II}]^+$ fragments.[10] In both of these cases, the original P_n ligands stay more or less intact. Therefore, it is of interest if oxidation of larger polyarsenic ligand complexes (n > 4) is also capable to afford extended cationic polyarsenic scaffolds and, if so, how will they react since arsenic, in comparison to phosphorus, has a larger tendency to reaggregate and form cluster compounds. One of the most famous representatives amongst polyarsenic ligand complexes is $[Cp^*Fe(\eta^5\text{-}As_5)]$ (**A**), which is the heavier congener of the ferrocene derivative **III**. The reactivity of **A** towards reducing agents[11] was already studied yielding a variety of anionic As_n ligand complexes (n = 4, 10, 14, 18). However, its oxidation remains unexplored but might show very promising results. Thus, in the following we will report on the synthesis of **A**, where we could isolate another, yet uncharacterized, product and moreover, on the reactivity of **A** and further polyarsenic ligand complexes towards one-electron oxidants.

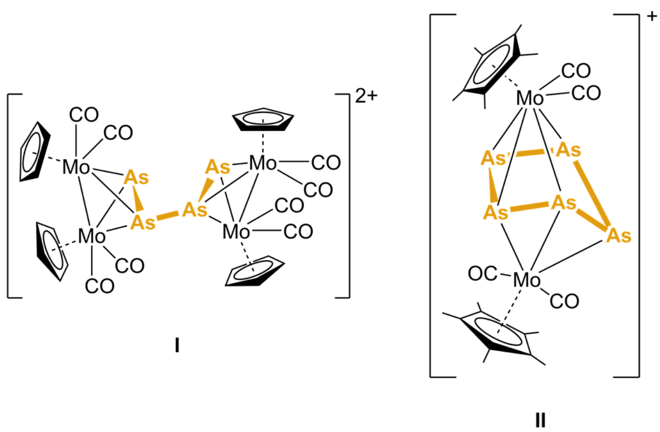

Scheme 1: Cationic polyarsenic ligand complexes.

8.2 Results and Discussion

Reaction of $[Cp^*Fe(CO)_2]_2$ with As_4

The reaction of $[Cp^*Fe(CO)_2]_2$ with solutions of yellow arsenic (As_4) in decalin is already known since 1990 leading to the formation of pentamethylpentaarsaferrocene $[Cp^*Fe(\eta^5\text{-}As_5)]$ (**A**) in 12 % yield.[12] However, side-products were not characterized or isolated. In 2011, our group identified two further products formed during this reaction. On one hand $[(Cp^*Fe)_3As_6\{Fe(\eta^3\text{-}As_3)\}]$ (**IV**) is obtained in 65 % yield by using toluene as eluent in column chromatography and on the other hand $[(Cp^*Fe)_3As_6]$ (**B**) in 10 % yield.[13] The latter compound though was only postulated by ^{1}H NMR spectroscopy and could not be separated from **IV**. Hence, we searched for a method to separate and isolate compound **B** as well. When we performed the reaction in an analogous manner and subjected the crude product to column chromatography, we likewise could isolate **A** as a green fraction with *n*-hexane but in a slightly higher yield of 16 % (Scheme 2). Interestingly, elution with *n*-hexane/toluene in a ratio of 2:1 (instead of pure toluene as used in the reported literature) afforded a brown fraction of pure **B** in 39 % isolated yield (Scheme 2), which, at the end, was mixed with a very dark brown fraction. ^{1}H NMR spectroscopic investigations of the latter show that a mixture of **B** and **IV** is present, however, this fraction was not isolated. Additional elution with pure toluene might have led to separation and isolation of **IV** as it was observed in literature before.[13]

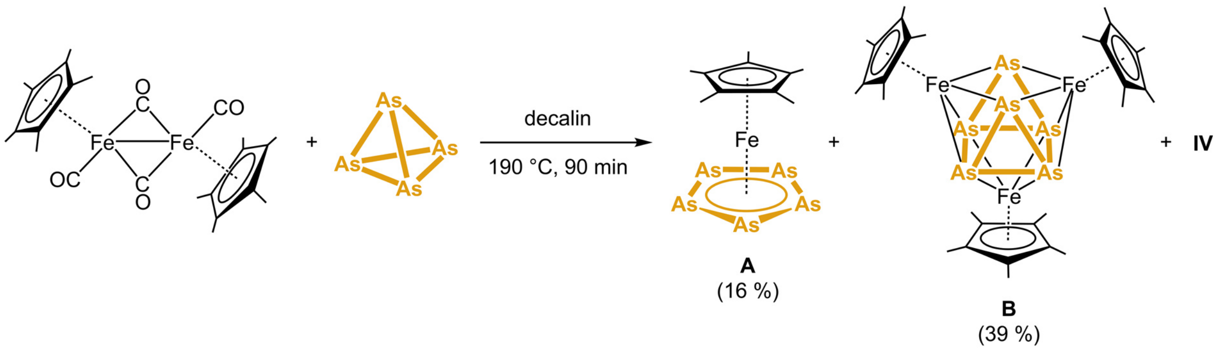

Scheme 2: Reaction of $[Cp^*Fe(CO)_2]_2$ with yellow arsenic (As_4).

The isolation of pure **B** now enabled its crystallization by cooling a concentrated solution in CH_2Cl_2 from room temperature to −30 °C and, thus, **B** could be characterized by single crystal X-ray diffraction. The molecular structure of **B** (Figure 1) reveals a cluster compound consisting of a central irregular As_6 prism, whose rectangular faces are each capped by a [Cp*Fe] fragment. The As_6 prism is slightly distorted with the As1–As2/2' (2.5130(4) Å) and As1'–As3/3' (2.5138(4) Å) distances being shorter than the As–As distances within the As2-As2'-As3'-As3 square (2.6367(4)–2.6888(3) Å). However, the As1–As1' distance of 3.5013(4) Å is very long, which rather excludes an As-As interaction. The same accounts for the Fe1 and Fe1' atoms (Fe1–Fe1': 3.2504(4) Å). The As–Fe distances (2.3706(4)-2.4530(4) Å) are in the range of As-Fe single bonds (2.37 Å).[14] Furthermore, the Fe_3As_6 cluster can be described by the *Wade´s* rules.[15] According to these the Fe_3As_6 core has 21 (= 2n+3)

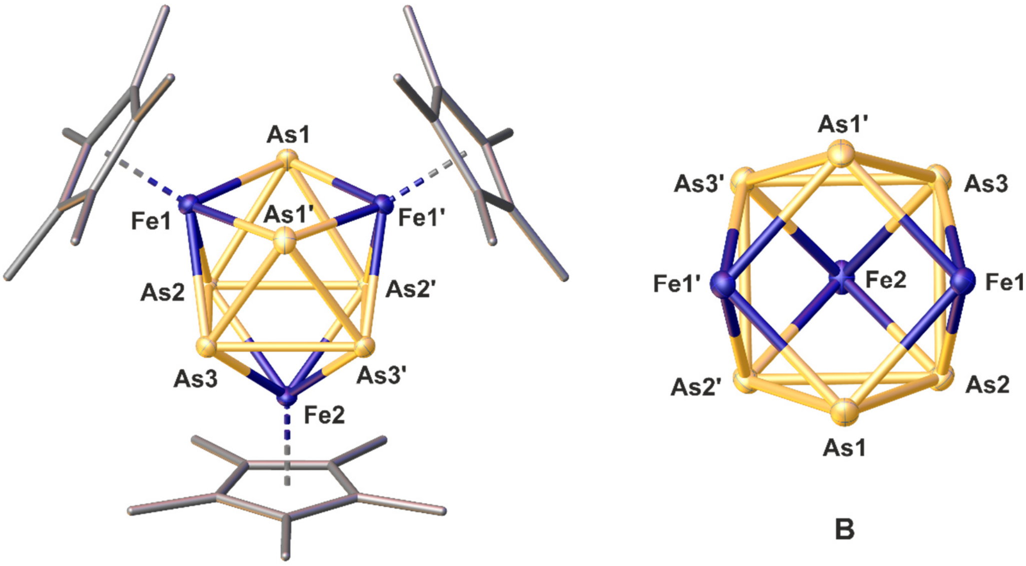

Figure 1: Left: Molecular structure of **B**. Anisotropic displacement is set to the 50% probability level. H atoms are omitted and Cp* ligands are drawn as connected tubes for clarity. Right: Top view of the central As_6Fe_3 core. Selected bond lengths [Å]: As1–As2/2' 2.5130(4), As1'–As3/3' 2.5138(4), As2–As2' 2.6411(4), As2/2'–As3/3' 2.6888(3), As3–As3' 2.6367(4), As1–As1' 3.5013(4), Fe1–Fe1' 3.2504(4).

skeletal electrons. This results in a *nido*-type cluster with one missing electron, which corresponds to a square antiprism with one capped side for n = 9. This perfectly describes the geometry in **B** with one As_2Fe_2 as well as one As_4 square and the third Fe atom capping the As_4 square (Figure 1). The angles withing the As_4 square are all about 90°, whereas the angles within the As_2Fe_2 square slightly deviate (85.53(1)–94.19(1)°), with the Fe-As-Fe angles being the smaller ones.

Similar structures are known for the Cp'' derivative of **B** [(Cp''Fe)$_3$As$_6$] (**V**)[13] and the formal oxidation product of **B** [(Cp*Fe)$_3$As$_6$][FeCl$_3$(thf)] (**VI**).[16] The latter was synthesized by *von Hänisch* and *Fenske* in 1998 by the reaction of $As_7(SiMe_3)_3$, $FeCl_2$ and LiCp*, which also afforded compound **IV**.[16] Although **V** contains the same Fe_3As_6 core as **B** and only varies in the substituents of the Cp ligand, its geometry differs remarkably as in **V** the As1–As1' distance is far shorter (2.8753(5) Å) leading to a perfect As_6 prism as central structural motif.[13] In contrast, **VI** is cationic and, thus, contains one valence electron less. Hence, it possesses 20 skeletal electrons resulting in a *closo*-type structure, which can be seen in an additional Fe1–Fe1' bond.[16]

In the ^{1}H NMR spectrum of **B** a broad singlet ($\omega_{1/2}$ = 640 Hz) at δ = 2.93 ppm for the methyl groups of the Cp* ligands is observed indicating a paramagnetic character of **B**. Thus, EPR measurements were conducted revealing an axial signal ($g_{x,y}$ = 2.139; g_z = 2.028), which corroborates the paramagnetic properties. Additionally, some hyperfine couplings were detected, although, they are not resolved and cannot be definitely attributed.

Redox chemistry of the cluster compound [(Cp*Fe)$_3$As$_6$]

Since **B** now is accessible in multigram scale and obtained in a pure form we investigated its redox chemistry. To get a first insight we recorded a cyclic voltammogram (CV, Figure 2), which reveals two reversible oxidations at 0.10 V and 0.75 V and two reversible reductions at −1.16 V and −1.76 V vs. $Cp_2Fe^{0/+}$, respectively, showing that $[C_{12}H_8S_2]^{\cdot+}$ ("thianthrenium", $[Thia]^{\cdot+}$, E = 0.86 V vs. $Cp_2Fe^{0/+}$)[17] and KC_8 (E = −2.38 V vs. $Cp_2Fe^{0/+}$), respectively, should be sufficient redox agents. Hence, we reacted **B** with one equivalent $[Thia]^{\cdot+}$ containing the weakly coordinating anions (WCA) $[Al\{OC(CF_3)_3\}_4]^-$ ($[TEF]^-$) or $[FAl\{OC(C_5F_5)(C_6F_{10})\}_3]$ ($[FAl]^-$) in CH_2Cl_2, which forms the salts [(Cp*Fe)$_3$As$_6$][X] (**1a**: X = TEF; **1b**: X = FAl) in 64 % and 82 % yield (Scheme 3), which correspond to **VI** and only differ in their respective counter ion. Reaction of **B** with two equivalents [Thia][X] (X = TEF, FAl) leads to double oxidation of **B** forming [(Cp*Fe)$_3$As$_6$][X]$_2$ (**2a**: X = TEF; **2b**: X = FAl) in 92 % and 85 % yield (Scheme 3). However, a further oxidation was not possible since reaction with an excess of [Thia][TEF] also yields **2**. Moreover, the compounds **2a** and **2b** can also be obtained by the respective reaction of **1a** or **1b** with another equivalent of $[Thia]^+$ (Scheme 3). Reduction of **B** was achieved by reacting it with one or two equivalents KC_8 in THF leading in the former case to the respective singly reduced species

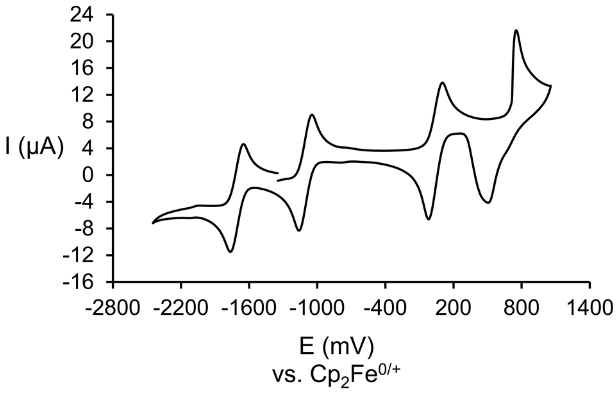

Figure 2: Cyclic voltammogram of **B**.

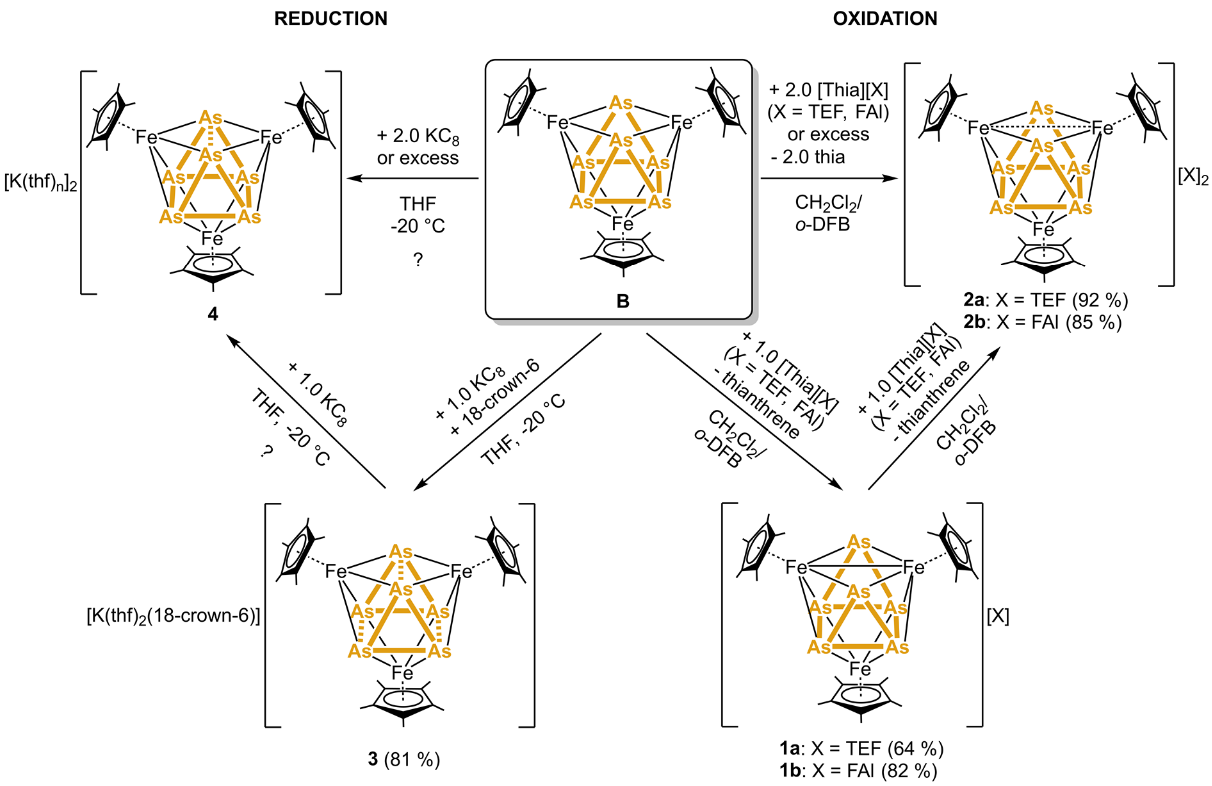

Scheme 3: Multiple oxidation (right) and reduction (left) of **B**. The exact structures of **2** and **4** are not determined yet. Isolated yields are given in parentheses.

$[K(thf)_2][(Cp^*Fe)_3As_6]$ (**3**) in 81 % yield, whereas the doubly reduced species could not be identified yet, but due to the cyclic voltammogram we assume that the analogous dianionic compound $[K(thf)_n]_2[(Cp^*Fe)_3As_6]$ (**4**) is formed (Scheme 3).

The products **1a**, **1b**, **2a** and **3** could also be crystallized by layering the respective solutions with *n*-hexane or *n*-pentane (in case of **3**, crown ether (18-crown-6) was added to coordinate the potassium cation and achieve better crystallization). The crystals were subjected to X-ray diffraction experiments to identify their molecular structure. However, the X-ray dataset of **2** was rather weak for which reason no detailed discussion of the geometry in the solid state is possible. In all cases the central Fe_3As_6 cores resemble that of the starting material **B** with some deviations (Figure 3). In **1a** and **1b** the former As1–As1' distance (3.7272(1) Å) is enlarged and in return the Fe1–Fe1' one is shortened to 2.8949(1) Å, which corresponds to the formation of an Fe–Fe bond upon oxidation as it was also observed in the derivative **VI** (*vide supra*). This leads to a distortion of the Fe1-As1-Fe2-As6 plane from a nearly perfect square to a rhomb with Fe-As-Fe angles of 75.6° and As-Fe-As angles of 104.3°. In contrast, in the anion **3** no Fe–Fe bond is formed as expected but, instead, reduction led to the formation of an additional As–As bond. Therefore, a perfect central As_6 prism is obtained, which is coordinated by the three [Cp*Fe] fragments. The As–As distances within the triangular surfaces are very similar (2.5384(1)–2.5913(1) Å). However, the As–As bonds connecting the two triangles (including the newly formed As–As bond) are significantly longer (2.7888(1)–2.8661(1) Å). Additionally, the Fe1-As1-Fe2-As6 square is not planar anymore. All in all, the structure of **3** is very similar to **V**, which surprises since the Fe_3As_6 cluster contains an additional skeletal electron (22 e^-). According to the *Wade´s* rules this leads to a *nido*-type structure.

The purity of **1a**, **1b** and **2** was proven by elemental analysis and the respective molecular ion peaks could be detected in mass spectra of **1a** and **1b**. In the ^1H NMR spectrum of **1b** only one sharp singlet at δ = 1.57 ppm can be detected, which can be assigned to the protons of the methyl groups of the Cp* ligands. This suggests that the monocationic $[(Cp^*Fe)_3As_6]^+$ cluster, in contrast to its neutral derivative, is diamagnetic. This is confirmed by $^{13}C\{^1H\}$ NMR spectroscopy where two sharp singlets for the methyl groups and the aromatic C atoms of the Cp* ligand are observed. Additionally, the

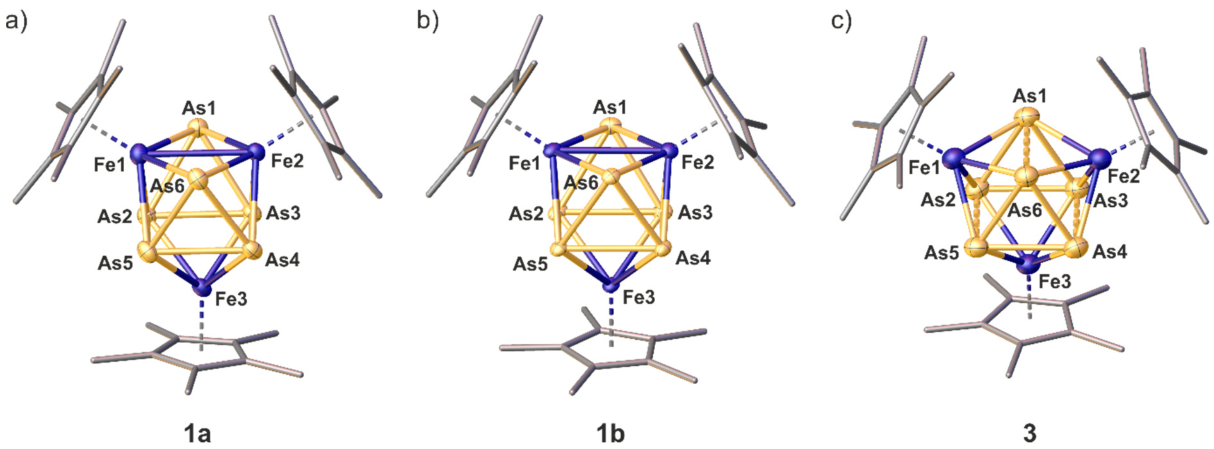

Figure 3: Molecular structures of the cationic parts in **1a**, **1b** and **3**. Anisotropic displacement is set to the 50% probability level. The H atoms and solvent molecules are omitted and the Cp* ligands drawn as connected tubes for clarity. Selected bond lengths [Å] and angles [°]: **1b** (**1a** and **1b** are isostructural): As1–As2 2.5090(1), As1–As3 2.5128(1), As2–As3 2.5878(1), As3–As4 2.6710(1), As4–As5 2.6042(1), As5–As2 2.6999(1), As4–As6 2.5097(1), As5–As6 2.4990(1), As1–As6 3.7272(1). Fe1–Fe2 2.8949(1).

characteristic signals for the [FAl]⁻ anion can be assigned in the $^{19}F\{^1H\}$ NMR spectrum. Additionally, EPR measurements of **1** are still to be done, which is part of future work as well as detailed analytical investigations of **2**, **3** and **4**, which could not be completed within the scope of this thesis.

Oxidation of [Cp*Fe(η^5-As_5)] (A)

Besides the redox chemistry of **B** we also investigated that of **A**. Since the reduction of **A** has already been reported[11] we focused on its oxidation. In previous work of our group **A** was reacted with [Ga(*o*-DFB)$_2$][TEF] in the hope that a 1D coordination polymer is formed as it was observed for analogous Tl^+ and In^+ salts. However, instead mostly precipitation of a dark solid was observed and once one single crystal could be obtained revealing the cationic compound [(Cp*Fe)$_2$(μ,η^5:η^5-As_7)][TEF] (**5a**). The structure refinement though was challenging due to severe disorder of the cation as well as the [TEF]⁻ anions and any attempts to reproduce **5a** failed. Furthermore, it could not be excluded that the observed reactivity may have been resulted from Ga(III) species or other decomposition products arisen from the starting material [Ga(*o*-DFB)$_2$][TEF], which have stronger oxidation properties. Therefore, we searched for a way to synthesize **5a** quantitatively and selectively. Reaction of **A** with the strong oxidant [Thia][TEF], however, only leads to the cationic triple-decker complex [(Cp*Fe)$_2$(μ,η^5:η^5-As_5)][TEF] (**VII**)[18] and Ag(I) or Cu(I) salts, respectively, form coordination compounds instead of serving as oxidant.[19] Thus, the question arose if a milder oxidant like 1,1'-diacetylferrocenium ([Fe(η^5-C_5H_4COMe)$_2$]$^+$ = [Fc^{Diac}]$^+$; E = 0.49 V vs. $Cp_2Fe^{0/+}$) can lead to the formation of **5a**. And indeed, reaction of a brownish green solution of **A** with [Fc^{Diac}][TEF] in CH_2Cl_2 or *o*-DFB results in a colour change to dark brown and precipitation of dark solid. After work-up and crystallisation **5a** can be obtained selectively in 82 % yield (Scheme 4). During the reaction formal elimination of an [As_3]$^+$ unit takes place, which might explain the brown precipitate. However, the latter could not be characterized until the end of this thesis. Although **5a** is now accessible selectively and in good yields, the determination of the molecular structure remains difficult since the [TEF]⁻ anions still show severe disorder in the solid state. Therefore, the introduction of other counterions like [FAl]⁻ could provide help. The oxidant [Fc^{Diac}]$^+$, though, is not known yet with [FAl]⁻ and had to be

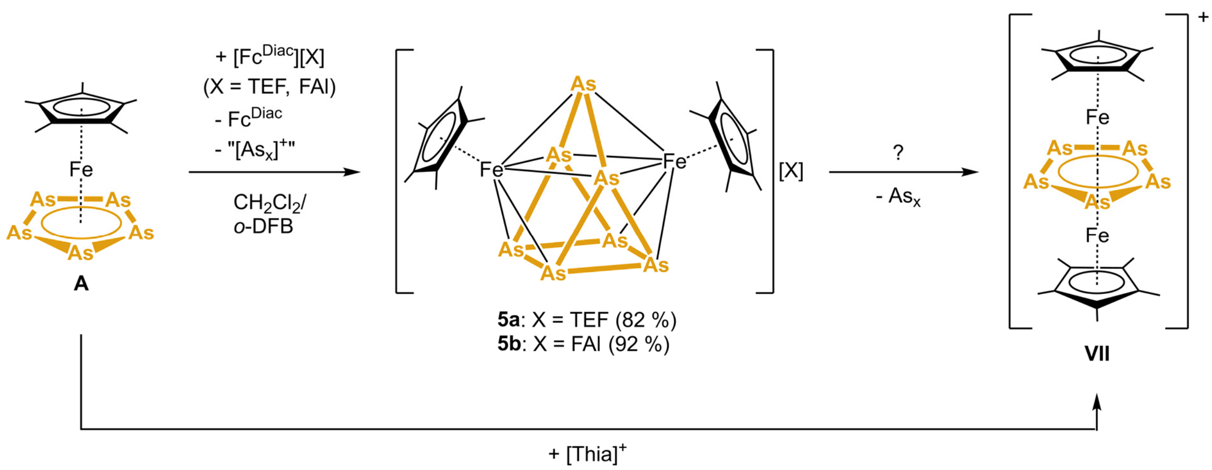

Scheme 4: Reaction of [Cp*Fe(η^5-As_5)] (**A**) with oxidants.

synthesized first. Analogous to the synthesis of $[Fc^{Diac}][TEF]$,[20] the reaction of an orange solution of 1,1'-diacetylferrocene with Ag[FAl] in CH_2Cl_2 results in a colour change to greenish blue. Additionally, grey powder precipitates, which indicates the formation of elemental silver. By layering the solution with *n*-hexane and storage at +4 °C $[Fc^{Diac}][FAl]$ can be isolated in 71 % yield as dark blue sticks.[20b] Additionally, the oxidant $[Fc^{Diac}][TEF^{Cl}]$ could be synthesized by the reaction of Fc^{Diac} with $[Thia][TEF^{Cl}]$ (see Supporting Information).

Respective oxidation of **A** with $[Fc^{Diac}][FAl]$ in CH_2Cl_2 leads to the formation of compound $[(Cp^*Fe)_2(\mu,\eta^5{:}\eta^5\text{-}As_7)][FAl]$ (**5b**) in 92 % yield (Scheme 4). By layering the CH_2Cl_2 solution with *n*-hexane **5b** can be obtained as dark red plates suitable for single crystal X-ray diffraction studies. In contrast to **5a** neither the As_7 cage nor the $[FAl]^-$ is disordered allowing a closer description of the molecular structure (Figure 4). The general geometry of the monocation in **5b** has already been described in the dissertation of Martin Fleischmann in 2015. It contains a central Fe_2As_7 cluster, whose bonding situation can generally be described by two ways, either as an $[As_7]^-$ cage which is coordinated by two $[Cp^*Fe]^+$ fragments in an η^5-fashion or by the *Wade´s* rules. According to these, the Fe_2As_7 cluster contains 22 (2n+4) skeletal electrons ($7 \cdot 5e^-$(As) + $2 \cdot 8e^-$(Fe) + $2 \cdot 5e^-$(Cp*) − $1e^-$(pos. charge) − $7 \cdot 2e^-$(As) − $2 \cdot 12e^-$(Fe) = $22e^-$) resulting in a *nido*-type cluster, which correlates with a monocapped square antiprism arrangement for the 9 cluster atoms exactly as it is observed in **5b**. The basal square consists of four As atom with As–As distances between 2.416(1) and 2.544(1) Å, while the top square is built up of two Fe and two As atoms in alternating fashion with similar Fe–As distances (2.529(1)–2.544(1) Å). The angles within both squares come very close to 90°. Ultimately, the As6 atom is capping the Fe_2As_2 square. Furthermore, the cation is similar to **B**, where one [Cp*Fe] fragment is removed and instead the As6 atom is added on top of the Fe_2As_2 square.

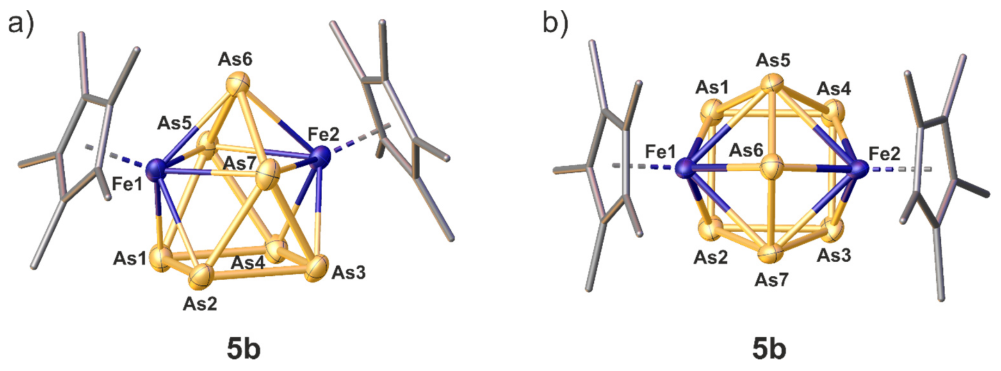

Figure 4: Side view (a) and top view (b) of the molecular structure of the cationic part in **5b**. Anisotropic displacement is set to the 50% probability level. The H atoms and solvent molecule are omitted and the Cp* ligands drawn as connected tubes for clarity. Selected bond lengths [Å] and angles [°]: **5b**: As1–As2 2.416(1), As2–As3 2.544(1), As3–As4 2.427(1), As4–As1 2.538(1), As1–As5 2.578(1), As4–As5 2.579(1), As2–As7 2.568(1), As3–As7 2.563(1), As5–As6 2.384(1), As6–As7 2.394(1), Fe1–Fe2 3.609(1).

When the crystallization solution of **5a** is stored for prolonged times the formation of the As_5 triple-decker complex **VII**, which was obtained by oxidation of **A** with [Thia][TEF] (*vide supra*), can be observed. This suggests that **5a** might be an intermediate within the synthesis of **VII** (Scheme 4).[18]

The cation 5^+ contains 60 VE ($7{\cdot}5e^-$(As) + $2{\cdot}8e^-$(Fe) + $2{\cdot}5e^-$(Cp*) − $1e^-$(pos. charge)), which indicates a diamagnetic character. This is confirmed by ^{1}H NMR spectroscopy, where only one sharp singlet (δ = 1.18 ppm) in the expected region for Cp* protons is observed. Additionally, the characteristic signals for the $[FAl]^-$ anion can be detected in the $^{19}F\{^1H\}$ NMR spectrum. To corroborate the assumption of the diamagnetic character of **5**, EPR measurements are still to be made, which is part of future work as well as mass spectrometric investigations, which could not be executed until the end of this thesis.

Oxidation of As_5 Triple-Decker Complexes

Since the oxidation of **A** led to rearrangement and aggregation yielding an enlarged polyarsenic cation it was of interest to expand our investigations towards other As_n ligand complexes. Cyclic As_5 ligands are not only known as end-decks within sandwich complexes, as in **A**, but, moreover, also as bridging ligands (middle-decks) within triple-decker complexes, for example, in $[(Cp^*Mo)_2(\mu,\eta^5{:}\eta^5\text{-}As_5)]$ (**C**) and $[(Cp^{Bn}Cr)_2(\mu,\eta^5{:}\eta^5\text{-}As_5)]$ (**D**; $Cp^{Bn} = C_5(CH_2\{C_6H_5\})_5$), which are synthesized by the reactions of the respective $[Cp^R(CO)_2M]_2$ (Cp^R = Cp*, Cp^{Bn}; M = Mo, Cr) dimers with solutions of yellow arsenic.[21] **D** contains a Cp analogous As_5 ring, whereas the middle-deck in **C** is a

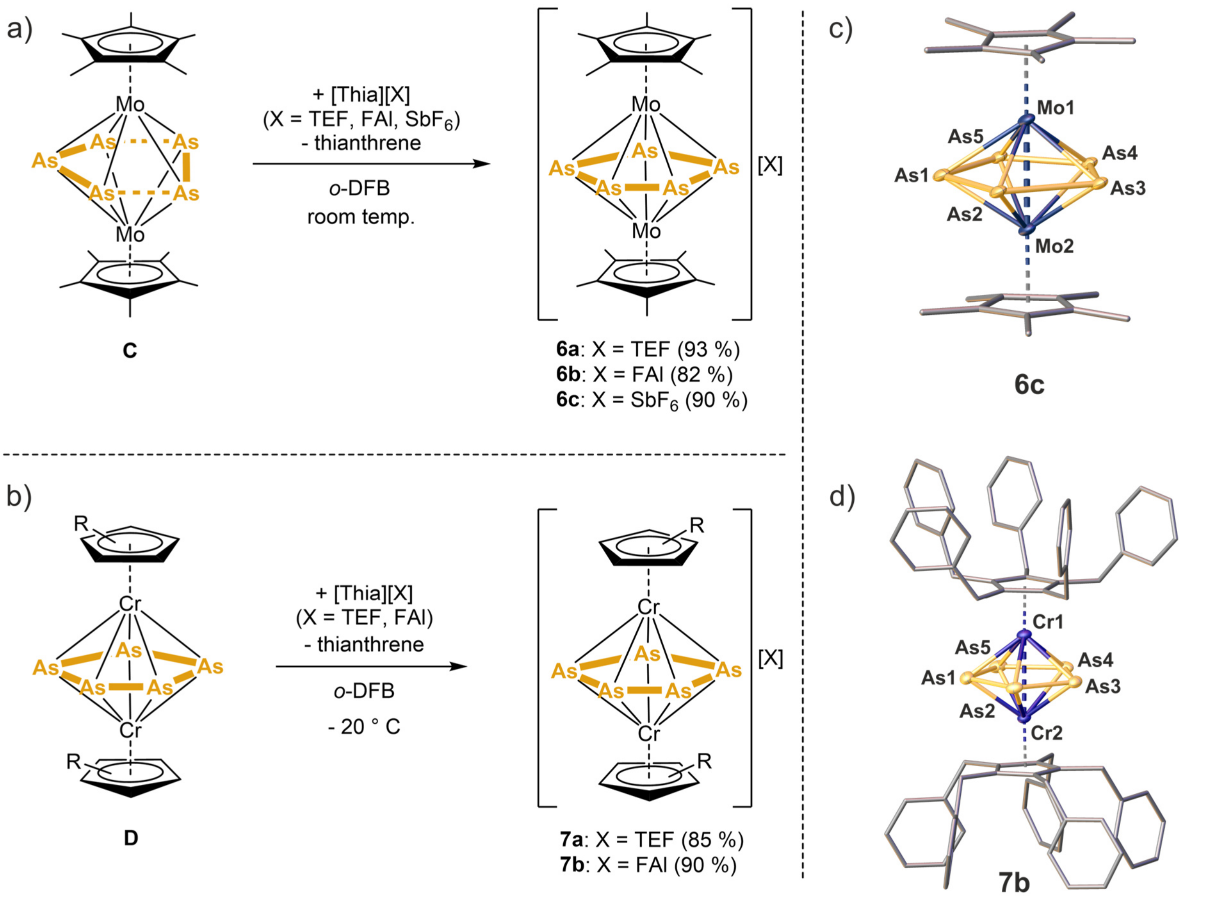

Figure 5: Oxidation of **C** (a) and **D** (b) with $[Thia]^+$ salts ($Cp^R = Cp^{Bn}$); Cationic parts of the molecular structures of **6c** (c) and **7b** (d). Anisotropic displacement is set to the 50% probability level. The H atoms and counterions are omitted and the Cp^R ligands drawn as connected tubes for clarity. Selected bond lengths [Å]: **6c**: Mo1–Mo2 2.825(2); **7b**: As1–As2 2.4135(5), As2–As3 2.4089(5), As3–As4 2.4056(5), As4–As5 2.4079(5), As5–As1 2.4079(5), Cr1–Cr2 3.0099(6).

pseudo five-membered arsenic ligand with two elongated As–As distances (Figure 5). To study the oxidation behaviour of **C** and **D** we reacted *o*-DFB solutions of them with dark purple [Thia][X] (X = TEF, FAl, SbF_6). This led to an immediate colour change from black (**C**) or green (**D**), respectively, to dark blue (**C**) or reddish brown (**D**) and the formation of the products $[(Cp^*Mo)_2(\mu,\eta^5:\eta^5\text{-}As_5)][X]$ (X = TEF (**6a**), FAl (**6b**), SbF_6 (**6c**)) and $[(Cp^{Bn}Cr)_2(\mu,\eta^5:\eta^5\text{-}As_5)][X]$ (X = TEF (**7a**), FAl (**7b**)) in yields of 82–93% (Figure 5a). After precipitation with *n*-pentane, washing with toluene and recrystallization from *o*-DFB/*n*-pentane blueish green (**6a**, **6c**) or reddish brown (**7b**) crystals, respectively, could be isolated and subjected to single crystal X-ray diffraction studies. In contrast to the oxidation of **A**, no rearrangement and aggregation of the As_5 ligands took place. Instead, in both cases the original triple-decker structure is preserved. The $[TEF]^-$ anions in **6a** exhibit severe disorder, which made the refinement of the crystal structure very difficult but it resembles the one of **6c**. Hence, only the structural parameters (Figure 5c/d) of **6c** and **7b** are discussed in the following. **6c** and **7b** crystallize in the triclinic space group *P*-1 with either four cations and four $[SbF_6]^-$ anions (**6c**) or one cation and one $[FAl]^-$ anion (**7b**), respectively, in the asymmetric unit. The As–As distances within the As_5 middle-deck in **7b** are all in the range of 2.4030(5)–2.4135(5) Å, which are slightly shorter than in the starting material **D**[21] and not considerably shortened compared to a calculated As–As single bond (2.42 Å).[14] In contrast, the Cr–Cr distance of 3.0099(6) Å is elongated by 0.2 Å in comparison to **D**[21] and matches the ones of other reported Cr–Cr distances like in $[\{CpCr(CO)_2\}_2(\mu,\eta^2:\eta^2\text{-}As_2)]$ (Cr–Cr 3.026(1) Å).[22] The As_5 ligands in **6c**, however, reveal rotational disorder, which could not be resolved until the end of this thesis. Therefore, the As_5 ligands cannot be described in detail and it could not be clarified if the pseudo five-membered ring structure of **C** is still existent or if now a Cp analogous As_5 ring as in **D** and **7b** is present. The Mo–Mo distance (2.825(2) Å), though, is also slightly elongated in comparison to the $[(CpMo)_2(\mu,\eta^5:\eta^5\text{-}As_5)]$ (2.764(2) Å), which is the Cp derivative of **C**.[23]

The triple-decker complexes **6** and **7** are both 26 VE complexes. Since the As_5 ligand as well as each Cp^R ligand are carrying a formal negative charge, an average oxidation state of +2 (d^4/d^4 system) is proposed for each molybdenum or chromium atom, respectively. The dark colours of the solutions, though, do not exclude the presence of radicals and/or high spin complexes. Hence, theoretical calculations and magnetic measurements, which are part of future investigation, still have to be executed to get a better insight into the electronic properties of **6** and **7**. In the ESI mass spectrum of **6a** the molecular ion peak can be detected and the purity of **6a** was proven by elemental analysis.

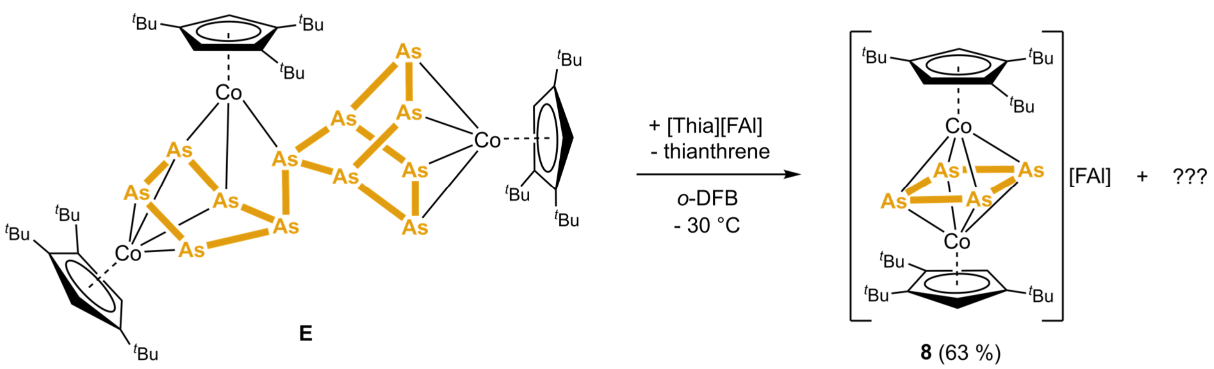

Scheme 5: Oxidation of $[(Cp'''Co)_3(\mu,\eta^{4:4:2:1}\text{-}As_{12})]$ (**E**) with [Thia][FAl]. The yield (given in parentheses) is referred to the limiting factor, which is the amount of available [Cp'''Co] fragments.

Analogous analytical investigations of **7** were unsuccessful since decomposition of the chromium triple-decker complex occurred during the measurements.

Oxidation of [(Cp'''Co)$_3$As$_{12}$]

Last but not least, it is of interest to investigate the reactivity of larger As_n frameworks towards one-electron oxidation. Therefore, to shed light into this area we reacted the compound [(Cp'''Co)$_3$(μ,η$^{4:4:2:1}$-As$_{12}$)] (**E**), which contains an As_{12} ligand, with [Thia][FAl] in *o*-DFB at −30 °C. After work up and recrystallization from *o*-DFB/*n*-hexane black blocks of the cationic triple-decker complex [(Cp'''CO)$_2$(μ,η^4:η^4-As$_4$)][FAl] (**8**) could be isolated in 63 % yield referred to the fact that two equivalents of **E** could potentially form three equivalents of **8** (Scheme 5). Hence, in case of **E** no aggregation to larger polyarsenic compounds takes place, but instead degradation to an As_4 ligand complex. Furthermore, during this reaction an As_8 unit as well as one [Cp'''Co] fragment are eliminated (Scheme 5). However, further products could not be identified until the end of this thesis. In order to avoid degradation, the use of less powerful oxidants, such as [Fc^{Diac}]$^+$, might be promising, which is subject of future research. The cationic triple-decker complex **8** (Figure 6) is already known in literature and was synthesized by our group in 2020 by oxidation of [(Cp'''Co)$_2$(μ,η^2:η^2-As$_2$)$_2$] with Ag[FAl].[24] Moreover, the respective dicationic as well as anionic As_4 triple-decker complexes are known as well.[24]

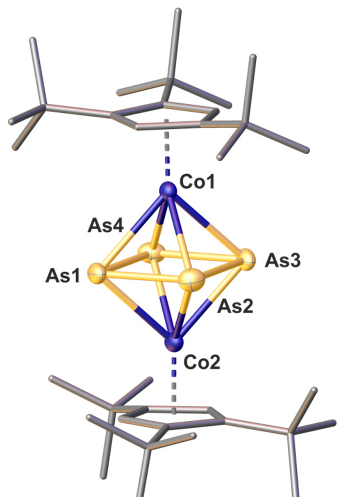

8

Figure 6: Molecular Structure of **8**. Anisotropic displacement is set to the 50% probability level. The H atoms and counterions are omitted and the Cp''' ligands drawn as connected tubes for clarity.

8.3 Conclusion

In summary, we have successfully expanded the rare class of cationic polyarsenic frameworks, which are free from organic substituents, *via* oxidation of transition metal complexes containing naked polyarsenic ligands. Reaction of [Cp*Fe(η^5-As$_5$)] (**A**) with the one-electron oxidant [Fc^{Diac}]$^+$ leads to fragmentation and reaggregation selectively forming a unique cationic Fe_2As_7 cluster (**5**), which was not accessible with other oxidation agents. Furthermore, **5** might be an intermediate product in the synthesis of the cationic triple-decker complex [(Cp*Fe)$_2$(μ,η^5: η^5-As$_5$)], which was obtained by reaction of **A** with the strong oxidant [Thia]$^{\cdot+}$. In contrast, oxidation of the dimolybdenum and dichromium As_5 triple-decker complexes **C** and **D** with [Thia]$^+$ results in the preservation of the As_5 middle-decks and the original triple-decker structure. Reaction of [(Cp'''Co)$_3$(μ,η$^{4:4:2:1}$-As$_{12}$)] (**E**) with [Thia]$^+$, however, leads again to fragmentation and the formation of a cationic Co_2As_4 triple-decker complex. Furthermore, we successfully isolated and characterized the cluster compound [(Cp*Fe)$_3$As$_6$] (**B**), which contains an As_6 prism, and investigated its redox chemistry. Oxidation or reduction, respectively, of **B** yields anionic or mono- and dicationic As_6 prisms, respectively, stabilized by three [Cp*Fe] fragments. In general, the oxidation of polyarsenic ligand complexes has been shown to be a powerful tool to gain access to the rare class of cationic polyarsenic scaffolds. Moreover, the reaction outcome can be managed by the choice of the right oxidant and its oxidation potential. Thus, future efforts will not only include the investigation of other As rich complexes and their heavier congeners towards oxidation, but also the development of new oxidants containing different WCAs.

8.4 Supporting Information

8.4.1 General remarks

All manipulations were carried out under an inert atmosphere of dried nitrogen/argon using standard Schlenk and glovebox techniques. The used Schlenk flasks were heated at 550 °C for at least 15-30 minutes under reduced pressure prior to use to get rid of water traces adhered to the glass surface. The starting materials $[Cp^*Fe(CO)_2]_2$,[25] [Thia][TEF],[7a] [Thia][FAl] (see chapter 6), KC_8,[26] $[Fc^{Diac}]$[TEF],[20a] $[(Cp^*Mo)_2(\mu,\eta^5{:}\eta^5\text{-}As_5)]$,[21] $[(Cp^{Bn}Cr)_2(\mu,\eta^5{:}\eta^5\text{-}As_5)]$,[21] $[(Cp'''Co)_3(\mu,\eta^{4:4:2:1}\text{-}As_{12})]$[27] and Ag[FAl][28] were synthesized *via* the respective literature procedures. $[Thia][SbF_6]$ was made by reaction of thianthrene with $[NO][SbF_6]$ in liquid SO_2. All other reagents were bought from commercial vendors. Solvents were freshly distilled under nitrogen after drying over CaH_2 (CH_2Cl_2, CD_2Cl_2), K or Na/K alloy (alkanes), P_4O_{10} (*ortho*-difluorobenzene = *o*-DFB) or NaH (toluene). Dried solvents were also taken from a solvent purification system from MBraun. For reactions in liquid SO_2, SO_2 gas cylinders were bought from Linde and SO_2 was condensed into Schlenk flasks with a Young valve at −196 °C under reduced pressure. Diatomaceous earth used for filtrations was stored at 130 °C for at least 24 h prior to use. Filtrations were also carried out by using Teflon tubes and glass fibre filters. NMR spectra were recorded at 300 K (if not stated otherwise) on a Bruker Avance 300 MHz NMR spectrometer (^{1}H: 300.132 MHz, ^{13}C: 75.468 MHz, ^{19}F: 282.404 MHz) or a Bruker Avance 400 MHz NMR spectrometer (^{1}H: 400.130 MHz, ^{13}C: 100.613 MHz, ^{19}F: 376.498 MHz) with external references of $SiMe_4$ (^{1}H, ^{13}C) and CCl_3F (^{19}F). The chemical shifts δ are presented in parts per million (ppm) and coupling constants J in Hz. ESI-MS spectra were either measured on a Finnigan Thermoquest TSQ 7000 mass-spectrometer by the MS department of the University of Regensburg or on a Waters Micromass LCT ESI-TOF mass-spectrometer by the first author. IR spectra were recorded as solids grinded together with dried KBr and pressed to pellets and measured on a VARIAN FTS-800 FT-IR spectrometer. Elemental analyses (EA) were performed by the micro analytical laboratory of the University of Regensburg.

8.4.2 Experimental details

8.4.2.1 Reaction of $[Cp^*Fe(CO)_2]_2$ with As_4

The following reaction steps were carried out under exclusion of light. Grey arsenic (~5 g) was heated to 550 °C and sublimed into 300 mL boiling decaline yielding a saturated solution of yellow As_4. This hot solution was transferred onto a orange brown solution of $[Cp^*Fe(CO)_2]_2$ (1.25 g, 2.53 mmol) in 15 mL decaline and refluxed for 90 minutes yielding a dark greenish brown solution, which is not light sensitive anymore. The solvent was condensed into another flask yielding a brown crude product.

This procedure was conducted for a total of six times and the crude products were combined. The brown powder was redissolved in 20 mL CH_2Cl_2, mixed with 20 g dried silica and the solvent removed under reduced pressure until a floating powder was obtained. The powder was transferred onto a chromatographic column (silica, 3x10 cm). Elution with *n*-hexane yields a dark green fraction of [Cp*Fe(η^5-As_5)] (**A**). Subsequently, by elution with *n*-hexane/toluene = 2:1 an additional brown fraction of [(Cp*Fe)$_3$As$_6$] (**B**) starts to arise, which can be separated by increasing the toluene percentage to 1:1. However, not all of **B** could be isolated since a further black fraction (probably containing [(Cp*Fe)$_3$As$_6${Fe(η^3-As_3)}] (**IV**)) is arising, which was not isolated. From both, the green as well as the brown fraction, the solvent was removed and the powders redissolved in 10 mL (**A**) or 40 mL (**B**), respectively, and stored at −30 °C yielding dark green (**A**) or brownish black (**B**) crystals. The latter were subjected to single crystal X-ray diffraction. The crystals were isolated and dried in vacuum for 3h. The solvents of the supernatants were removed under reduced pressure and the resulting powders again dried in vacuum for 3h.

A: Yield 2.78 g (4.91 mmol = 16 % referred to [Cp*Fe(CO)$_2$]$_2$).

B: Yield 4.03 g (3.94 mmol = 39 % referred to [Cp*Fe(CO)$_2$]$_2$). ^{1}H NMR (CD_2Cl_2) δ/ppm = 2.94 (s, $\omega_{1/2}$ = 640 Hz, Cp*). EPR spectra of **B** reveal an axial signal ($g_{x,y}$ = 2.139; g_z = 2.028), which shows some additional hyperfine couplings. However, the latter are not resolved and cannot be definitely attributed.

8.4.2.2 Redox Chemistry of [(Cp*Fe)$_3$As$_6$] (B)

Synthesis of [(Cp*Fe)$_3$As$_6$][TEF] (1a)

A brown solution of [(Cp*Fe)$_3$As$_6$] (**B**; 91 mg, 0.09 mmol, 0.9 eq.) in 5 mL CH_2Cl_2 was reacted with a dark purple solution of [Thia][TEF] (118 mg, 0.1 mmol, 1.0 eq.) in 5 mL CH_2Cl_2 leading to an immediate colour change to orange brown. The solution was stirred for 60 minutes. Addition of 50 mL *n*-hexane led to precipitation of a dark brown powder. The supernatant was removed and the residue washed with 30 mL *n*-hexane and 30 mL toluene. The powder was dried in vacuum and recrystallization from CH_2Cl_2/*n*-hexane at room temperature yielded pure **1a** as black needles suitable for single crystal X-ray diffraction. The solvent was removed by decanting and the crystals dried in vacuum for 3h.

Yield 105 mg (0.058 mmol = 64 %). Anal. calcd. for [$C_{30}H_{45}Fe_3As_6$][$AlO_4C_{16}F_{36}$]: C: 27.77, H: 2.28. Found: C: 27.90, H: 2.24. Positive ion MS *m/z* (%): 1022.69 (100) [**M**]$^+$. Negative ion MS *m/z* (%): 966.91 (100) [TEF]$^-$.

Synthesis of [(Cp*Fe)$_3$As$_6$][FAl] (1b)

A brown solution of [(Cp*Fe)$_3$As$_6$] (**B**; 182 mg, 0.18 mmol, 1.0 eq.) in 15 mL CH_2Cl_2 was reacted with a dark purple solution of [Thia][FAl] (118 mg, 0.18 mmol, 1.0 eq.) in 15 mL CH_2Cl_2 leading to an immediate colour change to orange brown. The solution was stirred for 60 minutes. Addition of 80 mL *n*-hexane led to precipitation of a dark brown powder. The supernatant was removed and the residue washed with 30 mL *n*-hexane and 30 mL toluene. The powder was dried in vacuum and recrystallization from CH_2Cl_2/*n*-hexane at room temperature yielded pure **1b** as black plates suitable for single crystal X-ray diffraction. The solvent was removed by decanting and the crystals dried in vacuum for 3h.

Yield 355 mg (0.148 mmol = 82 %). ^{1}H NMR (CD_2Cl_2) δ/ppm = 1.57 (s, Cp*). $^{13}C\{^1H\}$ NMR (CD_2Cl_2) δ/ppm = 10.66 (s, methyl groups), 95.68 (s, C atoms of Cp ring). Characteristic signals for the $[FAl]^-$ anion were detected in the $^{19}F\{^1H\}$ NMR spectrum in CD_2Cl_2. Anal. calcd. for $[C_{30}H_{45}Fe_3As_6][AlO_3C_{36}F_{46}]$: C: 33.00, H: 1.89. Found: C: 33.36, H: 1.88. Positive ion MS *m/z* (%): 1022.71 (100) [**M**]$^+$. Negative ion MS *m/z* (%): 1380.98 (100) $[FAl]^-$.

Synthesis of $[(Cp^*Fe)_3As_6][TEF]_2$ (2a)

A brown solution of $[(Cp^*Fe)_3As_6]$ (**B**; 91 mg, 0.09 mmol, 1.0 eq.) in 15 mL *o*-DFB was reacted with a dark purple solution of [Thia][TEF] (210 mg, 0.18 mmol, 2.0 eq.) in 5 mL *o*-DFB leading to an immediate colour change to dark orange red. The solution was stirred for 60 minutes. Addition of 80 mL *n*-hexane led to precipitation of a black powder. The supernatant was removed and the residue washed with 50 mL toluene. The powder was dried in vacuum and recrystallization from *o*-DFB/*n*-hexane at room temperature yielded pure **2a** as black sticks suitable for single crystal X-ray diffraction. The solvent was removed by decanting and the crystals dried in vacuum for 3h.
Compound **2a** can also be synthesized by analogous reaction in CH_2Cl_2, by using an excess (3.0 eq.) of [Thia][TEF] or by reacting **1a** with a further equivalent of [Thia][TEF].
Yield 245 mg (0.083 mmol = 92 %). Anal. calcd. for $[C_{30}H_{45}Fe_3As_6][AlO_4C_{16}F_{36}]_2$: C: 25.18, H: 1.53. Found: C: 25.33, H: 1.46.

Synthesis of $[(Cp^*Fe)_3As_6][FAl]_2$ (2b)

$[(Cp^*Fe)_3As_6]$ (**B**; 102 mg, 0.10 mmol, 1.0 eq.) and [Thia][FAl] (320 mg, 0.2 mmol, 2.0 eq.) were weighed together. Addition of 10 mL CH_2Cl_2 yielded a dark brown solution, which was stirred for 60 minutes. Addition of 50 mL *n*-hexane led to precipitation of a black powder. The supernatant was removed and the residue washed with 50 mL *n*-hexane. The powder was dried in vacuum and recrystallization from *o*-DFB/*n*-pentane at 4 °C yielded **2b** as black powder. The solvent was removed by decanting and the crystals dried in vacuum for 3h.
Compound **2b** can also be synthesized by reacting **1b** with a further equivalent of [Thia][FAl].
Yield 320 mg (0.085 mmol = 85 %).

Synthesis of $[K(thf)_2][(Cp^*Fe)_3As_6]$ (3)

$[(Cp^*Fe)_3As_6]$ (**B**; 204 mg, 0.20 mmol, 1.0 eq.), KC_8 (32 mg, 0.20 mmol, 1.0 eq.) and crown ether (18-crown-6) (52 mg, 0.20 mmol, 1.0 eq.) were weighed together and 20 mL THF were added at −20 °C yielding a dark orange brown solution and black precipitate. The suspension was stirred for 2h and the solid was separated by fitration. The solution was layered with 80 mL *n*-pentane and storage at 4 °C yielded pure **3**(18-crown-6) as dark brown blocks suitable for single crystal diffraction. The solvent was removed by decanting and the crystals dried in vacuum for 3h.
Compound **3** can also be synthesized without the crown ether in the same manner.
Yield 237 mg (0.161 mmol = 81 %).

8.4.2.3 Synthesis of salts of the mild oxidant $[Fe(\eta^5\text{-}C_5H_4COMe)_2]^+$ ($[Fc^{Diac}]^+$)

Synthesis of $[Fe(\eta^5\text{-}C_5H_4COMe)_2]$[FAl] ($[Fc^{Diac}]$[FAl])[20b]

An orange solution of $[Fe(\eta^5\text{-}C_5H_4COMe)_2]$ (1,1'-diacetylferrocene; Fc^{Diac}; 189 mg, 0.70 mmol, 1.0 eq.) in 10 mL CH_2Cl_2 was reacted with a colourless solution of Ag[FAl] (1042 mg, 0.70 mmol, 1.0 eq.) in 10 mL CH_2Cl_2 leading to a colour change to dark greenish blue and the precipitation of grey solid. The solution was filtered and layering with *n*-hexane at 4 °C yielded pure $[Fc^{Diac}]$[FAl] as blue sticks suitable for single crystal X-ray diffraction. The solvent was removed by decanting and the crystals dried in vacuum for 3h.

Yield 802 mg (0.5 mmol = 71 %). ^{1}H NMR (CD_2Cl_2) δ/ppm = −7.66 (s, $\omega_{1/2}$ = 180 Hz), 6.40 (s), 33.03 (s, $\omega_{1/2}$ = 2052 Hz). Characteristic signals for the $[FAl]^-$ anion were detected in the $^{19}F\{^1H\}$ NMR spectrum in CD_2Cl_2. ^{27}Al NMR (CD_2Cl_2) δ/ppm = 49.3 (s, $[FAl]^-$). Anal. calcd. for $[C_{14}H_{14}O_2Fe][AlO_3C_{36}F_{46}]$: C: 36.37, H: 0.85. Found: C: 36.77, H: 1.02. Positive ion MS *m/z* (%): 270.4 (100) $[\mathbf{M}]^+$. Negative ion MS *m/z* (%): 1379.7 (100) $[FAl]^-$. IR(KBr) $\tilde{\nu}$/cm^{-1} = 3125 (w), 2934 (vw), 1708 (m), 1655 (m), 1535 (s), 1486 (vs), 1407 (w), 1394 (m), 1318 (s), 1305 (s), 1267 (s), 1244 (s), 1204 (vs), 1159 (s), 1133 (s), 1108 (s), 1018 (vs), 954 (vs) 911 (m), 876 (w), 819 (w), 763 (s), 728 (s), 677 (w), 628 (m), 532 (m), 538 (w), 480 (w), 462 (m).

Synthesis of $[Fe(\eta^5\text{-}C_5H_4COMe)_2][TEF^{Cl}]$ ($[Fc^{Diac}][TEF^{Cl}]$)

An orange solution of $[Fe(\eta^5\text{-}C_5H_4COMe)_2]$ (1,1'-diacetylferrocene; Fc^{Diac}; 135 mg, 0.50 mmol, 1.0 eq.) in 10 mL CH_2Cl_2 was reacted with a purple solution of $[Thia][TEF^{Cl}]$ (700 mg, 0.50 mmol, 1.0 eq.) in 10 mL CH_2Cl_2 leading to a colour change to dark green. The solution was precipitated with 60 mL *n*-hexane and the solid washed with 5 mL toluene. The green powder was redissolved in 10 mL CH_2Cl_2 and again precipitated with *n*-hexane. The solvent was removed and the powder dried in vacuum. Dark green crystals of $[Fc^{Diac}][TEF^{Cl}]$ suitable for single crystal X-ray diffraction were obtained by dissolving a small amount of the powder in toluene (slightly soluble) and layering it with *n*-hexane (1:1) at 4° C.

Yield: 649 mg (0.45 mmol = 90 %). ^{1}H NMR (CD_2Cl_2) δ/ppm = no signals oberseved between −10 and 20 ppm. $^{19}F\{^1H\}$ NMR (CD_2Cl_2) δ/ppm = −69.0. Anal. calcd. for $[C_{14}H_{14}O_2Fe][AlO4C_{16}F_{24}Cl_{12}]$: C: 25.12, H: 0.98. Found: C: 25.45, H: 0.87.

8.4.2.4 Oxidation of $[Cp^*Fe(\eta^5\text{-}As_5)]$ (A)

Synthesis of $[(Cp^*Fe)_2(\mu,\eta^5\text{:}\eta^5\text{-}As_7)]$[TEF] (5a)

A green solution of $[Cp^*Fe(\eta^5\text{-}As_5)]$ (**A**; 44 mg, 0.078 mmol, 1.0 eq.) in 5 mL CH_2Cl_2 was reacted with a greenish blue solution of $[Fc^{Diac}]$[TEF] (84 mg, 0.068 mmol, 0.9 eq.) in 5 mL CH_2Cl_2 leading to an immediate colour change to dark orange brown and the precipitation of a brown solid. The solution was stirred for 60 minutes. The solution was filtered and addition of 40 mL *n*-hexane led to precipitation of brown powder. The supernatant was removed and the residue washed twice with 30 mL *n*-hexane. Recrystallization from CH_2Cl_2/*n*-hexane at 4 °C yielded **5a** as small dark brown plates

suitable for single crystal X-ray diffraction. The solvent was removed by decanting and the crystals dried in vacuum for 3h.
Yield 52 mg (0.028 mmol = 82 %).

Synthesis of [(Cp*Fe)$_2$(µ,η^5:η^5-As$_7$)][FAl] (5b)

A green solution of [Cp*Fe(η^5-As$_5$)] (**A**; 56 mg, 0.10 mmol, 1.0 eq.) in 5 mL CH_2Cl_2 was reacted with a greenish blue solution of [Fc^{Diac}][FAl] (168 mg, 0.10 mmol, 1.0 eq.) in 5 mL CH_2Cl_2 leading to an immediate colour change to dark orange brown and the precipitation of a brown solid. The solution was stirred for 60 minutes. The solution was filtered and addition of 40 mL *n*-hexane led to precipitation of brown powder. The supernatant was removed and the residue washed twice with 30 mL *n*-hexane. Recrystallization from CH_2Cl_2/*n*-hexane at 4 °C yielded **5b** as small dark brown plates suitable for single crystal X-ray diffraction. The solvent was removed by decanting and the crystals dried in vacuum for 3h.
Yield 106 mg (0.046 mmol = 92 %). ^{1}H NMR (CD_2Cl_2) δ/ppm = 1.18 (s, Cp*). Characteristic signals for the [FAl]$^-$ anion were detected in the ^{19}F{^{1}H} NMR spectrum in CD_2Cl_2. Anal. calcd. for [$C_{20}H_{30}Fe_2As_7$][$AlO_3C_{36}F_{46}$]: C: 29.40, H: 1.32. Found: C: 30.76, H: 1.51.

8.4.2.5 Oxidation of As$_5$ Triple-Decker Complexes

Synthesis of [(Cp*Mo)$_2$(µ,η^5:η^5-As$_5$)][TEF] (6a)

A black solution of [(Cp*Mo)$_2$(µ,η^5:η^5-As$_5$)] (**C**; 33 mg, 0.04 mmol, 1.0 eq.) in 3 mL o-DFB was reacted with a dark purple solution of [Thia][TEF] (47 mg, 0.04 mmol, 1.0 eq.) in 3 mL o-DFB leading to an immediate colour change to dark blue. The solution was stirred for 60 minutes. Addition of 40 mL *n*-hexane led to precipitation of blue powder. The supernatant was removed and the residue washed twice with 30 mL *n*-hexane. Recrystallization from *o*-DFB/*n*-hexane at 4 °C yielded pure **6a** as dark blue sticks suitable for single crystal X-ray diffraction. The solvent was removed by decanting and the crystals dried in vacuum for 3h.
Yield 67 mg (0.037 mmol = 93 %).

Synthesis of [(Cp*Mo)$_2$(µ,η^5:η^5-As$_5$)][FAl] (6b)

A black solution of [(Cp*Mo)$_2$(µ,η^5:η^5-As$_5$)] (**C**; 84 mg, 0.10 mmol, 1.0 eq.) in a mixture of 10 mL o-DFB and 5 mL CH_2Cl_2 was reacted with a dark purple solution of [Thia][FAl] (160 mg, 0.10 mmol, 1.0 eq.) in 20 mL o-DFB leading to an immediate colour change to dark blue. The solution was stirred for 60 minutes. The amount of solvent was reduced to 5 mL. Addition of 40 mL *n*-hexane led to precipitation of blue powder. The supernatant was removed, the residue dissolved in 5 mL *o*-DFB and again precipitated with *n*-hexane. The supernatant was removed and recrystallization from *o*-DFB/*n*-hexane at 4 °C yielded pure **6b** as dark blue powder. The solvent was removed by decanting and the powder dried in vacuum for 3h.
Yield 182 mg (0.082 mmol = 82 %).

Synthesis of [(Cp*Mo)$_2$(μ,η^5:η^5-As$_5$)][SbF$_6$] (6c)

A black suspension of [(Cp*Mo)$_2$(μ,η^5:η^5-As$_5$)] (**C**; 42 mg, 0.05 mmol, 1.0 eq.) in 10 mL o-DFB was transferred onto [Thia][SbF$_6$] (27 mg, 0.05 mmol, 1.0 eq.) yielding a dark blue solution. The solution was stirred for 60 minutes and addition of 40 mL *n*-hexane led to precipitation of greenish blue powder. The supernatant was removed, the residue washed with 30 mL toluene and dried in vacuum. Recrystallization from *o*-DFB/*n*-pentane at 4 °C yielded pure **6c** as dark blue needles suitable for single crystal X-ray diffraction. The solvent was removed by decanting and the crystals dried in vacuum for 3h.

Yield 48 mg (0.045 mmol = 90 %). Anal. calcd. for [$C_{20}H_{30}Mo_2As_5$][SbF_6]: C: 22.39, H: 2.82. Found: C: 22.25, H: 2.37.

Synthesis of [(Cp^{Bn}Cr)$_2$(μ,η^5:η^5-As$_5$)][TEF] (7a)

A dark purple solution of [Thia][TEF] (24 mg, 0.02 mmol, 1.0 eq.) in 3 mL o-DFB was transferred onto an olive green suspension of [(Cp^{Bn}Cr)$_2$(μ,η^5:η^5-As$_5$)] (**D**; 32 mg, 0.02 mmol, 1.0 eq.) in 5 mL o-DFB at −20 °C yielding an orange brown solution within 5 minutes. The solution was stirred for 30 minutes and addition of 30 mL *n*-pentane led to precipitation of brown powder. The supernatant was removed, the residue washed with 30 mL toluene and dried in vacuum. Recrystallization from *o*-DFB/*n*-pentane at 4 °C yielded **7a** as brown powder. The solvent was removed by decanting and the crystals dried in vacuum for 3h.

Yield 41 mg (0.017 mmol = 85 %).

Synthesis of [(Cp^{Bn}Cr)$_2$(μ,η^5:η^5-As$_5$)][FAl] (7b)

An olive green suspension of [(Cp^{Bn}Cr)$_2$(μ,η^5:η^5-As$_5$)] (**D**; 45 mg, 0.03 mmol, 1.0 eq.) in 15 mL o-DFB was transferred onto dark purple [Thia][FAl] (48 mg, 0.03 mmol, 1.0 eq.) at −20 °C yielding a red brown solution, which turn orange brown within 15 minutes. The solution was stirred for 30 minutes and addition of 30 mL *n*-pentane led to precipitation of brown powder. The supernatant was removed, the residue washed with 30 mL toluene and dried in vacuum. Recrystallization from *o*-DFB/*n*-pentane at 4 °C yielded pure **7b** as dark red brown sticks suitable for single crystal X-ray diffraction. The solvent was removed by decanting and the crystals dried in vacuum for 3h.

Yield 79 mg (0.027 mmol = 90 %). Decomposition of **7b** occurred during elemental analysis.

8.4.2.6 Oxidation of [(Cp'''Co)$_3$(μ,η$^{4:4:2:1}$-As$_{12}$)] (E)

An orange brown solution of [(Cp'''Co)$_3$(μ,η$^{4:4:2:1}$-As$_{12}$)] (**E**; 89 mg, 0.05 mmol, 1.0 eq.) in 10 mL o-DFB was reacted with a dark purple solution of [Thia][FAl] (80 mg, 0.05 mmol, 1.0 eq.) in 10 mL o-DFB at −30 °C yielding an orange brown solution. The solution was stirred for 60 minutes and the amount of solvent reduced to 5 mL Addition of 40 mL *n*-hexane led to precipitation of brown powder. The supernatant was removed, the residue washed twice with 30 mL *n*-hexane and dried in vacuum. Recrystallization from *o*-DFB/*n*-hexane at 4 °C yielded **8** as dark green blocks suitable for single crystal X-ray diffraction. The solvent was removed by decanting and the crystals dried in vacuum for 3h.

Yield 106 mg (0.047 mmol = 94 %). Anal. calcd. for [$C_{34}H_{58}Co_2As_4$][$AlO_3C_{36}F_{46}$]: C: 37.11, H: 2.58. Found: C: 36.18, H: 2.54.

8.4.3 NMR spectra

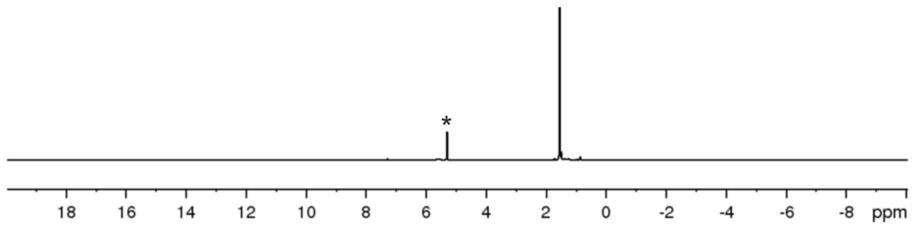

Figure S1: ^{1}H NMR spectrum of $[(Cp^*Fe)_3As_6][FAl]$ (**1b**) in CD_2Cl_2; * = CD_2Cl_2.

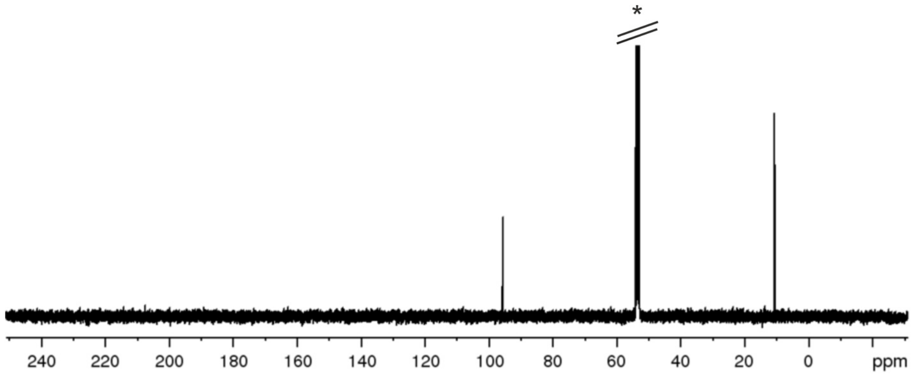

Figure S2: $^{13}C\{^1H\}$ NMR spectrum of $[(Cp^*Fe)_3As_6][FAl]$ (**1b**) in CD_2Cl_2; * = CD_2Cl_2.

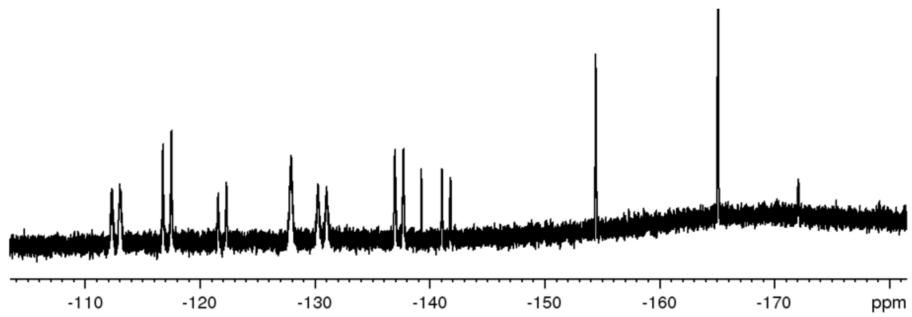

Figure S3: $^{19}F\{^1H\}$ NMR spectrum of $[(Cp^*Fe)_3As_6][FAl]$ (**1b**) in CD_2Cl_2.

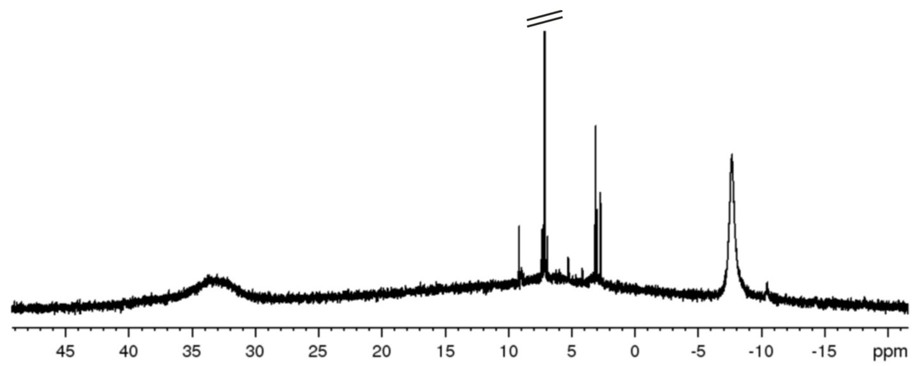

Figure S4: ^{1}H NMR spectrum of $[Fc^{Diac}][FAl]$ in CD_2Cl_2.

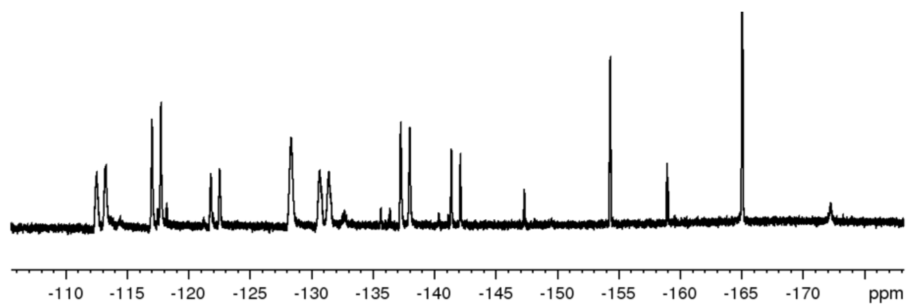

Figure S5: $^{19}F\{^1H\}$ NMR spectrum of $[Fc^{Diac}][FAl]$ in CD_2Cl_2.

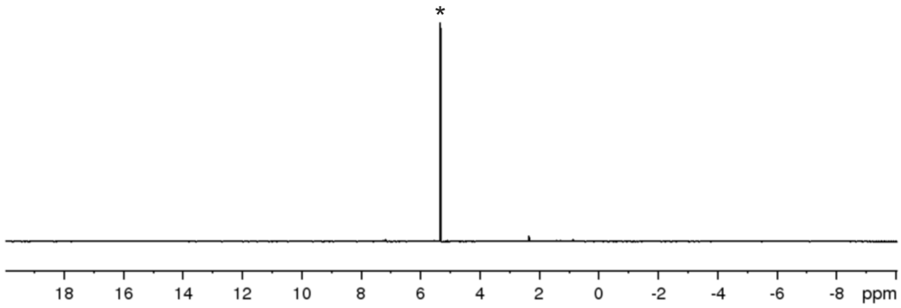

Figure S6: ^1H NMR spectrum of [Fc^{Diac}][TEF^{Cl}] in CD_2Cl_2.

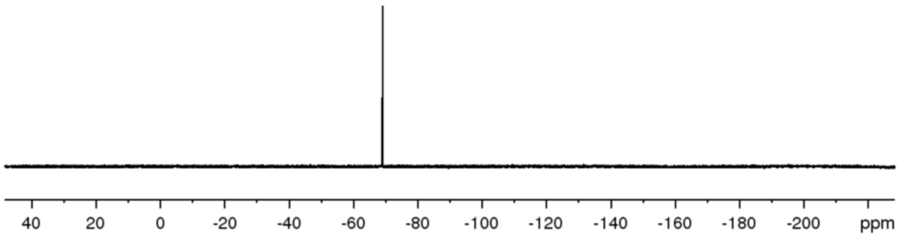

Figure S7: $^{19}F\{^1H\}$ NMR spectrum of [Fc^{Diac}][TEF^{Cl}] in CD_2Cl_2.

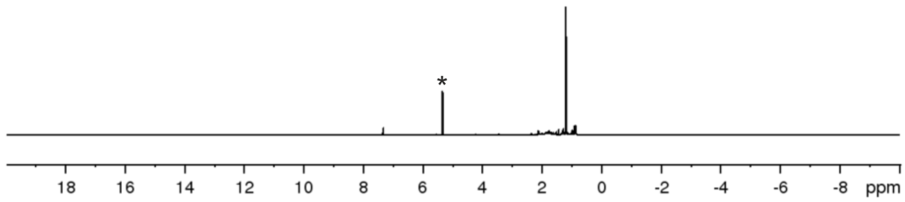

Figure S8: ^1H NMR spectrum of [(Cp*Fe)$_2$(μ,η^5:η^5-As$_7$)][FAl] (**5b**) in CD_2Cl_2; * = CD_2Cl_2.

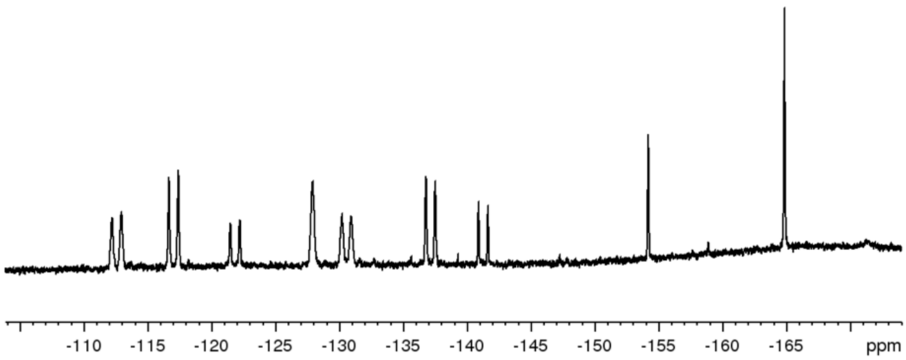

Figure S9: $^{19}F\{^1H\}$ NMR spectrum of [(Cp*Fe)$_2$(μ,η^5:η^5-As$_7$)][FAl] (**5b**) in CD_2Cl_2.

8.4.4 X-ray crystallography

All crystal manipulations were performed under mineral oil. The diffraction experiments were performed at 123 K (if not stated otherwise) either on a Rigaku (former Agilent Technologies or Oxford Diffraction) Gemini Ultra with an AtlasS2 detector, on a GV50 diffractometer with a TitanS2 detector or on a Gemini Ultra with an AtlasS2 detector using Cu-K_α, Cu-K_β or Mo-K_α radiation. Crystallographic data together with the details of the experiments are given in Table S1, Table S2 or Table S3. The cell determination, data reduction and absorption correction for all compounds were performed with the help of the CrysAlis PRO software.[29] All structures were solved by using the programs SHELXT[30] and Olex2.[31] The full-matrix least-squares refinement against F^2 was done using SHELXL[32] and Olex2.[31] If not stated otherwise, all atoms except hydrogen atoms were refined anisotropically. The H atoms were calculated geometrically, and a riding model was used during the refinement process.

Table S1: Crystallographic details for the compounds **B**, **1a**, **1b** and **2a**.

	B	**1a**	**1b**	**2a**
formula	$C_{30}H_{45}As_6Fe_3$	$C_{113}H_{114}Al_2As_{12}F_{72}Fe_6O_8$	$C_{66}H_{45}AlAs_6F_{46}Fe_3O_3$	
weight [g·mol^{-1}]	1022.73	4256.14	2404.07	
Temperature [K]	123.0(1)	123.0(1)	123.0(1)	
crystal system	monoclinic	monoclinic	triclinic	orthorhombic
space group	$P2_1/m$	$P2_1/c$	P-1	$Pmn2_1$
a [Å]	8.2946(4)	40.3103(3)	15.9679(4)	14.9557(3)
b [Å]	19.0247(6)	22.2643(2)	16.0682(4)	30.0333(5)
c [Å]	11.2462(4)	16.3724(2)	17.5789(5)	21.2085(3)
α [°]	90	90	70.388(2)	90
β [°]	108.558(5)	101.0640(10)	67.422(2)	90
γ [°]	90	90	73.953(2)	90
Volume [Å^3]	1682.40(12)	14420.8(2)	3866.17(19)	9526.2(3)
Z	2	4	2	
ρ_{calc} [g·cm^{-3}]	2.019	1.960	2.065	
μ [mm^{-1}]	7.152	6.901	8.884	
F(000)	1002.0	8328.0	2336.0	
crystal size [mm^3]	0.334 × 0.168 × 0.125	0.191 × 0.118 × 0.079	0.797 × 0.472 × 0.089	
diffractometer	Gemini Ultra	GV50	Gemini Ultra	GV50
absorption correction	analytical	gaussian	analytical	
T_{min} / T_{max}	0.528 / 0.743	0.390 / 0.790	0.257 / 0.810	
radiation [Å]	MoKα (λ = 0.71073)	Cu-Kβ (λ = 1.39222)	Cu-Kα (λ = 1.54184)	
2Θ range [°]	6.722 to 64.398	5.396 to 145.118	7.044 to 145.744	
completeness [%]	99.7	99.6	98.6	
reflns collected / unique	15838 / 5581	100774 / 37349	30671 / 14747	
R_{int} / R_{sigma}	0.0260 / 0.0334	0.0358 / 0.0382	0.0524 / 0.0640	
data / restraints / parameters	5581 / 0 / 249	37349 / 198 / 2311	14747 / 0 / 1141	
GOF on F^2	1.033	1.039	1.055	
R_1 / wR_2 [$I \geq 2\sigma(I)$]	0.0259 / 0.0495	0.0385 / 0.0868	0.0490 / 0.1323	
R_1 / wR_2 [all data]	0.0379 / 0.0530	0.0513 / 0.0937	0.0543 / 0.1399	
max / min $\Delta\rho$ [e·Å^{-3}]	0.64 / −0.51	1.24 / −1.11	1.56 / −1.35	
Identification code	CR177_F2	LD316_abs	LD325_abs	LD319_abs

Table S2: Crystallographic details for the compounds **3**, **5a**, **5b** and **6c**.

	3	**5a**	**5b**	**6c**
formula	$C_{50}H_{85}As_6Fe_3KO_8$	$C_{42}H_{34}AlAs_7F_{38}Fe_2O_4$	$C_{57}H_{32}AlAs_7Cl_2F_{46}Fe_2O_3$	$C_{20}H_{30}As_5F_6Mo_2Sb$
weight [g·mol^{-1}]	1450.94		2372.84	
Temperature [K]	100.0(1)		123.0(1)	
crystal system	triclinic	monoclinic	triclinic	triclinic
space group	*P*-1	*C*2/*c*	*P*-1	*P*-1
a [Å]	15.6462(2)	22.021(2)	11.5072(4)	18.4682(3)
b [Å]	17.4652(3)	19.852(2)	18.2843(7)	18.4687(3)
c [Å]	43.6064(5)	20.732(1)	19.3859(7)	20.5772(3)
α [°]	90.1450(10)	90	115.220(4)	107.656(1)
β [°]	90.9920(10)	102.28(1)	92.418(3)	107.651(2)
γ [°]	90.0660(10)	90	98.260(3)	108.917(1)
Volume [Å^3]	11914.2(3)	8855.5(1)	3627.3(3)	5664.3(2)
Z	8		2	
ρ_{calc} [g·cm^{-3}]	1.618		2.173	
μ [mm^{-1}]	7.880		9.081	
F(000)	5798.0		2284.0	
crystal size [mm^3]	0.842 × 0.421 × 0.326		0.129 × 0.094 × 0.022	
diffractometer	GV50	GV50	GV50	GV50
absorption correction	gaussian		gaussian	
T_{min} / T_{max}	0.006 / 0.468		0.481 / 0.823	
radiation [Å]	Cu-Kβ (λ = 1.39222)	Cu-Kα (λ = 1.54184)	Cu-Kα (λ = 1.54184)	Cu-Kα (λ = 1.54184)
2Θ range [°]	4.918 to 148.586		5.072 to 149.082	
completeness [%]	98.6		98.9	
reflns collected / unique	153397 / 64044		39839 / 14159	
R_{int} / R_{sigma}	0.1061 / 0.1068		0.0761 / 0.0713	
data / restraints / parameters	64044 / 0 / 2356		14159 / 0 / 1073	
GOF on F^2	1.648		1.027	
R_1 / wR_2 [$I \geq 2\sigma(I)$]	0.1717 / 0.4599		0.0833 / 0.2233	
R_1 / wR_2 [all data]	0.1922 / 0.4787		0.1017 / 0.2475	
max / min $\Delta\rho$ [e·Å^{-3}]	4.06 / −5.91		2.78 / −1.48	
Identification code	LD438_abs	LD208_abs	LD209_abs	LD416_aP

Table S3: Crystallographic details for the compounds **7b**, **8b** and [Fc^{Diac}][TEF^{Cl}].

	7b	**8b**	[Fc^{Diac}][TEF^{Cl}]
formula	$C_{131}H_{80}AlAs_5Cr_2F_{51}O_3$	$C_{76}H_{62}AlAs_4Co_2F_{48}O_3$	$C_{30}H_{14}O_6F_{24}AlCl_{12}Fe$
weight [g·mol^{-1}]	3174.51	2379.77	1434.64
Temperature [K]	123.0(1)	123.0(1)	123.0(1)
crystal system	triclinic	monoclinic	monoclinic
space group	P-1	$P2_1/c$	$P2_1/c$
a [Å]	16.2805(3)	13.1950(2)	12.0418(2)
b [Å]	18.6298(3)	33.6287(4)	29.4427(5)
c [Å]	21.4360(3)	19.2913(3)	13.2210(2)
α [°]	79.6380(10)	90	90
β [°]	69.3330(10)	92.5370(10)	100.2090(10)
γ [°]	84.2860(10)	90	90
Volume [Å^3]	5979.39(17)	8551.8(2)	4613.20(13)
Z	2	4	4
ρ_{calc} [g·cm^{-3}]	1.763	1.848	2.066
μ [mm^{-1}]	4.328	6.262	10.542
F(000)	3146.0	4692.0	2804.0
crystal size [mm^3]	0.355 × 0.08 × 0.063		0.258 × 0.138 × 0.081
diffractometer	GV50	GV50	GV50
absorption correction	gaussian	multi-scan	gaussian
T_{min} / T_{max}	0.399 / 1.000	0.323 / 1.000	0.620 / 0.843
radiation [Å]	Cu-Kα (λ = 1.54184)	Cu-Kα (λ = 1.54184)	Cu-Kα (λ = 1.54184)
2Θ range [°]	7.092 to 147.882	6.706 to 147.914	7.428 to 148.04
completeness [%]	99.4	99.2	99.1
reflns collected / unique	70937 / 23510	37204 / 16553	21869 / 8918
R_{int} / R_{sigma}	0.0264 / 0.0250	0.0418 / 0.0452	0.0473 / 0.0466
data / restraints / parameters	23510 / 2216 / 2026	16553 / 0 / 1186	8918 / 0 / 669
GOF on F^2	1.018	1.033	1.072
R_1 / wR_2 [$I \geq 2\sigma(I)$]	0.0443 / 0.1172	0.0576 / 0.1519	0.0457 / 0.1217
R_1 / wR_2 [all data]	0.0477 / 0.1206	0.0638 / 0.1580	0.0509 / 0.1354
max / min $\Delta\rho$ [e·Å^{-3}]	1.55 / −1.03	1.51 / −1.00	0.73 / −0.59
Identification code	LD417_abs	LD410	LD198_CR016_2_abs

Refinement details for B

Compound **B** crystallizes in the monoclinic space group *P*2/*m* with one half molecule in the asymmetric unit exhibiting a distorted As_6 prism with an open As–As bond. The square sides of the prism are coordinated by [Cp*Fe] fragments. The refinement could be done without any difficulty. One Cp* ligand shows rotational disorder in a ratio of 62:38.

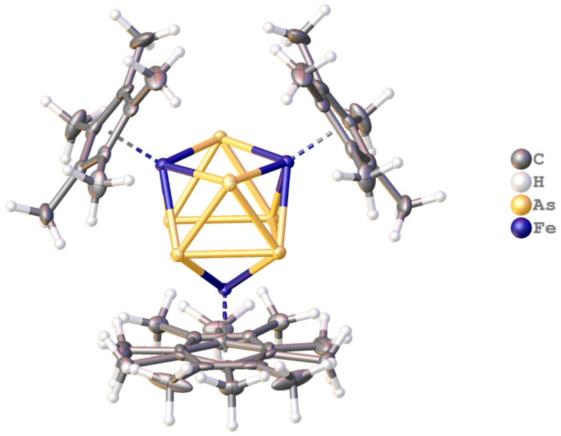

Figure S10: Molecular structure of **B**. The grown structure of the asymmetric unit is shown, which contains one half molecule of **B**.

Refinement details for 1a

Compound **1a** crystallizes in the monoclinic space group *P*2_1/*c* with two cations, two [TEF]⁻ anions and two solvent molecules toluene in the asymmetric unit. The refinement could be done without any difficulty. One [TEF]⁻ anion (including Al1) shows rotational disorder of three $OC(CF_3)_3$ groups in a ratio of 69:31, 63:37 and 56:44. The disordered parts were partially constrained with DANG and DFIX commands and the ADPs with SIMU commands during the refinement process.

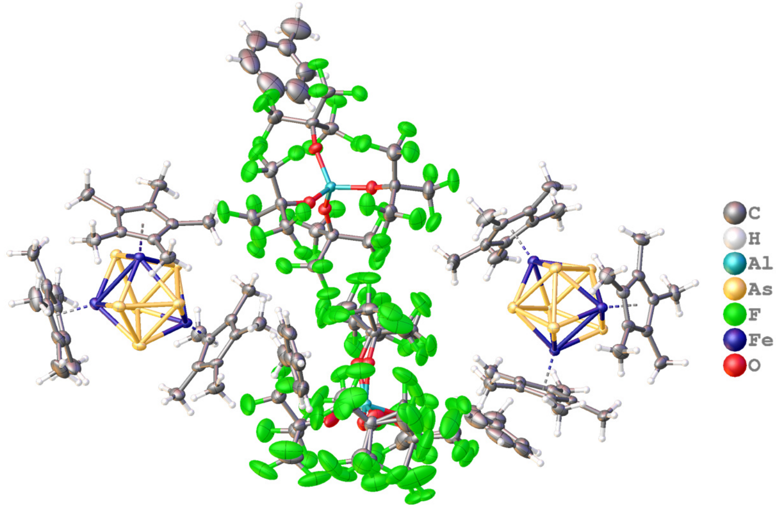

Figure S11: Molecular structure of **1a**. The asymmetric unit is shown containing two cations, two [TEF]⁻ anions and two solvent molecules toluene.

Refinement details for 1b

Compound **1b** crystallizes in the triclinic space group *P*-1 with one cation and one [FAl]⁻ anion in the asymmetric unit. The refinement could be done without any difficulty. No disordering was observed.

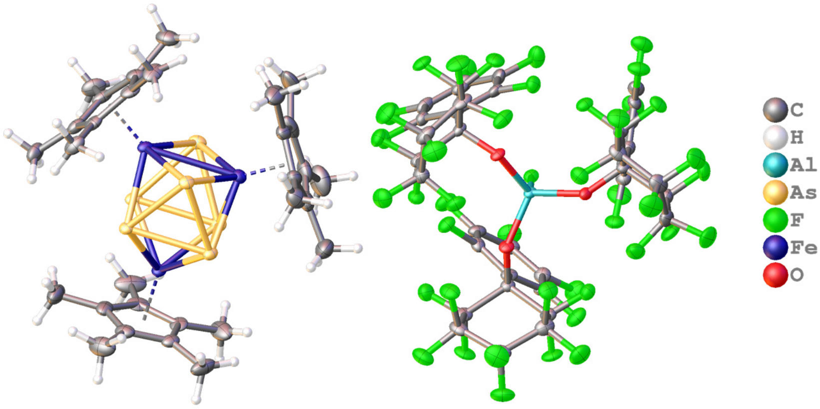

Figure S12: Molecular structure of **1b**. The asymmetric unit is shown containing one cation and one [FAl]⁻ anion.

Refinement details for 2a

Compound **2a** crystallizes as dark black sticks. The crystallographic data set was very weak and the [TEF]⁻ anions cause severe disorder. Therefore, the refinement could not be done allowing no description of the molecular structure. However, the heavy atom framework of the dication (Figure S13) shows that the original $(Cp^*Fe)_3As_6$ cluster of the starting material **B** is maintained.

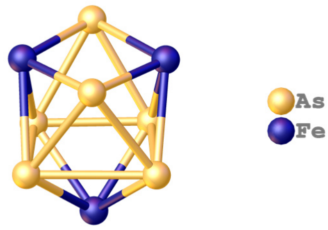

Figure S13: Heavy atom framework of the dication in **2a**.

Refinement details for 3

Compound **3** crystallizes in the triclinic space group *P*-1 with four anions and four $[K]^+$ in the asymmetric unit. Each of the latter are coordinated by one crown ether (18-crown-6) and two THF molecules. Some crown ethers and THF molecules are disordered, and their refinement could not be finished until the end of this thesis. However, the anionic parts are described well.

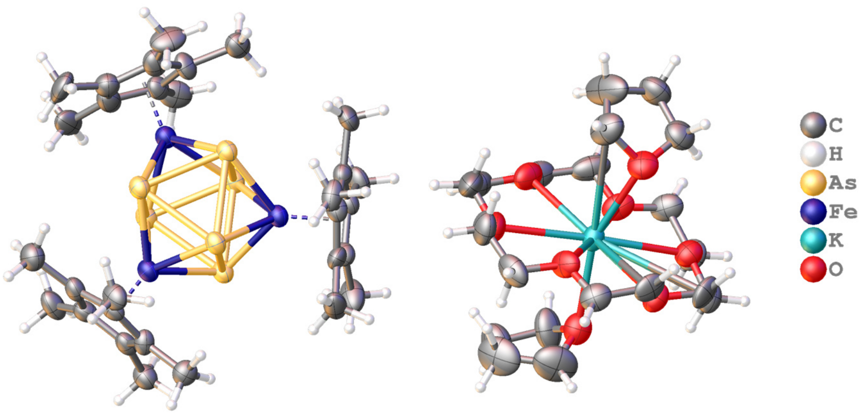

Figure S14: Molecular structure of **3**. A fourth of the asymmetric unit is shown, which contains four anions and four potassium cations each coordinated by one crown ether and two THF molecules.

Refinement details for 5b

Compound **5b** crystallizes in the triclinic space group *P*-1 with one cation, one $[FAl]^-$ anion and one solvent molecule CH_2Cl_2 in the asymmetric unit. The refinement could be done without any difficulty.

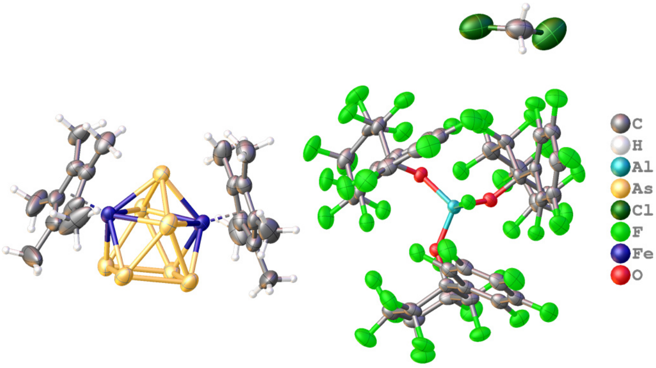

Figure S15: Molecular structure of **5b**. The asymmetric unit is shown containing one cation, one $[FAl]^-$ anion and one solvent molecule CH_2Cl_2.

Refinement details for 6c

Compound **6c** crystallizes in the triclinic space group *P*-1 with four cations and four $[SbF_6]^-$ anions in the asymmetric unit. The As_5 middle-decks within the cations exhibit manifold rotational disorder. Thus, the refinement could not be finished until the end of this thesis. However, it can be seen that the original triple-decker geometry of the starting material **C** is maintained.

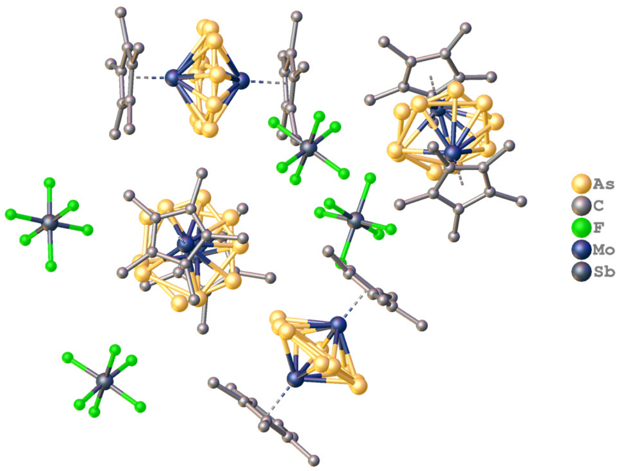

Figure S16: Molecular structure of **6c**. The asymmetric unit is shown containing four cations and four $[SbF_6]^-$ anions. The refinement was not finished until the end of this thesis.

Refinement details for 7b

Compound **7b** crystallizes in the triclinic space group *P*-1 with one cation, one $[FAl]^-$ anion and two and a half solvent molecules *o*-DFB in the asymmetric unit. The refinement could be done without any difficulty. Five benzyl groups of the Cp^{Bn} ligands show positional disorder in a ratio of 50:50, 50:50, 50:50, 55:45 and 62:38. The disordered parts were partially constrained with DFIX commands and the ADPs with SIMU commands during the refinement process.

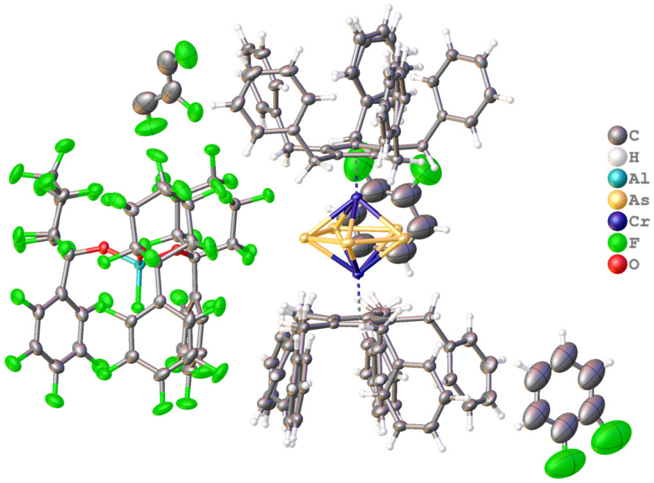

Figure S17: Molecular structure of **7b**. The asymmetric unit is shown containing one cation, one [FAl]⁻ anion and two and a half solvent molecules *o*-DFB. Some benzyl groups of the Cp^{Bn} ligands show positional disorder.

Refinement details for 8

Compound **8** crystallizes in the monoclinic space group $P2_1/c$ with one cation, one $[FAl]^-$ anion and one solvent molecule *o*-DFB in the asymmetric unit. The refinement could be done without any difficulty. No disorder was observed.

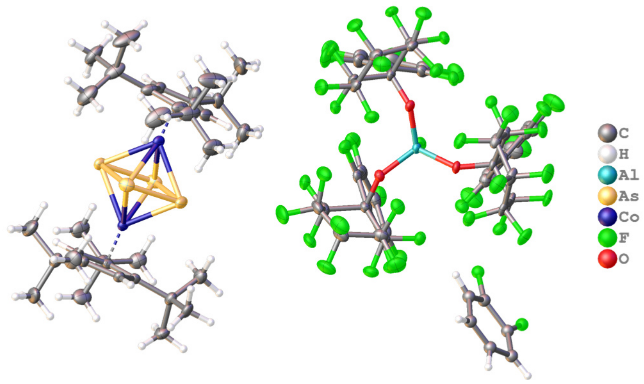

Figure S18: Molecular structure of **8**. The asymmetric unit is shown containing one cation, one $[FAl]^-$ anion one solvent molecule *o*-DFB.

Refinement details for $[Fc^{Diac}][TEF^{Cl}]$

$[Fc^{Diac}][TEF^{Cl}]$ crystallizes in the monoclinic space group $P2_1/c$ with one cation and one $[TEF^{Cl}]^-$ anion in the asymmetric unit. The refinement could be done without any difficulty. No disorder was observed.

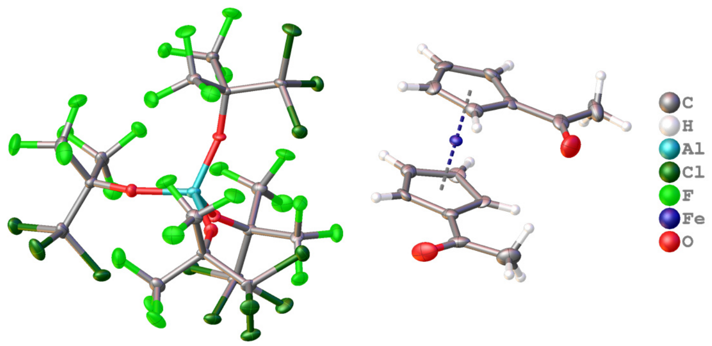

Figure S19: Molecular structure of $[Fc^{Diac}][TEF^{Cl}]$. The asymmetric unit is shown containing one cation and one $[TEF^{Cl}]^-$ anion.

8.5 References

[1] a) T. A. Engesser, I. Krossing, *Coord. Chem. Rev.* **2013**, *257*, 946-955; b) T. A. Engesser, M. R. Lichtenthaler, M. Schleep, I. Krossing, *Chem. Soc. Rev.* **2016**, *45*, 789-899.

[2] a) C. A. Dyker, N. Burford, *Chem. Asian J.* **2008**, *3*, 28-36; b) A. P. M. Robertson, P. A. Gray, N. Burford, *Angew. Chem. Int. Ed.* **2014**, *53*, 6050-6069; c) M. Donath, F. Hennersdorf, J. J. Weigand, *Chem. Soc. Rev.* **2016**, *45*, 1145-1172.

[3] a) M. H. Holthausen, J. J. Weigand, *J. Am. Chem. Soc.* **2009**, *131*, 14210-14211; b) M. H. Holthausen, J. J. Weigand, *Dalton Trans.* **2016**, *45*, 1953-1961; c) M. Gonsior, I. Krossing, L. Müller, I. Raabe, M. Jansen, L. v. Wüllen, *Chem. Eur. J.* **2002**, *8*, 4475-4492; d) M. Donath, E. Conrad, P. Jerabek, G. Frenking, R. Fröhlich, N. Burford, J. J. Weigand, *Angew. Chem. Int. Ed.* **2012**, *51*, 2964-2967.

[4] a) T. Köchner, T. A. Engesser, H. Scherer, D. A. Plattner, A. Steffani, I. Krossing, *Angew. Chem. Int. Ed.* **2012**, *51*, 6529-6531; b) T. Köchner, S. Riedel, A. J. Lehner, H. Scherer, I. Raabe, T. A. Engesser, F. W. Scholz, U. Gellrich, P. Eiden, R. A. Paz Schmidt, D. A. Plattner, I. Krossing, *Angew. Chem. Int. Ed.* **2010**, *49*, 8139-8143.

[5] I. Krossing, I. Raabe, *Angew. Chem. Int. Ed.* **2004**, *43*, 2066-2090.

[6] a) B. M. Cossairt, N. A. Piro, C. C. Cummins, *Chem. Rev.* **2010**, *110*, 4164-4177; b) M. Caporali, L. Gonsalvi, A. Rossin, M. Peruzzini, *Chem. Rev.* **2010**, *110*, 4178-4235; c) B. P. Johnson, G. Balázs, M. Scheer, *Coord. Chem. Rev.* **2006**, *250*, 1178-1195; d) O. J. Scherer, *Angew. Chem. Int. Ed.* **1990**, *29*, 1104-1122; e) O. J. Scherer, *Acc. Chem. Res.* **1999**, *32*, 751-762.

[7] a) L. Dütsch, M. Fleischmann, S. Welsch, G. Balázs, W. Kremer, M. Scheer, *Angew. Chem. Int. Ed.* **2018**, *57*, 3256-3261; b) L. Dütsch, C. Riesinger, G. Balázs, M. Seidl, M. Scheer, *Chem. Sci.* **2021**, *12*, 14531-14539.

[8] O. J. Scherer, H. Sitzmann, G. Wolmershäuser, *Angew. Chem. Int. Ed.* **1985**, *24*, 351-353.

[9] M. Fleischmann, F. Dielmann, L. J. Gregoriades, E. V. Peresypkina, A. V. Virovets, S. Huber, A. Y. Timoshkin, G. Balázs, M. Scheer, *Angew. Chem. Int. Ed.* **2015**, *54*, 13110-13115.

[10] a) R. F. Winter, W. E. Geiger, *Organometallics* **1999**, *18*, 1827-1833; b) M. V. Butovskiy, G. Balázs, M. Bodensteiner, E. V. Peresypkina, A. V. Virovets, J. Sutter, M. Scheer, *Angew. Chem. Int. Ed.* **2013**, *52*, 2972-2976.

[11] M. Schmidt, D. Konieczny, E. V. Peresypkina, A. V. Virovets, G. Balázs, M. Bodensteiner, F. Riedlberger, H. Krauss, M. Scheer, *Angew. Chem. Int. Ed.* **2017**, *56*, 7307-7311.

[12] O. J. Scherer, C. Blath, G. Wolmershäuser, *J. Organomet. Chem.* **1990**, *387*, C21-C24.

[13] H. Krauss, PhD thesis, University of Regensburg, Regensburg, **2011**.

[14] P. Pyykkö, *J. Phys. Chem. A* **2015**, *119*, 2326-2337.

[15] a) K. Wade, in *Advances in Inorganic Chemistry and Radiochemistry, Vol. 18* (Eds.: H. J. Emeléus, A. G. Sharpe), Academic Press, **1976**, pp. 1-66; b) K. Wade, *Inorganic and Nuclear Chemistry Letters* **1972**, *8*, 559-562; c) J. D. Corbett, in *Prog. Inorg. Chem.*, John Wiley & Sons, Inc., **2007**, pp. 129-158.

[16] C. v. Hänisch, D. Fenske, *Z. Anorg. Allg. Chem.* **1998**, *624*, 367-369.

[17] N. G. Connelly, W. E. Geiger, *Chem. Rev.* **1996**, *96*, 877-910.

[18] M. Fleischmann, PhD thesis, University of Regensburg, Regensburg, **2015**.

[19] M. E. Moussa, M. Fleischmann, G. Balázs, A. V. Virovets, E. Peresypkina, P. A. Shelyganov, M. Seidl, S. Reichl, M. Scheer, *Chem. Eur. J.* **2021**, *27*, 9742-9747.

[20] a) A. Straube, P. Coburger, L. Dütsch, E. Hey-Hawkins, *Chem. Sci.* **2020**, *11*, 10657-10668; b) L. Dütsch, master thesis, University of Regensburg, Regensburg, **2015**.

[21] M. Schmidt, PhD thesis, University of Regensburg, Regensburg, **2016**.

[22] L. Y. Goh, R. C. S. Wong, W. H. Yip, T. C. W. Mak, *Organometallics* **1991**, *10*, 875-879.

[23] A. L. Rheingold, M. J. Foley, P. J. Sullivan, *J. Am. Chem. Soc.* **1982**, *104*, 4727-4729.

[24] M. Piesch, C. Graßl, M. Scheer, *Angew. Chem. Int. Ed.* **2020**, *59*, 7154-7160.

[25] D. Catheline, D. Astruc, *Organometallics* **1984**, *3*, 1094-1100.

[26] W. Rüdorff, E. Schulze, *Z. Anorg. Allg. Chem.* **1954**, *277*, 156-171.

[27] C. Graßl, M. Bodensteiner, M. Zabel, M. Scheer, *Chem. Sci.* **2015**, *6*, 1379-1382.

[28] T. Köchner, N. Trapp, T. A. Engesser, A. J. Lehner, C. Röhr, S. Riedel, C. Knapp, H. Scherer, I. Krossing, *Angew. Chem. Int. Ed.* **2011**, *50*, 11253-11256.

[29] Agilent (2014). CrysAlis PRO. Agilent Technologies Ltd., Yarnton, Oxfordshire, England.

[30] G. Sheldrick, Acta Crystallographica Section A **2015**, 71, 3-8.

[31] O. V. Dolomanov, L. J. Bourhis, R. J. Gildea, J. A. K. Howard, H. Puschmann, *J. Appl. Cryst.* **2009**, *42*, 339-341.

[32] G. Sheldrick, Acta Crystallographica Section C **2015**, 71, 3-8.

Preface

The following chapter has not been published until the submission of this thesis.

Authors

Luis Dütsch and Manfred Scheer

Author Contributions

The main part (conceptualization, preparation of the compounds **1a**-**f**, **1g**$_{endo}$/**1g**$_{exo}$, **2**, **3a**[TEF], **3b**[TEF] and **5**[TEF], writing, visualization, and execution and evaluation of measurements) of this work was done by the first author (Luis Dütsch). Manfred Scheer supervised the research and revised the manuscript.

Acknowledgements

This work was supported by the Deutsche Forschungsgemeinschaft within the project Sche 384/36-2.

9 ELECTROPHILIC RING EXPANSION OF CYCLIC E_3 (E = P, AS) LIGANDS BY PHOSPHENIUM AND BORENIUM ION INSERTION

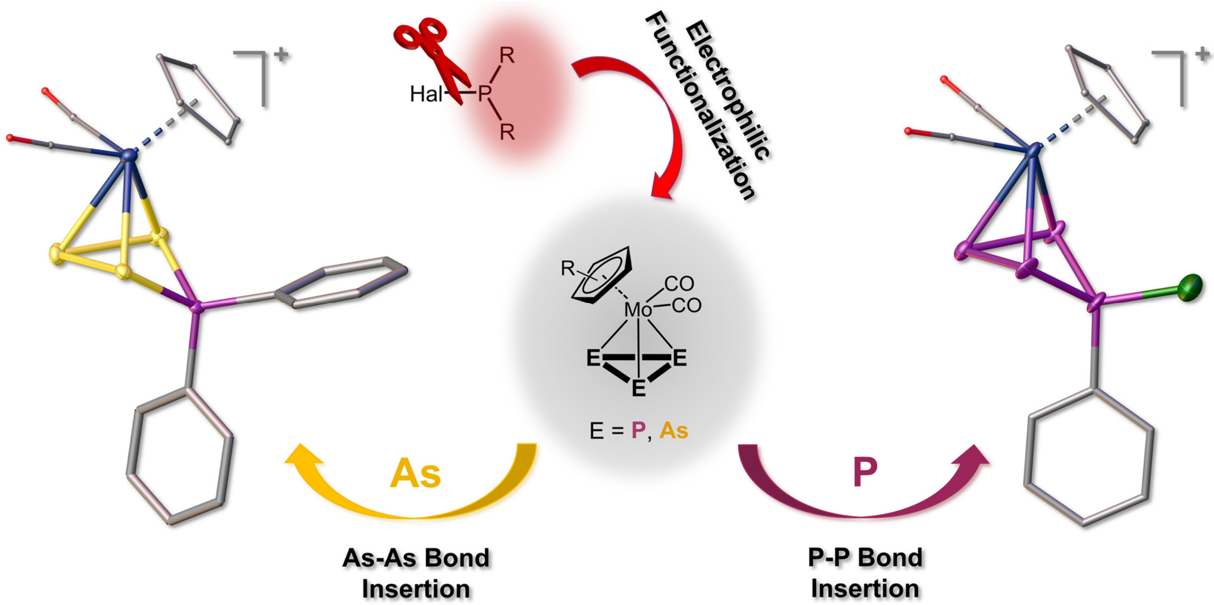

Abstract: *Electrophilic functionalization of naked P_3 ligand complexes is accomplished by the reaction of in situ generated phosphenium ions $[PRR']^+$ with $[Cp^RMo(CO)_2(\eta^3\text{-}P_3)]$ (**A**) yielding the polyphosphorus cations $[Cp^RMo(CO)_2(\eta^3\text{-}P_4RR')]^+$ via ring expansion reactions. By using different phosphenium ions a variety of substituents can be introduced into the newly formed P_4 ligands (R, R' = Ph, Me, Cy, Mes, 0.5 biphen, Br; RR' = PhCl). Additionally, for the first time also analogous As_3 ligand complexes were made accessible for electrophilic funtionalization by this procedure yielding unprecedented, cationic As_3PR_2 ligands. The central structural motifs of the products show "butterfly-like" folded E_3P rings stabilized in the coordination sphere of a $[Cp^RMo(CO)_2]$ fragment. Additionally, after prolonged storage CO elimination could be observed yielding dimerized species containing a P_7 or P_8 ligand. Furthermore, besides phosphenium ions also electrophilic functionalization of **A** with the borinium ion $[BBr_2]^+$ was applicable resulting in an unprecedented $P_6BBr_2(Br)$ ligand.*

9.1 Introduction

Organophosphorus compounds have become an essential part for industrial purposes and daily life since phosphorus is present in many products such as detergents, fertilizers or flame retardants.[1] However, their synthesis is associated with a multistep process, high energy consumption, the use of toxic or corrosive reagents and the generation of equimolar amounts of waste in terms of inorganic salts. Therefore, usually P_4 (whose synthesis itself is very energy consuming) is chlorinated to PCl_3 and then further reacted with organolithium compounds or Grignard reagents.[1b] For this reason, in recent research huge emphasis was put on the development of new procedures towards the functionalization of P_4,[1-2] in which the conversion with electrophiles is one of the most challenging, yet highly promising fields. This area was pioneered by the groups of *Weigand* and *Krossing* since they were able to functionalize P_4 *via* the electrophilic insertion of different phosphenium ions into one or multiple P–P bonds ($[P_4(PR_2)]^+$ (R = Br (**I**), Ph (**II**)), $[P_4(PPh_2)_2]^{2+}$ (**III**), $[P_4(PPh_2)_3]^{3+}$ (**IV**); Scheme 1a).[3] Thereby, the phosphenium ions are generated *in situ* from the respective halophosphines PBr_3 or PPh_2Cl, respectively, by halide abstraction using either Ag^+ salts in CH_2Cl_2 solutions or $GaCl_3$ in salt melts. Additionally, also $[PRCl]^+$ (R = various organic substituents) could be inserted into P–P bonds of white phosphorus.[4] Only recently, we were able to functionalize the nickel complex [Cp'''Ni(η^3-P_3)] (**V**), which bears a naked, *cyclo*-P_3 ligand, by reaction with phosphenium ions. These phosphenium ions insert into one P–P bond of the P_3 ligand yielding cationic P_4 ligands (**VI**), which carry two substituents and are stabilized by a coordinating [Cp'''Ni] fragment (Scheme 1b).[5] This approach could be expanded to a large amount of phosphenium ions containing a variety of organic substituents as well as halides. However, in some case the received products **VI** were unstable and formed dinuclear Ni complexes upon rearrangement reactions. Also decomposition of **V** to the cationic tripledecker complex $[(Cp'''Ni)_2(\mu,\eta^3{:}\eta^3\text{-}P_3)]^+$ (**VII**) was observed on various occasions. In order to suppress these

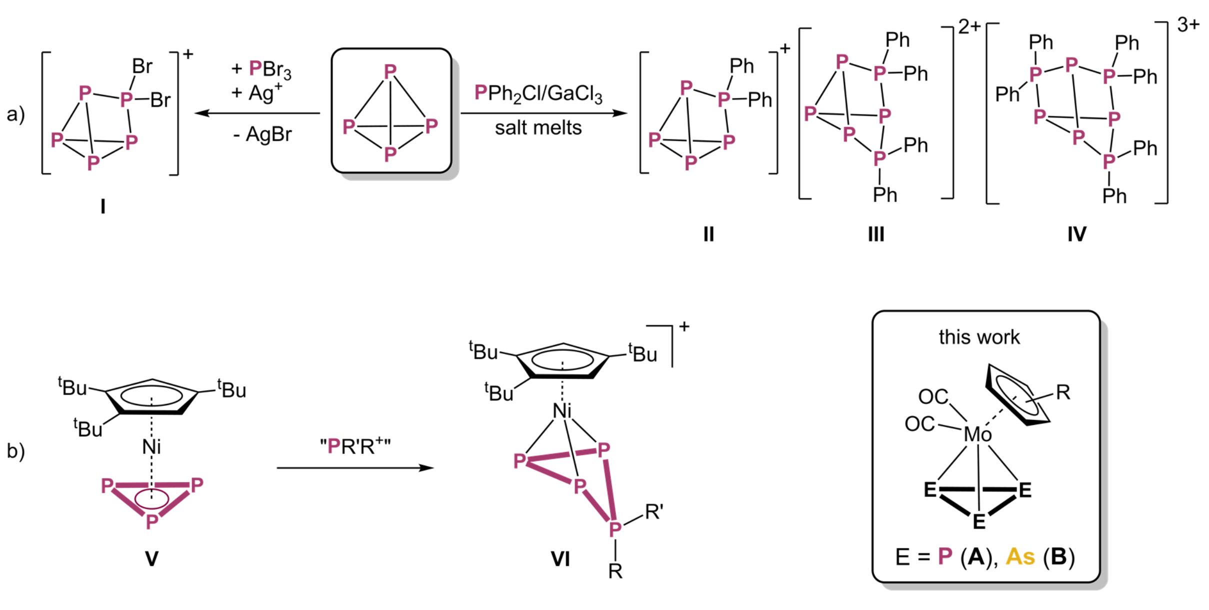

Scheme 1: a) Electrophilic functionalization of P_4 *via* phosphenium ion insertion; b) electrophilic functionalization of [Cp'''Ni(η^3-P_3)], phosphenium ions "in situ" generated by halide abstraction of the respective halophosphine; *this work*: electrophilic functionalization of the tetrahedral MoE_3 complexes [Cp^{R}Mo(CO)$_2$(η^3-E_3)] (Cp^R = Cp, Cp*; E = P, As).

rearrangement and side-reaction, we switched to the similar, yet more robust tetrahedral molybdenum complex $[Cp^RMo(CO)_2(\eta^3-P_3)]$ (Cp^R = Cp (**A1**), Cp* (C_5Me_5; **A2**)), which also bears a *cyclo*-P_3 ligand and, furthermore, is isolobal to P_4 (Scheme 1). In the following, we report on the electrophilic functionalization of **A** *via* reaction towards *in situ* generated phosphenium ions. Furthermore, we expanded these studies onto the reactivity of the analogous As_3 complexes $[Cp^RMo(CO)_2(\eta^3-As_3)]$ (Cp^R = Cp (**B1**), Cp* (**B2**)) and introduced different electrophiles including heavier group 15 cations and borinium ions.

9.2 Results and Discussion

When a yellow solution of **A1** and PPh_2Cl in CH_2Cl_2 is reacted with the halide-abstracting agent Tl[OTf] ($[OTf]^-$ = $[SO_3CF_3]^-$), immediate formation of a white precipitate (TlCl) occurs and the solution brightens up. Thereby, the phosphenium ion $[PPh_2][OTf]$ is formed *in situ*, which further reacts with **A1** *via* insertion of $[PPh_2]^+$ into the *cyclo*-P_3 ligand leading to a ring expansion (Scheme 2). After filtration and recrystallisation, $[CpMo(CO)_2(\eta^3-P_4Ph_2)][OTf]$ (**1a**[OTf]) can be isolated in 90 % crystalline yield (Scheme 2). The reaction is very selective and quantitative. A possible second or third insertion of the phosphenium ions $[PPh_2]^+$ into the P_3 ligand (analogous to the reaction of P_4 with $[PPh_2]^+$

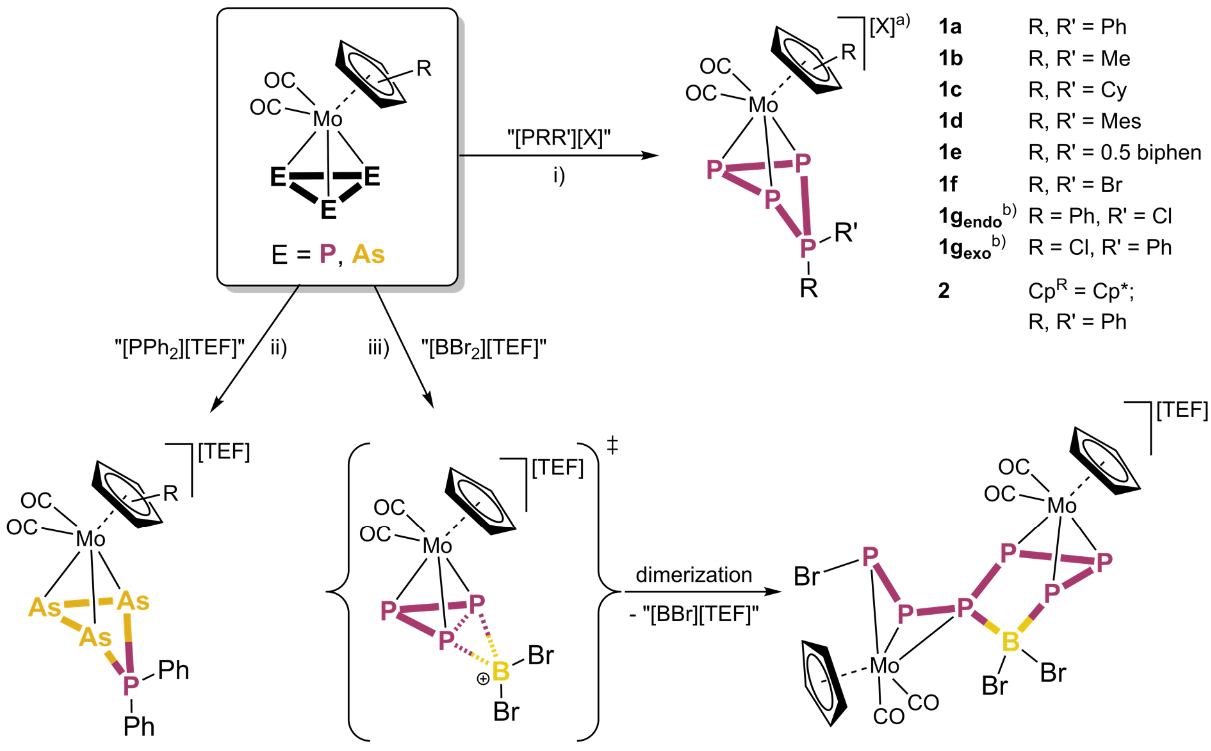

Scheme 2: Functionalization of a naked E_3 ligand (E = P, As) *via* insertion of phosphenium and borenium ions: i) E = P, Cp^R = $C_5H_5^-$ (**1**) or $C_5Me_5^-$ (**2**), "[PRR'][X]" *in situ* generated from PRR'Cl and Tl[TEF] (for other abstracting agents, see the Supporting Information); ii) E = As, Cp^R = Cp (**3a**) or Cp* (**3b**), "$[PPh_2]$[TEF]" from PPh_2Cl and Tl[TEF]; iii) E = P, Cp^R = Cp, "$[BBr_2]$[TEF]" from BBr_3 and Tl[TEF]; a) all compounds **1a-g** were prepared as their $[TEF]^-$ salts and **1a** additionally as its $[OTf]^-$ and $[GaCl_4]^-$ salt; b) Isomeric mixture of $\mathbf{1g_{endo}}$:$\mathbf{1g_{exo}}$ = 6:1 (with *endo* and *exo* referring to the position of the phenyl group at the P_4 ring).

(Scheme 1a) could not be observed even by using an excess of $[PPh_2]^+$. However, different anions can be introduced by using the halide-abstracting agents Tl[TEF] ($[TEF]^-$ = $[Al\{O(C(CF_3)_3\}_4]^-$) or $GaCl_3$ yielding the products **1a**[TEF] and **1a**$[GaCl_4]$ in isolated yields of up to 96 %. As **V** could be successfully functionalised with a big variety of phosphenium ions containing different organic substituents, we performed a systematic ^{31}P NMR screening in *o*-DFB (1,2-difluorobenzene) using PMe_2Cl, PCy_2Cl, $PMes_2Cl$ and P(biphen)Cl (Mes = 2,4,6-trimethylphenyl, Cy = cyclohexyl, biphen = 2,2'-biphenyl) as starting materials, which all proofed to be applicable for electrophilic functionalization of the P_3 unit after reaction with Tl[TEF] (*vide infra*, Figure 2), yielding the products $[CpMo(CO)_2(\eta^3\text{-}P_4R_2)]$[TEF] (R = Me (**1b**[TEF]), Cy (**1c**[TEF]), Mes (**1d**[TEF]); R_2 = biphen (**1e**[TEF]); Scheme 2). Also, by using PBr_3 as phosphenium ion precursor, insertion of the respective phosphenium ion $[PBr_2]^+$ into the P_3 ring can be observed selectively giving **1f**[TEF] (Scheme 2) in 75 % isolated yield. However, this contrasts the reactivity of $[PBr_2]^+$ with **V**, where a rearrangement reaction and elimination of white phosphorus took place. Therefore, the $[CpMo(CO)_2]$ fragment provides more stability for the $P_4R_2^+$ ligands than the [Cp'''Ni] fragment in **VI**. In order to extend the range of our approach we used dihalophosphines as precursor as well. Reaction of **A1** with $PPhCl_2$ in the presence of Tl[TEF] leads again to precipitation of a white powder (TlCl) and a colour change from yellow to an almost colourless solution is observed. After workup, the product $[CpMo(CO)_2(\eta^3\text{-}P_4PhCl)]$[TEF] (**1g**[TEF]) is obtained in 83 % isolated yield. The ^{31}P NMR spectrum of the crude solution (Figure 2) suggests the formation of two isomers of **1g** in a ratio of 1.6 to 1, where the phenyl group is either in *endo* or *exo* position referring to the P_4 cycle. The same behaviour was observed for the reaction of **V** with $[PPhCl]^+$. Due to steric reasons probably the *endo* isomer represents the major product. Interestingly, the amount of the sterically more accessible *endo* isomer increases during the crystallization as the NMR data of crystalline **1g** reveal a different ratio of **1g$_{endo}$**: **1g$_{exo}$** = 6:1 suggesting a possible free tumbling of the substituents (or an association/dissociation pathway of the phosphenium ion). An abstraction of the second chloride of $PPhCl_2$ by using two equivalents or even an access of Tl^+ was, however, not observed. When the same reaction was performed with $GaCl_3$ as halide abstraction agent, the ratio of **1g$_{endo}$**: **1g$_{exo}$** was already 6:1 in the crude solution indicating an influence of the counterion on the reaction outcome. Furthermore, we exchanged the Cp ligand in **A1** with the bulkier C_5Me_5 (Cp*) ligand. When $[Cp^*Mo(CO)_2(\eta^3\text{-}P_3)]$ (**A2**) is reacted with $[PPh_2]^+$ (*via* PPh_2Cl and $GaCl_3$) analogous insertion of the phosphenium ion into the P_3 ligand is observed giving $[Cp^*Mo(CO)_2(\eta^3\text{-}P_4Ph_2)][GaCl_4]$ (**2**; Scheme 2) in 82 % yield.

Interestingly, this approach can also be expanded to the analogous arsenic derivatives $[Cp^RMo(CO)_2(\eta^3\text{-}As_3)]$ (Cp^R = Cp (**B1**), Cp* (**B2**)). Reaction of **B1** and **B2**, respectively, with $[PPh_2]^+$ (*via* PPh_2Cl and Tl[TEF]) again lead to insertion of the phosphenium ion into one As–As bond of the As_3 ligand yielding $[Cp^RMo(CO)_2(\eta^3\text{-}As_3PPh_2)]$[TEF] ($Cp^R$ = Cp (**3a**), Cp* (**3b**); Scheme 2). To the best of our knowledge, this is the first example of an electrophilic functionalization of an As_n unit by a phosphenium cation. Furthermore, cationic As_3P cycles as complex ligands are completely unprecedented. The only As_3P cycles reported so far are the neutral phosphatriarsetanes $(^tBuAs)_3PR$ (R = Et, ^{i}Pr), which are received as a minor by-product in the synthesis of the respective phosphadiarsirane,[6] and within the neutral complex $[Cp'''Co(\eta^3\text{-}As_3PR_2)]$ (R = Ph, Cy, ^{t}Bu), which was synthesized only recently *via* electrophilic quenching of the respective anionic *cyclo*-As_3 complex.[7]

However, the latter are only accessible as product mixtures and, hence, could only be isolated in very low yields.

With these results in hand, we turned our interest towards heavier group 15 electrophiles. However, electrophilic functionalization of P_3 and As_3 ligands with arsenium ($[AsCl_2]^+$ and $[AsPh_2]^+$) and stibenium ($[SbPh_2]^+$) ions turned out to be unsuccessful since only uncharacterizable product mixtures were obtained probably due to the oxidative formation of the respective diarsonium and distibonium salts, in which the halide abstracting agents act as oxidants. Furthermore, switching from Group 15 to Group 13, we also used BBr_3 as an electrophile precursor for the functionalization of **A1**. The reaction of BBr_3 with Tl[TEF] leads to the formation of the borinium[8] ion $[BBr_2]^+$, which reacts in the presence of **A1** to the unexpected dinuclear compound $[\{CpMo(CO)_2\}_2(\mu,\eta^3{:}\eta^3\text{-}P_6BBr_2(Br))][TEF]$ (**5**[TEF]; Scheme 2). In this reaction the order, in which the reactants are added, is crucial. When BBr_3 is added to a solution of **A1** without Tl[TEF] immediately an orange precipitate is formed. It seems that **A1** and BBr_3 form a classical Lewis Acid/Base adduct, which is hardly soluble in CH_2Cl_2 or *o*-DFB. Therefore, it could not be characterized. However, when BBr_3 is added to **A1** in the presence of Tl[TEF], probably the bromide abstraction takes place before the adduct is formed and no precipitation is observed. In **5** a new catena P_6 ligand is formed, which is stabilized by two $[CpMo(CO)_2]$ fragments. Furthermore, one $[BBr_2]$ moiety bridges two P atoms leading to a five-membered P_4B ring and the external P atom carries one bromide substituent. Compound **5** is formally derived from the expected borinium insertion/adduct product $[CpMo(CO)_2(\eta^3\text{-}P_3BBr_2)]^+$ (**4**[TEF]; Scheme 2), which dimerizes under elimination of a formal cationic "BBr^+" moiety. An alternativ reaction pathway would be that after the initial formation of **4** a second P_3 ligand of **A1** inserts into one P–B bond leading to a P–P bond break-up of the second P_3 ligand, which is saturated by a bromide ion. A similar product is obtained in the reaction of **V** with $[PBr_2]^+$, where instead of a $[CpMo(CO)_2P_3]$ unit a [Cp'''Ni] fragment inserts into **VI** under elimination of P_4.[5] However, theoretical computations have to be carried out to get a better insight into the reaction pathway. Furthermore, the isolation or at least detection of the intermediate **4**, which was not accomplished yet, would be crucial. The use of **A1** and **A2** as starting material for electrophilic ring expansion additionally has the advantage that the formation of *cyclo*-P_3 triple-decker complexes, which were observed in similar reactions of **V** on various occasions, can be suppressed.[5]

In order to shed light into the molecular structure of these products, **1a**, **1f**, **1g** and **2** (Figure 1, top) as well as **3a**, **3b** and **5** (Figure 1, bottom) were crystallized as their $[GaCl_4]^-$ (**1a**, **2**), $[(OTf)_2H]^-$ (**1g$_{endo}$**), $[OTf]^-$ (**1a**) or $[TEF]^-$ (**1f**, **1g$_{exo}$**, **3a**, **3b**, **5**) salts. For **1g**, in contrast to its [Cp'''Ni] derivative **VI**,[5] both the *endo* and *exo* isomer could be crystallographically characterized. Interestingly, **1g$_{exo}$** crystallizes as completely colourless blocks, while **1g$_{endo}$** forms yellow crystals similar to the other products (except **1f**, which forms dark yellow to orange crystals). As all molecular structures of the complexes **1** and **2** are similar only the bond lengths of **1a**[OTf] are given in the following. The central structural motif in **1**, **2** and **3** consists of a bent, cationic P_4 (**1**, **2**) or As_3P (**3**) ring, respectively, with two substituents on the P1 atom. The former P_3 or As_3 units are still coordinated by the $[Cp^RMo(CO)_2]$ fragment in an η^3-fashion. The P_4 cycle in **1** and **2** is obtained by the insertion of the phosphenium cation into one P–P bond of **A1** or **A2**, respectively. Likewise, the As_3P cycle in **3** is obtained by the insertion into one As–As bond of **B**. This is clearly seen in the strongly widened P2–P4 distance (3.074(1) Å in **1a**) and As1–As3 distance (3.293(1) Å in **3a**) clearly indicating cleavage of the former E–E bonds. In contrast, the P–

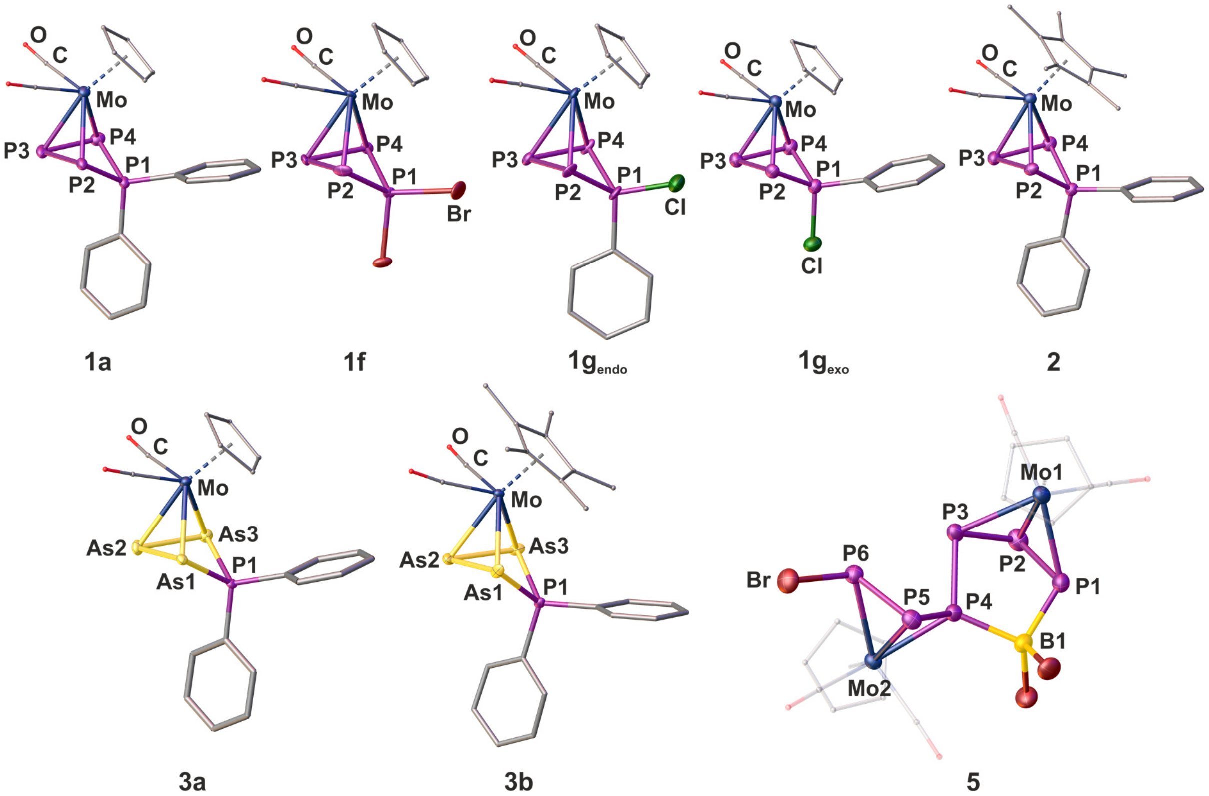

Figure 1: Molecular structures of **1a**, **1f**, **1g**$_{\mathbf{endo}}$, **1g**$_{\mathbf{exo}}$, **2**, **3a**, **3b** and **5**. Anisotropic displacement is set to the 50% probability level. H atoms, counter ions and solvent molecules are omitted and C as well as O atoms are drawn as small spheres for clarity. Selected bond lengths [Å]: **1a**: P1–P2 2.173 (1), P2–P3 2.205(1), P3–P4 2.211(1), P4–P1 2.176(1), P2–P4 3.074(1); **3a**: As1–As2 2.419(1), As2–As3 2.430(1), As3–P1 2.293(2), P1–As1 2.294(2), As1–As3 3.292(1); **5**: P1–P2 2.1550(1), P2–P3 2.1754(1), P3–P4 2.2122(1), P4–P5 2.1527(1), P5–P6 2.1611(1), P1–P3 3.0125(1), P4–P6 2.8736(1), P1–B1 1.9362(1), P2–B1 1.9663(1).

P distances within the P_4 unit (2.16624(4)–2.21922(3) Å) and the As–As (2.419(1)–2.431(1) Å) as well as As–P (2.291(2)–2.298(2) Å) distances within the As_3P ring are all in the range of a classical single bond,[9] with the ones involving P1 being slightly shorter. However, all P–P bond lengths in **1** and **2** are slightly elongated in comparison to free **A1** or **A2**, but comparably shorter than in **I** and **II**.[3] Additionally, the P–P bond lengths including the P1 atom are the shortest in **1f** (2.13440(3) and 2.13856(1) Å) and they are getting longer the bulkier the substituents are (**1f** < **1g**$_{\mathbf{exo}}$ < **1g**$_{\mathbf{endo}}$ < **1a**). Overall, the central structural motifs are very similar to those of the nickel derivatives **VI**.

The molecular structure in **5** (Figure 1, bottom right) differs significantly from those of **1**–**3** since it shows a dimeric unit, in which two P_3 ligands of **A1** are connected to an unprecedented, catena P_6 ligand *via* a new P–P bond, which bears an additional bromide substituent on the P6 atom. Thereby, the former P1–P3 and P4–P6 bonds are clearly broken, which is indicated by the elongated distances of 3.0125(1) and 2.8736(1) Å, respectively. The remaining P–P bond lengths within the former P_3 ligands (2.1527(1)- 2.1754(1) Å) are all slightly elongated compared to free **A1** but slightly shorter than a single bond,[9] while the newly formed P3–P4 bond (2.2122(1) Å) perfectly fits a single bond. The borinium ion $[BBr_2]^+$ is bridging the P_6 ligand between P1 and P4 leading to a five-membered P_4B cycle. This shows a distorted envelope structure, where the atoms P1, B1, P4 and P3 are almost within one plane and the P2 atom is bent out of that plane. The P–B distances are in the range of a classical single bond, which suggests rather a covalent than a dative character. However, theoretical calculations have to be carried out to affirm this assumption. The Mo–P distances in **1**, **2** and **5** as well as the Mo–As distances in **3** always remain the same as in the respective starting materials.

The complexes **1** and **2** represent very rare examples of ring expansion reactions from strained three-membered cycles to four-membered ones. Furthermore, **3** is the first representative for a ring expansion of a cyclic As_3 unit by a phosphenium ion.

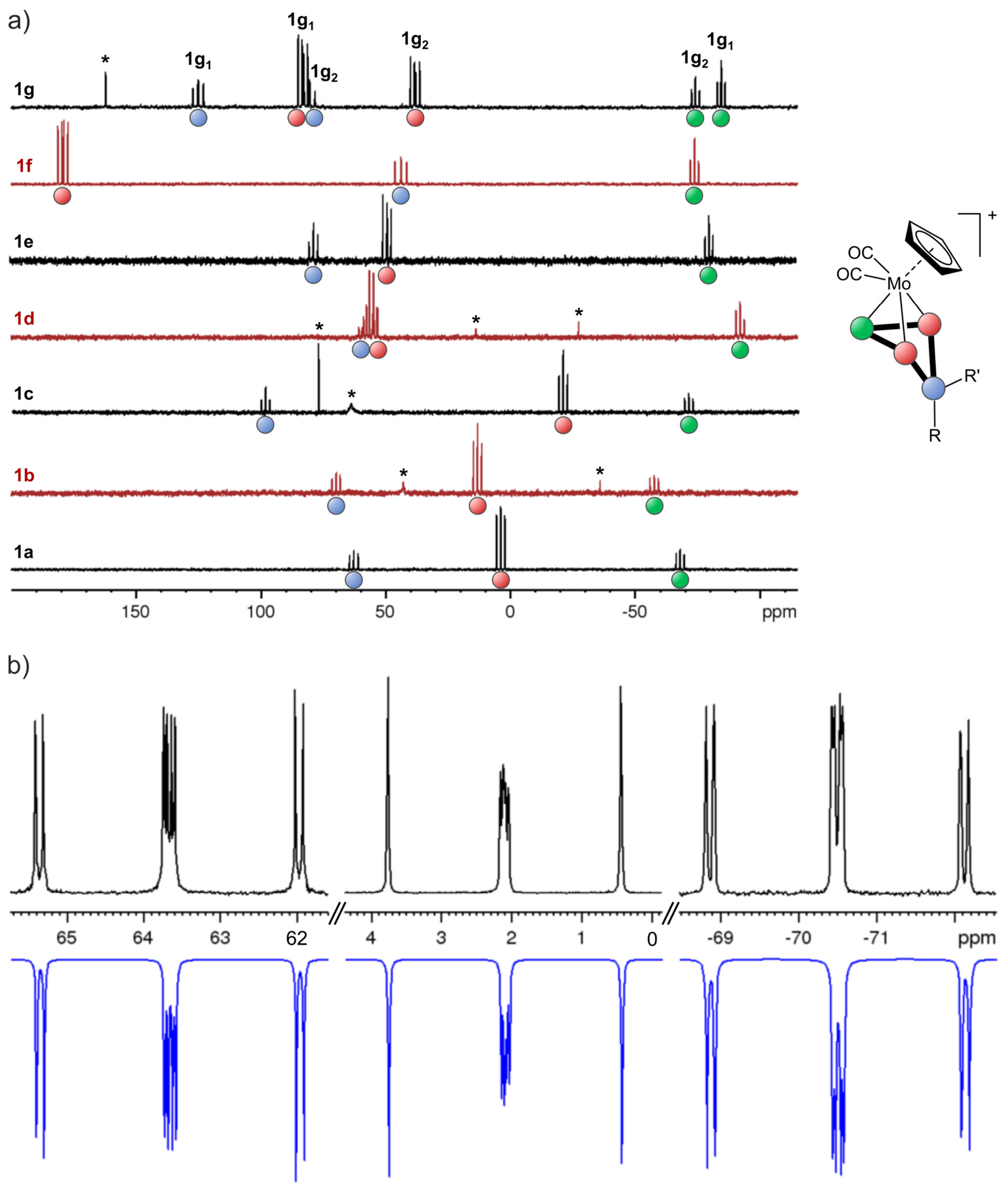

Figure 2: a) $^{31}P\{^1H\}$ NMR spectra of crude solutions of **1a-g** in *o*-DFB/C_6D_6. R = R' = Ph (**1a**), Me (**1b**), Cy (**1c**), Mes (**1d**), 0.5 biphen (**1e**), Br (**1f**); RR' = PhCl (**1g**). Two sets of signals observed for **1g** are labelled as **1g$_1$** and **1g$_2$**, with the former being most probably the *endo*-Ph and the latter the *exo*-Ph isomer (due to steric reasons). * = unidentified impurities or excess halophosphanes in minor ratio. b) $^{31}P\{^1H\}$ NMR spectra of crystalline **1a**[OTf]; top: measured, bottom: simulated.

The $^{31}P\{^1H\}$ NMR spectra of the crude solutions of the products **1a**–**g** all show an AMM'X spin system (Figure 2a), except for **1d** (ABB'X) and **1f** (AA'MX), which is in good agreement with the cyclic P_4R_2 ligands within these compounds. The same is observed in the $^{31}P\{^1H\}$ NMR spectrum of crystalline **1a**[OTf] in CD_2Cl_2 (Figure 2b). The assignment of the signals could be easily accomplished since additional P–H coupling could be observed in the ^{31}P NMR spectra for the signals corresponding to the P1 atom, which carries the organic substituents. The AMM'X spin system consists of a doublet of doublet of doublets (ddd) at δ = −70.5 ppm (P3 atom, green dot), two doublet of doublets at δ = 2.1 ppm (P2/P4 atoms, red dot) and a ddd at δ = 63.7 ppm (P1 atom, blue dot). The splitting patterns and the observed ^1J coupling constants (262–279 Hz) show that the P2 and P4 atoms are not fully magnetically equivalent. Additionally, a ^2J coupling (17 Hz) between P1 and P3 is observed. In contrast to **1a**–**g**, the signals for the P2/P4 (red) and the P1 atom (blue) in **2** are very broad and, therefore, not resolved. In **3a** and **3b** only a singlet for the P1 atom is observed as anticipated. All these reactions execute very selective and quantitative since only in some cases minor impurities were detected. For **1g** two sets of signals in a ratio of 1.6:1 are found suggesting the formation of two isomers, where the phenyl group is either in *endo* or *exo* position, with the *endo* isomer probably being the favoured one due to less steric hindrance. Upon crystallization the ratio of *endo*/*exo* increases to 6:1 (see …. in the Supporting Information). The chemical shifts are in between δ = −90 and 180 ppm (for exact values see the Supporting Information). The $^1J_{P\text{-}P}$ coupling constants in **1a-g** and **2** are slightly larger compared to the isolobal compounds $[P_4(PPh_2)]^+$ (**II**) and $[P_4(PRCl)]^+$,[3a, 4] and the varying sequence of the signals (in addition to electronic effects) may be attributed to similar "cross-ring through space" interactions as reported for $[P_4(PRCl)]^+$ and **VI**.[4-5]

In the ^1H NMR spectrum of **5** two singlets at δ = 5.95 and 6.09 ppm are observed for the Cp ligands. The $^{31}P\{^1H\}$ and ^{31}P NMR spectra reveal five signals at δ = −169.2 (m), −112.8 (dd), −51.2 to −42.8 (m), −9.5 (broad signal) and 79.5 (tqt) with an integral ratio of 1:1:3:1:1. A signal assignment could not be accomplished till the end of this thesis. NMR simulation and variable temperature NMR spectroscopy have to be carried out to get further insights. The $^{11}B\{^1H\}$ and ^{11}B NMR spectra show one triplet at δ = −14.5 ppm with a $^1J_{B\text{-}P}$ = 98 Hz for the B1 atom. Characteristic signals for the Cp ligands and the counterion $[TEF]^-$ are also detected in the $^{13}C\{^1H\}$ and $^{19}F\{^1H\}$ NMR spectra.

As mentioned before no crystals for the methyl (**1b**) and mesityl (**1d**) derivatives could be obtained (due to the formation of an yellow oil upon crystallization). However, after prolonged storage orange red, crystalline sticks are formed within the oil, which could be subjected to single crystal X-ray diffraction. These reveal the decarbonylation products $[\{CpMo(CO)_2(\eta^3\text{-}P_4Me_2)\}\{CpMo(CO)(\eta^3\text{-}P_3)\}][TEF]$ (**6b**[TEF]) and $[\{CpMo(CO)\}_2(\mu,\eta^3:\eta^1:\eta^3:\eta^1\text{-}P_8Mes_4)][TEF]_2$ (**6d**$[TEF]_2$). Compound **6b** (Figure 3, left) consists of one molecule **1b**, which substitutes one CO ligand of the MoP_3 tetrahedron in the starting material **A1** resulting in a new Mo–P bond. Due to a weak X-ray data set no further bond lengths and angles can be discussed. In contrast, the central structural motif in **6d** consists of a P_8 ligand, which contains four mesityl substituents (two on P1 and two on P8) and is coordinated by two [CpMo(CO)] fragments in an $\eta^3:\eta^1$ fashion. The motif is formally derived by the dimerization of two molecules of **1d** under elimination of one CO ligand per unit. Thereby, two new Mo–P bonds (Mo1–P5: 2.4911(1) Å, Mo2–P4: 2.4801(1) Å) are formed, which means that the Mo atoms remain their 18 valence electrons. Furthermore, an additional short P4···P5 contact (2.6439(1) Å) is observed, which is

0.4 Å longer than a respective single bond, but far below the sum of the van der Waals radii (Σ = 3.60 Å).[10] The other P–P distances within the P_4Mes_2 units are similar to those of **1** or **2**. The same is also observed for the Mo–P bond lengths. To gain a better insight into the bonding situation of **6b** and **6d** DFT computations have to be carried out. Also, the question arises, if these complexes can be synthesized selectively and quantitatively from **1b** and **1d** by systematic elimination of CO ligands (*e.g.*, *via* irradiation or heating) and if the complexes **1** with other substituents are also capable of CO elimination, which is part of future investigations.

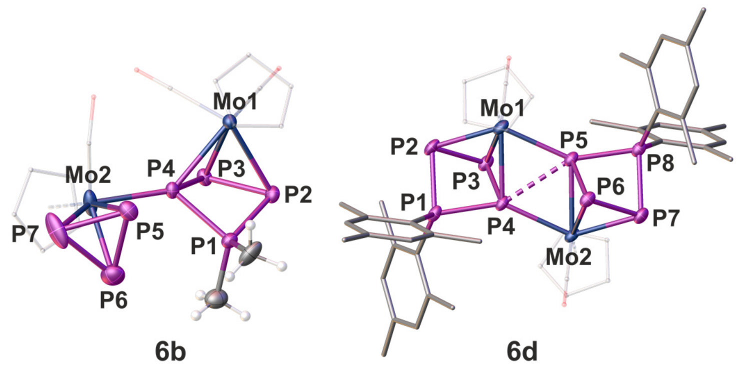

Figure 3: Molecular structures of the decomposition products **6b** and **6d**. Anisotropic displacement is set to the 50% probability level. H atoms, counter ions and solvent molecules are omitted and C as well as O atoms are drawn as small spheres and translucent for clarity. Selected bond lengths [Å] and angles [°]: **6d**: P1–P2 2.240(3), P2–P3 2.170(3), P3–P4 2.172(3), P4–P1 2.208(3), P4–P5 2.639(3), P5–P6 2.170(3), P6–P7 2.176(3), P7–P8 2.241(3), P5–P8 2.207(3), Mo1–P5 2.490(2), Mo2–P4 2.477(2), P2-P3-P4-P5 60.9(1).

9.3 Conclusion

In summary, the tetrahedral compound $[CpMo(CO)_2(\eta^3\text{-}P_3)]$ (**A**), which is isolobal to P_4, depicts an excellent precursor for ring expansion reactions of the P_3 ligand *via* electrophilic functionalization. Reaction of **A** with phosphenium ions gives quantitative access to new cationic polyphosphorus frameworks stabilized in the coordination sphere of $[CpMo(CO)_2]$ moieties. The substituents on the obtained P_4RR' ligand can be varied easily by using different halophosphines as phosphenium ion precursors. These functionalized P_n ligand complexes are very stable and do not undergo rearrangement reactions as analogous nickel complexes.[5] Furthermore, this system is also expandable to the respective As_3 ligand complexes allowing their electrophilic functionalization for the first time yielding unprecedented cationic As_3PR_2 rings. These findings open this area to polyarsenic ligands and it can be expected that this procedure can also be transferred to the analogous Sb_3 complex as well as to other polypnictogen ligand compounds of various ring sizes. In addition, we showed that borinium ions are capable of electrophilic functionalization as well yielding an unprecedented, substituted P_8B ligand upon dimerization. Thus, a large variety of main group electrophiles may be suitable for these reactions, which would give access to a large variety of functionalized E_n ligand complexes in a maintainable way.

9.4 Supporting Information

9.4.1 General remarks

All manipulations were carried out under an inert atmosphere of dried nitrogen/argon using standard Schlenk and glovebox techniques. The used Schlenk flasks were heated at 550 °C for at least 15-30 minutes under reduced pressure prior to use to get rid of water traces adhered to the glass surface. The starting materials [CpMo(CO)$_2$(η^3-P$_3$)] (**A1**),[11] [Cp*Mo(CO)$_2$(η^3-P$_3$)] (**A2**),[12] [CpMo(CO)$_2$(η^3-As$_3$)] (**B1**),[13] [Cp*Mo(CO)$_2$(η^3-As$_3$)] (**B2**),[14] (2,2'-biphen)PCl[15] and Tl[TEF][16] were synthesized according to literature procedures. All other chemicals were purchased from commercial vendors. $GaCl_3$ was sublimed and all halophosphanes as well as the boron tribromide BBr_3 were distilled prior to use. Solvents were freshly distilled under nitrogen after drying over CaH_2 (CH_2Cl_2, CD_2Cl_2), K or Na/K alloy (alkanes), P_4O_{10} (*ortho*-difluorobenzene = *o*-DFB) or NaH (toluene). Dried solvents were also taken from a solvent purification system from MBraun. For NMR spectra of crude solutions a C_6D_6 capillary was used. Filtrations were carried out using a glas fibre filter paper, which was wrapped around one end of a Teflon tube and fixed with a Teflon tape. The tube and filter paper were dried in a heating stove at 170 °C for at least 3h. Then the end with the glas fibre filter paper was put into the crude solution and the solution was transferred into another Schlenk flask by creating an overpressure on the starting side. NMR spectra were recorded at 300 K (if not stated otherwise) on a Bruker Avance 300 MHz NMR spectrometer (^{1}H: 300.132 MHz, ^{31}P: 121.495 MHz, ^{13}C: 75.468 MHz, ^{19}F: 282.404 MHz) or a Bruker Avance 400 MHz NMR spectrometer (^{1}H: 400.130 MHz, ^{31}P: 161.976 MHz, ^{13}C: 100.613 MHz, ^{19}F: 376.498 MHz, ^{11}B: 128.432 MHz) with external references of $SiMe_4$ (^{1}H, ^{13}C), CCl_3F (^{19}F), BF_3 (^{11}B) and H_3PO_4 (85%, ^{31}P). The chemical shifts δ are presented in parts per million (ppm) and coupling constants J in Hz. ESI-MS spectra were either measured on a Finnigan Thermoquest TSQ 7000 mass-spectrometer by the MS department of the University of Regensburg or on a Waters Micromass LCT ESI-TOF mass-spectrometer by the first author. Elemental analyses (EA) were performed by the micro analytical laboratory of the University of Regensburg.

9.4.2 Experimental details

9.4.2.1 Synthesis of the compounds [CpMo(CO)$_2$(η^3-P$_4$RR')][X] (1a-g)

[CpMo(CO)$_2$(η^3-P$_4$Ph$_2$)][OTf] (1a[OTf])

A yellow solution of [CpMo(CO)$_2$(η^3-P$_3$)] (47 mg, 0.15 mmol, 1.0 eq.; **A1**) and Tl[OTf] (63 mg, 0.15 mmol, 1.0 eq.) in 15 mL CH_2Cl_2 was stirred for 30 minutes before a colourless solution of PPh_2Cl in toluene (c = 0.122M, 1.23 mL, 0.15 mmol, 1.0 eq.) was added, which led to precipitation of white powder in the course of 5 minutes and the solution slightly brightens. The suspension was stirred for 1h, the amount of solvent reduced to 5 mL and filtered through glas fibre filter paper. Crystallization *via* layering the solution with *n*-hexane (5x) and storage at 4 °C for five days yielded pure **1a**[OTf] as yellow blocks suitable for single crystal X-ray diffraction. The solvent was removed by decanting and the crystals dried in vacuum for 3h.

Yield 87 mg (0.135 mmol = 90 %). ^{1}H NMR (CD_2Cl_2) δ/ppm = 5.83 (s, 5 H, Cp), 7.71 (m, 10 H, Ph). ^{31}P{^{1}H} NMR (CD_2Cl_2) δ/ppm = −70.5 (ddd, $^{1}J_{P3\text{-}P2/P4}$ = 268 Hz, $^{1}J_{P3\text{-}P2/P4}$ = 262 Hz, $^{2}J_{P3\text{-}P1}$ = 17 Hz, 1 P, P3 atom), 2.1 (two dd, $^{1}J_{P2/P4\text{-}P1}$ = 279 Hz, $^{1}J_{P2/P4\text{-}P1}$ = 273 Hz, $^{1}J_{P2/P4\text{-}P3}$ = 268 Hz, $^{1}J_{P2/P4\text{-}P3}$ = 262 Hz, 2 P, P2/P4 atoms), 63.7 (ddd, $^{1}J_{P1\text{-}P2/P4}$ = 279 Hz, $^{1}J_{P1\text{-}P2/P4}$ = 273 Hz, $^{2}J_{P1\text{-}P3}$ = 17 Hz, 1 P, P1 atom). ^{31}P NMR (CD_2Cl_2) δ/ppm = −70.5 (ddd, $^{1}J_{P3\text{-}P2/P4}$ = 267 Hz, $^{1}J_{P3\text{-}P2/P4}$ = 262 Hz, $^{2}J_{P3\text{-}P1}$ = 17 Hz, 1 P, P3 atom), 2.1 (two dd, $^{1}J_{P2/P4\text{-}P1}$ = 279 Hz, $^{1}J_{P2/P4\text{-}P1}$ = 272 Hz, $^{1}J_{P2/P4\text{-}P3}$ = 267 Hz, $^{1}J_{P2/P4\text{-}P3}$ = 262 Hz, 2 P, P2/P4 atoms), 63.7 (m (additional $^{3}J_{P\text{-}H}$ coupling to the protons of the phenyl rings), 1 P, P1 atom). ^{13}C{^{1}H} NMR (CD_2Cl_2) δ/ppm = 87.55 (s), 92.57 (s), 131.76 (ddd) 135.65 (d), 218.99 (s, CO). ^{19}F{^{1}H} NMR (CD_2Cl_2) δ/ppm = −77.1 (s, OTf).

[CpMo(CO)$_2$(η^3-P$_4$Ph$_2$)][TEF] (1a[TEF])

Synthesis of **1a**[TEF] was only conducted on an NMR scale for the purpose of the screening of different phosphenium ions:

A yellow solution of [CpMo(CO)$_2$(η^3-P$_3$)] (15 mg, 0.05 mmol, 1.0 eq.; **A1**) and Tl[TEF] (59 mg, 0.05 mmol, 1.0 eq.) in 5 mL *o*-DFB was stirred for 30 minutes before a colourless solution of PPh_2Cl in toluene (*c* = 0.2M, 0.25 mL, 0.05 mmol, 1.0 eq.) was added, which led to immediate precipitation of white powder and the solution slightly brightens. The suspension was stirred for 1h and filtered through glas fibre filter paper. The solvent was removed by evaporation and the yellow powder of **1a**[TEF] was dried in vacuum for 3h. All attempts to obtain single crystals of **1a**[TEF], however, failed.
Yield 57 mg (0.039 mmol = 78 %). ^{31}P{^{1}H} NMR of the crude solution (*o*-DFB/C_6D_6) δ/ppm = −68.2 (td, $^{1}J_{P3\text{-}P2/P4}$ = 265 Hz, $^{2}J_{P3\text{-}P1}$ = 17 Hz, 1 P, P3 atom), 3.7 (dd/pt, $^{1}J_{P2/P4\text{-}P1}$ = 278 Hz, $^{1}J_{P2/P4\text{-}P3}$ = 265 Hz, 2 P, P2/P4 atoms), 62.6 (ddd, $^{1}J_{P1\text{-}P2/P4}$ = 278 Hz, $^{1}J_{P1\text{-}P2/P4}$ = 272 Hz, $^{2}J_{P1\text{-}P3}$ = 17 Hz, 1 P, P1 atom). ^{31}P NMR of the crude solution (*o*-DFB/C_6D_6) δ/ppm = −68.2 (td, $^{1}J_{P3\text{-}P2/P4}$ = 263 Hz, $^{2}J_{P3\text{-}P1}$ = 17 Hz, 1 P, P3 atom), 3.7 (dd/pt, $^{1}J_{P2/P4\text{-}P1}$ = 278 Hz, $^{1}J_{P2/P4\text{-}P3}$ = 263 Hz, 2 P, P2/P4 atoms), 62.6 (m (additional $^{3}J_{P\text{-}H}$ coupling to the protons of the phenyl rings), 1 P, P1 atom). ^{19}F{^{1}H} NMR (*o*-DFB/C_6D_6) δ/ppm = −75.5 (s, CF_3).

[CpMo(CO)$_2$(η^3-P$_4$Ph$_2$)][GaCl$_4$] (1a[GaCl$_4$])

A colourless solution of PPh_2Cl in toluene (*c* = 0.2M, 0.5 mL, 0.10 mmol, 1.0 eq.) was transferred onto a yellow solution of [CpMo(CO)$_2$(η^3-P$_3$)] (32 mg, 0.10 mmol, 1.0 eq.; **A1**) in 5 mL *o*-DFB. To this solution $GaCl_3$ (18 mg, 0.10 mmol, 1.0 eq.) in 5 ml *o*-DFB was added and the solution was stirred for 18h (when $GaCl_3$ is added to **A1** in the absence of a halophosphane immediately orange precipitate is formed, which can be probably attributed to the adduct complex of **A1** and $GaCl_3$). The solution was filtered through glas fibre filter paper to get rid of potential impurities and layered with *n*-hexane (4x). Storage at room temperature for five days yielded pure **1a**[GaCl$_4$] as yellow, crystalline needles suitable for single crystal X-ray diffraction. The solvent was removed by decanting and the crystals dried in vacuum for 3h.
Yield 68 mg (0.096 mmol = 96 %). ^{31}P{^{1}H} NMR of the crude solution (*o*-DFB/C_6D_6) δ/ppm = −69.3 (td, $^{1}J_{P3\text{-}P2/P4}$ = 263 Hz, $^{2}J_{P3\text{-}P1}$ = 17 Hz, 1 P, P3 atom), 3.4 (dd/pt, $^{1}J_{P2/P4\text{-}P1}$ = 279 Hz, $^{1}J_{P2/P4\text{-}P3}$ = 263 Hz, 2 P, P2/P4 atoms), 62.3 (ddd, $^{1}J_{P1\text{-}P2/P4}$ = 279 Hz, $^{1}J_{P1\text{-}P2/P4}$ = 273 Hz, $^{2}J_{P1\text{-}P3}$ = 17 Hz, 1 P, P1 atom). ^{31}P NMR of the crude solution (*o*-DFB/C_6D_6) δ/ppm = −69.3 (td, $^{1}J_{P3\text{-}P2/P4}$ = 263 Hz, $^{2}J_{P3\text{-}P1}$ = 17 Hz, 1 P, P3 atom),

3.4 (dd/pt, $^{1}J_{P2/P4\text{-}P1}$ = 279 Hz, $^{1}J_{P2/P4\text{-}P3}$ = 263 Hz, 2 P, P2/P4 atoms), 62.3 (m (additional $^{3}J_{P\text{-}H}$ coupling to the protons of the phenyl rings), 1 P, P1 atom). Anal. calcd. for $[C_{19}H_{15}O_2MoP_4][GaCl_4]$: C: 32.29, H: 2.14. Found: C: 32.29, H: 2.03.

$[CpMo(CO)_2(\eta^3\text{-}P_4Me_2)][TEF]$ (1b[TEF])

Synthesis of **1b**[TEF] was only conducted on an NMR scale for the purpose of the screening of different phosphenium ions:

A yellow solution of $[CpMo(CO)_2(\eta^3\text{-}P_3)]$ (16 mg, 0.05 mmol, 1.0 eq.; **A1**) and $Tl[TEF]\cdot(CH_2Cl_2)$ (64 mg, 0.05 mmol, 1.0 eq.) in 5 mL *o*-DFB was stirred for 30 minutes before a colourless solution of PMe_2Cl in toluene (*c* = 0.122M, 0.43 mL, 0.05 mmol, 1.0 eq.) was added, which led to immediate precipitation of white powder and the solution brightens to pale yellow. The suspension was stirred for 24h and filtered through glas fibre filter paper directly underneath pure *n*-pentane. Storage at room temperature only led to the formation of a yellow oil containing pure **1b**[TEF]. Recrystallization of the oil by redissolving in 10 mL CH_2Cl_2, layering with *n*-hexane and storage at 4°C for three days again led to the formation of an yellow oil. However, after several months of storage crystals in form of orange to red sticks of $[\{CpMo(CO)_2(\eta^3\text{-}P_4Me_2)\}\{CpMo(CO)(\eta^3\text{-}P_3)\}][TEF]$ (**6b**[TEF]) were formed, which were suitable for single crystal X-ray diffraction. The crystals were manually separated from the oil and dried in vacuum for 3h.
$^{31}P\{^{1}H\}$ NMR of the crude solution (*o*-DFB/C_6D_6) δ/ppm = −57.5 (ddd, $^{1}J_{P3\text{-}P2/P4}$ = 272 Hz, $^{1}J_{P3\text{-}P2/P4}$ = 265 Hz, $^{2}J_{P3\text{-}P1}$ = 21 Hz, 1 P, P3 atom), 13.2 (dd/pt, $^{1}J_{P2/P4\text{-}P1}$ = 257 Hz, $^{1}J_{P2/P4\text{-}P3}$ = 271 Hz, 2 P, P2/P4 atoms), 69.9 (ddd, $^{1}J_{P1\text{-}P2/P4}$ = 264 Hz, $^{1}J_{P1\text{-}P2/P4}$ = 257 Hz, $^{2}J_{P1\text{-}P3}$ = 22 Hz, 1 P, P1 atom). $^{31}P\{^{1}H\}$ NMR of the crude solution (*o*-DFB/C_6D_6) δ/ppm = −57.5 (td, $^{1}J_{P3\text{-}P2/P4}$ = 267 Hz, $^{2}J_{P3\text{-}P1}$ = 21 Hz, 1 P, P3 atom), 13.2 (pt, $^{1}J_{P2/P4\text{-}P1/P3}$ = 267 Hz, 2 P, P2/P4 atoms), 69.9 (m (additional $J_{P\text{-}H}$ coupling to the protons of the methyl groups), 1 P, P1 atom). $^{19}F\{^{1}H\}$ NMR (*o*-DFB/C_6D_6) δ/ppm = −75.5 (s, CF_3).
6b[TEF]: Yield 7 mg (0.004 mmol = 8 % referred to **A1**). Anal. calcd. for $[Cp_2Mo_2(CO)_3P_7Me_2][TEF]$: C: 22.98, H: 1.00. Found: C: 21.89, H: 1.16.

$[CpMo(CO)_2(\eta^3\text{-}P_4Cy_2)][TEF]$ (1c[TEF])

Synthesis of **1c**[TEF] was only conducted on an NMR scale for the purpose of the screening of different phosphenium ions:

A yellow solution of $[CpMo(CO)_2(\eta^3\text{-}P_3)]$ (16 mg, 0.05 mmol, 1.0 eq.; **A1**) and $Tl[TEF]\cdot(CH_2Cl_2)$ (64 mg, 0.05 mmol, 1.0 eq.) in 5 mL *o*-DFB was stirred for 30 minutes before a colourless solution of PCy_2Cl in toluene (*c* = 0.1M, 0.5 mL, 0.05 mmol, 1.0 eq.) was added, which led to immediate precipitation of white powder and the solution brightens to pale yellow. The suspension was stirred for 24h and filtered through glas fibre filter paper directly underneath pure *n*-pentane. Storage at room temperature only led to the formation of a yellow oil containing pure **1c**[TEF]. All attempts to obtain single crystals of **1c**[TEF], however, failed.
$^{31}P\{^{1}H\}$ NMR of the crude solution (*o*-DFB/C_6D_6) δ/ppm = −68.8 (ddd, $^{1}J_{P3\text{-}P2/P4}$ = 273 Hz, $^{1}J_{P3\text{-}P2/P4}$ = 264 Hz, $^{2}J_{P3\text{-}P1}$ = 16 Hz, 1 P, P3 atom), −19.4 (pt, $^{1}J_{P2/P4\text{-}P1}$ = 266 Hz, 2 P, P2/P4 atoms), 97.6 (td, $^{1}J_{P1\text{-}P2/P4}$ = 266Hz, $^{2}J_{P1\text{-}P3}$ = 16 Hz, 1 P, P1 atom). ^{31}P NMR of the crude solution (*o*-DFB/C_6D_6) δ/ppm = −68.8 (ddd, $^{1}J_{P3\text{-}P2/P4}$ = 273 Hz, $^{1}J_{P3\text{-}P2/P4}$ = 264 Hz, $^{2}J_{P3\text{-}P1}$ = 16 Hz, 1 P, P3 atom), −19.4 (pt,

$^{1}J_{P2/P4\text{-}P1}$ = 266 Hz, 2 P, P2/P4 atoms), 97.6 (m (additional $J_{P\text{-}H}$ coupling to the protons of the cyclohexyl rings), 1 P, P1 atom). $^{19}F\{^{1}H\}$ NMR (*o*-DFB/C_6D_6) δ/ppm = −75.5 (s, CF_3).

[CpMo(CO)$_2$(η^3-P_4Mes_2)][TEF] (1d[TEF])

Synthesis of **1d**[TEF] was only conducted on an NMR scale for the purpose of the screening of different phosphenium ions:

A yellow solution of [CpMo(CO)$_2$(η^3-P_3)] (18 mg, 0.058 mmol, 1.0 eq.; **A1**) and Tl[TEF]·(CH_2Cl_2) (70 mg, 0.056 mmol, 1.0 eq.) in 5 mL *o*-DFB was stirred for 30 minutes before a colourless solution of $PMes_2Cl$ in toluene (*c* = 0.05M, 1.05 mL, 0.053 mmol, 1.0 eq.) was added, which led to immediate precipitation of white powder and the solution brightens to pale yellow. The suspension was stirred for 24h and filtered through glas fibre filter paper directly underneath pure *n*-hexane. Storage at room temperature only led to the formation of a yellow oil containing pure **1d**[TEF]. Recrystallization of the oil by redissolving in 10 mL CH_2Cl_2, layering with *n*-hexane and storage at 4°C for three days again led to the formation of an yellow oil. However, after several months of storage crystals in form of orange to red sticks of [{CpMo(CO)}$_2$(μ,η^3:η^1:η^3:η^1-P_8Mes_4)][TEF]$_2$ (**6d**[TEF]$_2$) were formed, which were suitable for single crystal X-ray diffraction. The crystals were manually separated from the oil and dried in vacuum for 3h.

$^{31}P\{^{1}H\}$ NMR of the crude solution (*o*-DFB/C_6D_6) δ/ppm = −92.3 (m, 1 P, P3 atom), 53.0–60.8 (m, 3 P, P2/P4 and P1). ^{31}P NMR of the crude solution (*o*-DFB/C_6D_6) δ/ppm = −92.3 (m, 1 P, P3 atom), 53.0–60.8 (m, 3 P, P2/P4 and P1). $^{19}F\{^{1}H\}$ NMR (*o*-DFB/C_6D_6) δ/ppm = −75.5 (s, CF_3).

6d[TEF]$_2$: Yield 4 mg (0.0013 mmol = 5 % referred to $PMes_2Cl$). Anal. calcd. for [$Cp_2Mo_2(CO)_2P_8Mes_4$][TEF]$_2$: C: 31.64, H: 1.79. Found: C: 32.57, H: 1.73.

[CpMo(CO)$_2$(η^3-P_4biphen)][TEF] (1e[TEF])

Synthesis of **1e**[TEF] was only conducted on an NMR scale for the purpose of the screening of different phosphenium ions:

A yellow solution of [CpMo(CO)$_2$(η^3-P_3)] (18 mg, 0.058 mmol, 1.0 eq.; **A1**) and Tl[TEF]·(CH_2Cl_2) (70 mg, 0.056 mmol, 1.0 eq.) in 5 mL *o*-DFB was stirred for 30 minutes before a colourless solution of P(biphen)Cl (12.5 mg, 0.058 mmol, 1.0 eq.) in 2 mL *o*-DFB was added, which led to immediate precipitation of white powder and the colour changes to orange yellow. The suspension was stirred for 24h and filtered through glas fibre filter paper directly underneath pure *n*-pentane. Storage at room temperature only led to the formation of a yellow oil containing pure **1e**[TEF]. All attempts to obtain single crystals of **1e**[TEF], however, failed.

$^{31}P\{^{1}H\}$ NMR of the crude solution (*o*-DFB/C_6D_6) δ/ppm = −80.0 (td, $^{1}J_{P3\text{-}P2/P4}$ = 260 Hz, $^{2}J_{P3\text{-}P1}$ = 21 Hz, 1 P, P3 atom), 48.9 (two dd, $^{1}J_{P2/P4\text{-}P1}$ = 290 Hz, $^{1}J_{P2/P4\text{-}P1}$ = 284 Hz, $^{1}J_{P2/P4\text{-}P3}$ = 266 Hz, $^{1}J_{P2/P4\text{-}P3}$ = 252 Hz, 2 P, P2/P4 atoms), 78.4 (ddd, $^{1}J_{P1\text{-}P2/P4}$ = 297Hz, $^{1}J_{P1\text{-}P2/P4}$ = 281Hz, $^{2}J_{P1\text{-}P3}$ = 21 Hz, 1 P, P1 atom). ^{31}P NMR of the crude solution (*o*-DFB/C_6D_6) δ/ppm = −80.0 (td, $^{1}J_{P3\text{-}P2/P4}$ = 260 Hz, $^{2}J_{P3\text{-}P1}$ = 21 Hz, 1 P, P3 atom), 48.9 (two dd, $^{1}J_{P2/P4\text{-}P1}$ = 290 Hz, $^{1}J_{P2/P4\text{-}P1}$ = 284 Hz, $^{1}J_{P2/P4\text{-}P3}$ = 266 Hz, $^{1}J_{P2/P4\text{-}P3}$ = 252 Hz, 2 P, P2/P4 atoms), 78.4 (m (additional $J_{P\text{-}H}$ coupling to the protons of the biphenyl rings), 1 P, P1 atom). $^{19}F\{^{1}H\}$ NMR (*o*-DFB/C_6D_6) δ/ppm = −75.5 (s, CF_3).

[CpMo(CO)$_2$(η^3-P$_4$Br$_2$)][TEF] (1f[TEF])

A yellow solution of [CpMo(CO)$_2$(η^3-P$_3$)] (31 mg, 0.1 mmol, 1.0 eq.; **A1**) and Tl[TEF]·(CH$_2$Cl$_2$) (126 mg, 0.1 mmol, 1.0 eq.) in 5 mL *o*-DFB was stirred for 30 minutes before pure PBr$_3$ (12 µL, 0.1 mmol, 1.0 eq.) was added, which led to immediate precipitation of white powder. The suspension was stirred for 24h leading to a colour change to ochre, and filtered through glas fibre filter paper. The solution was layered with *n*-hexane and storage at room temperature for two weeks yielded pure **1f**[TEF] as dark yellow to orange sticks and blocks suitable for single crystal X-ray diffraction. The solvent was removed by decanting and the crystals dried in vacuum for 3h.

Yield 110 mg (0.075 mmol = 75 %). ^{1}H NMR (CD$_2$Cl$_2$) δ/ppm = 6.22 (s, Cp). ^{31}P{^{1}H} NMR of crystalline **1f**[TEF] (CD$_2$Cl$_2$) δ/ppm = −73.7 (td, $^1J_{P3\text{-}P2/P4}$ = 257 Hz, $^2J_{P3\text{-}P1}$ = 27 Hz, 1 P, P3 atom), 43.9 (ddd, $^1J_{P1\text{-}P2/P4}$ = 384Hz, $^1J_{P1\text{-}P2/P4}$ = 377Hz, $^2J_{P1\text{-}P3}$ = 27 Hz, 1 P, P1 atom), 179.2 (dd, $^1J_{P2/P4\text{-}P1}$ = 381 Hz, $^1J_{P2/P4\text{-}P3}$ = 257 Hz, 2 P, P2/P4 atoms). ^{31}P{^{1}H} NMR of crystalline **1f**[TEF] (CD$_2$Cl$_2$) δ/ppm = −73.7 (td, $^1J_{P3\text{-}P2/P4}$ = 257 Hz, $^2J_{P3\text{-}P1}$ = 27 Hz, 1 P, P3 atom), 43.9 (ddd, $^1J_{P1\text{-}P2/P4}$ = 384Hz, $^1J_{P1\text{-}P2/P4}$ = 377Hz, $^2J_{P1\text{-}P3}$ = 27 Hz, 1 P, P1 atom), 179.2 (dd, $^1J_{P2/P4\text{-}P1}$ = 381 Hz, $^1J_{P2/P4\text{-}P3}$ = 257 Hz, 2 P, P2/P4 atoms). ^{19}F{^{1}H} NMR (CD$_2$Cl$_2$) δ/ppm = −75.5 (s, CF$_3$). ^{13}C{^{1}H} NMR (CD$_2$Cl$_2$) δ/ppm = 91.89 (s, Cp), 121.12 (q, $^1J_{CF}$ = 292 Hz; CF$_3$), CO signals to small. Anal. calcd. for [C$_7$H$_5$O$_2$MoP$_4$Br$_2$][TEF]: C: 18.82, H: 0.34. Found: C: 19.04, H: 0.42. Positive ion ESI-MS *m/z* (%): several not assignable. Negative ion ESI-MS *m/z* (%): 966.9 (100) [TEF]$^-$.

[CpMo(CO)$_2$(η^3-P$_4$PhCl)][TEF] (1g[TEF])

A yellow solution of [CpMo(CO)$_2$(η^3-P$_3$)] (31 mg, 0.1 mmol, 1.0 eq.; **A1**) and Tl[TEF] (118 mg, 0.1 mmol, 1.0 eq.) in 5 mL *o*-DFB was stirred for 30 minutes before a solution of PPhCl$_2$ in toluene (*c* = 0.147M, 0.68 mL, 0.1 mmol, 1.0 eq.) was added, which led to immediate precipitation of white powder and the solution brightens to an almost colourless solution. ^{31}P NMR spectroscopy reveals the presence of **1g$_{endo}$**[TEF]/**1g$_{exo}$**[TEF] in ratio of 1.6:1. The suspension was stirred for 24h and filtered through glas fibre filter paper directly underneath pure *n*-pentane. Storage at 4 °C for two weeks yielded a yellow oil and few colourless blocks of pure **1g$_{exo}$**[TEF] suitable for single crystal X-ray diffraction. The solvent was removed by decanting and the crystals as well as the oil dried in vacuum for 3h. ^{31}P NMR spectroscopy of the crystals and the oil reveals the presence of **1g$_{endo}$**[GaCl$_4$]/**1g$_{exo}$**[GaCl$_4$] in ratio of ~6:1.

Similar reaction with two equivalents of Tl[TEF] did not yield the abstraction of the second chloride atom and also **1g$_{endo}$**[TEF]/**1g$_{exo}$**[TEF] in a ratio of roughly 1:1 was obtained.

Yield 110 mg (0.075 mmol = 75 %). ^{1}H NMR (CD$_2$Cl$_2$) δ/ppm = 5.64 (s, 5H, Cp$_{exo}$), 6.22 (s, 5H, Cp$_{endo}$), 7.08-7.28 (m, 3H, Ph$_{o,p;exo}$), 7.37-7.44 (m, 2H, Ph$_{m;exo}$), 7.71-7.89 (m, 3H, Ph$_{o,p;endo}$), 8.17-8.27 (m, 2H, Ph$_{m;endo}$). ^{31}P{^{1}H} NMR of crystalline/oily **1g**[TEF] (CD$_2$Cl$_2$): two sets of signals in a ratio of ≈6:1 are observed, which are assigned to **1g$_{endo}$** and **1g$_{exo}$**: δ/ppm = −82.1 (td, $^1J_{P3\text{-}P2/P4}$ = 259 Hz, $^2J_{P3\text{-}P1}$ = 31 Hz, 1 P, P3$_{endo}$ atom), −72.3 (td, $^1J_{P3\text{-}P2/P4}$ = 261 Hz, $^2J_{P3\text{-}P1}$ = 21 Hz, 1 P, P3$_{exo}$ atom), 36.2 (two dd, $^1J_{P1\text{-}P2/P4}$ = 348 Hz, $^1J_{P1\text{-}P2/P4}$ = 334 Hz, $^1J_{P2/P4\text{-}P3}$ = 264 Hz, $^1J_{P2/P4\text{-}P3}$ = 255 Hz, 2 P, P2$_{exo}$/P4$_{exo}$ atoms), 80.4 (two dd, $^1J_{P1\text{-}P2/P4}$ = 357 Hz, $^1J_{P1\text{-}P2/P4}$ = 345 Hz, $^1J_{P2/P4\text{-}P3}$ = 263 Hz, $^1J_{P2/P4\text{-}P3}$ = 254 Hz, 2 P, P2$_{endo}$/P4$_{endo}$ atoms), 81.7 (ddd, $^1J_{P1\text{-}P2/P4}$ = 351 Hz, $^1J_{P1\text{-}P2/P4}$ = 334 Hz, $^2J_{P1\text{-}P3}$ = 21 Hz, 1 P, P1$_{exo}$ atom), 127.0 (ddd, $^1J_{P1\text{-}P2/P4}$ = 357 Hz, $^1J_{P1\text{-}P2/P4}$ = 345 Hz, $^2J_{P1\text{-}P3}$ = 31 Hz, 1 P, P1$_{endo}$ atom). ^{31}P NMR of crystalline/oily **1g**[TEF] (CD_2Cl_2): δ/ppm = −82.1 (td, $^1J_{P3\text{-}P2/P4}$ = 259 Hz, $^2J_{P3\text{-}P1}$ = 31 Hz, 1 P, P3$_{endo}$ atom), −72.3 (td, $^1J_{P3\text{-}P2/P4}$ = 261 Hz, $^2J_{P3\text{-}P1}$ = 22 Hz, 1 P, P3$_{exo}$ atom), 36.2 (two dd, $^1J_{P1\text{-}P2/P4}$ = 348 Hz, $^1J_{P1\text{-}P2/P4}$ = 334 Hz, $^1J_{P2/P4\text{-}P3}$ = 264 Hz, $^1J_{P2/P4\text{-}P3}$ = 255 Hz, 2 P, P2$_{exo}$/P4$_{exo}$ atoms), 80.4 (two dd, $^1J_{P1\text{-}P2/P4}$ = 357 Hz, $^1J_{P1\text{-}P2/P4}$ = 345 Hz, $^1J_{P2/P4\text{-}P3}$ = 263 Hz, $^1J_{P2/P4\text{-}P3}$ = 254 Hz, 2 P, P2$_{endo}$/P4$_{endo}$ atoms), 81.7 (m (additional $J_{P\text{-}H}$ coupling (16 Hz) to the protons of the phenyl ring), 1 P, P1$_{exo}$ atom), 127.0 (m (additional $J_{P\text{-}H}$ coupling (16 Hz) to the protons of the phenyl ring), 1 P, P1$_{endo}$ atom). $^{31}P\{^1H\}$ NMR of the crude solution of **1g**[TEF] (*o*-DFB/C_6D_6): two sets of signals in a ratio of ≈1.6:1 are observed, which are assigned to **1g$_{endo}$** and **1g$_{exo}$**: δ/ppm = −84.4 (td, $^1J_{P3\text{-}P2/P4}$ = 259 Hz, $^2J_{P3\text{-}P1}$ = 31 Hz, 1 P, P3$_{endo}$ atom), −74.1 (td, $^1J_{P3\text{-}P2/P4}$ = 261 Hz, $^2J_{P3\text{-}P1}$ = 21 Hz, 1 P, P3$_{exo}$ atom), 38.2 (two dd, $^1J_{P1\text{-}P2/P4}$ = 348 Hz, $^1J_{P1\text{-}P2/P4}$ = 334 Hz, $^1J_{P2/P4\text{-}P3}$ = 264 Hz, $^1J_{P2/P4\text{-}P3}$ = 255 Hz, 2 P, P2$_{exo}$/P4$_{exo}$ atoms), 81.7 (ddd, $^1J_{P1\text{-}P2/P4}$ = 351 Hz, $^1J_{P1\text{-}P2/P4}$ = 334 Hz, $^2J_{P1\text{-}P3}$ = 21 Hz, 1 P, P1$_{exo}$ atom), 83.2 (two dd, $^1J_{P1\text{-}P2/P4}$ = 357 Hz, $^1J_{P1\text{-}P2/P4}$ = 345 Hz, $^1J_{P2/P4\text{-}P3}$ = 263 Hz, $^1J_{P2/P4\text{-}P3}$ = 254 Hz, 2 P, P2$_{endo}$/P4$_{endo}$ atoms), 125.0 (ddd, $^1J_{P1\text{-}P2/P4}$ = 357 Hz, $^1J_{P1\text{-}P2/P4}$ = 345 Hz, $^2J_{P1\text{-}P3}$ = 31 Hz, 1 P, P1$_{endo}$ atom). $^{31}P\{^1H\}$ NMR of the crude solution of **1g**[TEF] (*o*-DFB/C_6D_6): δ/ppm = −84.4 (td, $^1J_{P3\text{-}P2/P4}$ = 259 Hz, $^2J_{P3\text{-}P1}$ = 31 Hz, 1 P, P3$_{endo}$ atom), −74.1 (td, $^1J_{P3\text{-}P2/P4}$ = 261 Hz, $^2J_{P3\text{-}P1}$ = 21 Hz, 1 P, P3$_{exo}$ atom), 38.2 (two dd, $^1J_{P1\text{-}P2/P4}$ = 348 Hz, $^1J_{P1\text{-}P2/P4}$ = 334 Hz, $^1J_{P2/P4\text{-}P3}$ = 264 Hz, $^1J_{P2/P4\text{-}P3}$ = 255 Hz, 2 P, P2$_{exo}$/P4$_{exo}$ atoms), 81.7 (m (additional $J_{P\text{-}H}$ coupling (16 Hz) to the protons of the phenyl ring), 1 P, P1$_{exo}$ atom), 83.2 (two dd, $^1J_{P1\text{-}P2/P4}$ = 357 Hz, $^1J_{P1\text{-}P2/P4}$ = 345 Hz, $^1J_{P2/P4\text{-}P3}$ = 263 Hz, $^1J_{P2/P4\text{-}P3}$ = 254 Hz, 2 P, P2$_{endo}$/P4$_{endo}$ atoms), 125.0 (m (additional $J_{P\text{-}H}$ coupling (16 Hz) to the protons of the phenyl ring), 1 P, P1$_{endo}$ atom). $^{19}F\{^1H\}$ NMR (CD_2Cl_2) δ/ppm = −75.5 (s, CF_3). $^{13}C\{^1H\}$ NMR (CD_2Cl_2) δ/ppm = 91.89 (s, Cp), 121.12 (q, $^1J_{CF}$ = 292 Hz; CF_3), CO signals to small.

[CpMo(CO)$_2$(η^3-P$_4$PhCl)][OTf] (1g[OTf])

A yellow solution of [CpMo(CO)$_2$(η^3-P$_3$)] (31 mg, 0.1 mmol, 1.0 eq.; **A1**) and Tl[OTf] (71 mg, 0.2 mmol, 2.0 eq.) in 20 mL CH_2Cl_2 was stirred for 15h before a solution of $PPhCl_2$ in toluene (c = 0.147M, 0.68 mL, 0.1 mmol, 1.0 eq.) was added, which led to precipitation of white powder in the course of 3 minutes. The solution was stirred for 7h leading to a colour change to almost colourless. The suspension was concentrated to 5 mL, filtered through glas fibre filter paper and layered with *n*-hexane. Storage at 4 °C for two weeks yielded yellow crystals of **1g$_{endo}$**[OTf] suitable for single crystal X-ray diffraction. The crystals, however, quickly melt at air, for which reason mounting has to be done very fast. The solvent was removed by decanting and the crystals dried in vacuum for 3h.

[CpMo(CO)$_2$(η^3-P$_4$PhCl)][GaCl$_4$] (1g[GaCl$_4$])

A solution of $PPhCl_2$ in toluene (c = 0.147M, 0.68 mL, 0.1 mmol, 1.0 eq.) was added to a yellow solution of [CpMo(CO)$_2$(η^3-P$_3$)] (31 mg, 0.1 mmol, 1.0 eq.; **A1**) in 5 mL *o*-DFB and stirred for 15 minutes before a solution of $GaCl_3$ (18 mg, 0.1 mmol, 1.0 eq.) in 5mL *o*-DFB was added (when $GaCl_3$ is added to **A1** in the absence of a halophosphane immediately orange precipitate is formed, which can be probably attributed to the adduct complex of **A1** and $GaCl_3$). The solution slightly gets darker (dark yellow) and small amounts of orange solid precipitates (probably the adduct complex of **A1** and $GaCl_3$), which almost redissolves upon stirring for 24h.

^{31}P NMR spectroscopy reveals the presence of **1g**$_{\mathbf{endo}}$[$GaCl_4$]/**1g**$_{\mathbf{exo}}$[$GaCl_4$] in ratio of ≈6:1. The supernatant was decanted and layered with *n*-pentane yielding a yellow oil. All attempts to afford crystals, however, failed.
^{31}P{^{1}H} NMR of the crude solution of **1g**[TEF] (*o*-DFB/C_6D_6): two sets of signals in a ratio of ≈6:1 are observed, which are assigned to **1g**$_{\mathbf{endo}}$ and **1g**$_{\mathbf{exo}}$: δ/ppm = −84.4 (td, $^1J_{P3\text{-}P2/P4}$ = 256 Hz, $^2J_{P3\text{-}P1}$ = 31 Hz, 1 P, P3$_{endo}$ atom), −76.0 (td, $^1J_{P3\text{-}P2/P4}$ = 255 Hz, $^2J_{P3\text{-}P1}$ = 21 Hz, 1 P, P3$_{exo}$ atom), 38.5 (two dd, $^1J_{P1\text{-}P2/P4}$ = 346 Hz, $^1J_{P1\text{-}P2/P4}$ = 332 Hz, $^1J_{P2/P4\text{-}P3}$ = 264 Hz, $^1J_{P2/P4\text{-}P3}$ = 247 Hz, 2 P, P2$_{exo}$/P4$_{exo}$ atoms), 80.1 (ddd, $^1J_{P1\text{-}P2/P4}$ = 351 Hz, $^1J_{P1\text{-}P2/P4}$ = 334 Hz, $^2J_{P1\text{-}P3}$ = 21 Hz, 1 P, P1$_{exo}$ atom), 82.6 (two dd, $^1J_{P1\text{-}P2/P4}$ = 364 Hz, $^1J_{P1\text{-}P2/P4}$ = 346 Hz, $^1J_{P2/P4\text{-}P3}$ = 263 Hz, $^1J_{P2/P4\text{-}P3}$ = 254 Hz, 2 P, P2$_{endo}$/P4$_{endo}$ atoms), 124.4 (ddd, $^1J_{P1\text{-}P2/P4}$ = 364 Hz, $^1J_{P1\text{-}P2/P4}$ = 346 Hz, $^2J_{P1\text{-}P3}$ = 31 Hz, 1 P, P1$_{endo}$ atom). ^{31}P{^{1}H} NMR of the crude solution of **1g**[TEF] (*o*-DFB/C_6D_6): δ/ppm = −84.4 (td, $^1J_{P3\text{-}P2/P4}$ = 259 Hz, $^2J_{P3\text{-}P1}$ = 31 Hz, 1 P, P3$_{endo}$ atom), −76.0 (td, $^1J_{P3\text{-}P2/P4}$ = 261 Hz, $^2J_{P3\text{-}P1}$ = 21 Hz, 1 P, P3$_{exo}$ atom), 38.5 (two dd, $^1J_{P1\text{-}P2/P4}$ = 346 Hz, $^1J_{P1\text{-}P2/P4}$ = 342 Hz, $^1J_{P2/P4\text{-}P3}$ = 264 Hz, $^1J_{P2/P4\text{-}P3}$ = 247 Hz, 2 P, P2$_{exo}$/P4$_{exo}$ atoms), 80.1 (m (additional $J_{P\text{-}H}$ coupling to the protons of the phenyl ring), 1 P, P1$_{exo}$ atom), 82.6 (two dd, $^1J_{P1\text{-}P2/P4}$ = 364 Hz, $^1J_{P1\text{-}P2/P4}$ = 346 Hz, $^1J_{P2/P4\text{-}P3}$ = 263 Hz, $^1J_{P2/P4\text{-}P3}$ = 254 Hz, 2 P, P2$_{endo}$/P4$_{endo}$ atoms), 124.4 (m (additional $J_{P\text{-}H}$ coupling to the protons of the phenyl ring), 1 P, P1$_{endo}$ atom).

9.4.2.2 Synthesis of [Cp*Mo(CO)$_2$(η^3-P_4Ph_2)][$GaCl_4$] (2[$GaCl_4$])

A solution of PPh_2Cl in toluene (*c* = 0.2M, 0.25 mL, 0.05 mmol, 1.0 eq.) was added to a yellow-orange solution of [Cp*Mo(CO)$_2$(η^3-P_3)] (20 mg, 0.05 mmol, 1.0 eq.; **A2**) in 5 mL *o*-DFB and stirred for 15 minutes before a solution of $GaCl_3$ (9 mg, 0.05 mmol, 1.0 eq.) in 5mL *o*-DFB was added. The solution was stirred for 18h leading to a colour change to dark yellow (brighter than before), and filtered through glas fibre filter paper. The solution was layered with *n*-hexane and storage at room temperature for two weeks yielded pure **2**[$GaCl_4$] as yellow to orange needles suitable for single crystal X-ray diffraction. The solvent was removed by decanting and the crystals dried in vacuum for 3h.
Yield 32 mg (0.041 mmol = 82 %). ^{31}P{^{1}H} NMR of the crude solution (*o*-DFB/C_6D_6) δ/ppm = −61.0 (td, $^1J_{P3\text{-}P2/P4}$ = 254 Hz, $^2J_{P3\text{-}P1}$ = 21 Hz, 1 P, P3 atom), 8.7 (broad multiplet, 2 P, P2/P4 atoms), ~65 (broad signal, 1 P, P1 atom). ^{31}P NMR of the crude solution (*o*-DFB/C_6D_6) δ/ppm = −61.0 (td, $^1J_{P3\text{-}P2/P4}$ = 254 Hz, $^2J_{P3\text{-}P1}$ = 21 Hz, 1 P, P3 atom), 8.7 (broad multiplet, 2 P, P2/P4 atoms), ~65 (broad signal, 1 P, P1 atom). Anal. calcd. for [$C_{24}H_{25}O_2MoP_4$][$GaCl_4$]: C: 37.10, H: 3.24. Found: C: 35.77, H: 3.17.

9.4.2.3 Synthesis of 3a[TEF] and 3b[TEF]

[CpMo(CO)$_2$(η^3-As_3PPh_2)][TEF] (3a[TEF])

A yellow solution of [CpMo(CO)$_2$(η^3-As_3)] (14 mg, 0.03 mmol, 1.0 eq.; **B1**) and Tl[TEF] (37 mg, 0.03 mmol, 1.0 eq.) in 10 mL *o*-DFB was stirred for 30 minutes before a solution of PPh_2Cl in toluene (*c* = 0.2M, 0.15 mL, 0.03 mmol, 1.0 eq.) was added. After 5 minutes white solid starts to precipitate. The suspension was stirred for 1h leading to an almost colourless (light yellow) solution. After filtration through glas fibre filter paper the solution was layered with *n*-hexane and storage at 4 °C for two weeks

yielded pure **3a**[TEF] as yellow sticks suitable for single crystal X-ray diffraction. The solvent was removed by decanting and the crystals dried in vacuum for 3h.
Yield 32 mg (0.02 mmol = 67 %).

[Cp*Mo(CO)$_2$(η^3-As$_3$PPh$_2$)][TEF] (3b[TEF])

A orange-yellow solution of [Cp*Mo(CO)$_2$(η^3-As$_3$)] (13 mg, 0.025 mmol, 1.0 eq.; **B2**) and Tl[TEF]·(CH_2Cl_2) (32 mg, 0.025 mmol, 1.0 eq.) in 5 mL *o*-DFB was stirred for 20 minutes before a solution of PPh_2Cl in toluene (*c* = 0.2M, 0.14 mL, 0.028 mmol, 1.0 eq.) was added, which led to immediate precipitation of white powder and the solution brightens to a lemon yellow solution. The suspension was stirred for 24h and filtered through glas fibre filter paper. Layering with *n*-hexane and storage at 4 °C for two weeks yielded pure **3b**[TEF] as yellow blocks suitable for single crystal X-ray diffraction. The solvent was removed by decanting and the crystals dried in vacuum for 3h.
Yield 22 mg (0.013 mmol = 43 %). $^{31}P\{^1H\}$ NMR of the crude solution (*o*-DFB/C_6D_6) δ/ppm = 3.0 (s, 1 P, P1 atom). ^{31}P NMR of the crude solution (*o*-DFB/C_6D_6) δ/ppm = 3.0 (s, 1 P, P1 atom). $^{19}F\{^1H\}$ NMR (*o*-DFB/C_6D_6) δ/ppm = −75.5 (s, CF_3).

9.4.2.4 Synthesis of [{CpMo(CO)$_2$}$_2$(μ,η^3:η^3-P$_6$BBr$_2$(Br))][TEF] (5[TEF])

A orange solution of [CpMo(CO)$_2$(η^3-P_3)] (31 mg, 0.1 mmol, 1.0 eq.; **A1**) and Tl[TEF] (118 mg, 0.1 mmol, 1.0 eq.) in 10 mL *o*-DFB was stirred for 15 minutes before pure BBr_3 (12 µL, 0.13 mmol, 1.3 eq.) was added, which led to immediate precipitation of white powder and a colour change to a golden yellow (when BBr_3 is added to **A1** in the absence of a halophosphane immediately orange precipitate is formed, which can be probably attributed to the adduct complex of **A1** and BBr_3). The suspension was stirred for 1h and filtered through glas fibre filter paper. The supernatant was transferred to another flask and layered with *n*-hexane. Storage at 4 °C for five days yielded **5**[TEF] as dark yellow sticks and blocks suitable for single crystal X-ray diffraction. The solvent was removed by decanting and the crystals dried in vacuum for 3h.
Yield 70 mg (0.038 mmol = 76 %). ^1H NMR (CD_2Cl_2) δ/ppm = 5.95 (s, Cp), 6.08 (s, Cp). $^{31}P\{^1H\}$ NMR of crystalline sample (CD_2Cl_2) δ/ppm = −169.2 (m, *J* = 17 Hz, 327 Hz, 361 Hz, ~1 P), −112.8 (dd, $^1J_{P\text{-}P}$ = 369 Hz, $^1J_{P\text{-}P}$ = 370 Hz, ~1 P), −51.2 to −42.8 (m, ~4 P), −9.5 (broad signal, ~1 P), 79.5 (tqt, $^1J_{P\text{-}P}$ = 368 Hz, $J_{P\text{-}P \text{ or } P\text{-}B}$ = 37 Hz, $J_{P\text{-}P}$ = 10 Hz, 1 P). ^{31}P NMR of crystalline sample (CD_2Cl_2) δ/ppm = −173.2 (m), −169.3 (m, ~1 P), −112. (dd, $^1J_{P\text{-}P}$ = 368 Hz, $^1J_{P\text{-}P}$ = 358 Hz, ~1 P), −51.5 to −40.4 (m, ~4 P), −9.0 (broad signal, ~1 P), 79.5 (tqt, $^1J_{P\text{-}P}$ = 368 Hz, $J_{P\text{-}P \text{ or } P\text{-}B}$ = 37 Hz, $J_{P\text{-}P}$ = 12 Hz, 1 P). $^{13}C\{^1H\}$ NMR (CD_2Cl_2) δ/ppm = 92.16 (s, Cp), 92.37 (small, s, Cp), 92.62 (s, Cp) 93.24 (small, s, Cp), 117, 67 (q, $^2J_{C\text{-}F}$ = 6.1 Hz, C_{quart} (TEF)), 121.70 (q, $^1J_{C\text{-}F}$ = 291 Hz, CF_3 (TEF)), 125.10 (t, *J* = 5.1 Hz). $^{19}F\{^1H\}$ NMR (CD_2Cl_2) δ/ppm = −75.5 (s, CF_3). $^{11}B\{^1H\}$ NMR (CD_2Cl_2) δ/ppm = −14.5 (t, *J* = 100 Hz, BBr_2). ^{11}B NMR (CD_2Cl_2) δ/ppm = −14.5 (t, *J* = 100 Hz, BBr_2). Anal. calcd. for [$C_{14}H_{10}O_4Mo_2P_6BBr_3$][TEF]: C: 19.61, H: 0.55. Found: C: 20.25, H: 0.90. Positive ion ESI-MS *m/z* (%): 872.48 (100) [**M**$^+$], 950.39 (10) [**M**$^+$+Br], 831.57 (6) [**M$_2$**$^{2+}$–Br] 792.57 (6) [**M**$^+$–Br].

9.4.2.5 Reaction of [CpMo(CO)$_2$(η^3-P_3)] (A1) with BBr_3

A orange solution of [CpMo(CO)$_2$(η^3-P_3)] (31 mg, 0.1 mmol, 1.0 eq.; **A1**) in 10 mL *o*-DFB was reacted with pure BBr_3 (12 µL, 0.13 mmol, 1.3 eq.), which led to immediate precipitation of orange powder and almost decolourization of the supernatant. The orange precipitate can be probably attributed to the adduct complex of **A1** and BBr_3. However, all attempts to crystallize the product failed due to the low solubility in many solvents and decomposition in MeCN.

^{31}P{^{1}H} NMR of the supernatant solution (*o*-DFB/C_6D_6) δ/ppm = −351.2 (s, ~2 P), −336.7 (s, ~0.2 P), −157.2 (t, $^1J_{P\text{-}B}$ = 372 Hz ~1 P), −152.0 (t, $^1J_{P\text{-}B}$ = 295 Hz ~0.1 P), additional small signals (see Figure S54). ^{31}P NMR of the supernatant solution (*o*-DFB/C_6D_6) δ/ppm = −351.2 (s, ~2 P), −336.7 (s, ~0.2 P), −157.2 (t, $^1J_{P\text{-}B}$ = 365 Hz ~1 P), −152.0 (t, $^1J_{P\text{-}B}$ = 295 Hz ~0.1 P), additional small signals (see Figure S55). ^{11}B{^{1}H} NMR of the supernatant solution (*o*-DFB/C_6D_6) δ/ppm = −15.8 (t, J = 125 Hz), 14.6 (t, J = 82 Hz). ^{11}B NMR of the supernatant solution (*o*-DFB/C_6D_6) δ/ppm = −15.8 (t, J = 125 Hz), 14.6 (t, J = 82 Hz).

9.4.3 NMR spectroscopy

Screening of the reaction of A1 with different phosphenium ions

To identify, which phosphenium ions are applicable for electrophilic functionalization of **A1**, an NMR screening was conducted. Therefore, ^{31}P{^{1}H} NMR spectra of the crude solutions of **1a**–**g** were recorded. The NMR samples were taken 1–2 hours after the phosphenium ion generation and before the filtration. The resulting spectra are shown in Figure S1 proofing that all used phosphenium ions can be inserted into the P_3 ligand of **A1**. The ^{31}P{^{1}H} NMR spectra of the crude solutions of the products **1a**–**g** all show an AMM'X spin system, except for **1d** (ABB'X) and **1f** (AA'MX), which is in good agreement with the cyclic P_4R_2 ligands within these compounds. The signal assignment could be easily accomplished since an additional P–H coupling could be observed in the ^{31}P NMR spectra for the signals corresponding to the P1 atom (labelled with a blue dot in Figure S1), which carries the organic substituents. The signal with an integral of two can be assigned to P2 and P4 (red dot), while the remaining signal belongs to P3 (green dot). For **1g** two sets of signals in a ratio of 1.6:1 are found suggesting the formation of two isomers, where the phenyl group is either in *endo* or *exo* position, with the *endo* isomer probably being the favoured one due to less steric hindrance. Upon crystallization the ratio of *endo*/*exo* increases to 6:1 (*vide infra*).

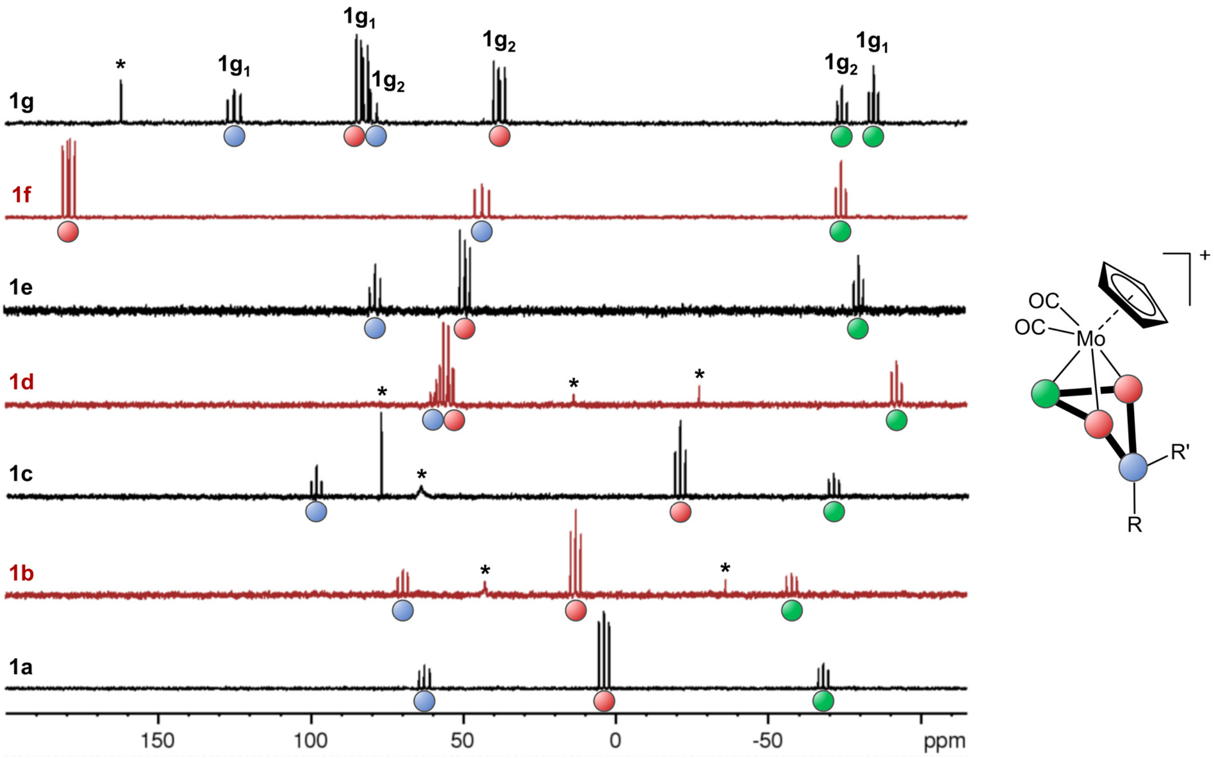

Figure S1: $^{31}P\{^1H\}$ NMR spectra of crude solutions of **1a-g** in *o*-DFB/C_6D_6. R = R' = Ph (**1a**), Me (**1b**), Cy (**1c**), Mes (**1d**), 0.5 biphen (**1e**), Br (**1f**); RR' = PhCl (**1g**). Two sets of signals observed for **1g** are labelled as **$1g_1$** and **$1g_2$**, with the former being most probably the *endo*-Ph and the latter the *exo*-Ph isomer (due to steric reasons). Signal assignment: blue dot = P1 (former phosphenium ion), red dots = P2 and P4, green dot = P3; * = unidentified impurities or excess halophosphanes in minor ratio.

NMR spectra

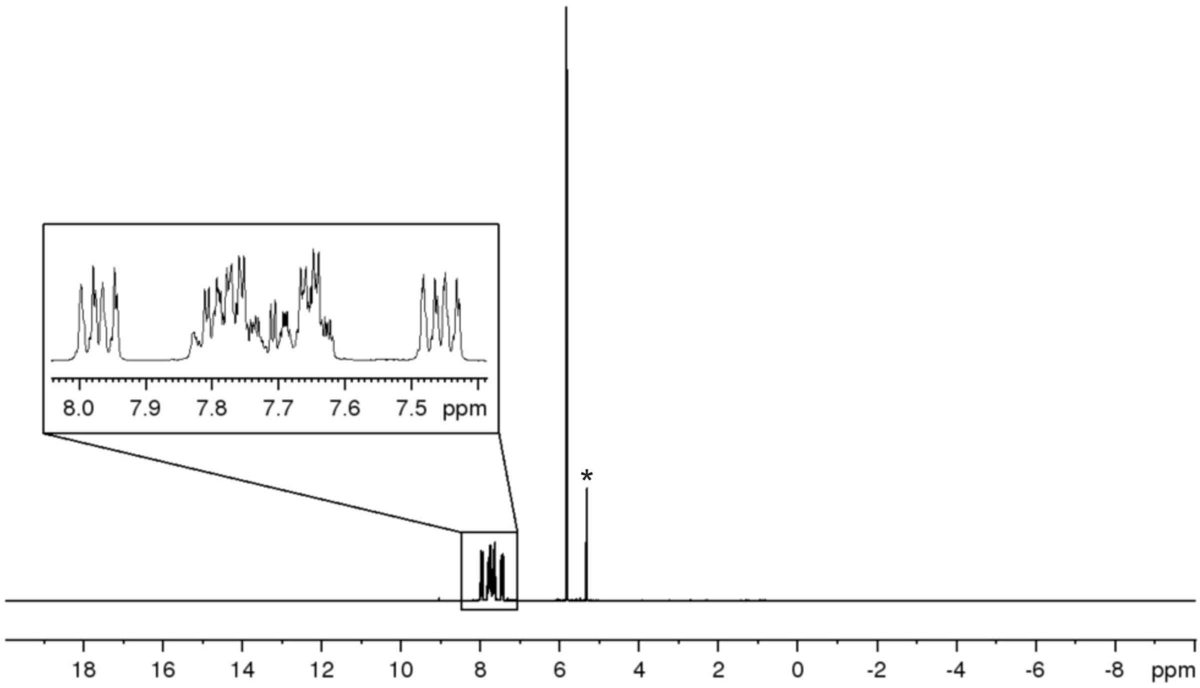

Figure S2: ^1H NMR spectrum of crystalline **1a**[OTf] in CD_2Cl_2; * = CD_2Cl_2.

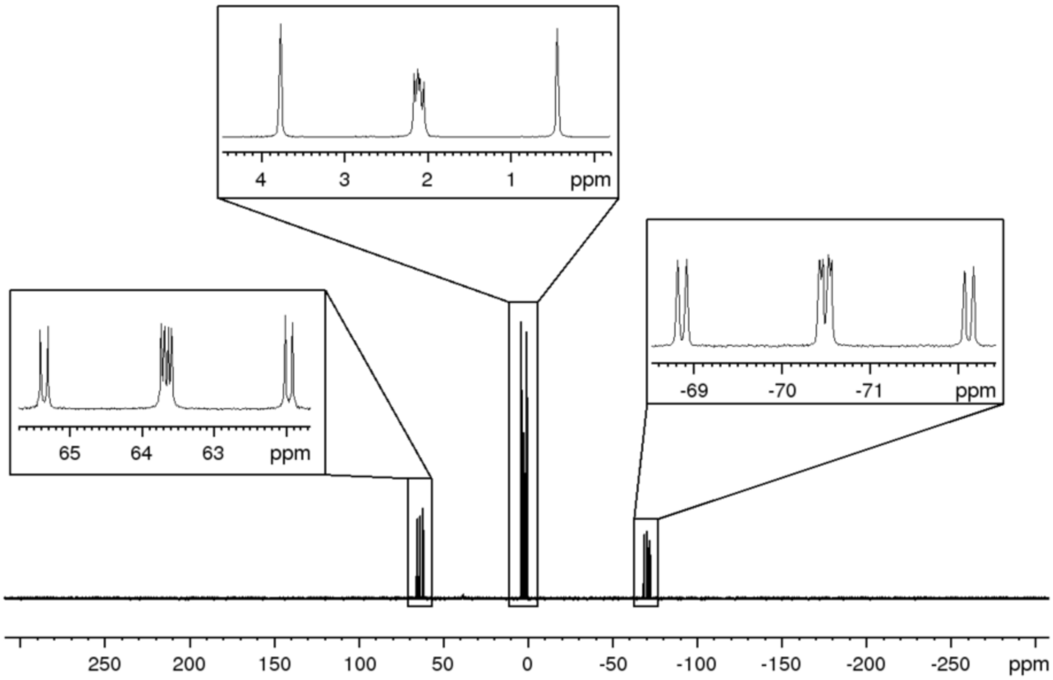

Figure S3: $^{31}P\{^{1}H\}$ NMR spectrum of crystalline **1a**[OTf] in CD_2Cl_2.

The $P_4Ph_2^+$ ligand in crystalline **1a** shows an AMM'X spin system (Figure S3) consisting of a doublet of doublet of doublets (ddd) at δ = −70.5 ppm (P3 atom), two doublet of doublets at δ = 2.1 ppm (P2/P4 atoms) and a ddd at δ = 63.7 ppm (P1 atom) in an integral ratio of 1:2:1. The splitting patterns and the observed ^{1}J coupling constants (262–279 Hz) show that the P2 and P4 atoms are not fully magnetical equivalent. Additionally, a ^{2}J coupling (17 Hz) between P1 and P3 is observed.

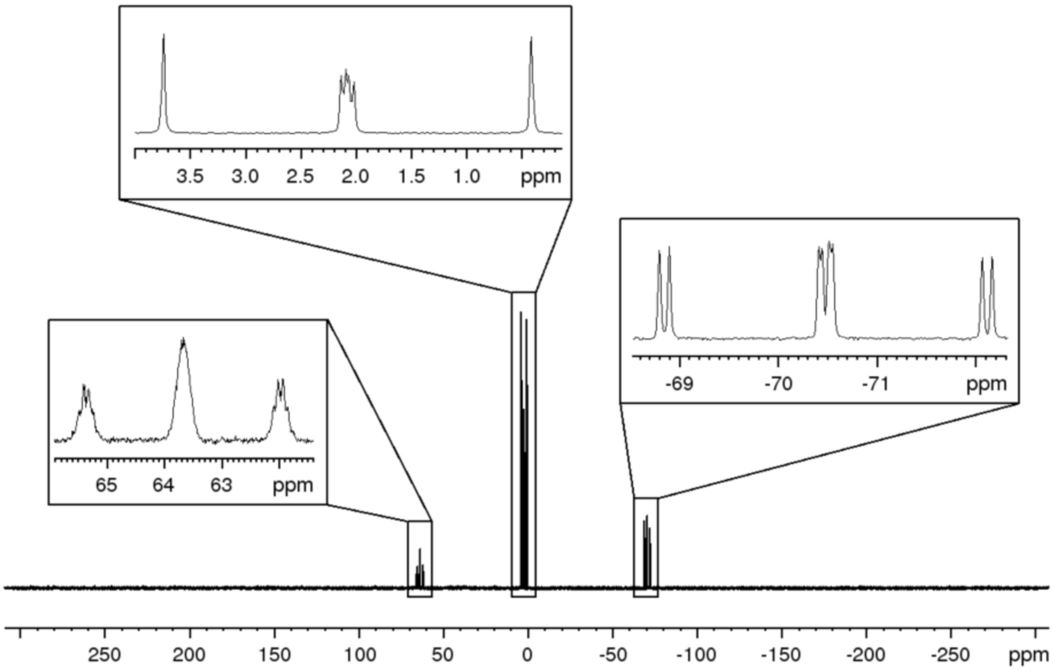

Figure S4: ^{31}P NMR spectrum of crystalline **1a**[OTf] in CD_2Cl_2.

The splitting patterns in the ^{31}P NMR spectrum (Figure S4) match those of the $^{31}P\{^{1}H\}$ NMR spectrum except the signal at δ = 63.7 ppm (corresponding to the P1 atom), which splits from a ddd to a multiplet upon additional $J_{P\text{-}H}$ coupling to the protons of the phenyl substituents.

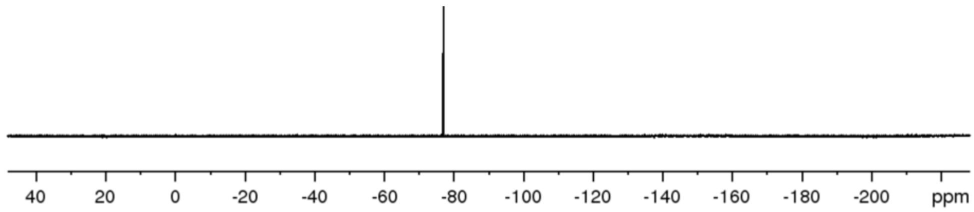

Figure S5: $^{19}F\{^1H\}$ NMR spectrum of crystalline **1a**[OTf] in CD_2Cl_2.

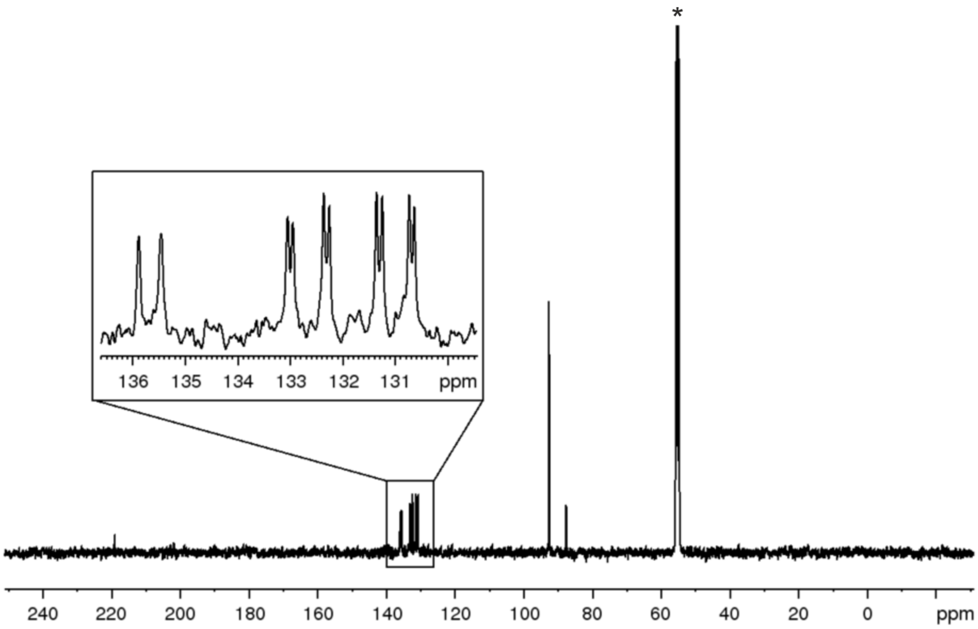

Figure S6: $^{13}C\{^1H\}$ NMR spectrum of crystalline **1a**[OTf] in CD_2Cl_2; * = CD_2Cl_2.

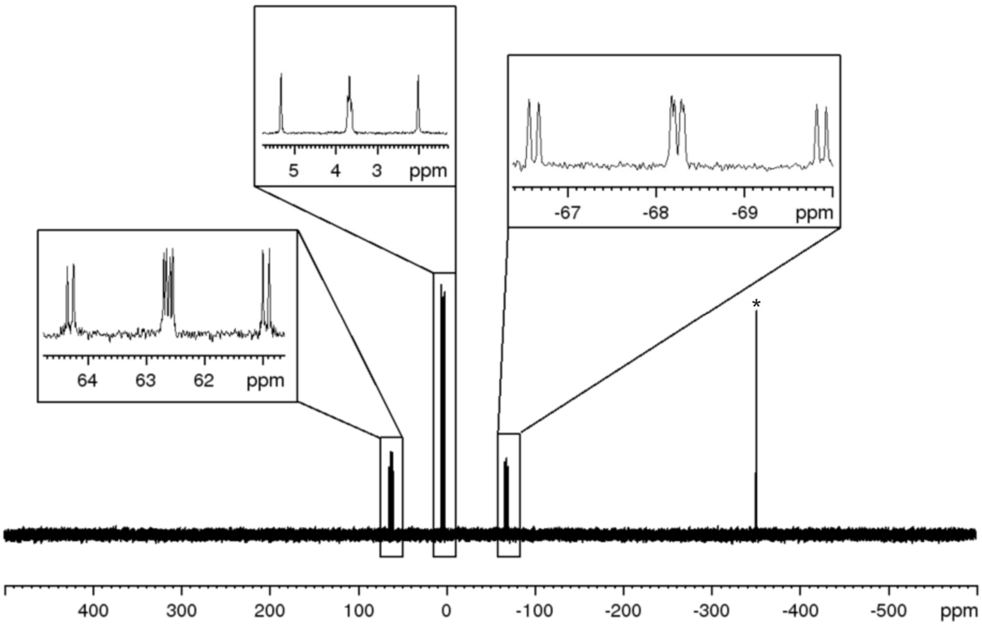

Figure S7: $^{31}P\{^1H\}$ NMR spectrum of the crude solution of **1a**[TEF] in *o*-DFB/C_6D_6; * = starting material **A1**.

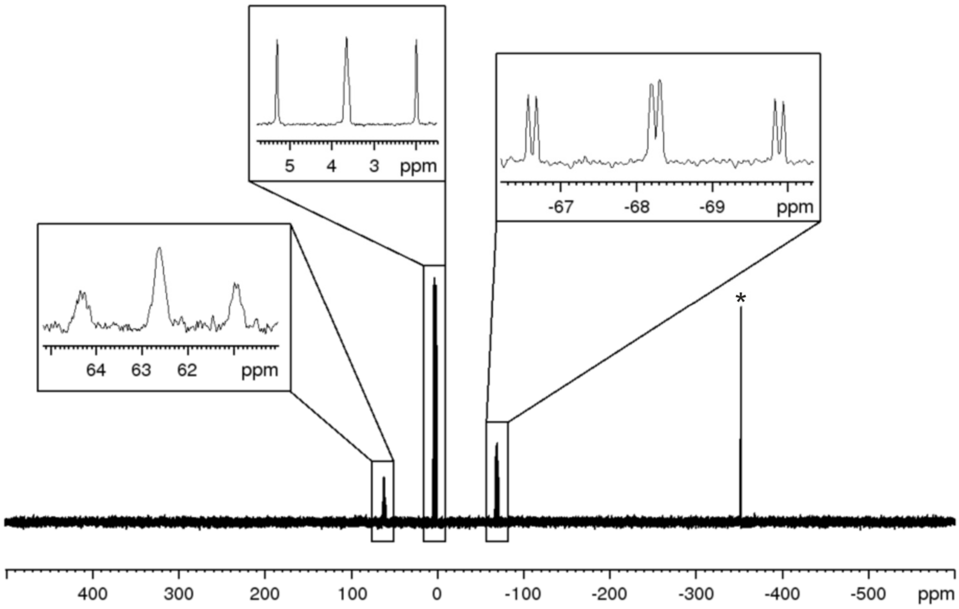

Figure S8: ^{31}P NMR spectrum of the crude solution of **1a**[TEF] in *o*-DFB/C_6D_6; * = starting material **A1**.

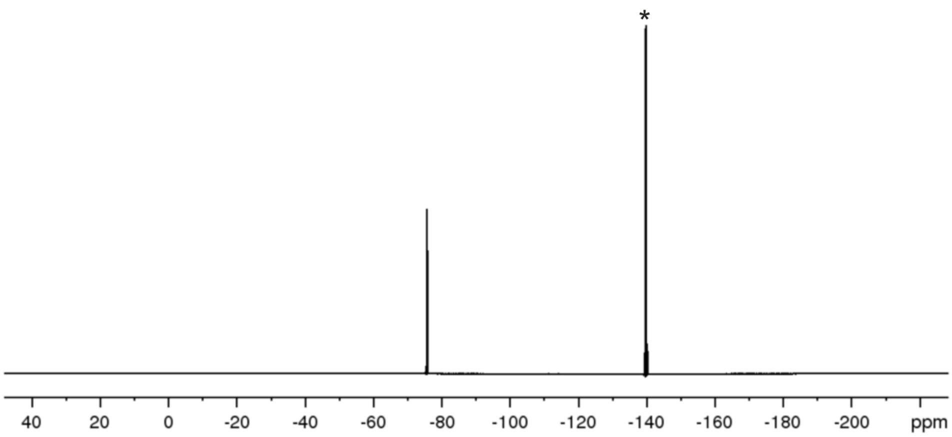

Figure S9: $^{19}F\{^1H\}$ NMR spectrum of the crude solution of **1a**[TEF] in *o*-DFB/C_6D_6; * = *o*-DFB.

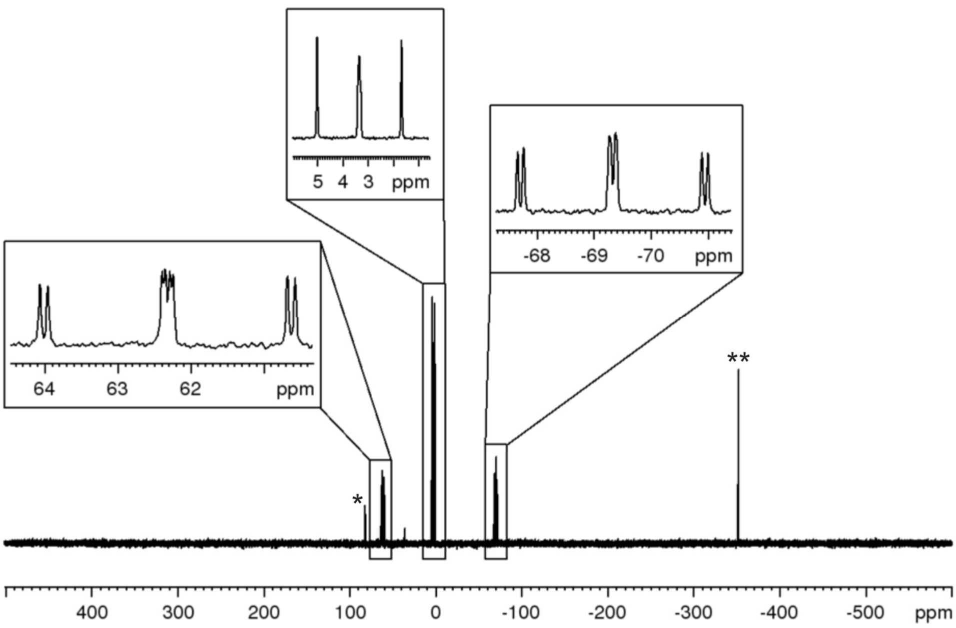

Figure S10: $^{31}P\{^1H\}$ NMR spectrum of the crude solution of **1a**[$GaCl_4$] in *o*-DFB/C_6D_6; * = unidentified impurity in minor ratio; ** = starting material **A1**.

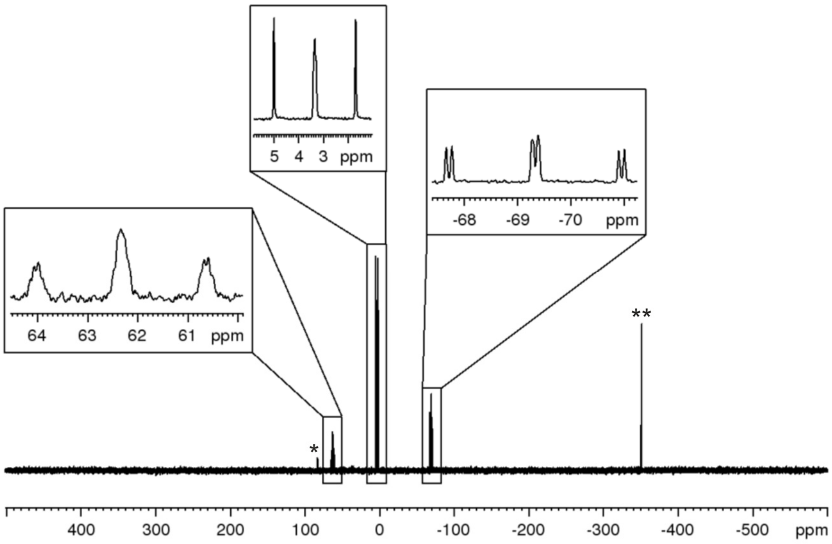

Figure S11: ^{31}P NMR spectrum of the crude solution of **1a**[$GaCl_4$] in *o*-DFB/C_6D_6; * = unidentified impurity in minor ratio; ** = starting material **A1**.

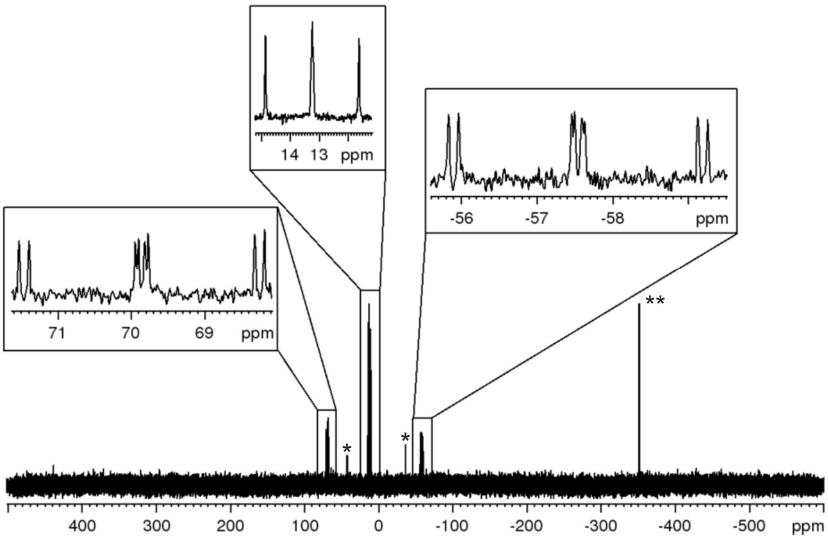

Figure S12: $^{31}P\{^1H\}$ NMR spectrum of the crude solution of **1b**[TEF] in *o*-DFB/C_6D_6; * = unidentified impurity in minor ratio; ** = starting material **A1**.

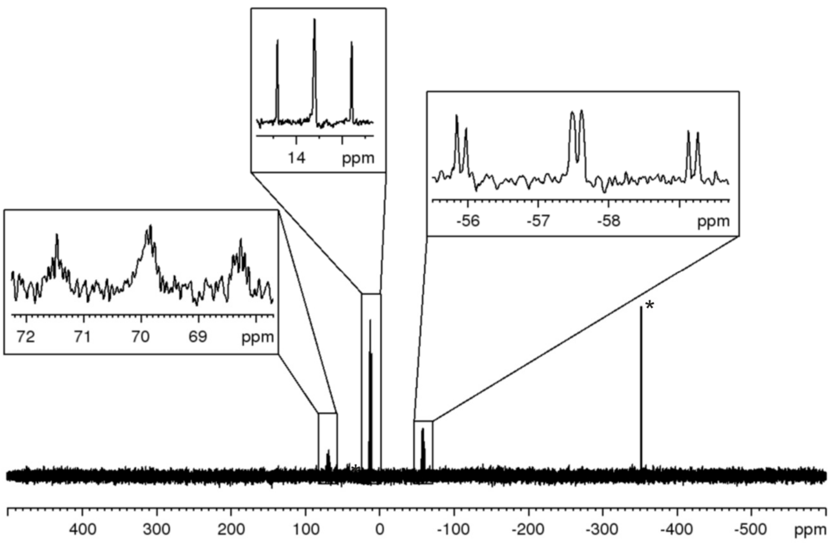

Figure S13: ^{31}P NMR spectrum of the crude solution of **1b**[TEF] in *o*-DFB/C_6D_6; * = starting material **A1**.

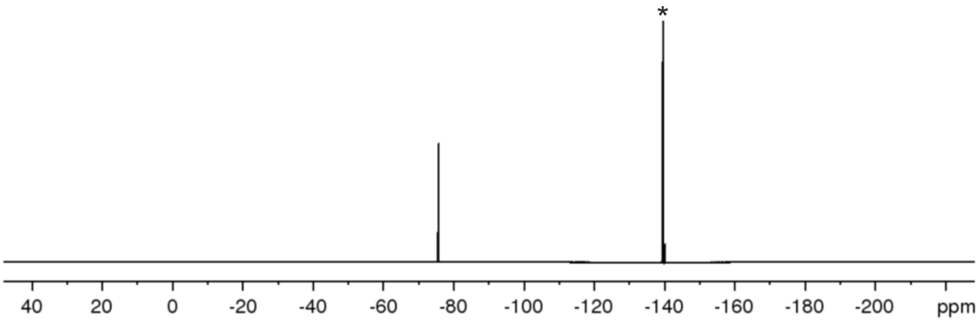

Figure S14: $^{19}F\{^1H\}$ NMR spectrum of the crude solution of **1b**[TEF] in *o*-DFB/C_6D_6; * = *o*-DFB.

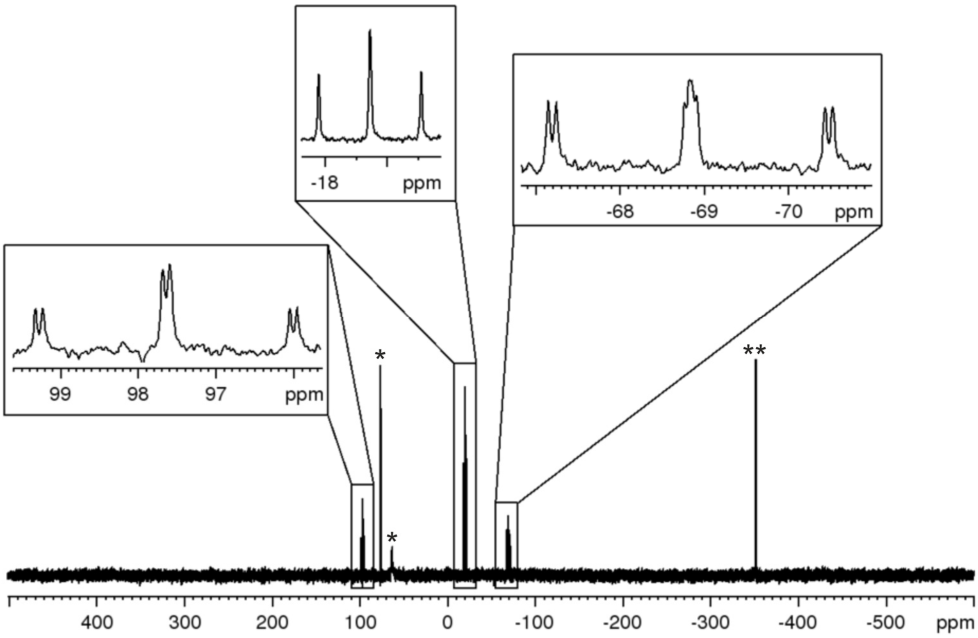

Figure S15: $^{31}P\{^1H\}$ NMR spectrum of the crude solution of **1c**[TEF] in *o*-DFB/C_6D_6; * = unidentified impurity in minor ratio; ** = starting material **A1**.

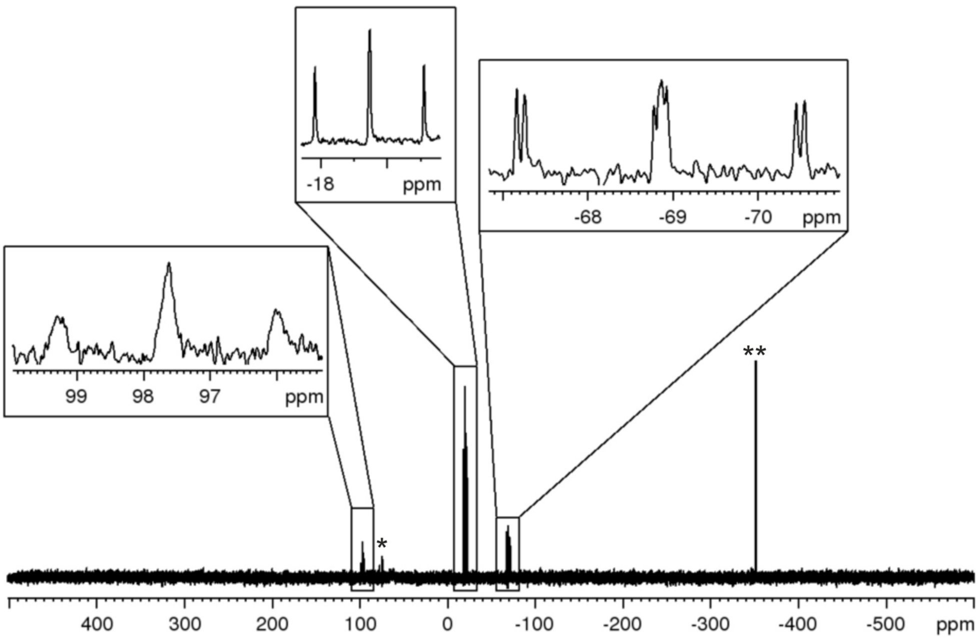

Figure S16: ^{31}P NMR spectrum of the crude solution of **1c**[TEF] in *o*-DFB/C_6D_6; * = unidentified impurity in minor ratio; ** = starting material **A1**.

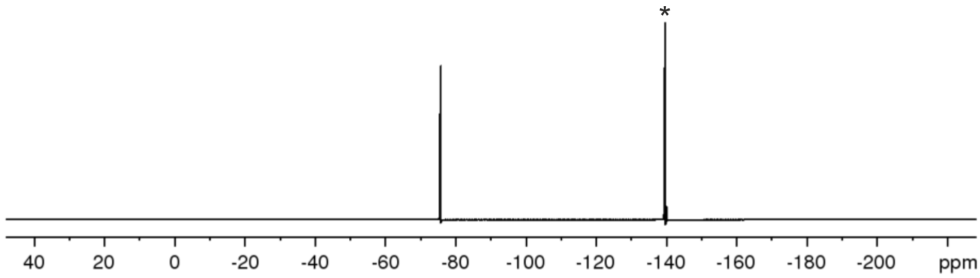

Figure S17: $^{19}F\{^1H\}$ NMR spectrum of the crude solution of **1c**[TEF] in *o*-DFB/C_6D_6; * = *o*-DFB.

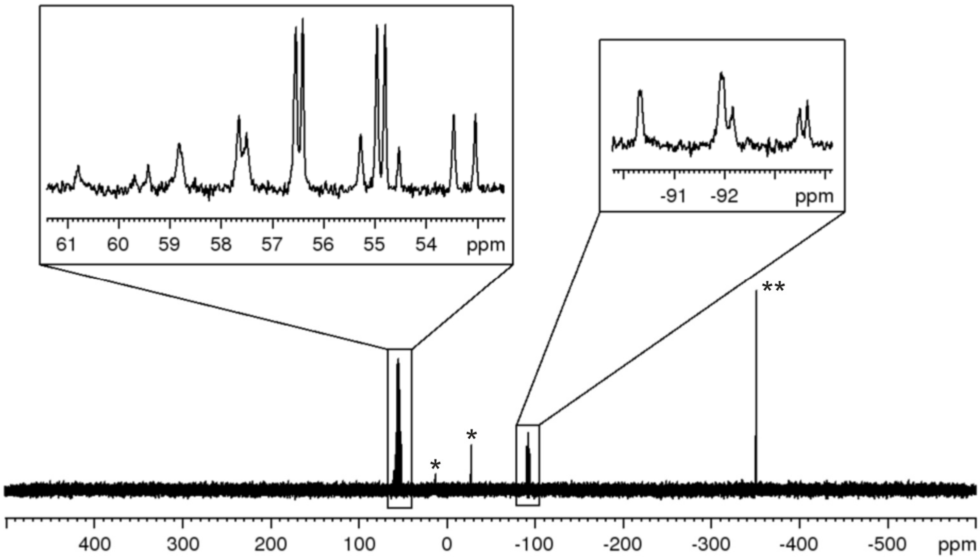

Figure S18: $^{31}P\{^1H\}$ NMR spectrum of the crude solution of **1d**[TEF] in *o*-DFB/C_6D_6; * = unidentified impurity in minor ratio; ** = starting material **A1**.

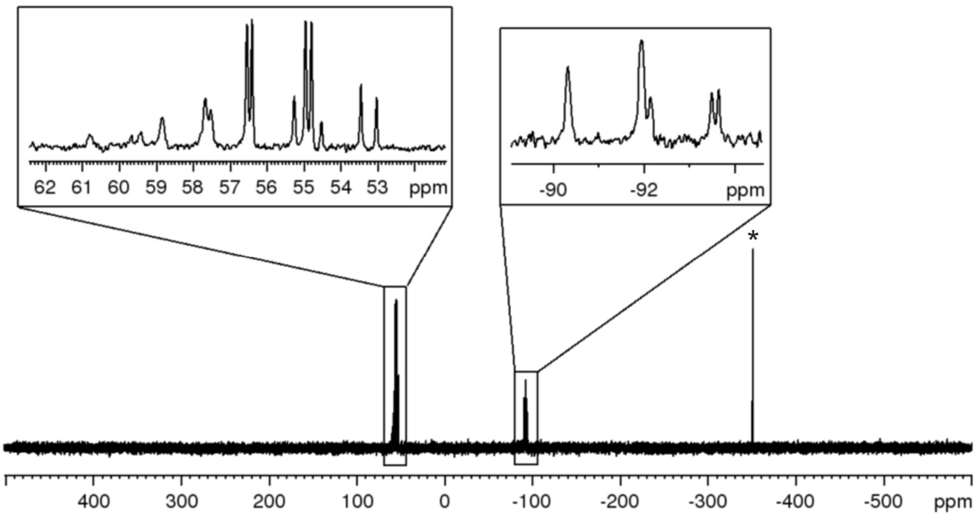

Figure S19: ^{31}P NMR spectrum of the crude solution of **1d**[TEF] in *o*-DFB/C_6D_6; * = starting material **A1**.

In the case of **1d**[TEF] (Figure S19), no further splitting of the signal at δ = 53–63 ppm is observed in the ^{31}P NMR spectrum (in comparison to the $^{31}P\{^1H\}$ spectrum) because the substituents (mesityl) have no *ortho*-protons.

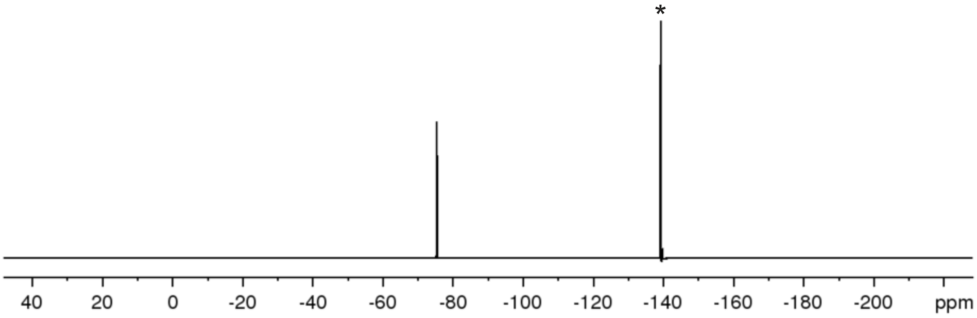

Figure S20: $^{19}F\{^1H\}$ NMR spectrum of the crude solution of **1d**[TEF] in *o*-DFB/C_6D_6; * = *o*-DFB.

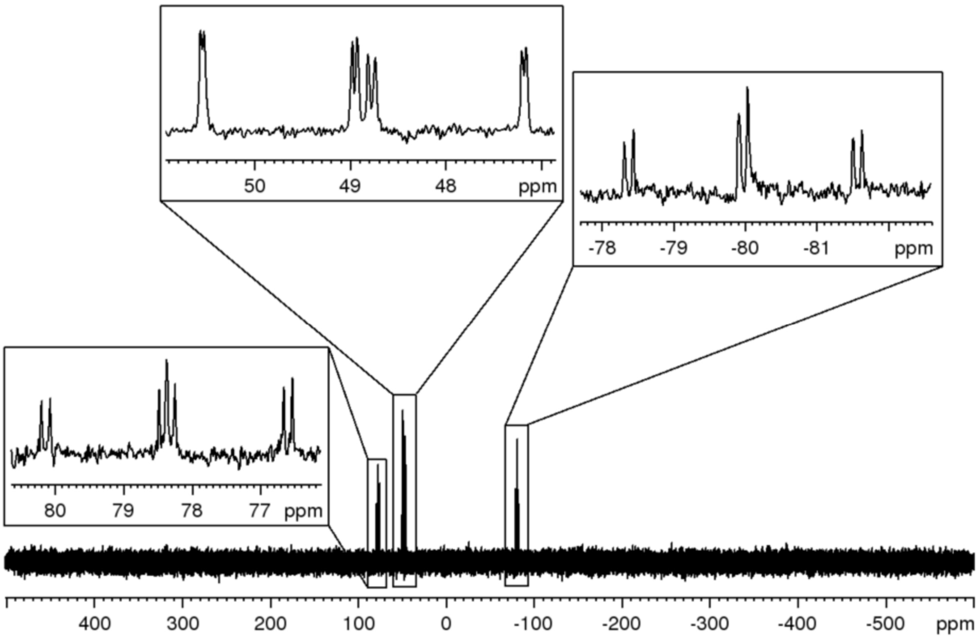

Figure S21: $^{31}P\{^1H\}$ NMR spectrum of the crude solution of **1e**[TEF] in *o*-DFB/C_6D_6.

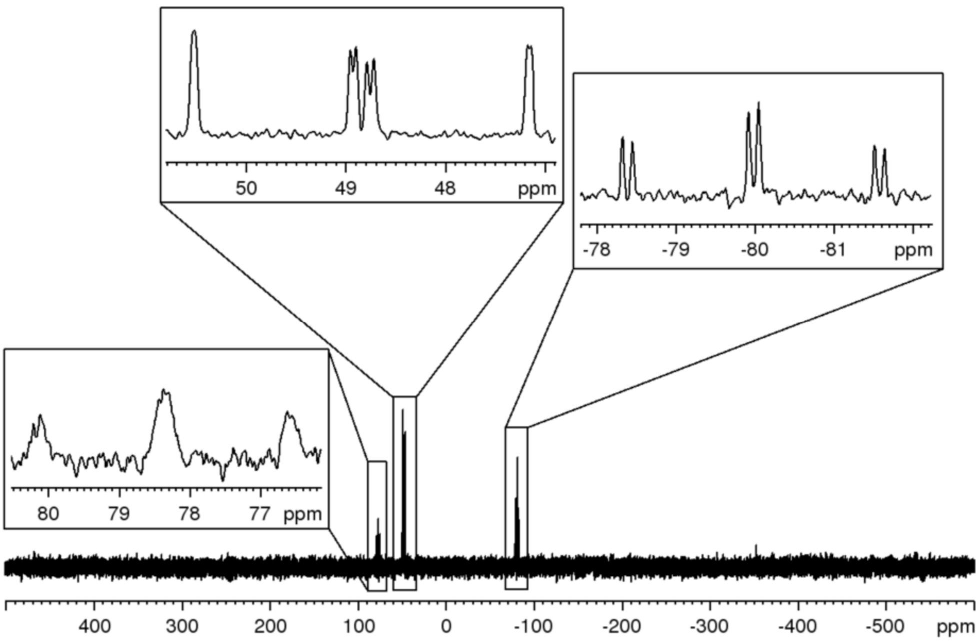

Figure S22: ^{31}P NMR spectrum of the crude solution of **1e**[TEF] in *o*-DFB/C_6D_6.

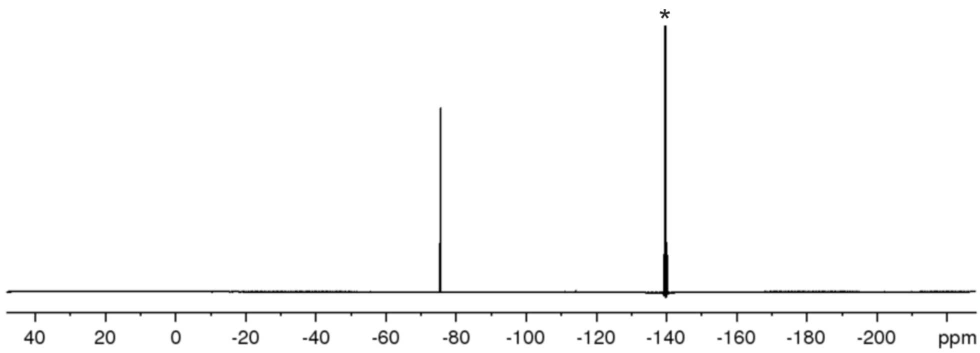

Figure S23: $^{19}F\{^1H\}$ NMR spectrum of the crude solution of **1e**[TEF] in *o*-DFB/C_6D_6; * = *o*-DFB.

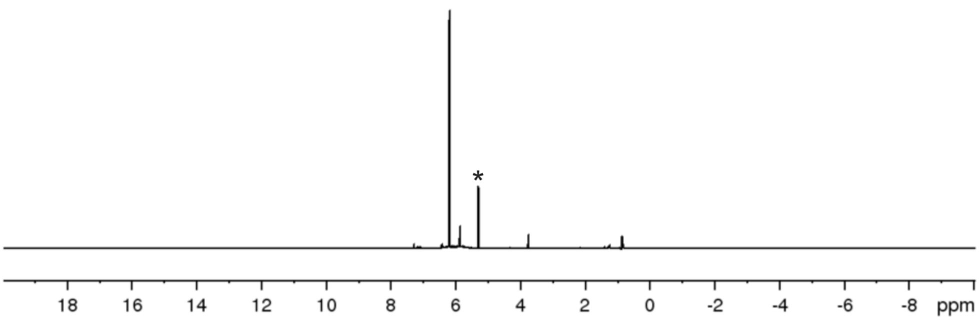

Figure S24: ^1H NMR spectrum of crystalline **1f**[TEF] in CD_2Cl_2; * = CD_2Cl_2.

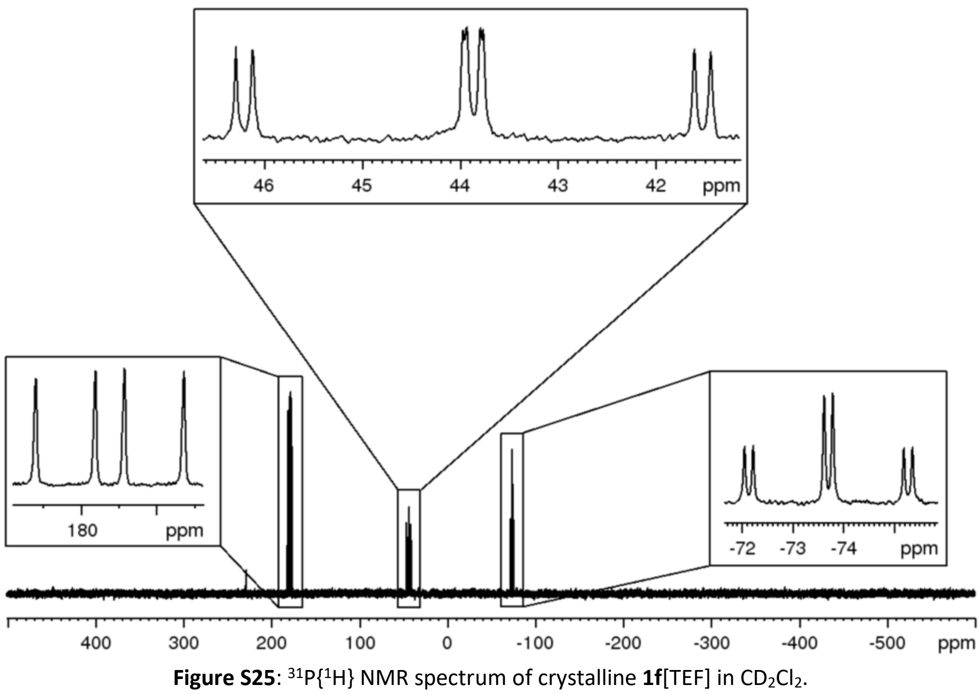

Figure S25: $^{31}P\{^1H\}$ NMR spectrum of crystalline **1f**[TEF] in CD_2Cl_2.

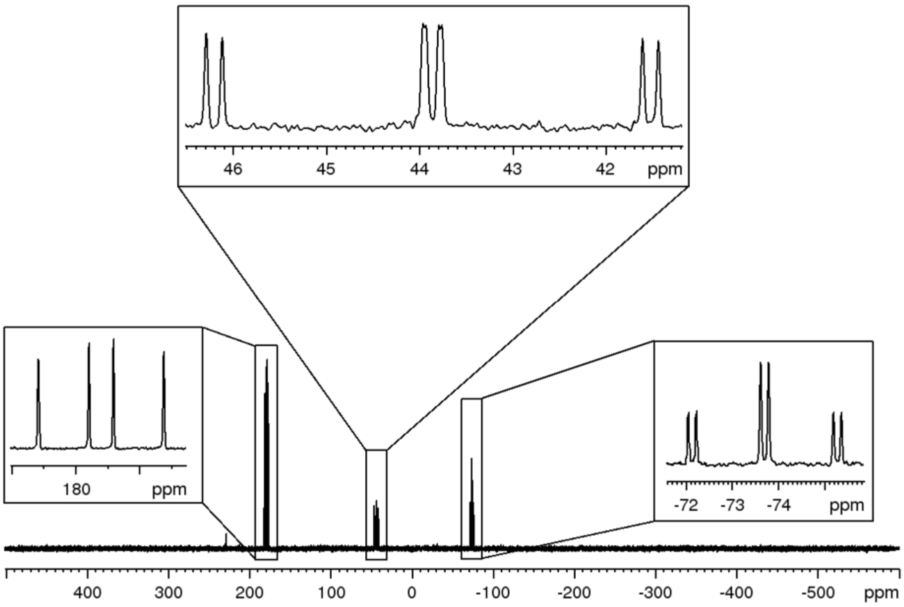

Figure S26: ^{31}P NMR spectrum of crystalline **1f**[TEF] in CD_2Cl_2.

In the case of **1f**[TEF] (Figure S26), no further splitting of the signal at δ = 40.3 ppm (corresponding to P1) is observed in the ^{31}P NMR spectrum (in comparison to the $^{31}P\{^1H\}$ spectrum) because of the absence of protons on the substituents (Br).

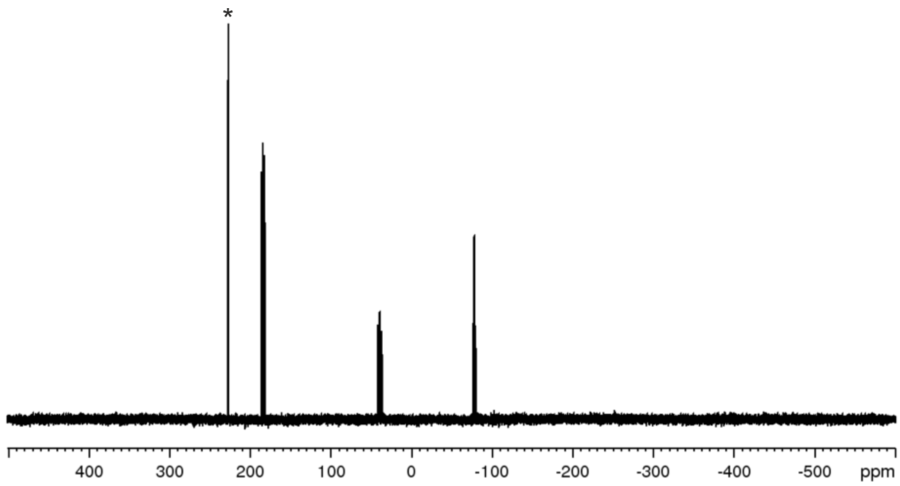

Figure S27: $^{31}P\{^1H\}$ NMR spectrum of the crude solution of **1f**[TEF] in CD_2Cl_2; * = PBr_3.

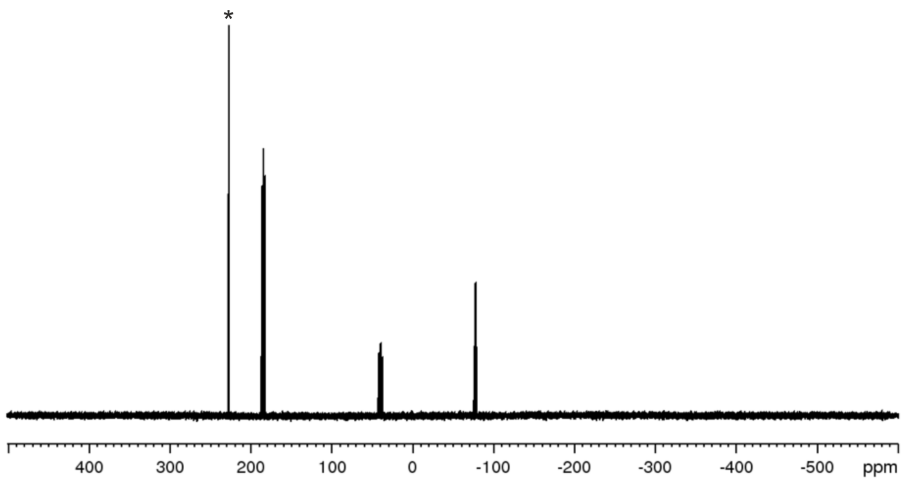

Figure S28: ^{31}P NMR spectrum of the crude solution of **1f**[TEF] in CD_2Cl_2; * = PBr_3.

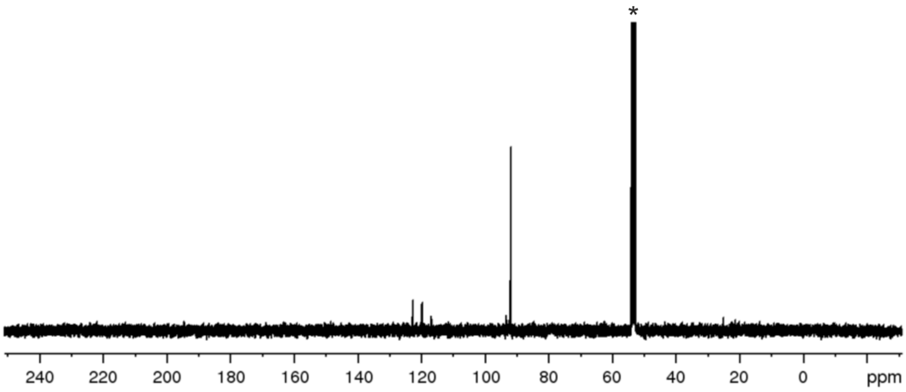

Figure S29: $^{13}C\{^{1}H\}$ NMR spectrum of crystalline **1f**[TEF] in CD_2Cl_2; * = CD_2Cl_2.

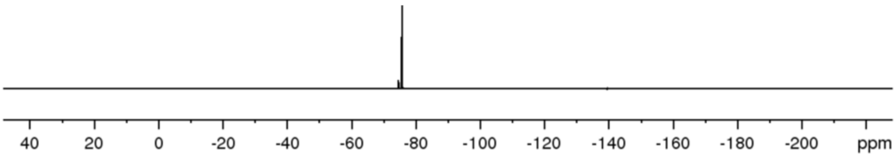

Figure S30: $^{19}F\{^{1}H\}$ NMR spectrum of crystalline **1f**[TEF] in CD_2Cl_2.

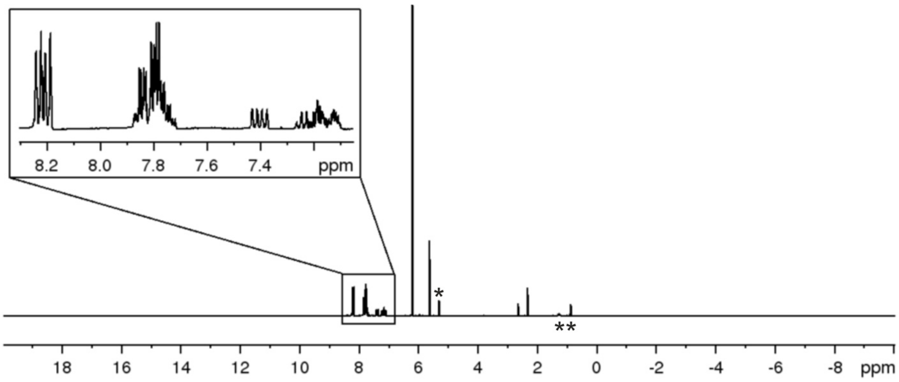

Figure S31: ^{1}H NMR spectrum of crystalline/oily **1g**[TEF] in CD_2Cl_2; * = CD_2Cl_2; ** = H-grease.

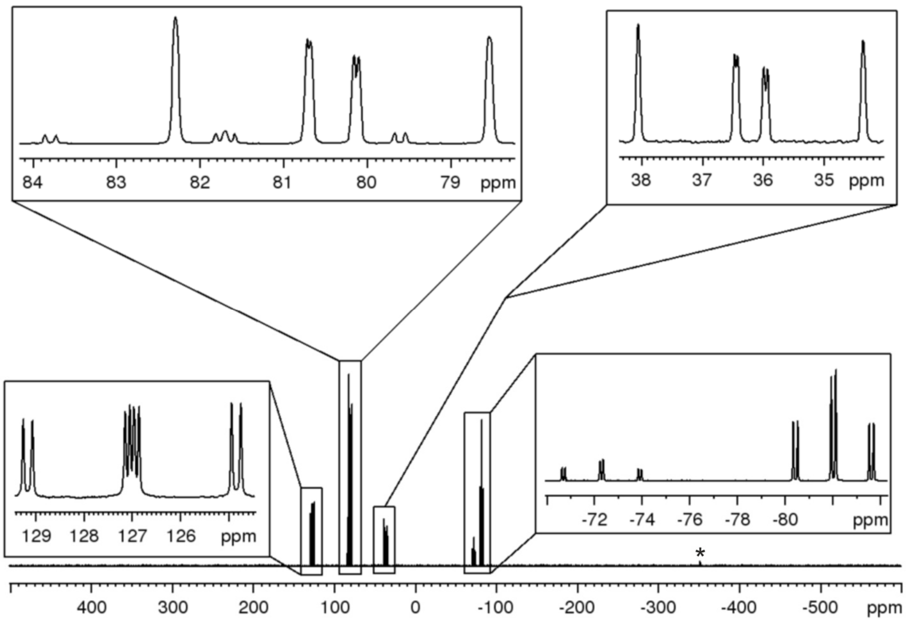

Figure S32: $^{31}P\{^{1}H\}$ NMR spectrum of crystalline/oily **1g**[TEF] in CD_2Cl_2; * = starting material **A1**.

Two sets of signals in a ratio of ≈6:1 are observed (Figure S32), which can be assigned to **1g**$_{\mathbf{endo}}$ and **1g**$_{\mathbf{exo}}$.

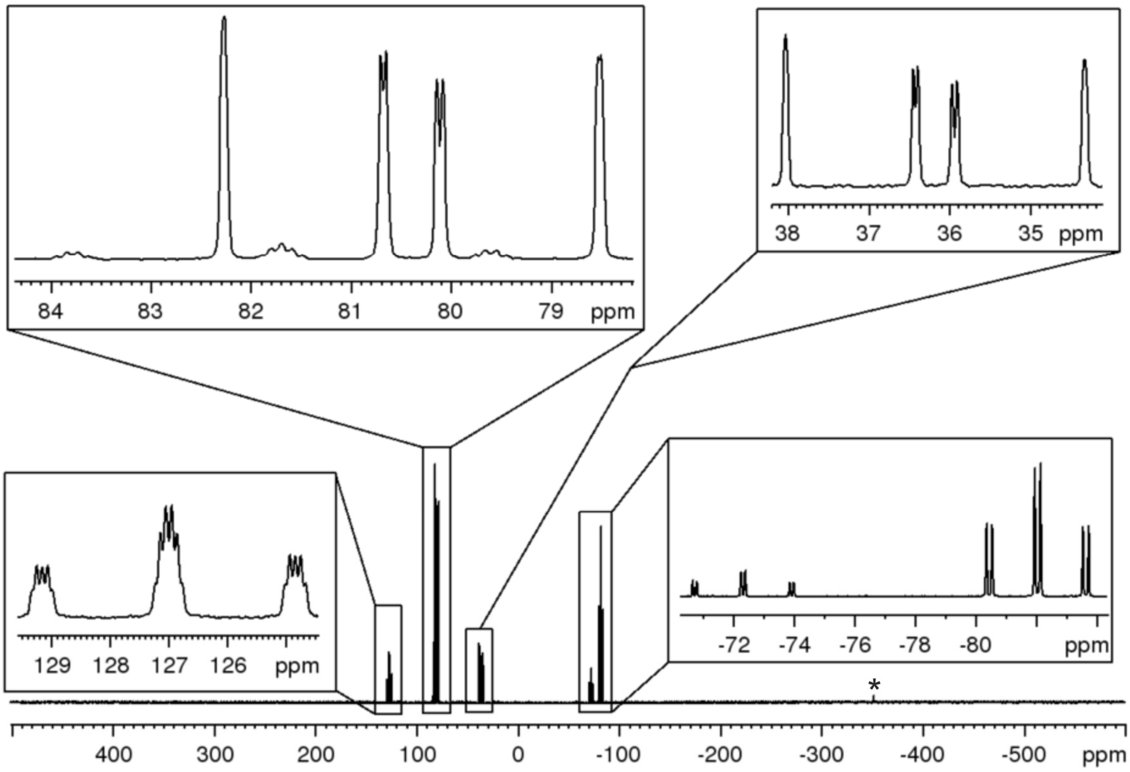

Figure S33: ^{31}P NMR spectrum of crystalline/oily **1g**[TEF] in CD_2Cl_2; * = starting material **A1**.

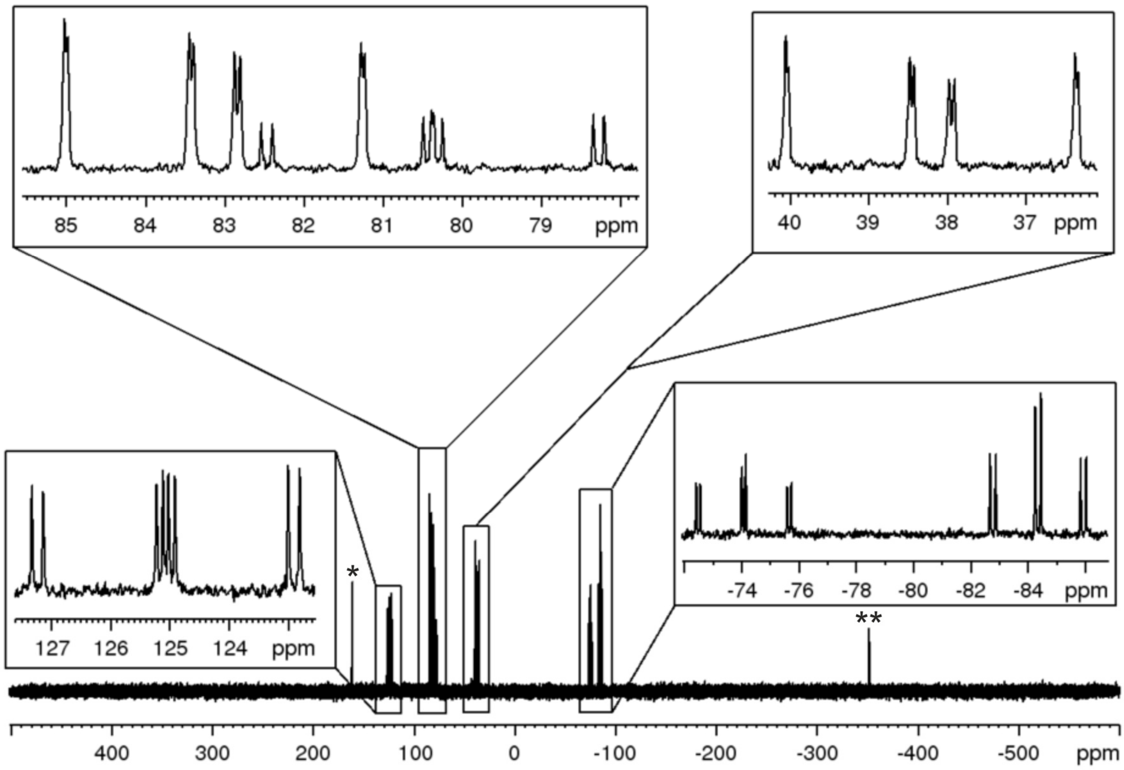

Figure S34: $^{31}P\{^1H\}$ NMR spectrum of the crude solution of **1g**[TEF] in o-DFB/C_6D_6; * = $PPhCl_2$ ** = starting material **A1**.

The ratio of the two sets of signals in the crude solution (Figure S34) differs from the one in the crystalline/oily product being roughly 1.6:1.

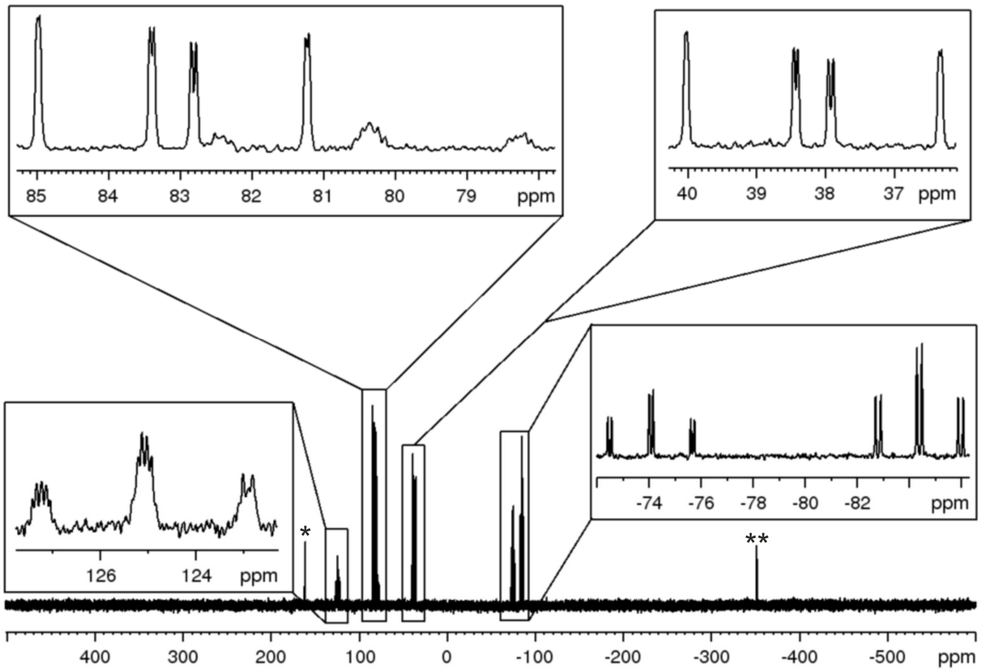

Figure S35: ^{31}P NMR spectrum of the crude solution of **1g**[TEF] in o-DFB/C_6D_6; * = $PPhCl_2$ ** = starting material **A1**.

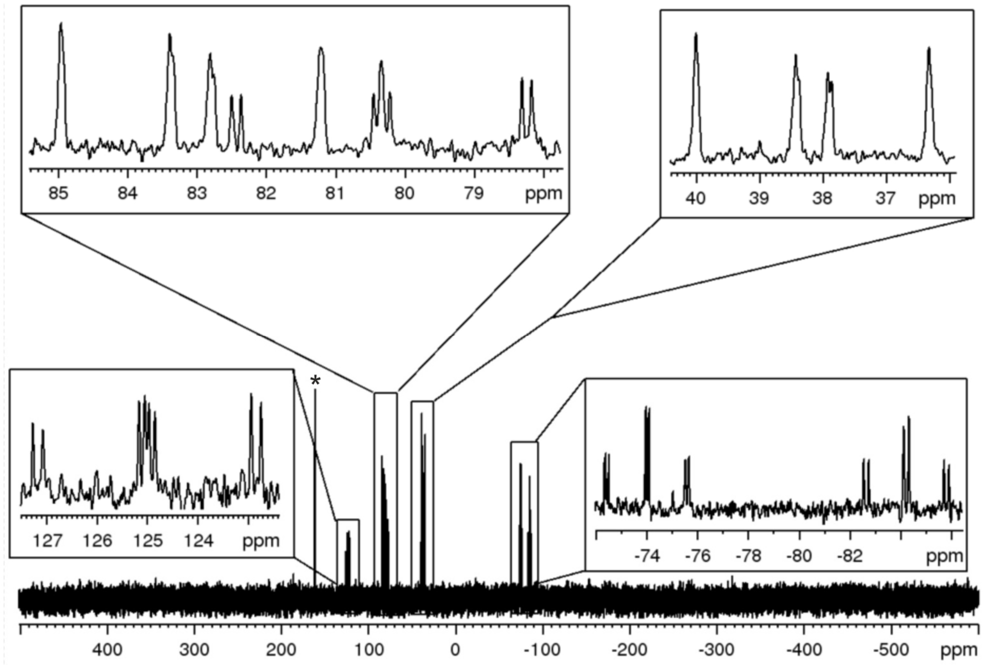

Figure S36: ^{31}P{^{1}H} NMR spectrum of the crude solution of **1g**[TEF], when two equivalents of Tl[TEF] were used, in o-DFB/C_6D_6; * = $PPhCl_2$.

When two equivalents of Tl[TEF] are used in the synthesis of **1g**[TEF], no abstraction of the second chloride atom occurs and the ratio of the two sets of signals is roughly 1:1 (Figure S36).

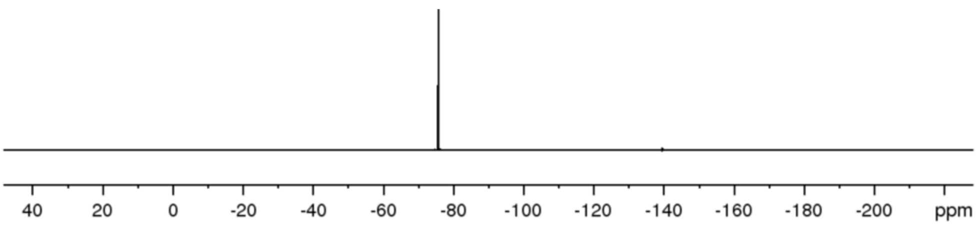

Figure S37: ^{19}F{^{1}H} NMR spectrum of crystalline/oily **1g**[TEF] in CD_2Cl_2.

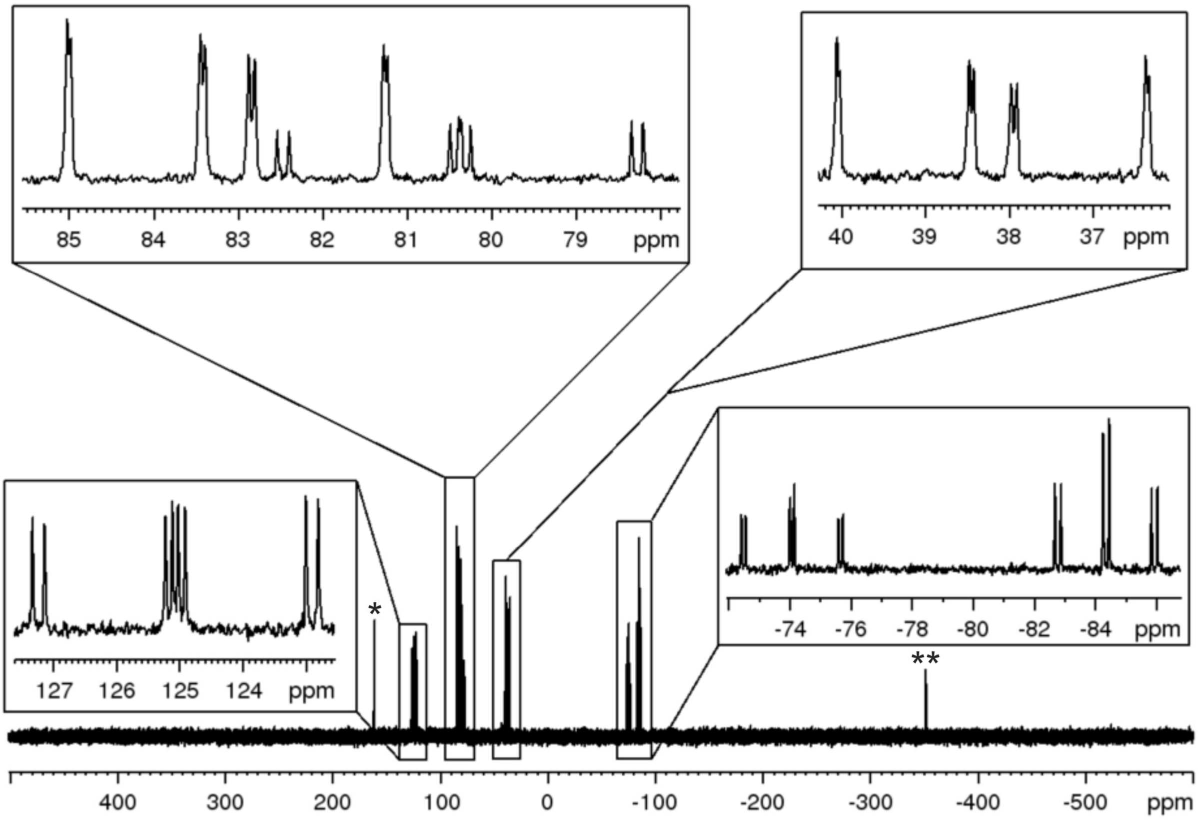

Figure S38: $^{31}P\{^{1}H\}$ NMR spectrum of the crude solution of **1g**[$GaCl_4$] in o-DFB/C_6D_6; * = $PPhCl_2$ ** = starting material **A1**.

Two sets of signals in a ratio of ≈4:1 are observed, which can be assigned to $\mathbf{1g_{endo}}$ and $\mathbf{1g_{exo}}$.

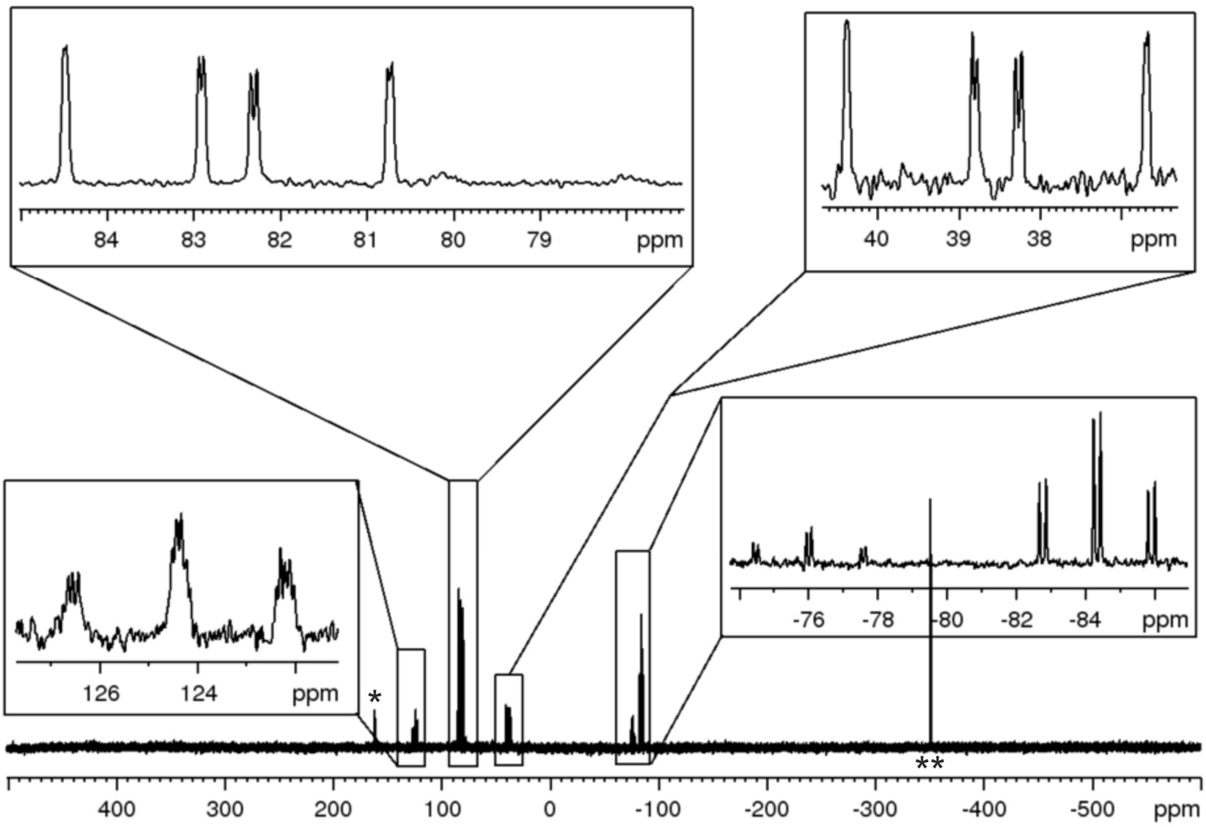

Figure S39: ^{31}P NMR spectrum of the crude solution of **1g**[$GaCl_4$] in o-DFB/C_6D_6; * = $PPhCl_2$ ** = starting material **A1**.

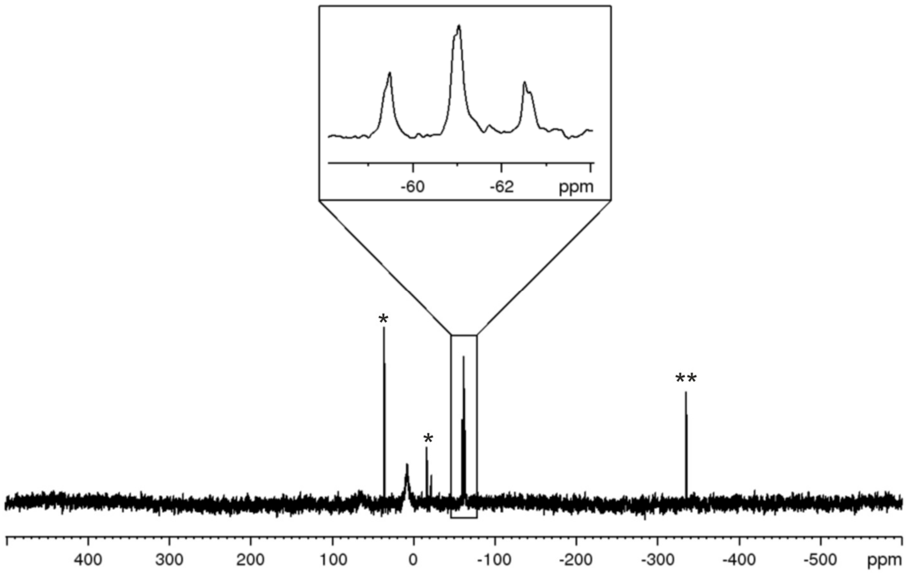

Figure S40: $^{31}P\{^{1}H\}$ NMR spectrum of the crude solution of **2**[$GaCl_4$] in o-DFB/C_6D_6; * = unidentified impurities in minor ratio; ** = starting material **A2**.

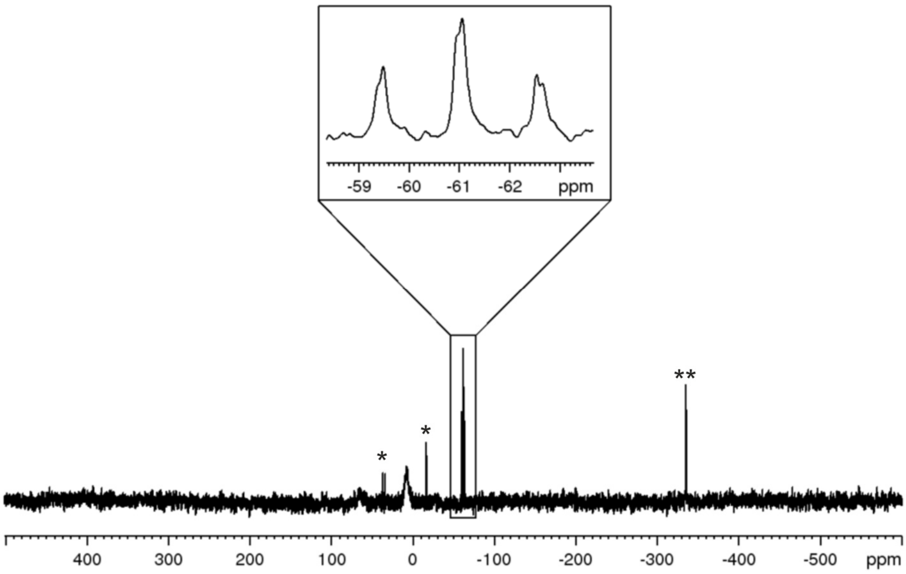

Figure S41: ^{31}P NMR spectrum of the crude solution of **2**[$GaCl_4$] in o-DFB/C_6D_6; * = unidentified impurities in minor ratio; ** = starting material **A2**.

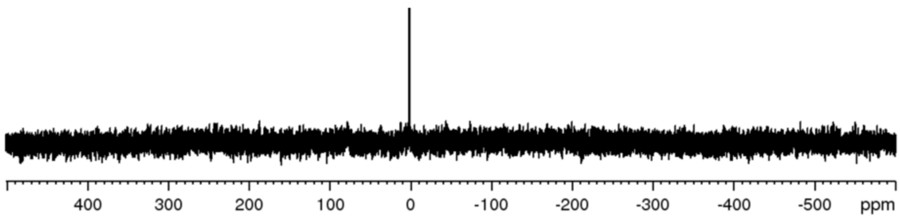

Figure S42: $^{31}P\{^{1}H\}$ NMR spectrum of the crude solution of **3b**[TEF] in o-DFB/C_6D_6.

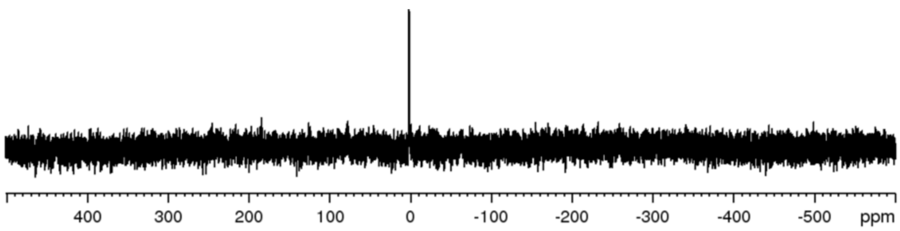

Figure S43: ^{31}P NMR spectrum of the crude solution of **3b**[TEF] in o-DFB/C_6D_6.

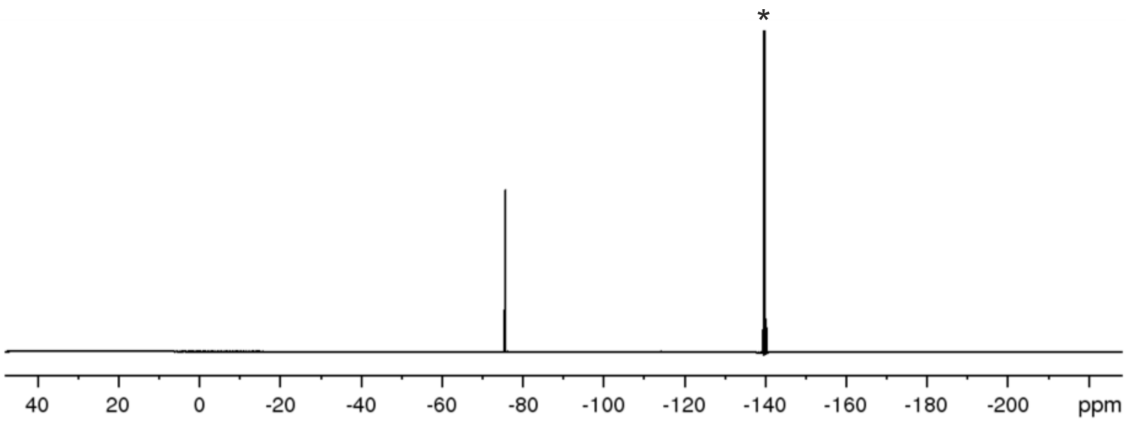

Figure S44: $^{19}F\{^{1}H\}$ NMR spectrum of the crude solution of **3b**[TEF] in o-DFB/C_6D_6; * = *o*-DFB.

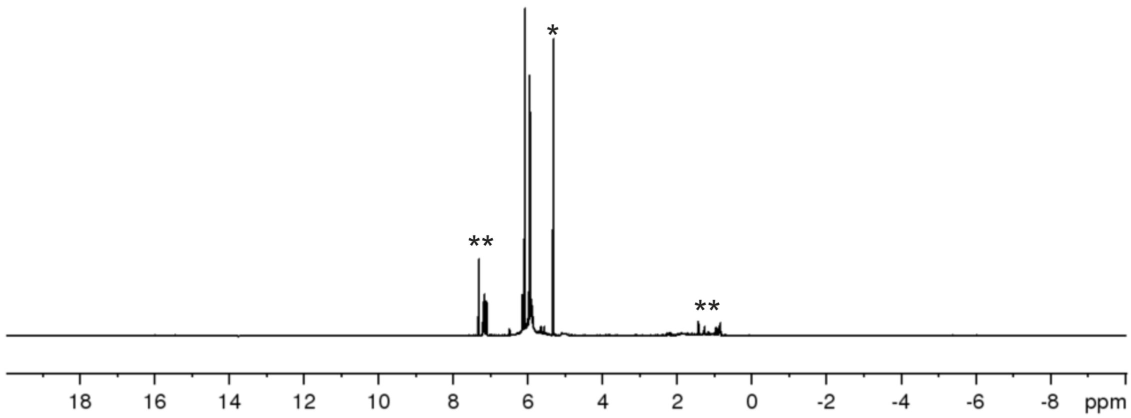

Figure S45: ^{1}H NMR spectrum of crystalline **5**[TEF] in CD_2Cl_2; * = CD_2Cl_2; ** = *o*-DFB/H

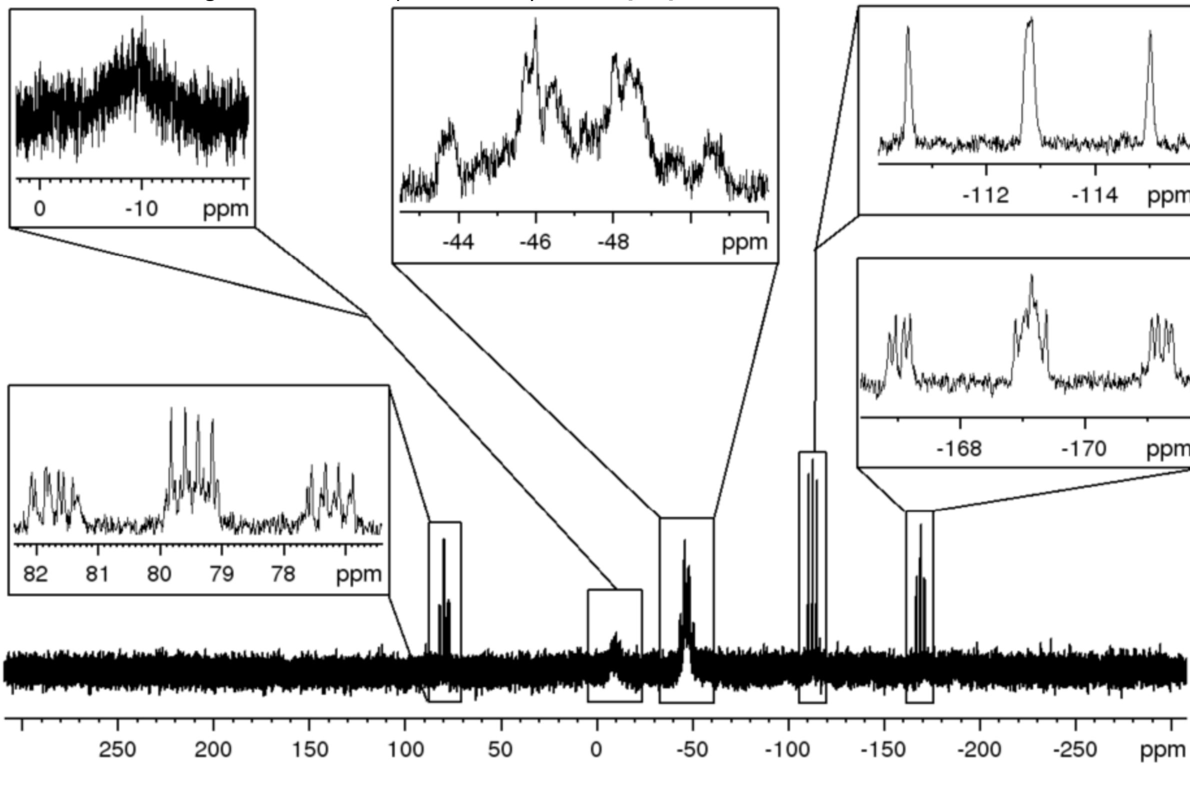

Figure S46: $^{31}P\{^1H\}$ NMR spectrum of crystalline **5**[TEF] in CD_2Cl_2.

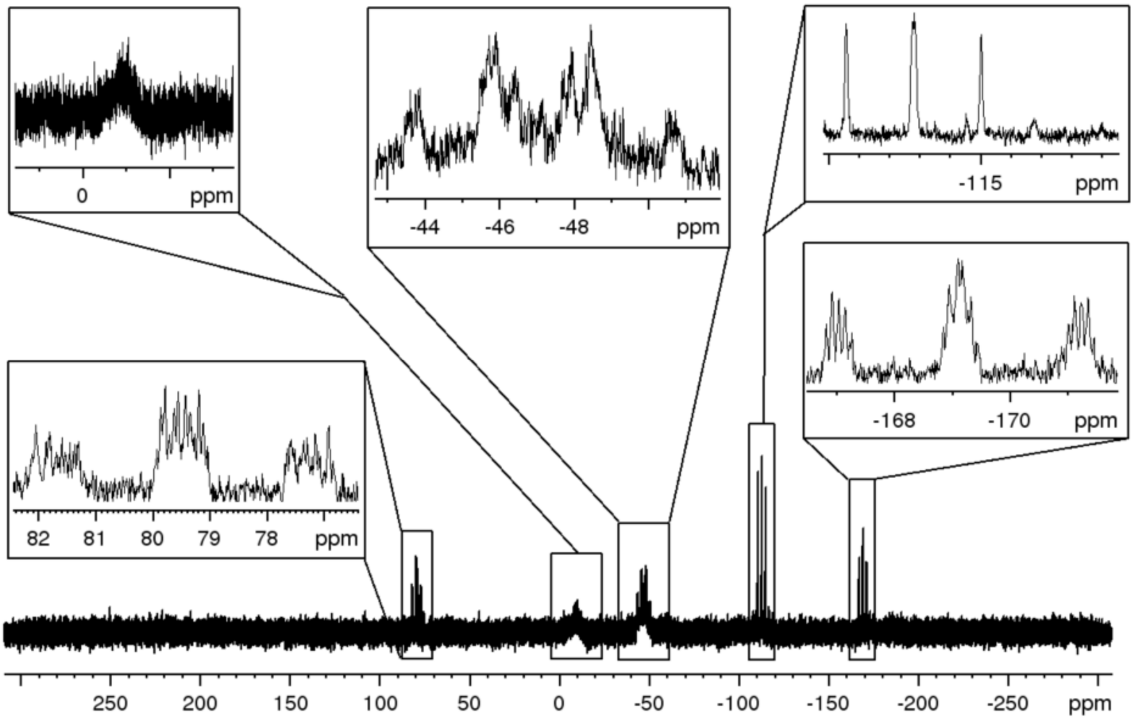

Figure S47: ^{31}P NMR spectrum of crystalline **5**[TEF] in CD_2Cl_2.

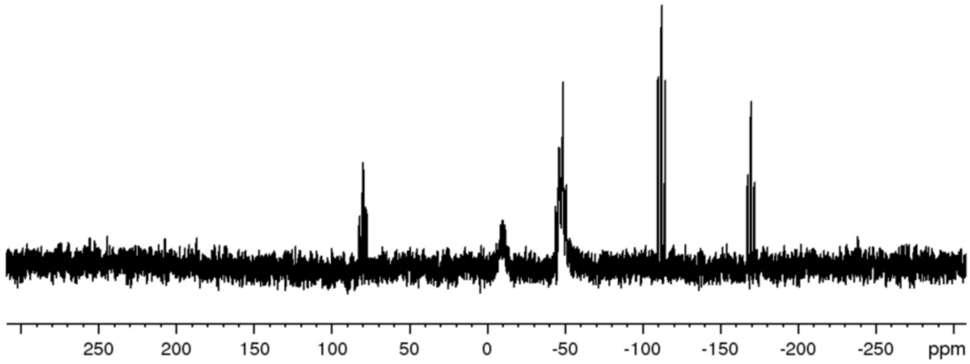

Figure S48: $^{31}P\{^1H\}$ NMR spectrum of the crude solution of **5**[TEF] in o-DFB/C_6D_6.

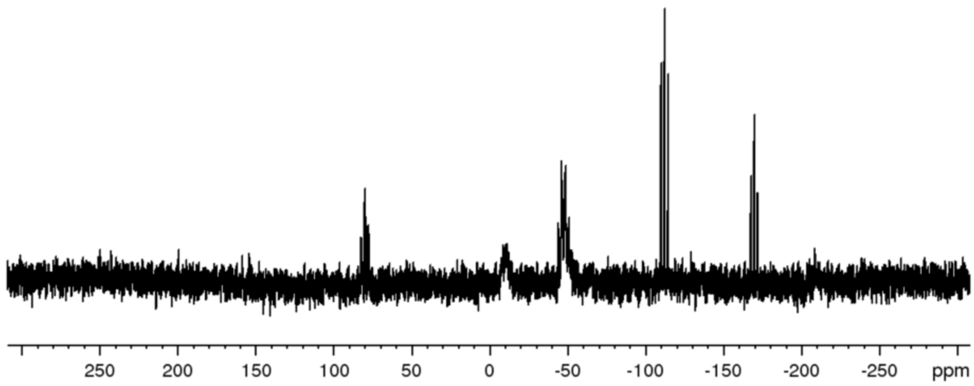

Figure S49: ^{31}P NMR spectrum of the crude solution of **5**[TEF] in o-DFB/C_6D_6.

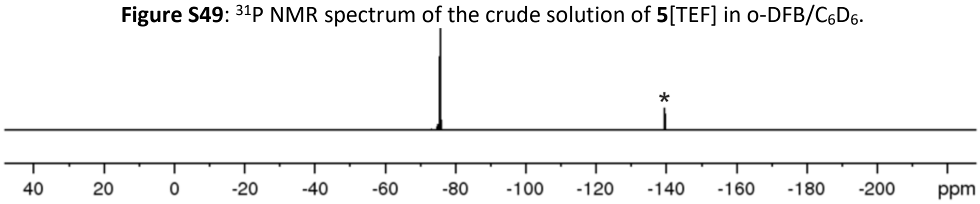

Figure S50: $^{19}F\{^1H\}$ NMR spectrum of crystalline **5**[TEF] in CD_2Cl_2; * = *o*-DFB.

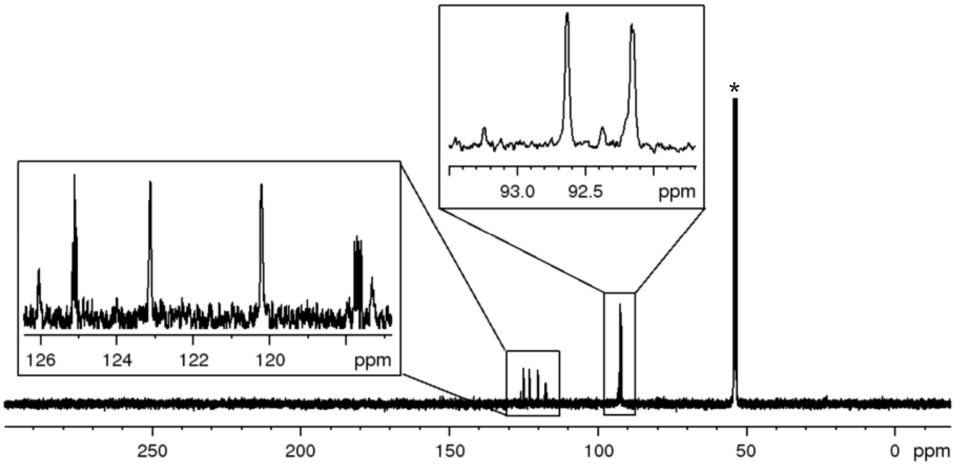

Figure S51: $^{13}C\{^1H\}$ NMR spectrum of crystalline **5**[TEF] in CD_2Cl_2; * = CD_2Cl_2.

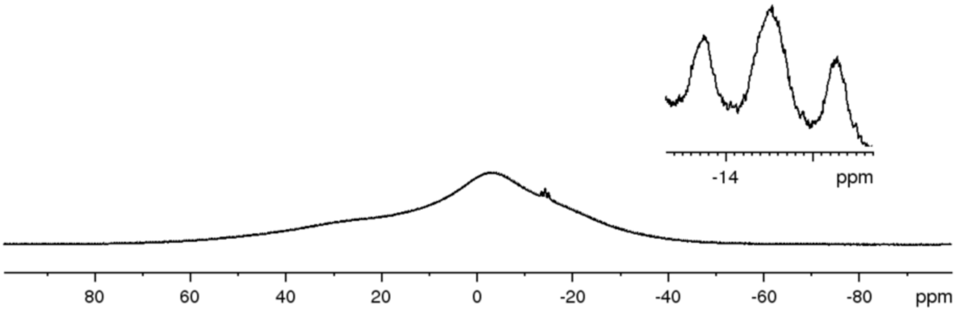

Figure S52: $^{11}B\{^1H\}$ NMR spectrum of crystalline **5**[TEF] in CD_2Cl_2.

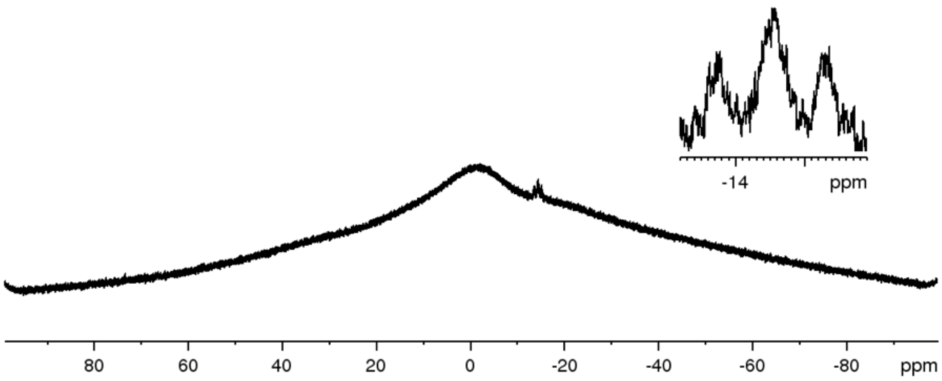

Figure S53: ^{11}B NMR spectrum of crystalline **5**[TEF] in CD_2Cl_2.

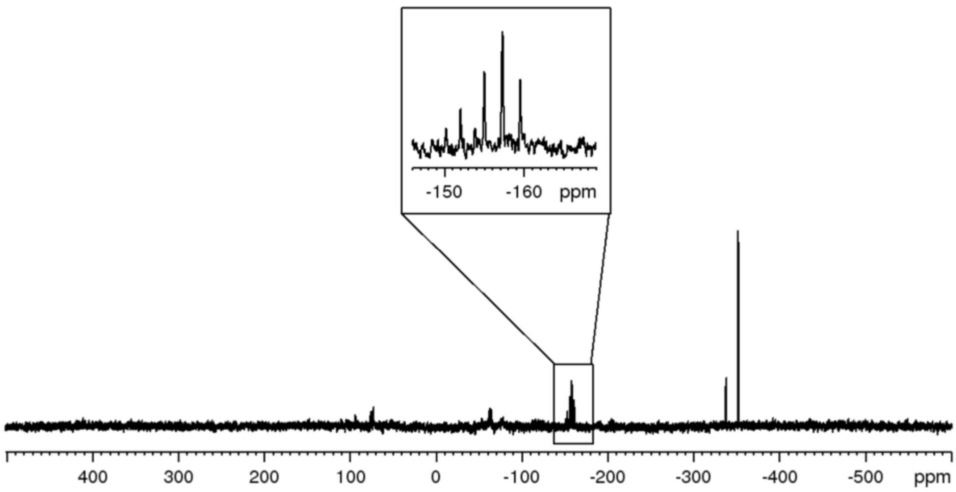

Figure S54: $^{31}P\{^{1}H\}$ NMR spectrum of the supernatant solution of the reaction of **A1** and BBr_3 in the absence of a halide abstraction agent (in o-DFB/C_6D_6).

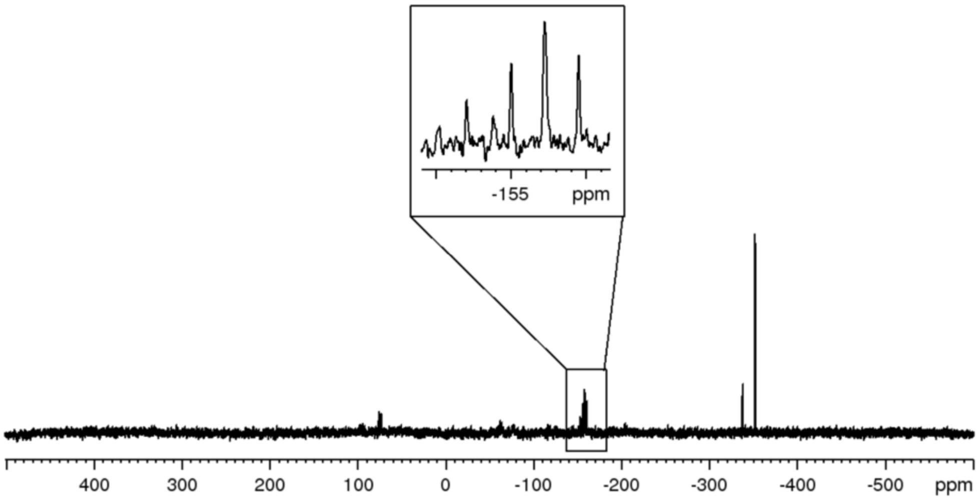

Figure S55: ^{31}P NMR spectrum of the supernatant solution of the reaction of **A1** and BBr_3 in the absence of a halide abstraction agent (in o-DFB/C_6D_6).

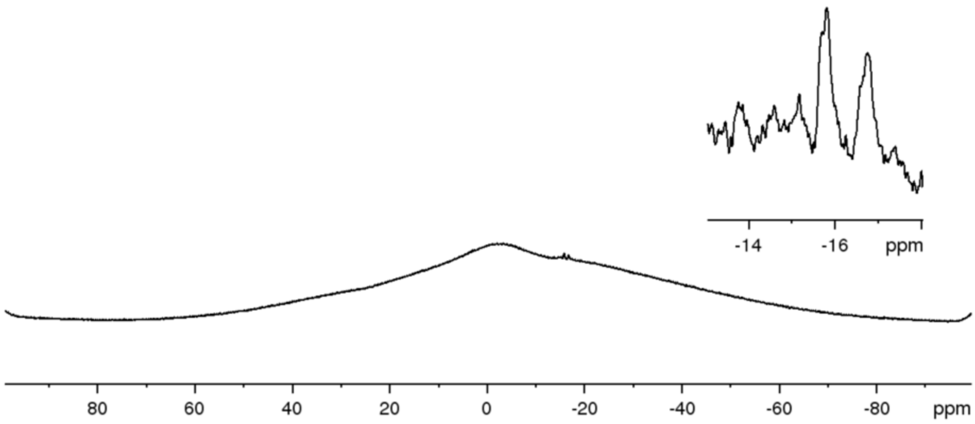

Figure S56: $^{11}B\{^{1}H\}$ NMR spectrum of the supernatant solution of the reaction of **A1** and BBr_3 in the absence of a halide abstraction agent (in o-DFB/C_6D_6).

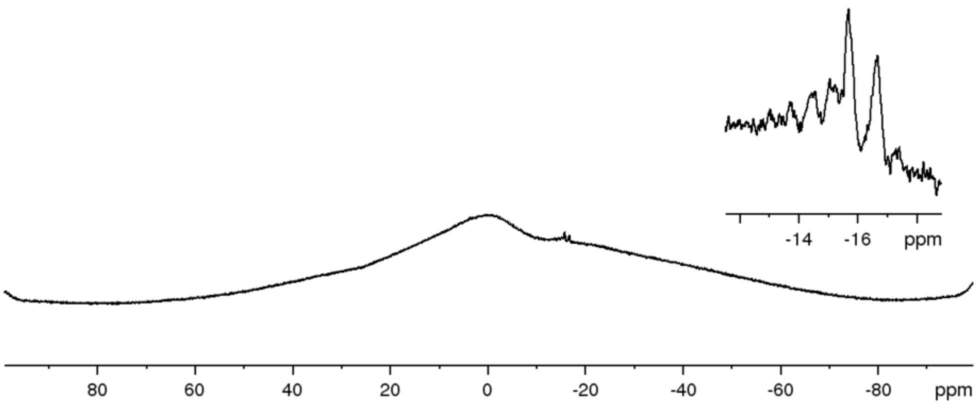

Figure S57: ^{11}B NMR spectrum of the supernatant solution of the reaction of **A1** and BBr_3 in the absence of a halide abstraction agent (in o-DFB/C_6D_6).

9.4.4 Mass spectrometry

The mass spectra were recorded by the mass spectrometry department of the University of Regensburg and are not available to the authors in a digital format and, therefore, could not be displayed.

9.4.5 X-ray crystallography

All crystal manipulations were performed under mineral oil. The diffraction experiments were performed at 123 K on a Rigaku (former Agilent Technologies or Oxford Diffraction) Gemini Ultra with an AtlasS2 detector or on a GV50 diffractometer with a TitanS2 detector using Cu-K_α, Cu-K_β or Mo-K_α radiation. Crystallographic data together with the details of the experiments are given in Table S1 and Table S2. The cell determination, data reduction and absorption correction for all compounds were performed with the help of the CrysAlis PRO software.[17] All structures were solved by using the programs SHELXT[18] and Olex2.[19] The full-matrix least-squares refinement against F^2 was done using SHELXL[20] and Olex2.[19] If not stated otherwise, all atoms except hydrogen atoms were refined anisotropically. The H atoms were calculated geometrically and a riding model was used during the refinement process.

Table S1: Crystallographic details for the compounds **1a**[$GaCl_4$], **1a**[OTf], **1f**[TEF], **1g$_{endo}$**[H(OTF)$_2$] and **1g$_{exo}$**[TEF].

	1a[$GaCl_4$]	**1a**[OTf]	**1a**[OTf] (2nd cell)	**1f**[TEF]	**1g$_{endo}$**[H(OTF)$_2$]	**1g$_{exo}$**[TEF]
formula	$C_{19}H_{15}Cl_4GaMoO_2P_4$	$C_{20.5}H_{16}ClF_3MoO_5P_4S$	$C_{20}H_{15}F_3MoO_5P_4S$	$C_{23}H_5AlBr_2F_{36}MoO_6P_4$	$C_{15}H_{11}ClF_6MoO_8P_4S_2$	$C_{29}H_{10}AlClF_{36}MoO_6P_4$
weight [g·mol^{-1}]	706.65	686.66		1467.89	752.63	1420.62
Temperature [K]	123.0(1)	123.0(1)	123.0(1)	123.0(1)	123.0(1)	123.0(1)
crystal system	monoclinic	triclinic	triclinic	monoclinic	orthorhombic	triclinic
space group	$P2_1/c$	P-1	P-1	$P2_1/c$	$P2_12_12_1$	P-1
a [Å]	19.8954(3)	9.4910(3)	10.321(3)	10.11870(10)	9.0886(3)	10.2166(7)
b [Å]	24.5243(4)	9.9195(4)	10.727(3)	28.7184(3)	10.0054(5)	14.7134(11)
c [Å]	10.6932(2)	13.9980(4)	24.315(6)	15.2530(2)	27.3887(8)	16.4139(13)
α [°]	90	80.132(3)	88.25(2)	90	90	80.780(6)
β [°]	95.053(2)	88.899(2)	84.03(2)	107.0790(10)	90	80.181(6)
γ [°]	90	74.649(3)	64.31(3)	90	90	76.965(6)
Volume [Å^3]	5197.16(15)	1251.56(8)	2412.5(1)	4236.95(9)	2490.59(17)	2349.4(3)
Z	8	2	4	4	4	2
ρ_{calc} [g·cm^{-3}]	1.806	1.822		2.301	2.007	2.008
μ [mm^{-1}]	8.506	6.641		6.072	10.130	0.676
F(000)	2768.0	682.0		2800.0	1480.0	1376.0
crystal size [mm^3]	0.404 × 0.258 × 0.221	0.405 × 0.241 × 0.181		0.53 × 0.399 × 0.362	0.365 × 0.219 × 0.153	0.382 × 0.329 × 0.217
diffractometer	GV50	GV50	GV50	GV50	GV50	Gemini Ultra
absorption correction	gaussian	gaussian		gaussian	gaussian	gaussian
T_{min} / T_{max}	0.074 / 0.439	0.295 / 0.807		0.403 / 1.000	0.178 / 0.573	0.836 / 0.984
radiation [Å]	Cu-Kβ (λ = 1.39222)	Cu-Kβ (λ = 1.39222)		Cu-Kβ (λ = 1.39222)	Cu-Kα (λ = 1.54184)	Mo-Kα (λ = 0.71073)
2Θ range [°]	5.176 to 148.824	8.474 to 131.3		5.558 to 148.21	9.41 to 146.442	7.16 to 58.424
completeness [%]	98.6	99.3		100.0	98.7	99.2
reflns collected / unique	36370 / 13953	13476 / 5665		34048 / 11434	8223 / 4469	14968 / 10412
R_{int} / R_{sigma}	0.0534 / 0.0492	0.0467 / 0.0542		0.0577 / 0.0492	0.0338 / 0.0397	0.0309 / 0.0717
data / restraints / parameters	13953 / 0 / 559	5665 / 0 / 331		11434 / 357 / 1117	4469 / 6 / 335	10412 / 73 / 793
GOF on F^2	1.059	1.036		1.023	1.141	1.079
R_1 / wR_2 [$I \geq 2\sigma(I)$]	0.0530 / 0.1455	0.0384 / 0.0999		0.0548 / 0.1443	0.0971 / 0.2558	0.0642 / 0.1512
R_1 / wR_2 [all data]	0.0561 / 0.1486	0.0405 / 0.1025		0.0590 / 0.1487	0.0985 / 0.2568	0.0867 / 0.1700
max / min $\Delta\rho$ [e·Å^{-3}]	1.44 / −1.66	1.36 / −1.28		1.32 / −1.29	4.36 / −4.04	2.20 / −1.54
Identification code	LD327_abs	LD287_abs	LD287_2. Zelle	LD340_abs	LD291_2_abs	LD398_exo_abs

Table S2: Crystallographic details for the compounds **2**[$GaCl_4$], **3a**[TEF], **3b**[TEF], **5** [TEF], **6b**[TEF] and **6d**[$TEF]_2$.

	2[$GaCl_4$]	**3a**[TEF]	**3b**[TEF]	**5**[TEF]	**6b**[TEF]	**6d**[$TEF]_2$
formula	$C_{24}H_{25}O_2P_4Cl_4GaMo$	$C_{35}H_{15}AlAs_3F_{36}MoO_6P$	$C_{40}H_{25}AlAs_3F_{36}MoO_6P$	$C_{36}H_{14}AlBBr_3F_{38}Mo_2O_8P_6$	$C_{31}H_{16}O_7F_{36}AlP_7Mo_2$	$C_{80.5}H_{54}Al_2ClF_{72}Mo_2O_{10}P_8$
weight [$g \cdot mol^{-1}$]	776.78	1594.12	1664.25	1951.69	1620.09	3206.68
Temperature [K]	123.0(1)	123(1)	123.0(1)	123.0(1)	123.0(1)	123.0(1)
crystal system	triclinic	orthorhombic	monoclinic	triclinic	monoclinic	triclinic
space group	P-1	$Pna2_1$	$P2_1/c$	P-1	$P2_1/n$	P-1
a [Å]	11.7348(2)	16.8787(4)	45.4511(4)	13.6041(3)	21.2779(5)	14.1537(5)
b [Å]	17.0922(3)	26.5532(6)	12.48280(10)	14.0096(3)	9.9873(2)	15.0522(4)
c [Å]	24.7913(4)	11.0660(2)	31.7213(3)	15.7113(3)	24.0381(4)	29.1712(7)
α [°]	72.641(2)	90	90	101.446(2)	90	78.832(2)
β [°]	84.7340(10)	90	95.5050(10)	92.464(2)	94.446(2)	83.396(2)
γ [°]	78.1730(10)	90	90	90.478(2)	90	78.385(2)
Volume [$Å^3$]	4642.75(15)	4959.60(19)	17914.3(3)	2931.68(11)	5092.94(18)	5953.5(3)
Z	6	4	12	2	4	2
ρ_{calc} [$g \cdot cm^{-3}$]	1.667	2.135	1.851	2.211	2.113	1.789
μ [mm^{-1}]	9.699	6.571	5.488	6.839	7.967	5.239
F(000)	2316.0	3064.0	9672.0	1866.0	3136.0	3152.0
crystal size [mm^3]	0.405×0.114×0.061	0.705×0.248×0.241	0.237×0.186×0.081	0.337×0.150×0.111	0.161×0.065×0.031	0.675×0.208×0.114
diffractometer	GV50	Gemini Ultra	GV50	GV50	GV 50	Gemini Ultra
absorption correction	gaussian	gaussian	gaussian	gaussian	gaussian	gaussian
T_{min} / T_{max}	0.181 / 0.887	0.053 / 0.610	0.400 / 0.824	0.347 / 0.888	0.409 / 0.868	0.225 / 1.000
radiation [Å]	Cu-Kα (λ = 1.54184)	Cu-Kα (λ = 1.54184)	Cu-Kα (λ = 1.54184)	Cu Kβ (λ = 1.39222)	Cu-Kα (λ = 1.54184)	Cu-Kα (λ = 1.54184)
2Θ range [°]	7.476 to 148.028	8.474 to 144.012	6.512 to 148.046	5.188 to 148.374	7.378 to 147.99	7.3 to 143.532
completeness [%]	99.7	99.9	99.0	99.2	98.9	98.5
reflns collected / unique	51773 / 18317	29084 / 9326	149810 / 36016	47761 / 15871	18637 / 9788	38428 / 22292
R_{int} / R_{sigma}	0.0375 / 0.0381	0.0429 / 0.0331	0.1431 / 0.0853]	0.0306/ 0.0318	0.0321 / 0.0429	0.0600 / 0.0722]
data / restraints / parameters	18317 / 6 / 1033	9326 / 31 / 748	36016 /1410 / 2392	15871 / 48 / 937	9788 / 801 / 1236	22292 / 162 / 1572
GOF on F^2	1.022	1.034	1.579	1.018	1.066	1.835
R_1 / wR_2 [$I \geq 2\sigma(I)$]	0.0274 / 0.0667	0.0476 / 0.1277	0.1348 / 0.3686	0.0383 / 0.1056	0.0729 / 0.1831	0.1853 / 0.4287
R_1 / wR_2 [all data]	0.0318 / 0.0693	0.0480 / 0.1282	0.1557 / 0.4026	0.0410 / 0.1084	0.0842 / 0.1919	0.2040 / 0.4615
max / min $\Delta\rho$ [$e \cdot Å^{-3}$]	0.61 / −0.90	1.10 / −1.55	7.27 / −3.14	2.89 / −1.50	1.22 / −0.88	17.28 / −5.39
Identification code	LD329_abs	LD443_abs	LD336_abs	LD375_abs	LD332_abs	LD334_abs

Refinement details for 1a[$GaCl_4$]

Compound **1a**[$GaCl_4$] crystallizes as dark yellow blocks in the monoclinic space group $P2_1/c$ with two cations **1a** and two [$GaCl_4$]$^-$ anions in the asymmetric unit. The refinement of the crystal structure could be done without any difficulty. No disorder was observed and no constraints or restraints had to be used.

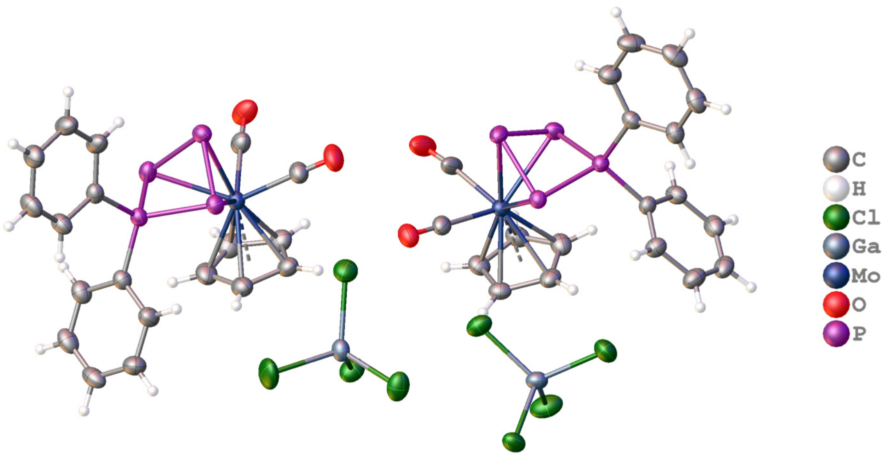

Figure S58: X-ray structure of **1a**[$GaCl_4$]. The asymmetric unit is shown containing two cations and two anions.

Refinement details for 1a[OTf]

Compound **1a**[OTf] crystallizes as yellow blocks in the triclinic space group $P\bar{1}$ with one cation **1a** one [OTf]$^-$ anion and one half CH_2Cl_2 in the asymmetric unit. The refinement of the crystal structure could be done without any difficulty. No disorder was observed and no constraints or restraints had to be used. As mentioned, one half molecule CH_2Cl_2 is present in the asymmetric unit. The chlorine atom has the occupancy 1, while the C and the H atoms have the occupancy 0.5.

An additional crystal species of **1a**[OTf] could be observed showing a different unit cell. Within that **1a**[OTf] crystallizes also as yellow blocks in the triclinic space group $P\bar{1}$, however, with two cations **1a** and two [OTf]$^-$ anions in the asymmetric unit (no CH_2Cl_2 molecule). For the second crystal species only an "What is this" and no complete experiment was conducted and, therefore, only the cell parameters are given in Table S1.

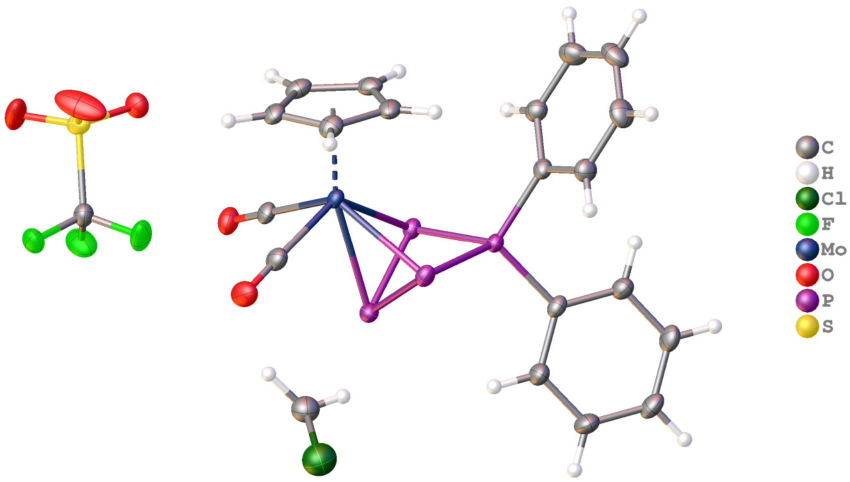

Figure S59: X-ray structure of **1a**[OTf]. The asymmetric unit is shown containing one cation, one anion and half CH_2Cl_2 molecule.

Refinement details for 1f[TEF]

Compound **1f**[TEF] crystallizes as orange blocks in the monoclinic space group $P2_1/c$ with one cation **1f** and one $[TEF]^-$ anion in the asymmetric unit. The $[TEF]^-$ anion exhibits rotational disorder of all four perfluorinated *tert*-butoxy groups in a ratio of 64:36, 66:34, 54:66 and 67:33. The disordered $C(CF_3)_3$ groups were restrained by DFIX and DANG, and the anisotropic displacement parameters (ADPs) by SIMU commands. One of the $C(CF_3)_3$ groups might show a third rotational disorder.

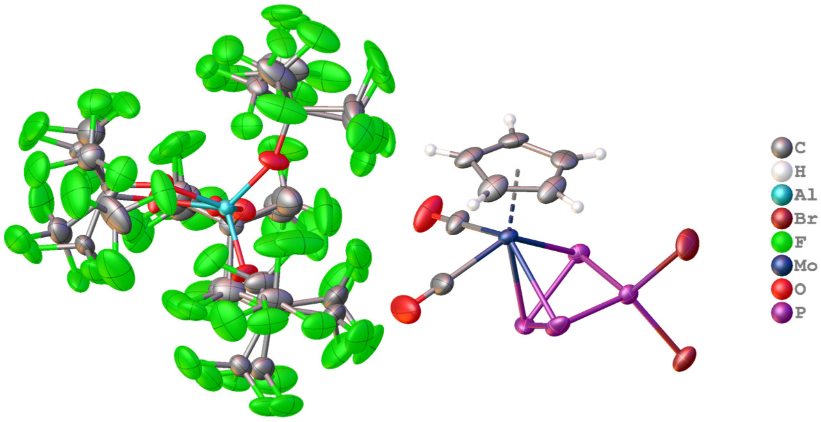

Figure S60: X-ray structure of **1f**[TEF]. The asymmetric unit is shown containing one cation and one fully disordered anion.

Refinement details for $\mathbf{1g_{endo}}$[H(OTf)₂]

Compound $\mathbf{1g_{endo}}[H(OTf)_2]$ crystallizes as yellow blocks in the orthorhombic space group $P2_12_12_1$ with one cation $\mathbf{1g_{exo}}$, one $[OTF]^-$ anion and one protonated triflate [HOTF] in the asymmetric unit. The proton of [HOTf] builds up a hydrogen bridge to the second $[OTF]^-$ anion. Therefore, it can be regarded as an $[H(OTf)_2]^-$. The refinement could be done without any difficulty. However, the *R* values are relatively high (R_1 = 9.71 %; wR_2 = 25.68 %). Additionally, a flack parameter of 0.48(2) is reported. Hence, a BASF/TWIN refinement should be done, which could not be finished until the end of this thesis. Therefore, the bond lengths and angles should be considered carefully.

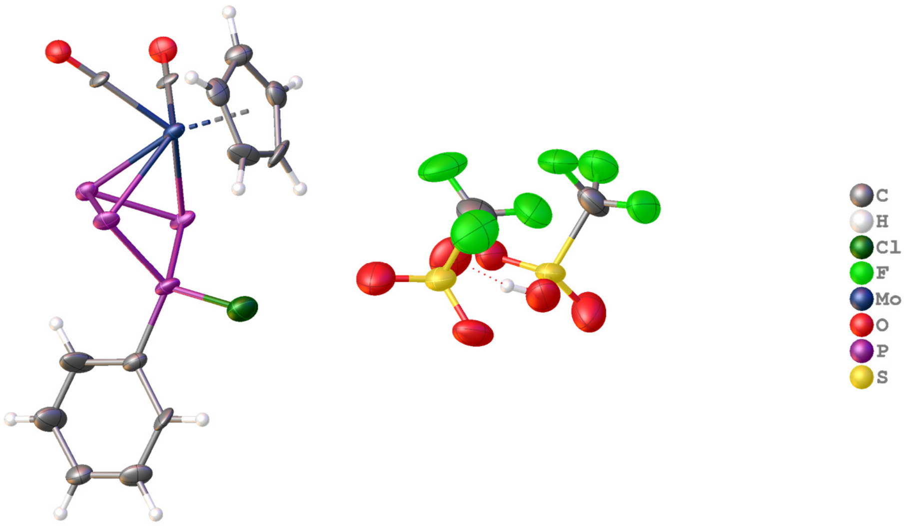

Figure S61: X-ray structure of $\mathbf{1g_{endo}}[H(OTf)_2]$. The asymmetric unit is shown containing one cation and two $[OTF]^-$ anion, where one of these is protonated and they are connected *via* a hydrogen bond.

Refinement details for $1g_{exo}$[TEF]

Compound **$1g_{exo}$**[TEF] crystallizes as colourless blocks in the triclinic space group $P\bar{1}$ with one cation **$1g_{exo}$** and one [TEF]$^-$ anion in the asymmetric unit. The [TEF]$^-$ anion exhibits rotational disorder of one of its perfluorinated *tert*-butoxy groups in a ratio of 73:27. The disordered $C(CF_3)_3$ group was restrained by DFIX and DANG, and the ADPs by SIMU commands.

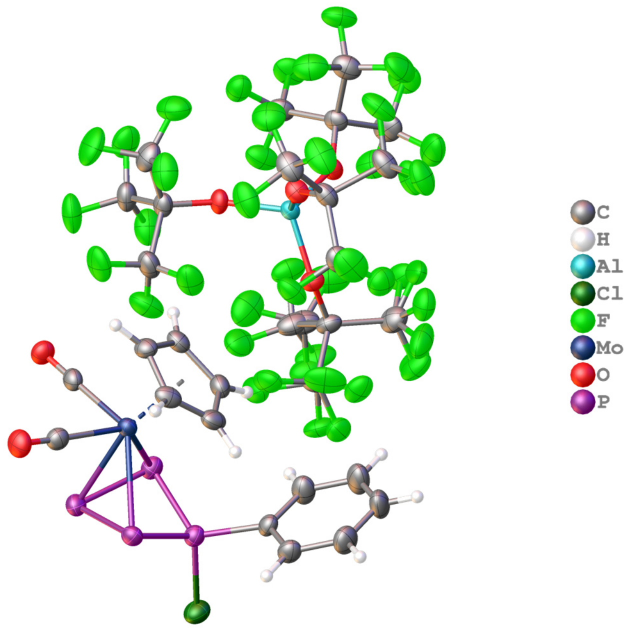

Figure S62: X-ray structure of **$1g_{exo}$**[TEF]. The asymmetric unit is shown containing one cation and one partially disordered anion.

Refinement details for 2[$GaCl_4$]

Compound **2**[$GaCl_4$] crystallizes as yellow sticks in the triclinic space group $P\bar{1}$ with three cations **2** and three [$GaCl_4$]$^-$ anions in the asymmetric unit. The refinement could be done without any difficulty. One [$GaCl_4$]$^-$ anion is disordered in a ratio of 55:45.

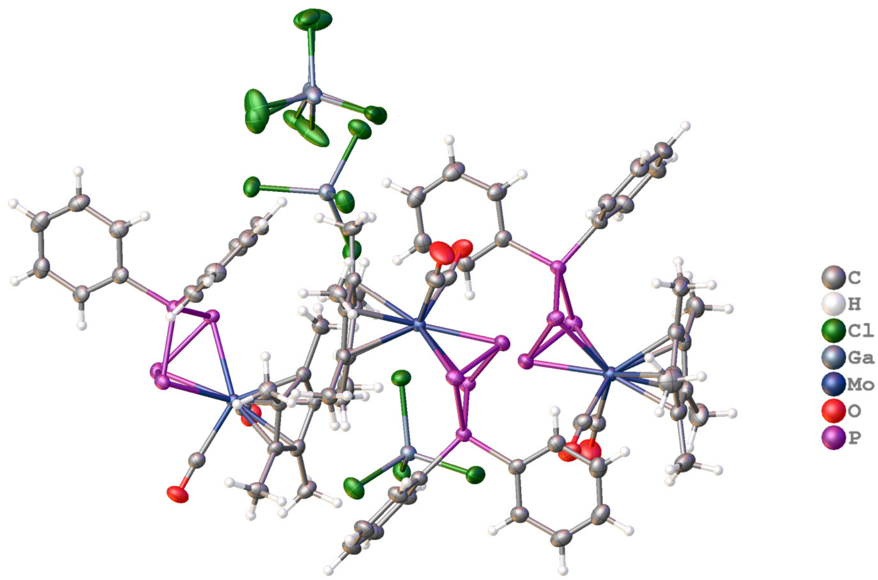

Figure S63: X-ray structure of **2**[$GaCl_4$]. The asymmetric unit is shown containing three cations and three anions.

Refinement details for 3a[TEF]

Compound **3a**[TEF] crystallizes as light yellow sticks in the orthorhombic space group *Pna*2_1 with one cation **3a** and one [TEF]$^-$ anion in the asymmetric unit. The refinement could be done without any difficulty. However, a flack parameter of 0.47(1) is reported suggesting a possible existence of an inversion twin. Hence, a BASF/TWIN refinement should be done, which could not be finished until the end of this thesis.

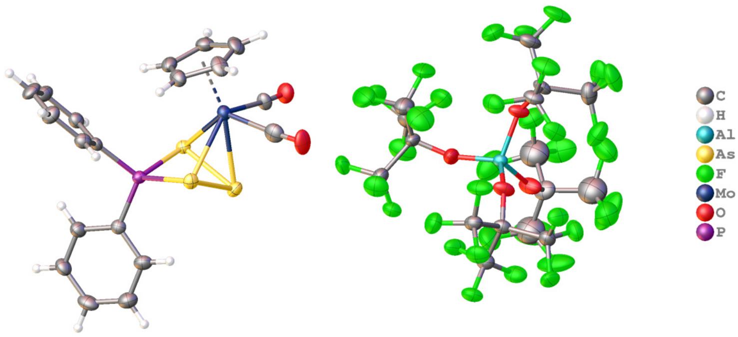

Figure S64: X-ray structure of **3a**[TEF]. The asymmetric unit is shown containing one cation and one anion.

Refinement details for 3b[TEF]

Compound **3b**[TEF] crystallizes as yellow blocks in the monoclinic space group $P2_1/c$ with three cations **3b** and three [TEF]$^-$ anions in the asymmetric unit. The experimental data set is very weak and, therefore, the refinement is difficult. Additionally, the [TEF]$^-$ anions show severe disorder, which could not be resolved until the end of this thesis. The [TEF]$^-$ anions were restrained with several DANG and DFIX, and the ADPs with SIMU commands. A solvent mask was calculated, and 632 electrons were found in a volume of 2742 Å^3 in 4 voids per unit cell. This is consistent with the presence of three *o*-DFB molecules per asymmetric unit. Overall, the bond lengths and angles should be considered carefully.

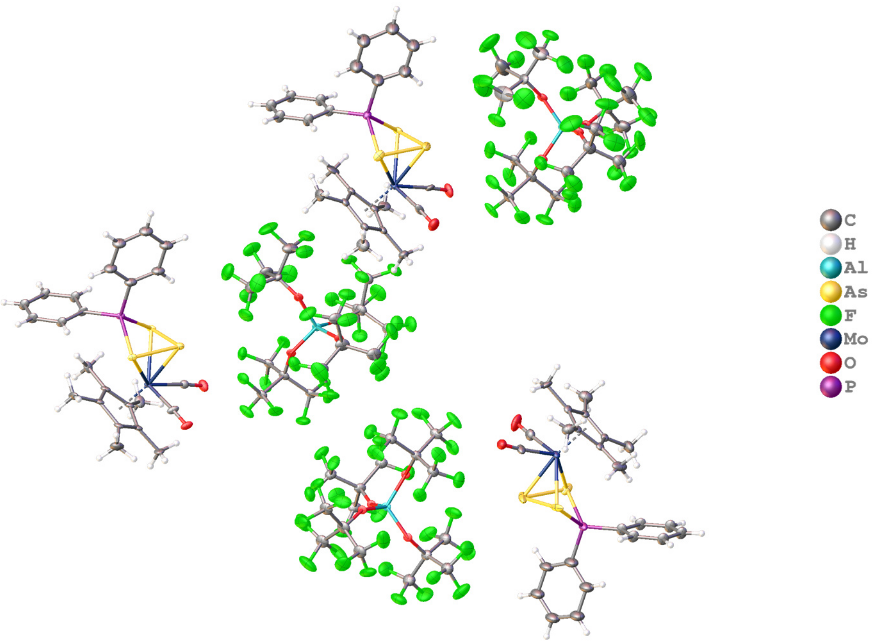

Figure S65: X-ray structure of **3b**[TEF]. The asymmetric unit is shown containing three cations and three anions. Additionally, solvent accessible voids were found, which perfectly fit for three *o*-DFB solvent molecules.

Refinement details for 5[TEF]

Compound **5**[TEF] crystallizes as intense yellow blocks in the triclinic space group $P\overline{1}$ with one cation **5**, one [TEF]⁻ anion and one *o*-DFB solvent molecule in the asymmetric unit. The refinement could be done without any difficulty. The [TEF]⁻ anion exhibits rotational disorder of one of its perfluorinated *tert*-butoxy groups in a ratio of 68:32. The disordered $C(CF_3)_3$ group was restrained by DFIX and DANG, and the ADPs by SIMU commands.

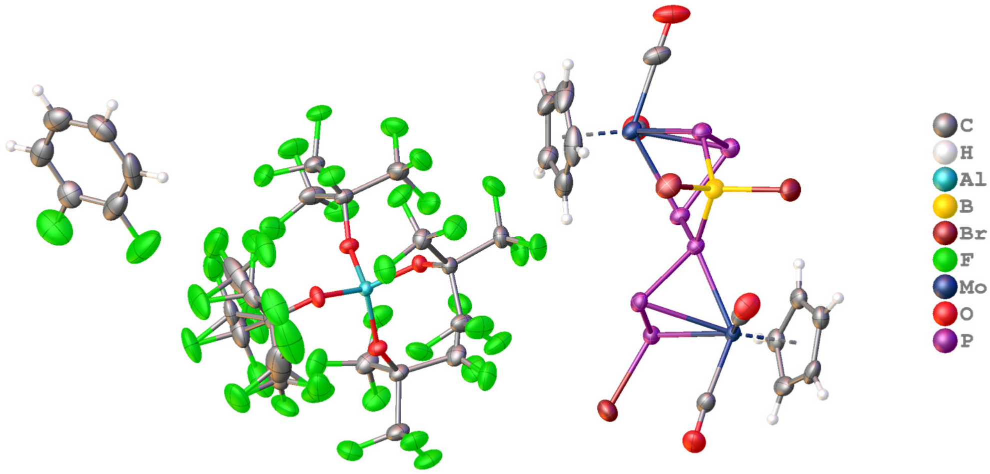

Figure S66: X-ray structure of **5**[TEF]. The asymmetric unit is shown containing one cation, one anion (with one disordered *tert*-butoxy group) and one *o*-DFB solvent molecule.

Refinement details for 6b[TEF]

Compound **6b**[TEF] crystallizes as orange to red sticks in the monoclinic space group $P2_1/n$ with one cation **6b** and one [TEF]⁻ anion in the asymmetric unit. The refinement could be done without any difficulty. The [TEF]⁻ anion exhibits rotational disorder of all four perfluorinated *tert*-butoxy groups in a ratio of 57:43, 58:43, 59:41 and 65:35. The $OC(CF_3)_3$ groups might also show a third rotational disorder in a very low percentage, which was not resolved. The disordered $OC(CF_3)_3$ groups were restrained by DFIX and DANG, and the ADPs by SIMU commands. Additionally, the MoP_3 unit and one CO ligand within the cation are disordered in a ratio of 65:35.

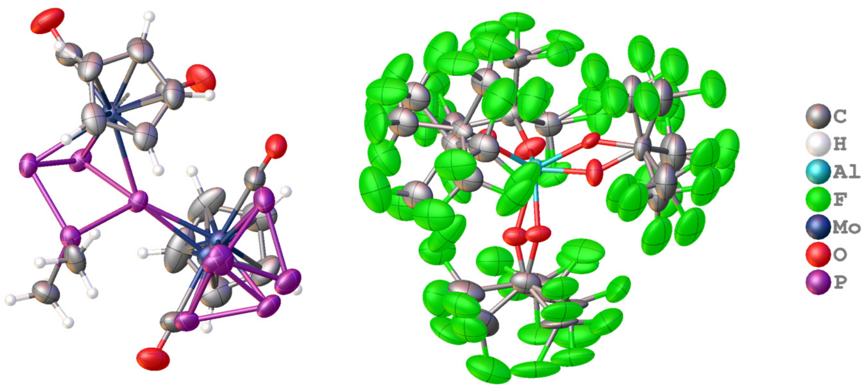

Figure S67: X-ray structure of **6b**[TEF]. The asymmetric unit is shown containing one cation (exhibiting a disorder of the MoP_3 unit and one CO ligand) and one anion (with at least doubly disordered *tert*-butoxy groups).

Refinement details for 6d[TEF]$_2$

Compound **6d**[TEF]$_2$ crystallizes as orange plates in the triclinic space group $P\bar{1}$ with one dication **6d**, two [TEF]$^-$ anions and one CH_2Cl_2 molecule in the asymmetric unit. The experimental data set is very weak and, therefore, the refinement is difficult. Additionally, the [TEF]$^-$ anions show severe disorder, which could not be completely resolved until the end of this thesis. The [TEF]$^-$ anions were restrained with several DANG and DFIX, and the ADPs with SIMU commands. Overall, the bond lengths and angles should be considered carefully.

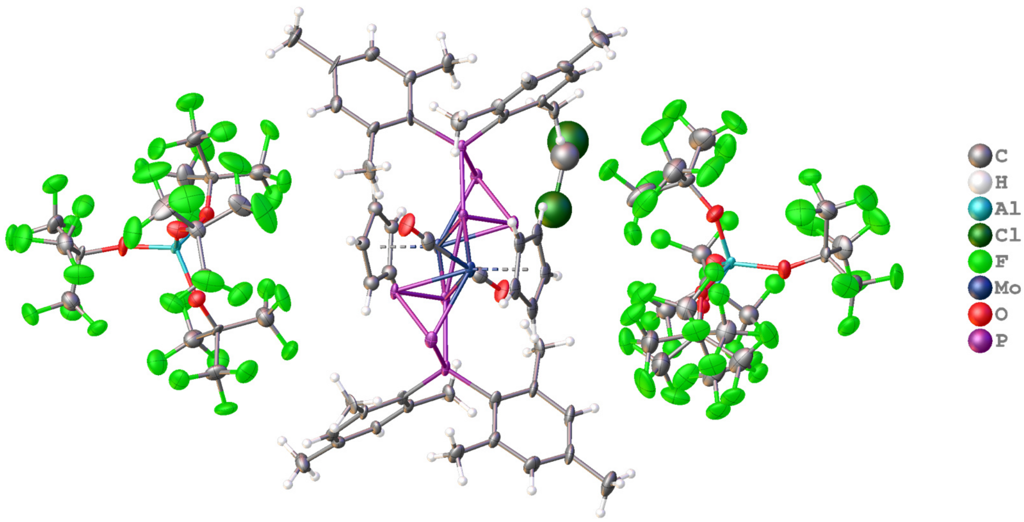

Figure S68: X-ray structure of **6d**[TEF]$_2$. The asymmetric unit is shown containing one dication, two disordered anions and one CH_2Cl_2 molecule.

9.5 References

[1] a) M. Peruzzini, L. Gonsalvi, A. Romerosa, *Chem. Soc. Rev.* **2005**, *34*, 1038-1047; b) C. M. Hoidn, D. J. Scott, R. Wolf, *Chem. Eur. J.* **2021**, *27*, 1886-1902.
[2] B. M. Cossairt, N. A. Piro, C. C. Cummins, *Chem. Rev.* **2010**, *110*, 4164-4177.
[3] a) J. J. Weigand, M. Holthausen, R. Fröhlich, *Angew. Chem. Int. Ed.* **2009**, *48*, 295-298; b) I. Krossing, I. Raabe, *Angew. Chem. Int. Ed.* **2001**, *40*, 4406-4409; c) M. Gonsior, I. Krossing, L. Müller, I. Raabe, M. Jansen, L. v. Wüllen, *Chem. Eur. J.* **2002**, *8*, 4475-4492.
[4] M. H. Holthausen, K.-O. Feldmann, S. Schulz, A. Hepp, J. J. Weigand, *Inorg. Chem.* **2012**, *51*, 3374-3387.
[5] C. Riesinger, L. Dütsch, G. Balázs, M. Bodensteiner, M. Scheer, *Chem. Eur. J.* **2020**, *26*, 17165-17170.
[6] M. Baudler, D. Habermann, *Angew. Chem. Int. Ed.* **1979**, *18*, 877-878.
[7] M. Piesch, S. Reichl, M. Seidl, G. Balázs, M. Scheer, *Angew. Chem. Int. Ed.*, *n/a*.
[8] W. E. Piers, S. C. Bourke, K. D. Conroy, *Angew. Chem. Int. Ed.* **2005**, *44*, 5016-5036.
[9] P. Pyykkö, *J. Phys. Chem. A* **2015**, *119*, 2326-2337.
[10] M. Mantina, A. C. Chamberlin, R. Valero, C. J. Cramer, D. G. Truhlar, *J. Phys. Chem. A* **2009**, *113*, 5806-5812.
[11] O. J. Scherer, H. Sitzmann, G. Wolmershäuser, *J. Organomet. Chem.* **1984**, *268*, C9-C12.
[12] P. Jutzi, R. Kroos, *Chem. Ber.* **1988**, *121*, 1399-1401.
[13] N. Reinfandt, C. Schoo, L. Dütsch, R. Köppe, S. N. Konchenko, M. Scheer, P. W. Roesky, *Chem. Eur. J.* **2021**, *27*, 3974-3978.
[14] O. J. Scherer, H. Sitzmann, G. Wolmershäuser, *J. Organomet. Chem.* **1986**, *309*, 77-86.
[15] H. T. Teunissen, C. B. Hansen, F. Bickelhaupt, *Phosphorus, Sulfur, and Silicon and the Related Elements* **1996**, *118*, 309-312.
[16] M. Gonsior, I. Krossing, N. Mitzel, *Z. Anorg. Allg. Chem.* **2002**, *628*, 1821-1830.
[17] Agilent (2014). CrysAlis PRO. Agilent Technologies Ltd., Yarnton, Oxfordshire, England.
[18] G. Sheldrick, Acta Crystallographica Section A **2015**, 71, 3-8.
[19] O. V. Dolomanov, L. J. Bourhis, R. J. Gildea, J. A. K. Howard, H. Puschmann, *J. Appl. Cryst.* **2009**, *42*, 339-341.
[20] G. Sheldrick, Acta Crystallographica Section C **2015**, 71, 3-8.

Preface

The following chapter has not been published until the submission of this thesis. This chapter should give a first insight into the reactivity of the complexes $[\{CpMo(CO)_2\}_2\{\mu,\eta^2:\eta^2\text{-}EE'\}]$ (E, E' = P, As, Sb; "**Mo_2EE'**") towards selected main-group electrophiles such as phosphenium and borinium ions. A lot of different combinations of **Mo_2EE'** and electrophiles were investigated. Therefore, some of the results are preliminary and have to be corroborated by further studies and computations, which have not been finished until the end of this thesis. Hence, it must be considered that some statements in this chapter are only assumptions. In general, the presented results should provide a basis for future research efforts.

Authors

Luis Dütsch, Christoph Riesinger and Manfred Scheer

Author Contributions

The main part (conceptualization, preparation of the compounds **1**, **2a**, **2b**, **3**, **4**, **5**, **6**, **7a**, **7b**, **8a**, **8b**, **9a**, **10a**, **11**, **12a** and **12b**, writing, visualization, and execution and evaluation of measurements) of this work was done by the first author (Luis Dütsch). Compound **1** was synthesized first by Stefan Welsch. Christoph Riesinger assisted in the synthesis and characterization of the compounds **8a** and **8b**, which are part of his Bachelor thesis. Manfred Scheer supervised the research and revised the manuscript.

Acknowledgements

This work was supported by the Deutsche Forschungsgemeinschaft within the project Sche 384/36-2. We thank Christoph Riesinger for providing $[(Et_3Si)H][B(C_6F_5)]$ for the synthesis of **12a** and **12b**.

10 Electrophilic Functionalization of Tetrahedral Dipnictogen Complexes with Phosphenium and Borinium Ions

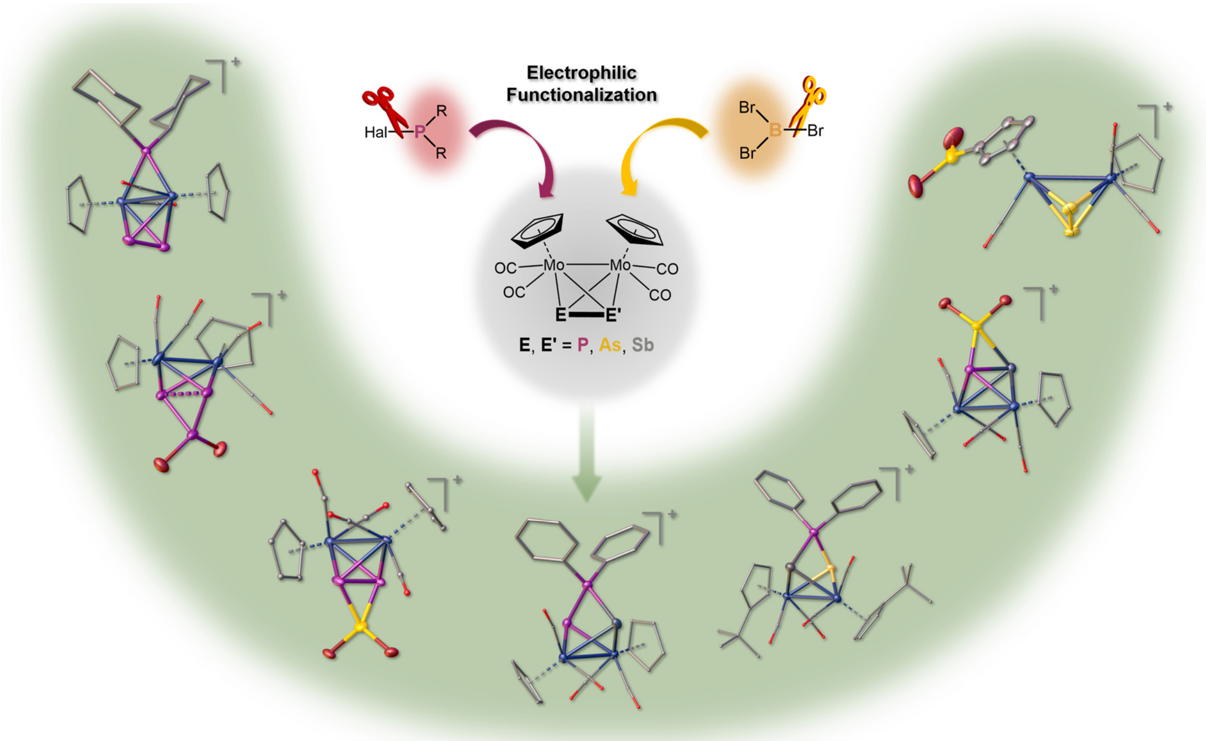

Abstract: *The reactivity of the tetrahedral dimolybdenum dipnictogen complexes [{CpMo(CO)$_2$}$_2${μ,η^2:η^2-EE'}] (E, E' = P, As, Sb; "**Mo$_2$EE'**") towards in situ generated phosphenium ([PR$_2$]$^+$) and borinium ([BBr$_2^+$]) ions is reported leading to electrophilic functionalization of the EE' ligand complexes. The resulting cationic products are stabilized by the weakly coordinating anion [Al{OC(CF$_3$)$_3$}$_4$]$^-$ (= [TEF]$^-$). Depending on the substituents of the phosphenium ions and the used **Mo$_2$EE'** complex different products can be obtained. Reaction of **Mo$_2$P$_2$** with [PPh$_2$]$^+$ gives a dimeric product [{CpMo(CO)}$_2${CpMo(CO)$_2$}$_2$(μ,η^2:η^2:η^2:η^1:η^1-2-(Ph$_2$P)P$_4$)(μ-PPh$_2$)]$^{2+}$ (**1**), which exhibits a isoprene analogous P$_5$ ligand. In contrast, reaction of [PCy$_2$] with **Mo$_2$P$_2$** as well as the reaction of [PPh$_2$]$^+$ with **Mo$_2$PAs** leads to CO elimination and the formation of the monomeric complexes [{CpMo(CO)}$_2$(μ,η^2:η^2-PE)(μ-PR$_2$)]$^+$ (**2a**: E = As, R = Ph; **3**: E = P, R = Cy), where the phosphenium ion is bridging the Mo–Mo bond. The phosphenium ion [PBr$_2$]$^+$ instead, partially inserts into the P–P bond of **Mo$_2$P$_2$** without CO elimination yielding [{CpMo(CO)$_2$}$_2$(μ,η^2:η^2-P$_3$Br$_2$)]$^+$ (**4**). Similar reaction is observed for the borinium ion [BBr$_2^+$] wit **Mo$_2$P$_2$** forming a three-membered P$_2$B ring, while electrophilic aromatic substitution of a proton on one Cp ligand occurs with **Mo$_2$As$_2$** and **Mo$_2$Sb$_2$**. Reaction of **Mo$_2$PSb** and **Mo$_2$AsSb** with [PPh$_2^+$] in CH$_2$Cl$_2$ leads to an attack towards the lighter pnictogen atom with subsequent HCl addition giving the products [{CpMo(CO)$_2$}$_2${μ-EH(PPh$_2$)}(μ-SbCl)]$^+$ (E = P (**8a**), As (**8b**)). The HCl addition can be suppressed by perfoming the reactions in o-DFB yielding [{Cp^{R}Mo(CO)$_2$}$_2$(μ,η^1:η^1-EP(Ph)$_2$Sb)]$^+$ (**10a**: E = P, Cp^R = Cp; **10b**: E = As, Cp^R = Cp') instead, where the phosphenium ions inserted into the E–Sb bonds forming rare PP(Ph$_2$)Sb and AsP(Ph$_2$)Sb chains. Reaction of **Mo$_2$PSb** with [BBr$_2^+$] leads to coordination of the P–Sb bond to the borinium ion forming a distorted PSbB ring. It was also possible to achieve selective protonation of **Mo$_2$P$_2$** and **Mo$_2$PAs** via reaction with [(Et$_3$Si)$_2$H][B(C$_6$F$_5$)$_4$], where the proton can be rather regarded as an hydride, which is bridging the Mo–Mo bond.*

10.1 Introduction

In the previous chapter it was shown that the E_3 ligand complexes [$Cp^RMo(CO)_2(\eta^3$-$E_3)$] (Cp^R = Cp, Cp*; E = P, As, "**MoE_3**") can be easily functionalized by reaction with the *in situ* generated phosphenium ions $[PR_2]^+$ (generated from PR_2X (X = halide) *via* reaction with a halide abstracting agent). The phosphenium ions insert into one of the P–P or As–As bonds, respectively, of the E_3 ligand leading to ring expansion reactions yielding substituted, cationic P_4 or As_3P rings stabilized by a [$Cp^RMo(CO)_2$] fragment and a weakly coordinating anion (**I** and **II**; Scheme 1). While this type of insertion reactions has been known for P_3 ligands before,[1] it was the first time that the electrophilic functionalization could be extended to neutral As_3 ligands. Only very recently we could also extend this to anionic As_3 rings.[2] By using different halophosphines as phosphenium ion precursors a lot of different substituents could be introduced into these rings enabling the access to numerous polyphosphorus and -arsenic ligand frameworks, which have been of high interest in recent research.[3] Additionally, this chemistry could be extended to group 13 electrophiles, where reaction of **MoP_3** with in situ generated $[BBr_2]^+$ led to the formation of a substituted P_6B^+ ligand (**III**; Scheme 1).

In chapter 3 we reported on the development of a facile synthesis of the isolobal tetrahedral dimolybdenum homo- and hetero-dipnictogen complexes [{$Cp^RMo(CO)_2$}$_2${$\mu,\eta^2:\eta^2$-E_2}] (Cp^R = Cp or Cp' ($^tBuC_5H_4$); E = P, As, Sb, Bi; "**Mo_2E_2**") and [{$Cp^RMo(CO)_2$}$_2${$\mu,\eta^2:\eta^2$-EE'}] (Cp^R = Cp or Cp'; E ≠ E' = P, As, Sb, Bi; "**Mo_2EE'**"), which increased the yield of the already known complexes **Mo_2E_2, Mo_2PAs** and **Mo_2PSb** dramatically and also realized their heavy pnictogen congeners with **AsSb**, **AsBi** and **SbBi**

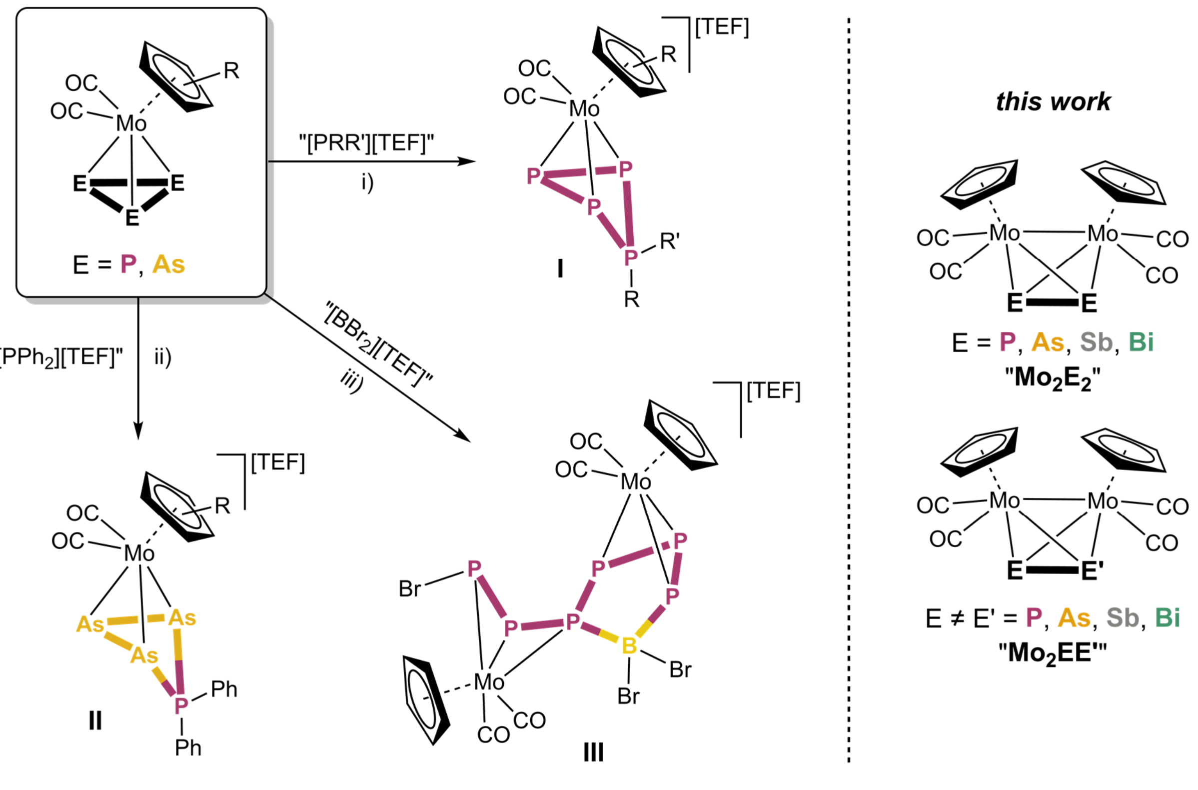

Scheme 1: Functionalization of a "naked" E_3 ligand (E = P, As) *via* insertion of phosphenium and borinium ions: i) E = P, Cp^R = $C_5H_5^-$ or $C_5Me_5^-$, "[PRR'][X]" *in situ* generated from PRR'Cl and Tl[TEF]; ii) E = As, Cp^R = Cp or Cp*, "[PPh_2][TEF]" from PPh_2Cl and Tl[TEF]; iii) E = P, Cp^R = Cp, "[BBr_2][TEF]" from BBr_3 and Tl[TEF]; *this work*: electrophilic attack on the tetrahedral dipnictogen complexes **Mo_2E_2** and **Mo_2EE'**.

ligands.[4] This easy and high yielding synthesis allowed us to investigate their reactivity. The complexes **Mo_2E_2** and **Mo_2EE'** already proofed to be excellent precursors for the formation of extended ionic polypnictogen frameworks upon oxidation (chapter 4–6)[5] and reduction.[6] Therefore, the question arose if they are also appropriate starting materials for electrophilic functionalization, like the **MoE_3** complexes, and if so, will the phosphenium ions react in an analogous manner *via* inserting into the E–E and E–E' bonds or just add on a pnictogen atom.

10.2 Results and Discussion

When an orange solution of **Mo_2P_2** and PPh_2Cl in CH_2Cl_2 is reacted with the halide-abstracting agent Tl[TEF] ($[TEF]^-$ = $[Al\{OC(CF_3)_3\}_4]^-$), formation of a white precipitate (TlCl) occurs and the solution turns red. Thereby, the phosphenium ion $[PPh_2][TEF]$ is formed *in situ*, which further reacts with **Mo_2P_2** to $[\{CpMo(CO)\}_2\{CpMo(CO)_2\}_2(\mu,\eta^2:\eta^2:\eta^2:\eta^1:\eta^1\text{-}2\text{-}(Ph_2P)P_4)(\mu\text{-}PPh_2)][TEF]_2$ (**1**; Scheme 2), which is formally derived by dimerization of **Mo_2P_2** under elimination of two CO ligands, followed by two phosphenium ions $[PPh_2]^+$ inserting into one of the **Mo_2P_2** tetrahedra. Thereby, one $[PPh_2]^+$ cation inserts into a Mo–P bond of the tetrahedron and the other one bridges the respective Mo–Mo bond. **1** contains a novel

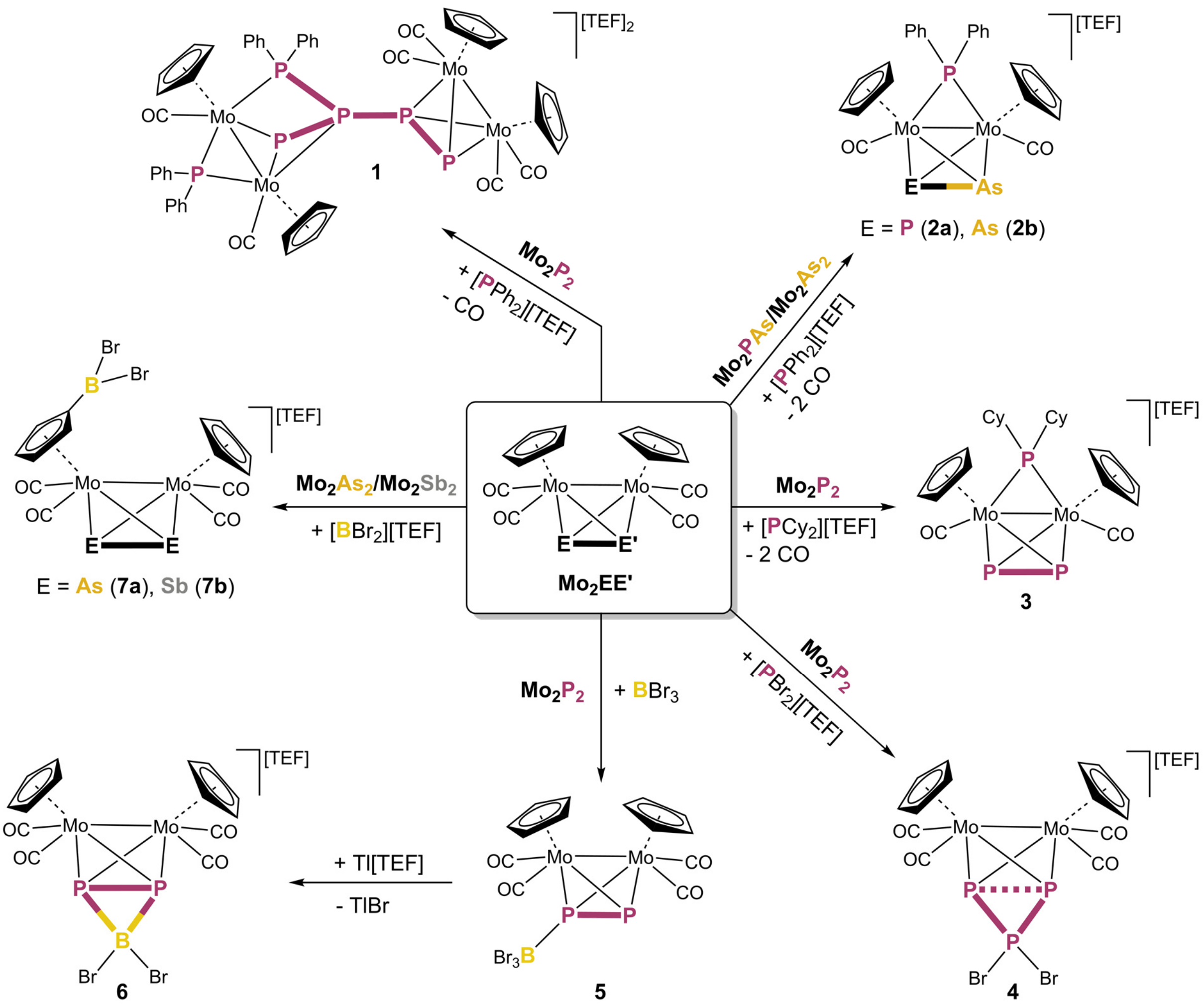

Scheme 2: Reaction of different tetrahedral dipnictogen complexes of the type $[\{CpMo(CO)_2\}_2\{\mu,\eta^2:\eta^2\text{-}EE'\}]$ (**Mo_2EE'**) towards phosphenium and borenium ions (*in situ* generated *via* the reaction of the respective halophosphane or borane with Tl[TEF]).

P_5 ligand, which is the phosphorus analogous to isopren carrying two phenyl substituents and only stabilized by dimolybdenum fragments. Compound **1** is the only product obtained by crystallization. However, it could not be proofed until the end of this thesis, if it is the only formed product in this reaction since signals in ^{31}P NMR spectra were very weak due to the use of diluted solutions. Hence, NMR spectra of concentrated solutions with a high number of scans have to be carried out to give a better insight into this reaction as well as further analytical studies of the crystalline product. Nonetheless, the existence of **1** shows that the reactivity of $[PPh_2]^+$ with **Mo_2P_2** differs from that of **MoP_3** since the phosphenium ion does not insert into the dipnictogen bond. Therefore, it was not surprising that by the reaction of $[PPh_2][TEF]$ with the mixed dipnictogen complex **Mo_2PAs** crystals of the product $[\{CpMo(CO)\}_2(\mu,\eta^2:\eta^2\text{-}PAs)(\mu\text{-}PPh_2)][TEF]$ (**2a**) could be obtained (Scheme 2), where the phosphenium ion bridges the Mo–Mo bond instead of inserting into the P–As bond and, thereby, two CO ligands are released. The dataset of the X-ray diffraction experiment though was weak, ruling out a detailed discussion of the molecular structure. However, the heavy atom framework could be determined (for further details see the Supporting Information). Furthermore, elemental analysis of the product is in confirmation with **2a**. In contrast, the reaction of the all arsenic congener **Mo_2As_2** with $[PPh_2][TEF]$ did not yield a crystalline product. Nonetheless, we assume that the similar product $[\{CpMo(CO)_2\}_2(\mu,\eta^2:\eta^2\text{-}As_2)(\mu\text{-}PPh_2)][TEF]$ (**2b**; Scheme 2) is formed since similar signals are observed in the ^{31}P and $^{31}P\{^1H\}$ NMR spectra as well as the elemental analysis of the purified precipitate fits to **2b**. However, to corroborate this assumption and also to proof if other products are formed during this reaction and in the reaction of **Mo_2PAs** as well, further studies have to be carried out. To extend the scope of this chemistry we used other phosphenium ions, namely in situ generated $[PCy_2]^+$ and $[PBr_2]^+$, which already proofed to be applicable for the electrophilic functionalization of **MoP_3**. The reaction of **Mo_2P_2** with $[PCy_2][TEF]$ only yields crystals of the product $[\{CpMo(CO)\}_2(\mu,\eta^2:\eta^2\text{-}P_2)(\mu\text{-}PCy_2)][TEF]$ (**3**), which differs from **1**, but is similar to **2a** and **2b**, where again the phosphenium ion bridges the Mo–Mo bond and two CO ligands are released (Scheme 2). However, no insertion either into a Mo–P or the P–P bond could be observed. Surprisingly, the reaction with $[PBr_2][TEF]$ leads to the initially desired insertion into the P–P bond and the formation of $[\{CpMo(CO)_2\}_2(\mu,\eta^2:\eta^2\text{-}P_3Br_2)][TEF]$ (**4**; Scheme 2). ^{31}P NMR spectra of the reaction solution reveal that the reaction, in contrast to the ones leading to **1** and **2**, is very selective and that **4** is the only product formed. The spectra show an AMX spin system featuring three dublets of dublets in a ratio of 1:1:1 with coupling constants of 169 Hz, 279 Hz and 311 Hz. This coupling pattern hints towards only a partial insertion/asymmetric coordination of the phosphenium ion into/to the P–P bond and that the bond is not completely broken. However, this has to be verified by theoretical calculations, which are still to be made. Overall, the reactivity of different phosphenium ions towards **Mo_2P_2, Mo_2As_2** and **Mo_2PAs** shows high diversity and the choice of the phosphenium ion guides the reaction outcome, which can be directed either to insertion reaction into E–E or Mo–E– bond or to phosphenium ions bridging the Mo–Mo bond.

Furthermore, we used haloboranes instead of halophosphines as electrophile precursor. However, already when a solution of **Mo_2P_2** with BBr_3 is reacted without the presence of a halide abstracting agent, immediate precipitation of an orange solid is observed, which is hardly soluble in *o*-DFB or CH_2Cl_2 and undergoes decomposition in THF or MeCN. Nonetheless, orange to red crystalline plates could be obtained from the supernatant revealing the Lewis acid/base adduct [{CpMo(CO)$_2$}$_2$(μ,η^2:η^2-P$_2$(BBr$_3$))] (**5**), where the lone pair of one P atom of the **Mo_2P_2** tetrahedron coordinates to BBr$_3$ (Scheme 2). However, if BBr$_3$ is added to a mixture of **Mo_2P_2** and Tl[TEF] precipitation of a white powder occurs instead and the product [{CpMo(CO)$_2$}$_2$(μ,η^2:η^2-P$_2$BBr$_2$)][TEF] (**6**) is formed (Scheme 2), with the *in situ* generated [BBr$_2$]$^+$ cation bridging the P–P bond in an η^2-fashion leading to a novel cyclic three-membered P$_2$B ligand, which carries two bromide substituents. In the ^{31}P as well as ^{11}B NMR spectra two singlets in a ratio of 2:1 are observed indicating the formation of a second species, which could not be identified yet. Two possibilities might be a compound, where the [BBr$_2$]$^+$ cation is either bridging the Mo–Mo bond or only coordinating to one P atom of the **Mo_2P_2** tetrahedron.

When [BBr$_2$][TEF] was reacted with the heavier pnictogen complexes **Mo_2As_2** and **Mo_2Sb_2** a completely different reactivity was observed, which yielded several crystals of the products [{(C$_5$H$_4$BBr$_2$)Mo(CO)$_2$}{CpMo(CO)$_2$}(μ,η^2:η^2-E$_2$)] (E = As (**7a**), Sb (**7b**)). Hereby, the borinium ion did not bridge the dipnictogen bond. Instead it undergoes electrophilic aromatic substitution of one proton of a Cp ligand (Scheme 2). However, no further analytical studies could be conducted until the end of this thesis. Therefore, it is not ensured that **7a** and **7b** are the only formed products in these reactions.

In order to shed light into the molecular structure of these complexes, **1**, **3** and **4** (Figure 1, top) as well as **5**, **6**, **7a** and **7b** (Figure 1, bottom) were crystallized and subjected to single crystal X-ray diffraction experiments. Also, crystals of compound **2a** were obtained, but the dataset was too weak to allow a detailed discussion of the structure. However, the central structural motif seems to be similar to **3**. The molecular structure of **1** (Figure 1a) reveals a dimeric and dicationic unit, which

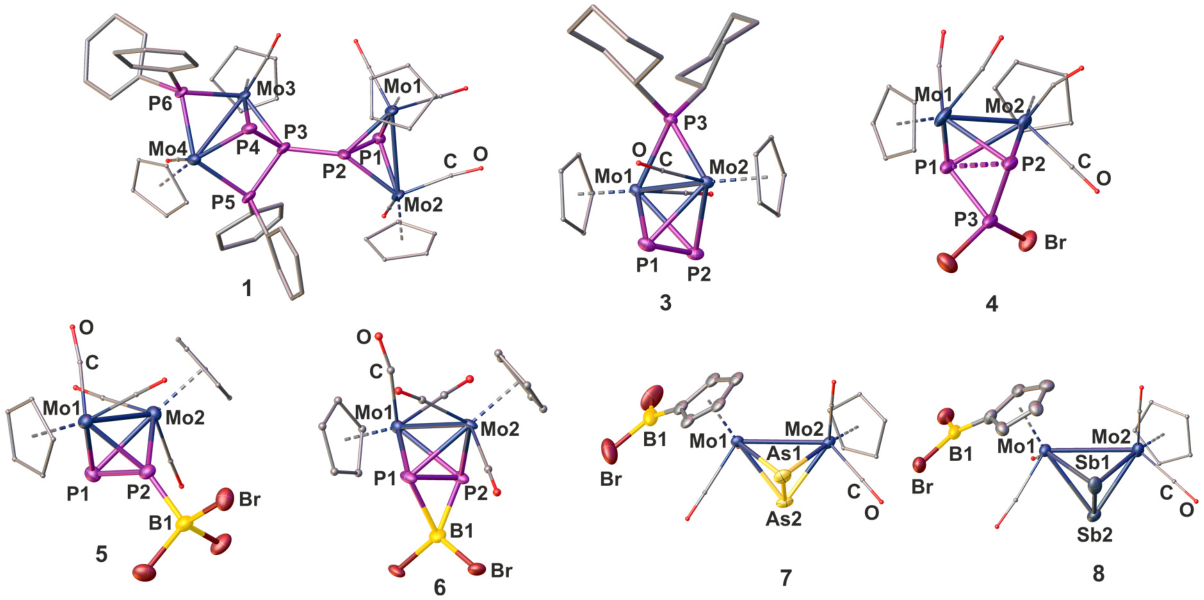

Figure 1: Molecular structures of **1** (a), **3** (b), **4** (c), **5** (d), **6** (e), **7a** (f) and **7b** (g). Anisotropic displacement is set to the 50% probability level. H atoms and counterions are omitted. Unsubstituted Cp and CO ligands are drawn as small spheres and phenyl substituents as connected tubes for clarity. Selected bond lengths [Å] and angles [°]: **1**: P1–P2 2.1077(1), P2–P3 2.1920(1), P3–P4 2.1307(1), P3–P5 2.1522(1), Mo4–P3 3.2315(1), Mo3–Mo4 3.0607(1), Mo3-P6-Mo4 77.519(1); **3**: P1–P2 2.03608(1), Mo1–Mo2 2.70196(2), Mo1-P3-Mo2 68.337(1); **4**: P1–P2 2.57(2), P1–P3 2.17(1), P2–P3 2.24(2), Mo1–Mo2 3.08(1); **5**: P1–P2 2.0823(1), P1–B1 1.97257(3), Mo1–Mo2 3.0956(1); **6**: P1–P2 2.18(1), P1–B1 2.15(4), P2–B1 1.98(4), Mo1–Mo2 3.111(3); **7a**: As1–As2 2.311(2), Mo1–Mo2 3.185(1), C–B1 1.52(2); **7b**: Sb1–Sb2 2.687(1), Mo1–Mo2 3.262(1), C–B1 1.54(1).

consists of two tetrahedra **Mo_2P_2** linked together *via* formation of a new P–P bond. Additionally, one PPh_2^+ unit is bridging the Mo3–Mo4 bond in an η^2-fashion and the second PPh_2^+ unit inserted into the Mo4–P3 bond leading to a branched P_5 chain, which could be regarded an all-phosphorus analogue of isopren. The newly formed P2–P3 bond (2.1920(1) Å) is in the range of a single bond,[7] while the other P–P distances are shorter being between a single and a double bond (2.1077(1)–2.1522(1) Å). The former P3–Mo4 bond is clearly broken (3.2315(1) Å). In contrast, all other Mo–P distances (2.3982(1)–2.5308(1) Å) are in the range of a single bond and similar to the ones in free **Mo_2P_2**,[8] as so are the Mo–Mo distances showing that the second phosphenium cation is only bridging the Mo–Mo bond. In contrast to **1**, the complexes **3**–**7b** all show monomeric structures with one phosphenium or borinium ion, or one borane attached to the starting material **Mo_2P_2**. However, the way they are attached to it differs significantly within those complexes. In **3** (Figure 1b) the Cy_2P^+ ion is bridging the Mo–Mo bond as it was observed for the second PPh_2^+ unit in **1**. Interestingly, this time this leads to shortening of the Mo–Mo bond by 0.3 Å compared to free **Mo_2P_2** and also the Mo–P distances are slightly shorter. The P–P bond length though remains the same. However, in **4** (Figure 1c) and **6** (Figure 1e) the PBr_2^+ or BBr_2^+ cation, respectively, bridges the P–P bond of **Mo_2P_2** *via* formation of two new P–P (**4**) or P–B (**6**) bonds.[9] While in the former case an elongation of the P–P bond by 0.5 Å compared to free **Mo_2P_2**[8] is observed indicating a partial insertion of the phosphenium ion, in the latter case the P–P bond length is only slightly elongated but still slightly shorter than a P–P single bond indicating rather a coordination of **Mo_2P_2** towards BBr_2^+.[7] However, theoretical calculations have to be executed to get a closer insight into the bonding situation. The newly formed P–P bonds in **4** represent single bonds, whereas only one of the new P–B bonds in **6** is in the range of a single bond and the other is elongated by 0.2 Å showing a slightly asymmetric coordination.[10] In the neutral complex **5** (Figure 1d) the borane BBr_3 is attached to **Mo_2P_2** only in an η^1-fashion to form a P–B bond, whose bond length indicates a P–B single bond.[7] The bond lengths inside the tetrahedron remain unchanged in comparison to free **Mo_2P_2** indicating only a coordination between the phosphorus and the boron atom building up a typical Lewis acid/base pair. In contrast to all aforementioned complexes, the boron electrophile in **7a** and **7b** (Figure 1f-g) did not attack the central Mo_2E_2 tetrahedron, but instead replaced a proton of the Cp ligand by an electrophilic aromatic substitution. Therefore, the Mo_2As_2 (**7a**) and Mo_2Sb_2 (**7b**) units remain intact. The respective E–E and Mo–E bonds remain the same as in free **Mo_2As_2** or **Mo_2Sb_2**, respectively, while the Mo–Mo bonds are widened up by roughly 0.15 Å. The newly formed C–B bonds are single bonds.[7]

Besides **Mo_2PAs** we were also interested in investigations of the reaction of its heavier hetero-dipnictogen congeners **Mo_2PSb** and **Mo_2AsSb** towards electrophilic functionalization. Therefore, we reacted them with *in situ* generated $[PPh_2][TEF]$ in CH_2Cl_2, which led to the formation of a product mixture of the compounds $[\{CpMo(CO)_2\}_2\{\mu\text{-}EH(PPh_2)\}(\mu\text{-}SbCl)][TEF]$ (E = P (**8a**), As (**8b**)) and $[\{CpMo(CO)_2\}_2(\mu\text{-}PH_2)(\mu\text{-}SbCl)][TEF]$(**9a**) as the main products (Scheme 3). In **8a** and **8b** no insertion of the phosphenium ion into the E–Sb bond was observed. Instead, $[PPh_2]^+$ is attached only to the P or As atom, respectively, which are additionally protonated. The former E–Sb bond is broken and a chlorine atom is bound to the Sb atom. These products are formally obtained by electrophilic attack of $[PPh_2]^+$ on **Mo_2ESb** and subsequent HCl addition leading to a $EH(PPh_2)$ and a SbCl unit coordinated by the dimolybdenum fragment $[CpMo(CO)_2]_2$. In **9a** the phosphenium ion is formally substituted by another proton yielding a PH_2 unit. This suggests that **8a** is an intermediate during the formation of **9a**.

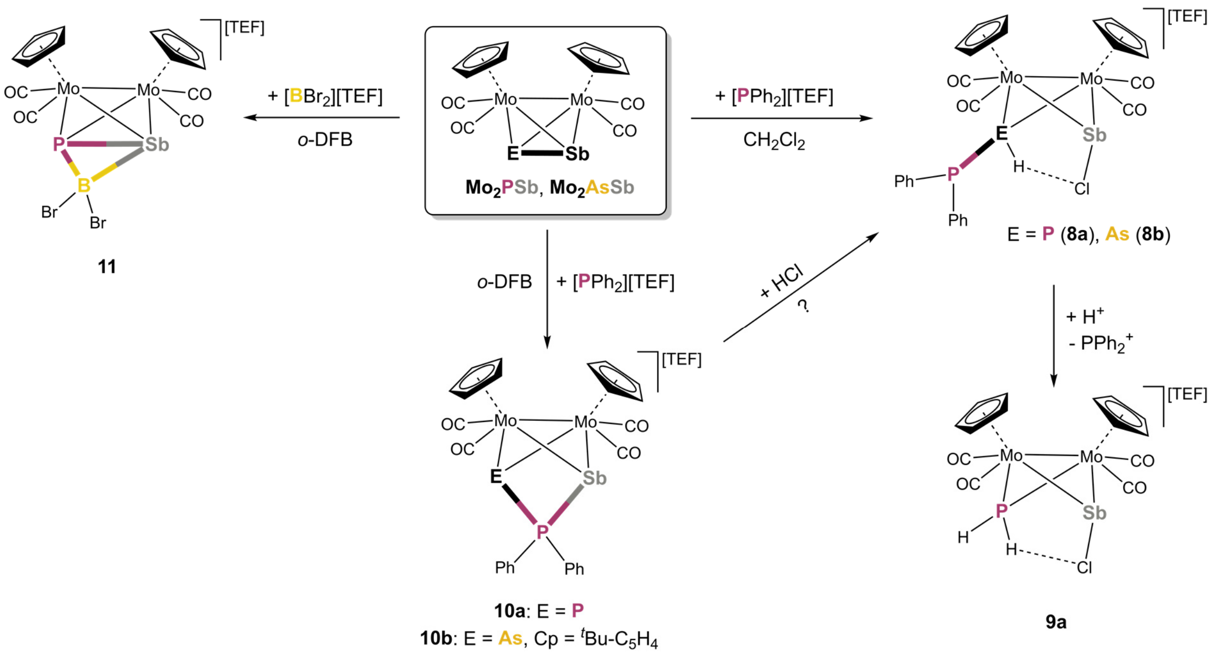

Scheme 3: Reaction of the tetrahedral hetero-dipnictogen complexes **Mo_2PSb** and **Mo_2AsSb** towards phosphenium and borinium ions (*in situ* generated *via* the reaction of the respective halophosphane or borane with Tl[TEF]).

Additionally, when the reaction solution is stirred for two weeks, **9a** is formed as the sole product suggesting full conversion of **8a** to **9a**.

However, it has to be clarified where the HCl is originating from. There are two possible ways, either it is released from solvent activation of CH_2Cl_2 or the protons descend from traces of moisture and the chlorine atom from the initial chlorophospane, which was abstracted by the Tl^+ cation. Therefore, we performed the same reactions (for **Mo_2AsSb** this time its Cp' (= $–C_5H_4{}^t$Bu) derivative was used due to availability) in *o*-DFB instead and, indeed, the formation of the HCl adducts **8a** and **8b** can be suppressed yielding the compounds [{Cp^RMo(CO)$_2$}$_2$(μ,η^1:η^1-EP(Ph)$_2$Sb)][TEF] (**10a**: E = P, Cp^R = Cp; **10b**: E = As, Cp^R = Cp') as the only products (Scheme 3). Therefore, this suggests that the HCl probably evolves from CH_2Cl_2. In **10a** and **10b** the phosphenium ion inserts into the E–Sb bond leading to a substituted, three-membered EPSb chain, which is coordinated to the dimolybdenum fragment [Cp^RMo(CO)$_2$]$_2$ *via* the E and the Sb atom. To the best of our knowledge, compound **10b** is only the second example of an phosphorus atom, which is bound to both an arsenic as well as an antimony atom and the first bearing a cationic charge (the first compound of this kind ^{t}Bu$_2$SbP(^{t}Bu)As^{t}Bu$_2$ was synthesized only recently by the group of *von Hänisch*).[11] Additionally, in contrast to the compound of *von Hänisch*, the As and Sb atoms in **10b** do not bear any organic substituents. We suggest that within the formation of **8** and **9** the insertion product **10** is generated first and then the subsequent HCl addition takes place. To affirm this assumption **10** should be reacted specifically with equimolar amounts of HCl to see if **8** can be obtained by this route, too. This could also be a possibility to synthesize **8** in a selective way. However, these investigations could not be conducted until the end of this thesis.

^{31}P{^{1}H} NMR studies of the crude solution of **8a** and **9a** reveal a singlet at δ = 28.1 ppm for **9a**, which splits into a triplet in the ^{31}P NMR spectra due to coupling to the two protons ($^1J_{P\text{-}H}$ = 405 Hz).

Additionally, two sets of signals, each consisting of two doublets in a ratio of 1:1, are observed, which both perfectly fit to **8a**. This suggests that two isomers of **8a** are present in solution. We assume that in one isomer a hydrogen bond between the proton and the chlorine atom is present (according to the short H–Cl distance in the molecular structure; *vide infra*), whereas it is not in the second isomer. The doublets at δ = 71.9 ppm and 103.4 ppm can be assigned to the respective PH groups of the two isomers since they split up into a triplet in the ^{31}P NMR spectrum due to coupling to the proton. Hence, the doublets at δ = −0.9 ppm and 3.6 ppm belong to the respective PPh_2 units of the two isomers of **8a**. All doublets show a $^1J_{P-P}$ coupling constant of about 330 Hz. Besides the signals for **8a** and **9a** other signals in minor ratio are detected, which could not be assigned. In contrast, in the ^{31}P{^{1}H} spectra of **10a** only two doublets at δ = −36.2 ppm and 139.5 ppm ($^1J_{P-P}$ = 323 Hz) are present, which additionally do not split up in the ^{31}P NMR proofing that no proton is attached to one of the two phosphorus atoms.

Last but not least, we also used the borinium ion [BBr_2][TEF] for electrophilic functionalization reactions towards **Mo_2PSb**. When an orange red solution of **Mo_2PSb** and Tl[TEF] in *o*-DFB is reacted with BBr_3 immediate precipitation of a white powder (TlBr) takes place and the colour changes to bright red. After filtration and crystallization [{CpMo(CO)$_2$}$_2$(μ,η^2:η^2-PSbBBr$_2$)][TEF] (**11**) can be obtained (Scheme 3). In contrast to the phosphenium ion, the [BBr_2]$^+$ cation is not inserting into the

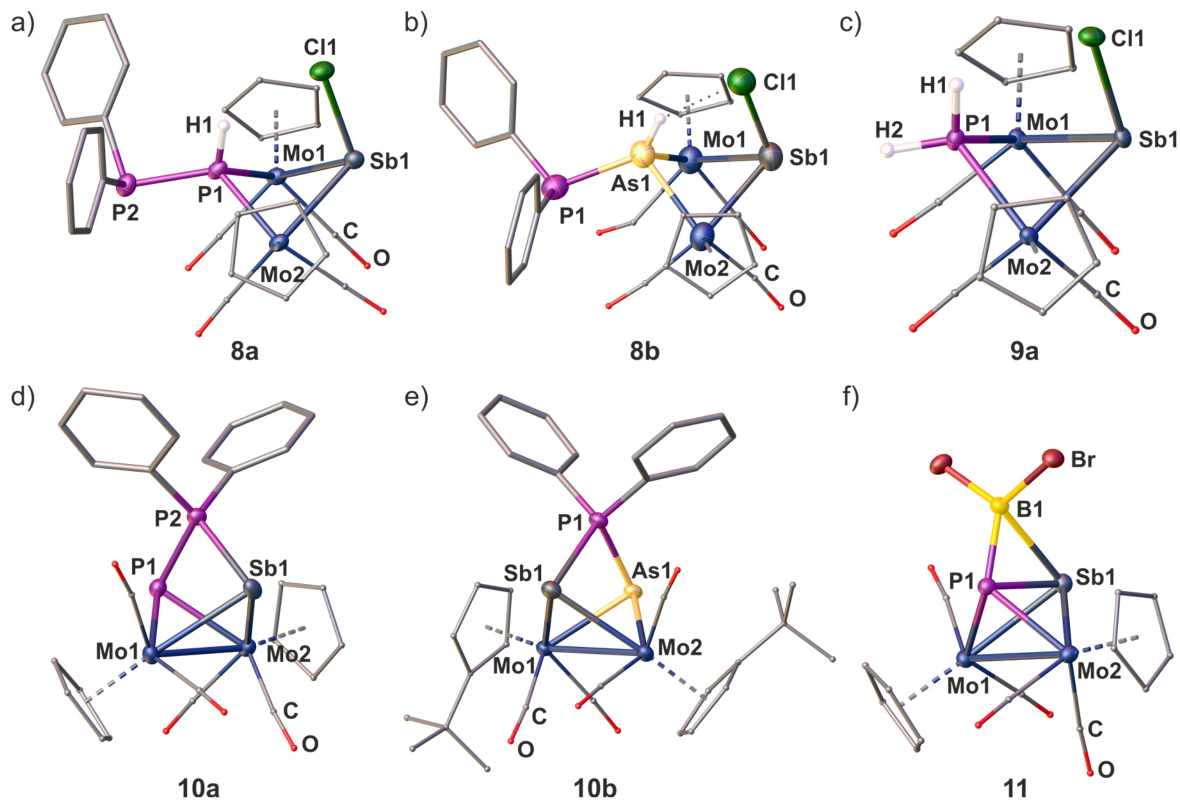

Figure 2: Molecular structures of **8a** (a), **8b** (b), **9a** (c), **10a** (d), **10b** (e) and **11** (f). Anisotropic displacement is set to the 50% probability level. H atoms bound to carbon and counterions are omitted. Cp and CO ligands are drawn as small spheres and phenyl substituents as connected tubes for clarity. Selected bond lengths [Å] and angles [°]: **8a**: P1–P2 2.200(2), P1–Sb1 3.240(1), Sb1–Cl1 2.430(1), Mo1–Mo2 3.2787(5), Cl1–H1 2.70(6); **8b**: P1–As1 2.3516(1), As1–Sb1 3.2248(1), Sb1–Cl1 2.4231(1), Mo1–Mo2 3.2838(1), Cl1–H1 2.3438(1); **9a**: P1–Sb1 3.2531(1), Sb1–Cl1 2.4202(1), Mo1–Mo2 3.2916(1), Cl1–H1 2.8184(1); **10a**: P1–P2 2.1736(1), P2–Sb1 2.5033(1), P1–Sb1 3.1900(1), Mo1–Mo2 3.0859(1); **10b**: As1–P1 2.3328(1), P1–Sb1 2.4943(1), As1–Sb1 3.2866(1), Mo1–Mo2 3.1547(1); **11**: P1–Sb1 2.5142(1), P1–B1 1.9074(1), Sb1–B1 2.6641(1), Mo1–Mo2 3.1998(1), P1-B1-Sb1 64.3(1).

P–Sb bond, but bridging it in an η^2 coordination mode like it was also observed in the reaction with **Mo_2P_2**. This yields a three-membered PSbB ring, which carries two bromide substituents on the boron atom and is attached to the dimolybdenum fragment $[CpMo(CO)_2]_2$.

The products **8**–**11** could be crystallized allowing their X-ray crystallographic characterization (Figure 2).[9] In **8a** (Figure 2a) and **8b** (Figure 2b) the phosphenium ion $[PPh_2]^+$ is attached to the P1 (**8a**) or As1 (**8b**) atom, respectively, of the former **Mo_2PSb** or **Mo_2AsSb** tetrahedron *via* formation of new P–P and P–As bonds, which are classic single bonds (**8a**: P1–P2 2.200(2) Å; **8b**: P1–As1 2.3516(1) Å). Additionally, in both cases a proton is bound to the P1 and As1 atoms, respectively, as well as a chlorine atom bound to the Sb atoms. The former E–Sb bonds within the tetrahedra are clearly broken. Hence, the SbCl units in **8a** and **8b** can be regarded as a stibinidene-like unit coordinated by a dimolybdenum fragment. The Sb–Cl bonds are again typical single bonds. Additionally, the Cl1–H1 distances are quite short (**8a**: Cl1–H1 2.70(6) Å; **8b**: P1–As1 2.3438(1) Å) indicating the presence of hydrogen bonding, which was already predicted to be the reason for the presence of two isomers observed in the ^{31}P NMR spectra (*vide supra*). The Mo–Mo bonds are elongated by about 0.2 Å compared to free **Mo_2PSb** and **Mo_2AsSb**. In **9a** the PPh_2^+ unit is substituted by another proton yielding a PH_2 unit. But besides this it resembles the molecular structure of **8a**. In contrast to **8a** and **8b**, within the complexes **10a** and **10b** the phosphenium ion PPh_2^+ is inserted into the E–Sb bond of **Mo_2PSb** and **Mo_2AsSb**, which is indicated by the again clearly broken E–Sb bonds and the formation of two additional bonds (P–P and P–Sb in **10a**; P–As and P–Sb in **10b**). These new bonds are all classical single bonds. Thus, three-membered pnictogen chains are obtained, which are quite rare. The AsPSb chain in **10b** is only the second example of a P atom, which is bound to both arsenic and antimony and the first where the As and Sb atoms do not bear organic substituents. In contrast to **8a**–**9a**, the Mo–Mo bonds in **10a**/**b** are not elongated compared to free **Mo_2PSb** and **Mo_2AsSb**. The borinium ion BBr_2^+ in **11** unlike the phosphenium ions does not insert into the P–Sb bond of **Mo_2PSb** and only bridges it by building up two new bonds, a P–B and a Sb–B bond. The same was observed for the reaction of $[BBr_2][TEF]$ with **Mo_2P_2** (**6**; *vide supra*). In **11**, the P–B bond is slightly shorter than a single bond, whereas the Sb–B distance exceeds the sum of the covalent radii by 0.4 Å revealing an asymmetric coordination of the pnictogen atoms towards the borinium cation with major contribution of the P atom. The P–Sb bond is slightly elongated by 0.1 Å compared to free **Mo_2PSb**, but still in the range of a single bond. Hence, a distorted, three membered PBSb ring is obtained, carrying two bromide substituents on the boron atom and stabilized by the dimolybdenum fragment $[CpMo(CO)_2]_2$. The Mo–Mo bond is slightly elongated by 0.1 Å. To get a better insight into the bonding situation in **11** and the complexes **8a**–**10a** as well, DFT calculations are in progress, which however could not be finished until the end of this thesis.

All the reported electrophilic functionalization reactions leading to the products **1**–**11** are very sensitive towards moisture especially the ones including borinium ions. In lot of these reactions yellow crystals can be obtained as decomposition products, which only show the starting materials **Mo_2EE'** (EE' = P_2, PAs, As_2, AsBi) bearing a cationic charge and one $[TEF]^-$ as counterion. We suggest that these are the protonated species of **Mo_2EE'**, $[\{CpMo(CO)_2\}_2(\mu,\eta^2{:}\eta^2\text{-EE'})H][TEF]$, which probably arise from the original insertion products or adducts. Therefore, the electrophiles could act as a sort of activator for the protonation reactions. However, the proton could not be detected by X-ray crystallography. To suppress these side and protonation reactions it requires extremely dry working methods especially

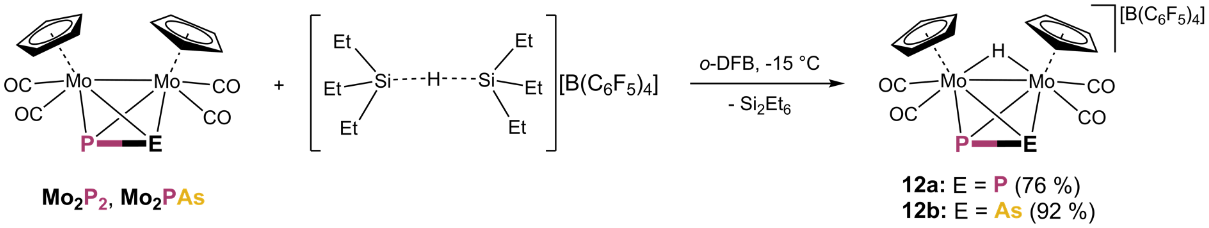

Scheme 4: Controlled protonation of **Mo_2P_2** and **Mo_2PAs** yielding **12a** and **12b**; isolated yields given in parentheses.

including very dry flasks and solvents. Since a proton is the smallest and most simple electrophile we aspired towards a selective synthesis of these protonated species. And, indeed, the compounds $[\{CpMo(CO)_2\}_2(\mu,\eta^2{:}\eta^2\text{-PE})(\mu\text{-H})][B(C_6F_5)_4]$ (E = P (**12a**), As (**12b**)) could also be obtained in a controlled manner in 76 % (**12a**) and 92 % (**12b**) isolated yield by reacting the respective compounds **Mo_2P_2** and **Mo_2PAs** with $[(Et_3Si)_2H][B(C_6F_5)_4]$ (Scheme 4). The cation of the latter consists of a triethylsilylium cation coordinated to triethylsilane and it can serve either as a source for silylium cations or like in this case for protons. However, a second possibility is that at first addition of the silylium takes place and that in a second step the silylated species is hydrolysed by water traces to yield the protonated compounds. Both **12a** and **12b** crystallize in the monoclinic space group $P2_1/n$ with one cation and one anion in the asymmetric unit. The molecular structures (Figure 3) show an intact Mo_2P_2 (**12a**) or Mo_2PAs (**12b**) tetrahedron, respectively, with the same P–E and slightly elongated Mo–Mo distances compared to free **Mo_2P_2**[8] and **Mo_2PAs**.[12] The protons in **12a** and **12b** are both bridging the respective Mo–Mo bonds. However, since the detection/localization of protons by X-ray diffraction is 0complicated, especially for transition metal hydrides, NMR spectroscopic investigations were conducted to get a more precise insight. In both ^{31}P and $^{31}P\{^1H\}$ NMR spectra of **12a** and **12b** only one singlet at $\delta = -33.0$ ppm (**12a**) or 26.4 ppm (**12b**), respectively, are observed, which is either downfield shifted by 10 ppm (**12a**) or upfield shifted by 5 ppm (**12b**) compared to free **Mo_2P_2** and **Mo_2PAs**, respectively.[4] The presence of singlets in the proton coupled spectra shows that no proton is bound to the phosphorus atoms. Also cooling to −80 °C does not lead to a splitting of the signal, only to a slight upfield shift to $\delta = -40.8$ ppm (**12a**) and 18.1 ppm (**12b**). In the ^1H NMR spectrum of **12a** two singlets at $\delta = -17.61$ and 5.57 ppm are shown in a ratio of 1:10. The letter can be assigned to the protons of the Cp ligands, while the former indicates the presence of a hydride, which is in good agreement with an H atom bridging the Mo–Mo bond. In contrast, for **12b** two signals for the Cp protons at $\delta = 5.30$ and 5.32 ppm as well as two signals for the Mo–Mo bridging hydride at $\delta = -18.54$ and −18.14 ppm are

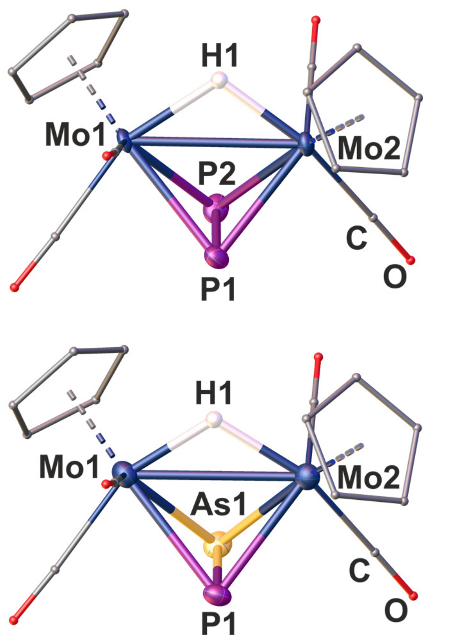

Figure 3: Molecular structure of **12a** (top) and **12b** (bottom). Anisotropic displacement is set to the 50% probability level. H atoms bound to carbon and counterions are omitted. Cp and CO ligands are drawn as small for clarity. Selected bond lengths [Å]: **12a**: P1–P2 2.0881(1), Mo1–Mo2 3.1218(2); **12b**: P1–As1 2.27995(2), Mo1–Mo2 3.1497(5).

observed indicating the presence of either two species or two isomers. The $^{13}C\{^1H\}$, $^{19}F\{^1H\}$ and $^{11}B\{^1H\}$ NMR spectra of **12a** also reveal the expected signals for the Cp ligands and the $[B(C_6F_5)_4]^-$ anion. Additionally, **12a** and **12b** were detected in mass spectrometry and their purity was proven by elemental analysis.

10.3 Conclusion

In summary, it could be shown that electrophilic functionalization of the complexes **Mo_2EE'** with *in situ* generated phosphenium and borinium ions is possible. In comparison to the similar tripnictogen complexes **MoP_3** and **$MoAs_3$**, the reactivity of the complexes **Mo_2P_2**, **Mo_2As_2**, **Mo_2Sb_2** and **Mo_2PAs** is much more diverse leading either dimeric, dicationic or monomeric, monocationic products, where the phosphenium ions either coordinate the Mo–Mo bond or insert into the Mo–P or P–P bond depending on the used phosphenium ion. Reaction of **Mo_2P_2** with the borinium ion $[BBr_2]^+$, instead, led to a side-on coordination of the P_2 ligand to the electrophile resulting only in a slight elongation of the P–P bond. In contrast, in case of **Mo_2As_2** and **Mo_2Sb_2**, $[BBr_2]^+$ undergoes electrophilic aromatic substitution of a Cp proton. Such behaviour has, to the best of our knowledge, not been observed before for organometallic complexes.

In contrast, reactions of $[PPh_2]$[TEF] with **Mo_2PSb** and **Mo_2AsSb** in CH_2Cl_2 led to an addition of $[PPh_2]^+$ to an P or an As atom, respectively, with subsequent HCl addition. The latter could be suppressed by performing the reaction in *o*-DFB only yielding the insertion products of $[PPh_2]^+$ into the E–Sb bond. Within that, the tripnictogen chains $PP(Ph_2)Sb$ and $AsP(Ph_2)Sb$ are formed, where the latter depicts only the second example of a P atom bound to both arsenic and antimony and, moreover, even the first example, where As and Sb do not bear any organic substituents. Furthermore, reaction of **Mo_2PSb** with $[BBr_2]^+$ yields a coordination product, where the $[BBr_2]^+$ unit bridges the P–Sb bond, but this time in an asymmetric fashion with stronger bonding to the P atom. Thereby, the P–Sb bond remains intact.

Finally, **Mo_2P_2** and **Mo_2PAs** could also be protonated in a selective reaction with $[(Et_3Si)_2H][B(C_6F_5)_4]$. The proton is not bound to the PE ligand but in fact bridging the Mo–Mo bond indicating its hydridic nature, which was corroborated by NMR spectroscopy.

Overall, the reactivity of main group electrophiles towards the complexes **Mo_2EE'** perfectly extends the chemistry of electrophilic functionalization of E_n ligand complexes leading to a variety of different cationic polypnictogen ligand complexes. However, since some reactions still seem to be unselective and the main studies in this chapter were conducted using the phosphenium ion $[PPh_2]$[TEF] this work must be expanded to other phosphenium ions with different substituents and counter ions. This could lead to more selective reactions and stable products. Furthermore, other pnictogenium ions and main group electrophiles should be introduced as well. In general, the combination of a wide range of E_n ligand complexes with numerous electrophiles bears the potential of countless functionalized polypnictogen complexes achievable.

10.4 Supporting Information

10.4.1 General remarks

All manipulations were carried out under an inert atmosphere of dried nitrogen/argon using standard Schlenk and glovebox techniques. The used Schlenk flasks were heated at 550 °C for at least 15-30 minutes under reduced pressure prior to use to get rid of water traces adhered to the glass surface. The starting materials $[\{CpMo(CO)_2\}_2(\mu,\eta^2:\eta^2\text{-}P_2)]$,[13] $[\{CpMo(CO)_2\}_2(\mu,\eta^2:\eta^2\text{-}As_2)]$,[13] $[\{CpMo(CO)_2\}_2(\mu,\eta^2:\eta^2\text{-}Sb_2)]$,[13] $[\{CpMo(CO)_2\}_2(\mu,\eta^2:\eta^2\text{-}PAs)]$,[13] $[\{CpMo(CO)_2\}_2(\mu,\eta^2:\eta^2\text{-}PSb)]$,[13] $[\{CpMo(CO)_2\}_2(\mu,\eta^2:\eta^2\text{-}AsSb)]$,[13] $[\{Cp'Mo(CO)_2\}_2(\mu,\eta^2:\eta^2\text{-}AsSb)]$[13] and Tl[TEF][14] were synthesized according to literature procedures. All other chemicals were purchased from commercial vendors. The halophosphanes as well as the boron tribromide BBr_3 were distilled prior to use. Solvents were freshly distilled under nitrogen after drying over CaH_2 (CH_2Cl_2, CD_2Cl_2), K or Na/K alloy (alkanes), P_4O_{10} (*ortho*-difluorobenzene = *o*-DFB) or NaH (toluene). Dried solvents were also taken from a MB SPS-800 solvent purification system from MBraun and degassed prior to use. For NMR spectra of crude solutions a C_6D_6 capillary was used. Filtrations were carried out using a glas fibre filter paper, which was wrapped around one end of a Teflon tube and fixed with a Teflon tape. The tube and filter paper were dried in a heating stove at 170 °C for at least 3h. Then the end with the glas fibre filter paper was put into the crude solution and the solution was transferred into another Schlenk flask by creating an overpressure on the starting side. NMR spectra were recorded at 300 K (if not stated otherwise) on a Bruker Avance 300 MHz NMR spectrometer (^1H: 300.132 MHz, ^{31}P: 121.495 MHz, ^{13}C: 75.468 MHz, ^{19}F: 282.404 MHz) or a Bruker Avance 400 MHz NMR spectrometer (^1H: 400.130 MHz, ^{31}P: 161.976 MHz, ^{13}C: 100.613 MHz, ^{19}F: 376.498 MHz, ^{11}B: 128.432 MHz) with external references of $SiMe_4$ (^1H, ^{13}C), CCl_3F (^{19}F), BF_3 (^{11}B) and H_3PO_4 (85%, ^{31}P). The chemical shifts δ are presented in parts per million (ppm) and coupling constants J in Hz. The following abbreviations were used for signal assignment: s = singlet, d = doublet, t = triplet, q = quartet, dd = doublet of doublets, ddd = doublet of doublet of doublets. ESI-MS spectra were either measured on a Finnigan Thermoquest TSQ 7000 mass-spectrometer by the MS department of the University of Regensburg or on a Waters Micromass LCT ESI-TOF mass-spectrometer by the first author. IR spectra were recorded either as solids using a ThermoFisher Nicolet iS5 FT-IR spectrometer with an iD7 ATR module and an ITX Germanium or ITX Diamond crystal, or grinded together with dried KBr and pressed to pellets and measured on a VARIAN FTS-800 FT-IR spectrometer. Elemental analyses (EA) were performed by the micro analytical laboratory of the University of Regensburg.

10.4.2 Experimental details

Synthesis of $[\{CpMo(CO)\}_2\{CpMo(CO)_2\}_2(\mu,\eta^2:\eta^2:\eta^1:\eta^1\text{-2-(diphenylphosphino)}P_4)(\mu\text{-}PPh_2)][TEF]_2$ (1)

An orange solution of $[\{CpMo(CO)_2\}_2(\mu,\eta^2:\eta^2\text{-}P_2)]$ (50 mg, 0.1 mmol, 1.0 eq.) and $Tl[TEF]\cdot(CH_2Cl_2)_{0.5}$ (121 mg, 0.1 mmol, 1.0 eq.) in 10 mL *o*-DFB was stirred for 15 minutes before a colourless solution of PPh_2Cl in toluene (c = 0.2M, 0.5 mL, 0.1 mmol, 1.0 eq.) was added, which led to precipitation of white powder and a colour change to red. The suspension was stirred for 18h and filtered through glas fibre filter paper. The red solution was precipitated with *n*-hexane, the supernatant removed and the residue dried in vacuum. Crystallization *via* layering an *o*-DFB solution with *n*-hexane (5x) and storage at 4 °C for five days yielded **1** as orange to red blocks suitable for single crystal X-ray diffraction. The solvent was removed by decanting and the crystals dried in vacuum for 3h.

Synthesis of [{CpMo(CO)}$_2$(μ,η^2:η^2-PAs)(μ-PPh$_2$)][TEF] (2a)

An orange red solution of [{CpMo(CO)$_2$}$_2$(μ,η^2:η^2-PAs)] (54 mg, 0.1 mmol, 1.0 eq.) and Tl[TEF] (117 mg, 0.1 mmol, 1.0 eq.) in 10 mL *o*-DFB was stirred for 60 minutes before a colourless solution of PPh_2Cl in toluene (*c* = 0.2M, 0.5 mL, 0.1 mmol, 1.0 eq.) was added, which led to immediate precipitation of white powder and a colour change to reddish brown in the course of 60 minutes. The suspension was stirred for 18h and filtered through glas fibre filter paper. Layering with *n*-hexane (5x) and storage at room temperature did not yield any crystals. However, recrystallization *via* layering a CH_2Cl_2 solution with *n*-hexane yielded **2a** as dark red sticks moderately suitable for single crystal X-ray diffraction. The solvent was removed by decanting and the crystals dried in vacuum for 3h.
Yield 118 mg (0.07 mmol = 70 %). ^{31}P{^{1}H} NMR of the crude solution (C_6D_6/*o*-DFB) δ/ppm = 152.1 (s), 183.6 (s). Anal. calcd. for [$C_{26}H_{20}O_4Mo_2P_2As$][TEF]: C: 29.81, H: 1.19. Found: C: 30.32, H: 1.40.

Synthesis of [{CpMo(CO)}$_2$(μ,η^2:η^2-As$_2$)(μ-PPh$_2$)][TEF] (2b)

A red solution of [{CpMo(CO)$_2$}$_2$(μ,η^2:η^2-As$_2$)] (58 mg, 0.1 mmol, 1.0 eq.) and Tl[TEF] (117 mg, 0.1 mmol, 1.0 eq.) in 10 mL *o*-DFB was stirred for 60 minutes before a colourless solution of PPh_2Cl in toluene (*c* = 0.2M, 0.5 mL, 0.1 mmol, 1.0 eq.) was added, which led to immediate precipitation of white powder. The suspension was stirred for 18h and the dark brown solution filtered through glas fibre filter paper. Layering with *n*-hexane (5x) and storage at room temperature yielded **2b** as brown powder. The solvent was removed by decanting and the residue dried in vacuum for 3h.
Yield 103 mg (0.06 mmol = 60 %). ^{31}P{^{1}H} NMR of the crude solution (C_6D_6/*o*-DFB) δ/ppm = 152.1 (s), 183.6 (s). Anal. calcd. for [$C_{26}H_{20}O_4Mo_2PAs_2$][TEF]: C: 29.05, H: 1.16. Found: C: 29.10, H: 1.13.

Synthesis of [{CpMo(CO)}$_2$(μ,η^2:η^2-P$_2$)(μ-PPh$_2$)][TEF] (3)

An orange solution of [{CpMo(CO)$_2$}$_2$(μ,η^2:η^2-P$_2$)] (49 mg, 0.1 mmol, 1.0 eq.) and Tl[TEF] (118 mg, 0.1 mmol, 1.0 eq.) in 10 mL *o*-DFB was stirred for 30 minutes before a colourless solution of PCy_2Cl in toluene (*c* = 0.1M, 1.0 mL, 0.1 mmol, 1.0 eq.) was added, which led to immediate precipitation of white powder. The suspension was stirred for 90 minutes and the dark red brown solution filtered through glas fibre filter paper. Layering with *n*-pentane (5x) and storage at 4 °C yielded **3** as dark red blocks suitable for single crystal X-ray diffraction. The solvent was removed by decanting and the crystals dried in vacuum for 3h.

Synthesis of [{CpMo(CO)$_2$}$_2$(μ,η^2:η^2-P$_3$Br$_2$)][TEF] (4)

An orange solution of [{CpMo(CO)$_2$}$_2$(μ,η^2:η^2-P$_2$)] (50 mg, 0.1 mmol, 1.0 eq.) and pure PBr_3 (10 µL, 0.1 mmol, 1.0 eq.) in 10 mL *o*-DFB was stirred for 15 minutes before a colourless solution of Tl[TEF]·(CH$_2$Cl$_2$]$_{0.5}$ (121 mg, 0.1 mmol, 1.0 eq.) in 5 mL *o*-DFB was added, which led to immediate precipitation of white powder. The suspension was stirred for 18 h and the orange solution filtered through glas fibre filter paper. Precipitation with *n*-hexane yielded a fluffy orange powder. The supernatant was removed, the powder dried in vacuum and redissolved in 5 mL *o*-DFB. Layering with *n*-hexane (4x) and storage at 4 °C yielded **4** as orange plates moderately suitable for single crystal X-ray diffraction. The solvent was removed by decanting, the crystals washed twice with *n*-hexane and dried in vacuum for 3h.

Yield 131 mg (0.079 mmol = 79 %). ^{1}H NMR (CD_2Cl_2) δ/ppm = 5.59 (s, Cp), 5.90 (s, Cp), 5.91 (s, Cp), 6.19 (s, Cp), 6.20 (s, Cp). ^{31}P{^{1}H} NMR (CD_2Cl_2) δ/ppm = 54.0 (dd, $^1J_{P\text{-}P}$ = 275 Hz, $^1J_{P\text{-}P}$ = 309 Hz, 1 P), 70.8 (dd, $^1J_{P\text{-}P}$ = 171 Hz, $^1J_{P\text{-}P}$ = 275 Hz, 1 P), 324.7 (dd, $^1J_{P\text{-}P}$ = 171 Hz, $^1J_{P\text{-}P}$ = 309 Hz, 1 P). ^{31}P NMR (CD_2Cl_2) δ/ppm = 54.0 (dd, $^1J_{P\text{-}P}$ = 275 Hz, $^1J_{P\text{-}P}$ = 309 Hz, 1 P), 70.8 (dd, $^1J_{P\text{-}P}$ = 171 Hz, $^1J_{P\text{-}P}$ = 275 Hz, 1 P), 324.7 (dd, $^1J_{P\text{-}P}$ = 171 Hz, $^1J_{P\text{-}P}$ = 309 Hz, 1 P). ^{13}C{^{1}H} NMR (CD_2Cl_2) δ/ppm = 89.36 (s, Cp), 91.17 (s, Cp), 93.75 (s, Cp). ^{19}F{^{1}H} NMR (CD_2Cl_2) δ/ppm = −75.6 (s, [TEF]$^-$). Anal. calcd. for [$C_{14}H_{10}O_4Mo_2P_3Br_2$][TEF]: C: 21.79, H: 0.61. Found: C: 22.22, H: 0.67. Positive ion ESI-MS *m/z* (%): 686.63 (100) [**M**$^+$]. Negative ion ESI-MS *m/z* (%): 966.9 (100) [TEF]$^-$.

Synthesis of [{CpMo(CO)$_2$}$_2$(μ,η^2:η^2-P$_2$)(η^1-BBr$_3$)] (5)

An orange solution of [{CpMo(CO)$_2$}$_2$(μ,η^2:η^2-P$_2$)] (50 mg, 0.1 mmol, 1.0 eq.) in 10 mL *o*-DFB was reacted with pure BBr_3 (22 µL, 0.2 mmol, 2.0 eq.), which led to immediate precipitation of a bright orange powder and almost decolourization of the supernatant. Upon addition of 10 mL CH_2Cl_2 the solution turns more orange again suggesting that a bit more precipitate is dissolved. The suspension was stirred for 2 d and the orange supernatant transferred to another flask. Layering with *n*-hexane and storage at 4 °C yielded **5** as red plates and blocks suitable for single crystal X-ray diffraction. The solvent was removed by decanting, the crystals washed twice with *n*-hexane and dried in vacuum for 3h.

The powder was dissolved in 20 mL THF, which probably led to decomposition of **5**.

Yield (crystals) 15 mg (0.02 mmol = 20 %).

Synthesis of [{CpMo(CO)$_2$}$_2$(μ,η^2:η^2-P$_2$BBr$_2$)][TEF] (6)

An orange solution of [{CpMo(CO)$_2$}$_2$(μ,η^2:η^2-P$_2$)] (50 mg, 0.1 mmol, 1.0 eq.) and Tl[TEF] (118 mg, 0.1 mmol, 1.0 eq.) in 10 mL *o*-DFB was stirred for 15 minutes before pure BBr_3 (11 µL, 0.11 mmol, 1.1 eq.) was added, which led to immediate precipitation of white powder and a colour change to orange red. The suspension was stirred for 3h and filtered through glas fibre filter paper. Layering with *n*-hexane (5x) and storage at 4 °C yielded **6** as orange plates suitable for single crystal X-ray diffraction (the crystals are very air sensitive and decompose rapidly at air and slowly in mineral oil by turning

yellow (hydride species of **Mo_2P_2**)). The solvent was removed by decanting and the crystals dried in vacuum for 3h.
$^{31}P\{^1H\}$ NMR of the crude solution (C_6D_6/*o*-DFB) δ/ppm = −32.6 (s, 2 P), −4.4 (s, 2 P). ^{31}P NMR of the crude solution (C_6D_6/*o*-DFB) δ/ppm = −32.6 (s, 2 P), −4.4 (s, 2 P). $^{19}F\{^1H\}$ NMR (C_6D_6/*o*-DFB) δ/ppm = −75.6 (s, [TEF]$^-$). $^{11}B\{^1H\}$ NMR (C_6D_6/*o*-DFB) δ/ppm = 38.4 (s), 56.4 (s).

Synthesis of [{($C_5H_4BBr_2$)Mo(CO)$_2$}{CpMo(CO)$_2$}(μ,η^2:η^2-As_2)] (7a)

A red solution of [{CpMo(CO)$_2$}$_2$(μ,η^2:η^2-As_2)] (59 mg, 0.1 mmol, 1.0 eq.) and Tl[TEF] (118 mg, 0.1 mmol, 1.0 eq.) in 10 mL *o*-DFB was stirred for 15 minutes before pure BBr_3 (11 µL, 0.11 mmol, 1.1 eq.) was added, which led to immediate precipitation of white powder and a colour change to orange brown. The suspension was stirred for 3h and filtered through glas fibre filter paper. Layering with *n*-hexane (5x) and storage at 4 °C yielded **7a** as orange sticks suitable for single crystal X-ray diffraction. The solvent was removed by decanting and the crystals dried in vacuum for 3h.

Synthesis of [{($C_5H_4BBr_2$)Mo(CO)$_2$}{CpMo(CO)$_2$}(μ,η^2:η^2-Sb_2)] (7b)

A dark red solution of [{CpMo(CO)$_2$}$_2$(μ,η^2:η^2-Sb_2)] (68 mg, 0.1 mmol, 1.0 eq.) and Tl[TEF] (118 mg, 0.1 mmol, 1.0 eq.) in 10 mL *o*-DFB was stirred for 15 minutes before pure BBr_3 (11 µL, 0.11 mmol, 1.1 eq.) was added, which led to immediate precipitation of white powder and a colour change to dark orange red. The suspension was stirred for 3h and filtered through glas fibre filter paper. Layering with *n*-hexane (5x) and storage at 4 °C yielded **7b** as orange sticks suitable for single crystal X-ray diffraction (the crystals undergo rapid decomposition in mineral oil by turning dark brown). The solvent was removed by decanting and the crystals dried in vacuum for 3h.

Synthesis of [{CpMo(CO)$_2$}$_2${μ-PH(PPh_2)}(μ-SbCl)][TEF] (8a) and [{CpMo(CO)$_2$}$_2$(μ-PH_2)(μ-SbCl)][TEF] (9a)

An orange red solution of [{CpMo(CO)$_2$}$_2$(μ,η^2:η^2-PSb)] (30 mg, 0.05 mmol, 1.0 eq.) and Tl[TEF] (59 mg, 0.05 mmol, 1.0 eq.) in 8 mL CH_2Cl_2 was stirred for 3h before pure PPh_2Cl (10 µL, 0.05 mmol, 1.0 eq.) was added, which led to immediate precipitation of white powder. The suspension (containing a product mixture of **8a**, **9a** and unidentified byproducts (see NMR section)) was stirred for 15 minutes and filtered through glas fibre filter paper. Layering with *n*-hexane (5x) and storage at 4 °C yielded **8a** as dark orange sticks suitable for single crystal X-ray diffraction. The solvent was removed by decanting and the crystals dried in vacuum for 3h.
When the filtered solution is stirred for two weeks, **9a** can be obtained as sole product and crystallized in the same manner as **8a**.
Yield (product mixture of **8a**, **9a** and unidentified byproducts) 51 mg (0.03 mmol = 60 % referred to a mixture of **8a** and **9a** in a ratio of 3:2). ^1H NMR (CD_2Cl_2) δ/ppm = 5.14 (s, Cp), 5.22 (s, Cp), 5.65 (s, Cp) 7.29–7.89 (m, Ph). $^{31}P\{^1H\}$ NMR (CD_2Cl_2) δ/ppm = −38.3 (s, unassignable), −1.0 (d, $^1J_{P\text{-}P}$ = 320 Hz, 1 P, P2 atom of **$8a_1$**), 3.4 (d, $^1J_{P\text{-}P}$ = 320 Hz, 1 P, P2 atom of **$8a_2$**), 28.2 (s, 1 P, **9a**), 36.5 (s, unassignable),

46.1 (s (broad), unassignable), 71.9 (d, $^1J_{P\text{-}P}$ = 320 Hz, 1 P, P1 atom of **8a₂**), 90.7 (s (broad), unassignable), 103.4 (d, $^1J_{P\text{-}P}$ = 320 Hz, 1 P, P1 atom of **8a₁**). ^{31}P NMR (CD_2Cl_2) δ/ppm = −38.3 (s, unassignable), −1.0 (d, $^1J_{P\text{-}P}$ = 320 Hz, 1 P, P2 atom of **8a₁**), 3.4 (d, $^1J_{P\text{-}P}$ = 320 Hz, 1 P, P2 atom of **8a₂**), 28.2 (t, $^1J_{P\text{-}H}$ = 405 Hz, 1 P, **9a**), 36.5 (s, unassignable), 46.1 (s (broad), unassignable), 71.9 (t, $^1J_{P\text{-}P}$ = 320 Hz, $^1J_{P\text{-}H}$ = 320 Hz, 1 P, P1 atom of **8a₂**), 90.7 (s (broad), unassignable), 103.4 (t, $^1J_{P\text{-}P}$ = 320 Hz, $^1J_{P\text{-}H}$ = 320 Hz, 1 P, P1 atom of **8a₁**). ^{19}F{^{1}H} NMR (CD_2Cl_2) δ/ppm = −75.6 (s, [TEF]$^-$). ^{31}P{^{1}H} NMR of the solution after 14 days (C_6D_6/*o*-DFB) δ/ppm = 26.8 (s, 1 P, **9a**). ^{31}P NMR of the solution after 14 days (C_6D_6/*o*-DFB) δ/ppm = 26.8 (dd, $^1J_{P\text{-}H}$ = 374 Hz, $^1J_{P\text{-}H}$ = 438 Hz, 1 P, **9a**). Anal. calcd. for [$C_{14}H_{10}O_4Mo_2PSb(PPh_2)HCl$][TEF]: C: 28.41, H: 1.19. Found: C: 28.41, H: 1.26. Positive ion ESI-MS *m/z* (%): 806.7 (70) [**8a**], 770.8 (100) [**8a**–HCl]$^+$/[**8a**–CO]$^+$, 742.8 (6) [**8a**−HCl−CO]$^+$, 714.8 (12) [**8a**−HCl−2CO]$^+$, 686.8 (28) [**8a**−HCl−3CO]$^+$, 658.8 (90) [**8a**−HCl−4CO]$^+$, 622.7 [**9a**]$^+$, 586.7 [**9a**-HCl]$^+$/[**9a**-CO]$^+$, 568.7 [**9a**-2CO]$^+$, 536.7 [**9a**-HCl-2CO]$^+$/[**9a**-3CO]$^+$, 508.7 [**9a**-HCl-3CO]$^+$/[**9a**-4CO]$^+$. Negative ion ESI-MS *m/z* (%): 966.9 (100) [TEF]$^-$. IR $\tilde{\nu}$/cm^{-1} = 2362 (vw), 2344 (vw), 2332 (vw), 2055 (m), 2044 (m), 2012 (m), 2006 (m), 1352 (w), 1297 (m), 1275 (s), 1241 (s), 1216 (vs), 1172 (w), 971 (vs), 849 (w), 834 (w), 822 (w), 756 (w), 727 (s), 702 (w); C-H around 3000 not observed (to small).

Synthesis of [{CpMo(CO)$_2$}$_2${µ-AsH(PPh$_2$)}(µ-SbCl)][TEF] (8b)

A red solution of [{CpMo(CO)$_2$}$_2$(µ,η^2:η^2-AsSb)] (32 mg, 0.05 mmol, 1.0 eq.) and Tl[TEF] (59 mg, 0.05 mmol, 1.0 eq.) in 10 mL CH_2Cl_2 was stirred for 15 minutes before a solution of PPh_2Cl (10 µL, 0.05 mmol, 1.0 eq.) in 10 mL CH_2Cl_2 was added, which led to immediate precipitation of white powder. The suspension was stirred for 18h and filtered through glas fibre filter paper. Layering with *n*-hexane (4x) and storage at 4 °C yielded **8b** as dark red sticks moderately suitable for single crystal X-ray diffraction. The solvent was removed by decanting and the crystals dried in vacuum for 3h.

^{1}H NMR (CD_2Cl_2) δ/ppm = 5.14 (s, **Mo_2AsSb**), 5.54 (s, 5 H, Cp), 7.40–7.90 (m, 10 H, Ph). ^{31}P NMR (CD_2Cl_2) δ/ppm = 36.9 (s), 47.2 (s (broad)). Negative ion ESI-MS *m/z* (%): 966.9 (100) [TEF]$^-$.

Synthesis of [{CpMo(CO)$_2$}$_2$(µ,η^1:η^1-PP(Ph)$_2$Sb)][TEF] (10a)

An orange red solution of [{CpMo(CO)$_2$}$_2$(µ,η^2:η^2-PSb)] (64 mg, 0.11 mmol, 1.0 eq.) and Tl[TEF] (124 mg, 0.11 mmol, 1.0 eq.) in 5 mL *o*-DFB was stirred for 20 minutes before a solution of PPh_2Cl in toluene (*c* = 0.2M, 0.5 mL, 0.10 mmol, 0.9 eq.) was added, which led to immediate precipitation of white powder and the solution slightly darkens. The suspension was stirred for 8h and filtered through glas fibre filter paper. Layering with *n*-pentane (4x) and storage at 4 °C yielded pure **10a** as dark red sticks suitable for single crystal X-ray diffraction. The solvent was removed by decanting and the crystals dried in vacuum for 3h.

^{1}H NMR of the crude solution (C_6D_6/*o*-DFB) δ/ppm = −36.4 (d, $^1J_{P\text{-}P}$ = 324 Hz, 1 P, P2 atom), 139.4 (d, $^1J_{P\text{-}P}$ = 324 Hz, 1 P, P1 atom). ^{31}P NMR of the crude solution (C_6D_6/*o*-DFB) δ/ppm = −36.4 (d, $^1J_{P\text{-}P}$ = 324 Hz, 1 P, P2 atom), 139.4 (d, $^1J_{P\text{-}P}$ = 324 Hz, 1 P, P1 atom).

Synthesis of [{Cp'Mo(CO)$_2$}$_2$(μ,η^1:η^1-AsP(Ph)$_2$Sb)][TEF] (10b)

A red solution of [{Cp'Mo(CO)$_2$}$_2$(μ,η^2:η^2-AsSb)] (32 mg, 0.043 mmol, 1.0 eq.) and Tl[TEF] (51 mg, 0.043 mmol, 1.0 eq.) in 5 mL *o*-DFB was stirred for 2h before a solution of PPh$_2$Cl (10 µL, 0.05 mmol, 1.1 eq.) in 1 mL *o*-DFB was added, which led to immediate precipitation of white powder and the solution slightly darkens to reddish brown. The suspension was stirred for 30 minutes and filtered through a frit. Layering with *n*-pentane (4x) and storage at room temperature yielded pure **10b** as dark red sticks suitable for single crystal X-ray diffraction. The solvent was removed by decanting and the crystals dried in vacuum for 3h.

Synthesis of [{CpMo(CO)$_2$}$_2$(μ,η^2:η^2-PSbBBr$_2$)][TEF] (11)

An orange red solution of [{CpMo(CO)$_2$}$_2$(μ,η^2:η^2-PSb)] (60 mg, 0.10 mmol, 1.0 eq.) and Tl[TEF] (118 mg, 0.10 mmol, 1.0 eq.) in 5 mL *o*-DFB was stirred for 20 minutes before pure BBr$_3$ (10 µL, 0.10 mmol, 1.0 eq.) was added, which led to immediate precipitation of white powder and the colour changes to bright red. The suspension was stirred for 8h and filtered through glas fibre filter paper. Layering with *n*-pentane (4x) and storage at 4 °C yielded pure **11a** as orange to red sticks and plates suitable for single crystal X-ray diffraction. The solvent was removed by decanting and the crystals dried in vacuum for 3h.

^{31}P{^{1}H} NMR of the crude solution (C$_6$D$_6$/*o*-DFB) *δ*/ppm = 35.6 (s), 35.8 (s). ^{31}P NMR of the crude solution (C$_6$D$_6$/*o*-DFB) *δ*/ppm = 35.6 (s), 35.8 (s). ^{11}B{^{1}H} NMR of the crude solution (C$_6$D$_6$/*o*-DFB) *δ*/ppm = 38.4 (s), 55.0 (s (broad)).

Synthesis of [{CpMo(CO)$_2$}$_2$(μ,η^2:η^2-P$_2$)(μ-H)][B(C$_6$F$_5$)$_4$] (12a)

An orange solution of [{CpMo(CO)$_2$}$_2$(μ,η^2:η^2-P$_2$)] (25 mg, 0.05 mmol, 1.0 eq.) in 5 mL *o*-DFB was reacted with a solution of [(Et$_3$Si)$_2$H][B(C$_6$F$_5$)$_4$] (46 mg, 0.05 mmol, 1.0 eq.) in 5 mL *o*-DFB at −15 °C yielding a light orange solution. The solution was stirred for 6h at −15 °C and layered with *n*-hexane (4x). Storage at 4 °C for 7 days yielded pure **12a** as light orange blocks suitable for single crystal X-ray diffraction. The solvent was removed by decanting, the crystals washed twice with *n*-hexane and dried in vacuum for 3h.

Yield 45 mg (0.038 mmol = 76 %). ^{1}H NMR (CD$_2$Cl$_2$) *δ*/ppm = −17.61 (s, 1 H, hydride), 5.57 (s, 10 H, Cp). ^{31}P{^{1}H} NMR (CD$_2$Cl$_2$) *δ*/ppm = −33.1 (s, P$_2$). ^{31}P NMR (CD$_2$Cl$_2$) *δ*/ppm = −33.1 (s, P$_2$). ^{13}C{^{1}H} NMR (CD$_2$Cl$_2$) *δ*/ppm = 89.33 (s, Cp). ^{19}F{^{1}H} NMR (CD$_2$Cl$_2$) *δ*/ppm = −167.3 (t, $^3J_{F\text{-}F}$ = 17.8 Hz, 2 F, meta position), −163.5 (t, $^3J_{F\text{-}F}$ = 20.4 Hz, 1 F, para position), −132.9 (s (broad), 2 F, ortho position). ^{11}B{^{1}H} NMR (CD$_2$Cl$_2$) *δ*/ppm = −16.8 (s). Positive ion ESI-MS *m/z* (%) 496.82 (100) [**12a**]$^+$. Negative ion ESI-MS *m/z* (%) 678.98 (100) [B(C$_6$F$_5$)$_4$]$^-$. Anal. calcd. for [C$_{14}$H$_{11}$O$_4$Mo$_2$P$_2$][B(C$_6$F$_5$)$_4$]: C: 38.81, H: 0.94. Found: C: 39.24, H: 0.89.

Synthesis of [{CpMo(CO)$_2$}$_2$(μ,η^2:η^2-PAs)(μ-H)][B(C_6F_5)$_4$] (12b)

An orange-red solution of [{CpMo(CO)$_2$}$_2$(μ,η^2:η^2-PAs)] (27 mg, 0.05 mmol, 1.0 eq.) in 5 mL *o*-DFB was reacted with a solution of [(Et_3Si)$_2$H][B(C_6F_5)$_4$] (46 mg, 0.05 mmol, 1.0 eq.) in 5 mL *o*-DFB at −15 °C yielding an orange to yellow solution. The solution was stirred for 6h at −15 °C and layered with *n*-hexane (4x). Storage at 4 °C for 7 days yielded pure **12b** as yellow plates suitable for single crystal X-ray diffraction. The solvent was removed by decanting, the crystals washed twice with *n*-hexane and dried in vacuum for 3h.

Yield 57 mg (0.046 mmol = 92 %). ^{1}H NMR (CD_2Cl_2) *δ*/ppm = −18.30 (s, 1 H, hydride), −17.90 (s, 1 H, hydride), 5.54 (s, 10 H, Cp), 5.56 (s, 10 H, Cp). ^{31}P{^{1}H} NMR (CD_2Cl_2) *δ*/ppm = −33.1 (s. trace impurity of **12a**), 26.4 (s, PAs). ^{31}P NMR (CD_2Cl_2) *δ*/ppm = −33.1 (s. trace impurity of **12a**), 26.4 (s, PAs). ^{19}F{^{1}H} NMR of crude solution (C_6D_6/*o*-DFB) *δ*/ppm = −167.7 (t, $^3J_{F\text{-}F}$ = 18.6 Hz, 2 F, meta position), −164.0 (t, $^3J_{F\text{-}F}$ = 20.3 Hz, 1 F, para position), −132.6 (s (broad), 2 F, ortho position). Positive ion ESI-MS *m/z* (%) 540.83 (4) [**12b**]$^+$, 584.72 (100) [$\mathbf{Mo_2As_2}$H]$^+$. Negative ion ESI-MS *m/z* (%) 679.04 (100) [B(C_6F_5)$_4$]$^-$. Anal. calcd. for [$C_{14}H_{11}O_4Mo_2PAs$][B(C_6F_5)$_4$]: C: 37.41, H: 0.91. Found: C: 37.42, H: 0.90.

10.4.3 NMR spectroscopy

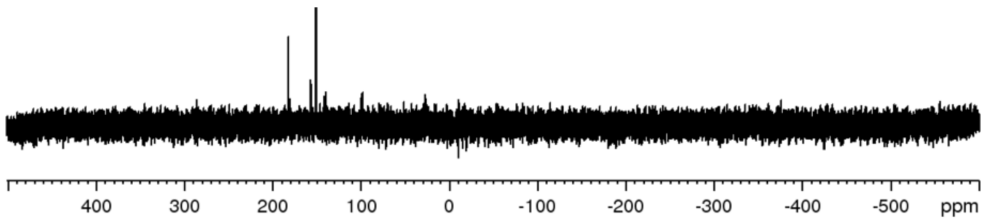

Figure S1: ^{31}P(^{1}H) NMR spectrum of the crude solution of **2a** in C_6D_6/*o*-DFB.

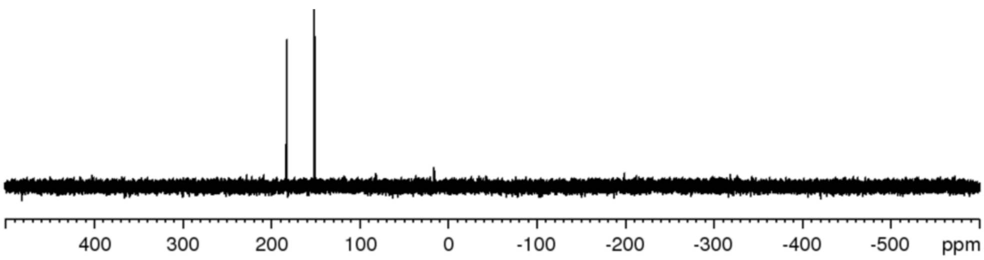

Figure S2: ^{31}P(^{1}H) NMR spectrum of the crude solution of **2b** in C_6D_6/*o*-DFB.

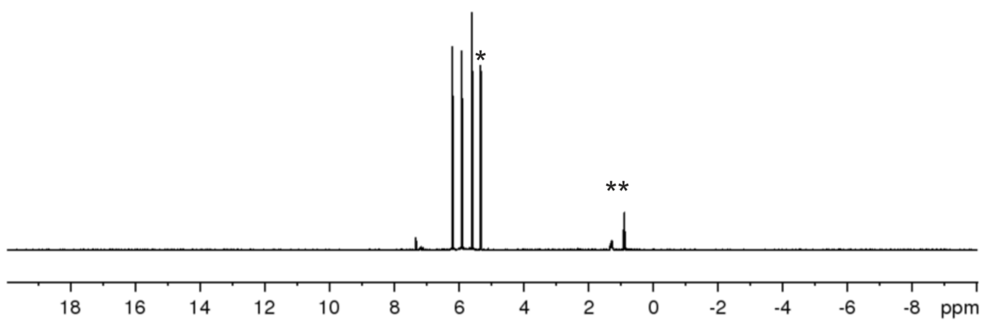

Figure S3: ^{1}H NMR spectrum of crystalline **4** in CD_2Cl_2; * = CD_2Cl_2, ** = H grease.

Surprisingly, five singlets for the Cp protons are observed, which cannot be explained yet, because the ^{31}P and ^{31}P{^{1}H} NMR spectra of **4** (Figure S4 and Figure S5) only show signals for one species.

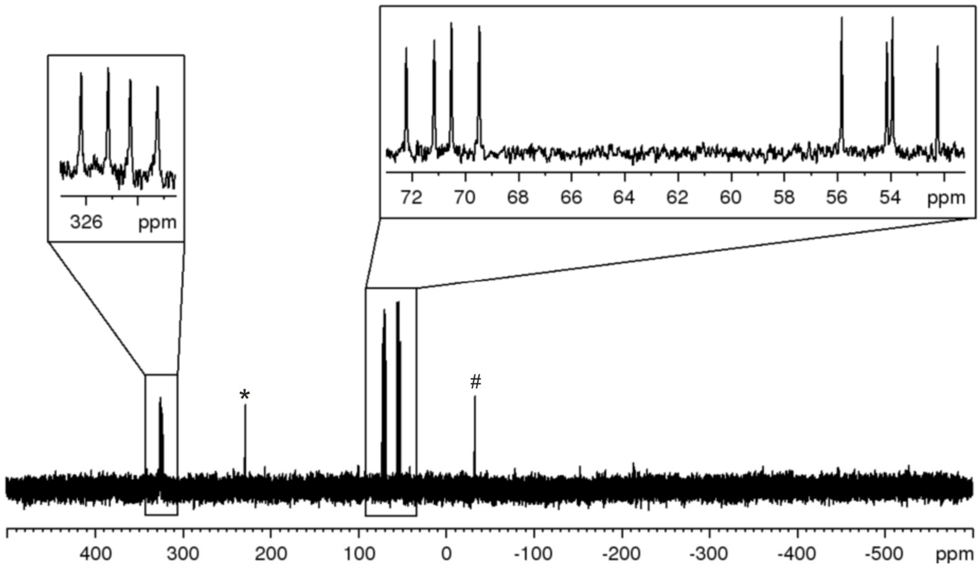

Figure S4: $^{31}P\{^1H\}$ NMR spectrum of crystalline **4** in CD_2Cl_2; * = traces of PBr_3, # = traces of **Mo_2P_2**.

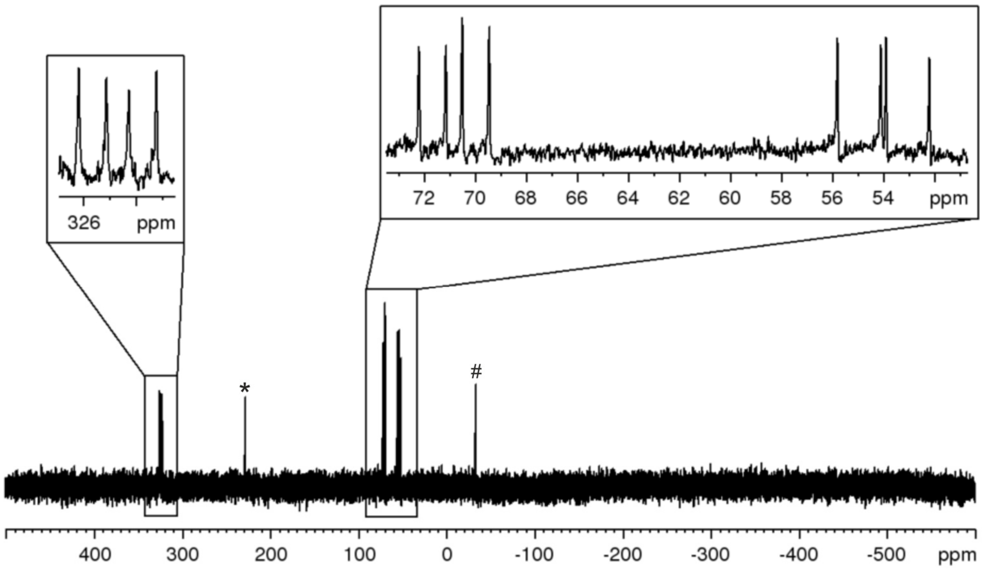

Figure S5: ^{31}P NMR spectrum of crystalline **4** in CD_2Cl_2; * = traces of PBr_3, # = traces of **Mo_2P_2**.

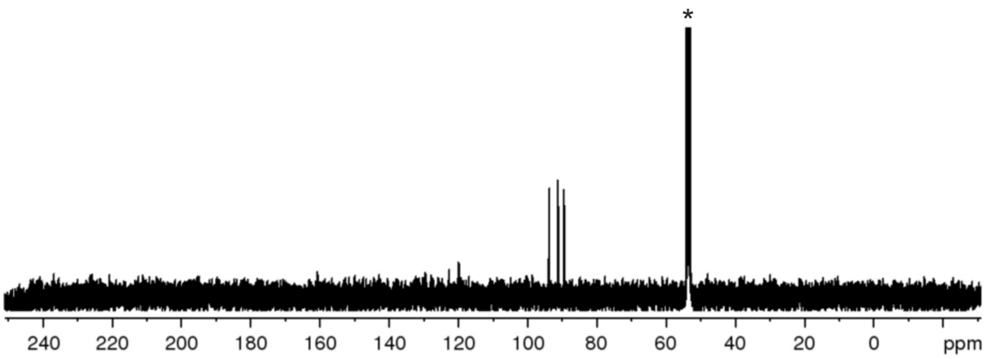

Figure S6: $^{13}C\{^1H\}$ NMR spectrum of crystalline **4** in CD_2Cl_2; * = CD_2Cl_2.

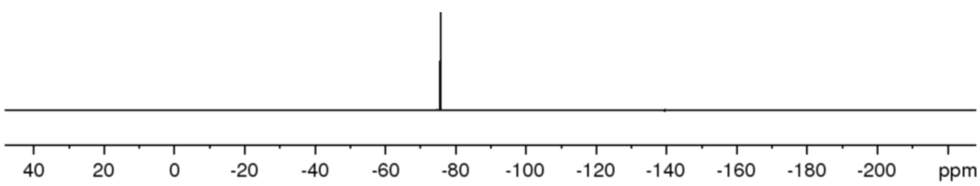

Figure S7: $^{19}F\{^1H\}$ NMR spectrum of crystalline **4** in CD_2Cl_2.

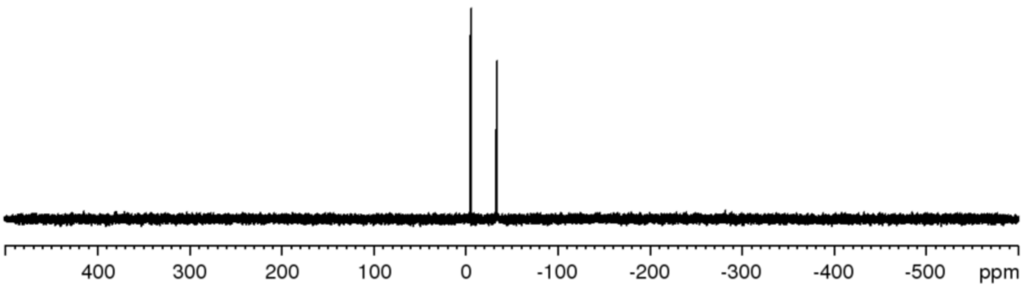

Figure S8: $^{31}P\{^1H\}$ NMR spectrum of the crude solution of **6** in C_6D_6/*o*-DFB.

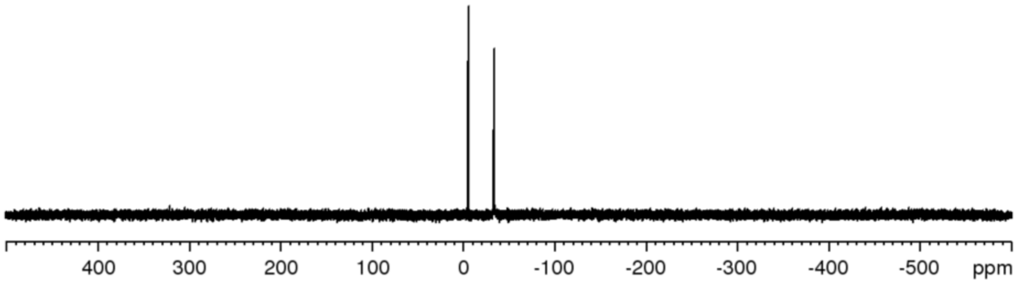

Figure S9: ^{31}P NMR spectrum of the crude solution of **6** in C_6D_6/*o*-DFB.

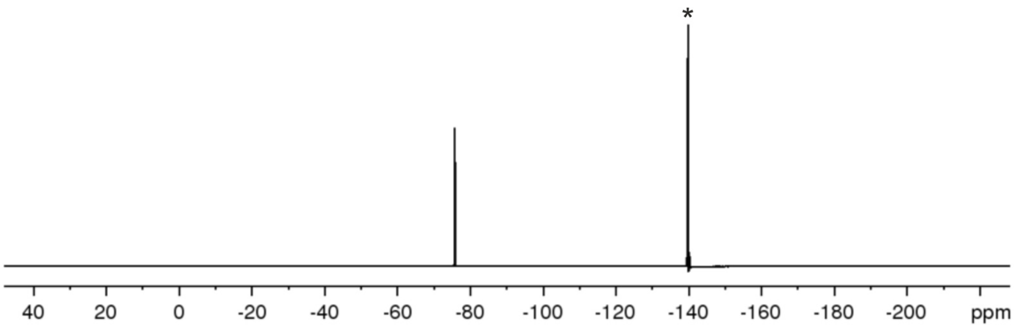

Figure S10: $^{19}F\{^1H\}$ NMR spectrum of the crude solution of **6** in C_6D_6/*o*-DFB; * = *o*-DFB.

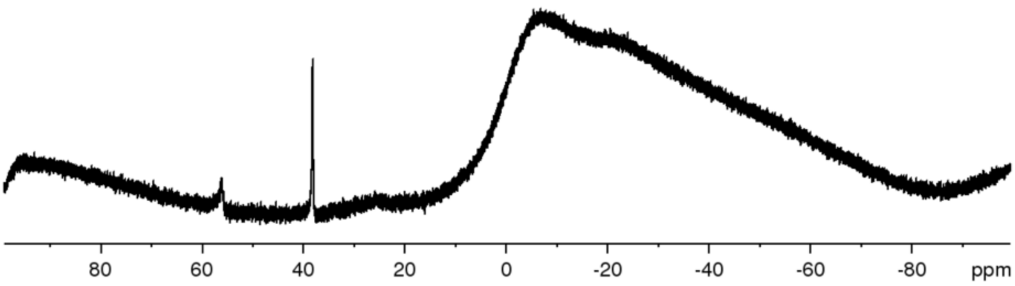

Figure S11: $^{11}B\{^1H\}$ NMR spectrum of the crude solution of **6** in C_6D_6/*o*-DFB.

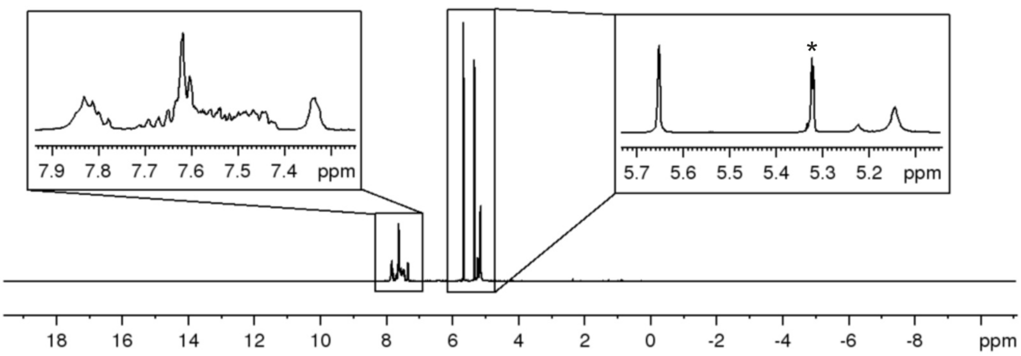

Figure S12: ^1H NMR spectrum of **8a** and **9a** in CD_2Cl_2; * = CD_2Cl_2.

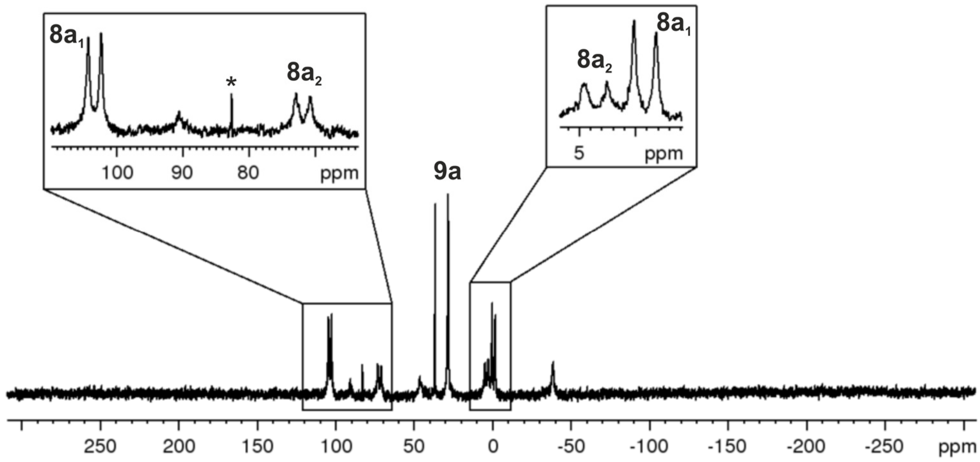

Figure S13: $^{31}P\{^{1}H\}$ NMR spectrum of **8a** and **9a** in CD_2Cl_2.

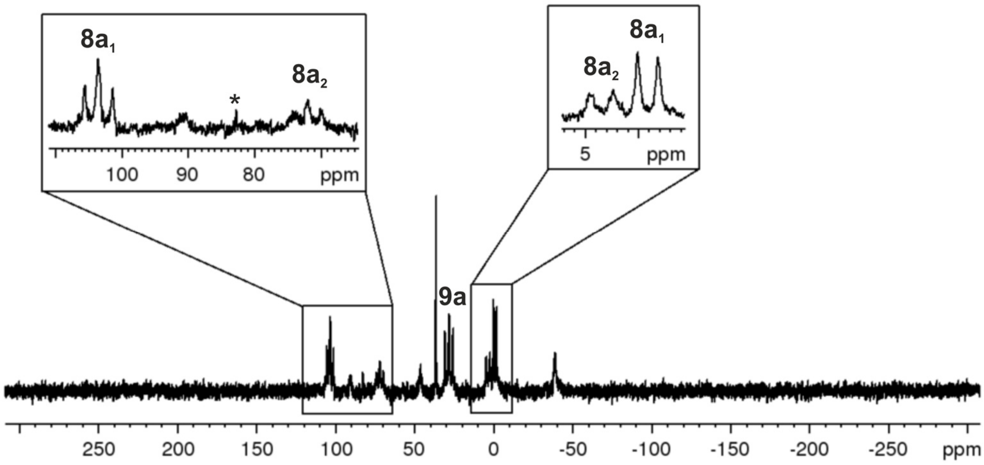

Figure S14: ^{31}P NMR spectrum of **8a** and **9a** in CD_2Cl_2.

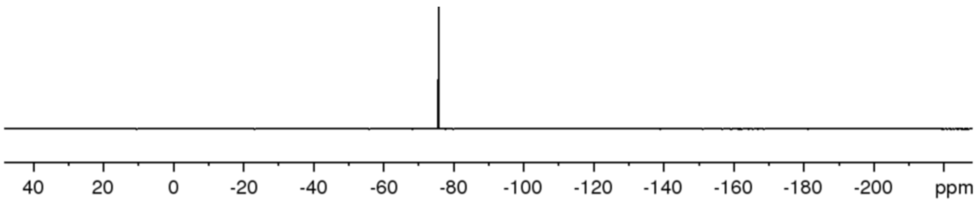

Figure S15: $^{19}F\{^{1}H\}$ NMR spectrum of **8a** and **9a** in CD_2Cl_2.

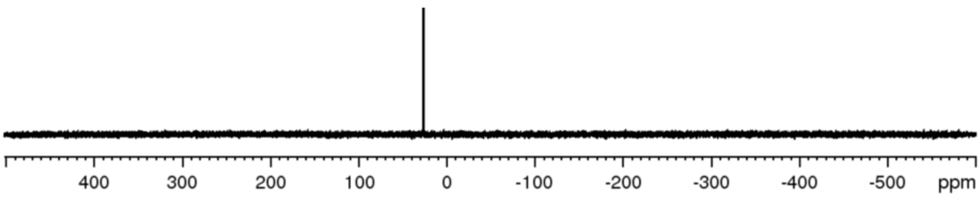

Figure S16: $^{31}P\{^{1}H\}$ NMR spectrum of the crude solution of **8a** and **9a** in C_6D_6/*o*-DFB after 14 days. Only **9a** is left.

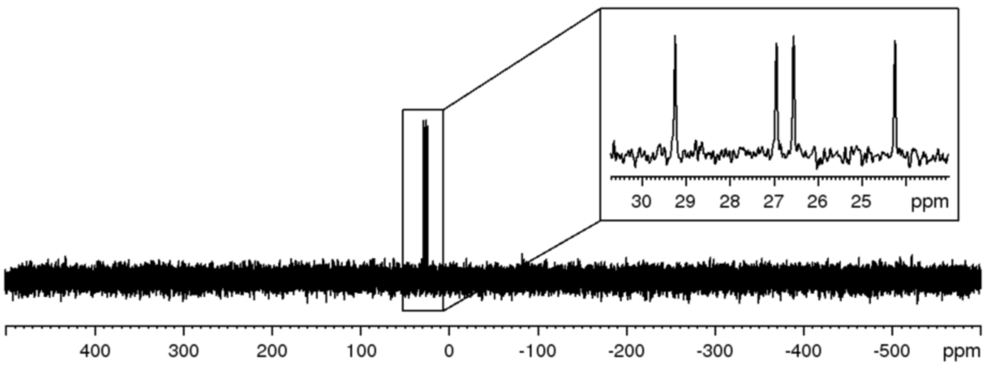

Figure S17: ^{31}P NMR spectrum of the crude solution of **8a** and **9a** in C_6D_6/*o*-DFB after 14 days. Only **9a** is left.

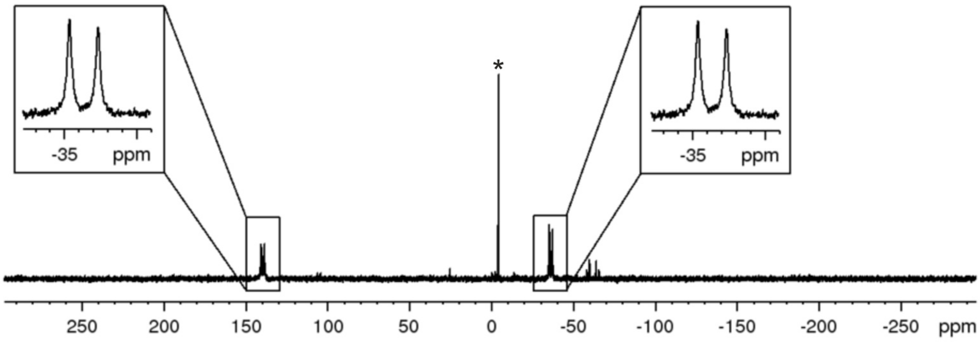

Figure S18: $^{31}P\{^1H\}$ NMR spectrum of the crude solution of **10a** in C_6D_6/*o*-DFB; * = unidentified trace impurity.

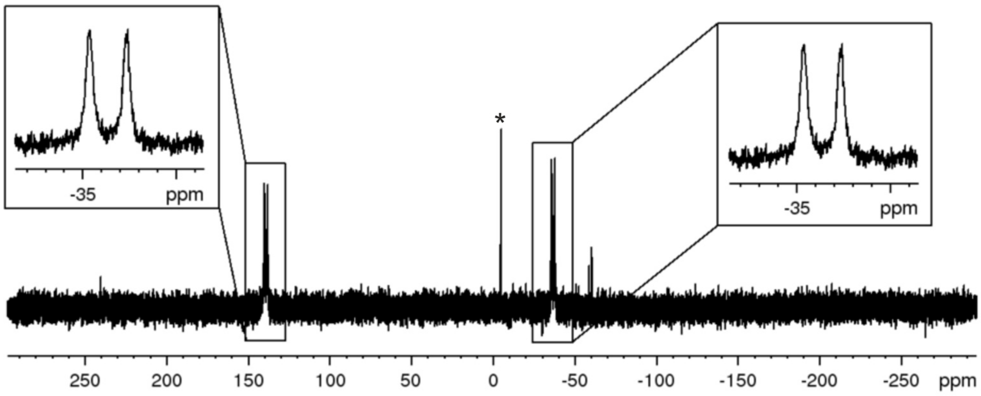

Figure S19: ^{31}P NMR spectrum of the crude solution of **10a** in C_6D_6/*o*-DFB; * = unidentified trace impurity.

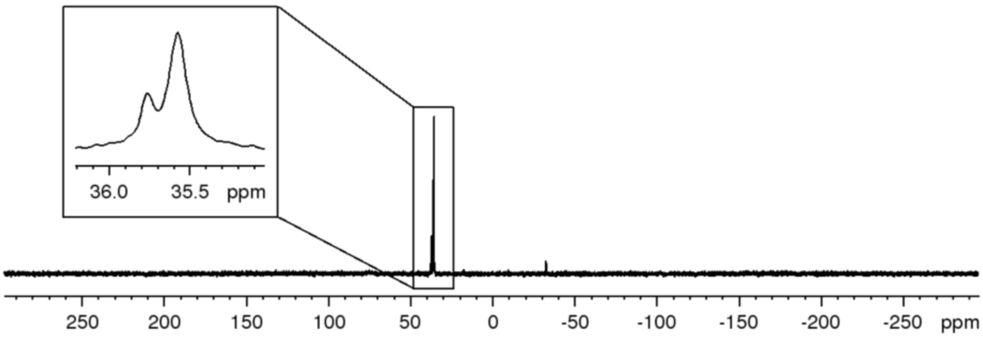

Figure S20: $^{31}P\{^1H\}$ NMR spectrum of the crude solution of **11** in C_6D_6/*o*-DFB.

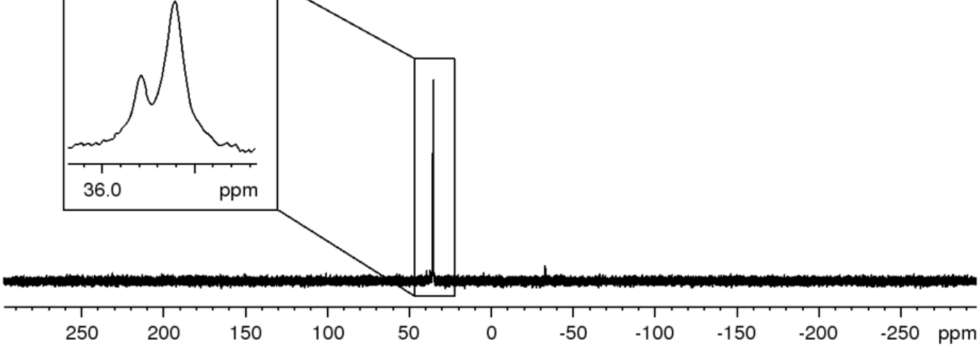

Figure S21: ^{31}P NMR spectrum of the crude solution of **11** in C_6D_6/*o*-DFB.

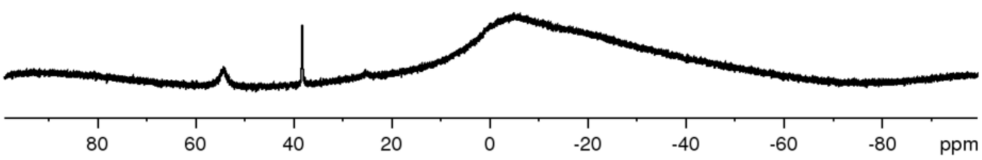

Figure S22: $^{11}B\{^1H\}$ NMR spectrum of the crude solution of **11** in C_6D_6/*o*-DFB.

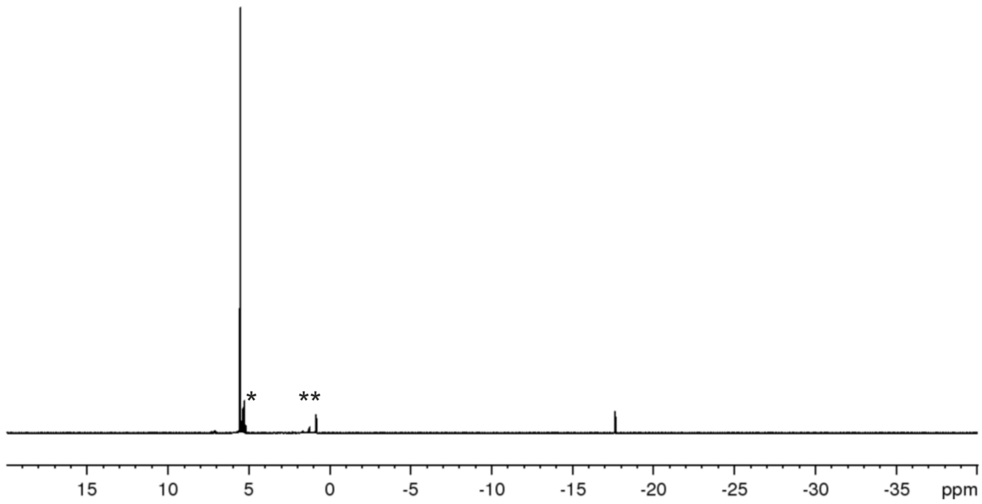

Figure S23: ^{1}H NMR spectrum of **12a** in CD_2Cl_2; * = CD_2Cl_2; ** = H grease.

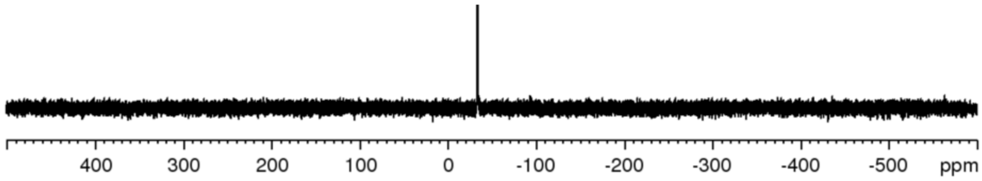

Figure S24: $^{31}P\{^{1}H\}$ NMR spectrum of **12a** in CD_2Cl_2.

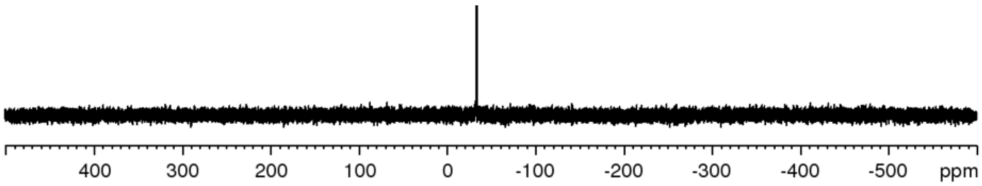

Figure S25: ^{31}P NMR spectrum of **12a** in CD_2Cl_2.

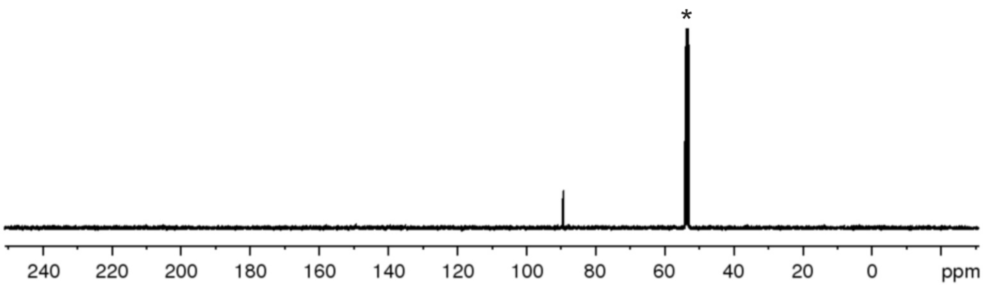

Figure S26: $^{13}C\{^{1}H\}$ NMR spectrum of **12a** in CD_2Cl_2; * = CD_2Cl_2.

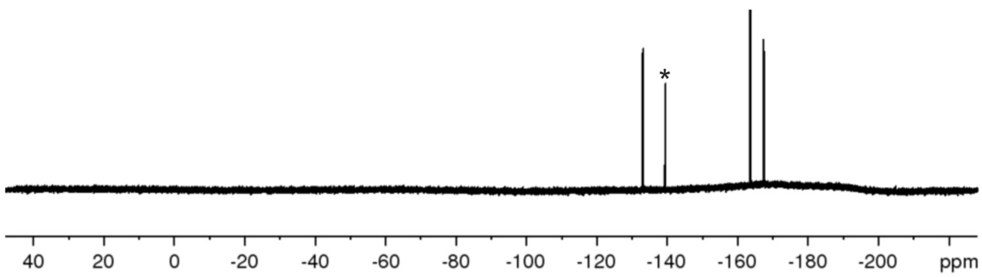

Figure S27: $^{19}F\{^{1}H\}$ NMR spectrum of **12a** in CD_2Cl_2; * = trace impurity.

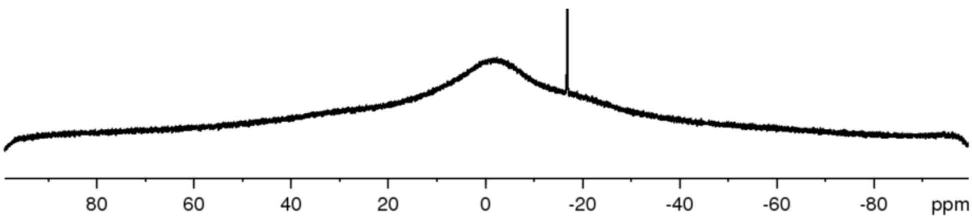

Figure S28: $^{11}B\{^{1}H\}$ NMR spectrum of **12a** in CD_2Cl_2.

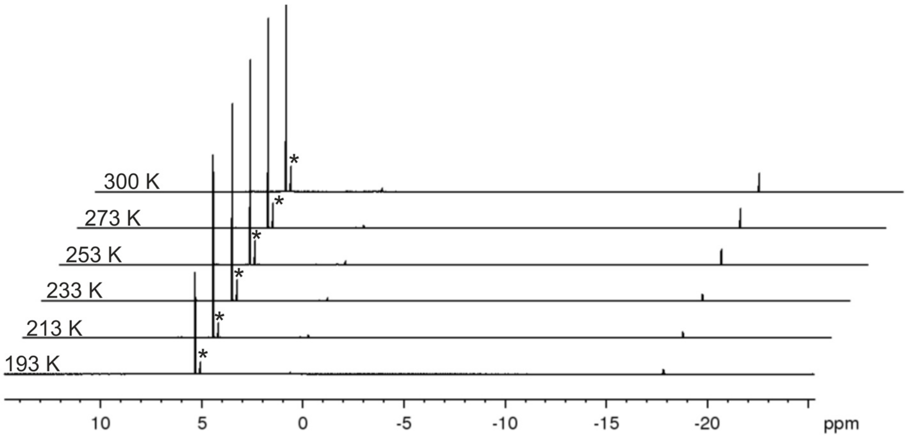

Figure S29: ^{1}H VT-NMR spectrum of **12a** in CD_2Cl_2; * = CD_2Cl_2; for the correct chemical shift +0.24 ppm must be added due to a calibration error.

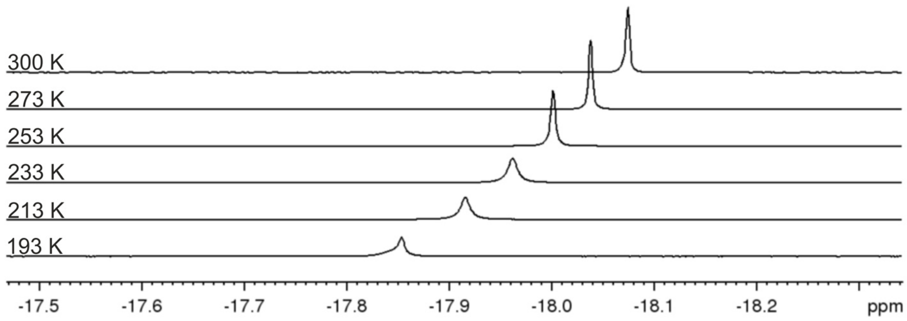

Figure S30: Hydride region of the ^{1}H VT-NMR spectrum of **12a** in CD_2Cl_2; for the correct chemical shift +0.24 ppm must be added due to a calibration error.

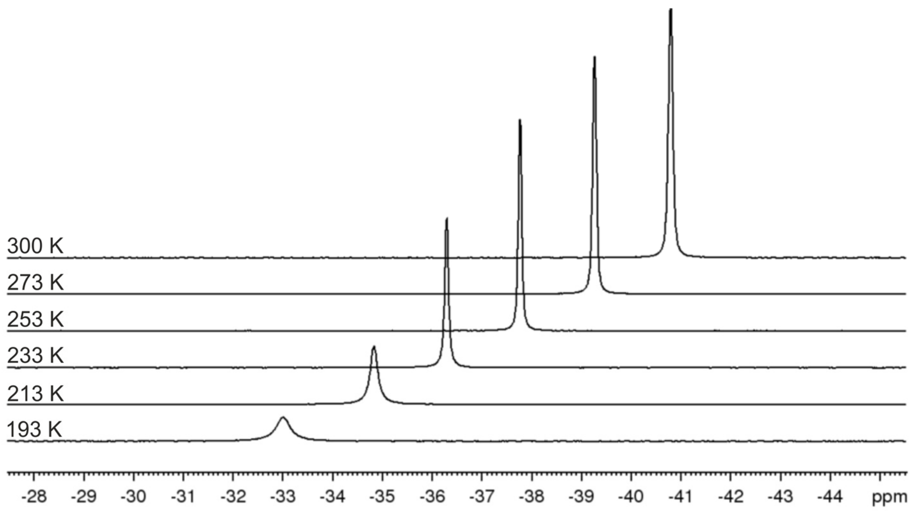

Figure S31: $^{31}P\{^{1}H\}$ VT-NMR spectrum of **12a** in CD_2Cl_2.

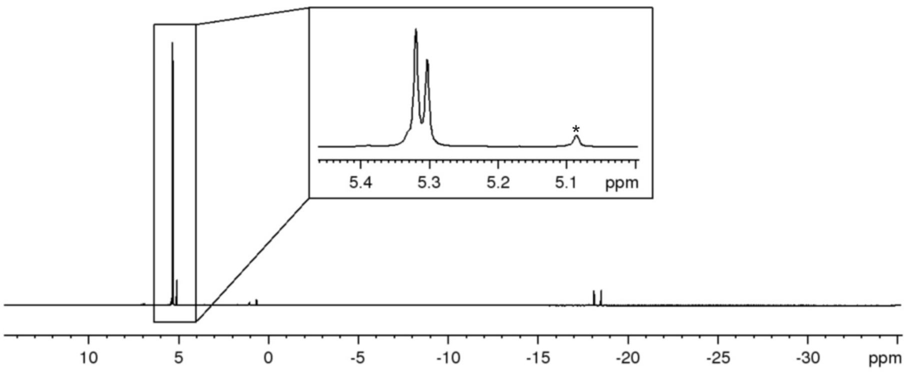

Figure S32: ^{1}H NMR spectrum of **12b** in CD_2Cl_2; * = CD_2Cl_2; for the correct chemical shift +0.24 ppm must be added due to a calibration error.

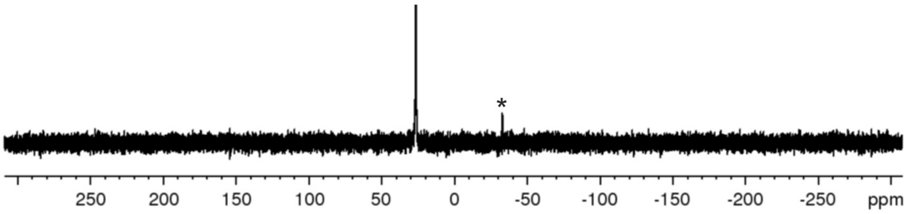

Figure S33: $^{31}P\{^1H\}$ NMR spectrum of **12b** in CD_2Cl_2; * = **12a** as trace impurity.

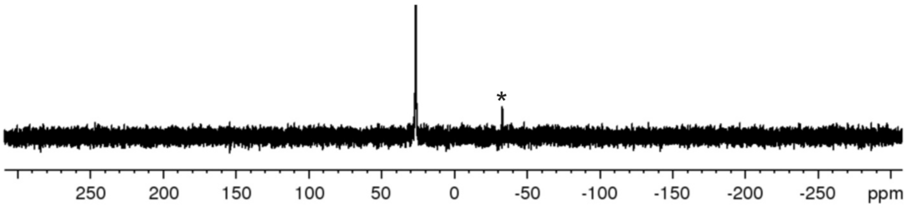

Figure S34: ^{31}P NMR spectrum of **12b** in CD_2Cl_2; * = **12a** as trace impurity.

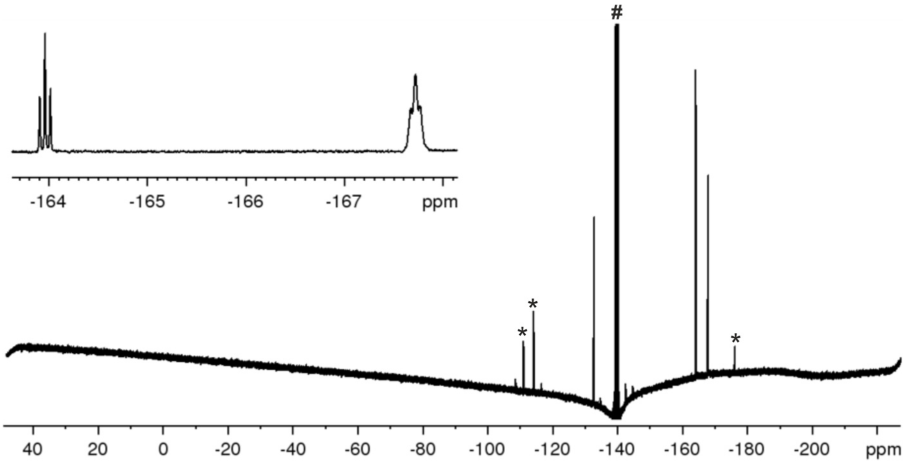

Figure S35: $^{19}F\{^1H\}$ NMR spectrum of the crude solution of **12b** in C_6D_6/*o*-DFB; * = trace impurities; # = *o*-DFB.

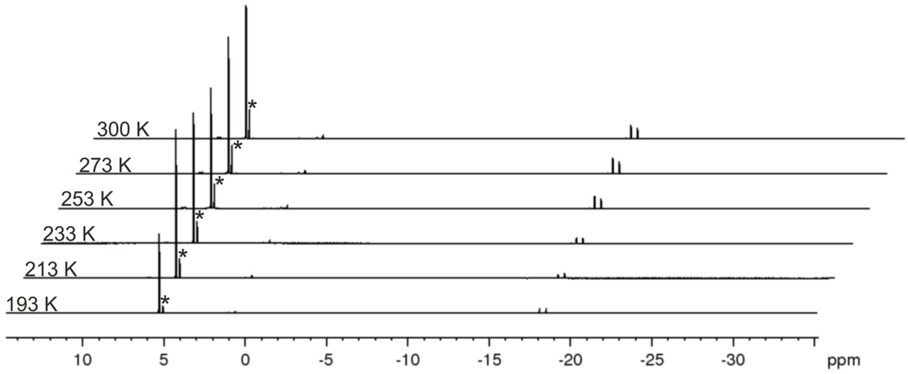

Figure S36: ^1H VT-NMR spectrum of **12b** in CD_2Cl_2; * = CD_2Cl_2; for the correct chemical shift +0.24 ppm must be added due to a calibration error.

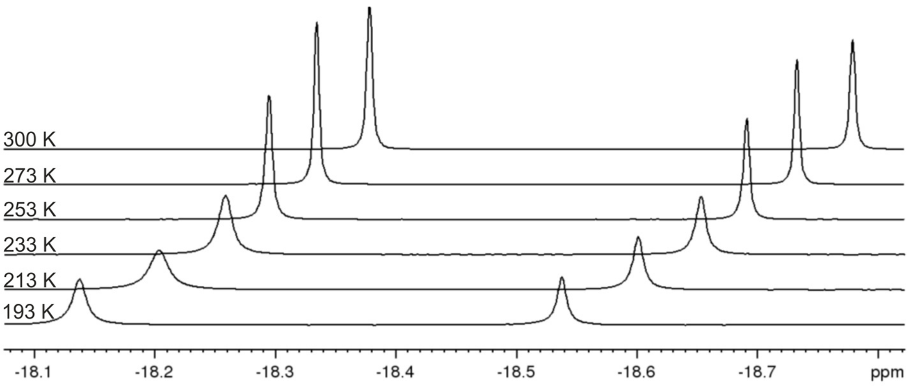

Figure S37: Hydride region of the ^1H VT-NMR spectrum of **12b** in CD_2Cl_2; for the correct chemical shift +0.24 ppm must be added due to a calibration error.

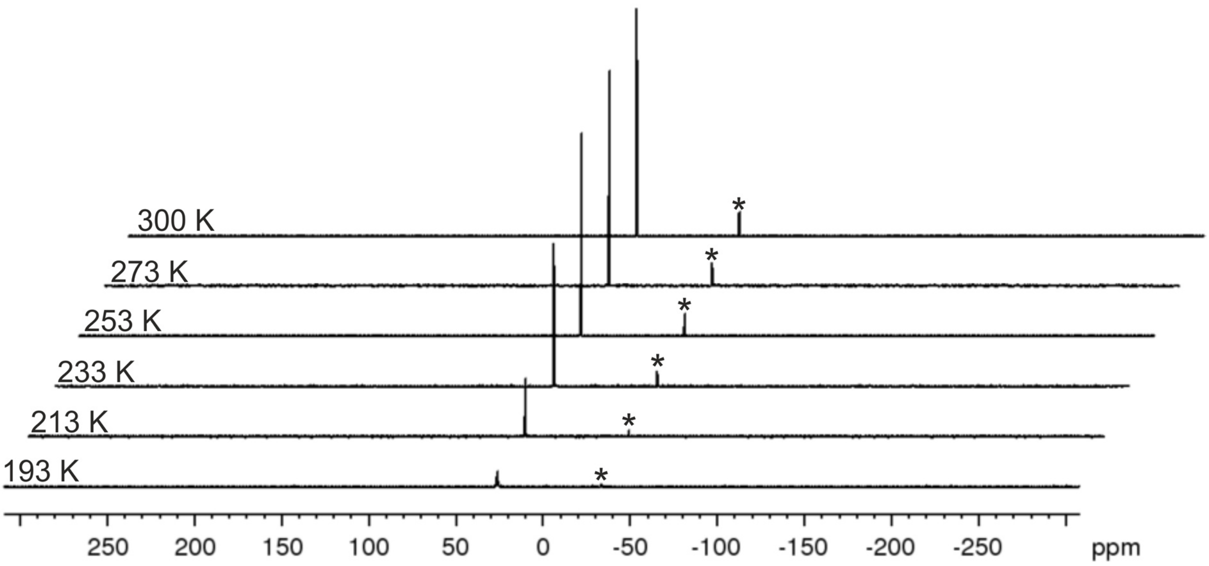

Figure S38: $^{31}P\{^{1}H\}$ VT-NMR spectrum of **12b** in CD_2Cl_2; * = **12a** as trace impurity.

10.4.4 Mass spectrometry

The mass spectra, which were recorded by the mass spectrometry department of the University of Regensburg are not available to the authors in a digital format and, therefore, could not be displayed. The following displayed spectra were recorded by the first author.

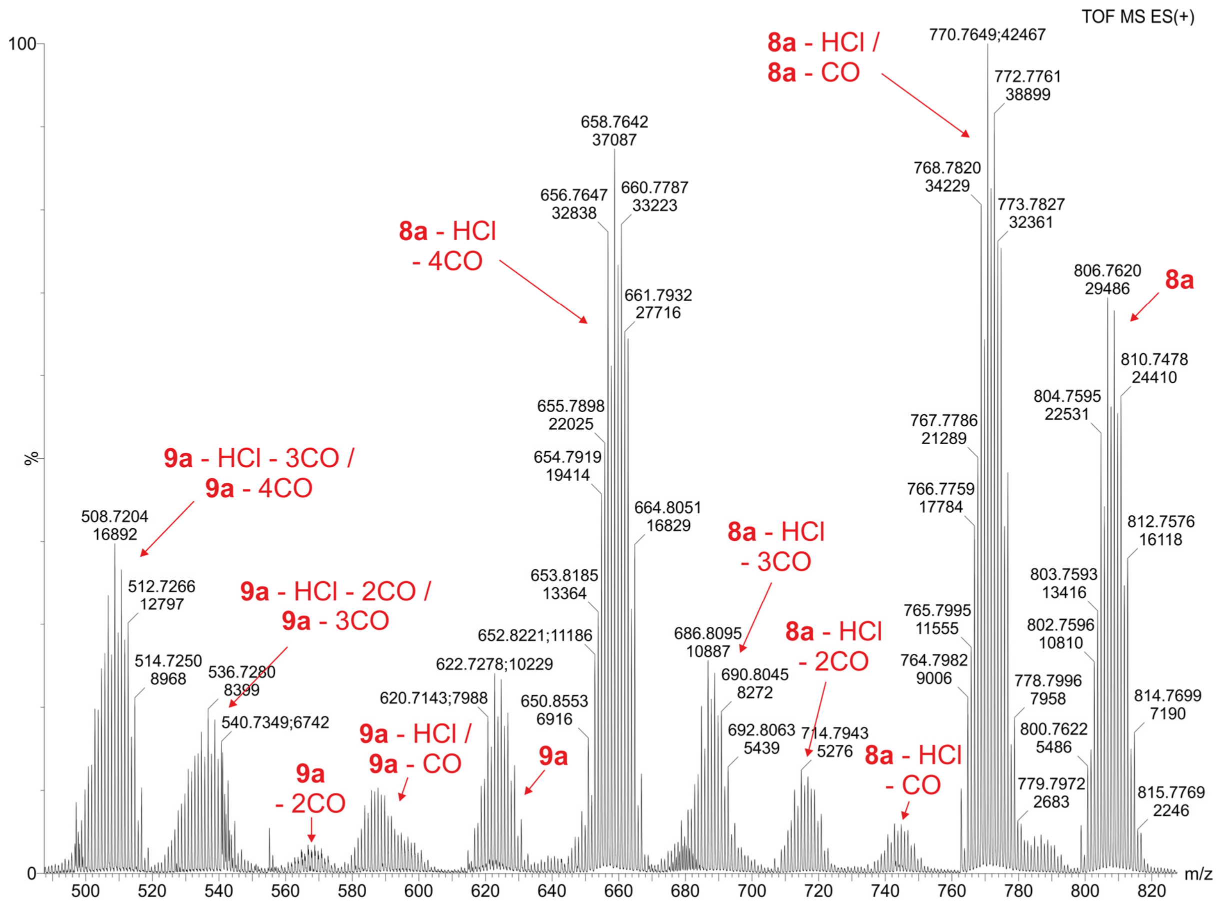

Figure S39: ESI MS(+) spectrum of **8a** and **9a**.

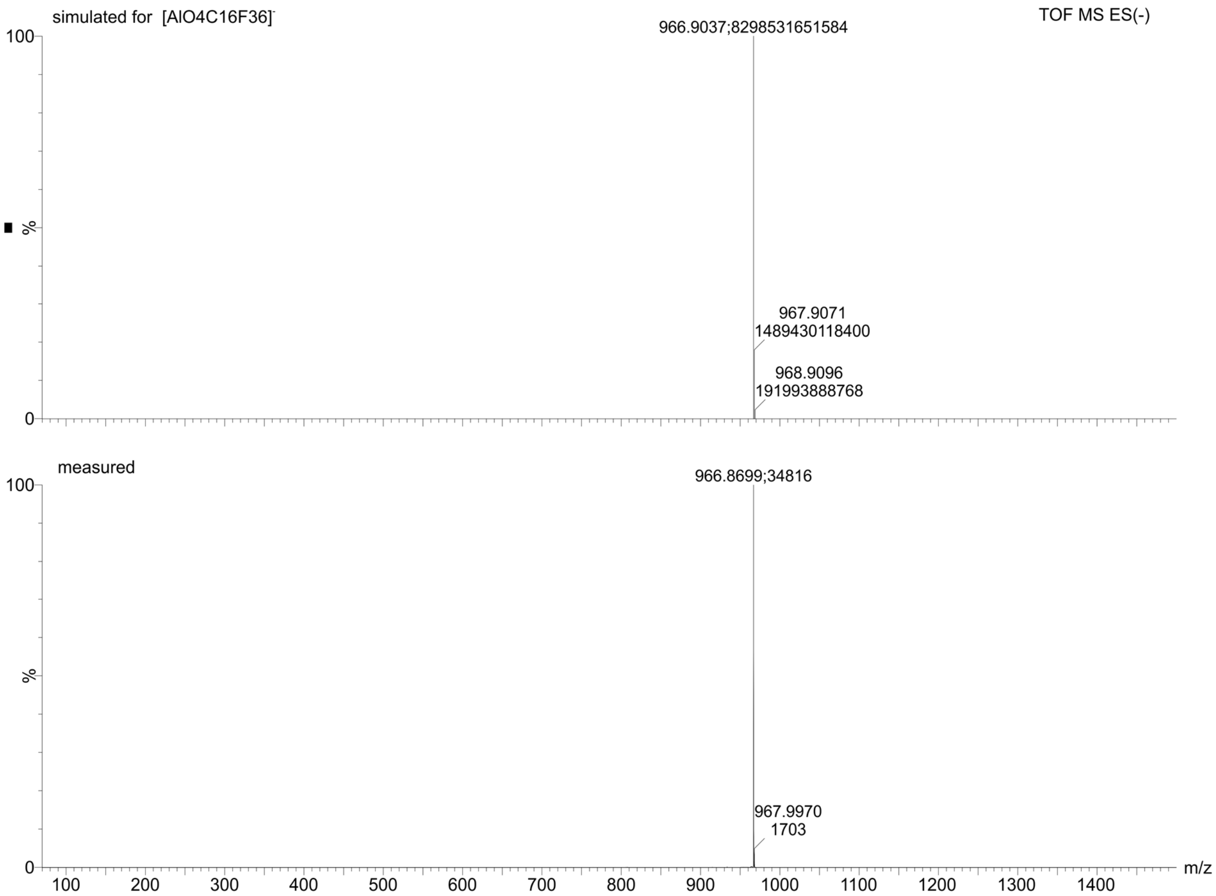

Figure S40: ESI MS(-) spectrum of **8a** and **9a**.

10.4.5 X-ray crystallography

All crystal manipulations were performed under mineral oil. The diffraction experiments were performed at 123 K (if not stated otherwise) on a Rigaku (former Agilent Technologies or Oxford Diffraction) Gemini Ultra with an AtlasS2 detector or on a GV50 diffractometer with a TitanS2 detector using Cu-K_α or Cu-K_β radiation. Crystallographic data together with the details of the experiments are given in Table S1, Table S2 and Table S3. The cell determination, data reduction and absorption correction for all compounds were performed with the help of the CrysAlis PRO software.[15] All structures were solved by using the programs SHELXT[16] and Olex2.[17] The full-matrix least-squares refinement against F^2 was done using SHELXL[18] and Olex2.[17] If not stated otherwise, all atoms except hydrogen atoms were refined anisotropically. The H atoms were calculated geometrically and a riding model was used during the refinement process (except of the H atoms in **12a** and **12b**, which are bridging the Mo–Mo bonds).

Table S1: Crystallographic details for the compounds **2a**, **3**, **4**, **5** and **6**.

	2a	**3**	**4**	**5**	**6**
formula		$C_{40}H_{32}AlF_{36}Mo_2O_6P_3$		$C_{14}H_{10}BBr_3Mo_2O_4P_2$	$C_{30}H_{10}AlBBr_2F_{36}Mo_2O_8P_2$
weight [g·mol^{-1}]		1604.42		746.58	1633.81
Temperature [K]		100.0(1)		123.0(1)	123.0(1)
crystal system	monoclinic	orthorhombic	monoclinic	monoclinic	monoclinic
space group	*Pn*	$Pca2_1$	$P2_1/c$	$P2_1$/n	$P2_1$
a [Å]	12.0709(5)	42.7542(4)	9.7473(1)	9.4108(2)	9.80980(10)
b [Å]	14.5369(5)	11.43180(10)	16.2131(3)	16.6561(2)	30.0495(2)
c [Å]	29.8627(9)	21.9904(2)	31.0231(4)	13.5923(2)	16.1599(2)
α [°]	90	90	90	90	90
β [°]	92.366(4)	90	91.775(1)	105.824(2)	93.1150(10)
γ [°]	90	90	90	90	90
Volume [Å^3]	5235.6(3)	10747.97(17)	4900.3(1)	2049.82(6)	4756.57(8)
Z		8		4	4
ρ_{calc} [g·cm^{-3}]		1.983		2.419	2.281
μ [mm^{-1}]		4.736		13.727	8.904
F(000)		6288.0		1400.0	3120.0
crystal size [mm^3]		0.32 × 0.101 × 0.091		0.341 × 0.313 × 0.074	0.693 × 0.417 × 0.106
diffractometer	GV50	GV50	GV50	GV50	Gemini Ultra
absorption correction		gaussian		gaussian	gaussian
T_{min} / T_{max}		0.371 / 0.991		0.066 / 0.887	0.056 / 0.773
radiation [Å]		Cu-Kβ (λ = 1.39222)		Cu-Kβ (λ = 1.39222)	Cu-Kα (λ = 1.54184)
2Θ range [°]		5.206 to 149.482		7.762 to 148.382	8.04 to 143.628
completeness [%]		99.7		98.6	99.5
reflns collected / unique		73153 / 27041		17451 / 5500	35890 / 17917
R_{int} / R_{sigma}		0.0372 / 0.0395		0.0405 / 0.0308	0.0486 / 0.0563
data / restraints / parameters		27041 / 133 / 1639		5500 / 0 / 235	17917 / 193 / 1375
GOF on F^2		1.025		1.087	1.640
R_1 / wR_2 [$I \geq 2\sigma(I)$]		0.0354 / 0.0902		0.0355 / 0.0958	0.1260 / 0.3432
R_1 / wR_2 [all data]		0.0367 / 0.0913		0.0379 / 0.0977	0.1281 / 0.3514
max / min $\Delta\rho$ [e·Å^{-3}]		1.10 / −1.34		1.32 / −1.07	12.46 / −2.26
Identification code	LD323	LD440_abs	LD354	LD377_abs	LD432_abs

Table S2: Crystallographic details for the compounds **7a**, **7b**, **8a**, **8b** and **9a**.

	7a	**7b**	**8a**	**8b**	**9a**
formula	$C_{30}H_9AlAs_2BBr_2F_{36}Mo_2O_8$	$C_{30}H_9AlBBr_2F_{36}Mo_2O_8Sb_2$	$C_{43}H_{23}AlCl_3F_{36}Mo_2O_8P_2Sb$		$C_{30}H_{12}AlCl_{36}Mo_2O_8PSb$
weight [g·mol^{-1}]	1720.70	1814.36	1860.51		1591.43
Temperature [K]	123.0(1)	100.0(1)	123.0(1)		123.0(1)
crystal system	triclinic	monoclinic	triclinic	monoclinic	monoclinic
space group	*P*-1	$P2_1/c$	*P*-1	$P2_1/n$	$P2_1/c$
a [Å]	10.3717(2)	20.2705(3)	10.7394(3)	27.5243(11)	11.1031(4)
b [Å]	17.9832(3)	23.8028(3)	15.9183(3)	16.1792(5)	28.0101(11)
c [Å]	26.2047(4)	20.6150(3)	17.4248(4)	28.2309(14)	15.1696(6)
α [°]	90.9410(10)	90	90.726(2)	90	90
β [°]	97.9600(10)	98.915(2)	93.147(2)	114.415(5)	94.729(3)
γ [°]	92.2290(10)	90	92.888(2)	90	90
Volume [Å^3]	4835.68(14)	9826.5(2)	2970.20(12)	11447.6(9)	4701.7(3)
Z	4	8	2	8	4
ρ_{calc} [g·cm^{-3}]	2.364	2.453	2.080		2.248
μ [mm^{-1}]	9.654	12.344	10.413		1.396
F(000)	3260.0	6808.0	1796.0		3040.0
crystal size [mm^3]	1.246 × 0.43 × 0.202	0.573 × 0.148 × 0.126	0.161 × 0.077 × 0.034		0.348 × 0.11 × 0.09
diffractometer	Gemini Ultra	GV50	GV50	GV50	Gemini Ultra
absorption correction	gaussian	gaussian	gaussian		multi-scan
T_{min} / T_{max}	0.056 / 0.773	0.033 / 0.801	0.612 / 0.863		0.941 / 1.000
radiation [Å]	Cu-Kα (λ = 1.54184)	Cu-Kβ (λ = 1.39222)	Cu-Kα (λ = 1.54184)		Mo-Kα (λ = 0.71073)
2Θ range [°]	6.814 to 144.298	5.156 to 149.26	7.476 to 148.21		6.774 to 65.458
completeness [%]	99.0	98.9	99.7		99.7
reflns collected / unique	46365 / 18352	49045 / 26150	33910 / 11706		37943 / 15654
R_{int} / R_{sigma}	0.0695 / 0.0550	0.0592 / 0.0758	0.0552 / 0.0476		0.0410 / 0.0684
data / restraints / parameters	18352 / 192 / 1429	26150 / 192 / 1477	11706 / 45 / 941		15654 / 0 / 729
GOF on F^2	1.026	1.209	1.023		1.025
R_1 / wR_2 [$I \geq 2\sigma(I)$]	0.0929 / 0.2477	0.1012 / 0.2762	0.0494 / 0.1297		0.0468 / 0.0850
R_1 / wR_2 [all data]	0.0946 / 0.2492	0.1193 / 0.3097	0.0565 / 0.1380		0.0747 / 0.0955
max / min $\Delta\rho$ [e·Å^{-3}]	2.95 / −1.84	5.38 / −1.94	3.92 / −1.34		1.40 / −1.21
*Id*Intification code	LD433_abs	LD434_abs	LD194_CR012_abs	LD199_CR017_abs	LD301_abs

Table S3: Crystallographic details for the compounds **10a**, **10b**, **11a**, **12a** and **12b**.

	10a	**10b**	**11a**	**12a**	**12b**
formula	$C_{42}H_{20}AlF_{36}Mo_2O_8P_2Sb$	$C_{56}H_{40}AlAsF_{38}Mo_2O_8PSb$	$C_{30}H_{10}AlBBr_2F_{36}Mo_2O_8PSb$	$C_{38}H_{11}BF_{20}Mo_2O_4P_2$	$C_{38}H_{11}AsBF_{20}Mo_2O_4P$
weight [g·mol^{-1}]	1739.13	2009.38	1724.59	1176.10	1220.05
Temperature [K]	123.0(1)	123.0(1)	123.0(1)	123.0(1)	123.0(1)
crystal system	monoclinic	triclinic	triclinic	monoclinic	monoclinic
space group	$P2_1/n$	P-1	P-1	$P2_1/n$	$P2_1/n$
a [Å]	24.3346(2)	15.2102(3)	9.8955(3)	16.8144(2)	16.8750(3)
b [Å]	16.15820(10)	15.9524(3)	15.0010(5)	13.32290(10)	13.2931(2)
c [Å]	30.0534(3)	16.6339(3)	17.3704(3)	17.4699(2)	17.4391(2)
α [°]	90	114.879(2)	75.744(2)	90	90
β [°]	111.0630(10)	106.072(2)	88.172(2)	93.9490(10)	93.491(2)
γ [°]	90	94.2280(10)	82.818(2)	90	90
Volume [Å^3]	11027.54(17)	3433.61(13)	2479.49(12)	3904.26(7)	3904.70(10)
Z	8	2	2	4	4
ρ_{calc} [g·cm^{-3}]	2.095	1.944	2.310	2.001	2.075
μ [mm^{-1}]	7.323	8.359	9.259	7.336	7.889
F(000)	6704.0	1956.0	1632.0	2280.0	2352.0
crystal size [mm^3]	0.87 × 0.206 × 0.085	0.409 × 0.302 × 0.206	0.515 × 0.19 × 0.082	0.897 × 0.642 × 0.212	0.338 × 0.259 × 0.054
diffractometer	GV50	GV50	GV50	Gemini Ultra	GV 50
absorption correction	gaussian	gaussian	gaussian	gaussian	gaussian
T_{min} / T_{max}	0.317 / 1.000	0.089 / 0.614	0.091 / 1.000	0.131 / 1.000	0.450 / 1.000
radiation [Å]	Cu-Kβ (λ = 1.39222)	Cu-Kα (λ = 1.54184)	Cu-Kβ (λ = 1.39222)	Cu-Kα (λ = 1.54184)	Cu-Kα (λ = 1.54184)
2Θ range [°]	5.256 to 148.39	6.196 to 148.72	4.74 to 149.212	7.058 to 145.714	7.078 to 148.038
completeness [%]	98.7	99.3	99.2	99.2	99.0
reflns collected / unique	98058 / 29663	36925 / 13458	27748 / 13226	20948 / 7517	18200 / 7531
R_{int} / R_{sigma}	0.0635 / 0.0508	0.0392 / 0.0344	0.0418 / 0.0444	0.0667 / 0.0623	0.0410 / 0.0389
data / restraints / parameters	29663 / 383 / 2278	13458 / 0 / 958	13226 / 0 / 739	7517 / 0 / 605	7531 / 0 / 607
GOF on F^2	1.025	1.032	1.069	1.072	1.036
R_1 / wR_2 [$I \geq 2\sigma(I)$]	0.0661 / 0.1774	0.0479 / 0.1245	0.0539 / 0.1543	0.0474 / 0.1166	0.0507 / 0.1467
R_1 / wR_2 [all data]	0.0779 / 0.1961	0.0490 / 0.1256	0.0602 / 0.1641	0.0500 / 0.1216	0.0556 / 0.1537
max / min $\Delta\rho$ [e·Å^{-3}]	6.12 / −2.17	2.10 / −1.93	2.81 / −2.42	1.60 / −1.27	2.04 / −1.72
Idenlification code	LD424_abs	LD205_abs	LD426_abs	LD359_abs	LD360_yellow_abs

Refinement details for 2a

Compound **2a** crystallizes as dark red sticks in the monoclinic space group *Pn*. The X-ray dataset was very weak and, furthermore, the cations and the [TEF]$^-$ anions were severely disordered. Thus, the refinement could not be finished and only the heavy atom framework could be determined (Figure S41). No bond lengths or angles could be described and only the cell parameters are given in Table S1.

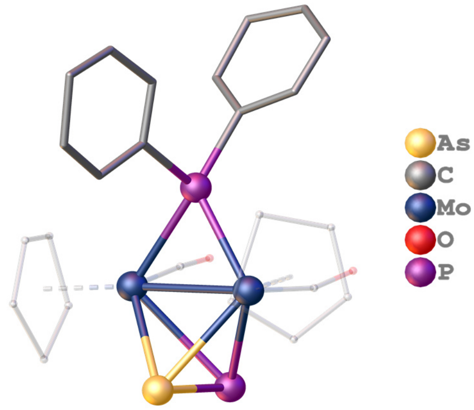

Figure S41: Heavy atom framework of the dicationic part in **2a** showing that the phosphenium ion is bridging the Mo–Mo bond. Cp and CO ligands are drawn translucent and the phenyl groups are represented as connected tubes.

Refinement details for 3

Compound **3** crystallizes as dark red sticks in the orthorhombic space group $Pca2_1$ with two cations and two [TEF]$^-$ anions in the asymmetric unit. The refinement could be done without any difficulties. In the [TEF]$^-$ anion including Al1 one of the -OC(CF_3)$_3$ groups exhibits a threefold rotational disorder in a ratio of 43:30:27. The disordered parts were partially restrained with DFIX and DANG commands and the anisotropic displacement parameters (ADPs) with SIMU and EADP commands.

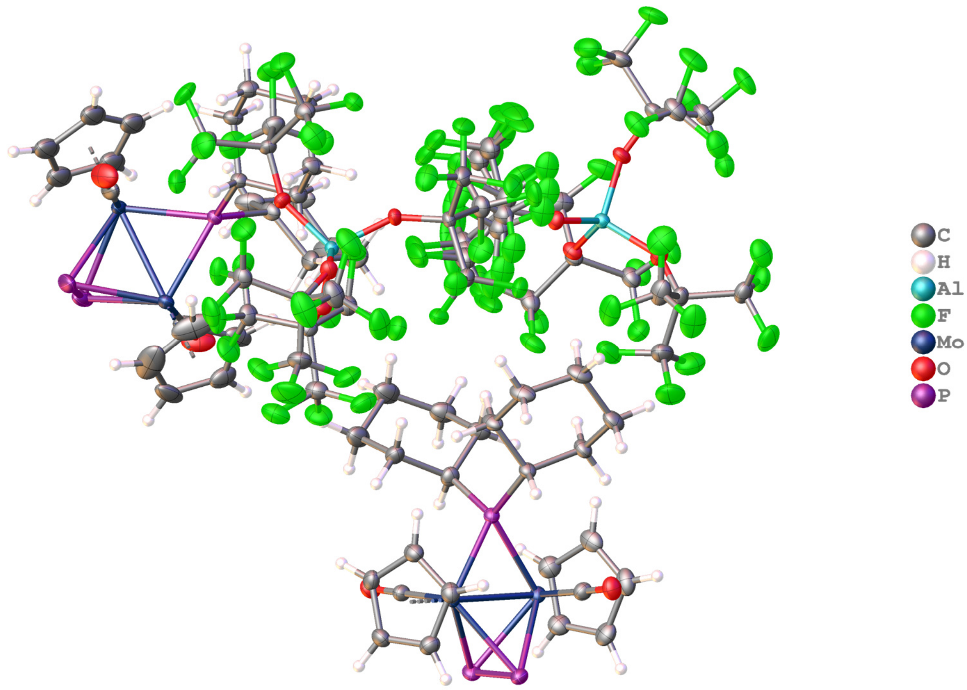

Figure S42: Molecular structure of **3**. The asymmetric unit is shown containing two cations and two [TEF]$^-$ anions.

Refinement details for 4

Compound **4** crystallizes as red brown plates in the monoclinic space group $P2_1/c$ with one cation and one $[TEF]^-$ anion in the asymmetric unit. The X-ray dataset was very weak and, furthermore, the cation and the $[TEF]^-$ anion were severely disordered. Thus, the refinement could not be finished and only a slight insight into the molecular structure of **4** can be given (Figure S43). No bond lengths or angles could be described and only the cell parameters are given in Table S1.

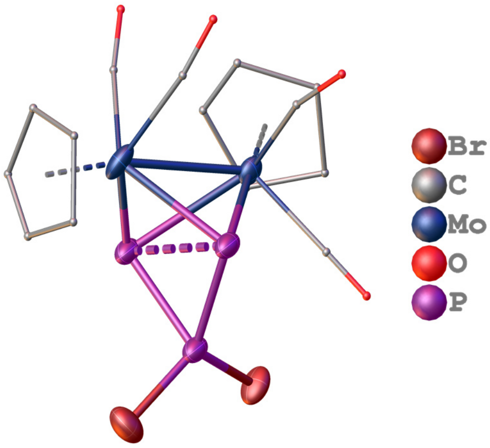

Figure S43: Molecular structure of the cationic part in **4** showing that the phosphenium ion is bridging/inserting into the P–P bond. Cp and CO ligands are drawn as small spheres.

Refinement details for 5

Compound **5** crystallizes as red brown plates in the monoclinic space group $P2_1/n$ with one molecule in the asymmetric unit. The refinement could be done without any difficulties. No disorder was observed.

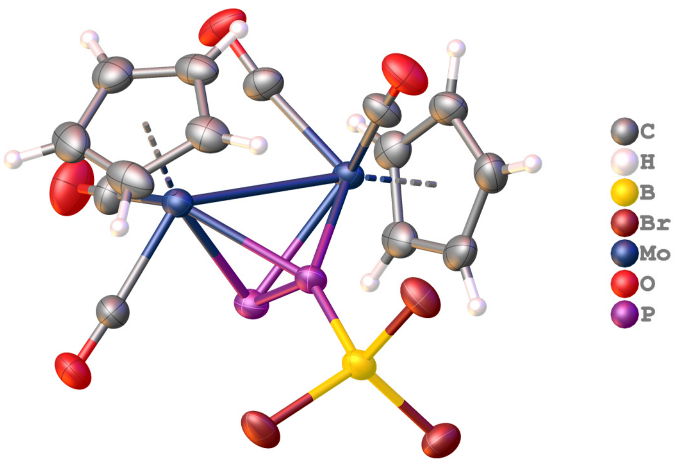

Figure S44: Molecular structure of **5**. The asymmetric unit is shown containing one molecule **5**.

Refinement details for 6

Compound **6** crystallizes as dark red plates in the monoclinic space group *P*2$_1$ with two cations and two [TEF]$^-$ anions in the asymmetric unit. The [TEF]$^-$ anions exhibit severe disorder. Therefore, the refinement could not be finished until the end of this thesis. However, the cationic part could be described well. Nevertheless, the bond lengths and angles should be considered carefully.

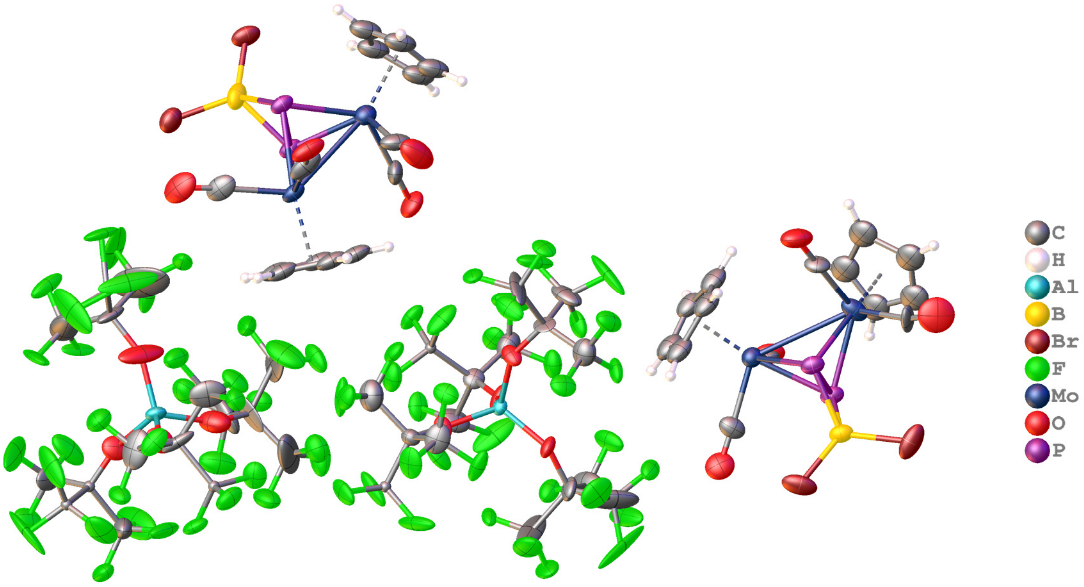

Figure S45: Molecular structure of **6**. The asymmetric unit is shown containing two cations and two [TEF]$^-$ anions.

Refinement details for 7a

Compound **7a** crystallizes as yellowish orange sticks in the triclinic space group *P*-1 with two cations and two [TEF]$^-$ anions in the asymmetric unit. The [TEF]$^-$ anions exhibit severe disorder. Therefore, the refinement could not be finished until the end of this thesis. However, the cationic part could be described well. Nevertheless, the bond lengths and angles should be considered carefully. The [TEF]$^-$ anions were partially restrained by DFIX and DANG commands.

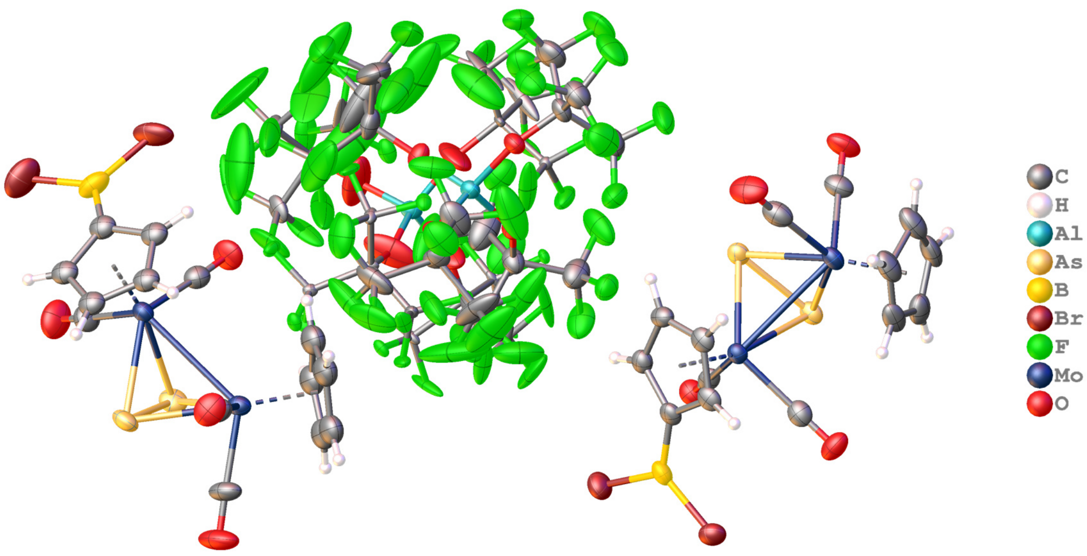

Figure S46: Molecular structure of **7a**. The asymmetric unit is shown containing two cations and two [TEF]$^-$ anions.

Refinement details for 7b

Compound **7b** crystallizes as orange sticks in the monoclinic space group $P2_1/c$ with two cations and two $[TEF]^-$ anions in the asymmetric unit. The $[TEF]^-$ anions exhibit severe disorder. Therefore, the refinement could not be finished until the end of this thesis. However, the cationic part could be described well. Nevertheless, the bond lengths and angles should be considered carefully. The $[TEF]^-$ anions were restrained by DFIX and DANG commands.

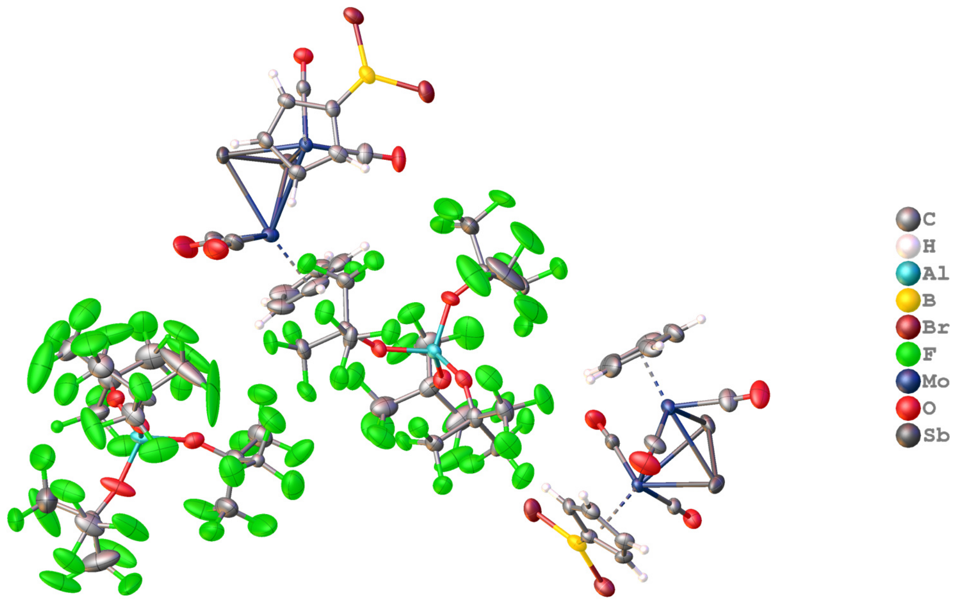

Figure S47: Molecular structure of **7b**. The asymmetric unit is shown containing two cations and two $[TEF]^-$ anions.

Refinement details for 8a

Compound **8a** crystallizes as dark red blocks in the triclinic space group *P*-1 with one cation, one $[TEF]^-$ anion and one solvent molecule CH_2Cl_2 in the asymmetric unit. The refinement could be done without any difficulties. In the $[TEF]^-$ anion one of the $-OC(CF_3)_3$ groups exhibits a rotational disorder in a ratio of 63:37. The disordered parts were partially restrained with DFIX and DANG commands during the refinement.

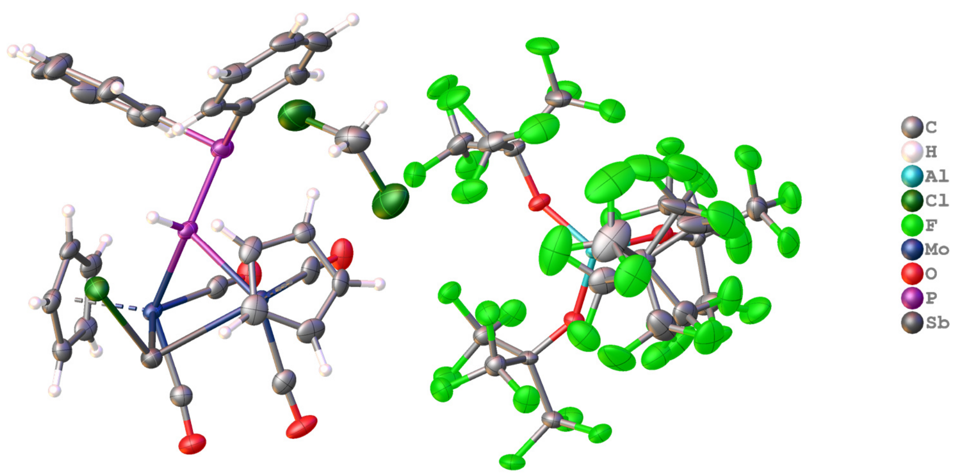

Figure S48: Molecular structure of **8a**. The asymmetric unit is shown containing one cation, one disordered $[TEF]^-$ anion and one solvent molecule CH_2Cl_2.

Refinement details for 8b

Compound **8b** crystallizes as dark red blocks in the monoclinic space group $P2_1/n$ with two cations and two [TEF]$^-$ anions in the asymmetric unit. The X-ray dataset was very weak and, furthermore, the [TEF]$^-$ anions were severely disordered. Thus, the refinement could not be finished and only a slight insight into the molecular structure of **8b** can be given (Figure S49). The bond lengths and angles should be considered very carefully and only the cell parameters are given in Table S2.

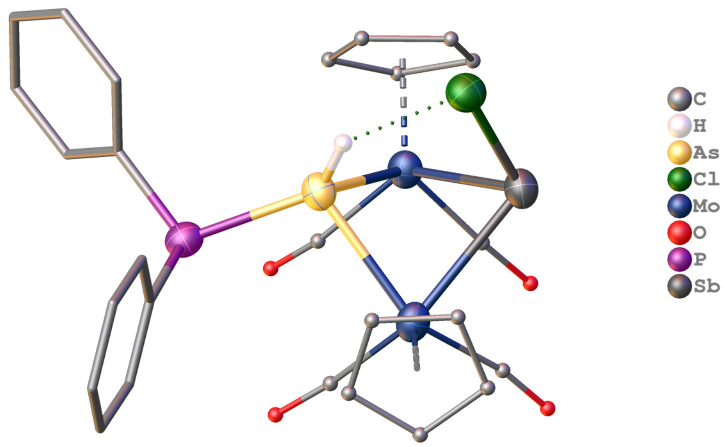

Figure S49: Molecular structure of the cation in **8b** showing that the phosphenium ion is attached to the arsenic atom and additional HCl addition took place analogous to **8a** Cp and CO ligands are drawn as small spheres and phenyl groups are presented as connected tubes.

Refinement details for 9a

Compound **9a** crystallizes as dark red blocks in the monoclinic space group $P2_1/c$ with one cation and one [TEF]$^-$ anion in the asymmetric unit. The refinement could be done without any difficulty. No disorder was observed.

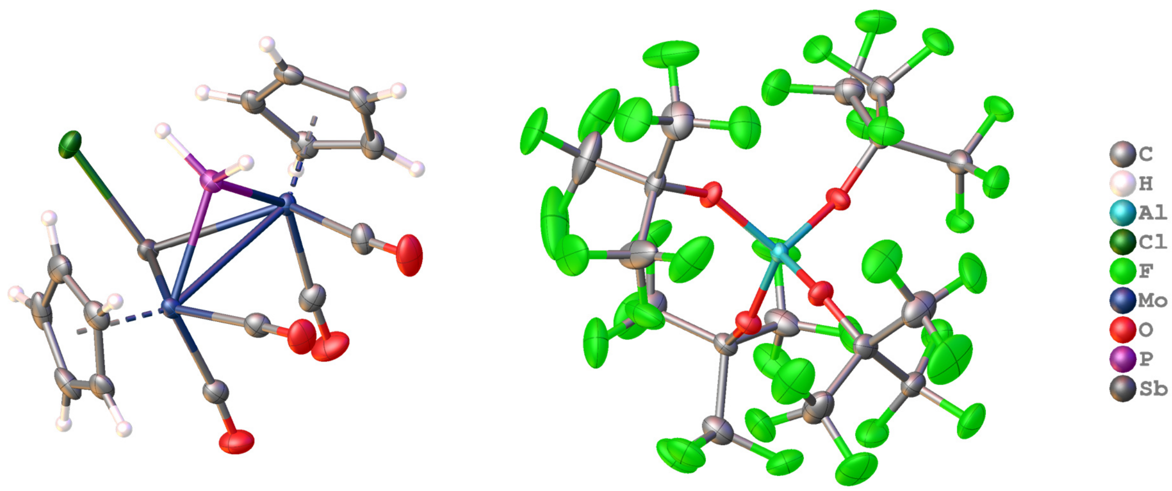

Figure S50: Molecular structure of **9a**. The asymmetric unit is shown containing one cation and one [TEF]$^-$ anion.

Refinement details for 10a

Compound **10a** crystallizes as dark red sticks in the monoclinic space group $P2_1/n$ with two cations and two [TEF]⁻ anions in the asymmetric unit. In the [TEF]⁻ anion including Al1 all four -OC(CF_3)$_3$ groups exhibit rotational disorder in ratios of 60:40, 57:43, 54:46 and 54:46. In the [TEF]⁻ anion including Al2 two of the -OC(CF_3)$_3$ groups exhibit rotational disorder in ratios of 57:43 and 57:43. The disordered parts were partially restrained with DFIX and DANG commands and the ADPs with SIMU commands during the refinement.

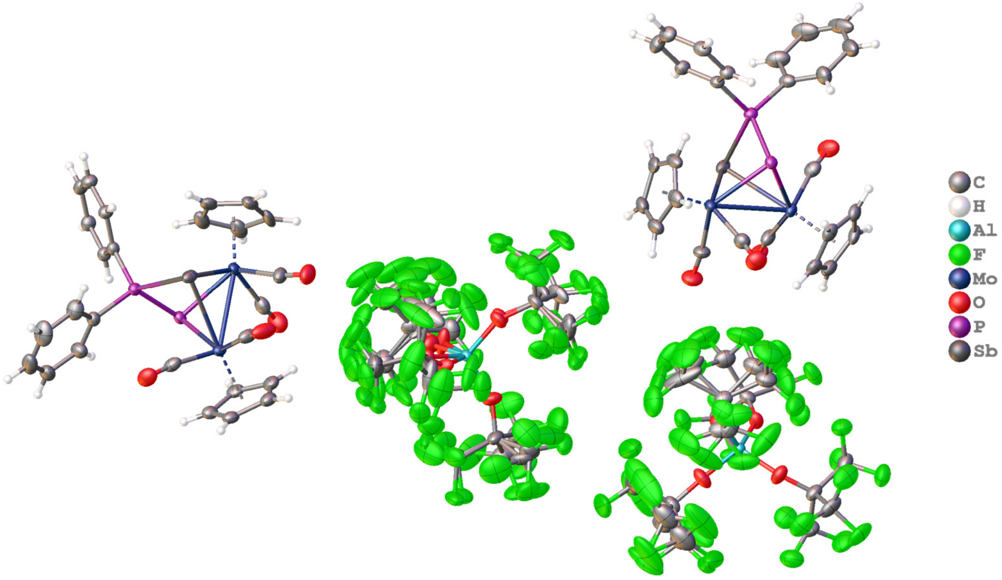

Figure S51: Molecular structure of **10a**. The asymmetric unit is shown containing two cations and two disordered [TEF]⁻ anions.

Refinement details for 10b

Compound **10b** crystallizes as dark red blocks in the triclinic space group *P*-1 with one cation, one [TEF]⁻ anion and one solvent molecule *o*-DFB in the asymmetric unit. The refinement could be done without any difficulty. The solvent molecule *o*-DFB exhibit rotational disorder in a ratio of 50:50. The ADPs of the disordered parts were partially restrained EADP commands during the refinement.

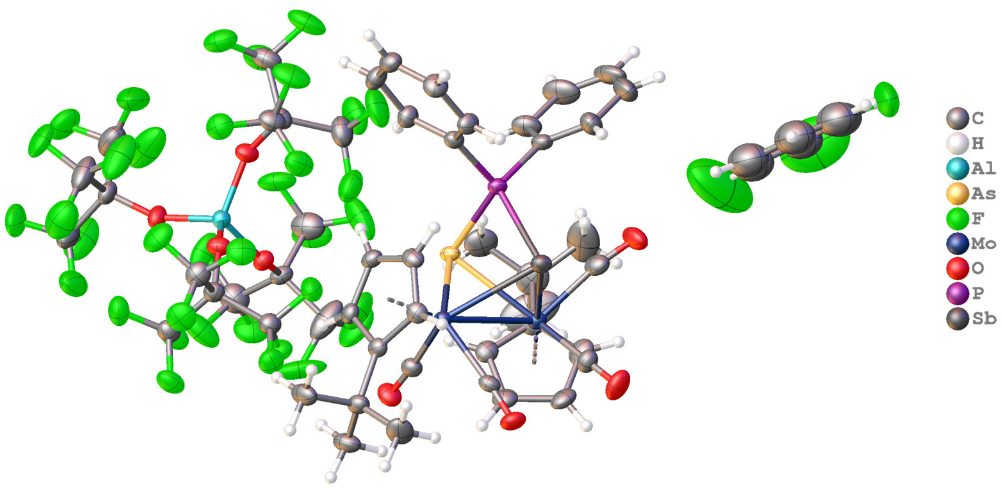

Figure S52: Molecular structure of **10b**. The asymmetric unit is shown containing one cation, one [TEF]⁻ anion and one disordered solvent molecule *o*-DFB.

Refinement details for 11a

Compound **11a** crystallizes as dark orange sticks in the triclinic space group *P*-1 with one cation and one $[TEF]^-$ anion in the asymmetric unit. The refinement could be done without any difficulties. No disorder was observed.

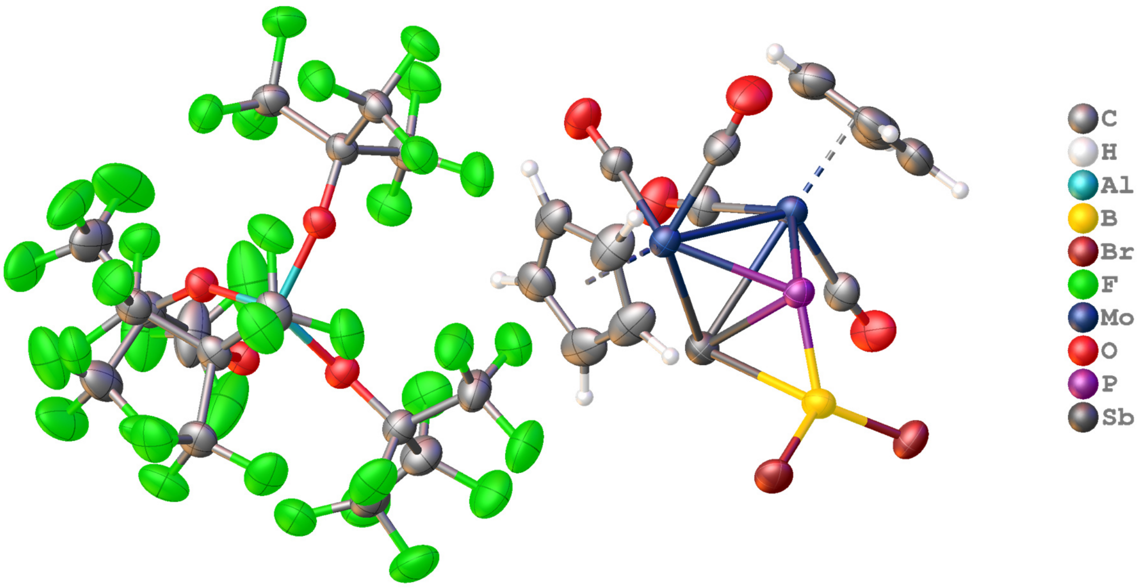

Figure S53: Molecular structure of **11a**. The asymmetric unit is shown containing one cation and one $[TEF]^-$ anion.

Refinement details for 12a

Compound **12a** crystallizes as light orange blocks in the monoclinic space group $P2_1/n$ with one cation and one $[BAr^F_4]^-$ anion in the asymmetric unit. The refinement could be done without any difficulties. No disorder was observed.

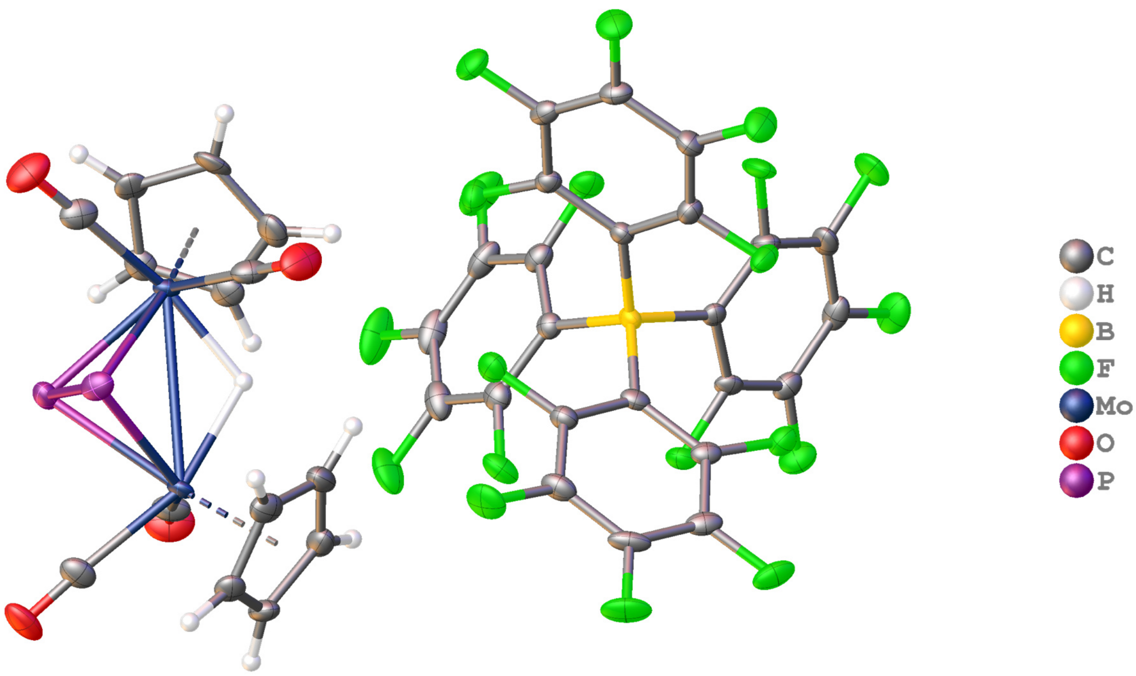

Figure S54: Molecular structure of **12a**. The asymmetric unit is shown containing one cation and one $[BAr^F_4]^-$ anion.

Refinement details for 12b

Compound **12b** crystallizes as light orange blocks in the monoclinic space group *$P2_1/n$* with one cation and one $[BAr^F_4]^-$ anion in the asymmetric unit. The refinement could be done without any difficulties. The PAs ligand exhibits a disorder over the two sites in a ratio of 50:50 and an EXYZ command was used for the refinement (see Figure S55). The ADPs of the H atom bridging the Mo–Mo bonds was restrained with an EADP command.

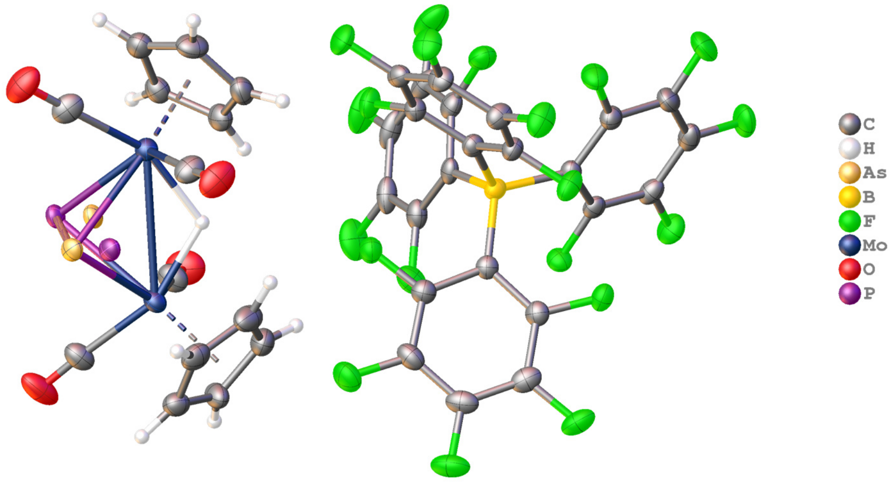

Figure S55: Molecular structure of **12b**. The asymmetric unit is shown containing one cation and one $[BAr^F_4]^-$ anion. The PAs ligand in the cation is disordered over the two sites in a ratio of 50:50.

10.5 References

[1] C. Riesinger, L. Dütsch, G. Balázs, M. Bodensteiner, M. Scheer, *Chem. Eur. J.* **2020**, *26*, 17165-17170.
[2] M. Piesch, S. Reichl, M. Seidl, G. Balázs, M. Scheer, *Angew. Chem. Int. Ed.* **2021**, *60*, 15101-15108.
[3] a) C. M. Hoidn, D. J. Scott, R. Wolf, *Chem. Eur. J.* **2021**, *27*, 1886-1902; b) M. Peruzzini, L. Gonsalvi, A. Romerosa, *Chem. Soc. Rev.* **2005**, *34*, 1038-1047; c) M. Caporali, L. Gonsalvi, A. Rossin, M. Peruzzini, *Chem. Rev.* **2010**, *110*, 4178-4235; d) B. M. Cossairt, N. A. Piro, C. C. Cummins, *Chem. Rev.* **2010**, *110*, 4164-4177; e) L. Giusti, V. R. Landaeta, M. Vanni, J. A. Kelly, R. Wolf, M. Caporali, *Coord. Chem. Rev.* **2021**, *441*, 213927; f) O. J. Scherer, *Acc. Chem. Res.* **1999**, *32*, 751-762; g) O. J. Scherer, *Angew. Chem. Int. Ed.* **1990**, *29*, 1104-1122; h) O. J. Scherer, *Chem. unserer Zeit* **2000**, *34*, 374-381.
[4] L. Dütsch, C. Riesinger, G. Balázs, M. Scheer, *Chem. Eur. J.* **2021**, *27*, 8804-8810.
[5] L. Dütsch, M. Fleischmann, S. Welsch, G. Balázs, W. Kremer, M. Scheer, *Angew. Chem. Int. Ed.* **2018**, *57*, 3256-3261.
[6] a) N. Arleth, M. T. Gamer, R. Koppe, N. A. Pushkarevsky, S. N. Konchenko, M. Fleischmann, M. Bodensteiner, M. Scheer, P. W. Roesky, *Chem. Sci.* **2015**, *6*, 7179-7184; b) P. W. Roesky, N. Reinfandt, C. Schoo, L. Dütsch, R. Köppe, S. N. Konchenko, M. Scheer, *Chem. Eur. J.* **2021**, *27*, proofs. https://doi.org/10.1002/chem.202003905.
[7] P. Pyykkö, *J. Phys. Chem. A* **2015**, *119*, 2326-2337.
[8] O. J. Scherer, H. Sitzmann, G. Wolmershäuser, *J. Organomet. Chem.* **1984**, *268*, C9-C12.
[9] The refinement of the crystal structures of **4**, **6** and **8b** have not been completely finished until the end of this thesis due to severe disorder. Therefore, the given bond lengths and angles should be considered carefully.
[10] It has to be mentioned that two molecules of **4** are present in the asymmetric unit, and that the coordination of the P-P bond towards the borinium ion is much more symmetric in the second molecule than in the one described in the text.
[11] B. Ringler, M. Müller, C. von Hänisch, *Eur. J. Inorg. Chem.* **2018**, *2018*, 640-646.
[12] J. E. Davies, L. C. Kerr, M. J. Mays, P. R. Raithby, P. K. Tompkin, A. D. Woods, *Angew. Chem. Int. Ed.* **1998**, *37*, 1428-1429.
[13] L. Dütsch, C. Riesinger, G. Balazs, M. Scheer, *Chem. Eur. J.*, *n/a*.
[14] M. Gonsior, I. Krossing, N. Mitzel, *Z. Anorg. Allg. Chem.* **2002**, *628*, 1821-1830.
[15] Agilent (2014). CrysAlis PRO. Agilent Technologies Ltd., Yarnton, Oxfordshire, England.
[16] G. Sheldrick, Acta Crystallographica Section A **2015**, 71, 3-8.
[17] O. V. Dolomanov, L. J. Bourhis, R. J. Gildea, J. A. K. Howard, H. Puschmann, *J. Appl. Cryst.* **2009**, *42*, 339-341.
[18] G. Sheldrick, Acta Crystallographica Section C **2015**, 71, 3-8.

11 THESIS TREASURY

11.1 Oxidation of the complex [{W(CO)$_4$}$_2$(μ-PH$_2$)] (A)

Since the tetrahedral tungsten compound [{CpW(CO)$_2$}$_2$(μ,η^2:η^2-P$_2$)] proofed to be a useful starting material for the synthesis of larger, dicationic polyphosphorus complexes upon oxidation, we looked to extend this chemistry to other tungsten diphorsphorus compounds. Thus, we reacted [{W(CO)$_4$}$_2$(μ-PH$_2$)] (**A**) with the strong one-electron oxidant [Thia][TEF] in CH_2Cl_2 solutions, which led to precipitation of a green powder. The precipitant is soluble in *ortho*-difluorobenzene (*o*-DFB) and crystallization *via* layering with *n*-pentane yields the monocationic compound [{W(CO)$_4$}$_2$(μ-PH$_2$)][TEF] (**1**) as green plates in good yields of 82 % (Figure 1, left), in which the frame of the original molecule **A** stays intact only carrying a positive charge. **1** crystallizes in the monoclinic space group $P2_1/c$ with one half cation and one half [TEF]$^-$ anion in the asymmetric unit. The molecular structure of **1** (Figure 1, right) reveals a central W$_2$(PH$_2$)$_2$ cycle similar to **A**. However, the W1–W1' bond is shortened by 0.2 Å to 2.894(1) Å upon oxidation in comparison to the starting material **A** (W1–W1' 3.068(3) Å).[1] In contrast, the W–P distances as well as the W-P-W and P-W-P angles stay nearly the same.

The cation in **1** has 33 valence electrons (12(2·W) + 16(8·CO) + 4(2·PH$_2$) + 2(W–W bond) – 1 (pos. charge)) suggesting a radical character. This is corroborated by NMR and EPR spectroscopy since the ^{1}H, ^{31}P and ^{31}P{^{1}H} spectra of **1** in *o*-DFB/C_6D_6 are all empty and the EPR spectra of **1** reveal a isotropic signal (g_{iso} = 2.142) at room temperature, which splits into a rhombic signal (g_x = 2.307, g_y = 2.186, g_z = 1.929) upon cooling to 77 K.

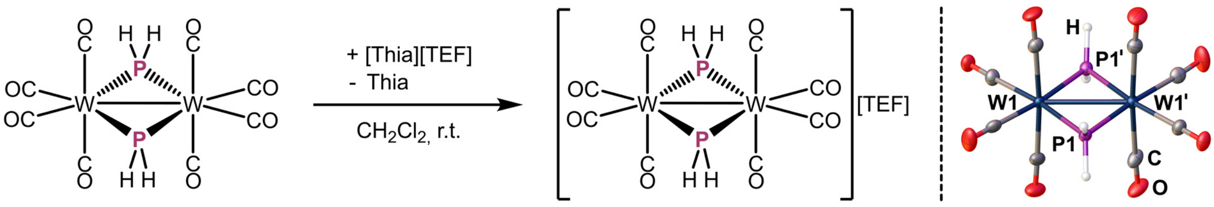

A **1** (82 %)

Figure 1: Left: One-electron oxidation of [{W(CO)$_4$}$_2$(μ-PH$_2$)] (**A**). Right: Molecular structure of **1**. Anisotropic displacement is set to the 50% probability level. The counter ion [TEF]$^-$ is omitted for clarity. Selected bond lengths [Å]: W1–W1' 2.894(1), W1–P1 2.432(3), W1–P1' 2.439(3), W1–P1–W1' 72.9(1), P1–W1–P1' 107(1).

11.2 Electrophilic functionalization of [Cp*Fe(η^5-P_5)] (B1) and [Cp''Fe(η^5-P_5)] (B2)

In the chapters 9 and 10 we reported on the electrophilic functionalization of the tetrahedral di- and tripnictogen complexes [{CpMo(CO)$_2$}$_2$(μ,η^2:η^2-E_2)] (E = P, As, Sb), [{CpMo(CO)$_2$}$_2$(μ,η^2:η^2-EE')] (E ≠ E' = P, As, Sb) and [Cp^{R}Mo(CO$_2$(η^3-E_3)] (Cp^R = Cp, Cp*; E = P, As) with phosphenium and borinium ion, which led to variety of functionalized, cationic E_n ligand complexes. Thus, we wanted to transfer this reactivity towards the P_5 complexes [Cp*Fe(η^5-P_5)] (**B1**) and [Cp''Fe(η^5-P_5)] (**B2**). The used phosphenium and borinium ions in previous work were synthesized *in situ* by reaction of the respective halophosphines and -boranes with halide abstractive agents. The latter are for example $GaCl_3$ and $AlCl_3$. Since **B1** and **B2** are Lewis bases and $GaCl_3$ and $AlCl_3$ are Lewis acids they should be able to form a Lewis pair. Therefore, we reacted **B1** and **B2** with $GaCl_3$ in CH_2Cl_2 solutions resulting brownish green solutions of the $GaCl_3$ adduct complex [Cp^{R}Fe(η^5-P_5GaCl$_3$)] (Cp^R = Cp* (**2a**), Cp'' (**2b**)) in good yields of 75 % and 82 % (Figure 2, left). Cooling of saturated solutions of **2a** and **2b** affords crystals suitable for single crystal X-ray diffraction. They crystallize either in the orthorhombic space group *Pnma* (**2a**) or in the triclinic space group *P*-1 (**2b**), respectively, with one half molecule (**2a**) or two molecules (**2b**) in the asymmetric unit. The P_5 ring as well as the $GaCl_3$ unit in **2a** exhibit severe disorder, for which reason the refinement could not be finished until the end of this thesis. Thus, only the molecular structure of **2b** (Figure 2, right) is discussed. The P–P bond lengths within the P_5 ligand are alle in the same range (2.096(2)–2.119(3) Å) and very similar to those in the free pentaphosphaferrocene derivative [Cp^{Et}Fe(η^5-P_5)] (Cp^{Et} = C_5Me_4Et).[2] The newly formed Ga–P1 bond (2.405(2) Å) is slightly elongated compared to a calculated Ga–P single bond (2.35 Å)[3] and also slightly longer than the Ga–P bond lengths in the phosphanylgallanes IDipp·Ga(H_2)PR_2 (R = H, Cy).[4] Additionally, the coordination of the P_5 ligand to $GaCl_3$ causes broadening ($\omega_{1/2}$ = 9150 Hz) of the signal in the ^{31}P{^{1}H} NMR spectrum of **2a**, which is observed at δ = 90–175 ppm.

With these results in hand, we also reacted **B1** with $AlCl_3$ in CH_2Cl_2. However, the solubility of $AlCl_3$ in CH_2Cl_2 is very limited and, thus, no analogous adduct complex was obtained. After prolonged storage of the reaction suspension though, the formation of few dark red blocks suitable for single crystal X-

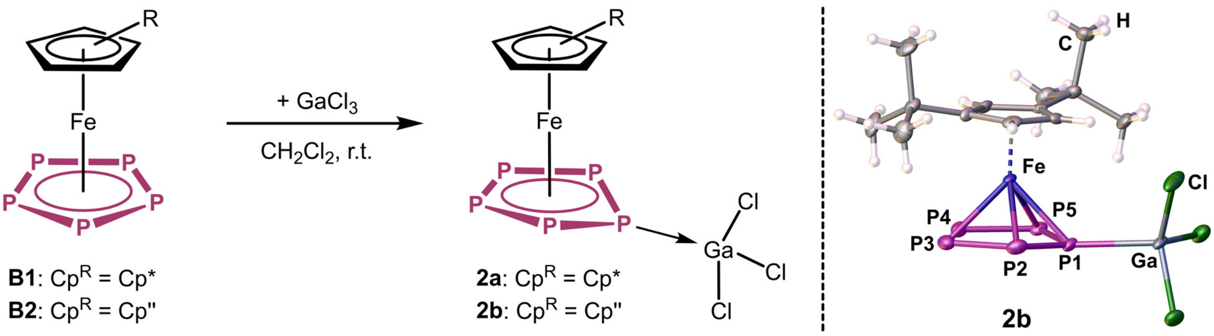

Figure 2: Left: Reaction of **B1** and **B2** with $GaCl_3$ in CH_2Cl_2. Right: Molecular structure of **2b**. Anisotropic displacement is set to the 50% probability level. Selected bond lengths [Å]: P1–P2 2.096(2), P2–P3 2.107(2), P3–P4 2.119(3), P4–P5 2.108(2), P5–P1 2.100(2), P1–Ga 2.405(2).

ray diffraction was observed revealing the product [Cp*Fe(η^5-P_5CH_2Cl)][$AlCl_4$] (**3**) (Figure 3). Here, activation of the solvent CH_2Cl_2 occurred, in which $AlCl_3$ abstracted one chloride forming the carbenium ion "[CH_2Cl][$AlCl_4$]" *in situ*. The latter than reacted with one of the phosphorus atoms of the P_5 ligand. **3** crystallizes in the monoclinic space group $P2_1/n$ with one cation and one [$AlCl_4$]$^-$ anion in the asymmetric unit. The P–P distances are all in the same range (2.101(1)–2.127(1) Å) and very similar to those in **2b** and the free pentaphosphaferrocene derivative [Cp^{Et}Fe(η^5-P_5)].[2] The newly formed P1–C1 bond (1.822(3) Å) is a classical carbon phosphorus single bond (1.86 Å).[3] The addition of the [CH_2Cl]$^+$ unit to the P_5 ring causes a distortion of the latter yielding an envelope structure. Thus, the P1 atom is bent out of the original P_5 ring by 21°. Unfortunately, the few crystals of **3** were not soluble in CH_2Cl_2 hampering further analytical investigations and it was not possible to reproduce **3** yet.

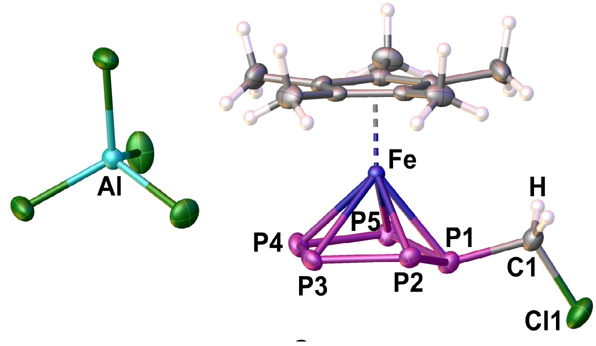

Figure 3: Molecular structure of **3**. Anisotropic displacement is set to the 50% probability level. Selected bond lengths [Å]: P1–P2 2.101(1), P2–P3 2.112(1), P3–P4 2.127(1), P4–P5 2.116(1), P5–P1 2.102(1), P1–C1 1.822(3).

The complexes **2a** and **2b** should be good precursors for electrophilic functionalization reaction of the P_5 ligands since in **2a** and **2b** the halide abstracting agent ($GaCl_3$) and the substrate (**B**) are already in close proximity. However, first reactions of **2a** with PPh_2Cl only resulted in the formation of the phosphinophosphonium salt [$ClPh_2P(PPh_2)$][$GaCl_4$] and **B1** is formed back, which was monitored by ^{31}P and ^{31}P{^{1}H} NMR spectroscopy. Additionally, no reaction between **B1** and the carbon electrophiles [Ph_3C]$^+$ (tritylium) and [C_7H_7]$^+$ (tropylium) was observed. However, in the meantime our group was able to functionalize the P_5 ligand complex **B1** with a variety of different main group electrophiles.[5]

11.3 Coordination of E_n ligand complexes to Ag(I) salts

In the reaction of [Fc^{Diac}][TEF] (Fc^{Diac} = [Fe(η^5-C_5H_4COMe)$_2$]) with [Cp*Fe(η^5-As_5)] (**D**) in *o*-DFB, which led to the formation of the cationic Fe_2As_7 cluster compound [{Cp*Fe}$_2$(μ,η^5:η^5-As_7)][TEF] (chapter …), once a dark red single crystal of a side-product was observed. The latter turned out to be the dinuclear coordination compound [Ag_2(η^5:$\eta^{2:1}$-**D**)$_2$(η^2:η^2-**D**)$_2$][TEF]$_2$ (**4**),which exists of two Ag(I) cations and four molecules **D**. The Ag(I) ions in this reaction probably arise from trace impurities in the starting material [Fc^{Diac}][TEF], which was prepared by the reaction of Fc^{Diac} and Ag[TEF]. However, the formation of **4** is very interesting since coordination compounds of **D** with Ag(I) salts containing WCAs are known but only different coordination modes were observed yet such as [Ag(η^5:η^2-**D**)$_2$][FAl] (**I**), [Ag(η^2-**D**)$_3$][FAl] (**II**) and [Ag_2(η^2:η^2-**D**)$_2$][FAl]$_2$ (**III**),[6] which were obtained by reaction of **D** with Ag[FAl] in CH_2Cl_2. Thus, it was of utmost interest to synthesize **4** selectively. Therefore, we reacted **D** with Ag[TEF] in *o*-DFB in a ratio of 2:1 (Figure 4, left) resulting in an immediate colour change from dark green to dark red. Cooling of saturated solutions from room temperature to 4 °C then yielded dark red crystals of **4** suitable for single crystal X-ray diffraction in 90 % yield. Compound **4** crystallizes in the monoclinic space group $P2_1/n$ with one dinuclear dication and two [TEF]$^-$ anions in the asymmetric unit. The molecular

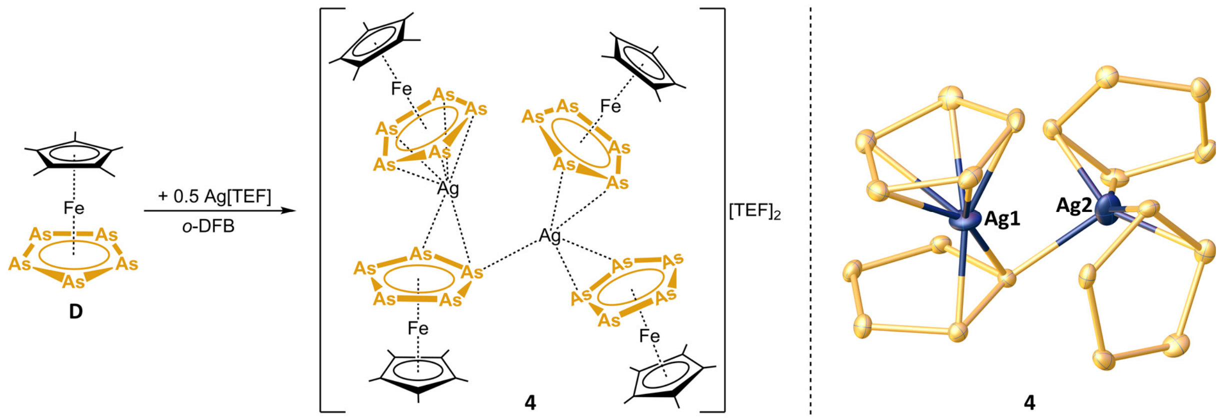

Figure 4: Left: Reaction of **D** with Ag[TEF] in *o*-DFB in a ratio of 2:1. Right: Molecular structure of **4**. Anisotropic displacement is set to the 50% probability level. The [Cp*Fe] fragments as well as the [TEF]⁻ anions are omitted for clarity. Selected bond lengths [Å]: As–As 2.323(1)–2.399(1), Ag1–Ag2 3.939(1).

structure of the cationic part of **4** (Figure 4, right) contains two Ag(I) cations and four molecules **D**. Thereby, the Ag1 atom is coordinated by two molecules **D** in a η^5:η^2 fashion (similar to **I**), while the Ag2 atom is coordinated by three molecules **D** in an η^2:η^2:η^1 coordination mode. Within that, one of the As_5 ligands is bridging the two Ag cations in an η^2:η^1 fashion. Overall, the dinuclear complex reminds on compound **II**, in which one molecule **D** is substituted by compound **I**. The As–As distances within the As_5 rings are very similar (2.323(1)–2.399(1) Å) with the ones coordinating to a silver cation in an η^2 mode being the longest. Additionally, they are resembling those of free **D**.[7] The Ag1–Ag2 distance (3.939(1) Å) is very long rather excluding any argentophilic interactions (*e.g.*, the Ag–Ag bond length in **III** is 2.88 Å).[6]

The question arises: What causes the change in the coordination mode in comparison to **II**, where the same Ag(I)/**D** ratio was used? This could either be caused by the different counterion ($[TEF]^-$ vs. $[FAl]^-$) or by the different solvent (*o*-DFB vs. CH_2Cl_2). Therefore, further investigations are part of future work to shed light into this topic. Moreover, **D** should be reacted with Ag[TEF] in various stoichiometries.

11.4 Supporting Information

11.4.1 General remarks

All manipulations were carried out under an inert atmosphere of dried nitrogen/argon using standard Schlenk and glovebox techniques. The used Schlenk flasks were heated at 550 °C for at least 15-30 minutes under reduced pressure prior to use to get rid of water traces adhered to the glass surface. The starting materials [{W(CO)$_4$}$_2$(μ-PH$_2$)] (**A**),[1] [Thia][TEF],[8], [Cp*Fe(η^5-P$_5$)],[9] [Cp''Fe(η^5-P$_5$)][10], Ag[TEF],[11] [Cp*Fe(η^5-As$_5$)][7] were synthesized according to literature procedures. $GaCl_3$ was purchased from commercial vendors. and prior to use. Solvents were freshly distilled under nitrogen after drying over CaH_2 (CH_2Cl_2, CD_2Cl_2), K or Na/K alloy (alkanes) or P_4O_{10} (*ortho*-difluorobenzene = *o*-DFB). Dried solvents were also taken from a solvent purification system from MBraun. For NMR spectra of crude solutions a C_6D_6 capillary was used. NMR spectra were recorded at 300 K (if not stated otherwise) on a Bruker Avance 300 MHz NMR spectrometer (^{1}H: 300.132 MHz, ^{31}P: 121.495 MHz, ^{19}F: 282.404 MHz) or a Bruker Avance 400 MHz NMR spectrometer (^{1}H: 400.130 MHz, ^{31}P: 161.976 MHz, ^{19}F: 376.498 MHz) with external references of $SiMe_4$ (^{1}H), CCl_3F (^{19}F) and H_3PO_4 (85%, ^{31}P). The chemical shifts δ are presented in parts per million (ppm) and coupling constants J in Hz. X-Band EPR spectra were recorded on a MiniScope MS400 device from Magnettech GmbH with a frequency of 9.5 GHz equipped with a rectangular resonator TE102.

11.4.2 Experimental details

Oxidation of [{W(CO)$_4$}$_2$(μ-PH$_2$)] (A)

A red solution of [{W(CO)$_4$}$_2$(μ-PH$_2$)] (**A**) (34 mg, 0.05 mmol, 1.0 eq.) in 5 mL CH_2Cl_2 was reacted with a dark purple solution of [Thia][TEF] (59 mg, 0.05 mmol, 1.0 eq.) in 5 mL CH_2Cl_2 leading to precipitation of a dark green solid. The suspension was stirred for 30 minutes, the supernatant was removed and the precipitate was dried in vacuum. The green powder was redissolved in 5 mL *o*-DFB and layering with *n*-pentane at +4 °C yields pure [{W(CO)$_4$}$_2$(μ-PH$_2$)][TEF] (**1**) as green plates suitable for single crystal X-ray diffraction. The solvent was removed and the crystals dried in vacuum.
Yield: 67 mg (0.041 mmol = 82 %). No signals observed in ^{1}H, ^{31}P and ^{31}P{^{1}H} NMR spectra. EPR spectra of **1** reveal a isotropic signal (g_{iso} = 2.142) at room temperature and a rhombic signal (g_x = 2.307, g_y = 2.186, g_z = 1.929) at 77 K.

Synthesis of [Cp*Fe(η^5-P$_5$GaCl$_3$)] (2a)

[Cp*Fe(η^5-P$_5$)] (**B1**) (35 mg, 0.10 mmol, 1.0 eq.) and $GaCl_3$ (18 mg, 0.10 mmol, 1.0 eq.) were dissolved in 15 mL CH_2Cl_2 yielding a brownish green solution. The solution was stirred for 15 minutes. The amount of solvent was reduced to 4 mL and the solution cooled to +4 °C yielding [Cp*Fe(η^5-P$_5$GaCl$_3$)] (**2a**) as green plates suitable for single crystal X-ray diffraction. The solvent was removed and the crystals dried in vacuum.
Yield: 39 mg (0.075 mmol = 75 %). ^{31}P{^{1}H} NMR (CH_2Cl_2/C_6D_6) δ/ppm = 90–175 (broad, $\omega_{1/2}$ = 9150 Hz).

Synthesis of [Cp''Fe(η^5-$P_5$$GaCl_3$)] (2b)

[Cp''Fe(η^5-P_5)] (**B2**) (39 mg, 0.10 mmol, 1.0 eq.) and $GaCl_3$ (18 mg, 0.10 mmol, 1.0 eq.) were dissolved in 5 mL CH_2Cl_2 yielding a brownish green solution. The solution was stirred for 15 minutes and then cooled to −30 °C yielding [Cp''Fe(η^5-$P_5$$GaCl_3$)] (**2b**) as green plates suitable for single crystal X-ray diffraction. The solvent was removed and the crystals dried in vacuum.
Yield: 46 mg (0.082 mmol = 82 %).

Reaction of Ag[TEF] with Cp*Fe(η^5-As_5) in a stoichiometry of 1:2 in *o*-DFB

A colourless solution of Ag[TEF] (125 mg, 0.1 mmol, 1.0 eq.) in 10 mL *o*-DFB was transferred onto a dark green solution of Cp*Fe(η^5-As_5) (114 mg, 0.2 mmol, 2.0 eq.; **D**) in 10 mL *o*-DFB yielding a colour change to dark red. After stirring for 3 days the amount of solvent was reduced to 3 mL and the solution layered with *n*-hexane. Storage at 4 °C yields dark red crystals of **4** suitable for single crystal X-ray diffraction. The solvent was removed by decanting and the crystals dried in vacuum.
Yield: 197 mg (0.045 mmol = 90 %).

11.4.3 NMR spectroscopy

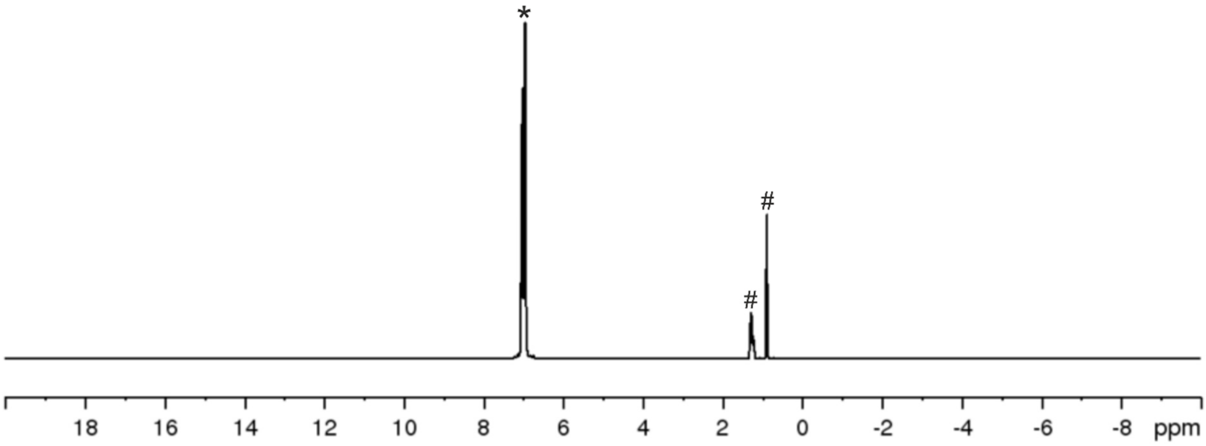

Figure S1: ^{1}H NMR spectrum of **1** in *o*-DFB/C_6D_6 showing no signal; * = *o*-DFB; # = *n*-pentane.

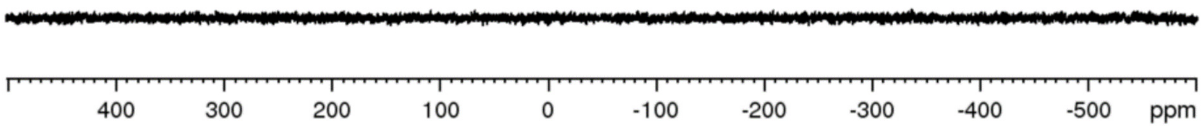

Figure S2: ^{31}P NMR spectrum of **1** in *o*-DFB/C_6D_6 showing no signal.

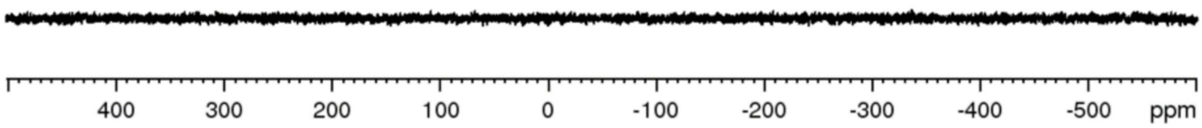

Figure S3: $^{31}P\{^{1}H\}$ NMR spectrum of **1** in *o*-DFB/C_6D_6 showing no signal.

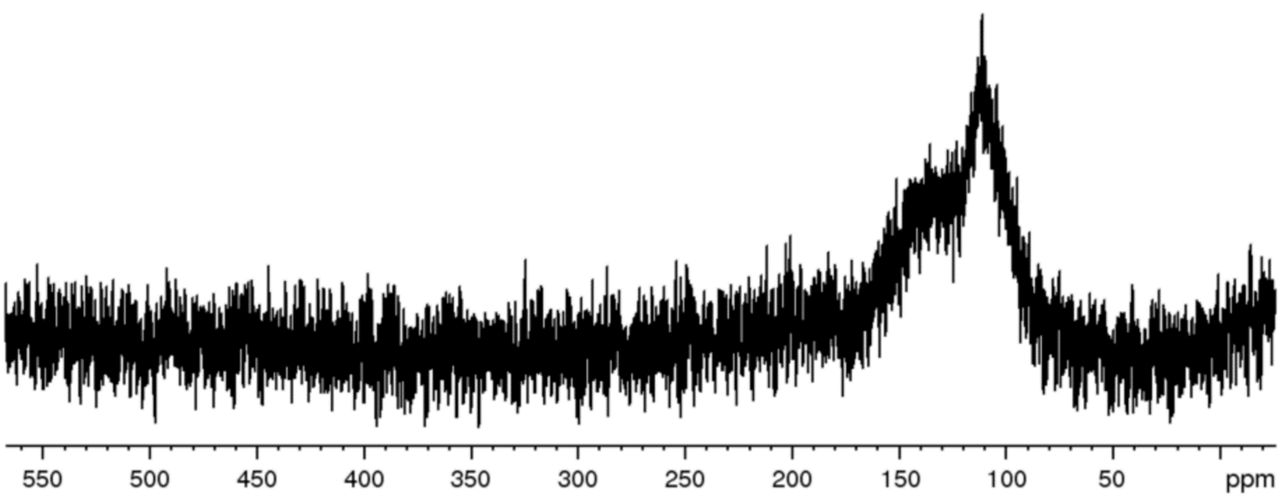

Figure S4: $^{31}P\{^{1}H\}$ NMR spectrum of **2a** in CH_2Cl_2.

11.4.4 EPR spectroscopy

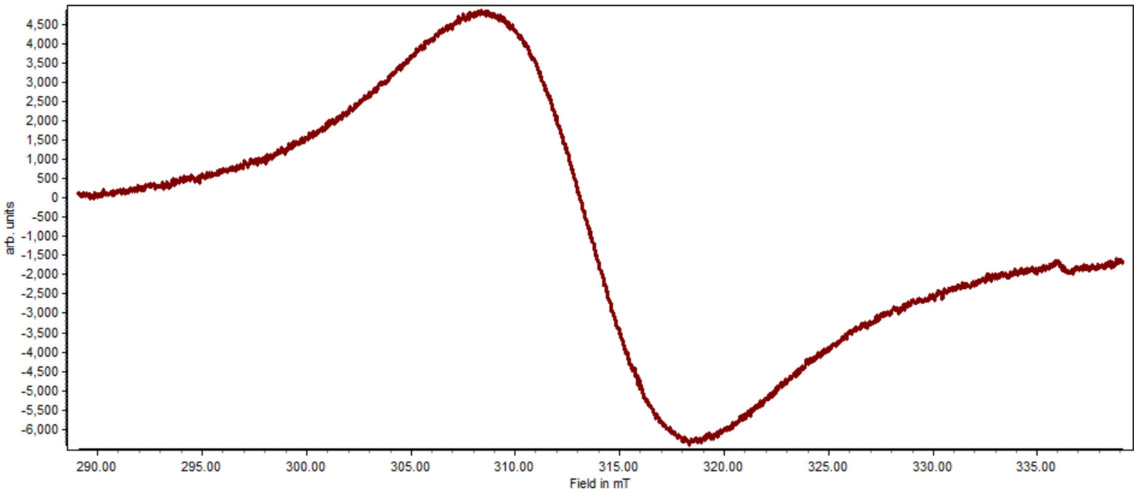

Figure S5: EPR spectrum of **1** in *o*-DFB at room temperature.

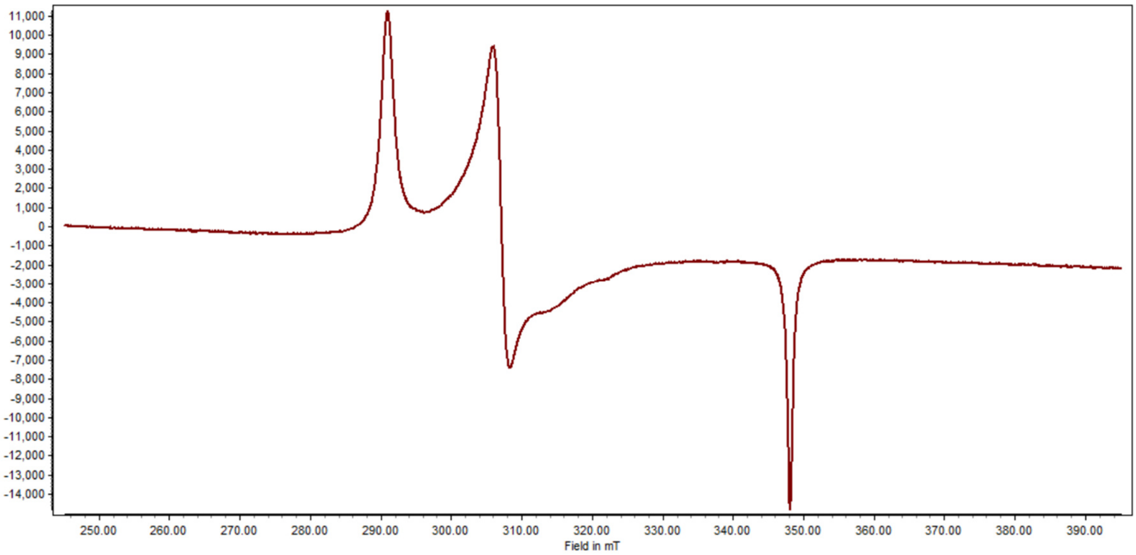

Figure S6: EPR spectrum of **1** in *o*-DFB at 77 K.

11.4.5 X-ray crystallography

All crystal manipulations were performed under mineral oil. The diffraction experiments were performed at 123 K (if not stated otherwise) either on a Rigaku (former Agilent Technologies or Oxford Diffraction) SuperNova SingleSource with an Atlas detector or on a GV50 diffractometer with a TitanS2 detector using Cu-K_{α} or Cu-K_{β} radiation. Crystallographic data together with the details of the experiments are given in Table S1. The cell determination, data reduction and absorption correction for all compounds were performed with the help of the CrysAlis PRO software.[12] All structures were solved by using the programs SHELXT[13] and Olex2.[14] The full-matrix least-squares refinement against F^2 was done using SHELXL[15] and Olex2.[14] If not stated otherwise, all atoms except hydrogen atoms were refined anisotropically. The H atoms were calculated geometrically and a riding model was used during the refinement process.

Table S1: Crystallographic details for the compounds **1**, **2a**, **2b**, **3** and **4**.

	1	**2a**	**2b**	**3**	**4**
formula	$C_{24}H_4AlF_{36}O_{12}P_2W_{21}$	$C_{10}H_{15}Cl_3FeGaP_5$	$C_{13}H_{21}Cl_3FeGaP_5$	$C_{11}H_{17}AlCl_5FeP_5$	$C_{72}H_{60}Ag_2Al_2As_{20}F_{72}Fe_4O_8$
weight [g·mol^{-1}]	1624.89		564.07	564.17	4412.70
Temperature [K]	123.0(1)	123.0(1)	123.0(1)	123.0(1)	112.0(3)
crystal system	monoclinic	orthorhombic	triclinic	monoclinic	monoclinic
space group	*P*2/*n*	*Pnma*	*P*-1	*P*2$_1$/*n*	P2$_1$/n
a [Å]	13.6690(2)	26.623(3)	9.8795(3)	9.2283(2)	17.68050(10)
b [Å]	9.8358(2)	9.7852(13)	14.1038(5)	18.3726(4)	21.5579(2)
c [Å]	16.4152(2)	7.0664(7)	16.4807(6)	13.1129(3)	35.2260(2)
α [°]	90	90	91.901(3)	90	90
β [°]	101.971(2)	90	100.749(3)	91.2915(18)	94.6930(10)
γ [°]	90	90	102.481(3)	90	90
Volume [Å^3]	2158.96(6)	1841.6(4)	2196.31(13)	2222.69(8)	13381.53(17)
Z	2	4	4	4	4
ρ_{calc} [g·cm^{-3}]	2.500		1.706	1.686	2.190
μ [mm^{-1}]	12.628		13.567	14.725	9.523
F(000)	1518.0		1128.0	1128.0	8352.0
crystal size [mm^3]	0.349 × 0.103 × 0.086		---	0.151 × 0.069 × 0.063	0.472 × 0.091 × 0.078
diffractometer	GV50	GV50	GV50	SuperNova	GV50
absorption correction	analytical		multi-scan	gaussian	gaussian
T_{min} / T_{max}	0.314 / 0.700		0.279 / 1.000	0.241 / 0.498	0.065 / 0.931
radiation [Å]	Cu-Kα (λ = 1.54184)	Cu-Kα (λ = 1.54184)	Cu-Kα (λ = 1.54184)	Cu-Kα (λ = 1.54184)	Cu-K*β* (λ = 1.39222)
2*Θ* range [°]	7.676 to 149.936		8.128 to 147.714	8.286 to 148.426	4.344 to 148.558
completeness [%]	99.0		98.7	99.4	98.8
reflns collected / unique	7407 / 4227		13238 / 8373	12609 / 4360	109474 / 36075
R_{int} / R_{sigma}	0.0250 / 0.0310		0.0564 / 0.0581	0.0258 / 0.0244	0.0330 / 0.0341
data / restraints / parameters	4227 / 2 / 356		8373 / 0 / 427	4360 / 0 / 213	36075 / 72 / 1968
GOF on F^2	1.255		1.075	1.062	1.054
R_1 / wR_2 [$I \geq 2\sigma(I)$]	0.0545 / 0.1493		0.0629 / 0.1805	0.0270 / 0.0692	0.0445 / 0.1422
R_1 / wR_2 [all data]	0.0568 / 0.1515		0.0720 / 0.1963	0.0319 / 0.0703	0.0526 / 0.1492
max / min $\Delta\rho$ [e·Å^{-3}]	2.71 / −2.80		1.72 / −1.90	0.98 / −0.47	2.52 / −2.10
Identification code	LD241_CR041_abs	LD138	LD139	LD123_abs	LD331_abs

Refinement details for 1

Compound **1** crystallizes in the monoclinic space group *P*2/*n* with one half cation and one half [TEF]$^-$ anion in the asymmetric unit. The refinement could be performed without any difficulty. No disorder was observed. The P–H bond lengths were constrained with DFIX commands.

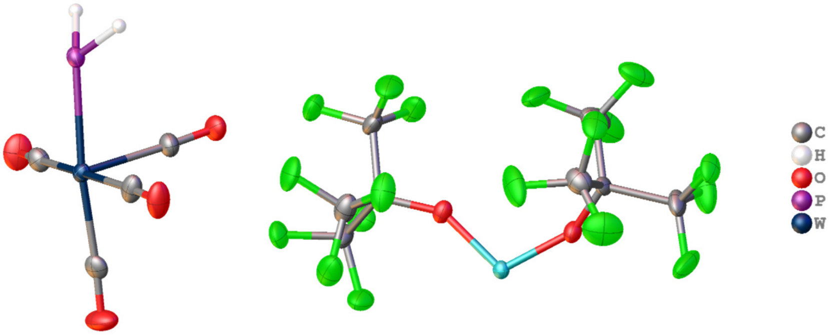

Figure S7: Molecular structure of **1**. The asymmetric unit is shown containing one half cation and one half [TEF]$^-$ anion.

Refinement details for 2a

Compound **2a** crystallizes in the orthorhombic space group *Pnma* with one half molecule in the asymmetric unit. The P_5 ligand and the $GaCl_3$ unit exhibit positional disorder in a ratio of 50:50. Thus, a pseudo-one-dimensional polymeric structure is formed (Figure S8). However, the refinement could not be finished until the end of this thesis. Therefore, no bond lengths and angles can be discussed.

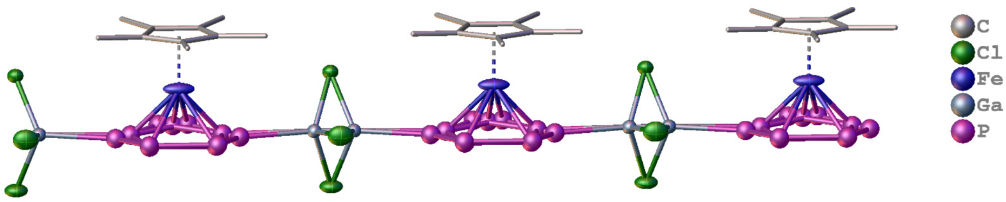

Figure S8: Molecular structure of **2a**. The grown structure is shown revealing pseudo-1D polymeric structure.

Refinement details for 2b

Compound **2b** crystallizes in the triclinic space group *P*-1 with two molecules in the asymmetric unit. The refinement could be done without any difficulty. No disorder was observed.

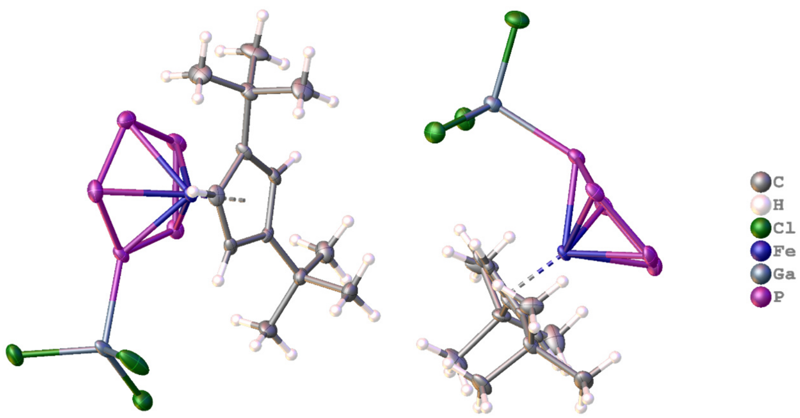

Figure S9: Molecular structure of **2b**. The asymmetric unit is shown containing two molecules of **2b**.

Refinement details for 3

Compound **3** crystallizes in the monoclinic space group $P2_1/n$ with one cation and one $[AlCl_4]^-$ anion in the asymmetric unit. The refinement could be done without any difficulty. No disorder was observed.

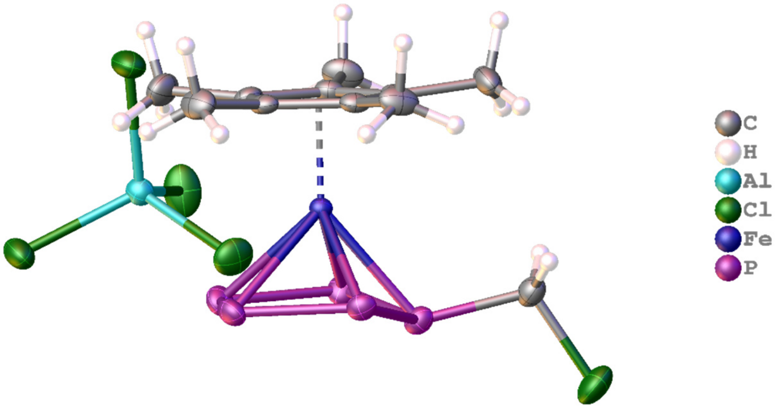

Figure S10: Molecular structure of **3**. The asymmetric unit is shown containing one cation and one $[AlCl_4]^-$ anion.

Refinement details for 4

Compound **4** crystallizes in the monoclinic space group $P2_1/n$ with one dicationic coordination compound $[Ag_2(\mathbf{D})_4]^+$ and two $[TEF]^-$ anions in the asymmetric unit. The refinement could be done without any difficulty. The $[Ag_2(\mathbf{D})_4]^+$ unit does not show any disorder. In contrast, the $[TEF]^-$ anion including Al1 exhibits rotational disorder of one of its -OC(CF$_3$)$_3$ groups in a ratio of 60:40. Furthermore, the $[TEF]^-$ anion including Al2 shows rotational disorder of two-OC(CF$_3$)$_3$ groups in ratios of 57:43 and 58:42. The disordered parts were constrained with DFIX and DANG commands and the anisotropic displacement parameters (ADPs) with SIMU or EADP commands during the refinement process.

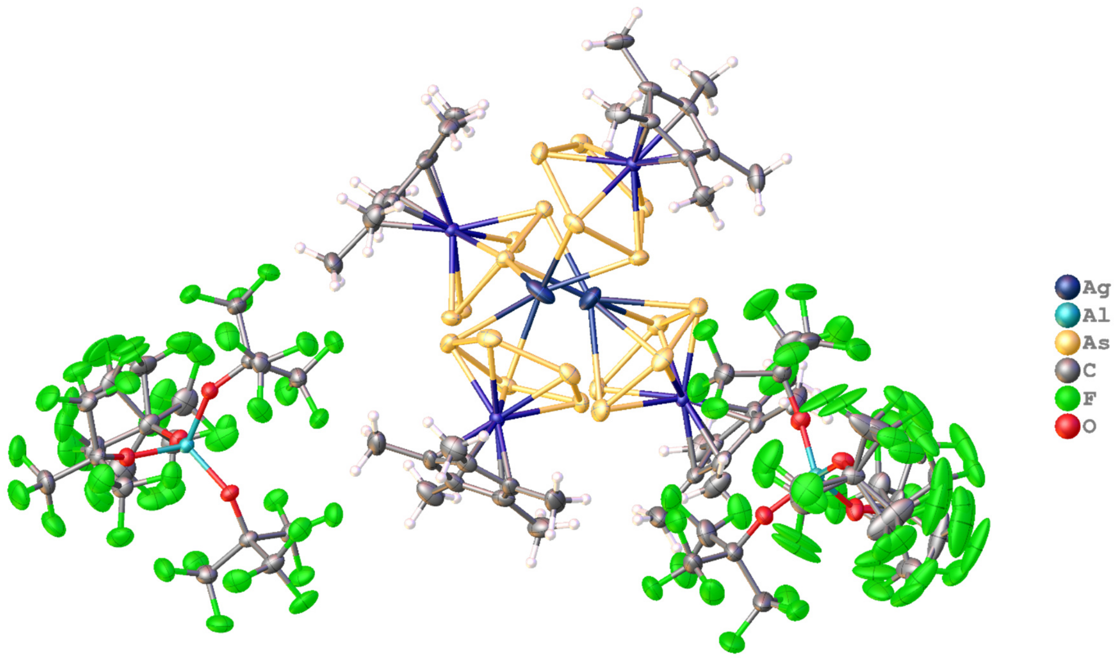

Figure S11: Molecular structure of **4**. The asymmetric unit is shown containing one dinuclear, dicationic coordination compound $[Ag_2(\mathbf{D})_4]^+$ and two disordered $[TEF]^-$ anions.

11.5 References

[1] S. Bauer, C. Hunger, M. Bodensteiner, W.-S. Ojo, A. Cros-Gagneux, B. Chaudret, C. Nayral, F. Delpech, M. Scheer, *Inorg. Chem.* **2014**, *53*, 11438-11446.

[2] O. J. Scherer, T. Brück, G. Wolmershäuser, *Chem. Ber.* **1988**, *121*, 935-938.

[3] P. Pyykkö, *J. Phys. Chem. A* **2015**, *119*, 2326-2337.

[4] M. A. K. Weinhart, A. S. Lisovenko, A. Y. Timoshkin, M. Scheer, *Angew. Chem. Int. Ed.* **2020**, *59*, 5541-5545.

[5] C. Riesinger, G. Balázs, M. Seidl, M. Scheer, *Chem. Sci.* **2021**.

[6] a) M. E. Moussa, M. Fleischmann, G. Balázs, A. V. Virovets, E. Peresypkina, P. A. Shelyganov, M. Seidl, S. Reichl, M. Scheer, *Chem. Eur. J.* **2021**, *27*, 9742-9747; b) M. Fleischmann, PhD thesis, University of Regensburg, Regensburg, **2015**.

[7] O. J. Scherer, C. Blath, G. Wolmershäuser, *J. Organomet. Chem.* **1990**, *387*, C21-C24.

[8] L. Dütsch, M. Fleischmann, S. Welsch, G. Balázs, W. Kremer, M. Scheer, *Angew. Chem. Int. Ed.* **2018**, *57*, 3256-3261.

[9] O. J. Scherer, T. Brück, *Angew. Chem.* **1987**, *99*, 59-59.

[10] M. Scheer, G. Friedrich, K. Schuster, *Angew. Chem. Int. Ed.* **1993**, *32*, 593-594.

[11] P. J. Malinowski, T. Jaroń, M. Domańska, J. M. Slattery, M. Schmitt, I. Krossing, *Dalton Trans.* **2020**, *49*, 7766-7773.

[12] Agilent (2014). CrysAlis PRO. Agilent Technologies Ltd., Yarnton, Oxfordshire, England.

[13] G. Sheldrick, Acta Crystallographica Section A **2015**, 71, 3-8.

[14] O. V. Dolomanov, L. J. Bourhis, R. J. Gildea, J. A. K. Howard, H. Puschmann, *J. Appl. Cryst.* **2009**, *42*, 339-341.

[15] G. Sheldrick, Acta Crystallographica Section C **2015**, 71, 3-8.

12 CONCLUSION

This thesis deals with the synthesis of new polypnictogen ligand (E_n ligand) complexes and, moreover, on the synthesis and stabilization of cationic homo- and hetero-polypnictogen complexes expanding the structural diversity of complexes containing elements of group 15. This class is rare and underdeveloped especially for the heavier representatives arsenic, antimony and bismuth. But also examples of hetero-polypnictogen complexes containing As–Sb, As–Bi or Sb–Bi bonds are scarce. Therefore, the herein reported products successfully extend this rare class and, furthermore, contain unique polypnictogen ligands, which exhibit unprecedented structural units and bonding properties.

The first objective (chapter 3) was the development of an improved synthesis for the tetrahedral complexes of the type [{CpMo(CO)$_2$}$_2$(μ,η^2:η^2-**E$_2$**)] ("**^{Cp}Mo$_2$E$_2$**"; E = P, As, Sb, Bi) and [{CpMo(CO)$_2$}$_2$(μ,η^2:η^2-**PE**)] ("**^{Cp}Mo$_2$PE**"; E = As, Sb), which is also transferable to their heavier analogues [{CpMo(CO)$_2$}$_2$(μ,η^2:η^2-**EE'**)] ("**^{Cp}Mo$_2$EE'**"; E ≠ E' = As, Sb, Bi). The main part of this thesis concerns the synthesis of cationic polypnictogen complexes, which were obtained by two general procedures, either by reaction of E_n ligand complexes with one-electron oxidation agents, like [$C_{12}H_8S_2$]$^{\cdot+}$ (= thianthrenium = [Thia]$^+$) or [Fe(C_5H_4COMe)$_2$]$^+$ ([Fc^{Diac}]$^+$), or *via* reaction with *in situ* generated main-group electrophiles, like [PR$_2$]$^+$ (R = organic substituent, halide) or [BBr$_2$]$^+$. In this sense, we investigated the oxidation behaviour of the complexes **^{Cp}Mo$_2$E$_2$** (chapter 4) and **^{Cp}Mo$_2$EE'** (chapter 5), as well as the influence of the metal atom, Cp ligand and counter ion on these reactions (chapter 6). Furthermore, the oxidation of the related tetrahedral complexes [{Cp^{R}Mo(CO)$_2$}(η^3-**E$_3$**)] ("**^{CpR}MoE$_3$**"; E = P, As; Cp^R = Cp, Cp*) (chapter 7) was studied as well as of different As$_n$ ligand complexes with n ≥ 5 (chapter 8). In addition, the electrophilic functionalization of **^{CpR}MoE$_3$** (chapter 9) and **^{Cp}Mo$_2$E$_2$**/**^{Cp}Mo$_2$EE'** (chapte 10) was examined.

12.1 Synthesis of tetrahedranes containing unique bridging hetero-dipnictogen ligands

Since the synthesis of the tetrahedral complexes **Mo$_2$PE** (E = As (**1**), Sb (**2**)) bears several disadvantages such as a multitude of reaction steps, side-reactions and a low overall yield, we developed a new and easy two step, one-pot synthesis (Scheme 1), which not only enhanced their

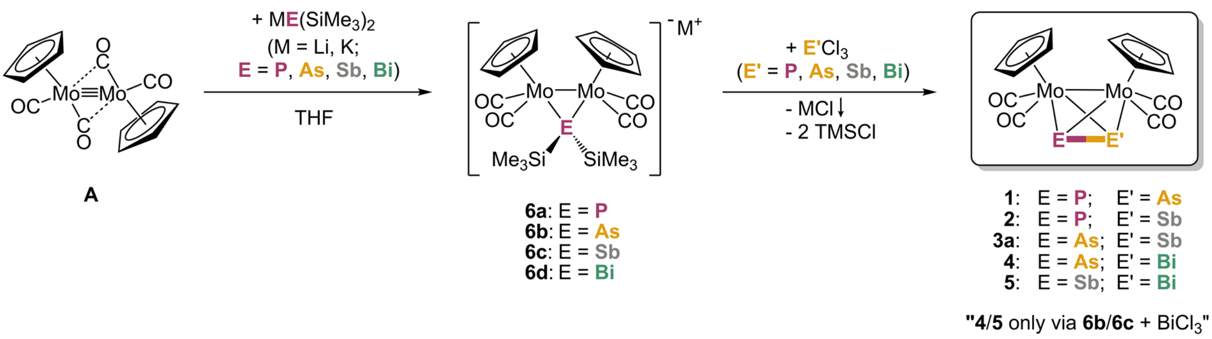

Scheme 1: Synthesis of **1**–**5**.

yield dramatically but also enabled the unprecedented heavier representatives containing **AsSb** (**3a**), **AsBi** (**4**) and **SbBi** (**5**) ligands. Reaction of $[CpMo(CO)_2]_2$ (**A**) with $ME(SiMe_3)_2$ (M = Li, K; E = P, As, Sb, Bi) gives the intermediates $M[\{CpMo(CO)_2\}_2\{\mu\text{-}E(SiMe_3)_2\}]$ (E = P (**6a**), As (**6b**), Sb (**6**c), Bi (**6d**))) in solution and subsequent addition of PCl_3, $AsCl_3$, $SbCl_3$ or $BiCl_3$, respectively, leads to formation of **1**–**5**. In the last reaction step elimination of two equivalents of trimethylsilyl chloride (Me_3SiCl = TMSCl) takes place, which does not lead to side reactions like analogous HCl evolution in the original synthesis of **1** and **2**. Furthermore, this procedure can be carried out in a multigram scale and could also be expanded to the homo-dipnictogen complexes $\mathbf{Mo_2E_2}$ (E = P, As, Sb, Bi) again leading to yield improvements (Table 1) compared to their literature procedures (except for $\mathbf{Mo_2Sb_2}$). Thus, all combinations of dipnictogen ligands can be synthesised by reacting the respective intermediate **6a**-**d** with the appropriate pnictogen-trihalide ECl_3 (except $\mathbf{Mo_2PBi}$). While the compounds **1**, **2** and **3a** can be obtained by two ways (*e.g.*, **3a** is formed either by combining **6b** with $SbCl_3$ or **6c** with $AsCl_3$), **4** and **5** are only received by the reaction of **6b** or **6c**, respectively, with $BiCl_3$, not by reacting **6d** with $AsCl_3$ or $SbCl_3$ (Table 1).

Table 1: All possible combinations of the intermediates **6a**-**d** with **E'**Cl_3 (E' = P, As, Sb, Bi) and the resulting products $[\{CpMo(CO)_2\}_2(\mu,\eta^2:\eta^2\text{-}\mathbf{EE'})]$ (= $\mathbf{Mo_2EE'}$). Yield improvements compared to the literature syntheses are given subjacent (referred to **A**).

	6a ("P")	**6b** ("As")	**6c** ("Sb")	**6d** ("Bi")
PCl_3	$\mathbf{Mo_2P_2}$ 20 % → 57 %	$\mathbf{Mo_2PAs}$ 5 % → 50 %	$\mathbf{Mo_2PSb}$ 6 % → 18 %	unsuccessful
$AsCl_3$	$\mathbf{Mo_2PAs}$ 5 % → 69 %	$\mathbf{Mo_2As_2}$ 35 % → 52 %	$\mathbf{Mo_2AsSb}$ 0 % → 63 %	unsuccessful
$SbCl_3$	$\mathbf{Mo_2PSb}$ 6 % → 59 %	$\mathbf{Mo_2AsSb}$ 0 % → 51 %	$\mathbf{Mo_2Sb_2}$ 76 % → 37 %	unsuccessful
$BiCl_3$	unsuccessful	$\mathbf{Mo_2AsBi}$ 0 % → 58 %	$\mathbf{Mo_2SbBi}$ 0 % → 46 %	$\mathbf{Mo_2Bi_2}$ 14 % → 25 %

Moreover, *via* this synthesis the bulkier *tert*-butylcyclopentadienyl (Cp') ligand could also be introduced into this class of compounds, which allows to vary their electronic and steric properties as well as their solubility, which extends the possibilities of further reactivity studies. Thus, by using $[Cp'Mo(CO)_2]_2$ as starting material instead of **A**, the complexes $[\{Cp'Mo(CO)_2\}_2(\mu,\eta^2:\eta^2\text{-}\mathbf{E_2})]$ ("$^{\mathbf{Cp'}}\mathbf{Mo_2E_2}$"; E = As (**7**), Sb (**8**)) and $[\{CpMo(CO)_2\}_2(\mu,\eta^2:\eta^2\text{-}\mathbf{AsSb})]$ ("$^{\mathbf{Cp'}}\mathbf{Mo_2AsSb}$"; **3b**) could be synthesized exemplarily.

The complexes **3**–**5** successfully expand the very scarce class of E_n ligand complexes of the heavy pnictogen elements and the exotic inorganic tetrahedrane analogues. Especially to be emphasized are their incorporated, very rare covalent bonds between two different heavy pnictogen atoms. The E–E' bond lengths of **1**–**5**, which were determined by single crystal X-ray diffraction, indicate a partial multiple bond character within the EE' ligands. This was nicely confirmed by DFT calculations. Compound **3** even contains the very first example of an As–Sb bond with a multiple bond character. Moreover, **3**–**5** depict the very first representatives, in which these covalent bonds could be stabilized without any organic substituents. Therefore, these compounds can be understood as the complexes of the exotic diatomic As≡Sb, As≡Bi and Sb≡Bi molecules with reduced E–E' bond order, which are the heavy hetero-pnictogen congeners of N_2.

Besides **1**–**5** also the intermediates **6a**-**c** could be characterized crystallographically revealing anionic $[E(SiMe_3)_2]^-$ units bridging a dimolybdenum fragment. Within that, the salt **6c** contains the first crystallographically characterized single stibenido unit of this kind.

12.2 Oxidation of E_n ligand complexes

During this thesis the oxidation chemistry of different E_n ligand complexes has been studied. In this process the use of WCAs in these reactions is crucial for the stabilization of the obtained reactive cationic species and, additionally, to ensure the solubility of the formed ionic compounds. For this reason, salts of the strong one-electron oxidant $[Thia]^+$ (0.86 V vs. $Cp_2Fe^{0/+}$) and the milder oxidant $[Fc^{Diac}]^+$ (0.49 V vs. $Cp_2Fe^{0/+}$) were synthesized with the WCAs $[TEF]^-$, $[TEF^{Cl}]^-$ and $[FAl]^-$. The former were received by a one-pot reaction of the respective lithium salts Li[X] (X = TEF, TEF^{Cl}, FAl) with $[NO][SbF_6]$ and thianthrene (Equation 1) in excellent yields up to 92 % ([Thia][TEF]). The reaction was performed in liquid SO_2 to assure the solubility of all reagents. Moreover, these syntheses can be carried out in a multigram scale.

The dark greenish blue oxidants $[Fc^{Diac}]$[TEF] and $[Fc^{Diac}]$[FAl] were prepared by simple reaction of 1,1'-diacetylferrocene (Fc^{Diac}) with Ag[TEF] and Ag[FAl], respectively, in CH_2Cl_2 (Equation 2). The analogous salt $[Fc^{Diac}][TEF^{Cl}]$ was synthesized *via* the reaction of Fc^{Diac} with $[Thia][TEF^{Cl}]$ (Equation 3).

$$\mathrm{Li[X] + NO[SbF_6] + Thia} \xrightarrow[\substack{\text{r.t., 24h} \\ \text{X = TEF, TEF}^{\text{Cl}}\text{, FAl}}]{\mathrm{SO_2(l)}} \mathrm{[Thia][X] + Li[SbF_6]\downarrow + NO\uparrow} \quad (1)$$

$$\mathrm{Fc^{Diac} + Ag[X]} \xrightarrow[\substack{\text{r.t., 24h} \\ \text{X = TEF, FAl}}]{\mathrm{CH_2Cl_2}} \mathrm{[Fc^{Diac}][X] + Ag\downarrow} \quad (2)$$

$$\mathrm{Fc^{Diac} + [Thia][TEF^{Cl}]} \xrightarrow[\text{r.t., 24h}]{\mathrm{CH_2Cl_2}} \mathrm{[Fc^{Diac}][TEF^{Cl}] + Thia} \quad (3)$$

12.2.1 Oxidation of tetrahedral di- and tripnictogen complexes

The oxidation of the tetrahedral dimolybdenum dipnictogen complexes $^{\mathbf{Cp}}\mathbf{Mo_2E_2}$ (E = P, As, Sb, Bi) was intensively studied. Their cyclic voltammograms (CV) all show one chemically pseudo-reversible oxidation with an oxidation potential below that of $[Thia]^+$, and the respective reduction peaks are significantly shifted to lower potentials. In general, the oxidation potential decreases by increasing the atomic number of the pnictogen. Reaction of the $^{\mathbf{Cp}}\mathbf{Mo_2E_2}$ complexes with the strong one-electron oxidant [Thia][TEF] leads to the selective formation of the complexes $[\{CpMo(CO)_2\}_4(\mu_4,\eta^2:\eta^2:\eta^2:\eta^2\text{-}E_4)][TEF]_2$ (E = P (**9**$[TEF]_2$), As (**10**$[TEF]_2$), Sb (**11**$[TEF]_2$), Bi (**12**$[TEF]_2$)) in quantitative yield (Scheme 2a and Scheme 2b), which reveal unprecedented dicationic E_4 chains free from organic substituents and only stabilized in the coordination sphere of transition metals. DFT calculations show that the potentially first formed radical monocations $[\mathbf{Mo_2E_2}]^{\cdot+}$ immediately dimerize in solution. In case of **9**$[TEF]_2$ and **10**$[TEF]_2$, this results in the formation of dicationic P_4 and As_4 zigzag chains, respectively, exhibiting an unusual gauche conformation with dihedral angles close to 130°. The dicationic Sb_4 and Bi_4 ligands in **11**$[TEF]_2$ and **12**$[TEF]_2$ also show a zigzag chain conformation, however, they feature two additional E···E interactions, what leads to a distorted “butterfly-like” (bicyclo[1.1.0]butane) geometry.

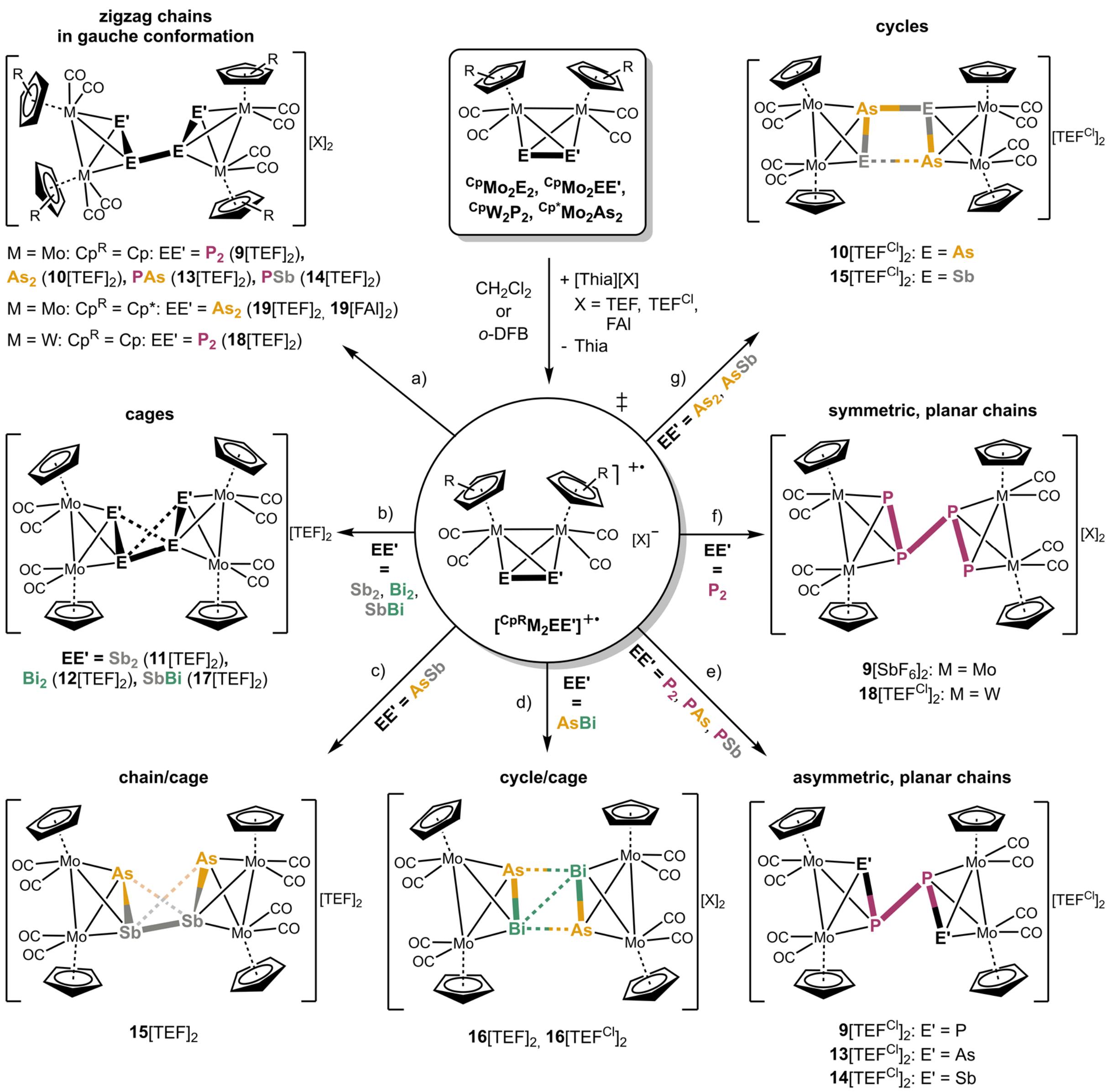

Scheme 2: One-electron oxidation of the complexes **$^{Cp}Mo_2E_2$**, **$^{Cp}Mo_2EE'$**, **$^{Cp*}Mo_2As_2$** and **$^{Cp}W_2P_2$** and stabilization of the dicationic products with different WCAs.

DFT calculations reveal that the rather weak central E–E bonds in **11**[TEF]$_2$ and **12**[TEF]$_2$ are supported by those additional interactions. Furthermore, the bonding within the Bi_4 unit in **12**$^{2+}$ is mainly based on the mixing of Bi-Bi σ and Mo-Bi orbitals of the two $[\{CpMo(CO)_2\}_2(Bi_2)]^+$ fragments and the same can be taken into account for **11**$^{2+}$. **11**[TEF]$_2$ represents the first example of a dicationic Sb_4 butterfly complex and **12**[TEF]$_2$ is the first Bi_4 buttefly complex in general, even though it is quite distorted. Moreover, an interesting feature for **9**[TEF]$_2$ could be observed, where the P_4 chain could be converted reversibly into a symmetric and an asymmetric form, respectively, by either precipitation or crystallization of **9**[TEF]$_2$ from CH_2Cl_2 solutions, which was monitored by $^{31}P\{^1H\}$ MAS NMR and IR spectroscopy. An analogous conversion could, however, not be detected for the heavier congeners **10**[TEF]$_2$–**12**[TEF]$_2$. A slight dissociation of the dicationic complexes to the free radical monocations [**$^{Cp}Mo_2E_2$**]$^{\cdot+}$ could only be observed for the arsenic derivative **10**[TEF]$_2$, which goes along with the dissociation/dimerization energies of the DFT calculations with **10**[TEF]$_2$ having the least exothermic dimerization energy (−89.52 kJ·mol^{-1}) and **12**[TEF]$_2$ the most exothermic one (−141.15 kJ·mol^{-1}).

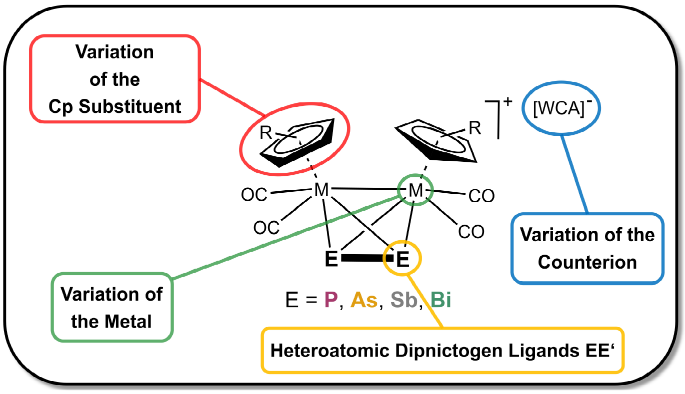

Scheme 3: Possible variations of the complexes **^{CpR}M$_2$EE'** and their influence on the reactivity towards oxidants with different WCAs.

Moreover, the electronic and steric properties of the **^{Cp}Mo$_2$E$_2$** complexes can be easily adjusted since they are known with different Cp ligands (*e.g.* **^{Cp*}Mo$_2$As$_2$**), metal atoms (*e.g.* **^{Cp}W$_2$P$_2$**) and also with mixed dipnictogen EE' ligands (**^{Cp}Mo$_2$EE'**; *vide supra*). During this thesis the influence of these adjustments on their reactivity towards oxidants was investigated as well as the impact of the stabilizing WCA (Scheme 3).

The oxidation of the unique EE' ligand complexes **^{Cp}Mo$_2$EE'** (EE' = PAs, PSb, AsSb, AsBi, SbBi) with [Thia][TEF] in CH_2Cl_2 solutions again leads to dimerization reactions of the initially formed radical monocations [**^{Cp}Mo$_2$EE'**]$^{\cdot+}$ *via* E–E or E'–E' bond formation giving the novel dicationic complexes [{CpMo(CO)$_2$}$_4$(μ_4,η^2:η^2:η^2:η^2-E'EEE')][TEF]$_2$ (EE' = PAs (**13**[TEF]$_2$), PSb (**14**[TEF]$_2$), SbAs (**15**[TEF]$_2$), BiAs (**16** [TEF]$_2$), SbBi (**17**[TEF]$_2$)), which reveal unprecedented four-membered hetero-pnictogen chains, which are only stabilized in the coordination sphere of transition metals (Scheme 2a-d). Remarkably, in **13**[TEF]$_2$, **14**[TEF]$_2$ and **17**[TEF]$_2$, the new bonds are formed between the respective lighter pnictogen atoms, whereas the aggregation in **15**[TEF]$_2$ and **16**[TEF]$_2$ takes place *via* the heavier pnictogen atoms. DFT calculations show that for **13**[TEF]$_2$ and **14**[TEF]$_2$ the P–P bond formation is favoured over E–E bond formation by 42 kJ·mol^{-1} (**13**[TEF]$_2$) and 38 kJ·mol^{-1} (**14**[TEF]$_2$), respectively, probably due to the higher P–P bond energy, although the heavier pnictogen atoms contribute more to the HOMO. Furthermore, the dimerization of the radical cations [**^{Cp}Mo$_2$EE'**]$^{\cdot+}$ is exothermic (**^{Cp}Mo$_2$PAs**: 147 kJ·mol^{-1}, **^{Cp}Mo$_2$PSb**: 158 kJ·mol^{-1}, **^{Cp}Mo$_2$AsSb**: 143 kJ·mol^{-1}, **^{Cp}Mo$_2$AsBi**: 144 kJ·mol^{-1} and **^{Cp}Mo$_2$SbBi**: 166 kJ·mol^{-1}).

The products **13**[TEF]$_2$ and **14**[TEF]$_2$ bear unique, unsubstituted P_2As_2 and P_2Sb_2 chains, respectively, in gauche conformation, which are similar to the P_4 and As_4 chains in **9**[TEF]$_2$ and **10**[TEF]$_2$. In contrast, **17**[TEF]$_2$ exhibits a distorted “butterfly-like” (bicyclo[1.1.0]butane) Sb_2Bi_2 cage with two additional Sb···Bi contacts, which resembles the dicationic Sb_4 and Bi_4 cages in **11**[TEF]$_2$ and **12**[TEF]$_2$. However, **15**[TEF]$_2$ represents a novel and very interesting intermediate stage between those two structural motifs (= mixture of chain and cage conformation), in which the additional As···Sb contacts are considerably longer and also the bond angles and the arrangement of the Cp substituents differ. Moreover, the central unit in **16**[TEF]$_2$ even reveals an entirely unknown structure exhibiting a planar As_2Bi_2 cycle, which can be interpreted as a planarized "butterfly-like" core.

The $E_2E'_2$ ligands in **13**[TEF]$_2$–**17**[TEF]$_2$ successfully extend the very rare class of hetero-polypnictogen compounds, especially of those containing covalent bonds between the heavy pnictogens arsenic, antimony and bismuth. Thus, **13**[TEF]$_2$ and **14**[TEF]$_2$ exhibit the first E_2P_2 (E = As, Sb) ligands that are free from organic substituents and only stabilized in the coordination sphere of transition metals. Going even further, the compounds **15**[TEF]$_2$, **16**[TEF]$_2$ and **17**[TEF]$_2$ contain the very first $E_2E'_2$ ligands of the heavy pnictogen elements As, Sb and Bi at all.

In addition, the influence of the metal atom and Cp ligand on the oxidation chemistry of the complexes **$^{CpR}M_2E_2$** was investigated using the tungsten and Cp* derivatives **$^{Cp}W_2P_2$** and **$^{Cp*}Mo_2As_2$**, respectively, as starting materials. However, no effect on the reactivity itself can be observed since again the dimeric products [{CpW(CO)$_2$}$_4$(μ_4,η^2:η^2:η^2:η^2-P_4)][TEF]$_2$ (**18**[TEF]$_2$) and [{Cp*Mo(CO)$_2$}$_4$ (μ_4,η^2:η^2:η^2:η^2-As_4)][TEF]$_2$ (**19**[TEF]$_2$) are obtained upon oxidation with [Thia][TEF] (Scheme 2a). The incorporated P_4 and As_4 ligands, respectively, exhibit a zigzag chain in gauche conformation resembling those of their Mo and Cp counterparts with only minor structural deviations in bond lengths and angles.

Also, when [Thia]$^{\cdot+}$ salts with other counterions ([TEF^{Cl}]$^-$, [FAl]$^-$, [SbF$_6$]$^-$) are used as oxidants in the reaction with **$^{CpR}M_2E_2$** and **$^{Cp}Mo_2EE'$**, very similar dimeric, dicationic E_4 and $E_2E'_2$ ligand complexes **9**–**19** are formed. However, it appears that the counterion has a dramatic impact on the molecular structure of the respective products in the solid-state. On the one hand, the [TEF^{Cl}]$^-$ anion causes nearly planarization of the gauche-conformed zigzag chain compounds leading to asymmetric P_4 (**9**[TEF^{Cl}]$_2$), P_2As_2 (**13**[TEF^{Cl}]$_2$) and P_2Sb_2 (**14**[TEF^{Cl}]$_2$) ligands with dihedral angles close to 180° (Scheme 2e). On the other hand, oxidation of **$^{Cp}Mo_2P_2$** with [Thia][SbF$_6$] as well as **$^{Cp}W_2P_2$** with [Thia][TEF^{Cl}] results in dimeric, dicationic products containing symmetric and planar P_4 zigzag chains (**9**[SbF$_6$]$_2$, **18**[TEF^{Cl}]$_2$; Scheme 2f). Moreover, in **10**[TEF^{Cl}]$_2$ and **15**[TEF^{Cl}]$_2$ (Scheme 2g) an interesting cyclization of the As_4 chain and the As_2Sb_2 cage-type ligand, respectively, occurred yielding a novel As_4 ring and an unprecedented As_2Sb_2 cycle. Thus, **10**[TEF^{Cl}]$_2$ represents the first cationic cyclic As_4 moiety known, which additionally is stabilized without any organic substituents. Furthermore, **15**[TEF^{Cl}]$_2$ contains the first cyclic As_2Sb_2 ligand in general. In contrast, in **16**[TEF^{Cl}]$_2$ (Scheme 2d) and **19**[FAl]$_2$ (Scheme 2a) the respective As_2Bi_2 cycle and As_4 zigzag chain remain mostly the same as in **16**[TEF]$_2$ and **19**[TEF]$_2$.

Interestingly, when **$^{Cp*}Mo_2As_2$** is reacted with [Thia][TEF^{Cl}] a completely different reactivity is observed (Scheme 4), in which formally a [Cp*Mo(CO)$_2$As] fragment was eliminated from the potentially first formed dimeric complex **19**[TEF^{Cl}]$_2$. This results in the formation of the product [{Cp*Mo(CO)$_2$}$_3$(μ_3,η^3:$\eta^{1:1}$:η^1-As_3)][TEF^{Cl}]$_2$ (**20**[TEF^{Cl}]$_2$), which contains a dicationic Mo_3As_3 unit. The latter consists of a square pyramidal Mo_2As_3 *nido*-type unit with an allylic As_3 ligand, and an additional Mo–As bond with multiple bond character. However, until the end of this thesis it could not be fully proven that **20**[TEF^{Cl}]$_2$ is the only product formed in this reaction. Therefore, further analytical investigations have to be executed.

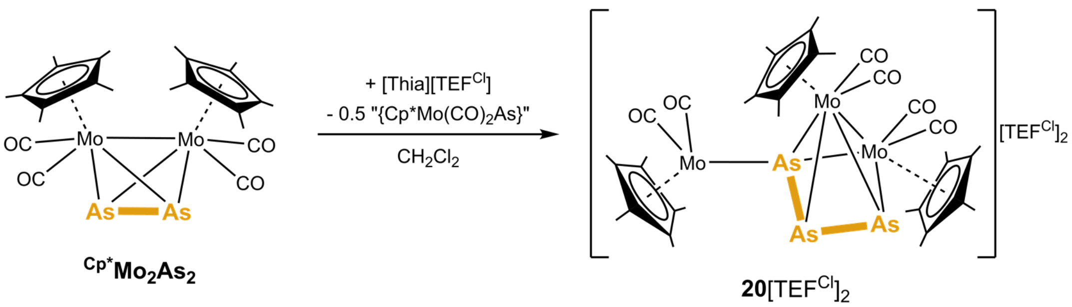

Scheme 4: Oxidation of **$^{Cp*}Mo_2As_2$** with [Thia][TEF^{Cl}].

A possible, irreversible double oxidation of the tetrahedral dipnictogen complexes, as it is predicted by CV studies, could not be observed. However, it was possible to interlink two different tetrahedra *via* oxidative dimerization by reacting a 1:1 mixture of **^{Cp}Mo$_2$P$_2$** and **^{Cp}Mo$_2$As$_2$** with equimolar amounts of [Thia][TEF] (Scheme 5). This leads to the formation of the three possible dimerization products **9**[TEF]$_2$ (= **^{Cp}Mo$_2$P$_2$** + **^{Cp}Mo$_2$P$_2$**), **10**[TEF]$_2$ (= **^{Cp}Mo$_2$As$_2$** + **^{Cp}Mo$_2$As$_2$**) and the novel compound [{CpMo(CO)$_2$}$_4$(μ_4,η^2:η^2:η^2:η^2-P$_2$As$_2$)][TEF]$_2$ (**21**[TEF]$_2$ = **^{Cp}Mo$_2$P$_2$** + **^{Cp}Mo$_2$As$_2$**) in a stochastic ratio of 1:1:1, which was proven by NMR spectroscopy. Hence, the oxidation of different **^{CpR}M$_2$E$_2$** as well as **^{CpR}M$_2$EE'** mixtures reveals to be a promising synthetic tool to gain access to a variety of dicationic polypnictogen complexes and, therefore, is part of future investigations, especially for the heavier pnictogen complexes **^{CpR}M$_2$EE'** (E, E' = As, Sb, Bi).

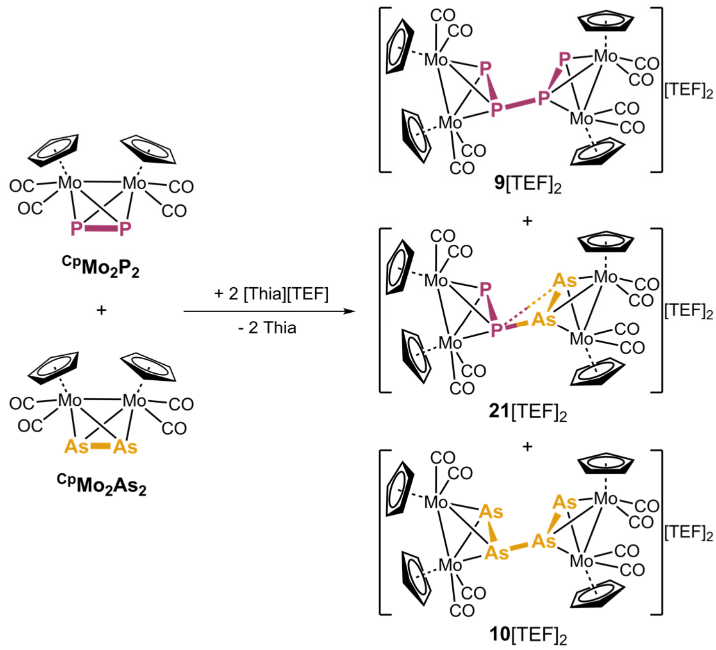

Scheme 5: Oxidation of a mixture of **^{Cp}Mo$_2$P$_2$** and **^{Cp}Mo$_2$As$_2$**.

Besides the dipnictogen complexes **^{CpR}M$_2$E$_2$** and **^{Cp}Mo$_2$EE'** we also studied the oxidation chemistry of the isolobal tetrahedral tripnictogen complexes [{Cp^{R}Mo(CO)$_2$}(η^3-**E$_3$**)] ("**^{CpR}MoE$_3$**"; E = P, As; Cp^R = Cp, Cp*). Interestingly, oxidation of **^{Cp}MoP$_3$** with [Thia][TEF] does not lead to dimerization reactions as observed for the analogous dipnictogen complexes (*vide supra*) but, moreover, it results in the selective and quantitative formation of the dicationic, trimeric product [{CpMo(CO)$_2$}$_3$(μ,η^3:η^3:η^3-P$_9$)][TEF]$_2$ (**22**[TEF]$_2$; Scheme 6). Due to crystallization problems with the counterion [TEF]$^-$, the dication **22**$^{2+}$ was also synthesized with different WCAs ([TEF^{Cl}]$^-$, [FAl]$^-$, [SbF$_6$]$^-$). Those dications contain a unique, unsubstituted P$_9$ ligand stabilized in the coordination sphere of three [CpMo(CO)$_2$] fragments. The P$_9$ ligand consists of two four-membered phosphorus rings, which are

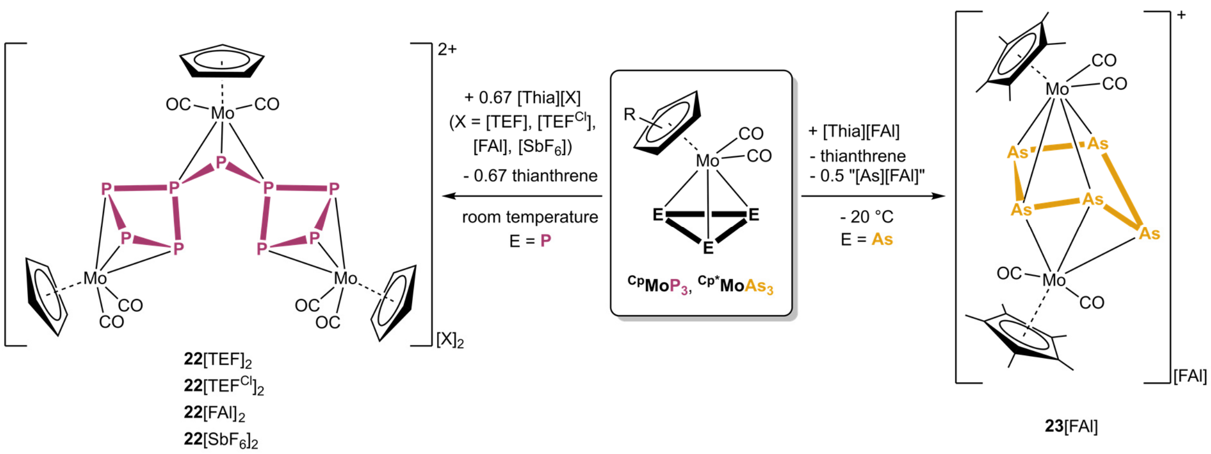

Scheme 6: Oxidation of the tetrahedral tripnictogen complexes **^{Cp}MoP$_3$** and **^{Cp*}MoAs$_3$**.

connected *via* a further phosphorus atom. This novel P_9 ligand is the largest unsubstituted polyphosphorus framework with an odd number of phosphorus atoms reported to date, which contains two positiv charges. Furthermore, ^{31}P and $^{31}P\{^1H\}$ NMR spectroscopy shows that the P_9 ligand remains intact in solution. Two possible reaction pathways for the formation of the dication **22**$^{2+}$ were postulated. On the one hand a double one-electron oxidation of $^{\mathbf{Cp}}$**MoP**$_3$ followed by two electrophilic insertion reactions into P–P bonds of two further molecules $^{\mathbf{Cp}}$**MoP**$_3$ and, on the other hand, a radical mechanism.

In contrast to $^{\mathbf{Cp}}$**MoP**$_3$, reaction of $^{\mathbf{Cp^*}}$**MoAs**$_3$ with [Thia][FAl] results in dimerization of the initially first formed radical monocation [$^{\mathbf{Cp^*}}$**MoAs**$_3$]$^{\cdot+}$ and subsequent elimination of a formal $\{As^+\}$ fragment, which results in reaggregation of the As_n ligand leading to the monocationic triple-decker complex $[(Cp^*Mo(CO)_2\}_2(\mu,\eta^4:\eta^3\text{-}As_5)]^+$ (**23**$[FAl]_2$) with an As_5 middle-deck in a distorted envelope geometry (Scheme 6). However, further investigations have to be carried out to exclude the possible formation of side-products, which is part of future work. Moreover, we plan to expand this chemistry to the heavier antimony analogue $^{\mathbf{CpR}}$**MoSb**$_3$.

Overall, it could be proven that the oxidation of homo- ($^{\mathbf{CpR}}$**M**$_2$**E**$_2$ and $^{\mathbf{CpR}}$**MoE**$_3$) as well as hetero-polypnictogen ligand complexes ($^{\mathbf{Cp}}$**Mo**$_2$**EE'**) leads to oxidative linkage of the starting materials and, thus, is a very useful synthetic tool to gain access to the class of unsubstituted, (di)cationic (hetero)polypnictogen frameworks stabilized in the coordination sphere of transition metals, which are not obtained by other ways.

12.2.2 Oxidation of arsenic rich E_n ligand complexes

We expanded the oxidation chemistry of E_n ligand complexes to larger As_n complexes with $n \geq 5$ in order to achieve larger cationic polyarsenic frameworks. In this manner, we investigated the pentaarsaferrocene derivative $[Cp^*Fe(\eta^5\text{-}As_5)]$ (**A**) and the complex $[\{Cp^*Fe\}_3As_6)]$ (**B**). The latter is formed as a byproduct in the synthesis of **A** and we could isolate and fully characterize it for the first time within the scope of this thesis. Compound **B** contains an As_6 prism with one open As–As bond. The geometry can be described as a *nido*-type cluster with one missing electron (2n+3 e^-) resulting in a square $As_6\{Cp^*Fe\}_2$ antiprism, in which one side is capped with another [Cp*Fe] fragment. The isolation of **B** allowed us to study its redox chemistry. The CV shows two reversible oxidations and two reversible reductions. Both, reduction with potassium graphite and single or multiple oxidation with [Thia][X] (X = TEF, FAl) results in the preservation of the original Fe_3As_6 cluster and the formation of the monocations $[\{Cp^*Fe\}_3As_6)][X]$ (**24**[X]), dications $[\{Cp^*Fe\}_3As_6)][X]_2$ (**25**$[X]_2$) and the monoanion $[K(thf)_2]$**26** (Scheme 7). The doubly reduced species **27** could not be isolated yet. Furthermore, it was not possible to achieve a triple oxidation of **B**. Overall, oxidation of **B** leads to the formation of an additional Fe–Fe bond within the Fe_3As_6 cluster, whereas reduction results in formation of an additional As–As bond.

Reaction of **A** with the one-electron oxidant $[Fc^{Diac}]^+$, however, affords the compounds $[(Cp^*Fe)_2(\mu,\eta^5:\eta^5\text{-}As_7)][X]$ (X = TEF (**28**[TEF]), FAl (**28**[FAl])) *via* dimerization, fragmentation (formal elimination of a cationic $[As_3]^+$ fragment) and reaggregation (Scheme 8). The monocation **28** contains a unique, substituent free As_7 ligand, which is stabilized by two [Cp*Fe] fragments. Additionally, the

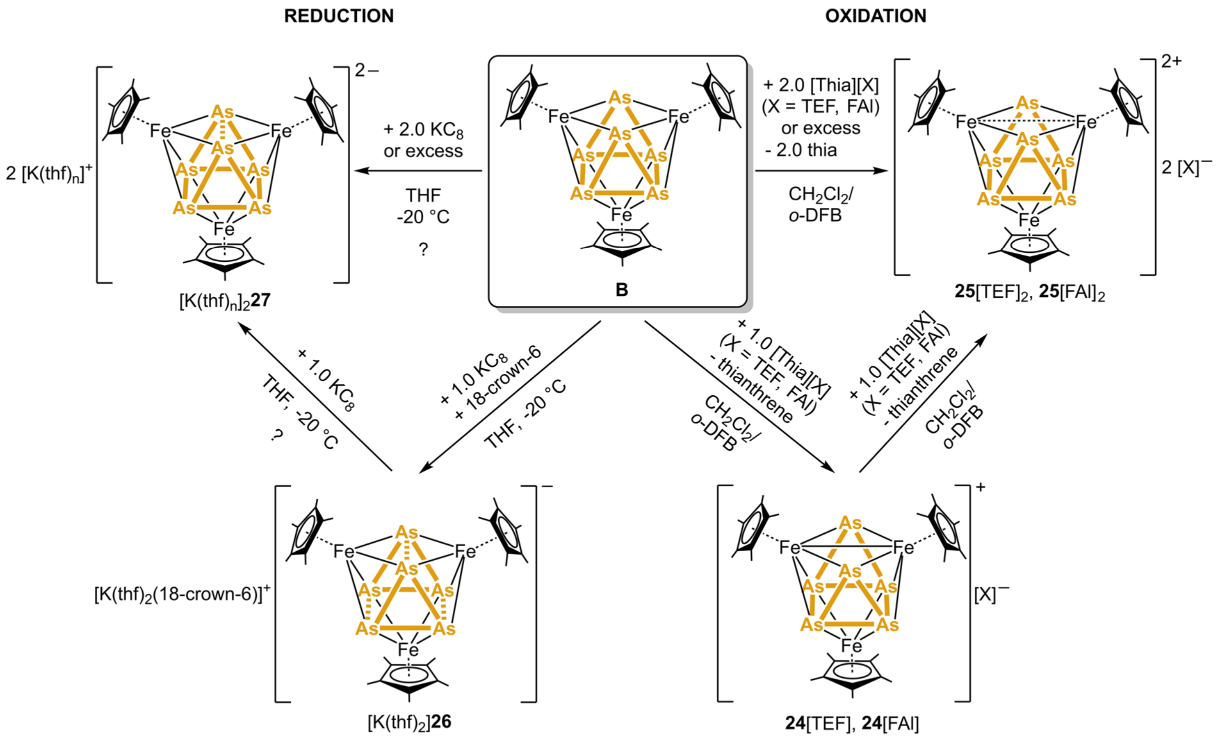

Scheme 7: Multiple oxidation and reduction of **B**.

geometry of **28** can be described as a *nido*-type cluster (2n+4 e⁻), which correlates with a monocapped square antiprism arrangement for the 9 cluster atoms with a basal As_4 and a top $As_2(Cp^*Fe)_2$ square as well as a [Cp*Fe] fragment bridging the latter. Compound **28**[TEF] was described before by Dr. Martin Fleischmann obtained by the reaction of **A** with [Ga(*o*-DFB)₂][TEF] but this synthesis could not be reproduced. Furthermore, prolonged storage of **28** or reaction of **A** with the strong oxidant $[Thia]^+$ result in the formation of the cationic triple-decker complex $[(Cp^*Fe)_2(\mu,\eta^5:\eta^5\text{-}As_5)]^+$ (**29**) assuming that **28** is an intermediate stage in the formation of **29**.

Besides As_5 ligand complexes, in which the As_5 ring is acting as an end-deck (like in **A**), also the triple-decker complexes $[(Cp^*Mo)_2(\mu,\eta^5:\eta^5\text{-}As_5)]$ and $[(Cp^{Bn}Cr)_2(\mu,\eta^5:\eta^5\text{-}As_5)]$ with an As_5 middle-deck

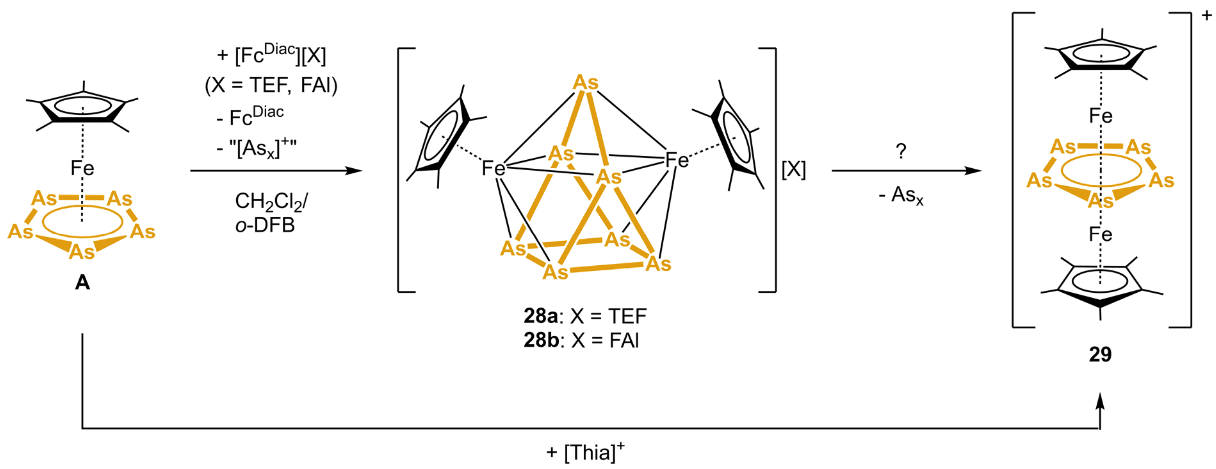

Scheme 8: Oxidation of **A**.

were reacted with [Thia]$^+$. In this case, no dimerization, fragmentation or reaggregation is observed but, instead, preservation of the original triple-decker geometry as well as the As_5 middle-decks. Furthermore, first studies on larger As_n ligand complexes show that oxidation of [(Cp'''Co)$_3$(μ,$\eta^{4:4:2:1}$-As_{12})] with [Thia][FAl] results in fragmentation and formation of the As_4 triple-decker complex [(Cp'''Co)$_2$(μ,η^4:η^4-As_4)][FAl]. However, it could not be clarified until the end of this thesis what happens with the remaining arsenic atoms, which are lost during the reaction, and what the side-products are.

In general, the oxidation of E_n and $E_nE'_m$ ligand complexes opens a unique access to new classes of cationic homo- and hetero-polypnictogen frameworks stabilized in the coordination sphere of transition metals, which are not received by other ways. These frameworks successfully expand the underdeveloped structural diversity of compounds containing covalent interpnictogen bonds, especially between the heavier group 15 elements arsenic, antimony and bismuth. Thus, future studies include the oxidation of further polypnictogen ligand complexes, *e.g.*, containing larger E_n ligands with $n \geq 5$ and, moreover, antimony and bismuth complexes, which are still scarcely explored. In addition, the synthesized cationic polypnictogen complexes should be studied to their follow-up chemistry, for example *via* nucleophilic quenching, irradiation (possible CO elimination) or thermolysis reactions.

12.3 Electrophilic functionalization of tetrahedral E_n ligand complexes

The reactivity of the tetrahedral E_n ligand complexes **^{CpR}MoE$_3$**, **^{CpR}Mo$_2$E$_2$** and **^{CpR}Mo$_2$EE'** towards phosphenium ions and other main group electrophiles was investigated within the scope of this thesis. Reaction of **^{Cp}MoP$_3$** with the phosphenium ion [PPh_2]$^+$, which was *in situ* generated from the respective chlorophosphine PPh_2Cl and the halide abstracting agent Tl[TEF], leads to insertion of [PPh_2]$^+$ into one P–P bond of the P_3 ligand and the selective and quantitative formation of the compound [CpMo(CO)$_2$(η^3-P_4Ph_2)][TEF] (**30a**; Scheme 9). Hence, a ring expansion from a P_3 to a P_4 cycle occurred, in which the latter is additionally functionalized by phenyl groups. By using other chlorophosphines as starting materials a variety of different substituents could be introduced into these systems ([PRR']$^+$: R, R' = Me (**30b**), Cy (**30c**), Mes (**30d**), 0.5 biphenyl (**30e**), Br (**30f**); Scheme 9). The asymmetric substituted phosphenium ion [PPhCl]$^+$ yields an isomeric mixture in a ratio of 6:1, in which the phenyl group at the P_4 ligand is either in *endo* (**30g$_{endo}$**) or *exo* position (**30g$_{exo}$**). Moreover, also the Cp* derivative **^{Cp*}MoP$_3$** could be used for electrophilic functionalization (forming **31**; Scheme 9). Overall, these functionalized P_n ligand complexes are very stable and do not undergo rearrangement reactions as similar nickel complexes. Interestingly, this system is also expandable to the respective As_3 ligand complexes **^{CpR}MoAs$_3$** (Cp^R = Cp, Cp*) allowing their electrophilic functionalization for the first time yielding unprecedented cationic As_3PR_2 rings (**32a** and **32b**; Scheme 9). These findings open this area to polyarsenic ligands, and we expect that this procedure can also be transferred to the analogous Sb_3 complex as well as to other polypnictogen ligand compounds of various ring sizes, which is part of future studies.

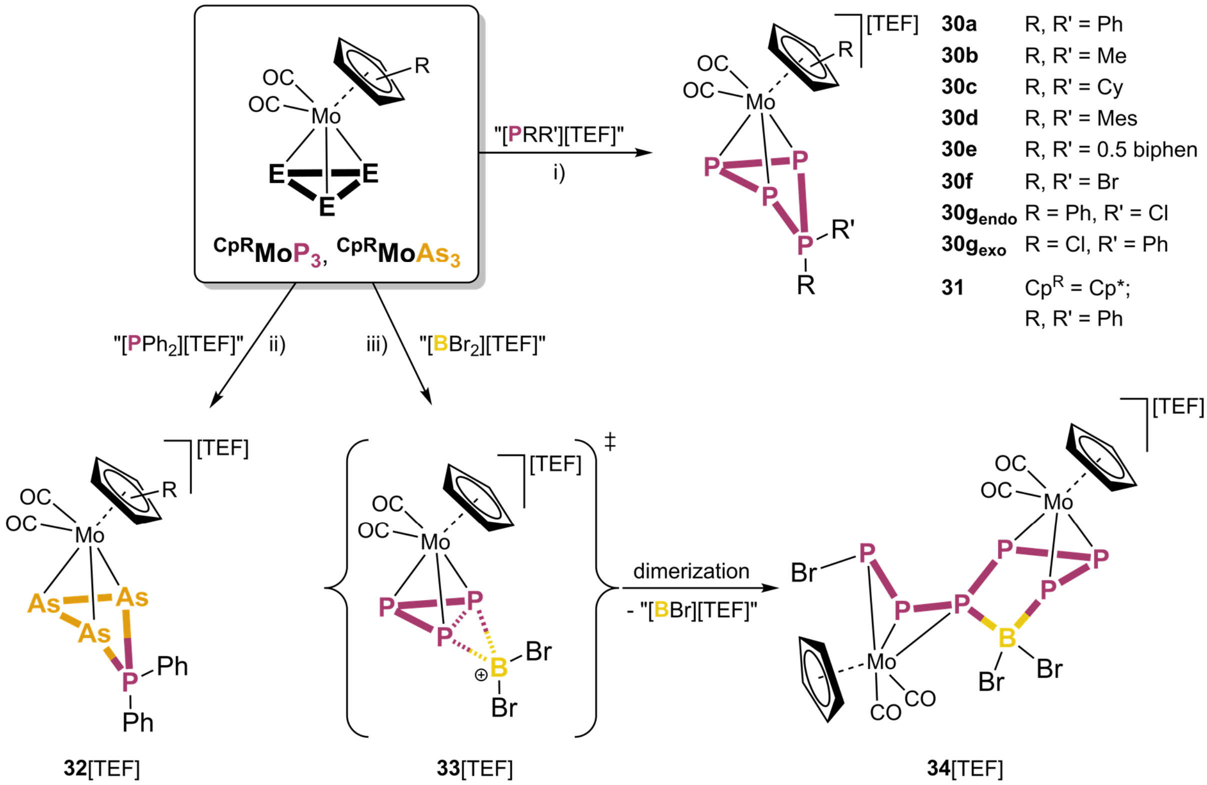

Scheme 9: Functionalization of a naked E_3 ligand (E = P, As) *via* insertion of phosphenium and borenium ions: i) E = P, Cp^R = $C_5H_5^-$ (**30**) or $C_5Me_5^-$ (**31**), "[PRR'][X]" *in situ* generated from PRR'Cl and Tl[TEF]; ii) E = As, Cp^R = Cp (**32a**) or Cp* (**32b**), "[PPh_2][TEF]" from PPh_2Cl and Tl[TEF]; iii) E = P, Cp^R = Cp, "[BBr_2][TEF]" from BBr_3 and Tl[TEF].

Analogous arsenium and stibenium ions, though, did not lead to the desired electrophilic functionalization but, instead, yielded uncharacterizable mixtures od products. But, finally, we were able to show that other main group electrophiles, namely borinium ions, are capable of electrophilic functionalization as well. However, this time reaction of **^{Cp}MoP$_3$** with *in situ* generated [BBr_2][TEF] (from BBr_3 and Tl[TEF]) results in the formation of the dinuclear compound [{CpMo(CO)$_2$}$_2$(μ,η^3:η^3-P_6BBr_2(Br))][TEF] (**34**; Scheme 9). This compound might be generated by the initially formed insertion/addition product [CpMo(CO)$_2$(η^3-P_3BBr_2)]$^+$ (**33**) followed by dimerization and formal elimination of "[BBr][TEF]".

This result suggests that a large variety of main group electrophiles may be suitable for these reactions, which would give access to a big variety of functionalized E_n ligand complexes in a maintainable way.

Last but not least, it could be shown that electrophilic functionalization with *in situ* generated phosphenium and borinium ions is also possible for the dipnictogen complexes **^{Cp}Mo$_2$EE'**, just as it was for the similar tripnictogen complexes **^{CpR}MoP$_3$** and **^{CpR}MoAs$_3$**. However, the reactivity of the complexes **^{Cp}Mo$_2$P$_2$**, **^{Cp}Mo$_2$As$_2$**, **^{Cp}Mo$_2$Sb$_2$** and **^{Cp}Mo$_2$PAs** is much more diverse but also more unselective. An overview of the electrophilic functionalization of **^{Cp}Mo$_2$EE'** with various phosphenium and borenium ions is presented in Scheme 10. The reaction of **^{Cp}Mo$_2$P$_2$** with [PR_2]$^+$ is dependent on the substituents of the phosphenium ions. On the one hand, reaction with [PPh_2][TEF] results in the formation of the dimeric, dicationic complex [{CpMo(CO)}$_2${CpMo(CO)$_2$}$_2$(μ,η^2:η^2:η^2:η^1:η^1-2-(Ph_2P)P_4)(μ-PPh_2)][TEF]$_2$

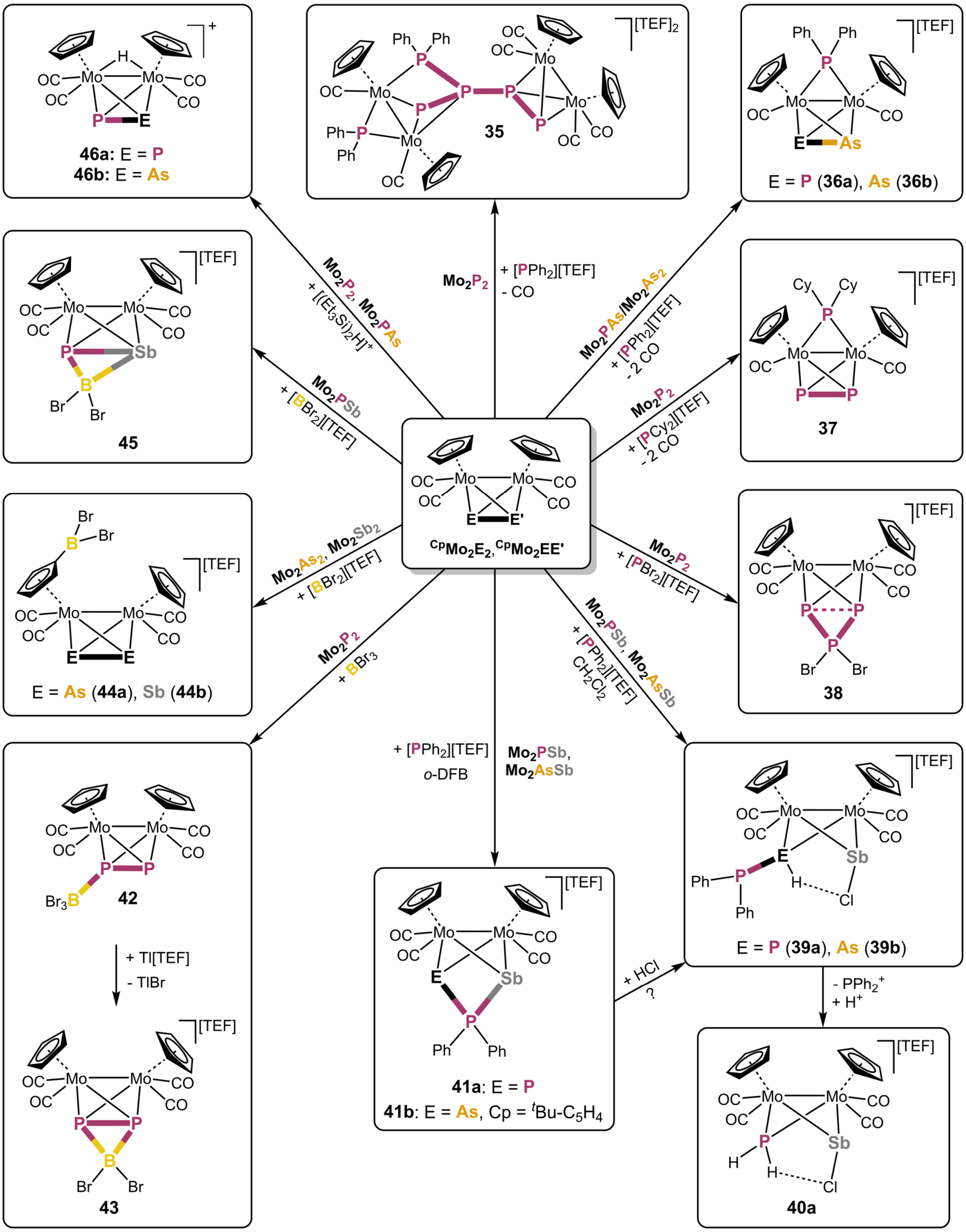

Scheme 10: Reaction of the complexes ^{Cp}**Mo$_2$E$_2$** and ^{Cp}**Mo$_2$EE'** with various main-group electrophiles (phosphenium ions, borinium ions and a proton transfer reagent).

(**35**), in which one $[PPh_2]^+$ ions was inserting into a Mo–P bond of ^{Cp}**Mo$_2$P$_2$** and the other phosphenium ion is bridging the Mo–Mo bond, which caused elimination of two CO ligands. Compound **35** contains an interesting isoprene analogous P_5 ligand. On the other hand, the use of $[PCy_2]^+$ instead leads to the release of two CO ligands and the selective formation of the monomeric complex

[{CpMo(CO)}$_2$(μ,η^2:η^2-P$_2$)(μ-PCy$_2$)][TEF] (**37**), in which the phosphenium ion is bridging the Mo–Mo bond (the same is observed in the reaction of [PPh$_2$][TEF] with **^{Cp}Mo$_2$PAs** (**36a**) and **^{Cp}Mo$_2$As$_2$** (**36b**), respectively). In contrast, the reaction of **^{Cp}Mo$_2$P$_2$** with [PBr$_2$]$^+$ results in the initially envisaged P–P bond insertion and the generation of the P$_3$ ligand complex [{CpMo(CO)$_2$}$_2$(μ,η^2:η^2-P$_3$Br$_2$)][TEF] (**38**).

In contrast to **^{Cp}Mo$_2$PAs**, reaction of [PPh$_2$][TEF] with **^{Cp}Mo$_2$PSb** and **^{Cp}Mo$_2$AsSb** in CH$_2$Cl$_2$ did not lead to a bridging of the Mo–Mo bond by the phosphenium ion but, instead, to addition of [PPh$_2$]$^+$ to the P or As atom, respectively, with subsequent HCl addition giving the compounds [{CpMo(CO)$_2$}$_2${μ-EH(PPh$_2$)}(μ-SbCl)][TEF] (E = P (**39a**), As (**39b**)). In the case of **^{Cp}Mo$_2$PSb** additionally the product [{CpMo(CO)$_2$}$_2$(μ-PH$_2$)(μ-SbCl)][TEF] (**40a**) is formed, which is formally derived from **39a** by replacing the [PPh$_2$]$^+$ group by a proton. Prolonged reaction times of the reaction mixture gave **40a** as sole product suggesting that **39a** is an intermediate in the formation of **40a**. The HCl probably originates from the solvent CH$_2$Cl$_2$ since reaction of **^{Cp}Mo$_2$PSb** and **$^{Cp'}$Mo$_2$AsSb** with [PPh$_2$][TEF] in *o*-DFB, instead, only gives the products [{Cp^{R}Mo(CO)$_2$}$_2$(μ,η^1:η^1-EP(Ph)$_2$Sb)][TEF] (E = P (**41a**), As (**41b**)), in which the phosphenium ion inserts into the E–Sb bond and the HCl addition is avoided. The question, which is still to be answered, arises, if treatment of **41a** with HCl results in a controlled synthesis of **39a**?

This chemistry could also be expanded to boron electrophiles. Reaction of **^{Cp}Mo$_2$P$_2$** with BBr$_3$ yields the adduct complex [{CpMo(CO)$_2$}$_2$(μ,η^2:η^2-P$_2$(BBr$_3$))] (**42**). However, when this reaction is conducted in the presence of the halide abstracting agent Tl[TEF], the borinium ion [BBr$_2$][TEF] is generated giving rise to [{CpMo(CO)$_2$}$_2$(μ,η^2:η^2-P$_2$BBr$_2$)][TEF] (**43**), in which the [BBr$_2$]$^+$ ion is bridging the P–P bond but no insertion takes place. The same is observed for the reaction with **^{Cp}Mo$_2$PSb** (forming compound **45**) but here the borinium ion bridges the P–Sb bond in an asymmetric fashion with a shorter P–B and a longer Sb–B distance. In contrast, in the reaction of [BBr$_2$][TEF] with **^{Cp}Mo$_2$As$_2$** and **^{Cp}Mo$_2$Sb$_2$** electrophilic aromatic substitution of a Cp proton was observed (Scheme 10; **44a** and **44b**).

Finally, **^{Cp}Mo$_2$P$_2$** and **^{Cp}Mo$_2$PAs** could also be protonated in a selective reaction with [(Et$_3$Si)$_2$H][B(C$_6$F$_5$)$_4$] forming the complexes [{CpMo(CO)$_2$}$_2$(μ,η^2:η^2-PE)(μ-H)][B(C$_6$F$_5$)$_4$] (E = P (**46a**), As (**46b**)). The proton is not bound to the PE ligand but in fact bridging the Mo–Mo bond indicating its hydridic nature, which was corroborated by NMR spectroscopy.

The reactivity of main group electrophiles with the complexes **^{Cp}Mo$_2$E$_2$**, **^{Cp}Mo$_2$EE'** and especially **^{CpR}MoE$_3$** proved to be a powerful synthetic tool to achieve a big variety of different cationic polypnictogen ligand complexes. Thus, future work will include the expansion of this chemistry to other electrophiles (phosphenium ions with other substituents, heavier pnictogenium ions and main group electrophiles in general) and other E$_n$ ligand complexes. This synthetic approach bears the potential to achieve countless functionalized polypnictogen complexes. Moreover, most of those products contain CO ligands, which might be accessible for controlled elimination upon irradiation and/or thermolysis. First results (chapter …) show that such CO elimination can lead to dimerization reactions and the formation of more extended cationic P$_n$ ligand complexes, for which reason this reactivity will be studied in more detail in future.

13 APPENDICES

13.1 Alphabetic List of Abbreviations

Å	Angstroem, 1 Å = $1\cdot10^{-10}$ m
ADP	anisotropic displacement parameters
ATP	adenosine triphosphate
br (NMR)	broad
°C	degree Celsius
Cp	cyclopentadienyl, $C_5H_5^-$
Cp*	pentamethylcyclopentadienyl, $C_5Me_5^-$
Cp'	mono-*tert*-butylcyclopentadienyl, $C_5H_4{}^tBu^-$
Cp''	1,3-di-*tert*-butylcyclopentadienyl, $C_5H_3{}^tBu_2^-$
Cp'''	1,2,4-tris-*tert*-butylcyclopentadienyl, $C_5H_2{}^tBu_3^-$
Cp^{Bn}	pentabenzylcyclopentadienyl, $C_5(PhCH_2)_5^-$
CV	cyclic voltammetry
d (NMR)	doublet
δ	chemical shift (NMR)
Da	dalton
DFT	density functional theory
dme	dimethoxyethane
DNA	deoxyribonucleic acid
e^-	electron, elemental charge
EA	elemental analyses
E_n	polypnictogen
eq.	equivalent(s)
ESI	electron spray ionization
Et	ethyl, $-C_2H_5$
$[FAl]^-$	falanate, $[FAl\{OC(C_5H_{10})(C_6F_5)\}_3]^-$
Fc	ferrocene, Cp_2Fe
Fc^{Diac}	diacetylferrocene, $(C_5H_4COMe)_2Fe$
FD	field desorption
gr.	ancient greek
h	hour(s)
Hal	halide
HOMO	highest occupied molecular orbital
Hz	Hertz
^{i}Pr	*iso*-Propyl, $-C_3H_7$
(FT-)IR	(Fourier-transform-) infrared spectroscopy
J	coupling constant
kJ	kiloJoule

L	ligand (specified in text)
LIFDI	liquid injection field desorption ionization
LUMO	lowest unoccupied molecular orbital
m (NMR)	multiplet
M	metal (specified in text)
$[M]^+$	molecular ion peak (MS)
MAS	magic angle spinning
Me	methyl, $-CH_3$
min	minute(s)
mL	milliliter
MS	mass spectrometry
m/z	mass to charge ratio
nm	nanometre
NMR	nuclear magnetic resonance (spectroscopy)
ν	freqency/wavenumber
o-DFB	*ortho*-difluorobenzene, $C_6H_4F_2$
Ph	phenyl, $-C_6H_5$
P_n	polyphosphorus
Pn	pnictogen
ppm	parts per million
q (NMR)	quartet
r	radius
R	(organic) substituent
r.t.	room temperature
s (NMR)	singlet
SI	supporting information
SOMO	singly occupied molecular orbital
t (NMR)	triplet
^{t}Bu	*tert*-butyl, $-C_4H_9$
$[TEF]^-$	teflonate, $[Al\{OC(CF_3)_3\}_4]^-$
$[TEF^{Cl}]^-$	teflonate, $[Al\{OC(CF_3)_2(CCl_3)\}_4]^-$
THF	tetrahydrofurane, C_4H_8O
Thia	thianthrene, $C_{12}H_8S_2$
V	volume
vdW	van-der-Waals
VE	valence electron
VT	various temperature
$\omega_{1/2}$	half width
WBI	wiberg bond indices
WCA	weakly coordinating anion
X	halide

13.2 Acknowledgements

Finally, I want to thank…

- Prof. Dr. Manfred Scheer for giving me the opportunity to work on this interesting research topic, providing excellent working conditions, enabling my research stay at the University of Victoria (British Columbia, Canada) as well as visits to national and international conferences.
- Prof. Dr. Henri Brunner (Zweitgutachter), Prof. Dr. Frank-Michael Matysik (Drittprüfer) and Apl. Prof. Dr. Rainer Müller (Vorsitz) for chairing the examination committee.
- Dr. Gábor Balázs to always have an open door when I encountered any problems during my research and providing useful solutions. I also thank him for proof reading, the performance of DFT calculations, the help with the interpretation of complex NMR and EPR spectra and the enjoyable conversations during the coffee breaks.
- Prof. Dr. Neil Burford from the University of Victoria for supervising me during my research stay and giving me the opportunity to work in a foreign country. Additionally, special thank goes to the Burford group members (Dr. Chris Frazee, Dr. Max Poller and Dr. Ricardo Suter) and all other amazing people I met there, especially Dr. Erica Hong, Joe Bellows and Brandon Manley, who became dear friends and made it a pleasant stay. Hope to see you soon again!!!
- my lab mate, former student and good friend Christoph Riesinger aka Christian Reisinger for all the good time, the interesting discussions, the proof reading, the help with X-ray problems and, especially, the countless "Feierabendbiere".
- Dr. Jana Schiller, Matthias Ackermann and Felix Lehnfeld for the good working atmosphere and the good music.
- Dr. Michael Seidl and Dr. Michael Bodensteiner for their help and the good advices whenever I faced serious difficulties with X-ray measurements and structure solutions.
- Prof. Dr. Werner Kremer for the measurement of MAS NMR spectra.
- my former lab supervisor Dr. Martin Fleischmann for all the stuff you taught me.
- all collaborators during these years.
- all staff members of the Central Analytical Services of the University of Regensburg.
- all staff members of the glass blowing, electronics and mechanics facilities of the University of Regensburg, especially Peter Fuchs for his enduring help with the mass spectrometre.
- all present and former members of the Scheer group for a good working atmosphere, enjoyable coffee and ice breaks at wright time and an unforgettable time.
- Maria Haimerl for her mental support during the final stage.
- my travel company at conferences and subsequent vacations: Chris, Helena, Pieschi, Annikka, Bertram, Armin, Andrea.
- Julian and Boi for being the best room mates at Hirschegg. I just say: "Two–O–Five!"

- the "AmongUs-Crew" for the weekly social zoom meetings during COVID-19.
- the "Quersties", especially Chris, Helena, Maria, Flo, Tobi, Schmidi, Theresa and all the others for the mental support from the beginning to the end, the unforgettable vacations we spent together and all the awesome memories we share.
- all my friends for the good times outside of work.
- my parents-in-law for their support during the last years.
- Rickie for keeping me company during writing this thesis, even if you were lieing on the keyboard sometimes.

And special thanks go to…

- my family simply for everything. Without you nothing would have been possible.
- my wife Lilly for your enduring support, your patience, for cheering me up when things didn´t went as planned and for always being at my side. I love you!!!